# ICANS

## *twelve*

*Volume 1*

*New Science at Pulsed Sources*
*Instrumentation Workshop*

*Rutherford Appleton Laboratory Report Number 94 — 025*

Proceedings of the Twelfth Meeting of the

# International Collaboration on Advanced Neutron Sources ICANS - XII

24 28 May 1993

held at the Cosener's House, Abingdon, Oxfordshire, U.K.

## Volume 1

New Science at Pulsed Sources
Instrumentation Workshop

**Editors:**
Uschi Steigenberger
Tim Broome
Grahame Rees
Alan Soper

Science and Engineering Research Council, Rutherford Appleton Laboratory

# Preface

The twelfth meeting of the International Collaboration on Advanced Neutron Sources - ICANS-XII- was held at the Cosener's House, Abingdon, UK, during the week of May 24 - 28, 1993, hosted by the Rutherford Appleton Laboratory.

The development of accelerator-based neutron sources is at an interesting and possibly critical point. The operational sources KEK, IPNS, LANSCE and ISIS continue to produce excellent science, fully justifying the original faith in these techniques and impressing supporters and critics alike. One new source, SINQ, is at an advanced stage of construction and is due to become operational in 1995, and advanced high power sources are under active consideration in Japan, Europe and America.

Technical experience from these sources and from the pulsed reactor IBR-2 are shared at ICANS meetings and common problems aired, often in a very frank and open way. This has contributed in no small measure to their successful developments, and will continue to be vital as next generation sources with beam powers in excess of 1 MW are planned.

The success of the Meeting resulted from the collective effort of many people. The Meeting would not have succeeded without the dedicated effort of the ISIS Organisation Committee and the suggestions of the ICANS contacts, but particular thanks must go to the participants themselves who made it such a stimulating week.

The ICANS collaboration is now over twenty years old: I look forward to a further twenty years of scientific interchange and international friendship.

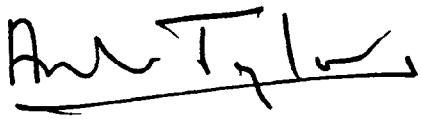

Andrew Taylor
Head, ISIS Facility

## Contents

## Volume 1

### Instrument Workshop


New Science from Pulsed Sources
J L Finney — I - 1

**New Instrument Ideas - Old Instrument Problems**

Reference Instrument Complement for IPNS Upgrade
R K Crawford — I - 24

A European Network for Neutron Instrumentation
M W Johnson — I - 32

The Use of Chopper Spectrometers for Cold-to-Epithermal Neutron Scattering at IPNS
C-K Loong, L I Donley, G E Ostrowski, R Kleb, J P Hammonds, L Soderholm, S Takahashi — I - 36

A New Chopper Spectrometer for Neutron Brillouin Scattering and Low-Angle Neutron Inelastic Scattering: PHAROS (Phase I)
R A Robinson, M Nutter, R L Ricketts, E Larson, J P Sandoval, P Lysaght, B J Olivier — I - 44

First Results from PHAROS, the New Chopper Spectrometer at LANSCE
B J Olivier, J P Sandoval, P Lysaght, M Nutter, R A Robinson — I - 52

MAPS: A Chopper Spectrometer to Measure High Energy Magnetic Excitations in Single Crystals
T G Perring, A D Taylor, R Osborn, D McK Paul, A T Boothroyd, G Aeppli — I - 60

Cold Neutrons on Pulsed Sources for High Resolution Spectroscopy and Long d-spacing Diffraction
C J Carlile, M A Adams, J B Forsyth, P S R Krishna — I - 73

Multicrystal Inverted Geometry Spectrometer NERA-PR at the IBR-2 Pulsed Reactor
I Natkaniec, S I Bragin, J Brankowski, J Mayer — I - 89

Performance of ROTAX
H Tietze-Jaensch, W Schmidt, R Geick — I - 97

Less Background, Better Contrast by Cooling Analyser Crystals
C J Carlile, M A Adams, P S R Krishna, M Prager, K Shibata, P Westerhuijs — I - 106

A new Beamline for Cold Neutron Storage Experiments on ISIS
E Jericha, H Rauch, M Schuster, C J Carlile — I - 118

The New Fourier Diffractometer at the IBR-2 Reactor: Design and First Results
V L Aksenov, A M Balagurov, V G Simkin, Yu V Taran, V A Trounov, V A Kudrjashev, A P Bulkin, V G Muratov, P Hiismaki, A Tiita, O Antson I - 124

SXD: Novel Single Crystal Studies using the Time-of-Flight Laue Technique
C C Wilson I - 132

Performance of the Amorphous Materials Diffractometer GLAD at IPNS
A J G Ellison, K J Volin, D L Price, R K Crawford I - 144

SPIDA - A Special Intense Diffractometer for Amorphous Materials
A C Hannon, A K Soper, R J Newport, W S Howells I - 152

ENGIN - An Engineering Strain Scanner at the ISIS Facility
M W Johnson , L Edwards, H G Priesmeyer, F Rustichelli, P J Withers, J S Wright I - 158

Small/Medium- Angle Diffractometer WINK
M Furusaka , K Suzuya, N Watanabe, M Osawa, I Fujikawa, S Satoh I - 166

A Very-Low-Q Diffractometer for an Advanced Spallation Source
P A Seeger, R P Hjelm I - 172

**Detectors and Data Acquisition**

ISIS Neutron Detectors
N J Rhodes, A J Boram, M W Johnson, E M Mott, A G Wardle I - 185

The Scintillation PSD JULIOS and its use in TOF-Diffractometry at ISIS
W Schäfer, E Jansen, A Szepesvary, R Skowronek, G Will, R Reinartz, K D Müller I - 200

Linearity and Calibration of Charge-Division and Rise-Time Encoded Gas PSDs
R K Crawford, P Thiyagarajan, J Chen I - 208

The ISIS Second Generation Data Acquisition Electronics System
J Norris, S Quinton, D Allen I - 216

**Measuring Techniques and Special Sample Environment**

Measurements of Strain in Individual Phases of Composites Before, During and After Mechanical Loading
J A Goldstone, M A M Bourke, D Davis, N Shi, A C Lawson, J E Allison I - 224

Time Resolved Studies on a Millisecond Time Scale: Transient Properties of the Ferroelectric Phase Transition in $Rb_2ZnCl_4$
U Steigenberger, G Eckold, M Hagen I - 232

The Effect of Inelastic Scattering upon Small Angle Diffraction Measurements
R K Heenan, A R Rennie I - 241

A Measurement of the Proton Wavefunction in Molecular Hydrogen by Neutron Compton Scattering
J Mayers I - 248

Development and Use of Pulsed Magnetic Fields for Neutron Diffraction Experiments
M Motokawa, M Arai, M Mino, K Ubukata, T Bokui, M Fujita I - 260

Neutron Diffraction to 10 GPa and Beyond: The State of the Art of the Paris-Edinburgh Cell
S Klotz, J M Besson, G Hamel, R J Nelmes, J S Loveday, R M Wilson, S Hull I - 268

**Data Analysis**

Rietveld Refinement of Magnetic Structures from Pulsed Neutron Source Powder Diffraction Data
R A Robinson, A C Lawson, A C Larson, R B von Dreele, J A Goldstone I - 273

A Dynamical Labelling Method for Extracting Partial Structure Factors
M Arai, A C Hannon, T Otomo I - 283

Applications of Bayesian Model Selection in Neutron Scattering
D Sivia I - 291

New Scans and Data Visualisation on ROTAX
W Schmidt , H Tietze-Jaensch, R Geick I - 292

Better Visualisation of Neutron Scattering Data using UNIRAS at ISIS
K Crennell I - 301

Using Databases for Improved Instrument Operations and Administration at ISIS
K Crennell I - 308

A Resolution Function Model for a Multi-Analyser Spectrometer
M Hagen, U Steigenberger I - 314

A Parametric Formulation of the Resolution Function of a Pulsed-Source Chopper Spectrometer
C-K Loong, J M Carpenter, S Ikeda I - 320

The Resolution Function of the Chopper Spectrometer HET at ISIS
T G Perring I - 328

**Polarized Beams and Beamline Devices**

$^3$He Nuclear Polarization and Neutron Spin Analysis
Y Masuda, K Asahi, M Doi, K Sakai, H Sato, Z Z Jian I - 338

Recent Progress in Supermirrors at PSI
P Böni, I S Anderson, P A Buffat, O Elsenhans, H P Friedli, H K Grimmer, R Hauert, K Leifer, J Penfold, J Söchtig I - 347

Polarized Neutron Reflection at LANSCE
M R Fitzsimmons, G S Smith, R Pynn, M A Nastasi I - 355

New Aspect in Employing Magnetic Anisotropic FeCo Thin Films as Neutron Polarizers
D A Korneev I - 363

User Dedicated Neutron Guide System at SINQ
W Wagner, J Duppich I - 368

Comparison of Neutron Efficiency of Reactor and Pulsed Source Instruments
F Mezei I - 377

## Contents

### Volume 2

### Proposals for new Spallation Neutron Sources


Study of a European Spallation Source
H Lengeler — P - 1

Plans for a New Pulsed Spallation Source at Los Alamos
R Pynn — P - 7

IPNS Upgrade - A 1 MW Spallation Neutron Source
B S Brown, J M Carpenter, Y Cho, R K Crawford, A E Knox — P - 13

An Intense Pulsed Spallation Neutron Source using a High-Power Proton Linac for Nuclear Transmutation
N Watanabe — P - 21

AUSTRON - a Spallation Neutron Source for Central and Eastern Europe
H Schönauer, H Aiginger, W H Breunlich, P J Bryant, K Hübner, W Pirkl, M Regler, G H Rees, K Schindl, A Wrulich — P - 26

Advanced Neutron Source for Physical Research
Yu Ya Stavissky, Yu V Senichev — P - 36


### Accelerator Workshop


Summary of the Accelerator Sessions
M K Craddock — A - 1

Reaching 200 μA on ISIS
C W Planner — A - 4

Study of Dual Harmonic Acceleration in ISIS
C R Prior — A - 11

Preliminary Report on the BNL Spallation Neutron Source Design Study
L N Blumberg — A - 20

Machine Studies at the Los Alamos Proton Storage Ring
R J Macek — A - 25

Overview of the NCNR Accelerator Studies
A J Jason — A - 33

Ion Source Development in the Culham Laboratory of AEA Technology
A J T Holmes — A - 41

Funneling Experience at Los Alamos: Experiments and Design
A J Jason, K F Johnson and S Nath A - 49

Conceptual Design for 1 MW Spallation Neutron Source at Argonne
Y Cho, J Bailey, B Brown, F Brumwell, J Carpenter, K Crawford, D Horan, D Jerng, R Kleb, A Knox, R Kustom, E Lessner, D McGhee, F Mills, H Moe, R Nielsen, C Potts, A Rauchas and K Thompson A - 57

IPNS - Upgrade RF System Design
R Kustom and D Horan A - 64

Study of 1 MW Neutron Source Synchrotron Dual Frequency Power Circuit for the Main Ring Magnets
D G McGhee A - 73

Basis for the Power Supply Reliability of the 1 MW Neutron Source
D G McGhee and M Fathizadeh A - 80

Performance of the 70 MeV Injector to the ISIS Synchrotron
N D West A - 85

Replacing a Popular Accelerator Control System
R P Mannix A - 93

Low Intensity and Injection Studies on the ISIS Synchrotron
C M Warsop A - 101

The ISIS Synchrotron RF System at High Intensity
P J S Barratt A - 109

Matching Problems between Linac and Compressor Ring
K Bongardt A - 115

Accelerator Studies at the KEK-PS Booster, Problems related with High Intensity Beam
I Yamane A - 124

Very Low Output Impedance RF System for High Intensity Accelerators
Y Irie A - 131

Operation of the RF System at the KEK PS
S Ninomiya A - 137

Room Temperature Vs Superconducting Linacs
H Heinrichs A - 144

FFAG Studies for a 5 MW Source
S A Martin, P F Meads, G Wustefeld, E Zaplatin and K Ziegler A - 153

A 2-Stage 5 MW FFAG
R Kustom A - 159

Compressor Ring Studies for a 5 MW Spallation Neutron Source
G H Rees A - 168

Choice of Proton Energy for New Sources
I S K Gardner A - 176

## Target Station Workshop

Experience with IPNS targets
J M Carpenter and A G Hins T - 1

Measurement of Cooling Characteristics of the ISIS Tantalum Target
G M Allen, T A Broome, M A Clarke-Gayther and C W Planner T - 12

Operational Consequences of Induced Activity on the ISIS Target Station
T A Broome T - 20

LAHET Code System/CINDER'90 Validation Calculations and Comparison with Experimental Data
T O Brun, C A Beard, L L Daemen, E J Pitcher, G J Russell, W B Wilson T - 26

Inclusion of Preequilibrium Calculation into High Energy Transport Code
K Ishibashi, H Takeda, Y Yoshizawa, N Matsufuji, T Nakamoto,
Y Wakuta and Y Nakahara T - 44

Pulsed Neutron Source of Moscow Meson Factory
M I Grachev, L V Kravchuk, A V Kuzin, S G Lebedev, V M Lobashev,
V G Miroshnichenko, V A Mateev, O V Ponomarev, V N Sazanov,
Yu V Senichev, S F Sidorkin, N M Sobolevsky, and Yu Ya Stavissky T - 53

Target-Moderator-Reflector Assembly for a High Power Pulsed Spallation Source
H Conrad T - 61

Pulsed Neutron Source of the Moscow Meson Factory on the base of Uranium Targets
A D Dementyev, V G Miroshnichenko, I Y Mosievskaya, S F Sidorkin,
N M Sobolevsky, Y Y Stavissky, I I Konovalov, A A Maslov, I T Tretyakov, V I Trushkin T - 71

Spallation Neutron Measurement at Incident Proton Energies of 0 8 to 3 GeV
T Nakamoto, K Ishibashi, N Matsufuji, K Maehata, Y Wakuta, N Numajiri, H Takeda,
S Meigo, S Chiba, Y Watanabe, T Nakamura and M Arai T - 80

Comparison of the Slow Neutron Intensity -0 8 GeV vs 3 GeV Protons
Y Kiyanagi, N Watanabe and M Arai T - 90

Conceptual Design of the Target Stations of the IPNS Upgrade
J M Carpenter, R K Crawford, R Kleb and A E Knox T - 95

Heat Generation and Neutron Beam Characteristics in a High Power Pulsed Neutron Source
D W Jerng and J M Carpenter T - 105

Target Station Design for a 1 MW Pulsed Spallation Neutron Source
G J Russell, G D Baker, R J Brewton, A Bridge, T O Brun, M Cappiello, C E Cummings, L L Daemen, D Davis, D Grisham, R P Hjelm, J S Elson, A Kernodle, M A Merrigan, E J Pitcher, H Robinson, L Walker and R Woods T - 115

The Choice of Optimum Proton Energy for a High Power Spallation Source - Issues for the Target Station
T A Broome T - 128

$D_2$ Cold Moderator System at SNQ
H Spitzer, K Geissmann, W Wagner and G S Bauer T - 132

First Experience of Cold Moderator Operation and Solid Methane Irradiation at the IBR-2 Pulsed Reactor
A A Beljakov, V G Ermilov, V L Lomidze, V V Melichov, and E P Shabalin T - 144

The ISIS Methane Moderator
T A Broome, J R Hogston, M Holding and W S Howells T - 156

Tailoring Intensities and Pulse shapes in Coupled Moderator-Reflector systems
J M Carpenter, Y Kiyanagi, N Watanabe H Iwasa and M Nakajima T - 164

Some Optimisation Studies on Flux-Trap Moderators for Increasing the Slow-Neutron Beam Intensity
Y Kiyanagi, N Watanabe and M Nakajima T - 172

Moderator Materials and Neutronic Performance
L L Daemen, G J Russell and E J Pitcher T - 181

Premoderator Studies for a Coupled Liquid-Hydrogen Moderator
Y Kiyanagi, N Watanabe, H Iwasa and Y Nakayama T - 196

A Hybrid Be/$D_2O$ Reflector for ISIS
L L Daemen, E J Pitcher, G J Russell, T A Broome and M Holding T - 202

Studies of Decoupled Composite Moderators of Liquid Hydrogen and Zirconium Hydride
Y Kiyanagi, J M Carpenter, N Watanabe H Iwasa and M Nakajima T - 206

# NEW SCIENCE FROM PULSED SOURCES

**J L Finney, Rutherford Appleton Laboratory, Chilton, Didcot, OX11 0QX**

## 1. Introduction

Four and a half years ago, at ICANS X in Los Alamos, we at ISIS were pretty pleased. ISIS was, for the first time, running at 100μA. More importantly, we were beginning to see new, exciting science coming from pulsed sources. In his summary talk at the end of that workshop Peter Egelstaff underlined the progress that had been made by announcing that pulsed sources had come of age[1].

Looking back from today, I believe that assessment was wrong. Understandably so, as when you are on a strongly rising curve whose future development you cannot know, it is difficult to assess your relative position on that curve. Pulsed spallation sources certainly had not come of age in 1988: at most, they were in early adolescence.

Since then, much has happened. ISIS has not only reached its design current of 200μA, but its reliability has increased significantly, and the number of scheduled instruments has more than doubled. The amount and variety of science being done each year has more than doubled, and many instruments have been improved beyond recognition, opening up the possibilities - and the realities - of more new science. We have learned much more how best to exploit the major advantages of pulsed sources. If we now look back from our present vantage point on the growth curve, at the quality and quantity of the science coming from pulsed sources, there is little comparison between the situation now and that 4½ years ago. Perhaps now, pulsed sources have come of age.

This review is therefore a celebration of pulsed source science. Using a necessarily very small selection of examples that I personally find particularly interesting, I will try to illustrate the advantages of pulsed sources through the new science they have made possible. I would emphasise this is a personal selection which inevitably must leave much out of interest and importance. I apologise for having to leave out so much.

## 2. The Advantages of Pulsed Spallation Sources

The conventional wisdom of pulsed sources tells us that the high energy (low wavelength) component in the delivered neutron spectrum is the key advantage. This allows us to perform inelastic scattering experiments with high energy transfer, for example in studying high energy magnetic excitations, as well as high momentum transfer elastic experiments which enables structural studies to very high resolution. These advantages are indeed powerful, allowing us to reach areas of science inaccessible to reactor neutrons. They are, however, only part of the story, as we have increasingly learned from recent experience. There are in addition other major advantages which all arise from the *pulsed* nature of the white beam of neutrons produced. In summary, these are:

- the high intrinsic resolution achievable in both space and time domains;

- a wide spectral range (meV→eV; 0.1Å → 20Å). This favours experiments exploring a wide dynamic range in both time and distance;

- the white beam allows fixed scattering geometries to be used. Not only is this ideal for background removal when working at 90° with pressure cells and reaction vessels but it also allows experiments to exploit other scattering angles for other optimisation reasons. Of particular importance are backscattering to maximise resolution in powder diffraction, and forward scattering to minimise inelasticity corrections in liquids;

- pulsed sources are essentially very low background sources: in essence the source is off when the data is collected. As signal/background ratio rather than intensity is often the determining quantity for a successful experiment, this low background allows more subtle effects to be seen more easily using by pulsed sources. This advantage is perhaps one whose potential value was not really appreciated before we started fully exploring the science that could be done.

In the examples that follow, the ways in which pulsed source instruments exploit the above advantages will be stressed.

## 3. High Energy Neutrons

Magnetic excitations provide one of the classic examples of the exploitation of high energy neutrons. One area which consequently has been opened up by pulsed sources is that of intermultiplet transitions in rare earth magnetic systems. As Fig 1 shows, only one transition ($^7F_0 \rightarrow {}^7F_1$ of europium) is of low enough energy to be studied using reactors. The figure also shows some of the transitions that have been explored using pulsed neutrons. Non-dipolar allowed transitions have been observed up to 1800meV (thulium)[2], and measured inelastic structure factors have been shown to be in good agreement with calculations for praseodymium[3]. In contrast, for light rare earths, significant shifts are found for transitions to different L quantum numbers (e.g. $^3H_4 \rightarrow {}^3F_2$ in Pr) due to the screening of coulomb interactions by the conduction electrons, an effect which is even greater for 5f electrons. The technique also has applications to intermediate valence systems (e.g. Ce, Sm) and crystal field levels.

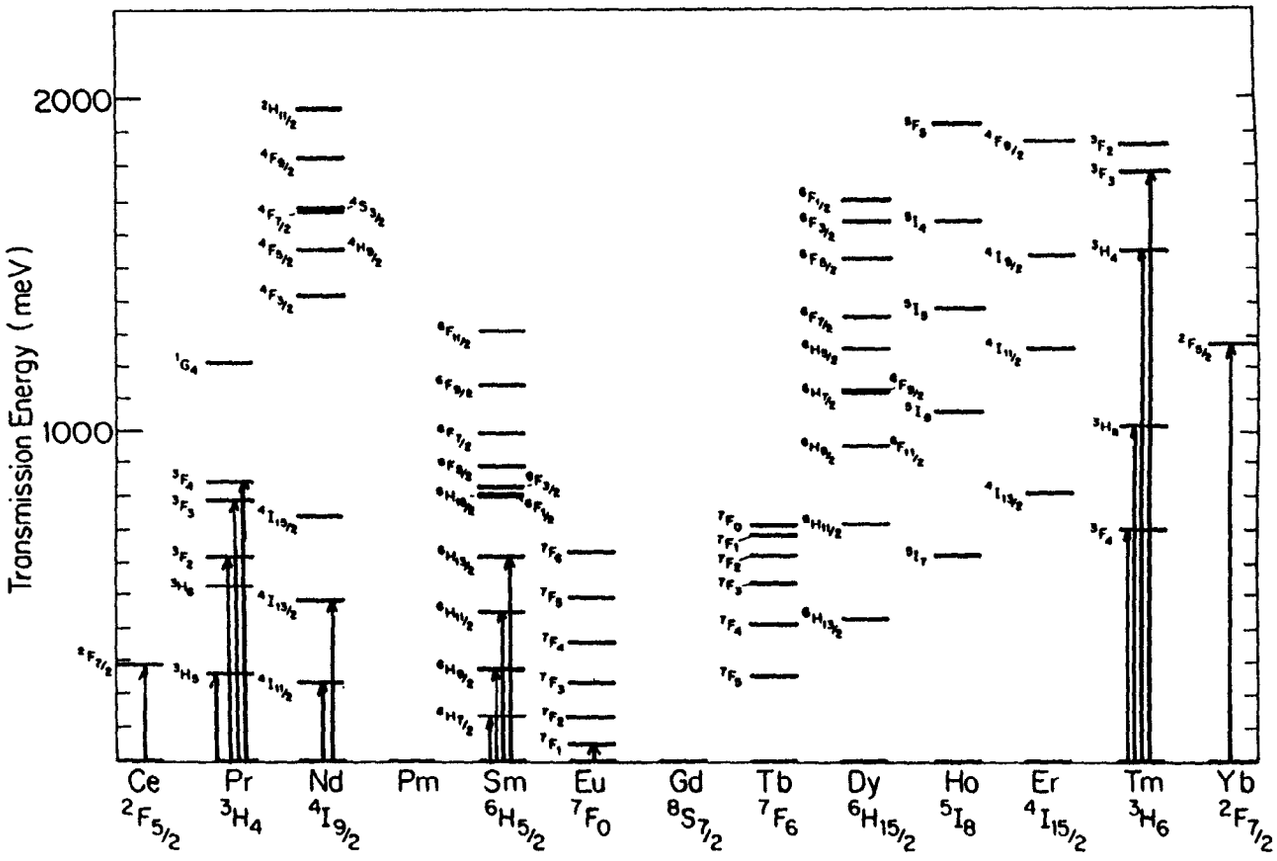


**Figure 1:** Intermultiplet levels in the rare earths. Transitions examined by neutrons are indicated. Only the $^7F_0 \rightarrow {}^7F_1$ transition in Eu is accessible to reactor neutrons.

From the early days of pulsed neutrons, it was believed that they would be at their best in excitation studies of materials presented as powders rather than single crystals, and instruments were therefore optimised for powder work. As reactor-based instruments are restricted to energy transfers of below about 200meV, however, attempts were made to explore magnetic dispersion relations above the reactor limit, with considerable success as illustrated by work on cobalt[4] to the zone boundary at around 300 meV, and iron[5] and chromium[6] up to 550meV. As the dimensionality of the magnetic system is reduced, however, it becomes possible to exploit the detector geometry to good effect, work[7] which has enabled the magnetic dispersion in the magnetically two-dimensional high $T_c$ parent compound $La_2CuO_4$ to be followed out to the zone boundary at 316meV (Fig 2), and the susceptibility of a Kagomé lattice system explored[8]. One dimensional magnetic systems are ideally suited to time of flight, as is illustrated by the case of $KCuF_3$[9]. Fig 3a illustrates the cut taken by incident 150meV neutrons while the results in Fig 3b indicate a quantum rather than a classical ground state. Fig 3b also underlines the low background, an advantage which is common - together with high intrinsic resolution - to most of these magnetic experiments.

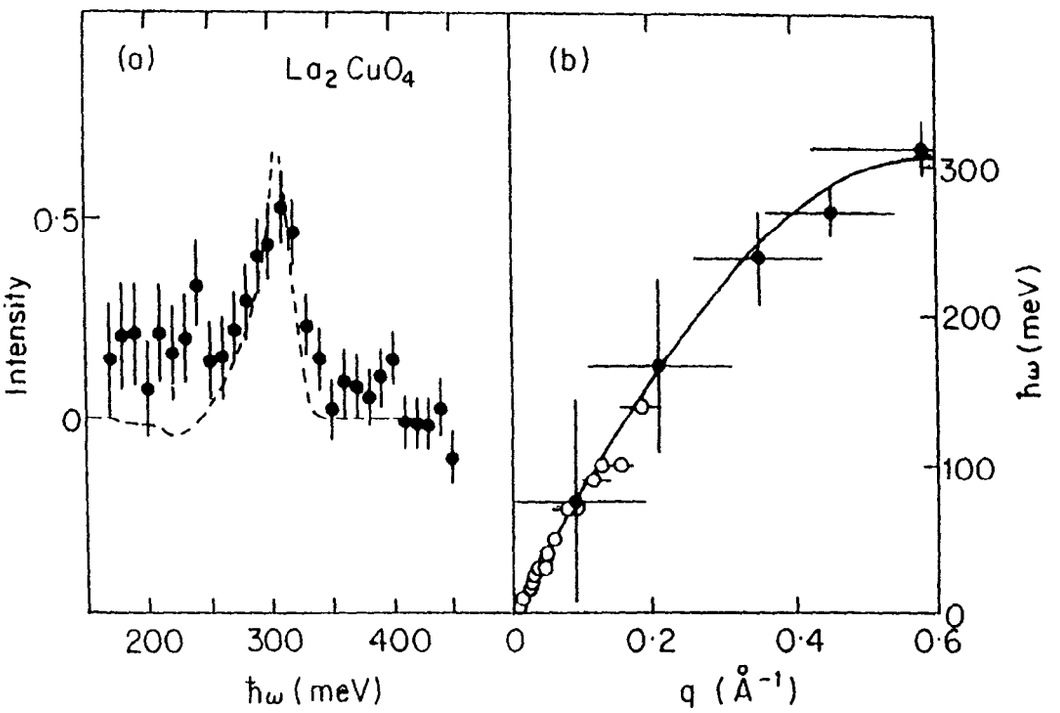


**Figure 2:** Magnetic excitation (left) and its dispersion (right) from a composite single crystal of $La_2CuO_4$. The response can be seen to be followed to the zone boundary at 316 meV.

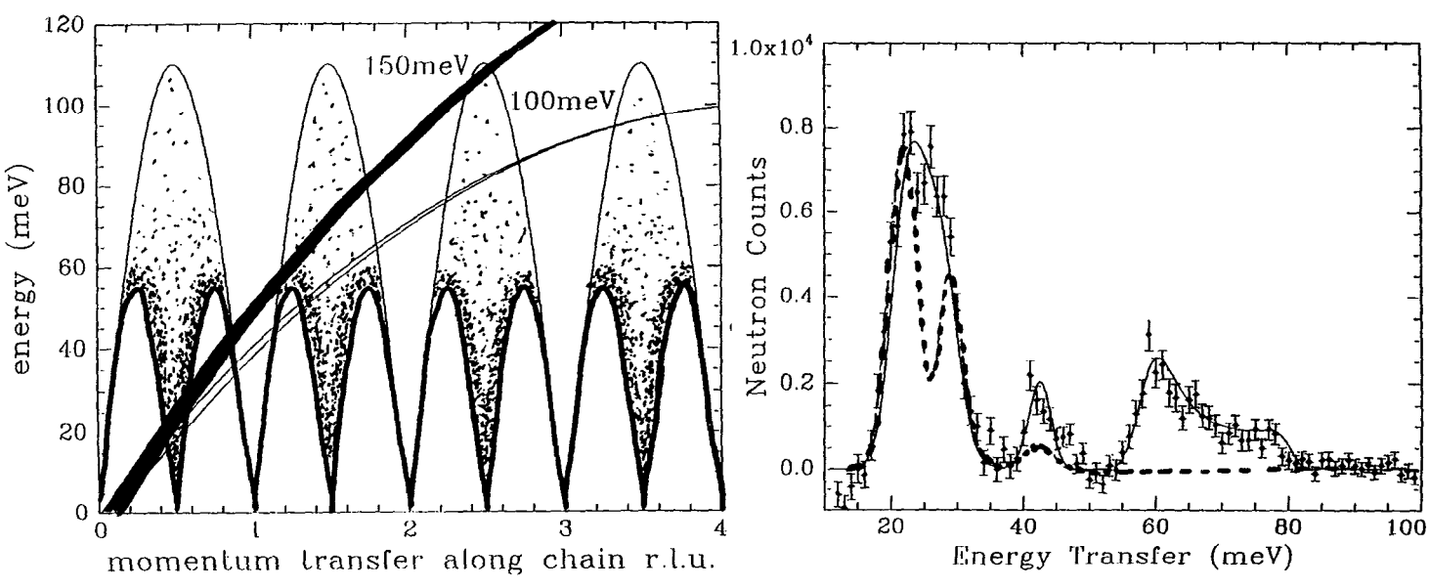


(a) (b)

**Figure 3:** Magnetic excitations in the one-dimensional $KCuF_3$ system. The dotted line in 3(b) indicates the expected response for the 150 meV cut (Fig 3(a)) for a classical ground state. The actual results indicate clearly a quantum ground state.

Moving away from magnetic systems and to even higher energy transfers, we come to the completely new area of electron volt spectroscopy. In effect, by scattering neutrons with very high energy and momentum transfer, we can probe directly the wave function. Here, a long standing problem has been to observe the Bose condensate in liquid $^4$He, and a series of experiments at IPNS and ISIS continue to tackle this problem. Fig 4 summarises the IPNS results[10], which, after correction for final state effects, are consistent with a Bose condensate fraction of about 9% in the superfluid at T=0K. Work on the new eVS instrument at ISIS allows higher momentum transfers to be accessed, and hence a closer approach to the impulse approximation. A significant amount of work has been done to probe the hydrogen wave function in hydrogen bonded systems[11] - both along and normal to the bond - and although still in the early stages of development, these studies promise much new and important information on a chemically and biologically very important interaction.

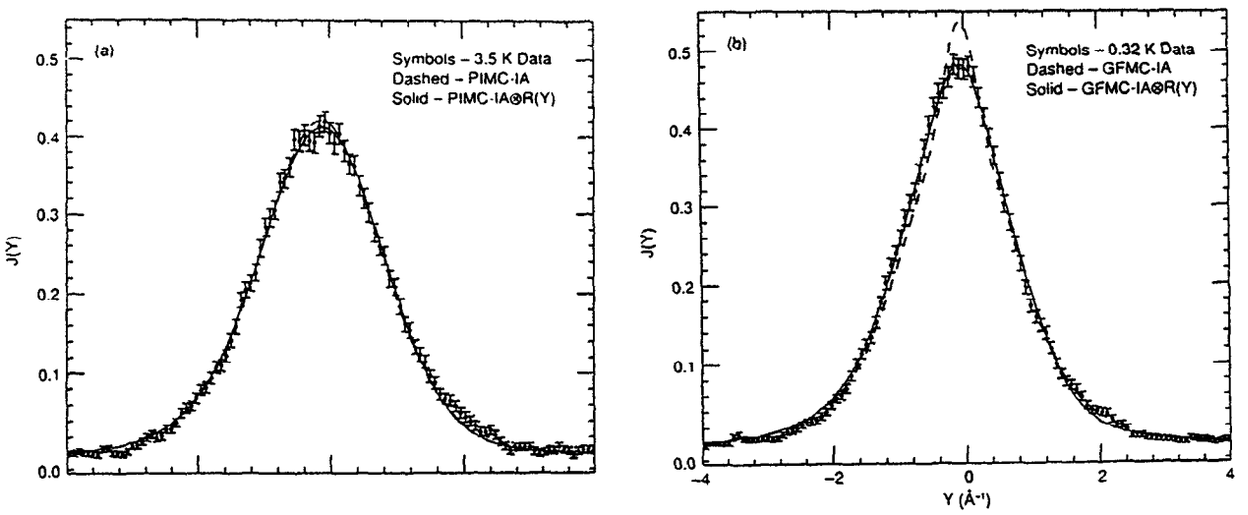


(a) (b)

**Figure 4:** The Compton profile for (a) normal liquid helium at 3.5 K and (b) superfluid helium at 0.35 K as a function of the scaling variable Y [$=(M/Q)(\omega-\omega_r)$, where $\omega_r$ $\{=Q^2/2M\}$ is the recoil energy]. The dashed lines are the theoretical predictions with instrumental resolution taken into account. The solid lines include final state effects in the comparison.

## 4. Very High Spatial Resolution

In pulsed source instruments, the spatial resolution achievable increases with time of flight, and hence with moderator-detector distance. The resolution achievable is illustrated well by the typical powder pattern taken from HRPD, situated nearly 100 m from the ISIS target, shown in Fig 5. Not only is the resolution, at $\Delta d/d \sim 4 \times 10^{-4}$, unmatched by any other neutron powder diffractometer, but, again characteristic of pulsed source instruments, this resolution is essentially constant with d-spacing. Thus, as a powder pattern is essentially a set of Fourier components of the crystal structure, as the number of "reflections" increases, the precision with which a structure can be refined also increases. Coupled with the wide dynamic range over which this high resolution is achievable, high resolution neutron powder instruments such as HRPD have little short of revolutionised powder diffractometry, allowing us to do science with powders that previously was not possible.

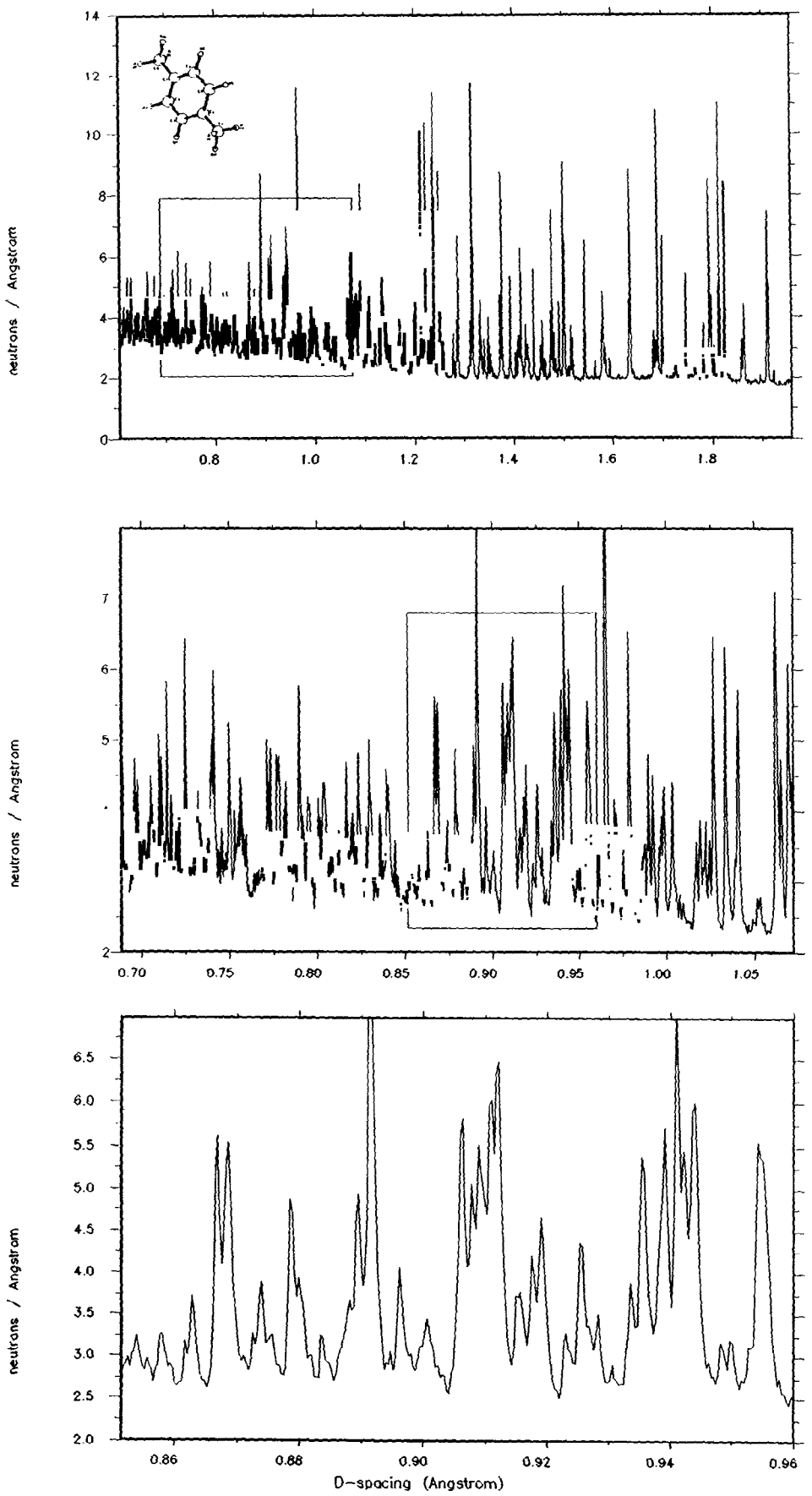


**Figure 5:** The powder diffraction of p-xylene taken on HRPD, illustrates both the very high - and constant - resolution, and the bandwith achievable in a single "shot". The two lower figures show blown-up the region framed in the figure above.

For example, more complex structures can be refined, and more subtle effects observed. An obvious example is structural studies of high temperature superconductors, where pulsed sources continue to make major contributions. Here, in addition to the work at ISIS,[12] the careful, thorough studies undertaken at Argonne are particularly noteable[13]. Secondly, we can now solve structures with powders and perform refinements of a quality that previously required single crystals. The "canonical" example is the refinement of the anistropic temperature factors of benzene from HRPD data[14], the comparison of which with single crystal measurements is shown in table 1. Within the quoted errors, the two sets of results are essentially the same. For this experiment, the standard deviations of the powder data are perhaps three times those of the single crystal figures, though longer data collection times would reduce this difference: in this case, the powder data was taken in 12 hours, the single crystal data over 3 weeks.

Time-of-flight powder neutron diffraction (4K)

HRPD $0.281\ \text{Å}^{-1} < \sin\theta/\lambda < 0.824\ \text{Å}^{-1}$

| Atom | $B_{11}$ | $B_{22}$ | $B_{33}$ | $B_{23}$ | $B_{13}$ | $B_{12}$ |
|---|---|---|---|---|---|---|
| C1 | 77 (7) | 42 (6) | 87 (7) | 1 (5) | 5 (5) | -3 (4) |
| C2 | 71 (7) | 58 (7) | 68 (6) | 9 (4) | 26 (5) | 12 (4) |
| C3 | 83 (7) | 57 (7) | 92 (7) | 0 (5) | 18 (5) | -1 (4) |
| D1 | 218 (8) | 121 (7) | 267 (9) | 19 (5) | 22 (6) | 31 (5) |
| D2 | 170 (8) | 212 (8) | 225 (9) | -2 (6) | 120 (6) | 33 (5) |
| D3 | 241 (9) | 155 (8) | 214 (8) | 75 (6) | 66 (7) | -20 (5) |

Single crystal neutron diffraction (15K)

BNL - 4-circle 1.0499 $\text{Å}^{-1}$. 0.403 $\text{Å}^{-1}$. $< \sin\theta/\lambda < 0.780\ \text{Å}^{-1}$

Jeffrey et al. Proc. R. Soc. Lond. **A 414** 47-57 (1987)

| Atom | $B_{11}$ | $B_{22}$ | $B_{33}$ | $B_{23}$ | $B_{13}$ | $B_{12}$ |
|---|---|---|---|---|---|---|
| C1 | 79 (2) | 67 (2) | 88 (2) | 4 (1) | 7 (2) | 6 (2) |
| C2 | 74 (2) | 81 (2) | 79 (2) | 0 (2) | 17 (2) | 9 (2) |
| C3 | 81 (2) | 75 (2) | 82 (2) | 10 (1) | 14 (2) | -3 (2) |
| D1 | 224 (3) | 114 (2) | 239 (3) | 12 (2) | 25 (2) | 46 (2) |
| D2 | 183 (2) | 204 (3) | 208 (3) | -8 (2) | 88 (2) | 35 (2) |
| D3 | 214 (3) | 171 (2) | 199 (3) | 58 (2) | 61 (2) | -18 (4) |

**Table 1:** Anistropic temperature factors ($10^4\text{Å}^2$) for deuterated benzene.

This ability to work with powders rather than single crystals promises to be a major step forward: growing the single crystals is often the rate determining step in a structural study, and often - e.g. in new materials synthesis such as zeolites - not possible. In elucidating drug structures, necessary if we are to determine the drug shape for correlation with its biological activity, pulsed neutron powder diffraction is beginning to make significant contributions: active drugs are often only available as powders, and may lose their activity in different crystal forms or when grown as single crystals. A recent example from HRPD is that of the neurotransmitter dopamine, for which accurate positions of both backbone and the interaction-important hydrogen atoms are obtained[15].

High resolution pulsed neutron diffraction has solved the low temperature structure[16] of Buckminsterfullerene, $C_{60}$. The high resolution also led to the uncovering of a dynamical phase transition through measuring to high precision the lattice constant as a function of temperature[17]. Fig 6 shows this temperature variation, in which each data point was measured in 15 minutes. In addition to the known transition around 260K, a second transition occurs at around 85K. Fig 7 illustrates the overall nature of these transitions. Above the higher temperature one, the molecules rotate with no preferential rotational axis, while below the 260K transition, rotation becomes restricted to a single axis. Below 85K, this motion freezes out, and the system adopts the low temperature structure. The quality of the powder data is further demonstrated by Fig 8, which shows how the "ideal" mutual orientation of nearest neighbour $C_{60}$ molecules (pentagon facing 6:6 bond: see Fig 8) is not fully achieved in the low temperature structure. Refining occupancies shows that ⅙ of the nearest - neighbour configurations do not adopt this "ideal": hence the zero temperature intercept of 0.833 in Fig 8.

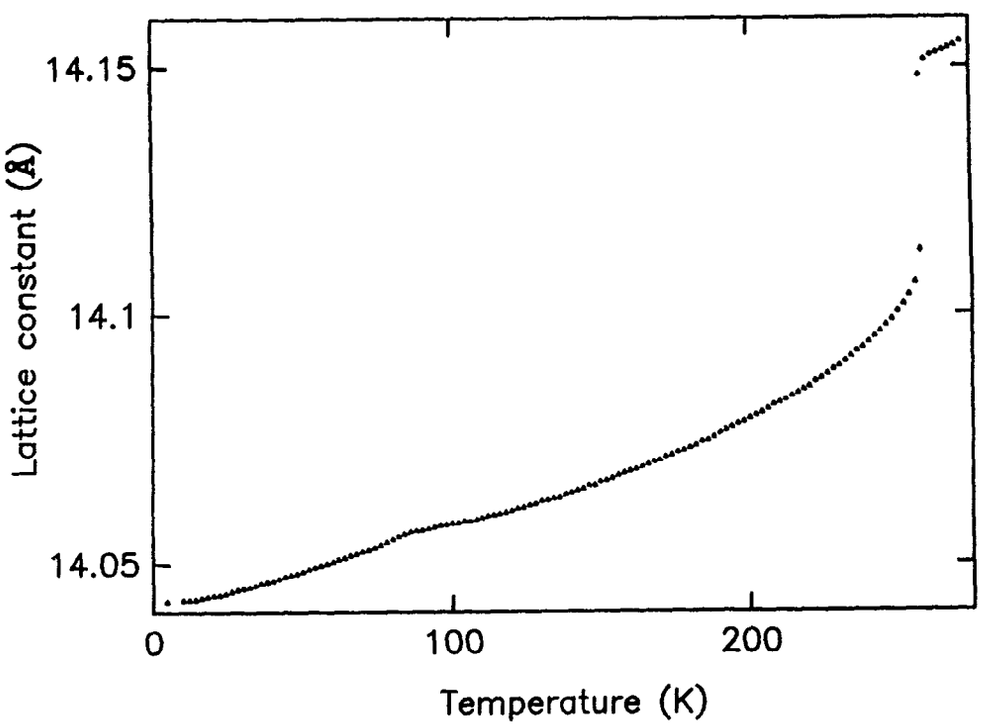


**Figure 6:** The temperature variation of the lattice parameters of $C_{60}$, showing transitions at around both 260K and 85K

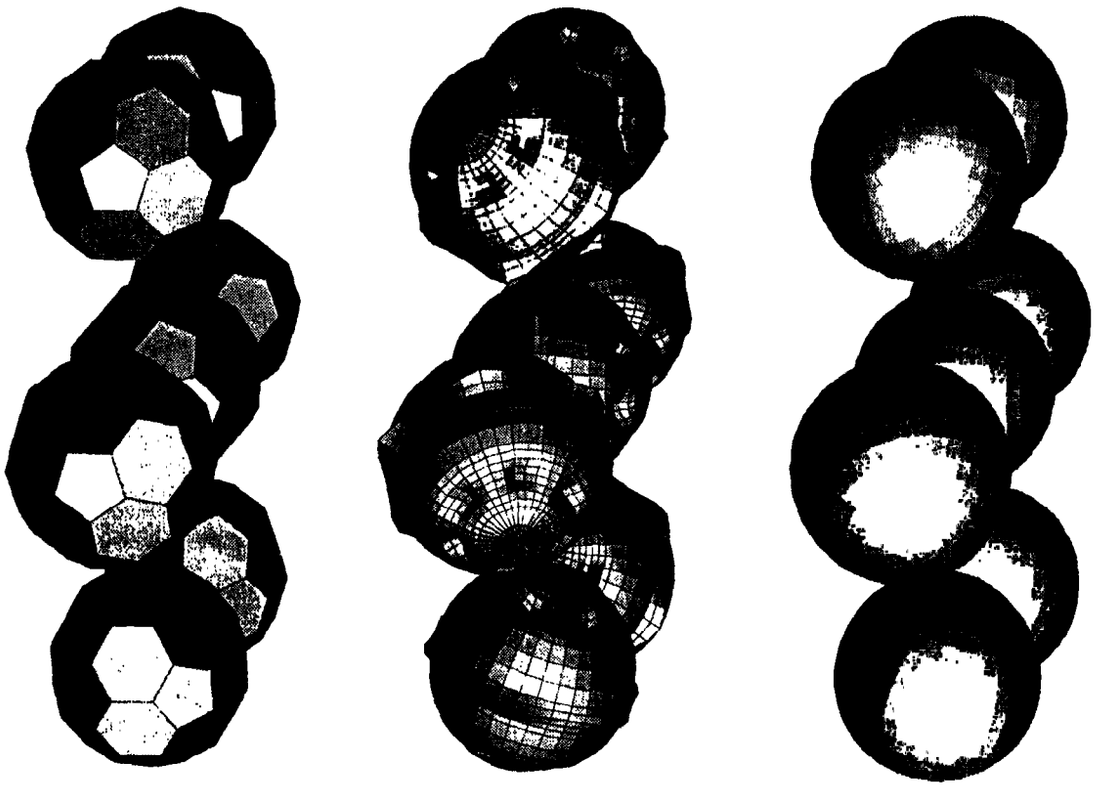

**Figure 7:** Above around 260K, $C_{60}$ molecules appear to rotate around no preferential axis (right). Below the upper transition, rotation becomes restricted to a single axis (centre) while below about 85K the low temperature structure is adopted (left).

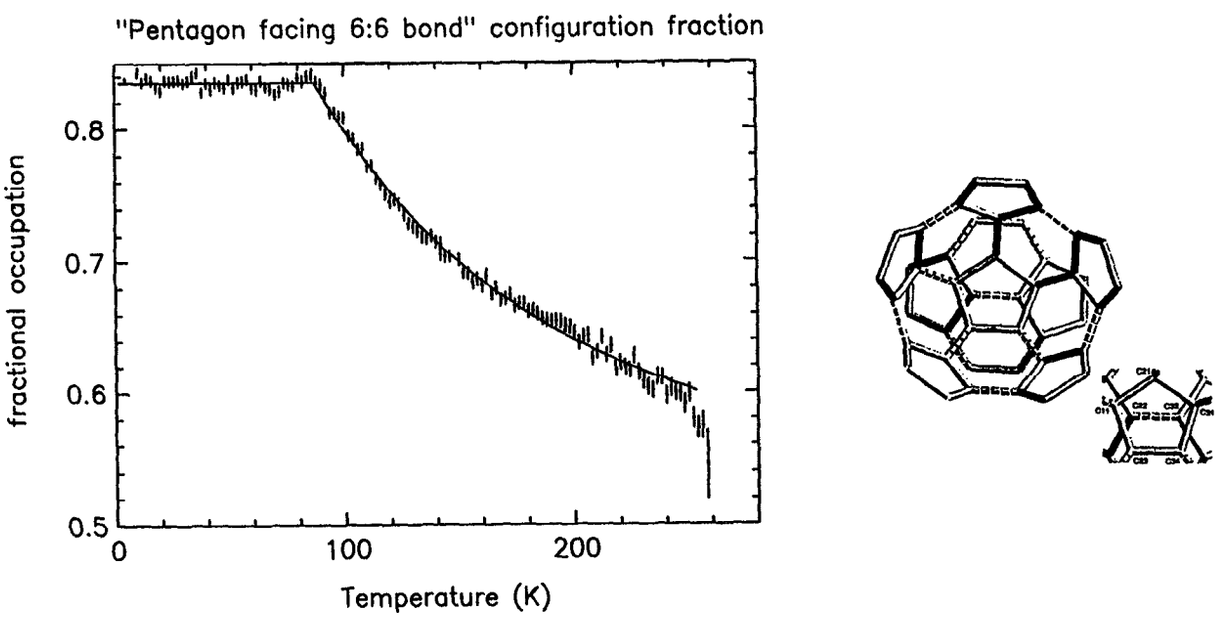


**Figure 8:** Even below 85K the low temperature structure is not fully ordered. Only $^5/_6$ of the local configurations (0.833) are in the "ideal" configuration shown.

Crystallography is recognised to be a very powerful technique, and when allied to pulsed neutrons can be even more powerful, as the above has underlined. It does however have limitations, and it is worth digressing a little to discuss this point. Broadly speaking, a crystallographic structure will give average positions of molecules, with "temperature factors" which themselves can often give us some information on disorder in the structure. This averaging of atomic position can, however, hide mechanistically useful information which other techniques can reveal. An example from IPNS - with similar work progressing at LANSCE - again concerns high $T_c$ materials[18]. In the $La_2CuO_4$ system, crystal structure determination tells us the $CuO_4$ conduction layer is planar. Using the crystal co-ordinates, we can calculate the distribution function of pairs of atoms (the probability of finding an atom at a given distance from any other atom), and the result for $Nd_{2-x}Ce_xCuO_4$ is given by the solid line in Figure 9. This distribution function can also be obtained by diffraction measurements, and in fact this is the standard way of looking at liquid and glass structures using neutrons or x-rays. The experimental results for $Nd_{2-x}Ce_xCuO_4$ both above (50K) and below (10K) the superconducting transition are also shown in Figure 9, and there are clear differences both from the "average" structure given us by crystallography and between the superconducting and non-superconducting states. The local structure is thus considerably different from the average crystallographic structure, and changes in local structure can be associated with the onset of superconductivity. Structural modelling indicates that the observed differences can be explained partly by oxygen atoms being displaced by small amounts perpendicular to the $CuO_4$ plane. With respect to this pair distribution technique, we should note that the degree of detail observable - the resolution - increases with increasing momentum transfer Q, and increased Q in turn requires short wavelength neutrons. This again underlines the power of pulsed spallation neutrons, where this high energy component is present in the incident spectrum.

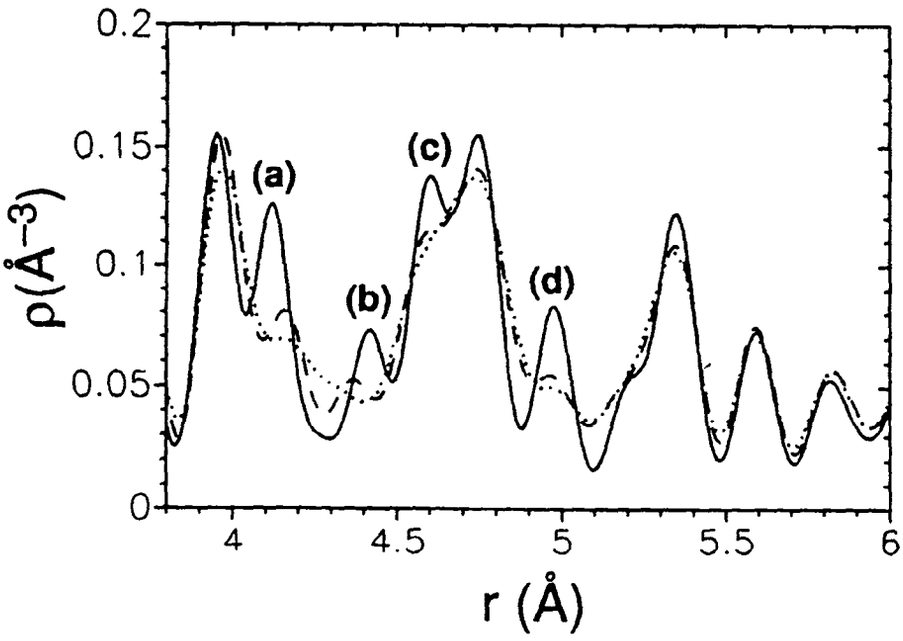


**Figure 9:** Calculated-PDF (solid line) of the crystal (T') structure superimposed on the data-PDFs from the 50K (dotted line) and 10K (dashed line) of the superconducting sample.

## 5. Fixed Scattering Geometry

By measuring diffraction from a sample at 90°, the collimation of incident and diffracted beams can be optimised to remove - in essence completely - parasitic scattering from the sample environment, which is perhaps a heavy pressure cell or chemical reaction vessel. This is illustrated dramatically by Fig 10, which shows powder patterns of ice VIII taken on a reactor source (ILL)[19] and at 90° at IPNS[20]. Although the reactor pattern looks superficially good, what is seen is largely scattering from the sample environment, which very much dominates the ten or so sample peaks that are marked. In comparison, the IPNS data show only the sample peaks - those from the pressure cell have been collimated out.

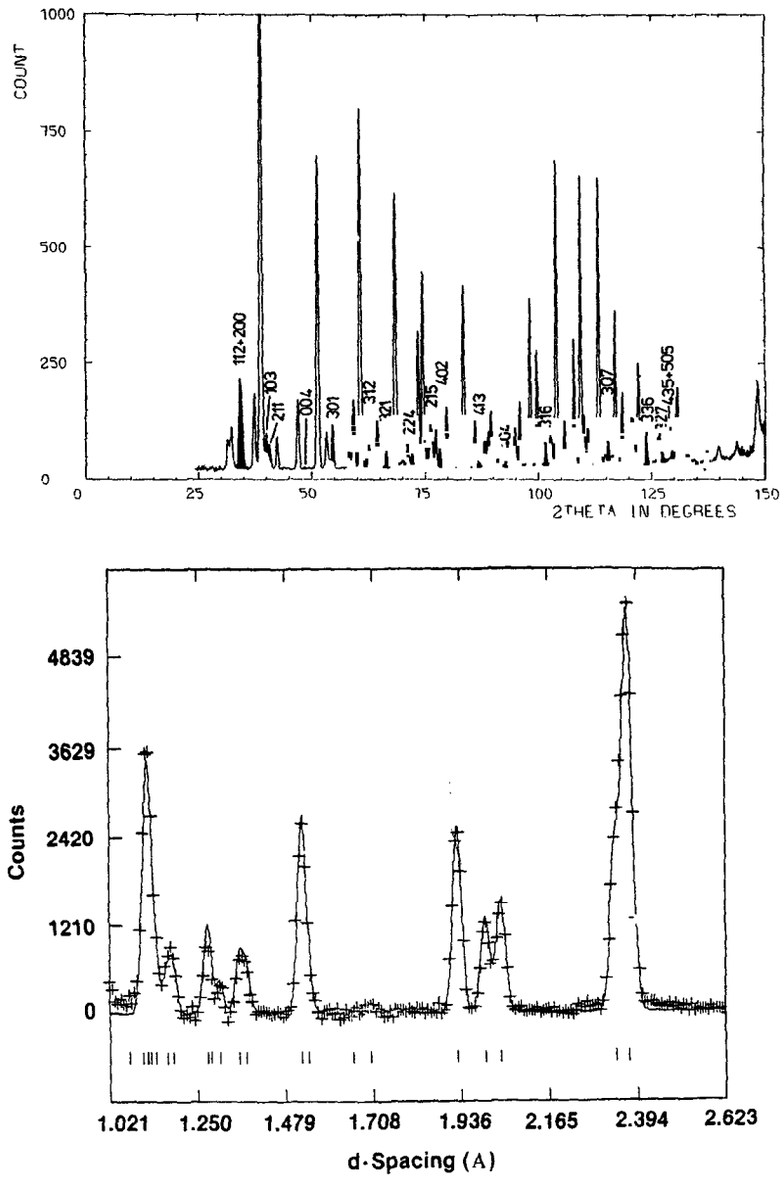


**Figure 10:** The powder diffraction patterns of ice VIII taken on a reactor source (ILL-upper) and a pulsed source (IPNS-below). Only the labelled peaks in the upper figure originate from the sample. The pressure cell peaks have been collimated out in the pulsed neutron pattern.

Small wonder, therefore, that high pressure studies on pulsed sources are expanding rapidly. A particularly interesting study from IPNS is on the high $T_c$ material $Tl_2Ba_2CuO_6$, for which $T_c$ depends on the oxygen concentration[21]. Applying pressure at room temperature also changes the critical temperature, while applying the same pressure changes at low temperature has very little effect on $T_c$. Preparing samples using different paths in (p,T) space (e.g. applying up to 6kbar at 295K and then cooling; cooling before applying pressure; intermediate paths by applying some pressure at 295K, cooling, and then increasing the pressure to 6kbar), crystallographic measurements showed clearly that the resulting structure depends on the path taken in (p,T) space. This work suggested that the interstitial oxygen defect mobility is reduced at reduced temperatures, and also perhaps that applying pressure at room temperature leads to defect ordering.

90° scattering geometry is being further exploited in a Paris-Edinburgh collaboration which is developing neutron high pressure techniques to reach much higher pressures than the present normal upper limit of around 25kbar[22]. Working with an anvil arrangement, data has been taken at pressures up to 250kbar, extending the accessible pressure range by an order of magnitude. In recent work at ISIS[23], refineable patterns from ice VIII were taken at 101kbar which gave a precision on the O-D bond length the same ($\pm$ 0.003Å) as at 25kbar. As this cell enters service as a user facility, further new advances are expected in high pressure exploitation.

Fixed geometry scattering is also exploited in making *in-situ* strain measurements. The strain is reported by small shifts in Bragg peak positions, so high resolution is also desirable. By measuring scattering from an appropriately aligned sample, strain both normal and parallel to the applied load can be measured simultaneously by taking data at both + and - 90° scattering positions. With appropriate collimation, strain can be measured pixel by pixel to give the spatial variation within the sample. However, using pulsed neutrons, strain can be measured for different lattice planes, again at the same time and orientation.

An example of work from LANSCE on a metal-matrix composite - aluminium reinforced with SiC whiskers - is shown in Fig 11, where the experimental results are compared with the results of finite element calculations[24]. For the parallel strain, theory and experiment are still some way apart, while for the normal strain, there is better agreement with the average strain deduced from profile refinements of the whole pattern However, in the latter case, there is a strong hkl dependence, which not only gives more detailed information, but also indicates the danger of drawing conclusions from the one hkl peak that is normally used in reactor studies of residual strain.

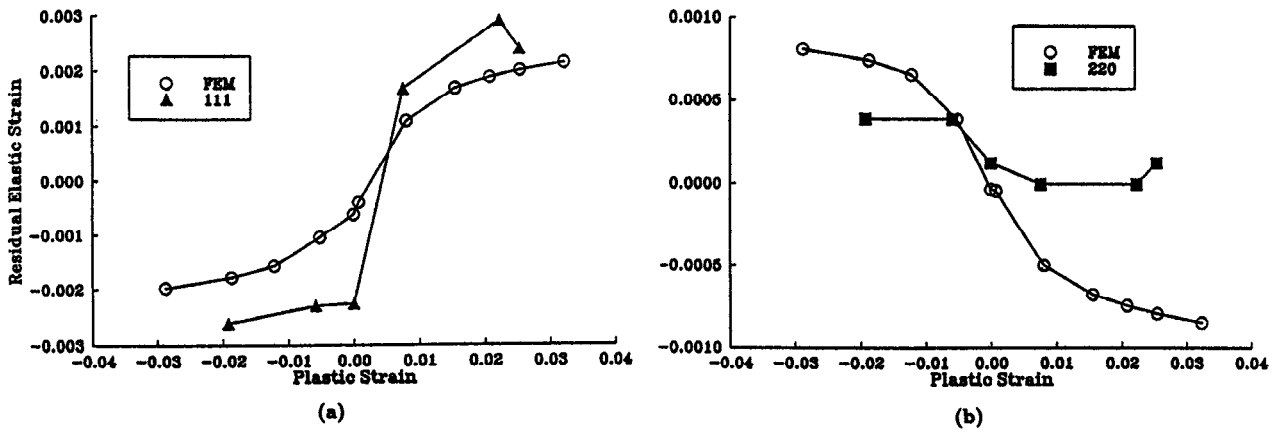


**Figure 11:** Measured and predicted values of average residual elastic strains in the matrix (a) parallel and (b) perpendicular to the deformation axis, from a 15% whisker composite strained in tension to a plastic strain of 0.018, deformed in compression and then unloaded.

These techniques are very much still under development: they promise much in evaluating the performance of increasingly complex engineering materials.

Although I shall say little further on the matter, structural studies of liquids and glasses using pulsed neutrons have also resulted in significant progress in the field. As mentioned above in the discussion of pair distribution studies of high $T_c$ materials, the much greater momentum transfer range accessible using the hot neutrons from a pulsed spallation source enables significantly greater structural detail to be obtained. When dealing with light atoms, pulsed neutrons have even greater advantages which result from working at "fixed" scattering geometry, in this case at low angles. This minimises troublesome inelasticity corrections and results in much improved data quality from such systems. These advantages have been exploited particularly in studies of aqueous solutions using hydrogen-deuterium and other atom substitution, and have told us a great deal about not only the hydration of charged, polar and non polar groups, but also how the water is or is not perturbed close to such groups[25].

## 6. Time Dependent Studies and Time Structure

The white beam of neutrons produced by a pulsed source enables the whole diffraction pattern to be measured simultaneously, rather than having to scan step by step as a function of scattering angle as is necessary on a standard monochromatic instrument on a reactor source. The ability to see the whole diffraction pattern build up over a relatively short time has natural advantages for time-dependent studies. Such work is of course possible on a reactor using multidetectors, but the white pulsed beam is more flexible for such studies, and, depending on neutron intensity, it is in principle possible to perform time dependent measurements on time scales as low as a few - or even perhaps a single - neutron pulse.

An example from Dubna of time resolved studies over intervals of 5 minutes concerns the synthesis of the yttrium 123 superconductor $YBa_2 Cu_3 O_x$[26]. Fig 12 shows the intensities of particular diffraction peaks identified with different compounds at five minute intervals. The interesting result here is that the synthesis proceeds not directly from the starting materials, but through three intermediate phases which coexist prior to the formation of the Y-123 end product. With intense pulses, it is easy to see how the time interval can be reduced, and a glimpse of the possibilities is given in Fig 13, which shows a diffraction pattern of molybdenum powder from (lower figures) 300 pulses (1 minute) and (upper figure) a single pulse. The diffraction pattern is clearly visible in the single pulse measurement, showing that in favourable cases single pulse measurements are already possible.

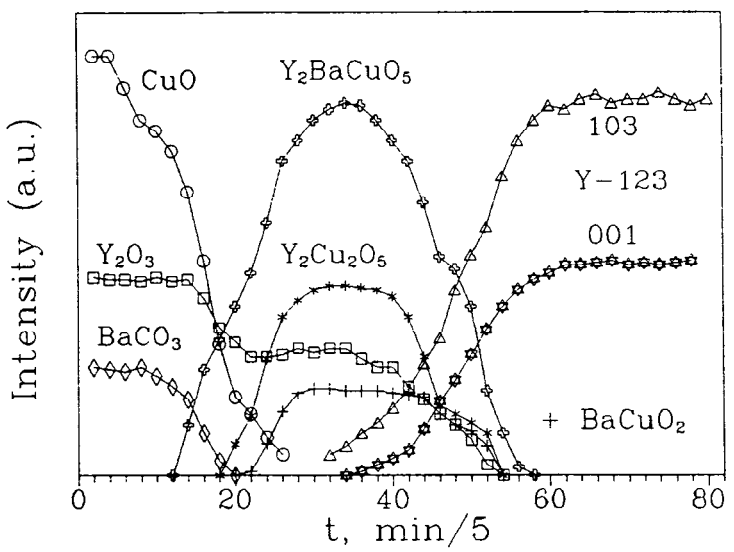


**Figure 12:** The intensities *vs* time of some diffraction peaks (relative units) which belong to different compounds during the synthesis of $YBa_2Cu_3O_x$ from raw materials $Y_2O_3$, CuO and $BaCO_3$. Three intermediate phases $Y_2BaCuO_5$, $Y_2Cu_2O_5$ and $BaCuO_2$ coexisted before the formation of Y-123 started.

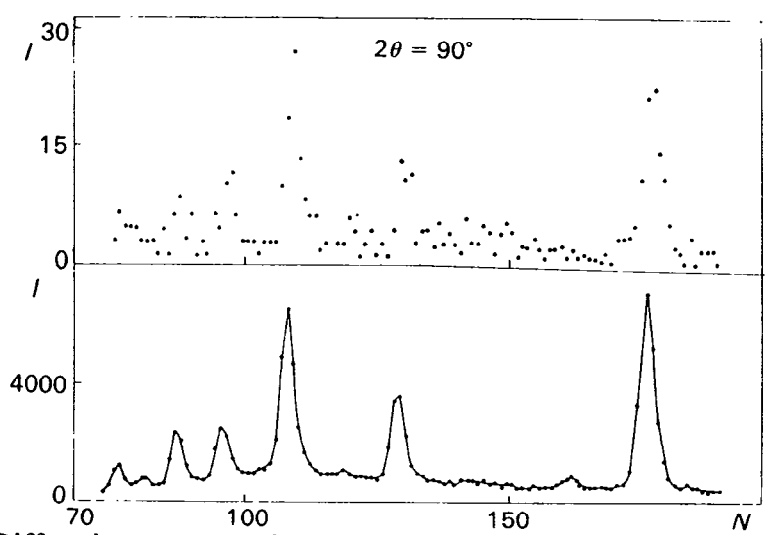


**Figure 13:** Diffraction patterns of Mo powder. The upper pattern was recorded in 1 pulse of the Dubna pulsed reactor, the lower one in 1 min (300 pulses of the pulsed reactor).

Also possible, but so far only exploited in limited degree, are "stroboscopic" - type measurements in which the sample is perturbed periodically by an external agent, in phase with the neutron pulse. This might be necessary when, as for example with very high magnetic fields, the sample perturbation cannot be obtained continuously and must therefore be pulsed. Pulsed magnetic field measurements have been pioneered at KEK, with some impressive results[27]. A recent example is the magnetic transition in the quasi one dimensional antiferromagnetic $CsCuCl_3$[28]. This system was expected to reveal enhanced quantum fluctuations in its magnetic properties, and the data taken on the magnetic transition at about 12 Tesla could be explained in terms of these fluctuations.

Another use of the time structure is illustrated by a recent experiment on ISIS. This addresses a system in which a phase transformation is restarted periodically and, consequently, time-resolved measurements on a millisecond time scale are possible. $Rb_2ZnCl_4$ has a ferroelectric transition close to 193K which is accompanied by a structural transition from incommensurate to commensurate. In the experiments on PRISMA - described in more detail elsewhere in these proceedings[29] - 5 pulses from ISIS are in effect ganged together, and an electric field applied with a frequency of 5Hz. The commensurate and incommensurate Bragg peaks can then be observed, and their relative intensities followed as a function of time at (variable) fixed temperature. The results at 193.5K are shown in Fig 14, and suggest a lag of a few milliseconds after applying or removing the field before the transition starts and, at this temperature, the transformation going to about 90% completion in the 100 ms time frame. Changes over periods as short as a few milliseconds can clearly be observed. Although this kind of use of pulsed sources has frequently been suggested, I believe this is the first effective demonstration of its implementation. Clearly it is capable of further development, for example to measure the kinetics of phonons in conjunction with a phase transition.

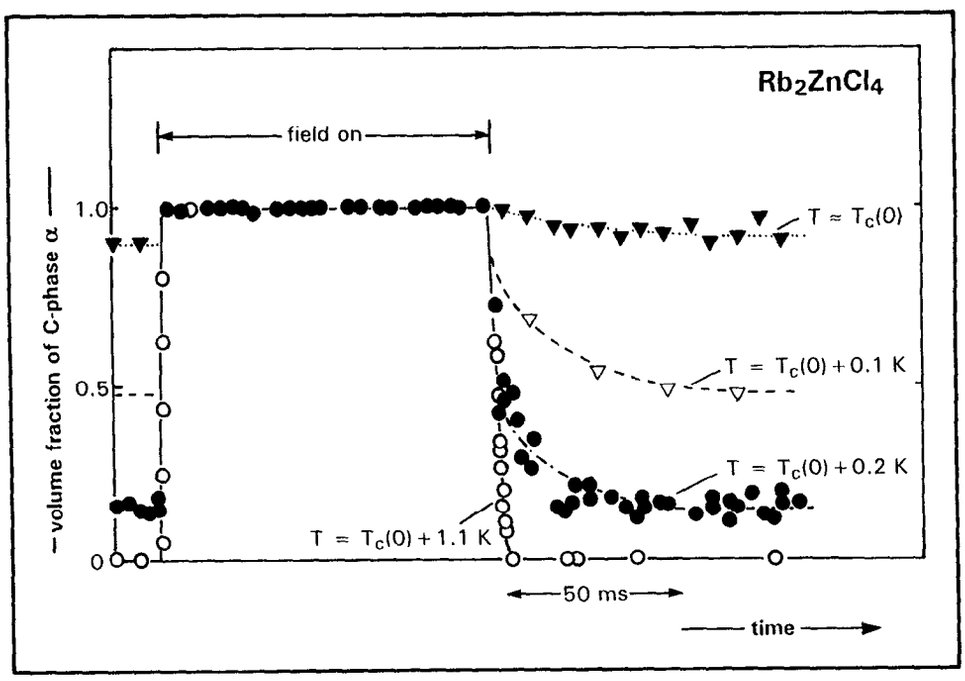


**Figure 14:** The relative intensities of the commensurate and incommensurate Bragg peaks during the ferroelectric transition in $Rb_2ZnCl_4$.

Pulsed spallation neutron sources also produce a variety of other particles. At ISIS for example, both neutrinos and muons are exploited, important aspects of their exploitation being again the time structure and associated low background.

In the KARMEN neutrino experiment at ISIS[30], three types of neutrinos are produced through pion decay as follows:

$$\pi^+ \xrightarrow[26\text{ns}]{} \mu^+ + \nu_\mu$$
$$\mu^+ \xrightarrow[2.2\mu s]{} e^+ + \nu_e + \bar{\nu}_\mu$$

Clearly, the $\nu_\mu$ is produced in a time window different from that in which the $\nu_e$ and $\bar{\nu}_\mu$ are formed, and hence they can be distinguished. In addition to searching for neutrino oscillations, cross-sections for some neutrino-induced interactions are being measured, for which the time structure is again crucial. An example is the neutral current nuclear excitation $^{12}C(\nu, \nu')^{12}C^*$, in which the resulting 15.1MeV $\gamma$ is measured as a signature of the C* decay. Fig 15 shows the measured events spectrum, and the looked-for $\gamma$ peak is clearly visible between 11 and 16 Mev. The resulting experimental cross-section - which is a new measurement - of [11.2 $\pm$ 1.3 (statistical) $\pm$ 1.0 (systematic)] x $10^{-42}cm^2$ is within the range of the theoretical prediction [9.9 - 11.5] x $10^{-42}cm^2$.

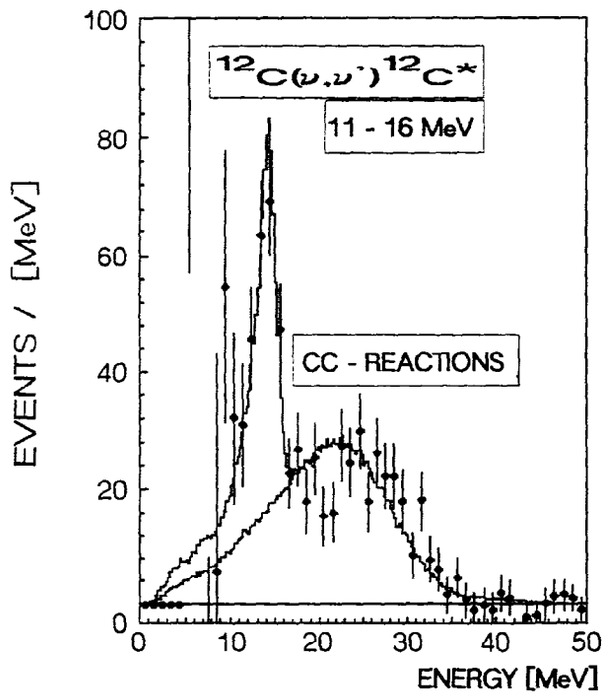


**Figure 15:** The events spectrum for the neutral current nuclear excitation of $^{12}C$. The C* decay signature - 15.1 MeV $\gamma$ - is clearly visible in a peak between 11 and 16 MeV.

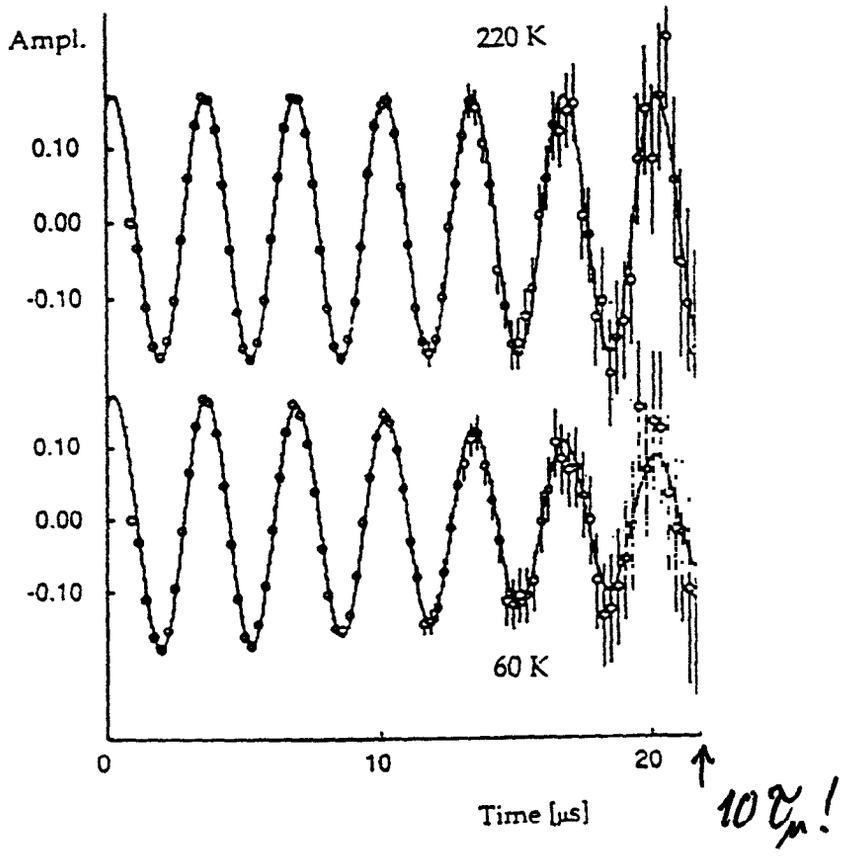


**Figure 16:** The muon spin rotation signals in Pt at two temperatures, showing damping at the lower temperature. Note that signals can be fitted to beyond 10 muon lifetimes.

KEK and ISIS both have pulsed muon sources. Here again the property of interest which gives rise to high quality spectra is the virtual absence because of the time structure of a background signal. This is illustrated in Fig 16 by muon spin rotation signals in platinum[31]. The signals can be fitted to beyond 10 muon lifetimes ($10\tau_\mu \simeq 22\mu s$), which is unprecedented in the μSR literature. In this case, it allows the weak damping at the lower temperature to be discerned. The temperature dependence of the fitted line width shows "textbook" behaviour, indicating static muons below about 100K and motional narrowing indicating the onset of diffusion at higher temperatures. The motion is by thermally activated hopping, with no sign of enhanced quantum diffusion at low temperature, in contrast to Cu and Al which also have f.c.c. structure. The static line width for muons in Pt is an order of magnitude less than in Cu, confirming that the dynamic range for such measurements is effectively extended by over a decade by the pulsed nature of the source.

## 7. Cold Neutrons

Just as the "old" conventional wisdom about pulsed sources asserts that hot neutrons are the major advantage, so also it says that cold neutron studies are not effectively performed on pulsed sources. And whereas the assertion on hot neutrons is found to be merely incomplete - as illustrated by many examples above - the statement on cold neutrons is demonstrably wrong. Experience at all operating pulsed sources has clearly demonstrated that they are indeed powerful engines for cold neutron diffraction and spectroscopy.

For example, reflectometry has been an outstanding success at pulsed sources world-wide. Taking advantage of the fixed geometry (which eases corrections) and low backgrounds, a tremendous amount of new science has been performed over a very wide range of chemistry, physics, materials science and biology. Through reflectometry, we have our first reliable view of the structure of surfactants at the air-liquid interface, polymer interdiffusion, and thin magnetic layers to list but three of a myriad possible examples. Moreover, the field is far from static, with new developments for example in liquid-liquid and liquid-solid interface studies, and exploration of the non-specular scattering. More comprehensive reviews can be consulted for detailed examples[32].

High resolution spectroscopy with pulsed cold neutrons has been a major success, led by the IRIS instrument at ISIS and LAM-80 at KEK. Both instruments have seen major improvements which have improved greatly the quality of spectra and opened up new areas. An example from KEK explores rotational tunnelling of a methane monolayer adsorbed on a graphite surface[33]. There are three spin species of the $CH_4$ molecule, the interconversion between them being forbidden. However, adding oxygen as a magnetic impurity catalyses the conversion. Fig 17(left) shows the non-equilibrium tunnelling spectrum at 0.32K, while fig 17(right) shows the effect of doping with 1% $O_2$: the impurity catalyses the attainment of equilibrium. Further work is planned to follow the time evolution to clarify the spin conversion mechanism.

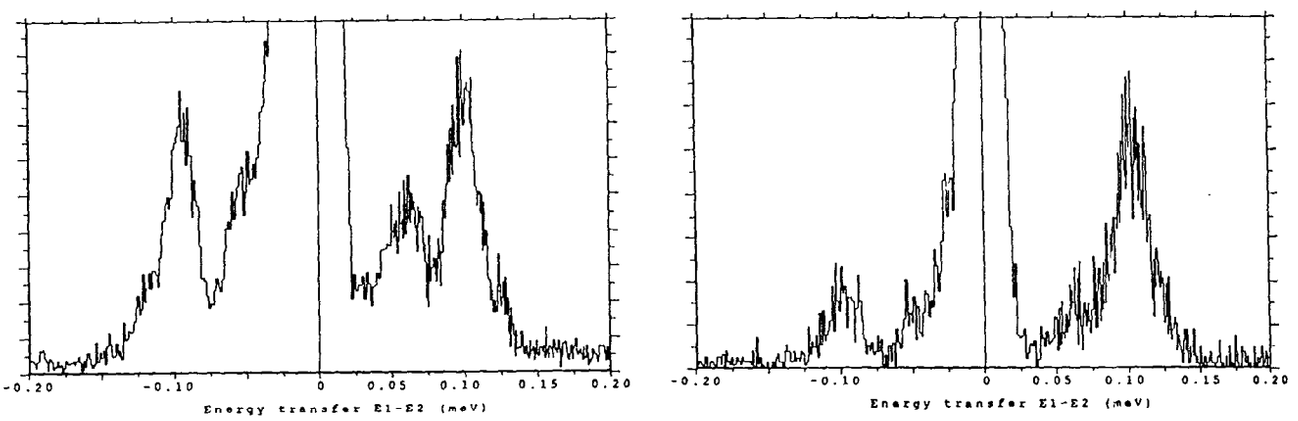


**Figure 17:** Rotational tunnelling spectra obtained at 0.32K for a $CH_4$ monolayer on graphite. Left: pure monolayer; right: doped with 1% $O_2$.

Because neutrons can be used to probe both structure and dynamics of a given system, lipservice has often been paid to the possibility of performing simultaneous elastic and inelastic experiments on the same sample. This is particularly appropriate for systems which are prepared in-beam, and when the conditions of production cannot necessarily be reproduced exactly for experiments on different instruments. Because a diffraction pattern can be measured in a single direction on pulsed sources, simultaneous diffraction and spectroscopy measurements are particularly suited to them. An example from IRIS - in which the diffraction detector was a single helium tube - is shown in Fig 18. The system is cesium intercalated graphite, to which is added increasing amounts of ammonia, which interacts directly with the cesium. Before adding $NH_3$ (x=0.0), two d-spacings show in the diffraction

pattern, and only the elastic line is evident in the inelastic spectrum. As $NH_3$ is added, an additional diffraction line begins to appear, while the inelastic spectrum shows a pair of tunnelling lines plus the free rotor line. Above x=0.42, further changes occur in both diffraction and inelastic signals, and these changes continue up to the maximum x=1.90. An interpretation of what is happening can be offered which involves the information obtained from the diffraction pattern[34].

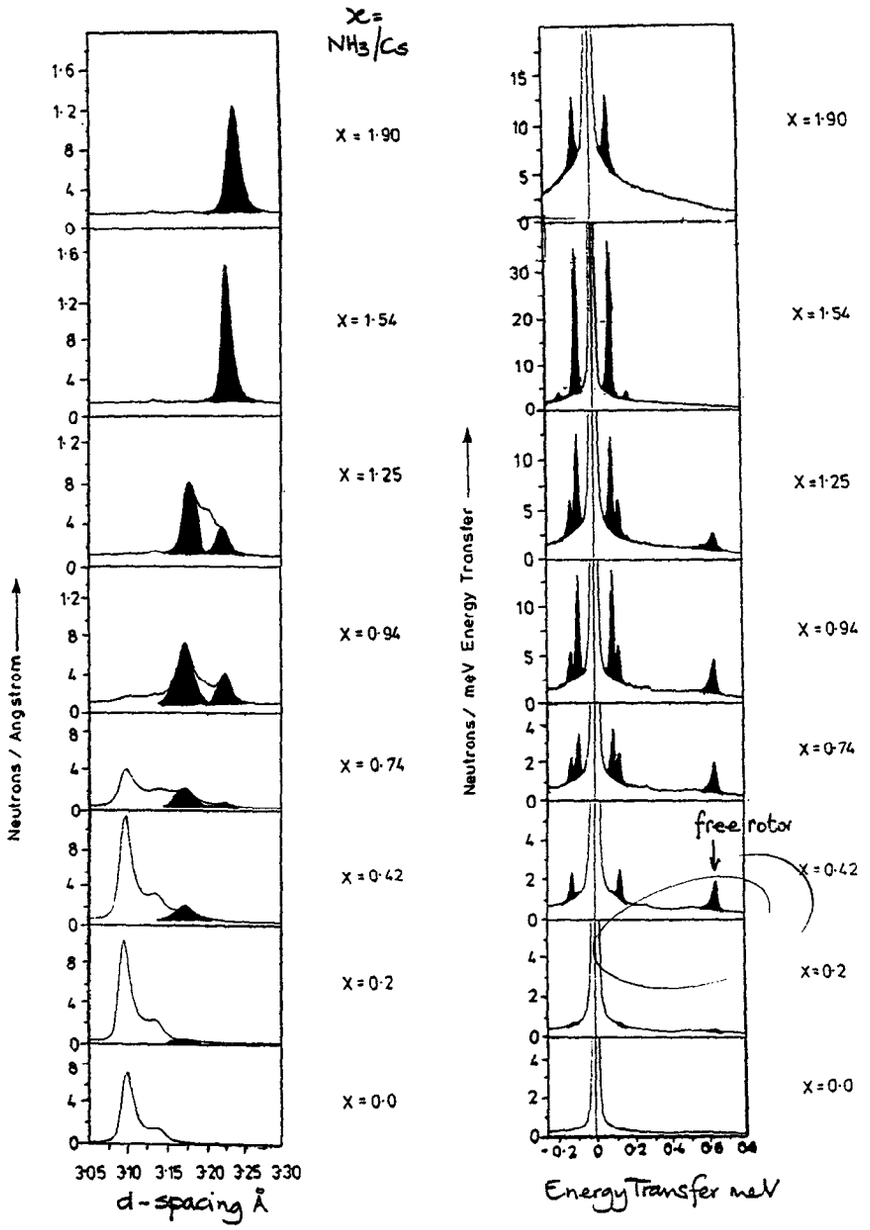


**Figure 18.** The tunnelling spectrum of Cs-intercalated graphite as the fraction x of $NH_3$ is increased (right). The left hand figure shows part of the diffraction pattern taken simultaneously, and assists in interpreting the tunnelling results.

A further example of the power of cold neutrons on pulsed sources is again from IRIS, but using only the diffraction detector to do long d-spacing crystallography. Figure 19 shows the pattern for $FeVO_4$ at 5K, with the magnetic peaks labelled. This spectrum has a good resolution of $\Delta d/d \sim 2.5 \times 10^{-3}$, uses wavelengths up to 18Å, and was taken in 4 hours. It is therefore possible to follow the two magnetic transitions as the temperature is raised, and more details of this are given elsewhere in these proceedings[35].

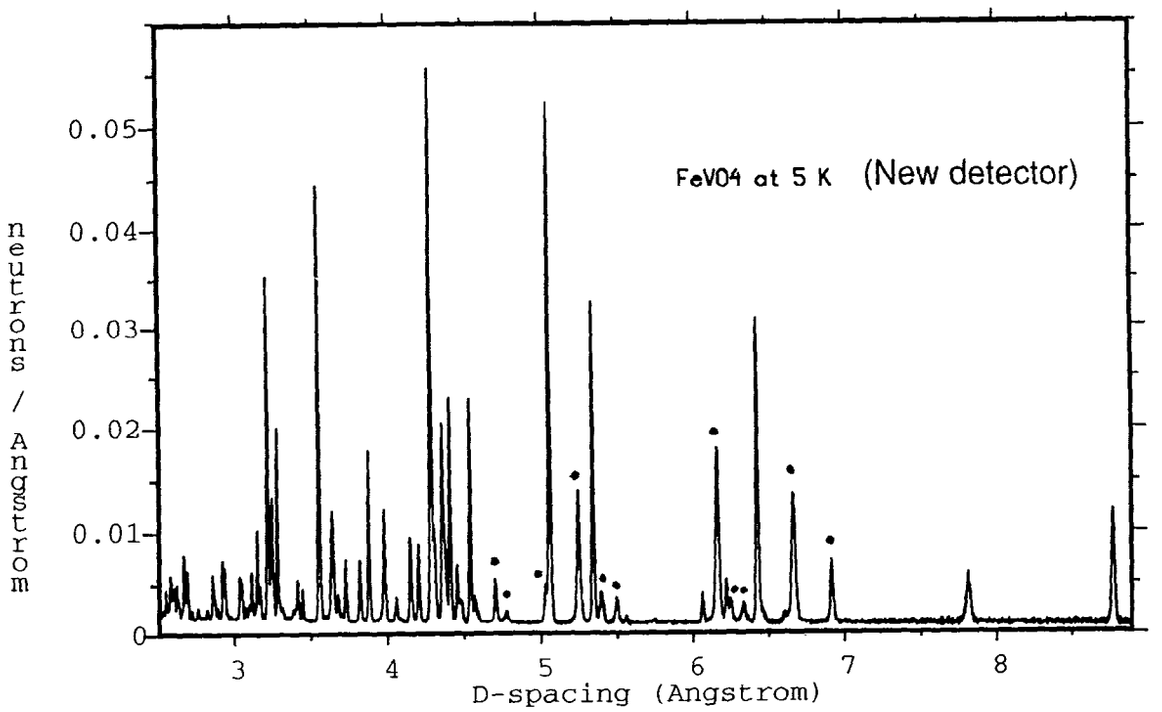


**Figure 19:** Magnetic ordering in $FeVO_4$ at 5K, taken on the inelastic spectrometer IRIS. The right hand edge of the spectrum corresponds to 18Å neutrons.

Long wavelength diffraction on pulsed sources is a very new area of work which promises much. In addition to the combined elastic and inelastic experiments and magnetic scattering examples above, other uses have included solution of "large" unit cell crystal structures and quality control of microgram samples of magnetic multilayers. More experiments are waiting to be done to further explore the potential of the technique.

## 8. Concluding Remarks

I am acutely aware that I have missed out much of importance in this rush through some of the highlights of the past few years of pulsed source science. This implies no value judgements. Reflectometry and liquids have only been touched upon, yet outstanding pulsed neutron science has been done in both areas. Single crystal diffraction - for which pulsed sources have major advantages, particularly in diffuse scattering studies - and small angle scattering - where the wide dynamic range is a big plus - have not even been mentioned. Perhaps the necessity to exclude so much just underlines the health and vigour of the science coming from pulsed sources, auguring well for the future.

A future which we are, of course, already preparing for. Discussions - both in Europe and the U.S.A - on a next generation pulsed source have raised the prospect of even more exciting new science, hopefully early in the next millennium. On a shorter timescale, new developments in instrumentation continue to widen the new science pulsed sources can tackle. For example, the design of the proposed MAPS instrument at ISIS was built on experience of utilising

existing instruments designed for powder measurements to tackle the difficult problems of efficient measurement of single crystal excitations.

We are still on not just one, but on several growth curves - of source strength, of instrumentation, and of learning how to exploit optimally this kind of source. Nethertheless, perhaps we now **can** say that pulsed sources have come of age.

## 9. Acknowledgements

This tour visited some of the high spots of pulsed sources as seen by me, but helped by Viktor Aksenov, Bruce Brown, Hiro Ikeda, Jim Jorgensen, Roger Pynn and many of my ISIS colleagues. The blame for the choice falls on me, the gratitude for producing so much to choose from goes to everyone else.

## References

1. P A Egelstaff, in Advanced Neutron Sources 1988, ed. D. K. Hyer, Inst. of Physics, Bristol, p.881 (1989).

2. R Osborn, K A McEwen, E A Goremychkin and A D Taylor, Physica B **163**, 37 (1990).

3. R Osborn, E Balcar, S W Lovesey and A D Taylor, in Handbook on the Physics and Chemistry of Rare Earths, eds K A Gschneider and L Eyring, 1991.

4. T G Perring, G L Squires, A D Taylor, R Osborn and Z A Bowden, in ISIS 1989, ed. A D Taylor, Rutherford Appleton Laboratory, RL-89-050, 1989, p. A116.

5. A T Boothroyd, T G Perring, A D Taylor, D McKPaul and H A Mook, J. Magn. Magn. Mater. **104,** 713 (1992).

6. P W Mitchell, R T Heap and J R Lowden, in ISIS 1993, ed C C Wilson, Rutherford Appleton Laboratory, RL-93-050, 1993, p.A256.

7. S M Hayden, G Aeppli, R Osborn, A D Taylor, T G Perring, S W Cheong and Z Fisk, Phys Rev Lett **67**, 3622 (1991).

8. T G Perring, G Aeppli, C Broholm and S Lee, in ISIS 1993, ed C C Wilson, Rutherford Appleton Laboratory, RL-93-050, 1993, p.A261. See also p.83.

9. S E Nagler, D A Tennant, R A Cowley, T G Perring and S K Satija, Phys. Rev. **B44**, 12361 (1991).

10. T R Sosnick, W M Snow, P E Sokol, and R N Silver, Europhys. Lett. **9**, 707 (1989).

11. P Postorino, F Fillaux, J Mayers, J Tomkinson and R S Holt, J Chem. Phys. **94**, 4411 (1991). See also F Fillaux, J Tomkinson and J Mayers in ISIS 1993, ed C C Wilson, Rutherford Appleton Laboratory, RAL-93-050, 1993, p. A302.

12. See for example: W I F David, W T A Harrison, J M F Gunn, O Moze, A K Soper, P Day, J D Jorgensen, D G Hinks, M A Beno, L Soderholm, D W Capone II, I K Schuller, C U Segre, K Zhang and J D Grace, Nature **327**, 310 (1987).

13. See for example: I K Schuller and J D Jorgenson, Mater. Res. Soc. Bull, Jan 1989, P.27; J D Jorgensen, M A Beno, D G Hinks, L Soderholm, K J Volin, C U Segre, K Zhang and M S Kleefisch, Phys. Rev. **B36**, 3608 (1987).

14. W I F David, in Proc. MRS Symposium on Neutron Scattering for Materials Science, Boston, November 1989, eds M Shapiro, S C Moss and J D Jorgensen, MRS Proc. **166**, 41 (1990). W I F David, R M Ibberson, G A Jeffrey and J R Ruble, Physica **B180/181**, 597 (1992).

15. W I F David, personal communication. See also ISIS 1993, ed C C Wilson, Rutherford Appleton Laboratory, RL-93-050, 1993, p.11.

16. W I F David, R M Ibberson, J C Matthewman, K Prassides, T J S Dennis, J P Hare, H W Kroto, R Taylor and D R M Walton, Nature **353**, 147 (1991).

17. W I F David, R M Ibberson and T Matsuo, Proc. Roy. Soc. Lond. **A442**, 129 (1993).

18. S J L Billinge and T Egami, in Lattice Effects in High Tc Superconductors, ed. Y Bar-Yam, World Scientific 1992.

19. W F Kuhs, J L Finney, C Vettier and D V Bliss, J. Chem. Phys. **81**, 3612 (1984).

20. J D Jorgensen, R A Beyerlin, N Watanabe and T G Worlton, J. Chem. Phys. **81**, 3211 (1984).

21. H Takahashi, J D Jorgensen, B A Hunter, R L Hitterman, Shiyou Pei, F Izumi, Y Shimakawa, Y Kubo and T Manako, Physica **C191** 248 (1992).

22. J M Besson, J R Nelmes, J S Loveday, G Hamel, P Pruzan and S Hull, High Press. Res. **9**, 179 (1992).

23. R J Nelmes and J M Besson, in ISIS 1993, ed C C Wilson Rutherford Appleton Laboratory, RAL-93-050, 1993, p.97.

24. G L Povirk, M G Stout, M Bourke, J A Goldstone, A C Lawson, M Lovato, S R MacEwen, S R Nutt and A Needleman, Acta Metal. Mater. **40**, 2391, (1992).

25. A K Soper and J Z Turner, Int. J. Mod. Phys. **B7**, 3049, (1993).

26. A M Balagurov, G M Mironova, V E Novozchilov, A I Ostrovnoy, V G Simkin and V B Zlokazov, J. Appl. Cryst. **24**, 1009 (1991).

27. H Nojiri, M Motokawa, N Nishida and Y Endoh, Physica **B180/181**, 31 (1992).

28. M Mino, M Arai and M Motokawa, to be published.

29. U E Steigenberger, M Hagen and G Eckold, this proceedings.

30. B Bodmann et al, Phys. Lett. **B280**, 198 (1992). See also ISIS 1993, ed C C Wilson Rutherford Appleton Laboratory, RAL-93-050, 1993, p.51.

31. S W Harris, O Hartmann and R Hempelmann, J. Phys. :Condens Matter **3** 5665 (1991).

32. J Penfold and R K Thomas, J. Phys. :Condens Matter **2**, 1369 (1990).

33. A Inaba, T Shirakami, K Shibata, and S Ikeda, KENS Report -IX, Japan National Laboratory for High Energy Physics, 1993, p.186.

34. C J Carlile, I Mc L, Jamie, G Lockhart and J W White, Molec. Phys. **76**, 173 (1992).

35. J B Forsyth, C Wilkinson, C J Carlile and P S R Krishna, personal communication.

**Reference Instrument Complement for IPNS Upgrade***

R. K. Crawford, for the Argonne Neutron Scattering Staff
Argonne National Laboratory, Argonne, IL 60439

ABSTRACT

A feasibility study for a new 1 MW pulsed neutron source has recently been completed at Argonne. As part of this feasibility study, an instrument package to instrument 24 of the 36 beam ports has been considered. This complement of instruments is outlined, and details of some of the instruments are discussed. Developments required before some of these instruments can be built are also indicated.

## I. Introduction

During the past year we at IPNS have been involved in analyzing the feasibility of the construction of a 1 MW pulsed neutron source, referred to as IPNS Upgrade, and in developing a workable design concept for such a source.[1] As the first part of this process, it was necessary to investigate the requirements imposed on such a source by the various types of neutron scattering instruments which are likely to be operated there. A list of 20-30 instruments was drawn up by the neutron scattering scientists at Argonne, including instruments which covered a broad spectrum of capabilities and which they would like to see at such a source. Realistic concepts for most of these instruments, based on currently available technologies, were developed to the point where the optimal source parameters (source pulse repetition rate, moderator type, angular separation between beamlines, etc.) could be assessed; this information was then used to fix the source parameters. Once the accelerator and target station concepts were more fully developed, it was possible to set up a fairly detailed Monte Carlo model of the target/moderator/reflector assembly and to use this model to calculate the expected intensities from each of the moderators. The instrument concepts were then re-evaluated to assess the instrument performance, and where necessary, the instrument parameters were adjusted to provide improved performance. The requirements imposed at these performance levels for various instrument components were then assessed to identify any problem areas and to provide realistic cost estimates. The various steps in this process are covered in some detail in the following sections.

## II. Choice of Source Parameters

The preliminary analysis of a reference set of instruments showed that very few could be optimized for operation at source pulsing frequencies greater than 30 Hz. A number of the instruments were well suited to 30 Hz operation, and nearly all of the remainder could be optimized for operation with a 10 Hz source pulsing frequency. This analysis resulted in the requirement that the primary operation of the accelerator systems should be at 30 Hz, with the proton pulses from the synchrotron being multiplexed between two target stations. One of these

* Work supported by U.S. department of Energy, BES, contract No. W-31-109-ENG-38.

target stations should receive every third pulse, and thus provide true 10 Hz operation. The other target station would receive two out of every three pulses, producing roughly twice the time-averaged neutron intensity as the 10-Hz station. However, the shortest interval between pulses governs frame-overlap conditions for the instruments, and for this high-intensity station the shortest interval would be that characteristic of 30 Hz operation, or 33 ms. This high-intensity station, referred to as the 30-Hz target station, is designed to be able to utilize the full 30 Hz accelerator output during periods when the 10-Hz station is not operating.

Analysis of the reference set of instruments also pointed out the need for a wide variety of moderator conditions; cryogenic and room-temperature moderators of different heights and volumes and with different types of poisoning and decoupling. Thus it was imperative that each target station provide positions for a number of different moderators, all having relatively high intensity, in order to permit optimal matching of the moderator performance to the requirements of each instrument. The horizontal-injection split-target geometry chosen, shown schematically in Fig. 1, allows the incorporation of six independent moderators in each target station (see the detailed discussion elsewhere in these proceedings). Two of these are tall moderators (20 cm x 10 cm) viewing the "flux trap" region between the two portions of the split target; these can provide greater intensity for those instruments which can utilize a large vertical divergence. The remaining four are wing moderators located above and below the front and back portions of the split target. The relatively high proton energy of 2.2 GeV distributes a considerable portion of the neutron production to the back target, so that the back wing moderators have good intensity (although not as high as that of the front wing moderators). Calculated time-averaged neutron beam currents at 1 eV from the moderators range from $2.4 \times 10^{13}$ n/sr-sec-eV to $4.7 \times 10^{13}$ n/sr-sec-eV, depending on the moderator position, geometry, and material, and on the degree of decoupling.

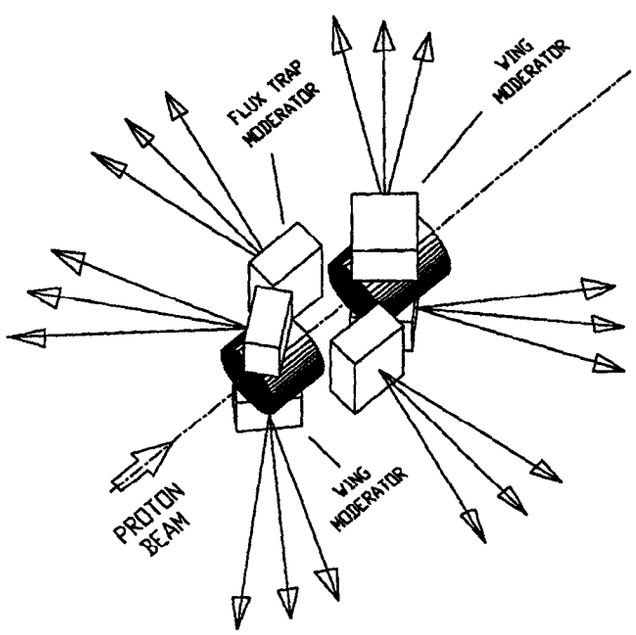


**Figure 1. Schematic representation of the split-target geometry for IPNS Upgrade.**

An analysis of heat deposition and radiolytic effects in the moderators has indicated that liquid $H_2O$, liquid $CH_4$, and liquid $H_2$ should all be viable moderator materials. Specific requirements regarding moderator material and configuration for the different instruments are addressed in the following section.

## III. Instrument Parameters and Performance

A reference set of instruments was selected for detailed study. This set was chosen to represent a reasonable mix of the types of science which might be expected at a source of this magnitude. These instruments were analyzed and roughly optimized based on the specified source performance. There are 27 instruments in this reference set, including two partially-instrumented development beams, and they occupy 24 of the 36 beam ports on the two target stations. This reference set includes 10 of the present IPNS instruments, which would undergo varying degrees of modification before relocation to the new source. All but one of these 27 instruments operates in the time-of-flight mode. The remaining instrument, a cold-neutron triple-axis spectrometer, operates in a quasi-steady-state mode making use of the relatively high time-averaged flux of cold neutrons from a large coupled liquid $H_2$ moderator at this source (equivalent to a reactor cold source flux of $5 \times 10^{13}$ n/cm$^2$-sec). The time structure of the source, while not used as the primary means of energy analysis in this instrument, provides discrimination against undesired orders from the monochromator and analyzer crystals as well as more general background reduction, resulting in an instrument with some unique capabilities.

Table 1 lists the 15 diffractometers and reflectometers in the reference set, and indicates their expected performance based on these source parameters. The five powder diffractometers are variously optimized for small samples (10-100 mg), high intensity, high resolution at 90° (0.2% in $\Delta d/d$), high resolution (0.08% in $\Delta d/d$), and for residual stress measurements on various types of samples. The general purpose small-angle diffractometer has an extremely broad dynamic range in Q, and it is complemented by a high-resolution instrument ($Q_{min} = 0.0005$ Å$^{-1}$) and by an instrument which can be reconfigured for various types of specialized small-angle scattering experiments (such as resonance small-angle scattering, measurements of inelastic effects, etc.). Additional diffractometers include a diffractometer for amorphous materials, and two single-crystal diffractometers, one of which is optimized for high real-space resolution (measurements made at Q values up to 30 Å$^{-1}$).

The suite of four reflectometers plus one reflectometer development beam is clustered on two beam ports, since the reflectometers are small and require only very narrow beams. This suite includes a polarized-neutron reflectometer, a general purpose reflectometer, a high-intensity reflectometer (reflectivities down to $10^{-4}$ in 1 min), and a reflectometer optimized for measurement of off-specular scattering. The latter three instruments have horizontal sample geometries, so that liquid samples can be accommodated.

Table 2 indicates the expected performance of the 10 remaining instruments, which are designed for inelastic scattering measurements. There are four chopper spectrometers including an instrument optimized for work with cold neutrons (better resolution but slightly lower intensity than IN5 at ILL) and one optimized for the study of excitations in single crystals, as

well as traditional general-purpose instruments in both low and high resolution versions. Included among the five crystal analyzer spectrometers is the cold-neutron triple-axis spectrometer which operates in a quasi-steady-state mode as discussed above. The other four crystal analyzer spectrometers are time-of-flight instruments. Two of these are optimized for

**Table 1 -- Reference Set of Diffractometers and Reflectometers**

| **Powder Diffractometers** | | | Range for d (Å) | Best Δd/d (%) | Measurement Time (min) |
|---|---|---|---|---|---|
| VSPD | very small samples (10-100 mg) | | 0.2 - 17 | 0.35 | 70 |
| SEPD[a] | high intensity | | 0.2 - 17 | 0.35 | 3 |
| GPPD[b] | medium resolution (excellent at 90°) | | 0.2 - 9 | 0.2 | 10 - 60 |
| HRPD | high resolution | | 0.2 - 5 | 0.08 | 50 |
| RSD | residual stress | (12-m position) | 0.3 - 6 | 0.55 | 50 |
| | | (25-m position) | 0.2 - 3 | 0.30 | 10 |

| **Small-Angle Diffractometers** | | $Q_{min}$ (Å$^{-1}$) | $Q_{max}$ (Å$^{-1}$) | Measurement Time (min) |
|---|---|---|---|---|
| SAND[a] | general purpose (wide Q range) | 0.002 | 2 | 1 - 90 |
| HRSAND | high resolution | 0.0005 | 0.4 | 60 -1800 |
| SPSAND | reconfigurable for special purposes | ---------- variable ---------- | | |

| **Amorphous Materials Diffractometer** | | Range for Q (Å$^{-1}$) | ΔQ/Q(%) | Measurement Time (min) |
|---|---|---|---|---|
| GLAD[a] | liquids and glasses | 0.07 - 120 | 1.2 - 10 | 10 - 50 |

| **Single-Crystal Diffractometers** | | Range for Q (Å$^{-1}$) | ΔQ/Q(%) | Measurement Time (min) |
|---|---|---|---|---|
| SCD[a] | general purpose | 0.9 - 17 | 0.6 - 0.9 | 20 - 200 |
| HQSCD | high real-space resolution | 2 - 30 | 0.4 | ~200 |

| **Reflectometers** | | Sample | Minimum Reflectivity | Measurement Time (min) |
|---|---|---|---|---|
| POSY-I[b] | polarized neutrons | vertical | $10^{-6}$ | 60 - 120 |
| POSY-II[b] | general purpose | horizontal | $10^{-7}$ | 60 - 120 |
| HIREF | high intensity | horizontal | $10^{-4}$ | < 1 |
| GREF | grazing incidence | horizontal | $10^{-7}$ | 60 - 120 |

[a] Transferred from IPNS with little change.
[b] Transferred from IPNS with some modification

medium resolution (70 μeV) and high resolution (1-5 μeV) measurements at low energies, one is optimized for relatively high resolution chemical spectroscopy at high energies, and one is a multi-angle spectrometer for the study of excitations in single crystals. The final instrument intended for inelastic scattering measurements is a spin-echo spectrometer. This instrument utilizes cylindrical field geometry, and is the time-of-flight counterpart to IN11 at ILL. Resolution is expected to be better than at IN11, while data rates are expected to be somewhat lower than at IN11.

Table 3 indicates the facility requirements (path lengths, moderator characteristics, source repetition rates) for this reference set of instruments. Based on these requirements, a reasonable assignment of the instruments to specific beam ports was found. This assignment, although not yet fully optimized, provided each instrument with its specified flight path lengths and grouped instruments sharing the same moderators in such a way as to require only small compromises from the optimum moderator characteristics. Figure 1 shows this arrangement of the reference set of instruments about the two target stations, and their possible locations within experimental halls which already exist at Argonne.

**Table 2 -- Reference Set of Inelastic Scattering Instruments**

| **Chopper Spectrometers** | | Range for $E_{inc}$ (meV) | $\Delta E/E_i$(%) | Measurement Time (h) |
|---|---|---|---|---|
| HRMECS[b] | high-resolution general purpose | 4 - 2000 | 2 - 4 | 2 |
| LRMECS[a] | low-resolution general purpose | 3 - 2000 | 4 - 7 | <1 |
| CNCS | high-resolution low energy | 0.3 - 20 | <1 | 12 |
| SCCS | excitations in single crystals | 50 - 2000 | ~1 | ~12 |
| **Crystal-Analyzer Spectrometers** | | Range for E (meV) | ΔE (meV) | Measurement Time (min) |
| TFCA | general purpose | 0 - 1000 | 0.5 - 30 | 20 - 80 |
| QENS[a] | quasielastic, medium resolution | 0 - 150 | 0.05 - 3 | 20 - 80 |
| HRBS | microvolt resolution | 0 - 10 | 0.005 - 0.06 | ~80 |
| MICAS | survey of single-crystal excitations | 0 - 20 | varies | |
| QSTAXC | cold-neutron triple axis (QSS) | | | |
| **Spin-Echo Spectrometer** | | Spectral Resolution (meV) | ΔQ/Q (%) | Measurement Time (h) |
| TOFNSE | TOF spin-echo, cylindrical geometry | $10^{-6}$ - $10^{-1}$ | 1.5 | 2 - 48 |

a Transferred from IPNS with little change.
b Transferred from IPNS with some modification
QSS Quasi-steady-state

**Table 3 -- Requirements for Instruments**

| 30-Hz Target | | | | | 10-Hz Target | | | | |
|---|---|---|---|---|---|---|---|---|---|
| Instrument | $L_i$(m) | $L_f$(m) | Moderator Specs[a] | | Instrument | $L_i$(m) | $L_f$(m) | Moderator Specs[a] | |
| SEPD | 12 | 1.5 | $CH_4$[b] | T | SAND | 12 | 2 | $H_2$ | C,N |
| GPPD | 25 | 1.5-4 | $CH_4$[b] | T | HRSAND | 20 | 5 | $H_2$ | C,N |
| HRPD | 50 | 2 | $CH_4$[b] | T | SPSAND | <40 | | $H_2$ | C,N |
| RSD | 25 | 1.5-3 | $CH_4$[b] | | POSY-I | 18 | <2 | $H_2$ | |
| VSPD | 12 | 0.75 | $CH_4$[b] | | HIREF | 18 | <2 | $H_2$ | |
| GLAD | 23.5[c] | 1.5 | $CH_4$ | T | POSY-II | 18 | <2 | $H_2$ | |
| SCD | 10 | 0.6 | $CH_4$[b] | | GREF | 18 | 5 | $H_2$ | |
| HQSCD | 30 | 0.7 | $CH_4$[b] | | REFD | 18 | | $H_2$ | |
| HRMECS | 18 | 4 | $CH_4$ | | CNCS | 20 | 4 | $H_2$ | |
| LRMECS | 12 | 2.5 | $CH_4$ | | HRBS | 30 | 3 | $H_2$ | T |
| SCCS | 16 | 4 | $H_2O$ | | TOFNSE | 16 | 4 | $H_2$ | C |
| QENS | 9 | <1 | $CH_4$[d] | T | DEVEL | | | $H_2$ | |
| TFCA | 16 | <1.5 | $CH_4$ | T | | | | | |
| QSTAXC | 17 | <2 | $H_2$ | C,T,N | | | | | |
| MICAS | 12 | 1.5 | $CH_4$ | | | | | | |

a Moderators are decoupled at 1 eV and poisoned unless otherwise indicated. C: coupled, T:can use a tall moderator, N:not poisoned.

b Could be $H_2O$.

c To low-resolution sample position.

d Could be poisoned $H_2$.

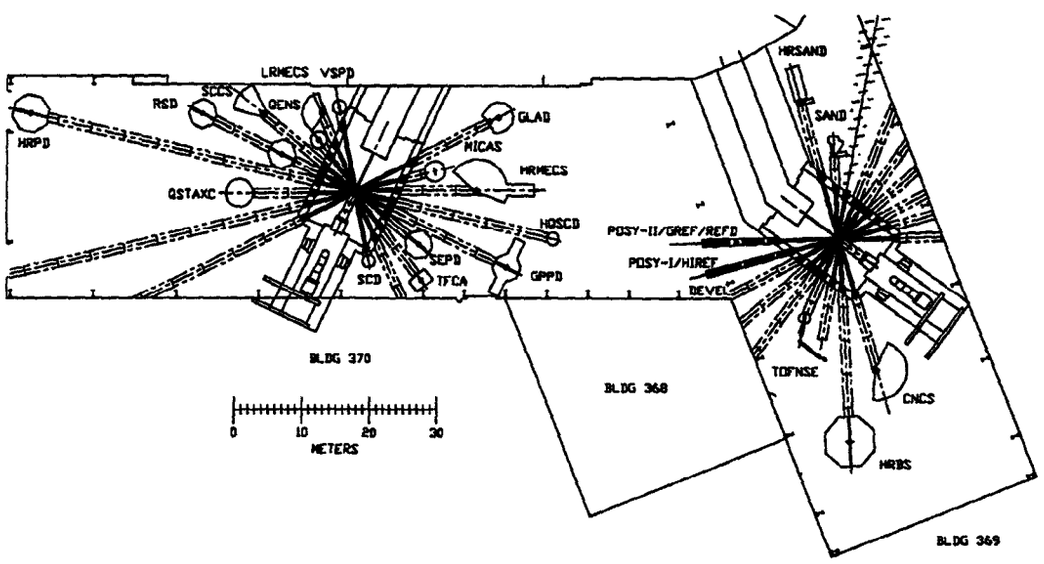


**Figure 2. Location of the reference set of instruments on the neutron beamlines.**

## IV. Requirements for Specific Instrument Components

The requirements for instrument components such as choppers, guides, beamline shielding, detectors, data acquisition, etc., were assessed for all the instruments in the reference set. With the exception of the detectors, all other components required for these 27 instruments appear to fall within the capabilities of current technology, although a number of areas were identified in which development efforts could lead to significant cost savings and/or improvements in performance. For example, considerable development will be required to produce reliable and cost-effective designs for the data acquisition electronics to handle the high data rates expected. Also, since the beamline shielding is a significant portion of the instrument cost, a development program to optimize the geometry and composition of this shielding will be worthwhile.

As an example of such assessments, Tables 4 and 5 indicate the detector requirements determined in this process. For this exercise, all detectors were considered to be $^3$He gas proportional counters, although other types of detectors such as scintillation detectors would work equally well in some (but not all) of these cases. Detector technology is currently available to meet all of the requirements for "standard" detectors indicated in Table 4. However, current

**Table 4 -- Standard[a] Detector Requirements**

| Instrument[b] | Number | Diameter (cm) | Length (cm) | Max rate per det (cts/sec)[c] Instantaneous | Time-avg. |
|---|---|---|---|---|---|
| SEPD | ~280 | 1.2 | 38 | ~$5\times10^4$ | ~$5\times10^3$ |
| GPPD | ~520 | 1.2 | 38 | ~$5\times10^3$ | ~$1\times10^3$ |
| HRPD | ~410 | 1.2 | 38 | ~$9\times10^2$ | ~$2\times10^2$ |
| RSD | ~250 | 1.2 | 38 | ~$4\times10^3$ | ~$7\times10^2$ |
| VSPD | ~560 | 0.6 | 19 | ~$2\times10^3$ | ~$3\times10^2$ |
| HRMECS | ~800 | 2.5 | 46 | ~$2\times10^5$ [d] | ~$3\times10^4$ [d] |
| LRMECS | ~160 | 2.5 | 46 | ~$7\times10^5$ [d] | ~$5\times10^4$ [d] |
| CNCS | ~1000 | 2.5 [e] | 25 | ~$4\times10^4$ [d] | ~$3\times10^3$ [d] |
| QENS | ~100 | 0.6 | 10 | ~$2\times10^3$ | ~$9\times10^1$ |
| HRBS | ~150 | 0.6 | 10 | ~$9\times10^1$ | ~$9\times10^0$ |
| TFCA | ~300 | 0.6 | 25 | ~$2\times10^3$ | ~$9\times10^1$ |
| QSTAXC | ~12 | 0.6 | 10 | ~$5\times10^4$ | ~$7\times10^2$ |
| MICAS | ~20 | 0.6 | 10 | ~$5\times10^4$ | ~$9\times10^3$ |
| TOFNSE | ~10 | 0.6 | 10 | ~$2\times10^2$ | ~$2\times10^1$ |

a Detectors are specified as cylindrical $^3$He gas proportional counters, but in some cases scintillation detectors such as those used on some instruments at ISIS can be substituted.

b Instruments not listed do not use any "standard" detectors.

c Scaled from IPNS rates where possible; otherwise estimated assuming the sample scatters 20% of the beam isotropically into a $4\pi$ solid angle.

d Maximum rates are for diffractometer mode (choppers removed). Rates in normal operation are much lower.

e This instrument uses "squashed" detectors with thickness ~1 cm and width ~3.5 cm.

**Table 5 -- Position-Sensitive Detector Requirements**

| Instrument[a] | Dimension | Number | Width (cm) | Length (cm) | Resolution (mm) | Max rate per det (cts/sec)[b] Instantaneous | Time-avg. |
|---|---|---|---|---|---|---|---|
| RSD | 2D | 4 | 30 | 30 | 2 | ~$1\times10^5$ | ~$2\times10^4$ |
| SAND | 2D | 1 | 40 | 40 | 4 | ~$2\times10^5$ | ~$7\times10^4$ |
| | 1D | 65 | 1.2 | 60 | 10 | ~$9\times10^3$ | ~$3\times10^3$ |
| HRSAND | 2D | 1 | 60 | 60 | 2 | ~$5\times10^3$ | ~$2\times10^3$ |
| | 1D | ~20 | 1.2 | 60 | 10 | ~$5\times10^2$ | ~$2\times10^2$ |
| SPSAND | 2D | 1 | 40 | 40 | 4 | ~$5\times10^4$ | ~$2\times10^4$ |
| GLAD | 1D | ~410 | 1.2 | 60 | 10 | ~$7\times10^3$ | ~$3\times10^3$ |
| SCD | 2D | 3 | 30 | 30 | 3 | ~$1\times10^6$ | ~$1\times10^5$ |
| HQSCD | 2D | 1 | 30 | 30 | 1.5 | ~$1\times10^5$ | ~$1\times10^4$ |
| POSY-I | 1D | 1 | 5 | 10 | 2 | ~$1\times10^3$ | ~$4\times10^2$ |
| POSY-II | 1D | 1 | 5 | 20 | 2 | ~$6\times10^3$ | ~$2\times10^3$ |
| HIREF | 1D | 1 | 5 | 10 | 2 | ~$1\times10^5$ | ~$3\times10^4$ |
| GREF | 2D | 1 | 60 | 60 | 2 | ~$1\times10^4$ | ~$3\times10^3$ |
| REFD | 2D | 1 | 3 | 3 | 0.5 | ~$1\times10^3$ | ~$4\times10^2$ |
| HRMECS | 1D | ~40 | 2.5 | 100 | 20 | ~$1\times10^5$ [c] | ~$2\times10^4$ [c] |
| LRMECS | 1D | ~30 | 2.5 | 46 | 20 | ~$8\times10^5$ [c] | ~$6\times10^4$ [c] |
| CNCS | 1D | ~30 | 2.0 [d] | 60 | 20 | ~$4\times10^4$ [c] | ~$3\times10^3$ [c] |
| SCCS | 1D | ~256 | 2.5 | 100 | 20 | ~$4\times10^4$ [c] | ~$8\times10^3$ [c] |

[a] Instruments not listed do not use any position-sensitive detectors.

[b] Scaled from IPNS rates where possible; otherwise estimated assuming the sample scatters 20 % of the beam isotropically into a $4\pi$ solid angle.

[c] Maximum rates are for diffractometer mode (choppers removed). Rates in normal operation are much lower than this.

[d] This instrument uses "squashed" cylindrical linear-position-sensitive detectors with thickness ~0.8 cm and width ~2 cm.

technology cannot provide all of the required position-sensitive detectors indicated in Table 5. In particular, the 2D detectors for HRSAND, SCD, HQSCD, and GREF all have either counting-rate requirements or resolution requirements which exceed the capabilities now available. Thus some improvements in detector technology will be required if these four instruments are to perform at their full potential at this 1 MW source. Fortunately, developments which are in progress[2] show promise of providing detector performance at these levels by the time these detectors would be needed.

## References


1. Full details of this feasibility study will be published as an Argonne Report.
2. A. Oed. *Nucl. Instrum. Meth.* **A263**, 351-359 (1988); P. Geltenbort and A. Oed. Proceedings of SPIE's 1992 International Symposium on Optical Applied Science and Engineering, San Diego, Calif., July 19-23, 1992, Vol. 1737, pp. 289-293.

# A European Network for Neutron Instrumentation

M W Johnson, Rutherford Appleton Laboratory, Chilton, Didcot, Oxon OX11 0QX

*Abstract*

A research proposal is described which has recently received EC funding. The proposal involves 7 European laboratories: HMI (Berlin), University of Rome, ILL (Grenoble), The Delft University of Technology, The Risø National Laboratory, EMBL (Grenoble) and RAL (Oxford, co-ordinator). The aim of the research is to provide the basis for improvements in neutron instrumentation in 3 areas: neutron detectors, neutron polarisation and data verification and visualisation.

*Introduction*

The network described here was conceived during a planning meeting for a next-generation neutron source, the ESS, held in 1992 at The Cosener's House, Abingdon. Although a new generation of neutron sources may be planned, the provision of new sources has a long lead time (10-20 years), and there is a need to improve the existing infrastructure of neutron instruments in the intervening period. The aims of the network are therefore twofold:

- to improve the instrumentation of European neutron facilities
- to train young scientists in the techniques of neutron instrumentation

It will achieve these aims by undertaking research in 3 key areas:

- detectors
- polarisation devices
- visualisation software

Each of these areas was chosen because of the major impact it will have on neutron instrumentation, and because in each area there are new ideas and techniques that require development. These 3 areas underpin the current development of neutron instrumentation and the overlapping expertise of each partner will result in an effective network of 7 leading European laboratories (see Table 1).

*Detectors*

Because of the high cost of neutron detectors, many existing facilities are equipped with less than their optimal detector complement. One of the central aims of this programme will therefore be the development of cheaper neutron detector technologies, together with improvements in their performance.

The programme on detectors will be the largest activity in the network, drawing together the expertise from 6 of the participating laboratories. Three key areas have been identified which will be studied:

- novel solid state detectors
- new scintillators/converters
- neutron image plate development

At the Instituto Nazionale di Fisica della Materia (INFM) in Italy the exciting possibilities of using amorphous silicon as a neutron detector will be explored. Amorphous silicon diode material, when coated (or doped) with a suitable neutron converter offers the promise of both fast and inexpensive neutron detectors. This possibility has recently been demonstrated by American research workers, although much work remains to be done in optimising both the materials and signal processing for such devices. The programme that will be followed in Italy will include:

- Studying the performance of position sensitive detectors based on a-Si:H diodes using various neutron-ionising converters. In this research, particular care will be devoted to developing position sensitive detectors (PSDs) with good efficiencies over a wide energy range.

- Investigating the possibility of building PSDs which are built up not by a single diode but by a stack of diodes. This solution is very important because it will allow, for example, the use of very thin boron coating so to accomplish both a high neutron absorption and high probability for $\alpha$ particle emission from the converter. In this way a PSD could be made with a high efficiency over a wide neutron energy range.

At Delft, in the Netherlands, new ideas on scintillator detectors will be pursued. In particular new inorganic neutron scintillators and techniques for the position sensitive detection of light will be explored.

Studies will be made of glasses and crystals containing Li and/or B, in low atomic-number scintillators to keep the background gamma ray efficiency small. Luminescence will be based on fast transfer of the excitation energy, produced by the neutron interaction in a host material, to low concentration rare earth ions. The intensity depends strongly on the host material as the efficiency of the transfer is governed by;

- the presence of competitive nonradiative processes that may occur in the host material and,
- the position of the 5d level of the rare earth ion in relation to the energy levels (bands) of the host material.

The main research task will be to find an optimal combination.

For emission in the UV region below 220 nm it is possible to use wire chamber technology or gas amplification micro strip detectors for the position sensitive detection of light (for which the response can be very fast). We will work on the development of the last type of detector since wire chamber technology is sufficiently understood.

At the Institut Laue-Langevin (ILL) in France, the detector programme will focus on the development of a neutron image plate. This is a neutron-sensitive analogue of the image plate which is increasingly being employed in X-ray diffraction. In order to use these image plates as neutron detectors, a scintillator is necessary to convert neutrons to electromagnetic radiation. A comprehensive experimental study to include the choice of scintillator materials, the production of special phosphors suitable for neutron diffraction and their characterisation using neutron beams will be pursued.

The considerable expertise of the Risø Laboratory and the Rutherford Appleton Laboratory (RAL), based on long standing programmes in neutron detectors, will be used to assist these programmes.

*Polarisation*

Polarised neutrons are crucially important in the study of spin dependant processes, such as occur in magnetism. Existing polarising devices (crystals, mirrors and super-mirrors) become increasingly inefficient below 3Å. The use of polarised $^3$He filters is an alternative approach, which could revolutionise the field of polarised neutron spectrometry. It could provide vastly improved intensities, particularly for polarisation analysis at thermal neutron wavelengths (1-3Å). Small filter units using this technique have been tested but there remains a variety of technical/physical problems to be solved, before a system of this kind could be of practical use. The research will focus on one of the schemes of optical pumping $^3$He, (i.e. via the exchange scattering on Rb vapour). The first goal is to set up a high power, stable laser facility on a neutron beam, in order to test and optimise various $^3$He cells. The goal of the test is to find the optimal efficiency and stability of working polarising filters of this kind, and to gain operational experience, a prerequisite for actual utilisation.

*Data Visualisation and Visualisation Software*

Four host laboratories (Table 1) will be involved, with an RA being employed at the Rutherford Appleton Laboratory in the UK. The objective of this research is to design software able to handle efficiently the complexity of data now being produced by neutron instruments.

Many spectrometers now employ large, positive sensitive detectors and routinely produce data sets of between 5-20 Mbytes. On some instruments, particularly those on white-beam pulsed sources, such data sets may be produced in minutes rather than hours. While raw computing power has increased significantly over recent years, there has not been a corresponding improvement in the software necessary to 'visualise' complex data. The efficient guiding of resource-limited neutron experiments requires specialised software, tailored closely to the instrument's and experimenter's needs. An

example of such successful software is in the 'GENE' language developed at RAL for manipulating 2-d spectra (e.g. I vs. momentum transfer Q, or energy ω).

An equivalent language for 3-d (I vs. $Q_x$,$Q_y$), 4-d (I vs. Q) and 5-d (I vs. ω,Q) intensity maps is now required and the research will concentrate on:

- selecting suitable visualisation techniques for the problems described above;
- defining the data analysis language;
- producing selective software prototypes.

The related problem of automatic data fault recognition (data verification) will also be investigated, since this now plays an important part in maintaining the efficient throughput of neutron experiments. A number of avenues will be explored. Many instruments now contain hundreds of individual detectors (e.g. MARI, SANDALS at ISIS) and manual surveys of the data are impractical. Such surveys are important since individual detector errors may be missed when the data is merged with that from other detectors. Instruments vary widely in their data rates and data 'profile'. Thus a different technique will be required to detect errors in sparse data than in intense data, for example. Suggested methods for testing, in increasing order of complexity, are:

- comparing total counts
- comparing information content
- comparing 'shape' using statistical or neural network techniques

The possibility of using neural networks to 'learn' normal data analysis patterns is being explored elsewhere, and could prove an effective tool for diagnosing error conditions within faulty neutron instrumentation.

Table 1

| Institute | Detectors | Polarisation | Visualisation |
|---|---|---|---|
| Delft (NL) | • | | |
| HMI (DE) | | ❷ | • |
| ILL (FR) | • | • | |
| INFM (I) | ❷ | | • |
| Risø (DK) | • | | • |
| RAL (GB) | • | | ❷ |
| Symbol: | • = participation | ❷ = 2yr RA | |

The total network, encompassing the interlinked areas of neutron instrumentation described above, will therefore employ 3 RAs. They will receive excellent training, in the techniques and technologies described at leading research centres throughout Europe. It is also clear that, resources permitting, further fellows could build upon this foundation and, following the creation of the network, will be bid for individually.

# The use of chopper spectrometers for cold-to-epithermal neutron scattering at IPNS

C.-K. Loong, L. I. Donley, G. E. Ostrowski, R. Kleb,
J. P. Hammonds, L. Soderholm, and S. Takahashi*
Argonne National Laboratory, Argonne, Illinois 60439-4814, U. S. A.

## Abstract

A multi-detector chopper spectrometer enables measurements of the scattering function S(Q,E) to be made over a wide range of momentum and energy transfer (Q,E). The application of pulsed-source chopper spectrometers for inelastic measurements at thermal and epithermal energies (50 meV < E < 1000 meV) is well known. Recently at IPNS, we have extended the energy-transfer region down to about 0.5 meV with a resolution of the order of 150 μeV. It is made possible by utilizing the cold-neutron incident spectrum of the 100 K methane moderator in conjunction with a dual beryllium-body rotor system. Neutron incident energies can be changed efficiently over the 4 to 1000 meV region while maintaining an undisturbed sample environment. We describe the operation of the IPNS chopper spectrometers (HRMECS and LRMECS), the instrumental resolution and the background-suppression performance. The capability of measuring inelastic features from 0.5 to 100 meV with an energy resolution of $\Delta E/E_0 = 2.5\%$ is demonstrated by experimental results of crystal-field excitation spectra of a high-$T_c$ superconductor $ErBa_2Cu_3O_7$. Preliminary data of quasielastic scattering from a room-temperature molten salt $AlCl_3$-EMIC are presented.

## I. Introduction

The dynamics of atomic and electronic systems of condensed matter is characterized by correlation functions over a large space-time domain. Neutron spectroscopy is capable of probing the dynamic response in a time scale of $10^{-8}$ to $10^{-14}$ sec, corresponding to an energy range of approximately 1 μeV to 1 eV. The coverage of spatial correlations, in terms of neutron momentum transfer $\hbar Q$, is determined by the scattering kinematics and the range of energies used. As far as experimental applications are concerned, the useful dynamic range of a spectrometer is affected by both the neutron source spectral distribution and the instrumental design. These factors have led to the design of a variety of instruments which are optimized individually for measurements in different regions of the (Q,E) space. As a result, experimenters are often required to perform measurements on the same samples using different spectrometers in order to collect the data needed to understand a system. For example, electronic transitions between states of transition-metal ion multiplets vary from a fraction of a milli-electron volt to many electron volts. Diffusional motion, atomic vibrations and deep-inelastic single-particle excitations within a molecular system have characteristic energies spanning decades in an energy

scale. In view of the need, frequently encountered, to study the properties of a system on several different spectral and dynamic scales, using a single instrument would ease efforts in scheduling, experimental set-up, data normalization and interpretation. This paper describes the results in applying the IPNS chopper spectrometers in a range of energies widely extended from what was originally conceived.

A pulsed-source multi-detector chopper spectrometer is a versatile instrument for two main reasons: 1) large fluxes of cold-to-epithermal neutrons are available from a pulsed source equipped with cold moderators; and 2) chopper (rotor) systems are an effective means to select neutron incident energies from a few meV to 1 eV. The applications of pulsed-source chopper spectrometers for inelastic measurements at thermal and epithermal neutron energies were recognized in the beginning of pulsed-source development.[1] Their routine usage in the cold-neutron regime, on the other hand, has been realized only recently. We will describe the operation of a dual chopper system, which enables cold-to-epithermal neutron scattering on the IPNS chopper spectrometers HRMECS and LRMECS, and present some recent scientific results of quasielastic, near elastic and inelastic scattering.

## II. Experimental Details

A chopper rotates at an angular frequency that is a multiple of the source repetition rate, i.e., from 30 Hz (fundamental) to 270 Hz (the 9th harmonic) at IPNS. The chopper aperture lines up with the source several times during the 33⅓ msec between successive bursts, but the curved multi-slits of the chopper window select a narrow energy-band of neutrons only at one opening. The neutron-absorbing slats are effective for energies up to a few eV. Higher-energy (fast, in the KeV range) neutrons at the time of the prompt burst are removed by scattering from the beryllium body of the rotor. Conceptually only one chopper is sufficient for the production of a monochromatic neutron beam. Unfortunately, the source also produces a small component of time-independent fast delayed neutrons that can pass through the chopper slit package at every opening. These fast neutrons scattered by substances intercepting the beam (container windows, samples, etc.), give rise to a background at the detectors with a time structure characteristic of the chopper's secondary openings, as shown in Fig. 1a. Moreover, the background level depends on the amounts of materials exposed to the beam, thus it cannot be corrected by using empty-cell runs.

### 1. $t_0$-choppers

A two-chopper system is called for to remedy the background problems. In this case a second, low-resolution chopper is placed upstream of the principle monochromating chopper to eliminate the secondary openings for delayed neutrons and to scatter prompt fast neutrons from the beam at a location farther from the sample than the principle chopper. The resulting background level, in a test run in 1987 as shown in Fig. 1b, improves significantly even though at that time the upstream chopper was not designed for optimal delayed neutron suppression. In 1988 the first background suppression chopper (coined "$t_0$-chopper", as opposed to the high-

resolution energy selecting "$E_0$-chopper") was fabricated and operated on the PHENICS chopper spectrometer at IPNS. The $t_0$-chopper has a slightly larger beryllium body than that of the $E_0$-chopper but has no slit package, (see Fig. 2). Both the $t_0$- and the $E_0$-choppers are mounted in identical housings and controlled by the same drive system. The $t_0$-chopper serves to remove the delayed and the prompt-pulse fast neutrons. Currently, all three chopper spectrometers at IPNS are equipped with similar $t_0$-choppers.

2. $E_0$-choppers

A unique feature of IPNS $E_0$-choppers is the large (up to 7.5 X 10 cm) aperture of the slit packages and the rather massive beryllium body, which provide effective stopping power for neutron removal. The disadvantage of such a design is the large energy required for high-speed rotation. The current drive system using mechanical bearings constrains the maximum speed to 270 Hz. An important criterion is to match the chopper opening time with the neutron pulse width so as to maximize the intensity without sacrificing the resolution. If a chopper is to be maintained at the maximum speed (always desirable in principle), it requires different slit packages for different energy selection, i.e., larger slit radii of curvature and tighter slits at higher energies. Six $E_0$-choppers have been built for the three chopper spectrometers at IPNS.[2] The energy resolution $\Delta E/E_0$ varies from about 4% at the elastic position for HRMECS and PHENICS (7% for LRMECS) to about 2% near the end of the neutron-energy-loss spectrum for HRMECS and PHENICS (4% for LRMECS). Better resolution, especially for $E_0 > 300$ meV, can be achieved by running with higher chopper speeds but this would require a new drive-control system.

3. Variable-speed dual chopper operation

Two major factors come into play for low energy ($E < 50$ meV) operations: 1) The pulse widths are broader so it allows a chopper window assembled with wider slits (and less curvature); and 2) The lower neutron speeds require much extended background-free time fields for energy analysis (e. g., over 20,000 μs for a 4-meV run on HRMECS). If a chopper maintains the same speed, say 270 Hz, a change of the neutron energy requires switching $E_0$-chopper during the experiment. More importantly, it becomes difficult to eliminate all the simultaneous openings of both the $t_0$- and $E_0$-choppers for fast delayed neutrons over such large time intervals.

The conditions for low-energy operation can be accommodated easily if the choppers can be run and controlled at lower speeds. An $E_0$-chopper that is optimized for high energy at 270 Hz operation becomes an efficient chopper for lower energies when its speed is reduced to lower harmonics of 30 Hz. At a lower angular speed, the sweeping time of the chopper slits across the beam increases and the curved slits transmit neutrons having a lower energy. Moreover, a lower chopper frequency reduces the number of secondary openings, which makes background control manageable over the larger time field (see Fig. 3). Changing chopper speeds takes a fraction of an hour as compared to a several hour job for switching choppers. Consequently, a variable-speed dual rotor system enables efficient operations between 4 to 1000 meV without a

significant loss of intensity or resolution. The sample environment is not disturbed throughout measurements using cold-to-epithermal neutrons.

In 1991 the chopper controller circuitry was modified to allow chopper rotation at any harmonics between 30-270 Hz.[3] We find that the IPNS 100 K methane moderators provide usable fluxes of neutrons for effectual experiments from 4 meV to 2 eV.[4] We show in Fig. 3 the neutron "time schedules" for 110 and 4 meV runs using the same $t_0$- and $E_0$-choppers on HRMECS. Table I lists examples of chopper speeds usable for HRMECS and LRMECS experiments over the 4 to 400 meV energy region.

Table I. Examples of chopper angular frequencies to be used for HRMECS and LRMECS experiments with incident energies ranging from 4 to 400 meV. The same $E_0$-chopper (the 250-3 rotor for HRMECS and the 160-2 rotor for LRMECS) is used throughout for each spectrometer.

| Incident energy | HRMECS | | LRMECS | |
|---|---|---|---|---|
| ( meV) | $t_0$-chopper (Hz) | $E_0$-chopper (Hz) | $t_0$-chopper (Hz) | $E_0$-chopper (Hz) |
| 4 | 90 | 30 | 60 | 30 |
| 8 | 30 | 60 | 60 | 60 |
| 20 | 30 | 90 | 60 | 90 |
| 40 | 60 | 90 | 90 | 120 |
| 60 | 60 | 150 | 120 | 180 |
| 80 | 60 | 150 | 120 | 180 |
| 110 | 90 | 210 | 120 | 210 |
| 140 | 90 | 210 | 150 | 240 |
| 170 | 90 | 240 | 150 | 270 |
| 200 | 90 | 240 | 150 | 270 |
| 250 | 90 | 270 | 150 | 270 |
| 400 | 90 | 270 | 150 | 270 |

## III. Results and Discussion

We present some recent HRMECS and LRMECS experimental results to illustrate the merits of performing measurements using cold-to-epithermal neutrons on the same spectrometer. Fig. 4 show the observed excitation spectra of a magnetic superconductor $ErBa_2Cu_3O_7$.[5] Four incident energies, 4, 8, 20 and 110 meV, were used to resolve transitions between the crystal-field states of the $Er^{3+}$ ionic ground multiplet which spans an 80-meV interval with uneven splittings (see Fig. 5). It is essential to perform experiments with a wide range of incident

energies at various temperatures in order to confirm the energy level structure. Furthermore, since the data were taken from the same spectrometer, the observed intensities were normalized in a straightforward manner, and the whole data set can be compared quantitatively with results from model calculation.[5]

Fig. 6 displays the quasielastic spectra for a room-temperature molten salt $AlCl_3$-1-ethyl-3-methyl imidazolium chloride (EMIC) measured by LRMECS with an incident energy of 4 meV.[6] The quasielastic scattering, measured as a function of Q from 0.2 to 2 $Å^{-1}$ at 25 ° C, provides information regarding to the diffusional motion of the molecular species in the liquid phase. The inelastic spectra[6] (not shown), measured with $E_0$ of 60, 160 and 400 meV at 25 K and room temperature, reveal features corresponding to collective excitations and internal molecular vibrations which afford a quantitative comparison with results of *ab initio* calculations.[7]

In summary, we describe the application of a dual chopper system on HRMECS and LRMECS for energy selections from the cold-to-epithermal neutron spectrum provided by the IPNS 100 K methane moderators. We also present some results of recent scientific studies which have taken advantage of this improved operation of the chopper spectrometers.

## Acknowledgment

We are indebted to many colleagues at Argonne for instrumental development and scientific collaborations. In particular, we wish to thank R. K. Crawford, J. M. Carpenter, P. E. Sokol, M.-L. Saboungi, D. L. Price, S. Kern, D. J. Leach and D. J. LePoire for many helpful suggestions and assistance. Work performed at Argonne National Laboratory is supported by the U. S. DOE, Office of Basic Energy Sciences, under the contract No. W-31-109-ENG-38.

## References:

* On leave from Nisshin Steel Co. Ltd., 7-1 Koya-shinmachi, Ichikawa, Chiba 272, Japan.
1. D. L. Price, in *Proceedings of the 1984 Workshop on High-Energy Excitations in Condensed Matter*, complied by R. N. Silver, Los Alamos National Laboratory Report LA-10227-C, Vol. 1, p. 30 (1984).
2. C.-K. Loong, S. Ikeda and J. M. Carpenter, Nucl. Instr. and Meth. **A260**, 381 (1987).
3. L. I. Donley, Proc. ICANS-VIII, RAL-85-110, vol. 3, 689 (1986).
4. C.-K. Loong, J. M. Carpenter and S. Ikeda, this Proceedings.
5. L. Soderholm, C.-K. Loong, and S. Kern, Phys. Rev. B **45**, 10062 (1992).
6. S. Takahashi, M.-L. Saboungi, and C.-K. Loong, submitted to the International Symposium on Molten Salts Chemistry and Technology, Honolulu, Hawaii, 1993.
7. S. Takahashi, L. A. Curtiss, D. Gosztola, and M.-L. Saboungi, submitted to the International Symposium on Molten Salts Chemistry and Technology, Honolulu, Hawaii, 1993.

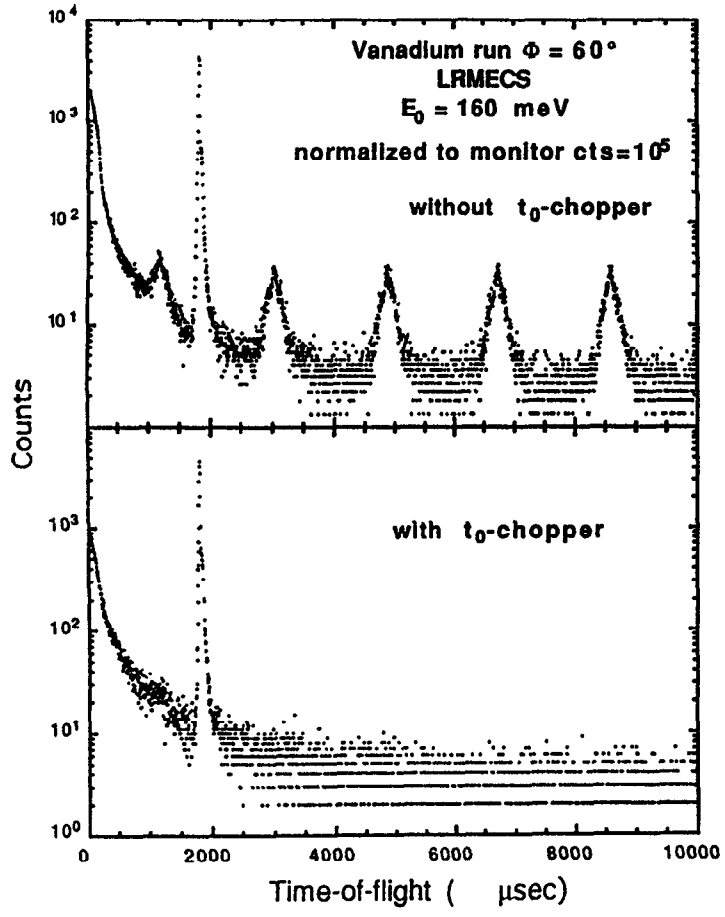


Figure 1. Observed detector spectra of a vanadium standard run (a) without and (b) with a background suppression $t_0$-chopper.

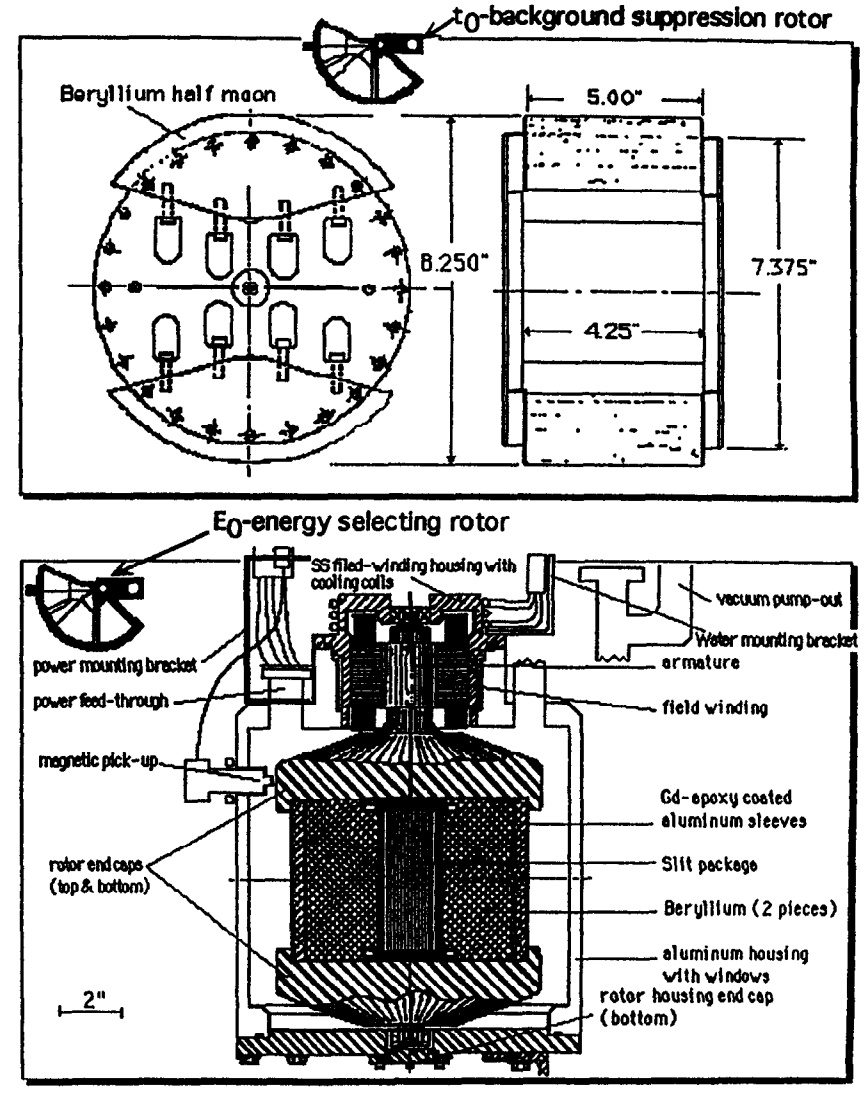


Figure 2. The IPNS $t_0$-background suppression chopper and the $E_0$-energy selecting chopper (with housing).

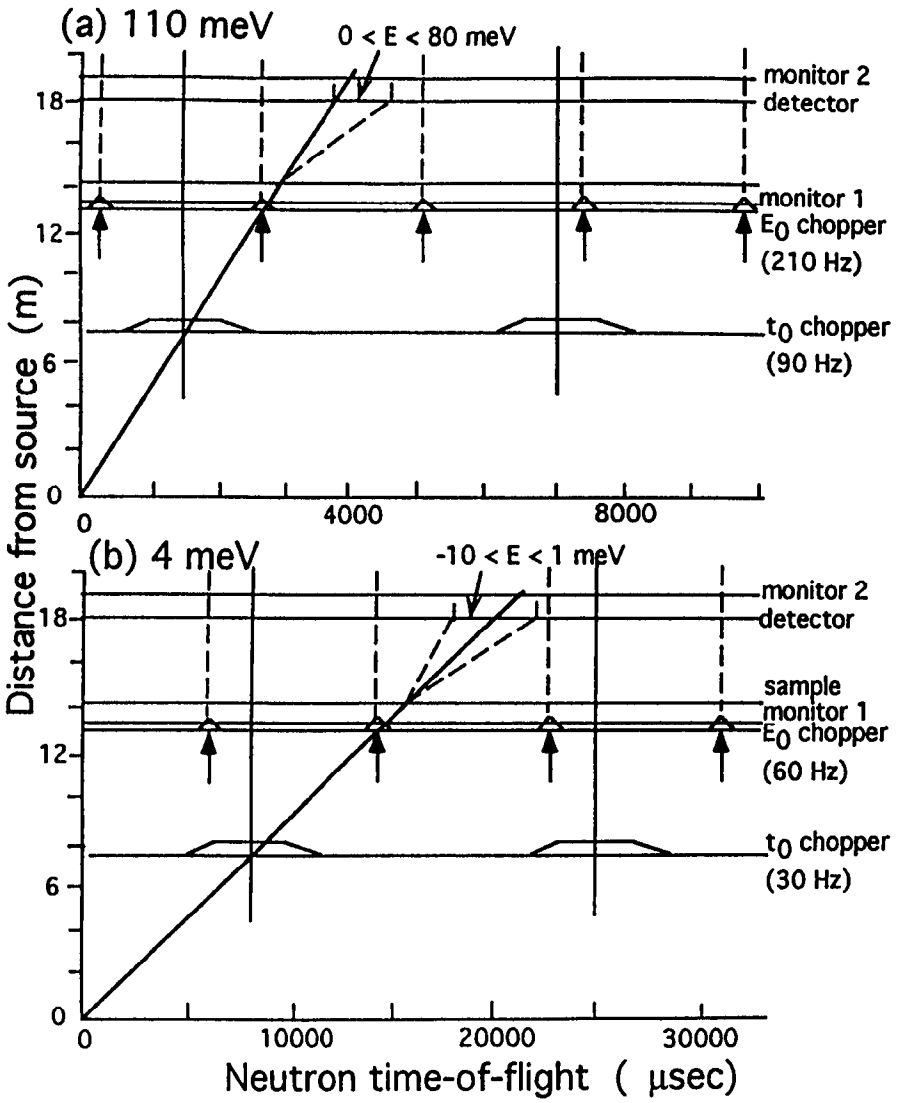


Figure 3. Neutron flight distance versus time for (a) 110 meV and (b) 4 meV operation. The $E_0$-chopper, optimized for 250 meV at 270 Hz, can be effectively used for 110 and 4 meV at reduced speeds.

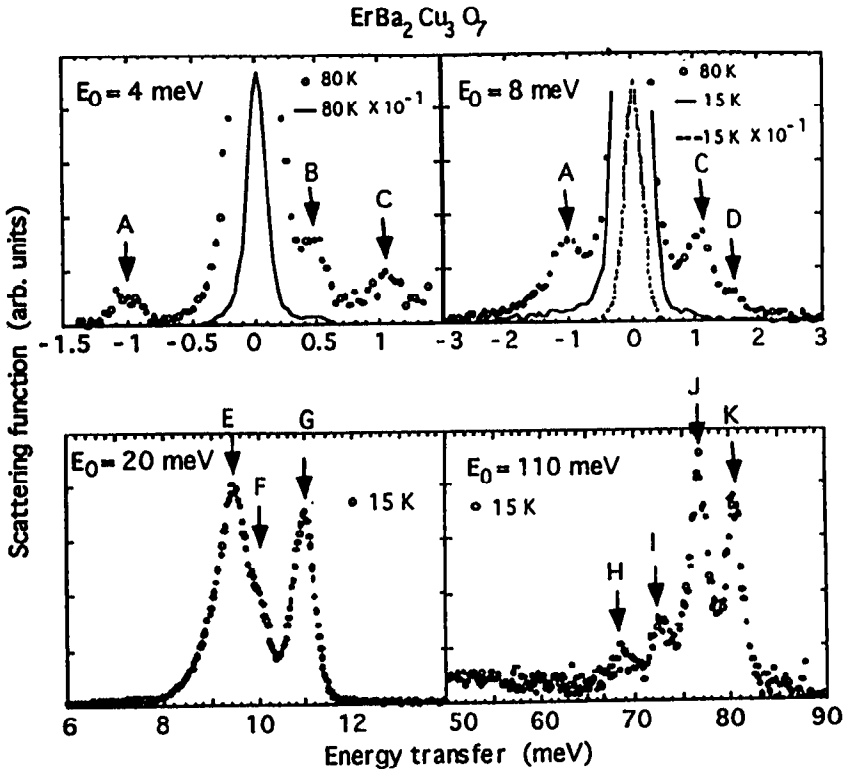


Figure 4. The observed excitation spectra of magnetic superconductor $ErBa_2Cu_3O_7$. The peaks labeled correspond to crystal-field transitions between the energy levels of the $Er^{3+}$ ionic ground multiplets $^4I_{15/2}$, as shown in Fig. 5.

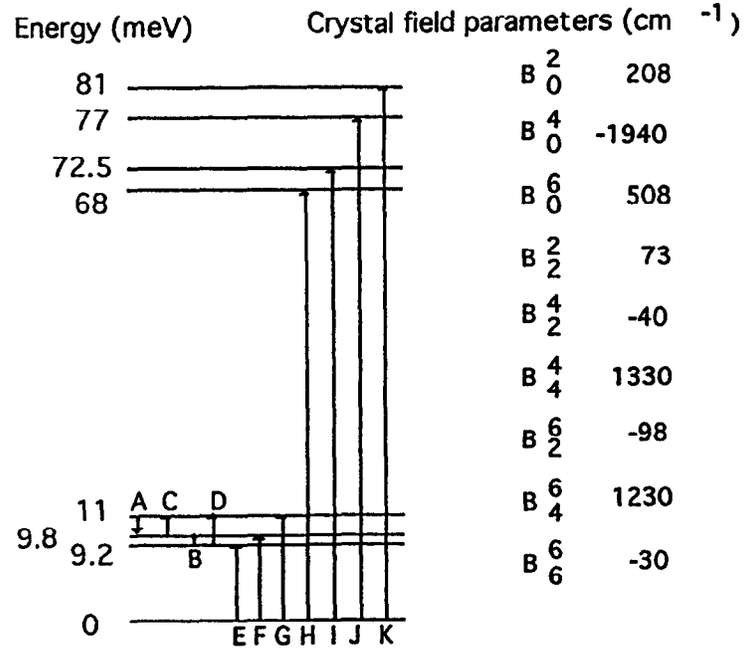


Figure 5. A schematic diagram of the crystal-field levels for the ground multiplet $^4I_{15/2}$ of $Er^{3+}$ ions in $ErBa_2Cu_3O_7$. The transitions labeled correspond to the observed peaks shown in Fig. 4, and the $B_q^k$ are the crystal-field parameters derived from the neutron data.

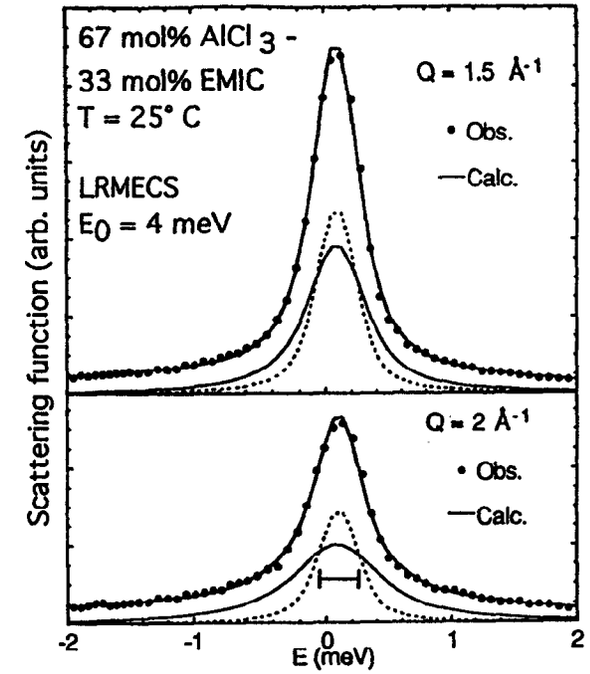


Figure 6. The quasielastic spectra for 67 mol% $AlCl_3$ - 54 mol% EMIC obtained using LRMECS with an incident neutron energy of 4 meV. The data were analyzed by a composition of a sloppy background and two Lorentzian functions.[6] The energy resolution (FWHM) is indicated by the horizontal bar in the lower panel.

# A NEW CHOPPER SPECTROMETER FOR NEUTRON BRILLOUIN SCATTERING AND LOW-ANGLE NEUTRON INELASTIC SCATTERING: PHAROS (PHASE I)

R. A. Robinson, M. Nutter, R. L. Ricketts, E. Larson, J. P. Sandoval, P. S. Lysaght and B. J. Olivier
Los Alamos National Laboratory, Los Alamos, NM 87545, U. S. A.

Abstract

Phase I of PHAROS, the new chopper spectrometer at LANSCE, is described in detail. The main components are a water moderator, a 60-Hz double-bladed T-zero chopper, a 600Hz magnetic-bearing Fermi chopper, a 6m-long vacuum vessel with thin aluminium-alloy vacuum window and a 1.2m$^2$ array of linear position-sensitive detectors.

## 1. Introduction

In this article, we describe the design, construction and components of the new high-resolution chopper spectrometer, PHAROS, which is installed on flight path 16 at the Los Alamos spallation neutron source LANSCE. PHAROS is not an acronym, but refers instead to the famous lighthouse[1] of Alexandria, one of the seven wonders of the ancient world. This is in reference to the "lighthouse" effect[2] for Fermi choppers which rotate, along with an acceptance zone, rather like lighthouses and their beams of light[3].

The spectrometer design follows that outlined conceptually by a workshop held in 1987[4]. This specified that the spectrometer should have high incident-energy resolution ($\Delta E_I/E_I$ = 0.5% FWHM), use incident neutron energies between 100meV and 2eV and have complete continuous detector coverage at a radius of 4m from the sample, between scattering angles of -10$^o$ and 140$^o$, but that it should also have the option of extending the low-angle section of the spectrometer to a secondary flight path of 10m. The decision was taken to build the primary spectrometer (incident beam line and choppers) and the 6-m low-angle extension first, as Phase I of the project. The design of the wide-angle spectrometer, Phase II, has been going on concurrently with that of Phase I but is not the subject of this article, except in as far as it has had major consequences for Phase I.

Perhaps the prime example of the potential utility of such a high-resolution low-angle spectrometer is to do "neutron Brillouin scattering", which has been variously defined as "neutron inelastic scattering from acoustic phonons in the first Brillouin zone"[5] and "inelastic neutron scattering at smaller Q-values than is currently customary"[6]. The idea is that one will be able to measure acoustic phonon dispersion curves, along with phonon linewidths and intensities, at small values of the wave-vector Q. This is of particular importance for amorphous materials[7], in which the low-temperature specific heat is not well-understood and where a study of the dispersive excitations may provide crucial information beyond that available from measurements of the density of phonon states. Indeed, such experiments have been attempted on the metallic glass $Mg_{70}Zn_{30}$[8], but the existing spectrometers with sufficient resolution can only reach scattering angles of 3.5$^o$ or more. In this case it was only possible to reach the pseudo-zone boundary.

Similar questions arise in the damping of magnetic excitations in amorphous ferromagnets [9] and it has long been recognised[10] that there is a need to follow spin-wave dispersion curves beyond the limits reached on current reactor triple-axis spectrometers. The kinematic constraints imposed by such experiments have been analysed in detail [6] and are quite severe: one needs scattering angles of the order of 1$^o$ or less, good resolution and relatively high incident energies. For sound waves, one needs an incident neutron velocity between 1 and $\sqrt{2}$ times the sound velocity of the phonon to be observed. Phase I of PHAROS has been designed expressly for such studies.

However it will also be useful for high-resolution studies of sharp magnetic excitations like crystal-field levels and single-crystal problems in low-dimensional magnetic materials. PHAROS has two potential advantages for the latter. Firstly, the coverage of the available solid angle is almost complete and secondly, the use of position-sensitive detectors means that the vertical divergence in the secondary flight path can be chosen after the experiment is finished, in software. Current practice elsewhere is to mask the detectors with absorbing material. Other design constraints have been that the spectrometer should be completely evacuated, that it should fit into

the available floor space at LANSCE on an existing moderator, and that a T-zero chopper should be employed.

## 2. Source, Collimation and General Layout

The overall characteristics of PHAROS are given in Table 1 and the spectrometer layout is shown in Figure 1. The spectrometer is situated on flight path 16 at LANSCE, with the sample position 20m from the source. It currently views a "high-resolution" water moderator[11] which is heterogeneously poisoned with gadolinium at 1.5cm and has a boron decoupler and liner. It is hoped that this moderator will be replaced with a liquid-methane moderator before too long. A conventional mercury shutter is installed within the bulk shield and the beam is defined with sintered-boron-carbide apertures along its whole length. These are backed up with 35% boron-loaded polyethylene and the fast-neutron beam (which is larger) is defined by fillers made of steel or 5% boron-loaded polyethylene. Following normal practice, the apertures prevent the sample from viewing any filler surfaces. The whole incident flight path is evacuated, except for the spaces immediately before and after the two choppers, where beam monitors are installed, and within the shutter which is helium-filled when open.

Two crucial mechanical choppers are installed in the incident beam, a *fast, monochromating, Fermi* chopper at 18m from the source and a *T-zero* or *background-suppression* chopper at 14m. These are described in more detail in sections 3 and 4 respectively. In fact the shielding and beam line have been designed in such a way that the fast chopper could be installed at 16m rather than 18m. This might be advantageous for Brillouin scattering experiments if one wanted to work at smaller scattering angles and needed to collimate the incident beam more tightly. The extra length between the chopper and sample would make that task easier. An additional cavity has been provided close to the bulk shield for a second Fermi chopper, if required. Its function would be for *pulse-shaping* the incident time distribution from the moderator, which is highly asymmetric[12]. The chopper would symmetrise the time distribution and the spectrometer resolution could even be tightened in an optimised manner: this is not possible at present because it is not possible to sharpen or degrade the moderator pulse width at high neutron energies to any great extent. We have no immediate plans to do this, not least because the beam cross-section at this distance is larger than our existing rotor size, which is in turn determined by considerations of mechanical strength and safety.

Immediately after the fast chopper, the main vacuum vessel starts. This consists of up to three 2-m long rectangular cross-section steel vessels. The sample is mounted in the first vessel via a 0.74m-diameter standard flange. The detector module can be mounted 5.5m, 3.5m or 1.5m after this, dependent upon whether extra sections of vessel are used. Between the sample position and the fast chopper is a smaller section of vacuum vessel, with good vertical access, which is intended to provide a flexible way of changing the incident-beam collimation: soller collimators or apertures can easily be placed there and an optical-bench rail is provided for this purpose. The internal surfaces of all vacuum vessels are lined with sheets of 1cm-thick boron carbide bonded with 10% epoxy resin. The whole vacuum-vessel assembly is surrounded on all sides, as well as on top and underneath, with 30cm of borated paraffin wax within large custom-designed steel cans. Each section of vacuum vessel can be removed independently of the others, and can be reinstalled reproduceably. This is achieved by mounting each vessel on four self-locating high-precision roller-bearing systems. These permit approximately 20cm of travel parallel to the neutron beam, which allows sufficient clearance to remove any one section by crane. The external shielding is also removeable in a simple way to allow access to all the bolts holding any two vessels together.

The detector module can be mounted on the downstream end of each and any of the vessels and consists of a large thin aluminium-alloy window, with its supports and frame, a short section of get-lost pipe, 56 linear position-sensitive detectors together with two shadow bars used for positional calibration, and a small scintillator beam monitor. The whole assembly is designed to be moved as one piece, though the detectors are mounted in banks of eight. Each detector bank includes 2 preamplifiers for each detector and boron carbide/epoxy resin shielding is built into it, immediately behind the detector. The window is described in more detail in Section 5 and the detectors in Section 6.

After the detector module, there are several sections of evacuated get-lost pipe and the straight-through beam ends up in a large steel/polyethylene beam stop. Again, this is evacuated and the illuminated surface is covered with boron carbide/10% epoxy resin, to reduce the number of neutrons scattered back into the spectrometer. The sections of get-lost pipe are modular and can be assembled to accomodate all possible vacuum-vessel configurations of Phase I and Phase II. The beam stop will not need to be moved when Phase II is installed.

3. Fast Chopper System

The single most important component in the spectrometer is the fast chopper, which acts like the shutter of a camera, in that it opens briefly to transmit radiation (neutrons) and then closes again. The time at which it opens can be chosen by the experimentalist and governs the energy of the incident neutrons $E_I$:

$$E_I = \frac{m_n L_1^2}{2 t_c^2} \qquad (1)$$

where $L_1$ is the distance from source to chopper and $t_c$ is the phase of the fast chopper. The chopper is a Fermi chopper[2], which rotates about a vertical axis. It contains a set of absorbing slats that define the beam. While the neutron trajectory is a straight line in the lab frame, it is curved in the frame of reference of the rotor, and therefore the slit package is curved, with a radius of curvature R given by

$$R = v_I / 2\omega \qquad (2)$$

which is energy dependent. As for the slit width, we have chosen to match the pulse width $\sigma_M$ of the moderator pulse to that of the chopper $\sigma_C$, which is due both to the sweep time $\sigma_S$ across an individual slit and to the sweep time $\sigma_m$ across the moderator.

$$\sigma_M = \sigma_C = \sqrt{(\sigma_S^2 + \sigma_m^2)} \qquad (3)$$

where

$$\sigma_S = d/(2 \times 2.45 \times \omega\, r) \qquad (4)$$
$$\sigma_m = a_m / (\sqrt{12}\, \omega\, L_1) \qquad (5)$$

and d is the slot width and r the effective radius of the Fermi chopper and $a_m$ is the width of the moderator. The fast chopper system is based on a commercial squirrel-cage induction motor and magnetic bearing system bought from S2M. A Fermi chopper, with a 5cm x 7.5 cm curved slit package embedded in a 10cm diameter aluminium body is suspended on the active bearings in vacuum. The absorbing slats are 1mm thick boron-fibre/epoxy-resin composite sheets made by Composites Inc. The motor is water-cooled. At present we have three rotors, with matched vacuum vessel/motor/bearing systems, optimised to operate at neutron energies of 100meV, 300meV and 1000meV. Their characteristics are given in Table 2. The chopper system can operate at multiples of 60Hz from 60Hz to 600Hz. Part of the control system is commercial and part is home-built.

Phasing to the accelerator system is achieved in several steps. Power considerations make it favourable to fire the accelerator near the zero-crossing of the mains supply, within a window of ±100μs. On the other hand the inertia of the chopper makes it easiest to spin the chopper at a steady angular velocity. We therefore try to follow the low-frequency fluctuations in the power supply line by accelerating and decelerating the chopper, while the high-frequency fluctuations are accomodated by triggering the accelerator system.

4. T-zero Chopper System

The T-zero chopper is a large paddle-wheel arrangement which places approximately 30cm of inconel in the neutron beam at the time (t-zero) when protons strike the LANSCE target. Its purpose is to stop the high energy neutrons upstream of the spectrometer and thereby reduce the background due to scattering and moderation of these neutrons in the spectrometer and its

shielding. Its design is the descendant of previous such choppers at Rutherford Appleton Laboratory and at LANSCE, but it is somewhat larger in diameter. It is symmetrically balanced and runs at 3,600 r.p.m. (60Hz) - that is, the beam is interrupted with a frequency of 120Hz, the fundamental frequency of the LAMPF linac. Therefore we do not have to pay attention to which particular proton pulses are delivered to LANSCE, which can operate at 12, 15, 20 or 24 Hz. It is driven by a shaft-mounted motor and control system supplied by Rexroth Indramat. The full characteristics are given in Table 3.

## 5. Vacuum window

The vacuum window is a large (1.0 x 1.2 $m^2$) flat sheet of 1.3 mm thick aluminium-alloy (7075-T6), with a small rectangular hole near the centre to allow the straight-through beam uninterrupted passage on to the beam stop. A window of this size is too large to support the atmospheric load, even at an elevation of more than 2000m, without extra support. This is provided by five 4.7mm-thick ribs, each made of aluminium alloy (6061) but coated on both surfaces with 5 layers of boron fibre-aluminium alloy laminate. They are mounted vertically and are parallel to the detectors, with a depth of 15cm and a length of 1m. Laterally, they occur every 22.3cm, this being the width of a set of 8 detectors, and the ribs are angled such that they all point to a focus at 4m. This is to minimise shadowing of the detectors by the ribs. For this arrangement, the safety factor is not sufficient to allow unrestricted access to the loaded window and we have an interlock system to prevent such access.

## 6. Detector System

The characteristics of the array of postion-sensitive detectors are given in Table 4. There are 40 full-length detectors, arranged vertically in banks of 8. The arrangement is asymmetric, there being three banks covering left-hand scattering and only two for right-hand scattering. There is a reason for this: when the window/detector module is installed in Phase II, there is necessarily a large flange in the range of angles that would be covered by a third set of detectors for right-hand scattering and we thereby lose continuous coverage. But if the scattering is symmetric about the incident beam, as it will be for all but single crystal experiments, the same information can be obtained from data taken on the left-hand side.

Above and below the get-lost pipe there are shorter sets of detectors mounted in the same way as the other detectors. Indeed, the whole assembly is designed in such a way that a full window (with no get-lost pipe) could be used, along with a full-length detector bank in place of the two short ones and get-lost pipe. This exposes those detectors to the direct beam, even if it is collimated specially for Brillouin scattering experiments. While this is unusual for inelastic scattering spectrometers, it is normal practice on small-angle scattering spectrometers and has been employed on the glass diffractometer[13] at Argonne National Laboratory. Of course, one would then need to place a small beam stop of suitable size in front of the detector, as in small-angle scattering machines. But, in our case it might be possible to use a resonant absorber, as we use monochromatic radiation: the absorption cross-sections are much higher on resonance, as are the ratios of absorption to scattering, so a small amount of material could be quite effective. A port has been provided in the top of the window frame to allow such access.

## 7. Discussion

It is also worthwhile to compare PHAROS with the ideas prevalent at the time the spectrometer was in its conceptual design stages. For instance, in 1985, Lander and Carpenter[14] proposed a similar spectrometer for a next-generation neutron source. Its principal aim would be for low-Q inelastic magnetic scattering with good resolution and they envisaged a 20-m machine with secondary flight paths of 20m at low angles and 7m for wide angle scattering, together with full polarisation analysis. PHAROS looks very modest in comparison: but it will still cost $2.5-3.0M, by the time Phase II is complete. Of that, a total of $1.3M, excluding labour, has been spent on Phase I.

Acknowledgements

Many people at Los Alamos have contributed significantly to the design and construction of PHAROS and we are grateful to all of them. But in particular, R. N. Silver played a major role in the very early stages, R. Pynn provided the vision to concentrate on the low-angle spectrometer (Phase I), L. Robeson did much of the design work, along with D. Clark. G. Russell gave invaluable advice on shielding and D. Davis made sure that much of the procurement occurred smoothly. We have also benefitted greatly from the advice of many colleages at Argonne National Laboratory and Rutherford Appleton Laboratory, with whom we have had numerous enlightening discussions. We are particularly indebted to J. M. Carpenter and A. D. Taylor. This work was funded in part by the division of Basic Energy Sciences of the U.S. Department of Energy.

References

[1] See for instance P. Clayton and M. Price, *The Seven Wonders of the Ancient World,* Routledge, London (1988).

[2] C. G. Windsor, *Pulsed Neutron Scattering*, Taylor and Francis, London (1981), Ch. 8.

[3] Ironically, the lighthouse effect turns out to be of little consequence on a high-resolution spectrometer like PHAROS.

[4] J. M. Carpenter, K. Crawford, R. Kleb, C. -K. Loong, G. Ostrowski, D. L. Price, M. Nutter, R. Pynn, R. A. Robinson, R. N. Silver, J. M. Rowe, P. Sokol and A. D. Taylor, Los Alamos Report LA-UR-87-2582 (1987).

[5] B. Dorner, Th. Plesser and H. Stiller, Discussions of the Faraday Society 43, 160 (1967).

[6] R. A. Robinson, Physica B 156 & 157, 557 (1989). R. A. Robinson, in *Advanced Neutron Sources 1988*, Inst. of Physics Conf. Ser. 97, 311 (1989).

[7] See for instance, U. Buchenau, Physica B 174, 131 (1991)

[8] J. -B. Suck, P. A. Egelstaff, R. A. Robinson, D. S. Sivia and A. D. Taylor, J. Non-Cryst. Solids 150, 245 (1992). J. -B. Suck, P. A. Egelstaff, R. A. Robinson, D. S. Sivia and A. D. Taylor, Europhys. Lett. 19, 207 (1992).

[9] J. J. Rhyne and J. W. Lynn in *Spin Waves and Magnetic Excitations*, eds. A. S. Borovik-Romanov and S. K. Sinha, North-Holland, Amsterdam, 1988, Part 2, Ch. 4.

[10] J. R. D. Copley, W. Gläser, W. S. Howells, D. L. Price, J. J. Rhyne, K. Sköld and C. Wagner, in Proc. of Workshop on Scientific Opportunities with Advanced Facilities for Neutron Scattering, Shelter Island, October 23-26 1984, CONF-8410256, p. 83.

[11] G. J. Russell, J. S. Gilmore, H. Robinson, G. L. Legate, A. Bridge, R. J. Sanchez, R. J. Brewton, R. Woods and H. G. Hughes, in *Advanced Neutron Sources 1988*, Inst. of Physics Conf. Ser. 97, 483 (1989).

[12] S. Ikeda and J. M. Carpenter, Nucl. Instrum. Methods A239, 536 (1985).

[13] R. K. Crawford, J. M. Carpenter, R. Dejus, J. R. Haumann, R. Kleb, D. G. Montague, D. L. Price and S. Susman, in Proc. XIth Meeting of ICANS, Tsukuba 22-26th October 1990, KEK Report 90-25, Vol. II p.820 (1991).

[14] G. H. Lander and J. M. Carpenter, in *Neutron Scattering in the 'Nineties*, I.A.E.A, Vienna 1985, p.17.

Table 1. Overall Characteristics of PHAROS (Phase I)

| | | |
|---|---|---|
| Moderator[11]: | "High-resolution" water<br>Poisoned with Gd at 1.25cm<br>Decoupled and lined with boron<br>Flight path is angled 15° away from the normal to the moderator surface | |
| Nominal Distances: | Moderator-Sample | 20m |
| | Sample-Detector | 1.5, 3.5 or 5.5m |
| | Moderator- Fast Chopper | 18m (16m is also possible) |
| | Moderator-T-zero Chopper | 14m |
| | Sample-Beam Stop | 11.3m |
| Beam size at sample | | 5cm x 7.5cm |
| Available volume for sample environment equipment | | 0.736m diameter, 0.45m below sample. |
| Detector area | | $1.2m^2$ |

Table 2. Characteristics of rotors for PHAROS fast choppers

| | |
|---|---|
| Materials: | |
| Rotor body | 7075-T6 Aluminium Alloy |
| Absorbing slats | boron fibre - epoxy resin composite 5 ply |
| Other characteristics | |
| Distance from source | 18m |
| Speeds | multiples of 60Hz up to 600Hz |
| Diameter of rotor | 10cm |
| Height of rotor | 12.5cm |
| Beam width | 5cm |
| Beam height | 7.5cm |
| Positional pick-up | magnetic |
| Phasing error, relative to accelerator system | <1μs FWHM |
| Veto rate | <0.5% |

| Rotor | A | B | C |
|---|---|---|---|
| Nominal energy(meV) | 100 | 300 | 1000 |
| slot width (mm) | 3.6 | 2.1 | 1.0 |
| radius of curvature (m) | 0.58 | 1.00 | 1.83 |
| Sweep time across one slot $\sigma_s$ at 600Hz (μs) | 3.93 | 2.23 | 1.14 |

Table 3. Characteristics of PHAROS T-zero chopper

| | |
|---|---|
| Materials: | |
| Rotor material | Inconel |
| Bearings | self-aligning ball bearing with vacuum-rated lubricant |
| Motor | Indramat brushless AC servomotor |
| Positional pick-up optical | optical |
| Other characteristics | |
| Distance from source | 14m |
| Speed | 60Hz |
| Diameter of rotor | 0.7m |
| Mass of rotor | 341kg |
| Width of active section | 11.6cm |
| height of active section | 11cm |
| Beam width | 7.25cm |
| Beam height | 9.0cm |
| Phasing error, relative to accelerator system | 20μs FWHM |
| Characteristic energies (assuming perfect phasing) | |
| Neutron energy at which chopper starts to open | 37eV |
| Neutron energy at which chopper is fully open | 3.4eV |
| Neutron energy at which the rotor next intercepts the beam | 14.75-17.65meV |

Table 4. Characteristics of PHAROS position-sensitive detectors and electronics

| | |
|---|---|
| material | 10-atmosphere $^3$He, stainless-steel walled |
| active length | 0.914m (and 0.248 m above/below straight-through beam) |
| diameter | 2.54 cm |
| manufacturer | Reuter-Stokes |
| positional resolution | 5cm FWHM with present electronics |

Figure Captions

Figure 1 Schematic diagram of PHAROS: (a) Phase I, with detector positions at 1.5, 3.5 and 5.5m from sample, (b) Phase II, with wide-angle detectors at 4m from sample and low angle detector positions at 4, 6, 8 and 10m.

(a)

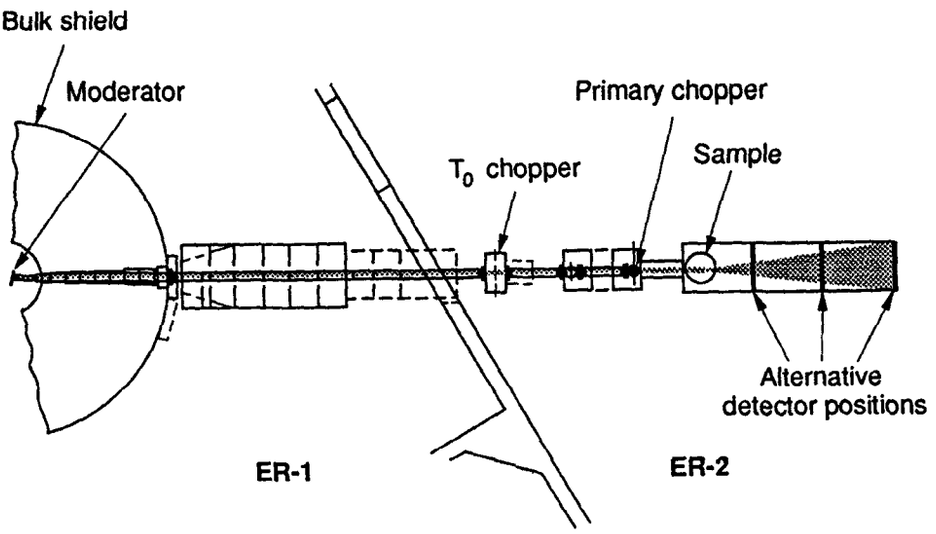
Bulk shield
Moderator
Primary chopper
Sample
$T_0$ chopper
Alternative
detector positions
ER-1
ER-2

(b)

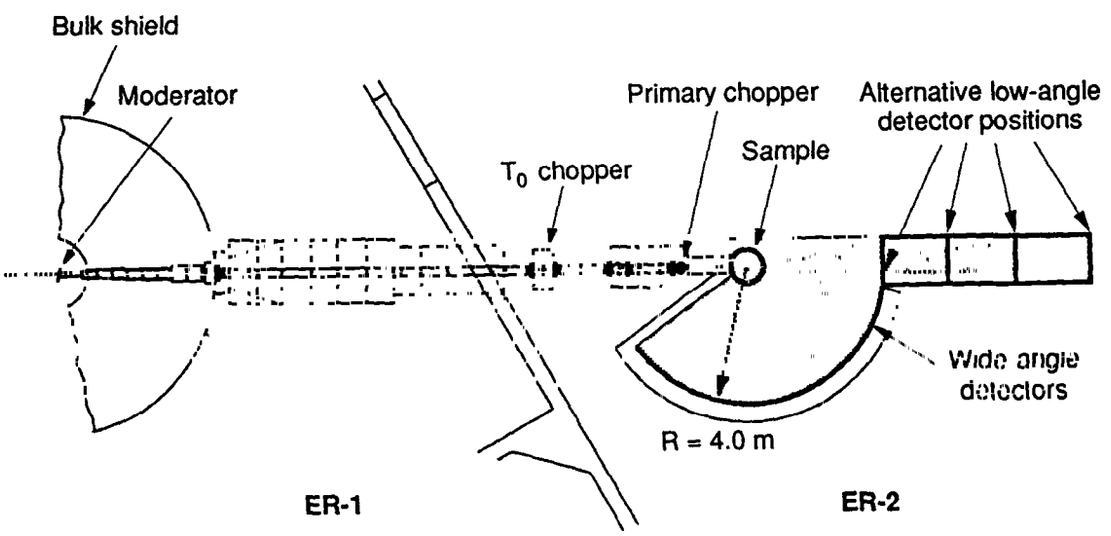
Bulk shield
Moderator
Primary chopper
Alternative low-angle
detector positions
Sample
$T_0$ chopper
Wide angle
detectors
R = 4.0 m
ER-1
ER-2

# FIRST RESULTS FROM PHAROS, THE NEW CHOPPER SPECTROMETER AT LANSCE

B. J. Olivier, J. P. Sandoval, P. S. Lysaght, M. Nutter and R. A. Robinson
LANSCE, Los Alamos National Laboratory, Los Alamos, NM 87545, USA.

Abstract

In this article we present the first experimental measurements obtained on PHAROS during the 1992 run cycle at LANSCE. These are data on the phasing of the choppers relative to the accelerator system along with the consequent neutronic resolution, data on the real-space position resolution of the main detectors, a white-beam nickel powder calibration, and our first inelastic scattering measurement made on $TiH_2$ with an incident energy of 300meV. The characteristic features of the new chopper spectrometer PHAROS, designed for low-angle inelastic neutron scattering and neutron Brillouin scattering, are described elsewhere in these proceedings[1].

## 1. Phasing of the High Speed Chopper Relative to the LAMPF/PSR Accelerator System

As stated in Ref. 1, we have developed a scheme whereby our fast chopper system electronics triggers both the firing of the main LAMPF linear accelerator and the extraction of protons from the proton storage ring. This phasing of the fast chopper allows one to select an incident neutron energy, $E_i$, on the sample. Figure 1(a) shows the signal from the magnetic pickup of the fast chopper, measured with respect to the arrival time of protons on the target. A vetoing system has been employed for uncertainties outside a 10μs time window, and a vetoing rate less than 0.5% was observed. We expect a phase error somewhat greater than the 0.37μs which corresponds to the circumference of the storage ring. Furthermore, since the chopper must accelerate or decelerate to follow a smoothed electrical-supply line frequency, there will be additional dephasing. Our data show a phasing error of approximately 1.1μs FWHM, which is less than the moderation time at all relevant neutron energies.

Figure 1(b) shows the signal from the beam monitor directly down stream from the fast chopper (186mm behind). The data in (b) were fit to $c(t) = A \exp(-(t-t_o)^2/2\sigma^2_{meas})$ where $\sigma^2_{meas} = \sigma^2_{mon} + \sigma^2_t$. $\sigma_{mon}$ results from the finite monitor thickness while $\sigma_t$ is the true energy resolution in time units. After correcting for the width (25.4mm) of the $BF_3$ monitor we find $\sigma_t = 1.46 \pm 0.05$μs (FWHM = $3.44 \pm 0.12$μs). This value is in good agreement with the calculated resolution of $\sigma_{calc} = 1.32$μs.

## 2. Position Resolution of Main Detectors

The main detector bank consists of forty, 0.914m active length, 10atm linear position-sensitive $^3He$ detectors. The detector array covers $1.2m^2$ in the forward scattering direction. A mapping of the detector array is shown in Fig. 2. The spectrometer design specifies 2.5cm spatial resolution along the length of each of these tubes. To investigate the spatial resolution, we have performed experiments in which the detectors were completely covered with absorbing material, except for 2 widely separated 5-cm slots, as shown in Figure 3(a). the results for a white beam, scattered from an isotropic (hydrogenated) scatterer are shown in Figure 3(b). Since the absorbing mask used was cadmium, we have chosen to integrate the incident spectrum only over energies where we are sure the cadmium is black i.e. from $10 < E_i <$ 150meV. The peaks in (b) were fit to $c(y) = A \exp(-(y-y_o)^2/2\sigma^2_{meas})$ where $\sigma^2_{meas} = \sigma^2_{det} + \sigma^2_{cad}$. $\sigma_{cad}$ results from the 5cm wide apertures while $\sigma_{det}$ represents the true intrinsic detector resolution. The measured resolution is given by a FWHM of 9.9cm, which after correcting for the size of the 5cm aperture gives an intrinsic detector resolution of approximately 8.9cm FWHM. Since October 1992, we have been working on improving this

resolution by increasing the detector gain, adjusting the discrimination levels in the channel logic boards and load matching the pre-amp to detector couplings.

## 3. White-Beam diffraction measurements

In order to investigate the position sensitivity and to calibrate the scattering angle scale on the detector plane, we performed total diffraction measurements on a standard nickel powder sample. The results are shown in Figure 4. The ordinate represents time-of-flight measured in a given pixel of the detector plane. The low-order nickel reflections have been indexed as shown. Each band along the abscissa represents a particular detector (a certain value of x measured horizontally away from the straight-through beam), with the 32 pixels ( the y-variation in the vertical direction along the length of each detector) represented within each band. The crescent shaped Bragg reflections, merely reflect the Debye-Scherrer cones projected onto particular detectors. For any given Bragg reflection, the observed time is a minimum at the center of each detector, because the Bragg angle is a minimum there. For detectors closer to the straight-through beam, that minimum time also decreases with scattering angle $\phi$.

## 4. Inelastic Measurements

Figure 5 shows our first inelastic scattering measurement from a 24g $TiH_2$ sample[2], using a nominal incident energy of 300meV. The calibration simply used the rigid body distances in the spectrometer, and the nominal timing of the fast chopper electronics. The elastic energy is close to zero indicating an incident energy of $304.2 \pm 0.15$meV. Inelastic features around 140 meV are indicative of the Einstein mode that has been previously studied elsewhere[2]. The observed width is significantly greater than the spectrometer resolution and the structure is due to dispersion. It is worth noting that the relative intensities of the two peaks are different from those reported in reference[2]. In our data, the lower energy transfer peak is more intense. This is a Q-dependent effect and in a similar system, $ZrH_2$, the inelastic structure at low-Q is similar to ours[3].

Note, however, that the observed elastic resolution (4%) for this measurement is significantly worse than the calculated (1.7%). We can account for this discrepancy in two ways. First, the trigger to the proton-storage ring was not connected. This was realized because our phasing to the accelerator was only 4.5μs FWHM, rather than the 1.0μs shown in Figure 1(a). Even after accounting for the phasing error, however, the resolution is still poorer than expected. We believe that this additional width is caused by the leakage of neutrons around the outside of the slit package of the fast chopper. The slit package has the same nominal size (5 x 7.5 $cm^2$) as the final boron composite aperture before the fast chopper, and we had found it necessary to place slightly smaller apertures before and after the fast chopper. When the 300meV chopper was installed, and these measurements taken, these apertures were inadvertently left out. Support for this view can be found in the strange shape of the elastic line, which is quite sharp at the center but with significant wings on either side.

## 5. Conclusions

In conclusion, we have fully operated all aspects of the spectrometer simultaneously: fast chopper, T-zero chopper, vacuum system with vacuum window, position-sensitive detectors and beam monitors. Satisfactory results have been obtained and with resolution improvements currently being made, we believe PHAROS will be ready for original experiments during 1993.

Acknowledgments

This work was supported in part by the Division of Basic Energy Sciences of the US Department of Energy.

References

1. R. A. Robinson, M. Nutter, R. L. Ricketts, E. Larson, J. P. Sandoval, P. Lysaght and B. J. Olivier, in these proceedings.
2. C. Korn and D. Zamir, *J. Phys. Chem. Solids*, **34**, 725 (1973).
3. J. G. Couch, O. K. Harling and L. C. Clune, *Phys. Rev.* **B4**, 2675 (1971).

Figure Captions

Figure 1. Plots of (a) the magnetic pick-up signal for the fast Fermi chopper (18m from the source), (b) signal in a 2.54cm-thick $BF_3$ beam monitor 0.186m downstream from the fast chopper.

Figure 2. Schematic of the PHAROS detector map to be used during the 1993 beam cycle at LANSCE. The gray scale gives the scattering angle spread.

Figure 3. Plots of intensity versus length along a linear position-sensitive detector. (a) shows the experimental setup, in which the detector is illuminated through two 5cm wide apertures. (b) shows in-beam results from October 1992. The spectra were summed over the energy range $10 < E_i < 150$meV.

Figure 4. Plots of intensity versus x, y, and t as measured in a few detectors on PHAROS. The fast chopper was removed in this measurement and the sample was 38g of nickel powder. The low-order reflections are indexed on the left hand side of the figure. The vertical axis represents observed time-of-flight in each pixel, while the horizontal axis represents both the x and y variations in the detector. The fine variation (32 pixels) is along the length (y) of each detector, while each band represents an individual tube (x-variation).

Figure 5. Plot of inelastically scattered intensity from $TiH_2$, using an incident energy of 300meV. (a) includes the elastic scattering while (b) focuses on the inelastic structure. The data in (b) show an order of magnitude increase in the signal over the background.

Fig.1

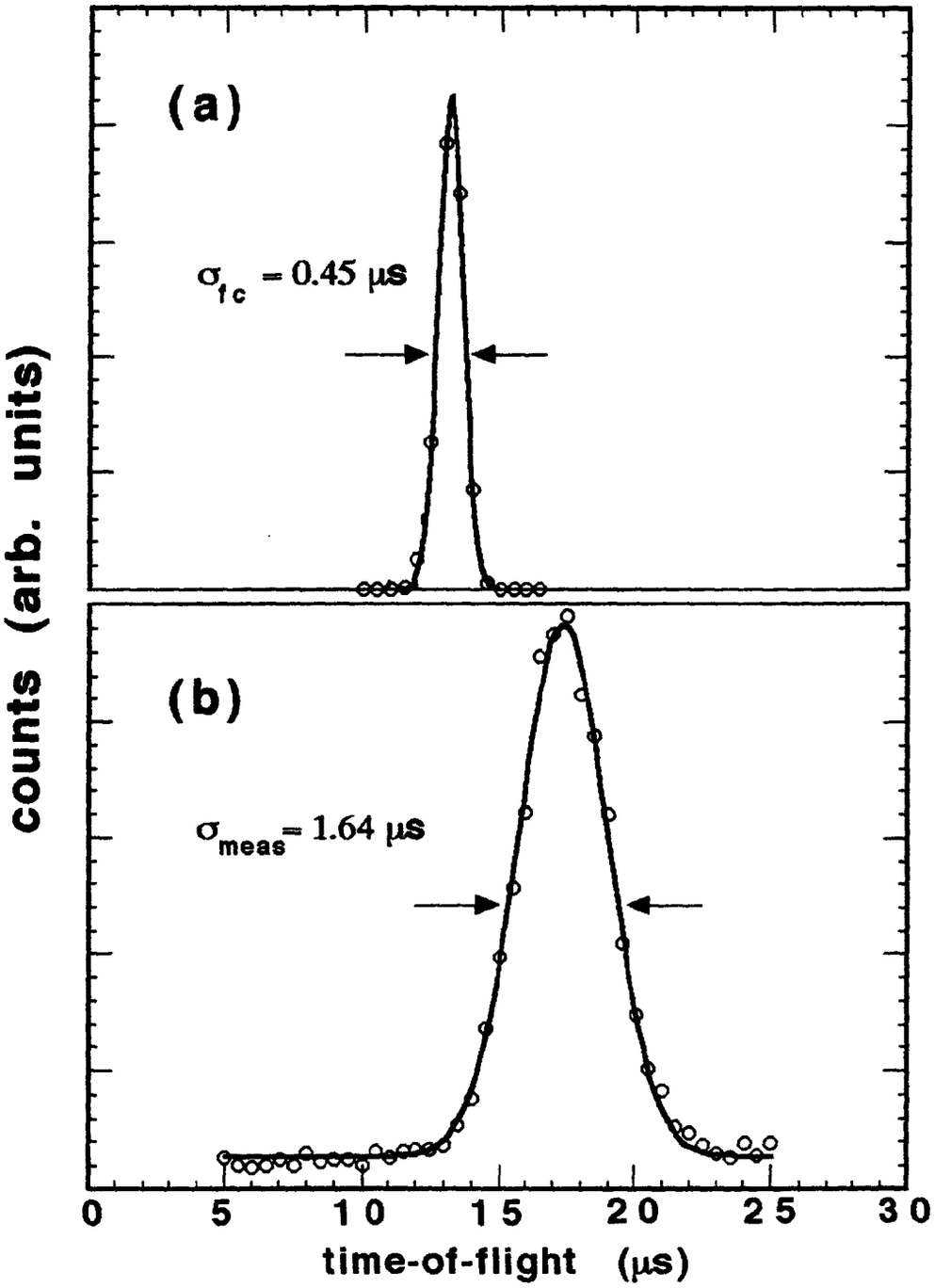
(a)
$\sigma_{fc}$ = 0.45 μs
(b)
$\sigma_{meas}$ = 1.64 μs
counts (arb. units)
0
5
10
15
20
25
30
time-of-flight (μs)

Fig.2

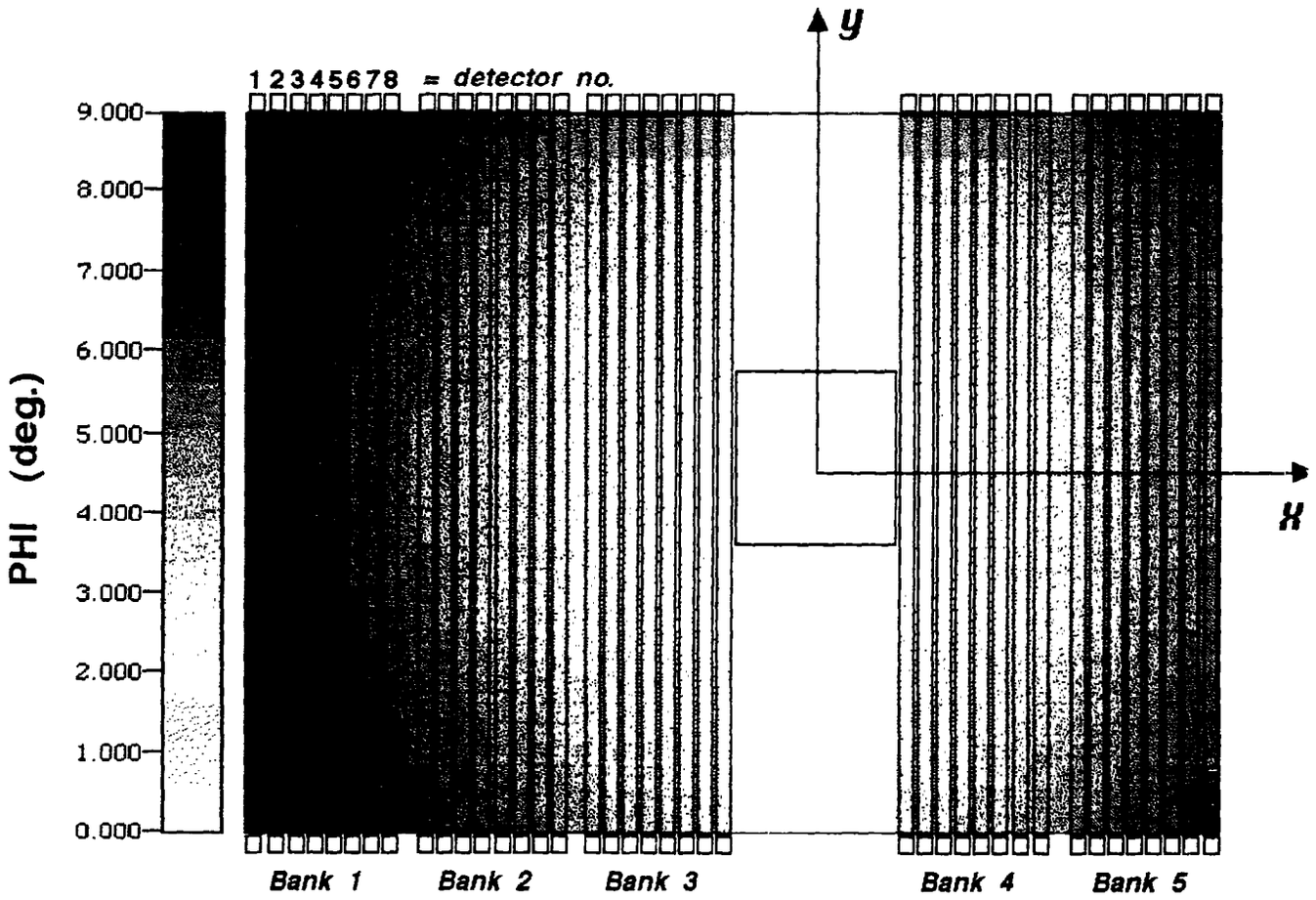
y
1 2 3 4 5 6 7 8 = detector no.
9.000
8.000
7.000
6.000
5.000
4.000
3.000
2.000
1.000
0.000
PHI (deg.)
x
Bank 1
Bank 2
Bank 3
Bank 4
Bank 5

Fig.3

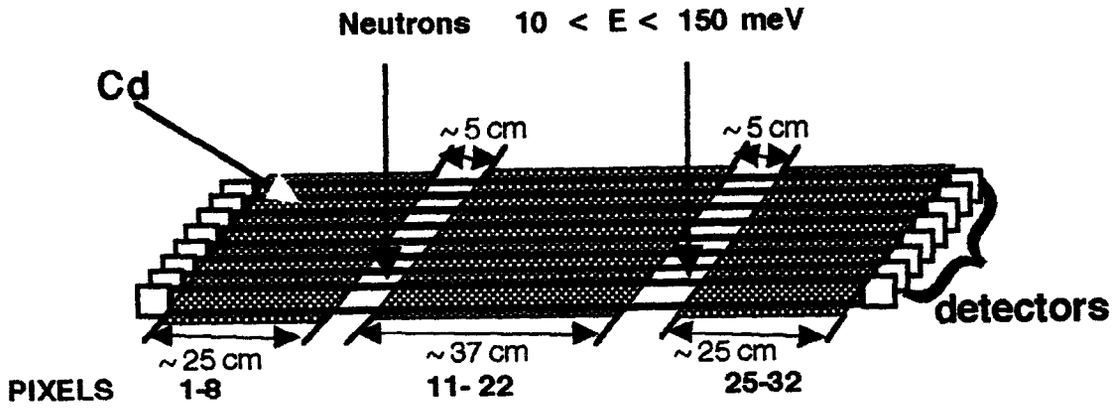
Neutrons 10 < E < 150 meV
Cd
~5 cm
~5 cm
detectors
~25 cm
~37 cm
~25 cm
PIXELS
1-8
11-22
25-32

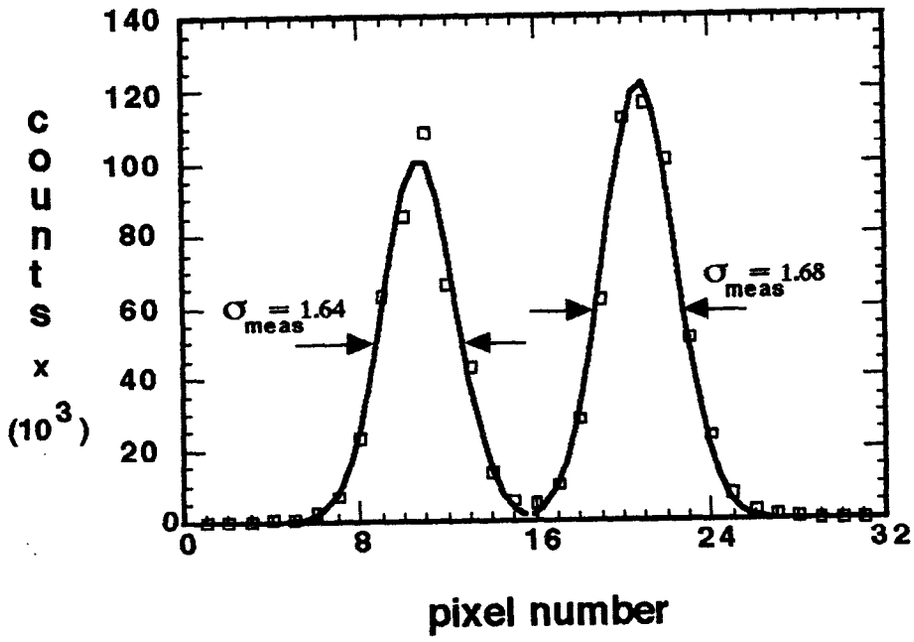
counts x (10^3)
140
120
100
80
60
40
20
0
0
8
16
24
32
pixel number
σ meas = 1.64
σ meas = 1.68

Fig.4

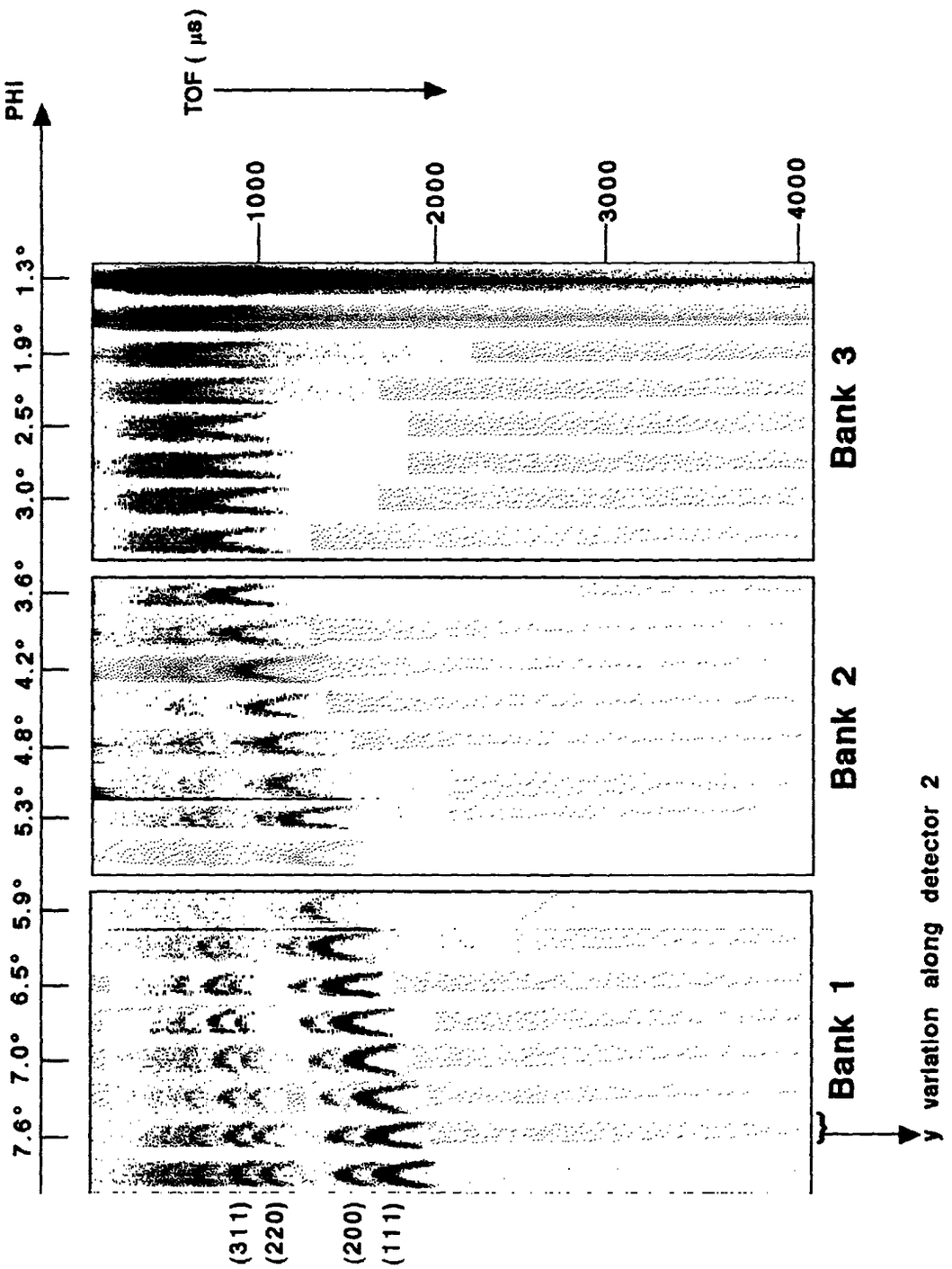
PHI
TOF ( μs)
1000
2000
3000
4000
1.3°
1.9°
2.5°
3.0°
3.6°
4.2°
4.8°
5.3°
5.9°
6.5°
7.0°
7.6°
Bank 3
Bank 2
Bank 1
y variation along detector 2
(311)
(220)
(200)
(111)

Fig.5

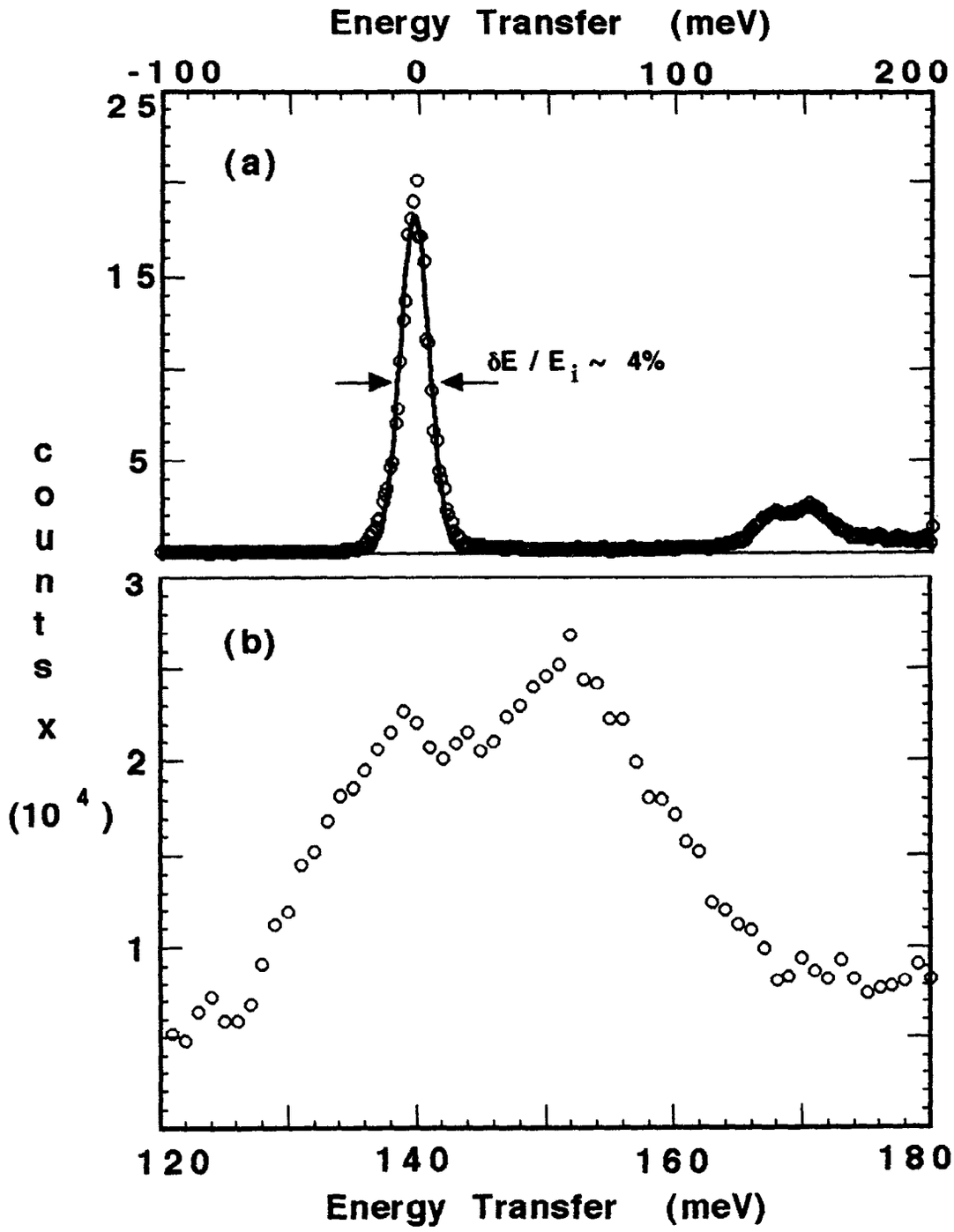
Energy Transfer (meV)
-100
0
100
200
25
15
5
(a)
δE / E_i ~ 4%
counts x (10^4)
3
2
1
(b)
120
140
160
180
Energy Transfer (meV)

# MAPS: A Chopper Spectrometer to Measure High Energy Magnetic Excitations in Single Crystals

T.G. Perring, A.D. Taylor, R. Osborn*
ISIS Facility, Rutherford Appleton Laboratory,
Chilton, nr. Didcot, Oxon OX11 0QX, U.K.

D.McK. Paul
Dept. of Physics, University of Warwick, Coventry, CV4 7AL, U.K.

A.T. Boothroyd
Dept. of Physics, University of Oxford,
Clarendon Laboratory, Parks Road, Oxford OX1 3PU

G. Aeppli
AT&T Bell Labs., 600 Mountain Avenue, Murray Hill, New Jersey 07974, USA

## 0. ABSTRACT

An increasing amount of the scheduled time of both HET and MARI has been spent measuring high energy magnetic excitations in single crystals. Despite the inherent limitations of current instruments, which were never optimised for such experiments, a growing number of experiments have been successfully carried out in 1-, 2- and 3-dimensional magnetic systems. The proposed spectrometer MAPS aims to dramatically increase the efficiency of these experiments and thereby to open the 100-1000meV energy transfer range in the same way that the triple axis spectrometer opened the 1-50meV range.

## 1. INTRODUCTION

The triple axis spectrometer has for three decades been the instrument of choice at reactors to investigate collective excitations in single crystals. It offers full flexibility in the choice of scan through (**Q**,ω)-space and, through collimation and monochromator

* Current address: Materials Science Division B223, Argonne National Laboratory, Argonne, Illinois 60439-4845, USA

changes, the instrument resolution can be adjusted to suit the problem being investigated. However, at high energy transfers the kinematic constraints placed by the requirement of small |Q| in magnetic experiments means that a large incident energy is needed, when the flux from a reactor is low and monochromator reflectivities are small. The small scattering angles at the monochromators and sample mean that the background from air scattering is large and a rapidly changing function of scattering angle. Single crystal experiments have occasionally been performed on time-of-flight chopper spectrometers, but because the paths in Q and ω are correlated, the spectrometers have almost exclusively been used with polycrystalline samples where the only Q dependency of the excitations is due to the magnetic form factor, or to measure excitation density of states.

Pulsed sources offer a number of advantages at high incident neutron energies over reactors, particularly a large epithermal neutron flux and low background between the pulses. However, it was not envisaged that high energy experiments in single crystals would form a large part of the experimental program at ISIS, and accordingly the principal considerations in the design of the HET spectrometer centred on its utility for measuring dispersionless excitations in polycrystalline samples. Nevertheless, experimental techniques have been developed that use the accessed volume of (Q,ω)-space in single crystals to advantage, and a wide range of highly succesful experiments have been performed on 1-, 2- and 3D magnetic systems [2-8].

Such experiments require considerable beam-time, and now account for a significant proportion of the time requested on HET and MARI. Accordingly, it was considered timely to request funds to build a spectrometer purpose designed to measure high energy magnetic excitations in single crystals [1], because in the light of the experience gained on HET and MARI significant optimisations can be made in the basic design that should allow a large increase in the efficiency of data collection. Advantage can be taken of the proposed flexibility of instrument configuration to allow easy incorporation of new beam components, either for test purposes (e.g. improved collimation) or as technological improvements occur (e.g. white beam polarisation). MAPS will act as a test bed for future developments of the time-of-flight chopper spectrometer both in hardware and data visualisation software.

In section 2 an outline is given of the methods used to perform single crystal experiments on HET and MARI, and the instrument developments that could be made to increase the effectiveness of the experiments are detailed with reference to experience gained on HET and MARI. Section 3 gives details of the proposed design of MAPS, and in section 4 the questions of software and data visualisation needs are briefly considered.

## 2. DESIGN CRITERIA

### 2.1 Performing single crystal experiments [1]

The most common method used with **3D systems** (e.g. Fe [2], Co [3], Cr [4]) is to arrange for a high symmetry direction of the crystal to lie along the direction of $\mathbf{k}_f$ within a chosen detector in the scattering plane (high symmetry plane)of the crystal. The path of energy transfer as a function of Q along this direction is an inverted parabola and where this parabola intersects the dispersion relation peaks in intensity will be observed (figure 1). Several detectors may be added together to improve the statistics, but as the **Q** resolution is degraded perpendicular to the symmetry direction, and hence perpendicular to the gradient of the dispersion relation, the peaks can remain sharp. To intersect the dispersion relation at a higher energy transfer, the incident energy is increased. To maintain the symmetry direction along $\mathbf{k}_f$ requires rotating the crystal a few degrees so that the symmetry direction is now along $\mathbf{k}_f$ in a detector with scattering angle also a few degrees different. With a series of runs at different $E_i$ the full dispersion relation can be mapped out.

In **2D systems** the scattering is independent of the component of **Q** perpendicular to the 2D plane so forming rods of scattering in that direction. In some experiments (e.g. $La_2NiO_4$ [5]) the same technique as with 3D systems has been used, with the rods perpendicular to the scattering plane. An alternative arrangement (e.g. $La_2CuO_4$ [6]) has been to align the rods along $\mathbf{k}_f$ in a chosen detector, and compare the signal in adjacent detectors. The differences in the spectra arise from the different points of intersection of the detectors on the dispersion relation, and models for the dispersion relation can be tested by comparing the calculated and observed differences. In **1D systems** (e.g. $KCuF_3$ [7], $KFeS_2$ [8]) the chains are aligned along $\mathbf{k}_i$ so the scattering has azimuthal symmetry. A large solid angle of detectors can be summed with little degradation of **Q** along the chain. The background can be estimated from detectors in the vertical plane after the crystal has been rotated through 90 degrees because in these detecotrs the component of **Q** along the chains is zero.

The success of HET and MARI with single crystal experiments is due to the low background and the large detector area. The sample and detector tanks are evacuated to eliminate air scattering and so the bulk of the background is from multiple scattering within the sample. Data is gathered over a wide range of momentum and energy transfers simultaneously, so all points on a scan are gathered at once. The broad coverage in $(\mathbf{Q},\omega)$-space, together with the low background, explains how the performance can be competitive with a triple axis spectrometer. but it also allows a better understanding of the behaviour of the background scattering processes. This has been crucial to the analysis of some experiments e.g. Cr, where the scattering in out-of-plane detectors, where no magnetic signal was expected, was subtracted from the in-plane detectors at the same scattering angle to leave magnetic scattering that was otherwise far from clear.

## 2.2 Instrument inprovements

The experience on HET and MARI has shown that there are a number of ways in which a purpose designed spectrometer could be improved to enhance the effectiveness of single crystal experiments.

- **Eliminating gaps in the detector arrays.** In the most common method of performing single crystal experiments it often occurs that in order to observe spin waves at the desired energy transfer the required detector angle corresponds to a gap in the coverage. Additionally, one can in principle construct scans by combining data from different detectors at different energy transfers (for example by integrating over an energy window in each detector a constant-E scan can be simulated). Gaps in the detector array prevents this.

- **Ensuring the same secondary flight path for different detector banks.** On HET the detectors with scattering angle 9°-29° have a 2.5m flight path, whereas those between 3°-7° degrees are at 4m. They have worse resolution as a result, and mostly have not been used in the analysis of single crystal data. In low energy experiments the resolution is acceptable, but the discontinuity in resolution between the low and higher angle banks makes comparison of the data difficult. On MARI, all detectors are at 4m from the sample and the continuity of resolution has been used, for instance with Fe, to extrapolate the multi-phonon scattering at high energy from higher scattering angles back to low scattering angle to perform a background subtraction.

- **Position sensitive detector arrays.** On HET and MARI the $^3$He gas tubes are 30cm in length. At high energies this leads to poor **Q** resolution along their length (1.5Å$^{-1}$ FWHH for 1eV neutrons). Position sensitive detectors would permit the resolution to be adjusted in software, both during and after the experiment. The out-of-plane detectors are generally used only for background estimates because the detector length integrates along a direction in reciprocal space that is not generally related to the crystal symmetry. It often occurs that their paths in (**Q**,ω)-space intersect the dispersion relation and so cannot be used for this purpose. Position sensitive detectors would allow scans to be constructed in software that made use of out-of-plane scattering just as much as the in-plane scattering. Scans could be constructed either to explore regions where magnetic scattering instensity is expected or to avoid magnetic intensity in order to provide an estimate of the background.

- **Increasing the total detector area.** A larger detector area at low scattering angles will greatly increase the possibility of constructing useful scans in (**Q**,ω)-space. In some experiments the gain is directly quantifiable: the count rate can improve by a factor of 6 over MARI if there is continuous coverage to 30° scattering angle (figure 2 gives an example). Coverage to this scattering angle would be an important gain, especially in low dimensional experiments for which only small samples are available.

- **Increasing the spectrometer flexibility.** Part of the success of the triple axis spectrometer comes from the ability to change collimation and monochromators in order to trade intensity for resolution. On HET and MARI the only flexibility is to change the incident energy and the chopper package. On MAPS the ability to alter the primary and secondary flight paths will permit wider intensity / resolution compromises. Adjustable apertures to control the beam size appear on triple aixs spectrometers to control the background, and these will also be a feature of MAPS.

## 3 SPECTROMETER SPECIFICATION

The principal spectrometer parameters are summarised in Table 1, along with those of HET and MARI.

### 3.1 Energy transfer range

The motivation for the proposal to build MAPS is to measure magnetic excitations at energy transfer $100\text{meV} \leq \varepsilon \leq 1000\text{meV}$, and the design of MAPS should be optimised for this range. It is also worthwhile that the MAPS design be tested at lower energies with an eye on instrumentation at proposed high power pulsed sources such as the ESS, so consideration should be made in the design for

$$5\text{meV} \leq \varepsilon \leq 1000\text{meV}$$

with $10\text{meV} \leq E_i \leq 2000\text{meV}$

so long as this does not compromise the efficiency of the spectrometer in its design energy transfer range.

The required energy resolution is that of HET/MARI or better, ie $\Delta\varepsilon/E_i \approx 2\%$ FWHH at the elastic line decreasing to $\Delta\varepsilon/E_i \approx 1\%$ at full energy transfer. The spectrometer flight paths should be flexible enough to permit optimisation of the flux for a given energy resolution.

### 3.2 Moderator and beamline

It is proposed that MAPS be sited on a beamline viewing an ambient temperature water moderator poisoned at 2cm depth. There is an alternative beamline which views a 77K methane moderator, which will have increased flux at $E_i$ less than about 20meV, but the minimum moderator-chopper flight path is 12m at this site, whereas 7.5m is achievable on the proposed beamline. In the high $E_i$ range for which MAPS is intended the flux from the moderator face is the same in either case.

3.3 Primary spectrometer

Figure 3 is a schematic plan of the MAPS spectrometer. The primary beam components will be heavily shielded modules running on rails, effectively a large optical bench. Spacer modules will be available to alter the distances between the components and the total flight path to the sample. The flight path will be evacuated. The minimum configuration (T=0 chopper, Fermi chopper, 1m collimation from chopper to sample) gives the moderator - sample distance $L_1 \approx 9$m. The energy resolution of MAPS can be improved to 2/3 of the value for HET or MARI by allowing $L_1$ to increase to 15m while maintaining the sample-detector distance $L_2 = 4$m (and hence keeping the maximum detector solid angle - see "Secondary spectrometer" below). The minimum requirement is that the beamline can be reconfigured on a time scale at least as fast as the norm for the current changeover time between experiments at ISIS (4-5hrs) It is highly desirable that reconfiguration is fast enough to be considered routine within an experiment.

- Collimation

The beam at the sample position should be at least 6cm by 6cm, to allow the largest available samples (often 100g - 200g) to be used. There will be several motorised adjustable apertures along the beamline to permit a tightened beam when small samples are used. A soller collimator should be available after the Fermi chopper to tighten the cone of neutrons that are scattered by the chopper body.

- Choppers

MAPS will have a t=0 chopper (ie closed for the fast neutron flash), to be sited as close to the bulk shielding as possible (flight path 6.5m). A second background chopper before the Fermi chopper will be available. This will perform a coarse energy selection but will remain closed for most of the frame to attenuate fast neutrons that penetrate the Fermi chopper in its closed position.

A selection of Fermi choppers will be available suitable for high and low energy resolution configurations of the spectrometer. The design of those currently used on HET and MARI works well for $E_i \leq 700$meV but above these energies the slats become 'grey'. An improved design using $^{10}B$ instead of natural boron is currently being explored.

- Monitors

The usual array of beam monitors will be required -

- in the unmonochromated beam before the coarse chopper
- after the Fermi chopper
- behind the sample

It is very important for the monitors to be highly stable. Many single crystal experiments rely on the subtraction of one large signal from another to leave a small magnetic signal.

This can only be performed with confidence if the normalisation of data sets is very accurate. Improved or alternative monitor designs will be explored. Absolute calibration of the monitors is highly desirable so that throughput of components such as choppers and collimation can be readily assessed.

3.4 Secondary spectrometer

It is proposed to have two detector banks:

1. Low angle bank with $0° < \phi \leq 30°$ covering all azimuthal angles with secondary flight path $L_2 = 4m$.
   This will require $11m^2$ of detectors (figure 4). Suitable resolution is 2cm pixelation. The bank could therefore be covered with 1m long position sensitice gas tubes with diameter 2.5cm and with resolution 1/64 of their length. One possible problem with gas tubes is the dead time. If a Bragg's law is satified at one point in a detector, then it becomes inactive along its whole length for $\approx 10\mu s$. The alternative of ZnS detectors is also being investigated.

   At high $E_i$ the angular coverage is rather generous for seeing purely magnetic scattering e.g. at $E_i$=1000meV $Q = 7.6Å^{-1}$at the elastic line at 20° and $Q=9.1Å^{-1}$ at $\varepsilon$ =500meV. However, higher angle data will be important for determining the behaviour of the multi-phonon background. Also, at lower $E_i$ magnetic scattering will be observed in the entire bank e.g. at $E_i$=100meV $Q = 3.60Å^{-1}$at the elastic line at 30° and $Q=3.64Å^{-1}$ at $\varepsilon$=50meV.

2. (In a future expansion) a high angle bank, with $30° \leq \phi \leq 120°$ (say) with $L_2$=4m
   These would be important for studies of phonons on MAPS. They would also be useful in magnetic experiments e.g. in an experiment in Fe on MARI data up to $\phi$=75° was used to understand the multi-phonon background, where the $E_i$ used ranged up to about 800meV.

The low angle bank should have variable $L_2$, increasing up to 8m. With the optimum choice of chopper, this would allow, for instance, $L_1$ to be shortened to 10m so as to retain the same energy resolution as on HET but double the flux at the sample position. Alternatively, the flux can be maintained but the energy resolution improved to 2/3 of its HET/MARI value. The solid angle coverage will be reduced, but at $L_2$=8m it will still cover all $\phi < 15°$. The variable flight path can be achieved either by having removable sections beyond $L_2$=4m, or by mounting the detector array on rails within a SANS type vacuum vessel. In the former case, the detectors should nevertheless be mounted inside the vacuum vessel so as to eliminate the need for a large vacuum window with supporting ribs.

Space considerations restrict the maximum $L_2$ for the high angle bank to 4m. Depending on cost constraints, the high angle tank could be built as part of the low angle tank or as a unit to be bolted on at a future date.

## 4. DATA COLLECTION, COMPUTING AND SOFTWARE

### 4.1 Data Acquisition Electronics (DAE)

In the low angle bank MAPS will have about $10m^2$ of detectors with pixel elements of about 4 $cm^2$, giving about 25000 spectra, a factor of 50 greater than on MARI. With energy bins corresponding to 1/10 of the resolution ( $\Delta\varepsilon/E_i \approx 1\%$) this gives a minimum requirement of 1000 time channels. Typically, on HET and MARI 3000 time channels are used. The total number of data bins will be between 25,000,000 and 75,000,000. A new Data Acquisition Electronics, DAE-II, is currently being designed at RAL, and this has sufficient power to cope with this number of histogram bins.

### 4.2 Visualisation and data manipulation

Significant computing power and advanced data visualisation methods will be needed to extract the full information from data gathered on MAPS, and must be considered an integral part of the spectrometer. The problem of data visualisation has yet to be tackled, but some points emerge-

- The current procedure for setting up most experiments is to produce a plot of contours of constant $\varepsilon$ in the scattering plane of the crystal (figure 5). The reciprocal lattice of the crystal is overlaid so that the accessible $(\mathbf{Q},\omega)$ points in any detector can be seen. This plot cannot indicate what is observable in the out-of-plane detectors. MAPS will access a volume of (Qx,Qy,Qz) space (at any point of which $\varepsilon$ is determined). A generalised version of the plot is needed in which one chooses a plane in reciprocal space, fixes the third component of **Q** and plots contours of constant $\varepsilon$. Alternatively, a value of $\varepsilon$ can be chosen, and contours of one component of **Q** plotted as a function of the other two (figure 2 earlier is an example of this plot, where $\varepsilon$ was fixed at 250meV and contours of constant component of **Q** along the rods of scattering plotted on the 2D Cu-O planes).

- Data will be viewed by choosing a plane or direction in $(\mathbf{Q},\omega)$-space and integrating the counts in a resolution volume constructed from many pixels in detector element-timebin space about each point.When the algorithm that determines the resolution function in the plane or along the direction has been specified the data can be converted to $S(\mathbf{Q},\omega)$. (Many pixels will be needed because the counts in any one will be so few. The gain of MAPS over HET/MARI is that the plane in $(\mathbf{Q},\omega)$-space and the resolution function can be freely chosen). The form of the resolution function will

in general be decided in an interactive analysis session, perhaps from a menu or a user-written library, so significant computing power will be required to perform the calculations in real time.

- Calculation of the $S(\mathbf{Q},\omega)$ data will be within a manipulation and display package. Routine manipulations that can be envisioned include, for instance, adding multi-dimensional data corresponding to symmetry related parts of reciprocal space, and adding runs or subtracting data from runs performed at different temperatures. At ISIS an in-house package, GENIE, is used to manipulate and display 1D workspaces of time-of-flight or processed data. It is an excellent toolbox, as it permits command files containing many GENIE commands to be run and can access external pre-compiled programs to transform workspaces, but to be suitable for MAPS it needs to be improved to handle multi-dimensional data sets. There is a project to write a greatly enhanced version of GENIE at ISIS which would satisfy the requirements of MAPS.

REFERENCES


[1] "MAPS - A Multi-Angle Position Sensitive Spectrometer" D.McK. Paul, A.T. Boothroyd. A proposal submitted to the SERC.

[2] T.G. Perring et al , *J.Appl. Phys* **69** 6219 (1991)
A.T. Boothroyd et al, *J. Magn. Magn. Mater.* **104-107** 713 (1992)

[3] T.G.Perring Ph.D. thesis, University of Cambridge, (1991)

[4] R.T.Heap et al, *Physica B* **174** 22 (1991)

[5] K. Yamada et al, *J.Phys. Soc. Japan* **60** 1197 (1991)

[6] S.M. Hayden et al, *Phys. Rev. Letts.* **67** 3622 (1991)

[7] S.E.Nagler et al, *Phys. Rev.* **B44** 12361 (1991)
D.A.Tennant et al, *Phys. Rev. Letts.* **70** 4003 (1993)

[8] D.Welz et al, *Phys. Rev.* **B45** 12319 (1992)

**Table 1.**

**Spectrometer specification and comparison with HET and MARI**

| | MAPS | HET/MARI |
|---|---|---|
| moderator: | Ambient water (poisoned) | HET: Ambient water (poisoned)<br>MARI: Methane 77K (poisoned) |
| Energy range: | $10meV \leq E_i \leq 2000meV$<br>$5meV \leq \varepsilon \leq 1000meV$ | HET: $10meV \leq E_i \leq 2000meV$<br>MARI: $10meV \leq E_i \leq 1000meV$ |
| Resolution: | $\Delta\varepsilon / E_i \leq 2\%$ @ elastic posn. | $\Delta\varepsilon / E_i = 2\%$ @ elastic posn. |
| Choppers | t=0 chopper<br>coarse chopper<br>Fermi chopper | t=0 chopper<br>coarse chopper (MARI)<br>Fermi chopper |
| Primary flight path $L_0$ | $9m \rightarrow 15m$ | 11.8m |
| Beam size | 6cm x 6cm (max.) | HET: 4cm x 4cm<br>MARI: 5cm x 5cm |
| Secondary flight path $L_2$ | $4m \rightarrow 8m$ | HET: 4m $3.5° \leq \lvert\phi\rvert \leq 7°$<br>$110° \leq \phi \leq 120°$<br>2.5m $9° \leq \lvert\phi\rvert \leq 29°$<br>$120° \leq \phi \leq 140°$<br><br>MARI: 4m $3.5° \leq \lvert\phi\rvert \leq 135°$ |

Detectors and scattering angle range:

| | |
|---|---|
| 10atm. $^3$He gas tubes<br>100cm position sensitive | 10atm. $^3$He gas tubes.<br>30cm long |
| $\lvert\phi\rvert \leq 30°$<br>all azimuthal angles | HET: $3.5° \leq \lvert\phi\rvert \leq 7°$; $9° \leq \lvert\phi\rvert \leq 29°$<br>MARI: $3.5° \leq \lvert\phi\rvert \leq 15°$ |
| $30° \rightarrow 120°$<br>plane array | HET: high angle bank<br>MARI: $15° \leq \lvert\phi\rvert \leq 135°$ |

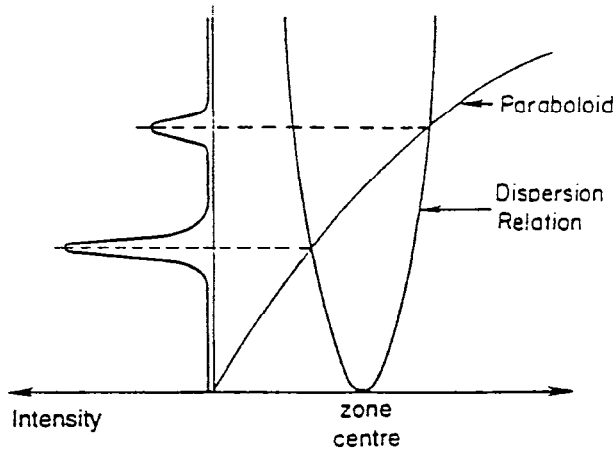


Fig. 1

*A section through the paraboloid for a detector which accepts $K_f$ that lie along a symmetry direction of a crystal. At those energy transfers where the paraboloid intersects the dispersion relation peaks in scattered intensity are expected.*

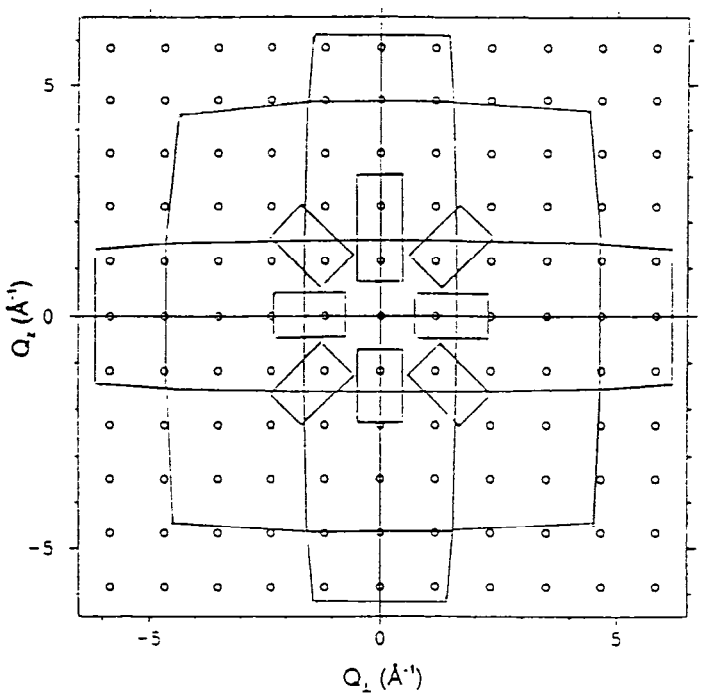


Fig. 2

*The relative solid angles of the low angle detectore on MARI and the proposed spectrometer MAPS as viewed along the incident neutron pateh. The momentum transfer scale is set by assuming $E_i$=650 meV and an energy transfer of 250 meV, approximately the condictions required to observe the zone boundary magnon in $La_{1.85}Ba_{0.15}CuO_4$. The circles mark the zone centres of this material when the 2D axis is aligned along $K_i$. The number of centres enclosed by the detector areas of MARI and MAPS give an idea of the relative data collection rates for the two instruments*

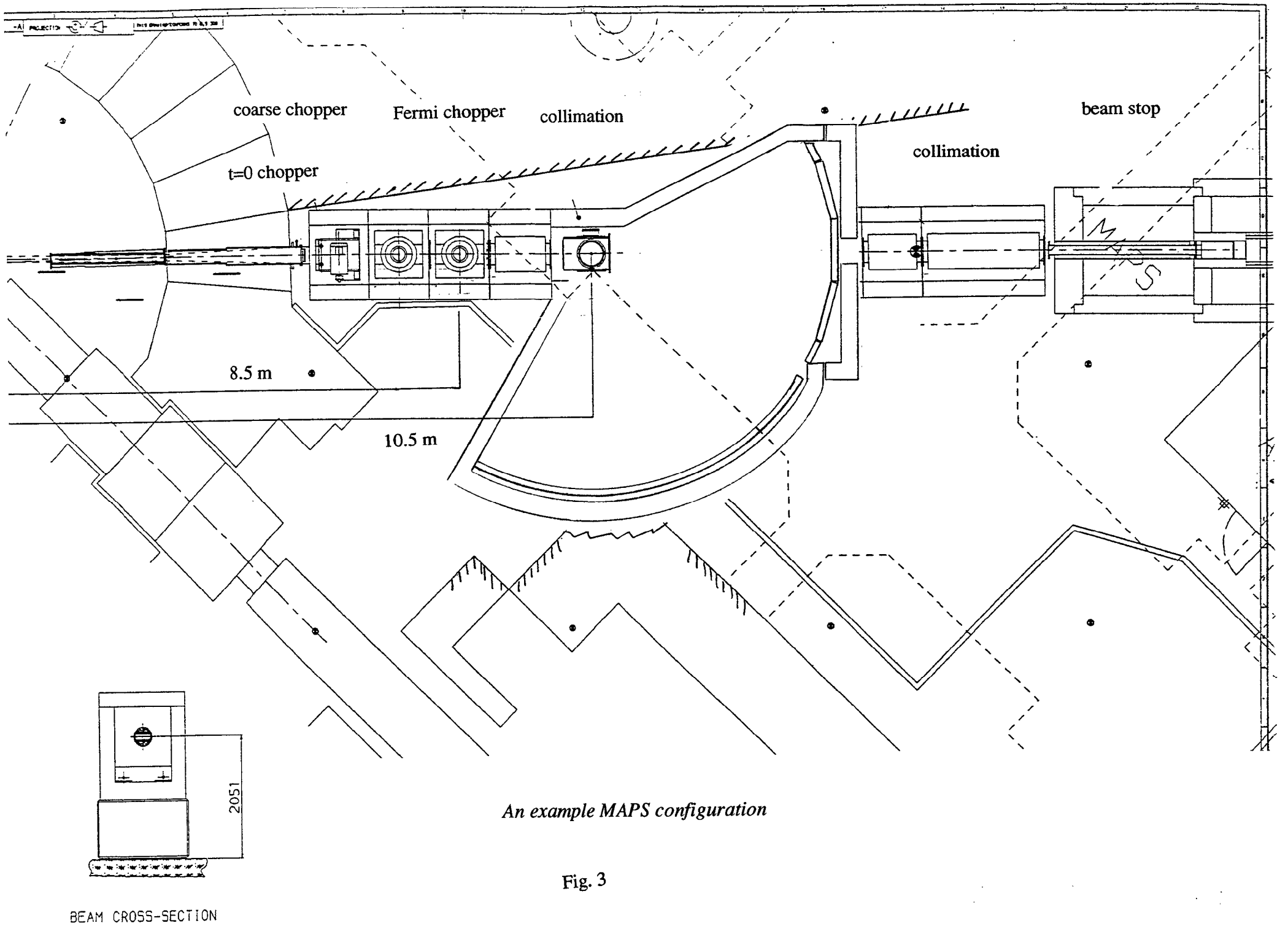


*An example MAPS configuration*

Fig. 3

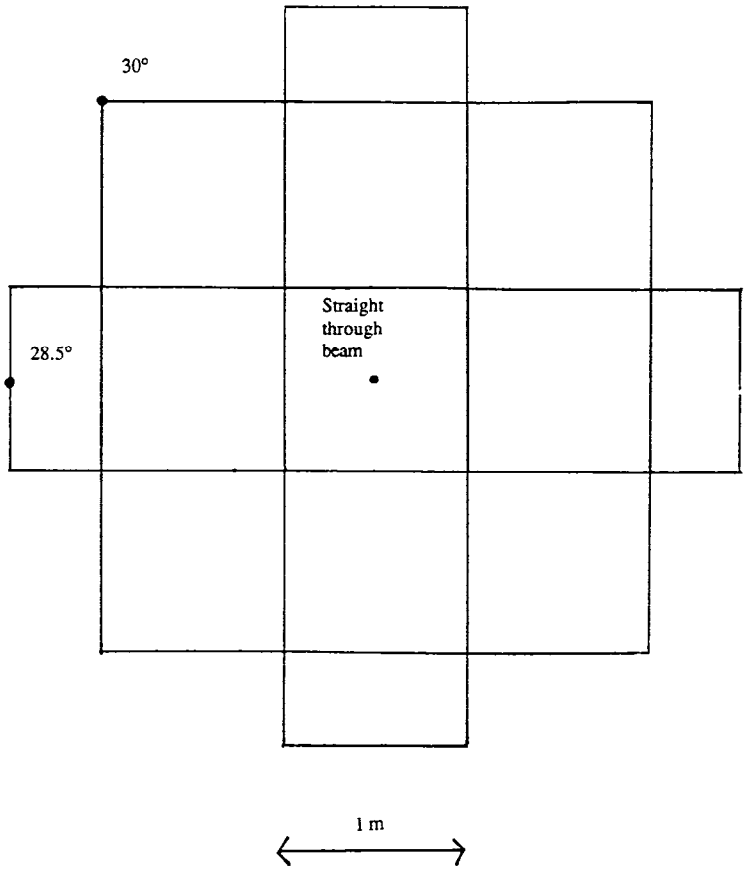


Fig. 4

*MAPS low angle detector bank. The scattering angles are shown at the extremities of the bank.*

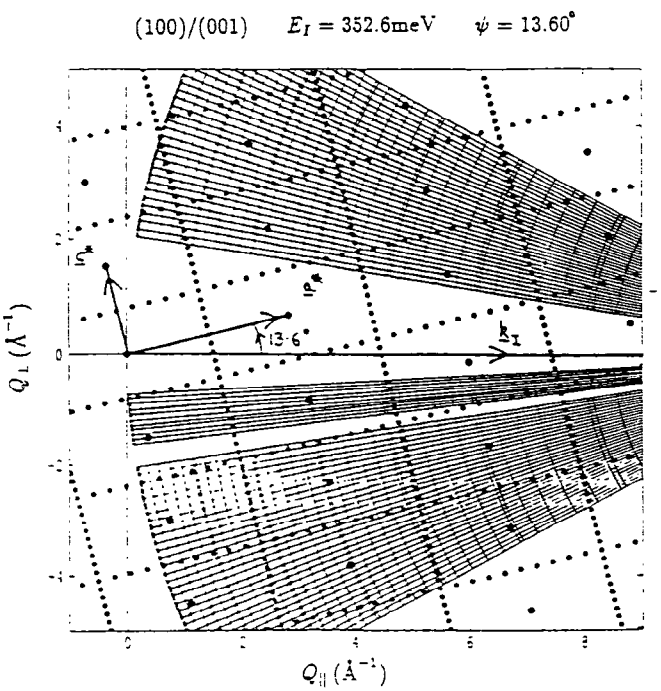


Fig. 5

*A plot of the accesible region of (Q,ω )-space in the (100)-(001) plane of h.c.p. cobalt with* $\mathbf{a}^*$ *at 13.6° to* $\mathbf{k}_i$ *and* $E_i$*=350meV on HET. The radial lines correspond to the locus of vector Q intercepted by different detectors and the circular contours are lines of equal energy transfer in 10meV intervals (50meV for the double lines). The spots mark reciprocal lattice points. The crystal is oriented so that the* $\mathbf{a}^*$ *symmetry direction through (1,0,-1) lies approximately along* $\mathbf{k}_f$ *for one of the central low angle detectors.*

# Cold Neutrons on Pulsed Sources for High Resolution Spectroscopy and Long d-spacing Diffraction

C J Carlile, M A Adams, J B Forsyth and P S R Krishna

The ISIS Pulsed Source, Rutherford Appleton Laboratory, Chilton, Oxfordshire, OX11 0QX, U.K.

**Abstract**

Using the IRIS spectrometer on the ISIS pulsed neutron source as an example it is demonstrated that, in the area of cold neutron production, the present generation of pulsed sources and their instruments can produce fluxes and count rates which are at least equal to those of the most powerful reactors. This is contrary to the generally accepted view and therefore is important when sources such as the European Spallation Source and AUSTRON are being considered by funding bodies. The instrumentation on pulsed sources can be quite novel, leading to new scientific applications, and there is still an immense amount of potential for instrument development which has not yet even been glimpsed.

## Introduction

Cold neutrons have traditionally been defined as those which will pass relatively unattenuated through a polycrystalline beryllium block beyond its Bragg edge. Beryllium was often used in order to filter out of a reactor beam the long wavelength or cold neutrons. Conveniently this means that those neutrons whose wavelengths are longer than 4Å, whose energies are greater than 5meV and whose reciprocal velocities exceed 1000μsec/metre (i.e. velocities less than Mach 3) are defined as *cold*. In an ambient temperature research reactor the flux of such neutrons is relatively low and not until low temperature "cold moderators" were installed in reactors could the use of cold neutrons for scattering experiments be properly developed. These cold moderators (hence the name cold neutrons) were normally composed of liquid hydrogen or deuterium and served to shift the peak of the Maxwell-Boltzmann spectrum to lower energies.

Their early development was a strictly European venture, taking place in the late 1950's and early 1960's at laboratories such as Mol, Saclay, Jülich and Harwell. The availability of intense cold neutron beams led directly to significant progress in instrumentation in Europe which resulted, for example, in the development of neutron guides, and the exploitation of small angle scattering and high resolution time of flight and backscattering spectrometers by the physics and, significantly, the chemistry community. These instrumentational advances can now be seen as milestones on the road to the building of the Institut Laue-Langevin with its strong emphasis on the imaginative use of cold neutrons and its resulting *flagship* status in neutron scattering world-wide during the 1970's and 1980's.

During this period the perceived saturation of technological advances in the development of reactors led to a revival in interest in accelerator-driven pulsed neutron sources, which promised higher effective fluxes than reactors, in the U.S.A., Japan and the U.K. This led to the building of IPNS at Argonne, LANSCE at Los Alamos, KENS at Tsukuba and ISIS at Rutherford. ISIS has been operating now for seven years and has reached its design goal: 200uamps of 800MeV protons at 50 Hz which yield a fast neutron source flux of $3 \times 10^{16}$ n/sec ISIS is recognised as the premier pulsed source in the world, standing side by side with ILL as two of the world's leading neutron scattering laboratories.

Experience on pulsed sources in the late 1970's when ISIS was being designed, was very limited and it was inconceivable then that it, or indeed any pulsed source, could challenge the supremacy of ILL in the cold neutron field. Accordingly pulsed sources, with their harder fast

neutron source fluxes and undermoderated slow neutron fluxes, were seen primarily as sources of epithermal neutrons and therefore as being naturally complementary to reactor sources.

Comparisons on paper of pulsed sources and reactors are fraught with difficulty as is any simplistic comparison of basically dissimilar objects. Although more complex algorithms have been developed, the enduring *performance indicator* for a reactor is its time-averaged flux and for a pulsed source its peak flux, and a comparison of these two quantities provides a broad-brush indication of relative instrument performance. These single numbers cannot represent the full story, and there are examples which run counter to it, but they are generally realistic.

The liquid hydrogen moderator on ISIS was designed at a time and in a climate when little could be reliably predicted about the performance of pulsed source instruments and cold neutrons instruments on pulsed sources were foreseen at best as providing local facilities for testing out and selecting those experiments which could be better done on high flux reactors. Accordingly the liquid hydrogen moderator was situated downstream on the ISIS target in the lower fast neutron flux position with a flux penalty, in comparison to the prime moderators, approaching a factor of two.

Therefore, if we take the published average and peak fluxes of ILL (1) and ISIS (2) respectively, we can produce a performance ratio which does indeed show, in figure 1, an increasing advantage of pulsed sources as neutron energy increases, approaching a factor of 100 at 1eV. What is surprising however is that the crossover between reactors and pulsed sources occurs well into the cold neutron regime, at a neutron energy of 3meV (or 5Å wavelength). If the ISIS hydrogen moderator were to have been situated in an upstream position this crossover would have occurred at 1meV (or 9Å wavelength).

Clearly the only proper method to compare instruments and sources is by scientific output and enough experience has now been gained to do this, even though it is still early days for the blossoming techniques of pulsed neutrons. We will illustrate the power of cold neutrons on pulsed sources by reference to the high resolution spectrometer and long d-spacing diffractometer IRIS (3) currently operational at ISIS.

## The IRIS Instrument

High resolution incoherent neutron spectroscopy is used for the study of diffusional processes in a wide variety of materials ranging from hydrogen in metals and superionic conductors to liquid crystals and

biological materials such as tRNA. The technique is also widely used for the study of quantum tunnelling processes in molecular crystals, crystal field splitting in magnetic materials, including high $T_c$ superconductors, and dispersion curves in quantum fluids such as helium. The demand for such instruments is high, partly because their capabilities appeal to a broad distribution of specialities, and such measurements continue to expand into new areas of science. High absolute resolutions in the μeV range are achieved by using slow (i.e. cold) neutrons when small changes in the neutron's energy can be detected with high accuracy.

Energy analysis of a neutron beam by Bragg reflection from a single crystal is a common procedure used, for example, in triple axis spectroscopy. When the Bragg angle is increased towards 90° the energy resolution becomes extremely good, limited only by the uncertainty in d-spacing of the crystal itself. Therefore backscattering analysers have been used to achieve the highest direct resolutions yet reached in neutron spectroscopy - 0.3 μeV. The neutron energy of the incident beam can be scanned by a number of different methods. In the earliest instruments Döppler shifting of the monochromatic beam reflected from a silicon crystal, again in backscattering geometry, was used. This method was developed at Munich and Jülich before being incorporated into the IN10 backscattering machine at ILL. A later development of this method was to scan the temperature of the backscattering monochromator thereby using the expansion of the lattice parameter to select a continuous range of energies. On pulsed sources the incident beam is naturally energy-sorted when observed some distance from the moderator. The further from the moderator, the higher the resolution achievable and this is the method used on the IRIS spectrometer to obtain high resolutions.

The energy transfer range $\Delta E$ accessible by Döppler shifting is quite limited because of the ultimate strengths of materials to withstand the high accelerations. Typically $\Delta E \sim 0.015E_a$. For temperature scanning the energy transfer range is higher, but limited to $\Delta E \sim 0.06E_a$ by the coefficients of expansion and melting points of most materials. Scanning the incident energy by time-of-flight however, as is done on pulsed source instruments, gives a higher accessible energy transfer range because of the ability to dispense with a crystal monochromator. In this case the energy transfer range is typically $\Delta E \sim 0.6E_a$.

The IRIS instrument is fully described in reference (3). IRIS views the liquid hydrogen moderator on the ISIS pulsed neutron source. The incident beam is transported by a curved neutron guide to the sample position about 36 metres from the moderator. Overlap of neutrons from pulse to pulse is avoided by the use of two disc choppers situated

close to the target station. The second disc chopper serves to eliminate ISIS pulses thus allowing very long wavelengths to be used. The neutron guide terminates in the analyser tank with a 2.5 metre long supermirror converging guide, which increases the flux on the sample by a factor close to 3. The guide is well shielded along its full length and earlier anxieties about the contamination of the beam with very energetic spallation neutrons have been shown to be unfounded. The beam at the sample position can be stopped by a sheet of cadmium. The sample sits in the white beam delivered by the guide. Scattered neutrons are analysed by two arrays of analyser crystals - pyrolytic graphite and mica - on either side of the 2 m diameter analyser vacuum tank. The analyser crystals are close to backscattering geometry to benefit from the optimum resolution of this geometry but sufficiently offset ($\theta_B$=87.5°) to install a large number of detectors (51 on each side) and to avoid the need for a beam modulation chopper in the incident beam (as on IN10 and IN13 at ILL) to discriminate against neutrons scattered directly into the detectors. This latter measure improves the usable flux on the sample by a factor of 2.5. Resolutions of 15 and 50 μeV are available with the pyrolytic graphite analysers and 11, 4 and 1 μeV with the mica analysers. The 1 μeV resolution uses neutrons of 20 Å wavelength. The 2.25 metre-long graphite analyser has been cooled to 25K resulting in a ten-fold reduction in background from Thermal Diffuse Scattering (TDS).

At scattering angles around 170° a small 10-tube diffraction detector is installed. This facility was included to allow the crystallographic phase of the sample under spectroscopic study to be monitored during measurements. It has proved to have important consequences when studying unique samples prepared in-beam or samples in unusual sample environment conditions (such as high pressures) where unexpected crystallographic changes can occur. *Simultaneous* dynamic and structural measurements of equal quality can therefore be carried out. Equally well the diffraction capability can be used in its own right for long d-spacing diffraction with very good resolution. The resolution is constant at 2.5 $10^{-3}$ in $\Delta d/d$ over a d-spacing range from 2 to 12 Å using neutrons with wavelengths out to 24Å. A diagram of the IRIS analyser tank is shown in Figure 2. In order to emphasis the intense cold fluxes coming from the ISIS hydrogen moderator a plot of the flux at the sample position for both IRIS and the high resolution powder diffractometer is shown in figure 3. The $\lambda^4$-dependence of the structure factor for Bragg scattering means that, even though the flux is falling considerably beyond 10 Å on IRIS, the detected data rate is still acceptably high.

## Scientific Examples

The scientific programme of the instrument is very broad but this can be illustrated with the aid of a few examples.

More than half the work done on the instrument is carried out using the graphite analysers at 6.7Å where the flux delivered by the guide is highest. Nevertheless the very long wavelength neutron flux is remarkably intense. Since this is the precise wavelength range in which pulsed sources are thought *not* to perform well (or even at all), all examples will be taken from this range. It is particularly important when considering instrument designs for AUSTRON that they are assessed taking advantage of the latest developments on pulsed sources rather than relying on outdated notions.

Nitromethane $CH_3NO_2$ represents one of the most well-studied materials by tunnelling spectroscopy. It contains only one type of $CH_3$ group in the orthorhombic unit cell having space group $P2_12_12_1$ and 4 molecules per unit cell. Thus the tunnel spectrum contains one single line. The profile is resolution limited, which is interpreted as meaning that direct methyl-methyl interactions are negligible. This sample was re-examined using the mica (002) reflection on IRIS to investigate the feasibility of this instrument option for tunnelling spectroscopy. The resolution of 1.2 μeV is attained using very slow neutrons (19.8Å or 208 μeV) which consequently provides low momentum transfers Q from 0.1 $Å^{-1}$ to 0.6 $Å^{-1}$ where form factors can be low. The spectrum is shown in figure 4 where a sharp single line spectrum is clearly seen at 35.4 μeV, broadened by about 1.5 μeV.

Quasielastic scattering spectroscopy is ideal for the study of random translational and rotational diffusive motions in solids and liquids on a time scale between $10^{-9}$ and $10^{-12}$ s. Because of the high incoherent cross-section of hydrogen, hydrogenous organic materials and hydrogen-containing samples, in general, have benefited from this technique. Some studies of the diffusion of other atoms such as silver and sodium are feasible but only very few have successfully been carried out. A recent experiment (4) on IRIS has observed what may be the lowest diffusion constant observed with neutron quasielastic neutron scattering, 3.1 $10^{-8}$ $cm^2/s$. A sample of sodium silicate glass was studied as a function of temperature, again using the mica (002) analysers, and line broadenings of 0.1 to 0.5 μeV were observed at low Q in exact agreement with macroscopic tracer measurements of the sodium self-diffusion. The data is now being analysed to determine the precise details of the diffusional jumps. This experiment was served by a fair degree of serendipity since the sample has a high coherent scattering

cross-section which ought to have drowned the relatively weak incoherent cross-section of sodium. Because of the long wavelength used however, the Q-range of the measurement was well below the first peak of the coherent structure factor so that no contamination was present in the data.

Small molecules such as hydrogen, methane and ammonia will absorb, in an apparently continuous and non-stoichiometric manner, into the large two-dimensional galleries in graphite intercalation compounds. In the second stage caesium compound (two layers of graphite and one layer of caesium) ammonia chemically binds to the caesium atom, in what is thought to be a tetrammine molecule. Thermodynamic limits on gas uptake also point to a $Cs(NH_3)_4$ molecule and this is consistent with the evolution of the tunnelling spectra with ammonia concentration, and the simultaneous high resolution neutron diffraction studies. The inelastic spectra out to an energy transfer of 2meV and the diffraction pattern in the region of the *(003)* interplanar reflections were studied simultaneously using IRIS (5). The data are shown in figure 6 as a function of $NH_3$ concentration up to 1.9 molecules of ammonia per caesium atom. The diffraction patterns show that the absorption process is not continuous as might be inferred from the thermodynamic data. Instead there exist at least two well-defined intermediate phases with distinct c-axis swellings and probably more, and these phases coexist over wide concentration ranges.

The inelastic spectra show a similar variation of distinct features with ammonia concentration and these features can be directly linked to the changes in the structure indicated by the diffraction data. The conclusion that there is a direct causal link between the structural evolution of the absorption process and the dynamical behaviour of the $NH_3$ groups is clearly valid when simultaneous measurements are carried out.

There are a wide range of experiments which can benefit from the extended d-spacing coverage which can be accessed using long wavelength time of flight diffraction with good resolution. These include the investigation of superstructures in ordered magnetic materials, the study of large unit cell organic samples such as clathrated compounds and biomolecular materials, and the study of certain materials in massive sample environment equipment such as pressure cells, where it is possible to measure beyond the Bragg edge of the materials surrounding the sample. An example is the study of magnetic ordering in ferric vanadate $FeVO_4$ (7) which exhibits two ordering transitions at low temperatures (9.5K and 14.5K). A temperature scan

of the diffraction pattern from 4K to 20K in Fig 7 shows the onset of ordering in both phases and the disappearance of all magnetic Bragg lines above the second transition temperature. In similar measurements split lines at 11.9Å, using almost 24Å neutrons, have been clearly observed, underlining the need for such resolutions at long d-spacings.

## Conclusions

Cold neutron intensities on pulsed sources, in contrast to the accepted view only 2 or 3 years ago, have been demonstrated to be very high and data rates on high resolution spectrometers are at least as high as those available on the best reactor-based instruments. Unique instrumentation providing simultaneous diffraction capabilities or long d-spacing diffraction, and white beam reflectometry can and has taken advantage of these fluxes. More significantly this demonstration shows that pulsed neutron sources have the potential to be complete neutron sources and not just speciality generators of thermal and epithermal neutrons. This has important consequences as decisions are taken on the next generation of neutron sources in Europe such as the European Spallation Source, ESS, and AUSTRON.

## References

(1) "A Guide to Facilities at the ILL" The ILL yellow book. B Maier and H Blank ILL Scientific Secretariat.

(2) A D Taylor Rutherford Appleton Laboratory report RAL-120-1984

(3) C J Carlile and M A Adams Physica B 182 (1992) 431

(4) D Beyer, Ch Kaps, C J Carlile and R Hempelmann Z für Physik 1993 (submitted)

(5) C J Carlile, I McL Jamie, G Lockhart and J W White, Mol. Phys. 76 (1992) 173

(6) J B Forsyth, C Wilkinson and C J Carlile to be published.

## Figure Captions

Fig 1. A comparison of the peak fluxes at ISIS with the average fluxes at ILL

Fig 2. The IRIS analyser tank showing the two sets of analyser/detectors and the diffraction detector at high scattering angles.

Fig 3. The flux at the sample position as a function of neutron wavelength on the IRIS spectrometer and the HRPD diffractometer on the ISIS pulsed source. IRIS views the 20K hydrogen moderator and HRPD views the 120K methane moderator.

Fig 4. Tunnelling in nitromethane measured using the mica (002) analyser with a resolution of 1.2 μeV at a final analysed wavelength of 19.8 Å.

Fig 5. The diffusional broadening in sodium silicate glass caused by the self-diffusion of sodium.

Fig 6. Simultaneous diffraction patterns around the *(003)* reflection, and tunnelling spectra from $C_{28}Cs(NH_3)_x$ as a function of $NH_3$ concentration $x$ showing the parallel evolution of structural and dynamic features.

Fig 7. The onset of magnetic ordering in Ferric Vanadate using cold neutron diffraction showing the two phase transitions at 9.5K and 14.5K.

## ISIS Peak Flux / ILL Mean Flux as Function of Energy

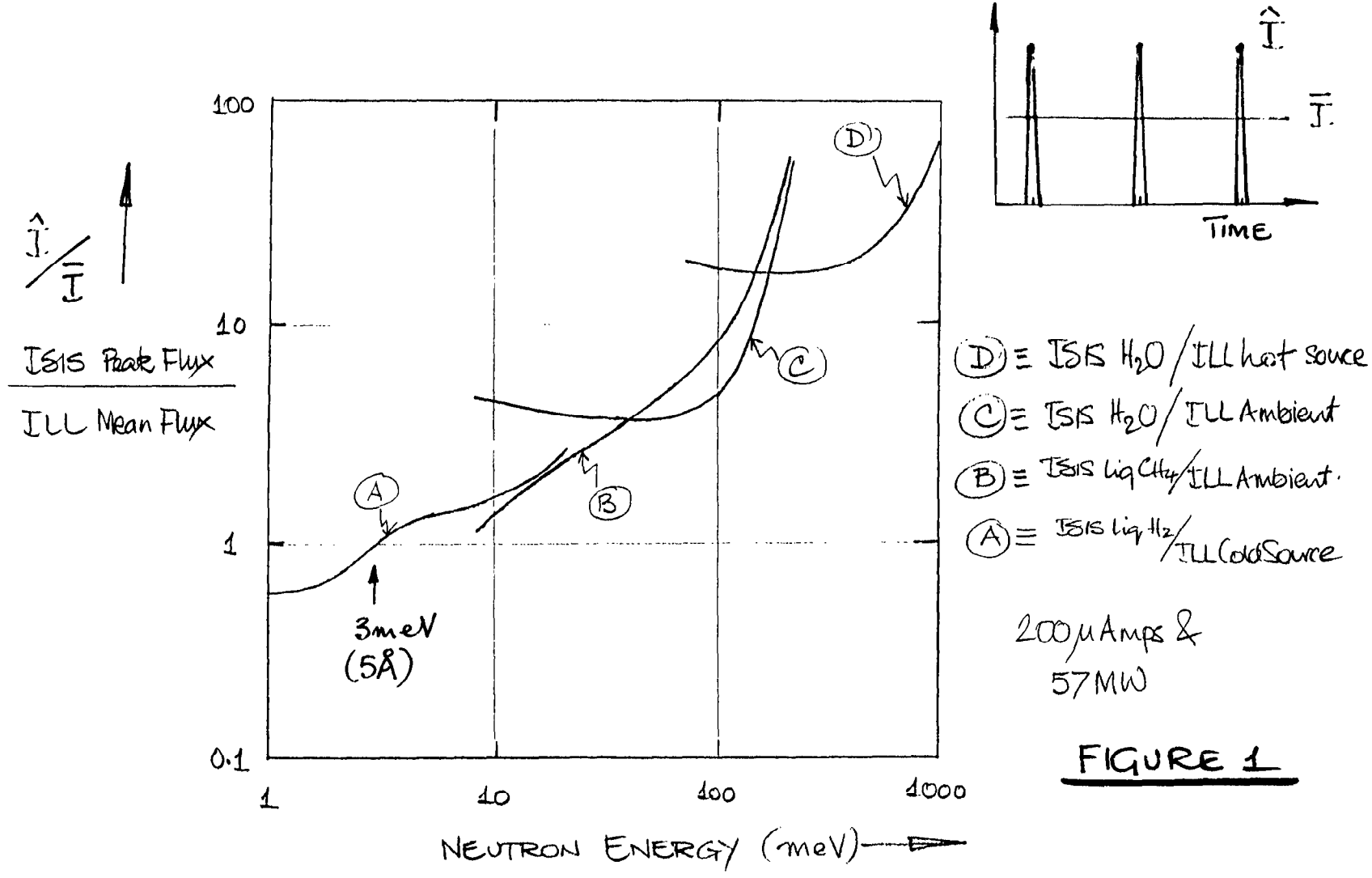


FIGURE 1

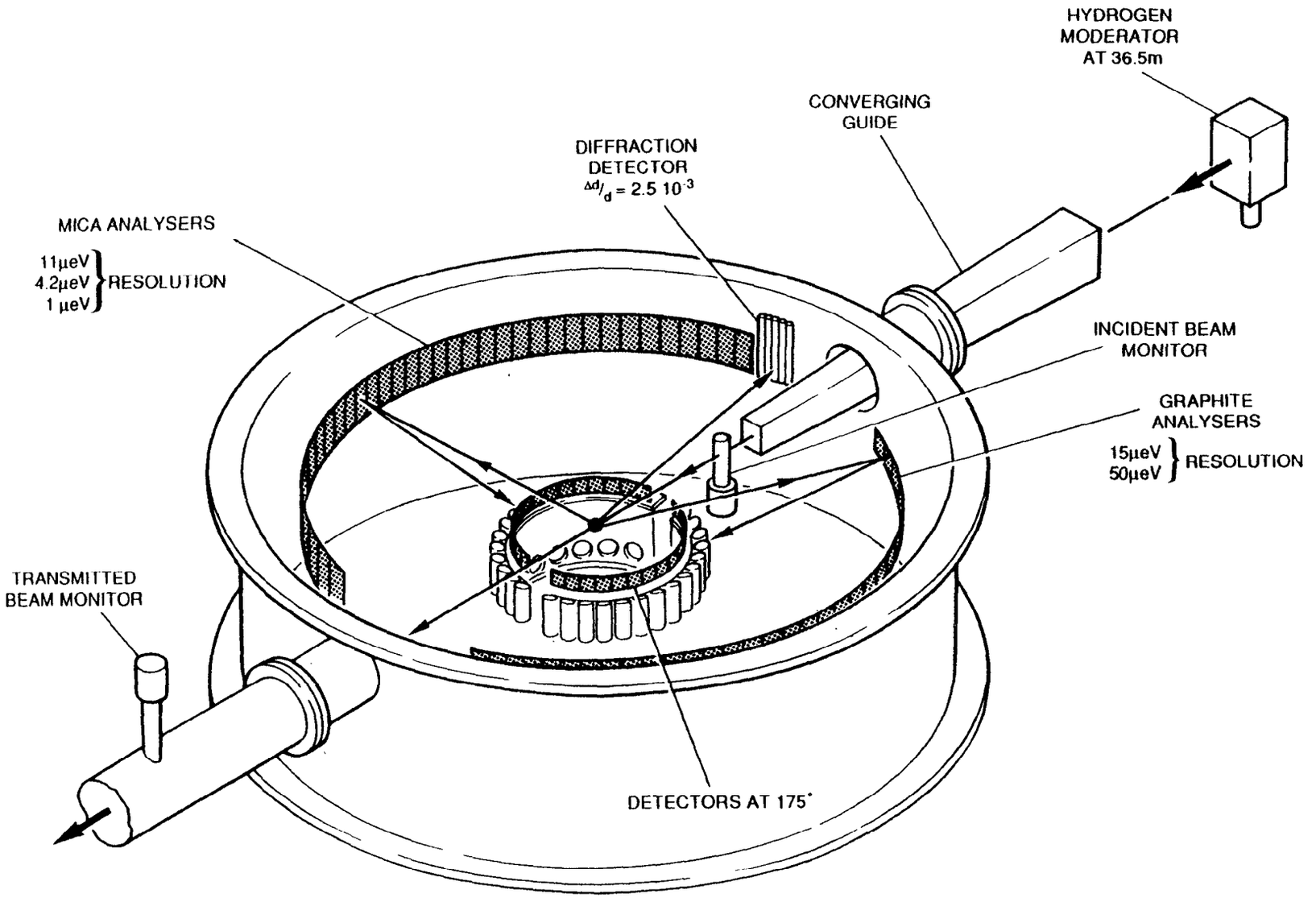


THE IRIS SPECTROMETER

FIGURE 2

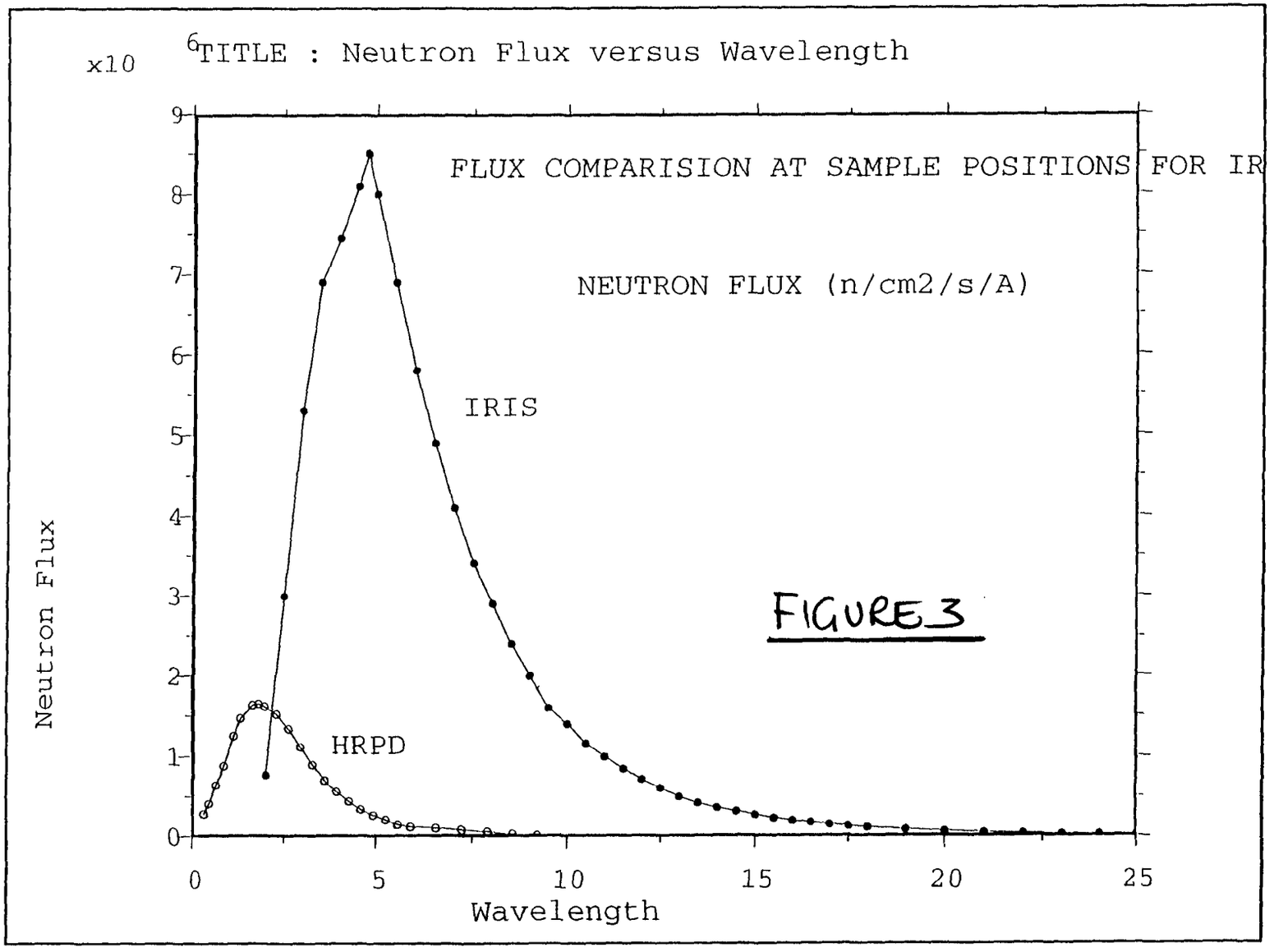
x10
6
TITLE : Neutron Flux versus Wavelength
FLUX COMPARISION AT SAMPLE POSITIONS FOR IR
NEUTRON FLUX (n/cm2/s/A)
IRIS
HRPD
FIGURE 3
Neutron Flux
Wavelength
0
1
2
3
4
5
6
7
8
9
0
5
10
15
20
25

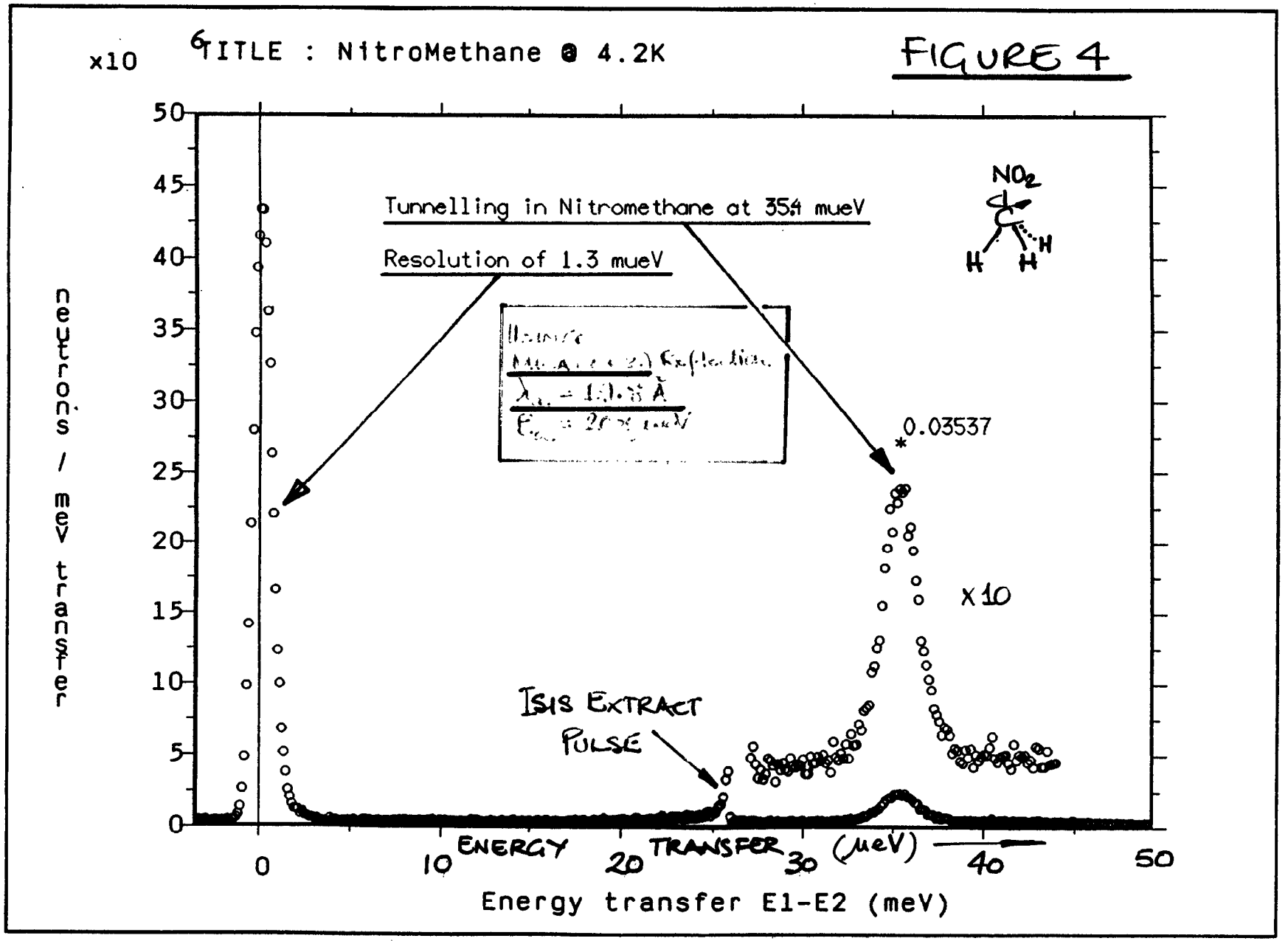
x10
TITLE : NitroMethane @ 4.2K
FIGURE 4
Tunnelling in Nitromethane at 354 mueV
Resolution of 1.3 mueV
0.03537
x10
ISIS EXTRACT PULSE
ENERGY TRANSFER (μeV)
neutrons / mev transfer
Energy transfer E1-E2 (meV)
0
5
10
15
20
25
30
35
40
45
50
NO2
H
H
H

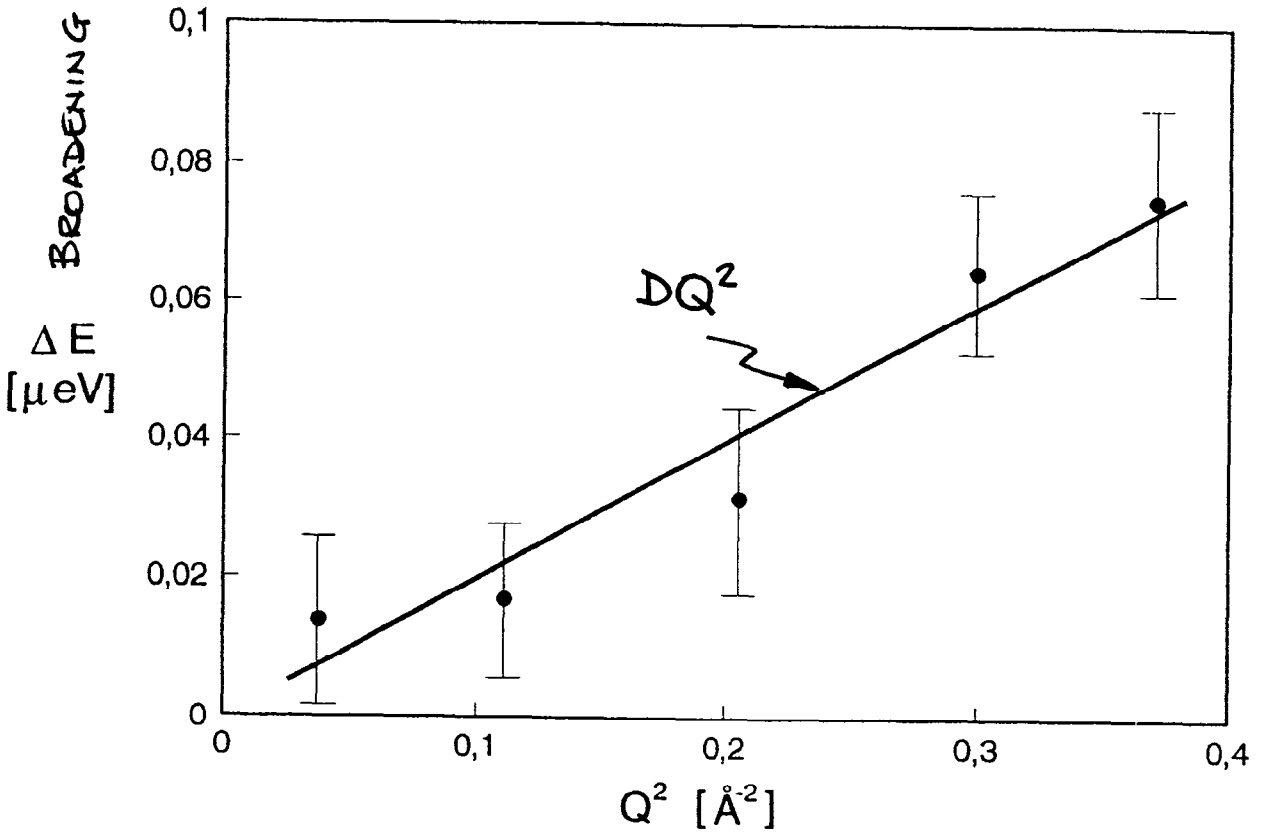
BROADENING
ΔE
[μeV]
0,1
0,08
0,06
0,04
0,02
0
0
0,1
0,2
0,3
0,4
DQ²
Q² [Å⁻²]

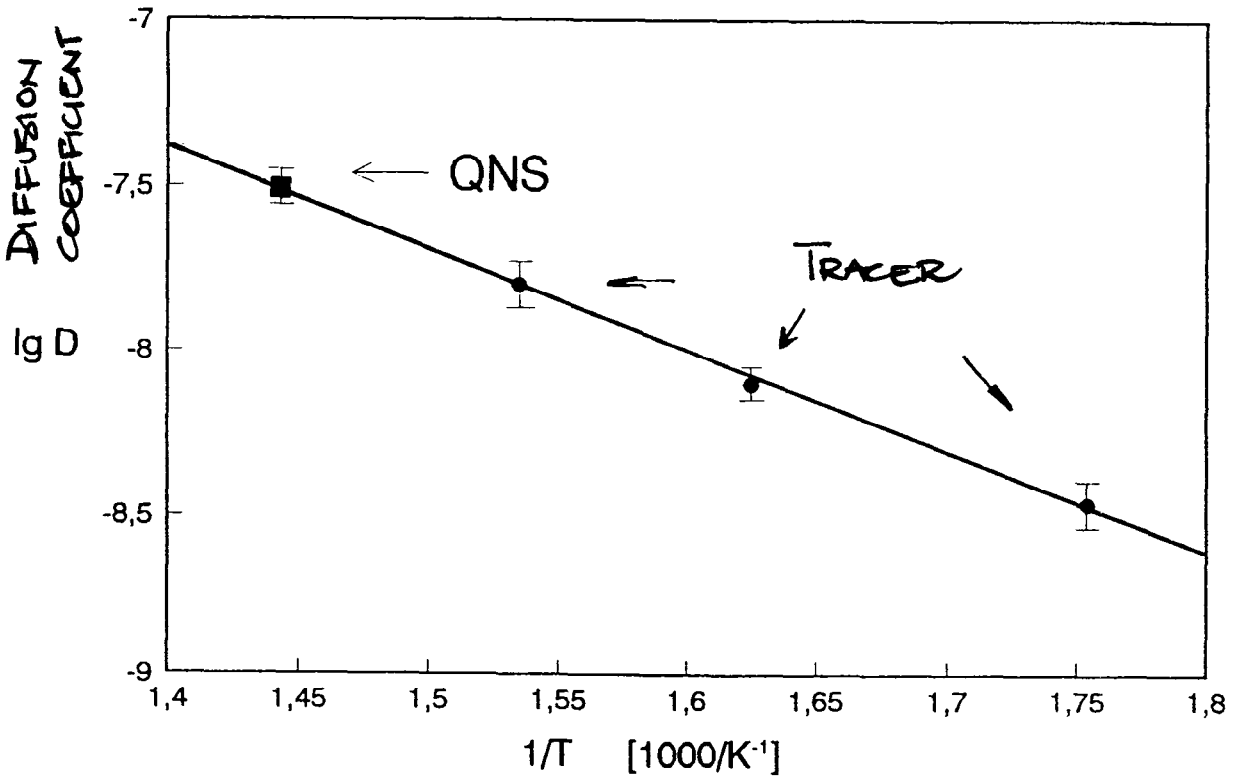
DIFFUSION COEFFICIENT
lg D
-7
-7,5
-8
-8,5
-9
1,4
1,45
1,5
1,55
1,6
1,65
1,7
1,75
1,8
QNS
TRACER
1/T [1000/K⁻¹]

FIGURE 5

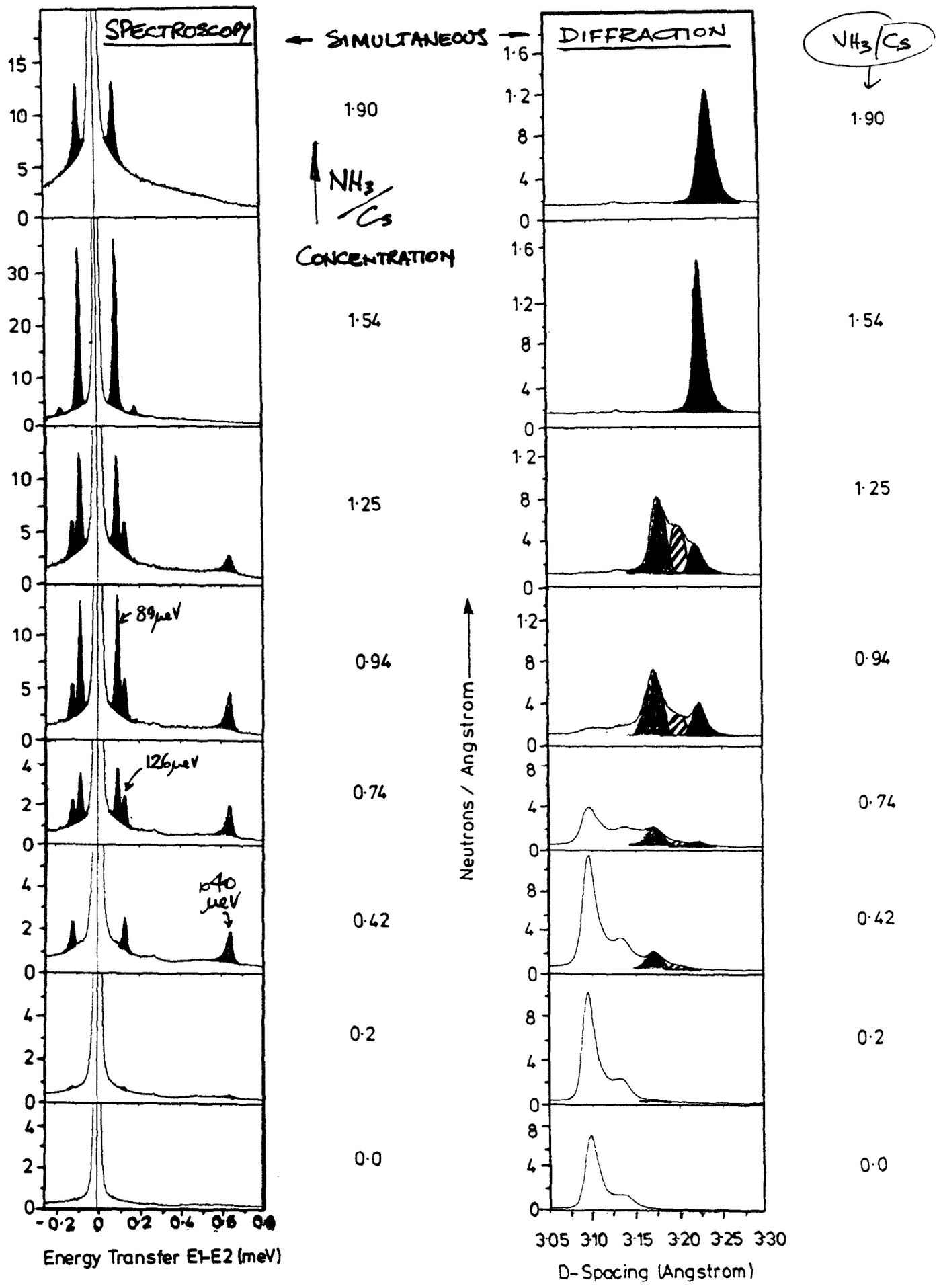
SPECTROSCOPY
← SIMULTANEOUS →
DIFFRACTION
NH3/Cs
1·90
1·54
1·25
0·94
0·74
0·42
0·2
0·0
NH3/Cs
CONCENTRATION
89μeV
126μeV
40 μeV
Neutrons / Angstrom
-0·2 0 0·2 0·4 0·6 0·8
Energy Transfer E1-E2 (meV)
3·05 3·10 3·15 3·20 3·25 3·30
D-Spacing (Angstrom)

**FIGURE 7** *Repeat pattern of FeVO4 at 5 K taken with new detector.*

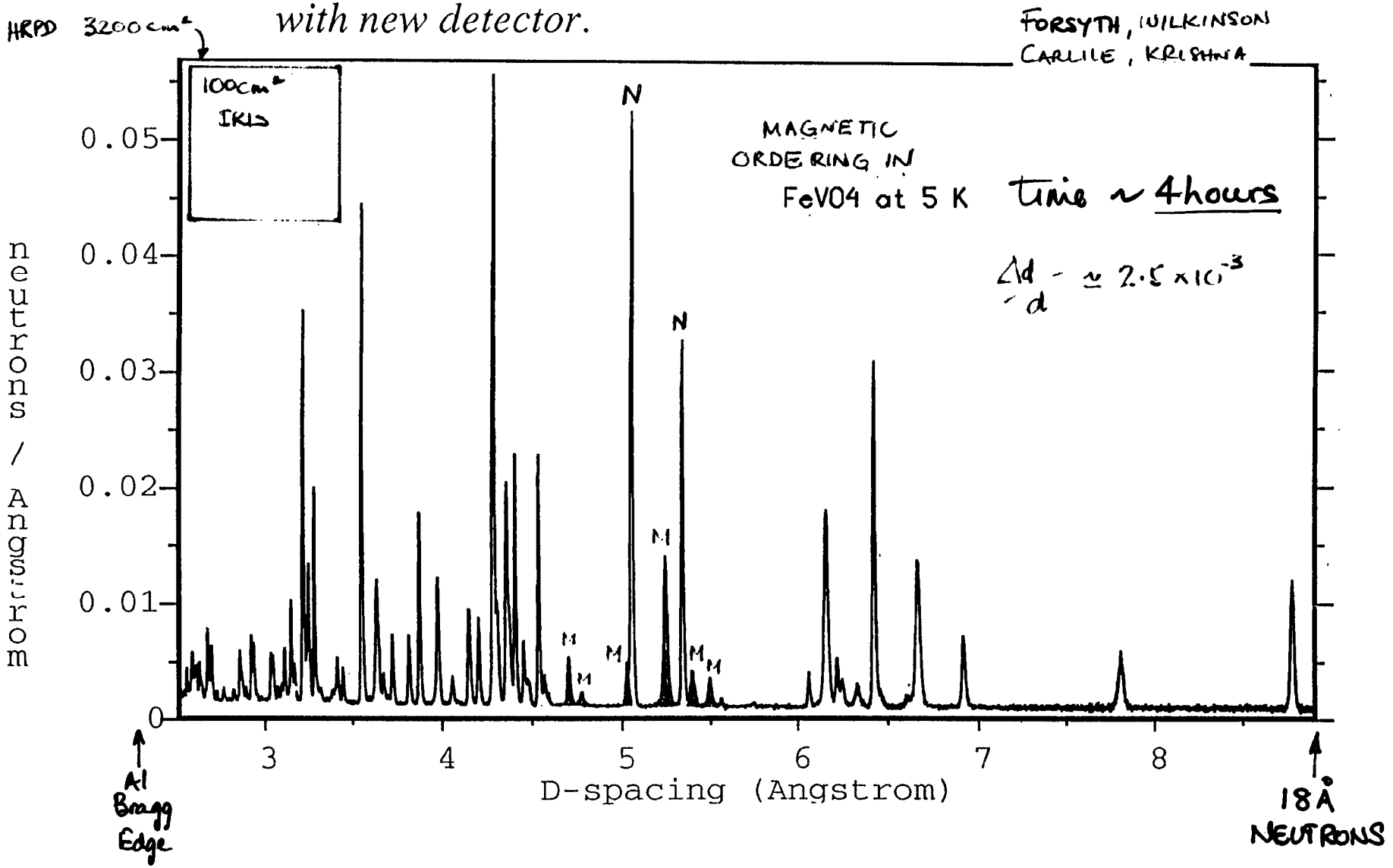

# MULTICRYSTAL INVERTED GEOMETRY SPECTROMETER NERA-PR AT THE IBR-2 PULSED REACTOR

I.Natkaniec[1,2], S.I.Bragin[1], J.Brankowski[2], J.Mayer[2]

[1] Frank Laboratory of Neutron Physics, JINR, 141980 Dubna, Russia
[2] H.Niewodniczanski Institute of Nuclear Physics, 31-342, Cracow, Poland

## Abstract

The NERA-PR spectrometer is intended for inelastic (INS) and quasielastic (QNS) neutron scattering research with simultaneous check of sample structure by powder neutron diffraction (ND). The wavelength spectrum of incident neutrons is analyzed by time of fight on the 109 m reactor - sample flight path. Beryllium filters and pyrolitic graphite or Al, Cu and Zn monocrystals in front of the detectors are used as monochromators of the scattered neutrons. This permits wide variation of the spectrometer's resolution. The design and performance details of the spectrometer are reported. The variable configuration of the spectrometer setup allows simultaneous performance of INS, QNS and ND experiments which fact extremely suits the aims of investigation of substances exhibiting phase polymorphism.

## 1. Introduction

The inverted geometry spectrometers developed for the instrument suit of the JINR pulsed reactors in Dubna are the result of evolution of a simple energy loss inelastic spectrometer with a beryllium filter towards a difference Be-BeO filter [1] and, finally, a combination of a beryllium filter and crystal monochromator in front of the detector [2]. The idea of simultaneous investigation of the dynamics and structure of solids [3] that B. Buras suggested in 1966 was experimentally tested in the next two years [4] at the IBR pulsed reactor. However, wide demand for and high cost of electronics hindered construction of multipurpose spectrometers at that time. The obstacles were removed with appearance of semiconductor-based memories and mini-computers for data collection and instrument control in neutron scattering experiments. The new generation of multi-detectors inverted geometry spectrometers [5-7] made routine the simultaneous investigations of the structure and dynamics of complex molecular crystals [7,8], superionic compounds [9], metal hydrides [10] etc. at the IBR-2 high flux pulsed reactor.

The inverted geometry spectrometer KDSOG-M [6] on the 30 m flight path of the IBR-2 reactor has high luminosity, but limited resolving power of both inelastic and diffraction spectra because of rather large duration of the thermal neutron pulse (about 300 μsec). Considerable resolution improvement, especially for the INS investigations in the region of energy transfers above 20 meV, could be achieved by making essentially longer (by about a factor of 3) the flight path to be traveled by the incident on sample neutrons. The design of the NERA-PR spectrometer [11] exploits the idea. It was realized after mirror vacuum neutron guides have been manufactured and installed to guide thermal neutrons to this long distance without essential loss of the flux intensity. The arrangement of this spectrometer additionally allows investigation of stochastic motions of molecules or their fragments with the help of quasielastic scattering of neutrons. The beam of scattered by sample neutrons is reflected on monocrystal energy analyzers in the direction of the detector, i.e. "nearly backward", and allows one to reach the resolving power of about 40 μeV.

## 2. Description of the Spectrometer

The schematical lay-out of the spectrometer is shown in Fig.1. The neutron beam having been formed in the active core of the reactor and thermalized when passing through the moderator is guided by the vacuum, mirror neutron guide to a distance of 2.5 m from the sample (1) which is positioned at a distance of 109.05 m from the moderator. The aperture of the nickel mirror neutron guides is 50 mm wide by 160 mm high. On the path of the primary neutron beam at a distance of 5.5 m and 15.5 m from the moderator, respectively, two choppers are installed: the disk which rotation about the horizontal and the drum about the vertical axis is synchronized with reactor pulses. This arrangement allows effective reduction of the background of fast neutrons.

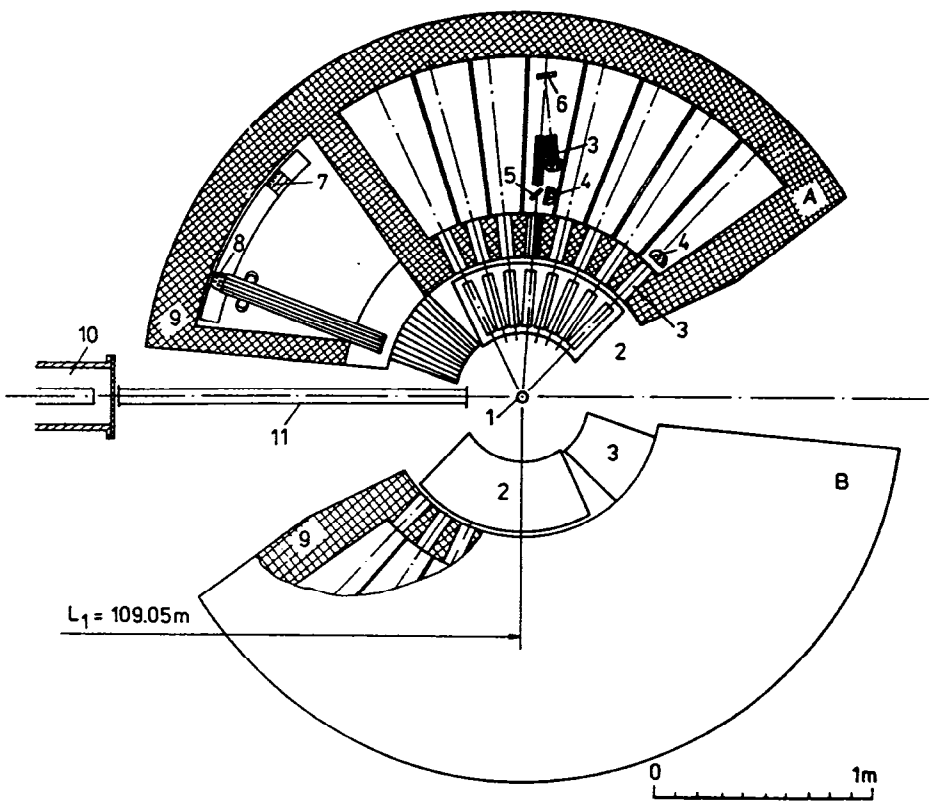


**Fig.1.** Sketch of the spectrometer NERA-PR:
1 - sample, 2 - Be-filters, 3 - collimators, 4 - $^3$He detectors (INS and QNS), 5 - pyrolitic graphite analyzer, 6 - single crystal QNS analyzer, 7 - detector for high intensity diffraction, 8 - detector for high resolution diffraction, 9 - spectrometer shielding, 10 - Ni-coated mirror neutron guide in a vacuum tube, 11 - vacuum neutron guide.

The spectrometer has the two shoulders A and B of like built. Each has eight sections for neutron elastic and quasielastic scattering and one for diffraction measurements. Rails allow displacements of both shoulders about the spectrometer's (1) axis and variation of the angle between the neutrons incident and scattered on the sample. The diffraction sections of A and B for the scattering angles $170 \geq 2\theta \geq 110$ and $70 \geq 2\theta \geq 10$, respectively have neutron detectors which permit one to carry out the measurements with either high luminosity (7) or high resolution (8). The detectors (8) are the assemblies of five $^3$He proportional counters (SNM-17) arranged in a chess order for the detector to have the area equal to the beam cross section (50 mm x 160 mm) and the thickness about 20 mm. Collimation of the scattered neutron beam is accomplished with a 750 mm length soller collimator with a minimum vertical width of slit of 5 mm giving an angular divergence of about 20'. The detectors (7) are the assemblies of four counters operating independently with an

angular shift of 1.2 degrees. In the latter case the collimation of the scattered beam depends on the diameter of a single counter and the distance between the radialy converging plates of the collimator (3) to make 45'.

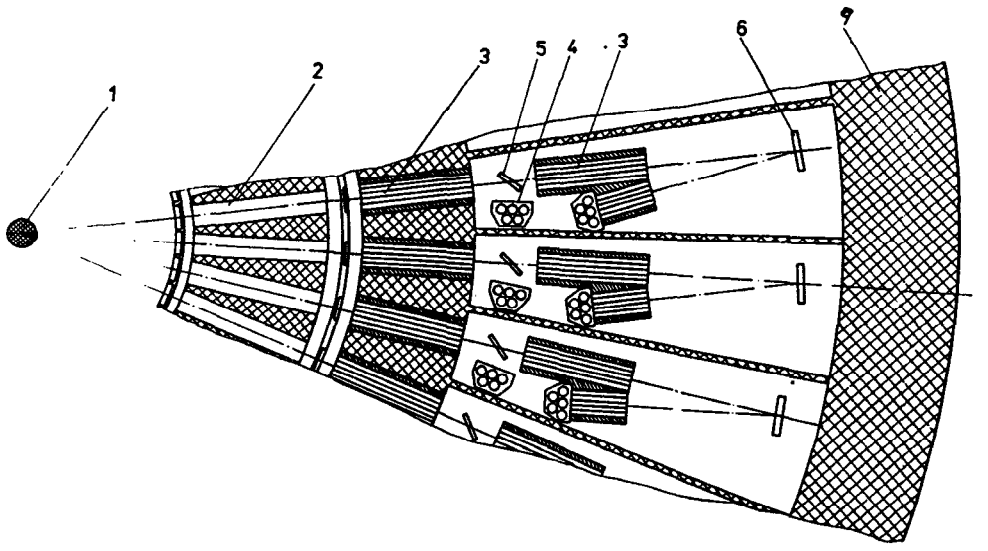


**Fig.2.** The INS and QNS neutron energy analyzers and detectors of the spectrometer NERA-PR. The numbers indicate the same options as in Fig.1.

The sections for neutron inelastic and quasielastic measurements are detailed in Fig.2. The neutrons scattered by sample (1) pass through a common for eight scattering angles beryllium filter-collimator (2) which is being cooled with liquid nitrogen. It is made of polycrystalline beryllium plates and cadmium sandwiched between every 20 mm. The total thickness of beryllium is 240 mm and the window is 40 mm x 160 mm. Behind the filter the soller collimators (3) with a minimum slit width of 5 mm are positioned which having the length of 200 mm ensure the horizontal collimation of 1.2°. The design of this sections allows analysis of scattered neutron energies to be carried out in three ways:

a) With the help of the beryllium filter, only. The neutron detector (4) having the analogous with (8) design (Fig.1) is installed immediately after the collimator (3). In this case the spectrometer has high luminosity at low energy resolution.

b) With the help of monocrystal analyzers (5) which exploit the Bragg reflection on a given crystallographic plane. The energy for analysis is usually selected in the immediate vicinity of the beryllium edge by rotating the crystal analyzer (5). The filter allows suppression of higher order reflections. Plates of pyrolytic graphite are conventionally used as analyzers, because of their high reflectivity. The analyzers are composed of four plates having the total size of 50 mm x 200 mm.

c) By making use of the Bragg reflection on a monocrystal (6) in the direction "nearly backscattering" ($2\theta$ = 172°). This version can be carried out simultaneously with the second one because the positions of elastic lines for the monocrystals of Al(111) or Zn(002) are sufficiently different from those of neutron energies reflected on a pyrolytic graphite at the scattering angle of about 43°. The elastic peak width is determined by both the TOF resolution of the reflected neutron wavelength and the mosaicity of the used monocrystals. For tested Zn(002) and Cu(111) monochromators it reaches the value of 30 and 50 μeV, respectively. This method has rather limited luminosity and, therefore, is mainly applied to investigation of the quasielastic scattering of neutrons.

All spectra of scattered neutrons are measured with two-dimensional analyzers, "number of detector - TOF". The analyser's units (different for diffraction, quasielastic and inelastic scattering) are made in the CAMAC standard. Control of analyzers and data files accumulation are performed by a PC/AT-386 linked to the local ETHERNET network.

## 3. Luminosity and Resolution

The thermal neutron intensity at the exit of a mirror neutron guide measured with the neutron activation analysis method makes $4.6\times10^6$ n/cm$^2$sec and it is comparable with the neutron flux $6.6\times10^6$ n/cm$^2$sec in a 30 m vacuum neutron guide of the spectrometer KDSOG-M [6] in agreement with the estimates made when designing the mirror guide. The geometry of neutron distribution on a sample was investigated using neutron sensitive photo-films. It appears to be very homogeneous and the beam divergence from the mirror guide edge to the spectrometer axis does not exceed 5 mm.

The intensity of scattered neutrons $N(t_0)$ detected at the time $t_0$ after the start of the time analyser is described with good approximation by the formula [2]:

$$N(t_0) = \Delta t_0 \iiint de\, E_i\, dE_f\, dt\, F(E_i, E_f, t_0, t)\, \sigma(E_i, E_f, \phi, T), \tag{1}$$

where $\Delta t_0$ is the time interval corresponding to the width of the time channel of the analyser, $F(E_i, E_f, t_0, t)$ is the apparatus function describing the resolution of the spectrometer, $\sigma(E_i, E_f, \phi, T)$ describes the neutron scattering law, which in its general form depends on the energy, $E_i$ and $E_f$, of incident and scattered neutrons, on the scattering angle, $\phi$, and the temperature of the sample, T.

To calculate the resolution of the spectrometer we used the scattering law in the form $\delta(E_i - E_f - \omega)$ at a given value of energy transfer, $\omega$. The apparatus function has the form:

$$F(E_i, E_f, t_0, t) = \rho(E_i, t)\, \Phi(E_i)\, n(E_f)\, \delta\left(t_0 - t - \frac{\alpha L_1}{\sqrt{E_i}} - \frac{\alpha L_2}{\sqrt{E_f}}\right), \tag{2}$$

where $\rho(E_i, t)$ describes the time distribution of incident neutrons with the energy $E_i$, $\phi(E_i)$ represents the energy distribution of the neutrons leaving the moderator; $n(E_f)$ is the distribution of neutrons after scattering. The function

$$\delta\left(t_0 - t - \frac{\alpha L_1}{\sqrt{E_i}} - \frac{\alpha L_2}{\sqrt{E_f}}\right),$$

gives the conditions of registration at the moment $t_0$ of a neutron leaving the source with the energy $E_i$ at the moment t to have after being scattered by the sample the energy $E_f$ ($L_1$ and $L_2$ denote the moderator-to-sample and sample-to-detector flight paths, respectively, $\alpha$ is the energy to velocity conversion coefficient).

The time distribution of incident neutrons $\rho(E_i, t)$ is calculated as convolution of an IBR-2 fast neutron pulse shape function (the Gauss function with the width 215 μsec) with the function describing the process of neutron moderation.

$$Z(t, E) \sim \frac{1}{\tau(E_i)} exp[-t/\tau(E_i)]U_+(t), \tag{3}$$

The value of

$$\tau(E_i) = 210.[1 - exp(-E_i/113.2)], \tag{4}$$

for the cock-shaped moderator of IBR-2 was taken from [12]. The energy distribution of neutrons leaving the moderator $\phi(E_i)$ was determined in accord with the results of fit to the experimental spectra of elastic scattering by vanadium. The energy distribution of detected neutrons $n(E_f)$ was

obtained with account of the transmission function of the beryllium filter [1] and the gaussian distribution of neutrons reflected on a crystal analyser. The width of this distribution was considered equal to the energy width at half maximum of an elastic peak. In this way the collimations of beams were taken into account, though not entering directly in the formulas (1) and (2).

The resolution functions calculated after these formula for different analysers of scattered neutron energy are shown in Fig.3. It is seen that at energy transfers above 100 meV the resolution analysing crystal are determined by the power pulse width from the IBR-2 reactor.

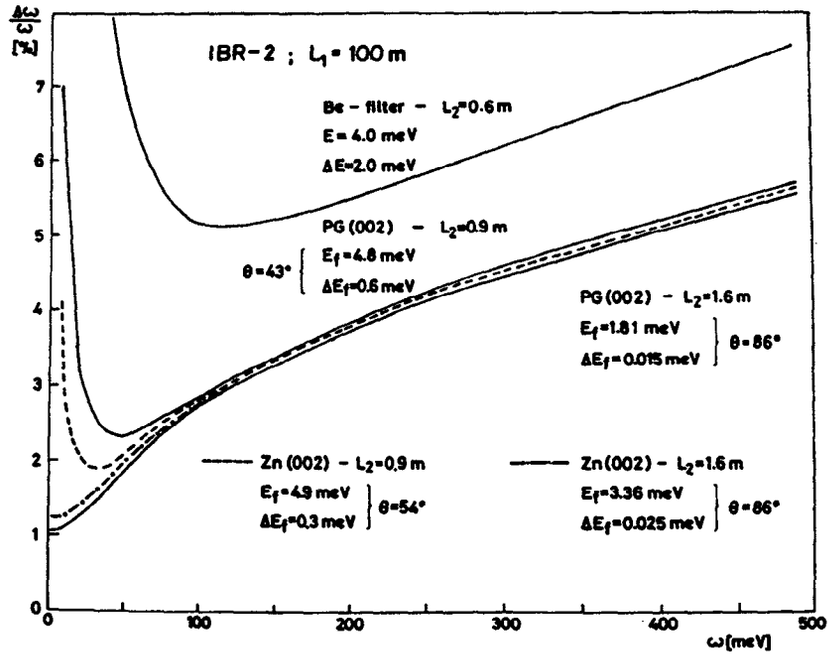


**Fig.3.** The resolution functions vs energy transfer for different analysers: upper solid curve — for Be filter; middle and lower solid curves — for pyrolytic graphite at different angles; dashed and dot-dashed lines — for zinc analyzer.

Figure 4 compares the INS resolutions of the NERA-PR and KDSOG-M spectrometers with pyrolytic graphite analysers. At energy transfers above 10 meV the resolution of the NERA-PR spectrometer becomes three times better and makes 3-5 % up to the energy transfer of the order of 500 meV.

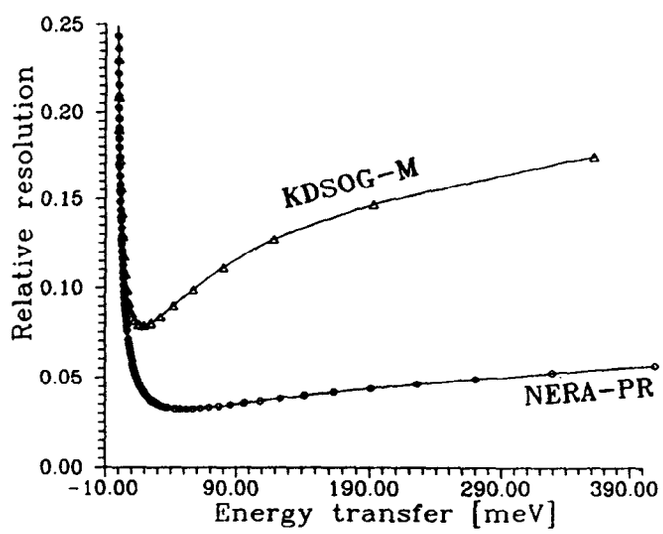


**Fig.4.** Relative INS resolutions $\Delta\omega/\omega$ of the KDSOG-M and NERA-PR inverted geometry spectrometers with pyrolytic graphite analysers at the IBR-2 pulsed reactor.

Calculated resolution functions are in good agreement with those measured with standard samples for all three types of spectra: inelastic and quasielastic scattering and diffraction of neutrons.

Figure 5 illustrates the spectrum of $NH_4Cl$ measured on the KDSOG-M spectrometer with graphite analysers in comparison with that measured on the NERA-PR spectrometer with a beryllium filter. This experiment confirms the prediction that under these conditions both spectrometers are comparable in resolution and luminosity.

Figure 6 shows comparative high resolution spectra of the hydrazine sulfate sample measured on the NERA-PR spectrometer at IBR-2 and the TXFA [13] spectrometer at the neutron spallation source ISIS. In the region of energy transfer below 100 meV both spectrometers have practically coinciding resolution and luminosity. At higher energy transfers the TXFA luminosity is higher thanks to optimization of the moderator for epithermal neutrons.

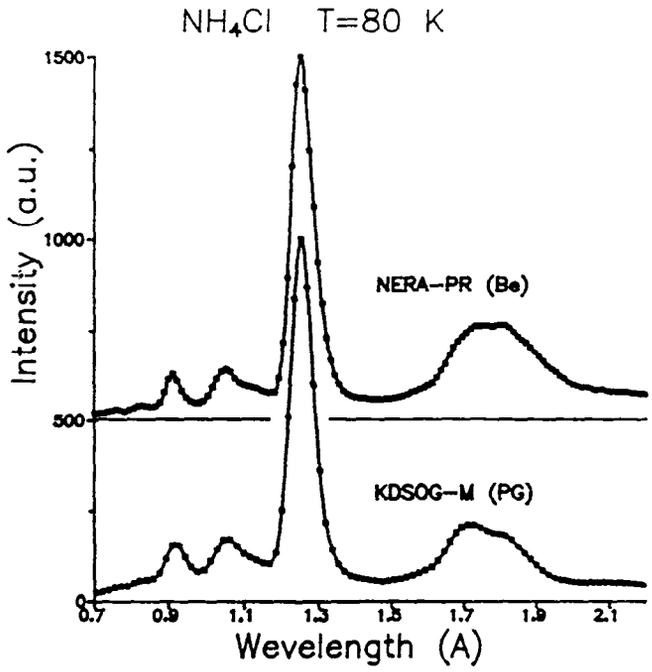


Fig.5.The INS spectra of ammonium chloride at 80 K measured on NERA-PR with beryllium filter analysers and on KDSOG-M with pyrolytic graphite analysers.

Figure 7 shows the neutron quasielastic scattering spectra of an ammonium chloride sample measured with a Cu(111) analyzer. At nitrogen temperature $NH_4Cl$ is in the ordered phase and the elastic peak at the energy $E_0$ = 4.69 meV corresponds to the resolution of the spectrometer and its full width at half maximum is 48 μeV. One can see that this resolution is sufficient for observing diffusion jumps of ammonium groups in a disordered phase at room temperature. Investigation of QNS intensities in dependence on momentum transfer allows one to study the geometry of diffusion jumps and their frequency determines the broadening of the QNS peak. The spectrometer NERA-PR permits study of QNS in the range of scattering angles from 20° to 160° with the energy resolution of about 1% in characteristic energies of the first order reflections on a monocrystal used as analyser.

The ND spectra simultaneously measured at scattering angles ranging from 20° to 70° and from 110° to 170° allow one to study the phase state of an investigated sample together with the behaviour of structural parameters in dependence on temperature, in particular. Figure 8 illustrates the diffraction spectrum of a Ni powder measured with a high resolution detector at the scattering angle of 160°.

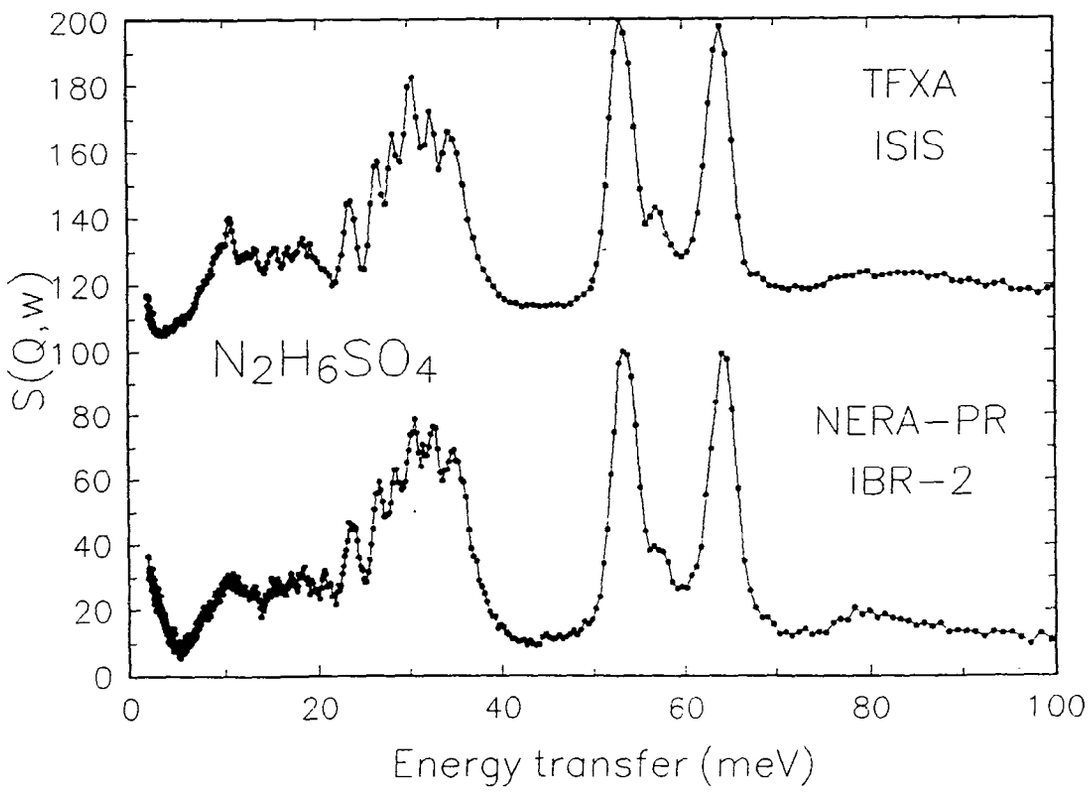


Fig.6. The high resolution INS spectra of hydrazine sulfate measured on the TFXA (ISIS) and NERA-PF (IBR-2) spectrometers with pyrolytic graphite analysers.

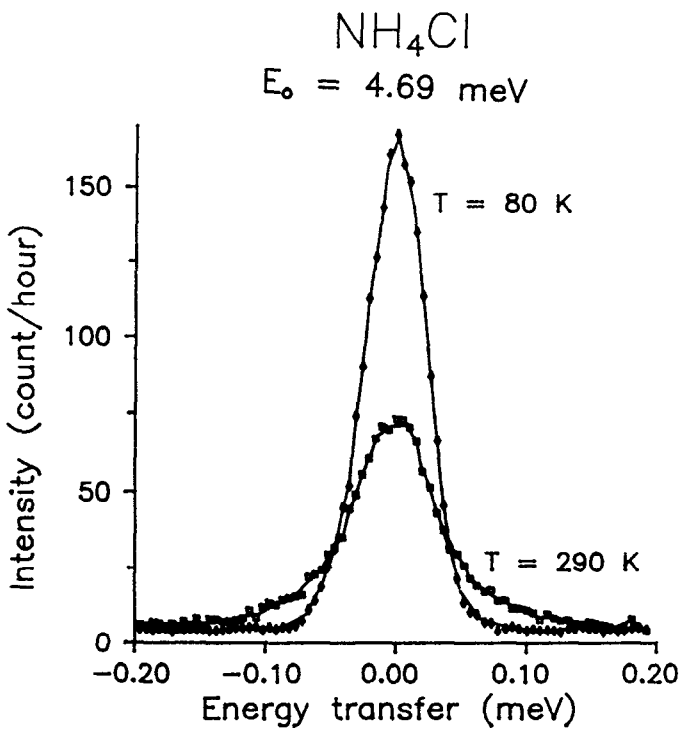


Under these conditions the resolution of the diffractogram is $\Delta d/d$ <0.5% for $d_{hkl}$ <1Å. With such resolution of the NERA-PR spectrometer one can measure the interplane distances up to 4Å. By measuring ND spectra in the angular range from 20° to 70° one can study the interplane distances up to 15Å with the resolution of the order of 1 to 3%.

Fig.7. The QNS spectra of ammonium chloride measured with a Cu(111) analyser at the scattering angle 80°.

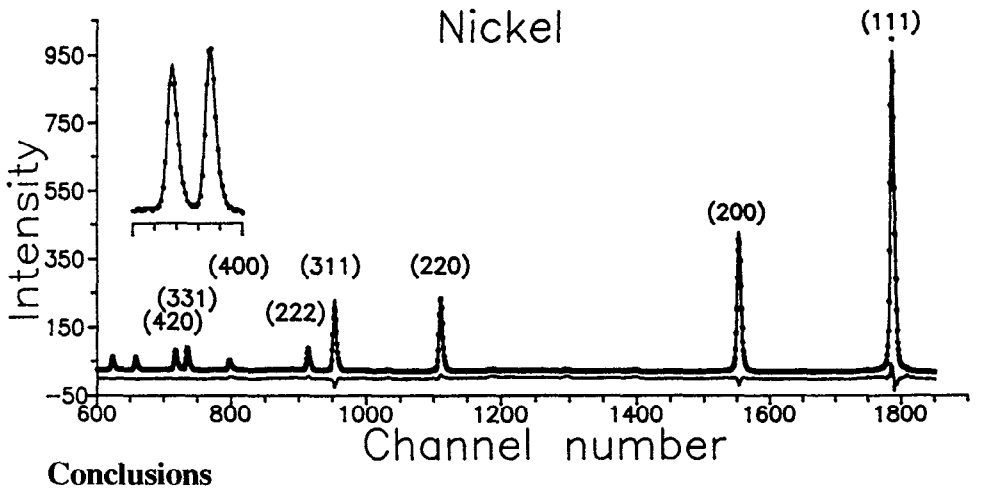


Fig.8.The Ni powder diffraction spectrum normalized to the incoming neutron spectrum measured at 160° scattering angle by a high resolution detector (8). Solid line represents a difference between the experimental and calculated by Rietveld method [14] spectra.

## 4. Conclusions

The NERA-PR design is optimized for operation at the high flux pulsed reactor IBR-2 producing neutron pulses of ca. 215 μ sec at a frequency of 5Hz. Of the period of 200 msec between the neutron pulses 95% of the time is allocated for neutron spectra analysis and about 5% i.e. about 10 μsec, for automatic control of the experimental conditions. Incoming neutrons in the wavelength range from 0.5 to 7 Å are effectively analysed.

The reported results of the test measurements of the physical parameters of the NERA-PR spectrometer show that this universal facility for measuring simultaneously INS, QNS and ND spectra of scattered neutrons belongs to the class of neutron spectrometers of relatively high resolution at good luminosity. These results confirm the calculated parameters laid in the basis of the spectrometer's design. Their comparison with the results obtained for other spectrometers show that all necessary experimental parameter are chosen correctly and the instrument can be transferred to the user's regime of operation. For instrument details see the updated edition of the FLNP User's guide [15].

Last year's experience of operation of the NERA-PR spectrometer has demonstrated usefulness of simultaneous investigation with the INS, QNS and ND methods of the dynamics and structure of

solids. It is especially suitable for investigation of substances, where phase transitions are followed by changes in the structure, lattice dynamics or stochastic motion behaviour of molecules or molecular groups.

**Acknowledgements**

The authors are sincerely grateful to Prof. J A Janik and the late Prof. Yu M Ostanevich for continuous interest and support in realization of this project; to Dr J Sciesinski and Dr S Urban for helpful discussions and comments in the time of preparation of the project; to eng. J Dec and the late eng. J Pawelczyk for the assistance in preparation of design documentation and manufacture of spectrometer parts; to technicians: R Pukala, H Zdziarski and the late T Pukala for the assistance in adjustment of the mirror neutron guides and assembly of the spectrometer; to engs. B Motyka, A P Sirotin, J Sokolowski and A I Zhuravlev for the assistance in manufacture and adjustment of detecting tracks and electronic systems for data storage and control of experimental conditions; to engs. W Iwanski and M L Tchelnokov for development and upgrading of the program for control of spectrometer operations; to Drs A V Belushkin, J Krawczyk. A Pawlukojc and W Zajac for the assistance in development of data procession programs and interest in the utmost use of this instrument's advantages in a physical experiment.

**References**

[1] A Bajorek, T A Matchekina, K Parlinski, F L Shapiro, in: Inelastic Neutron Scattering, IAEA, Vienna 1965, Vol. II, p. 519-535.
[2] K Parlinski, M Sudnik-Hrynkiewicz, A Bajorek, J A Janik, W Olejarczyk, in: Research Applications of Nuclear Pulsed Systems, IAEA, Vienna 1967, p. 179-185.
[3] B. Buras, in: Research Applications of Nuclear Pulsed Systems, IAEA, Vienna 1967, p. 17-34.
[4] I Natkaniec, K Parlinski, J A Janik, A Bajorek, M Sudnik-Hrynkiewicz, in: Neutron Inelastic Scattering, Vienna 1968, Vol. I, p. 65-78.
[5] A V Belushkin, J A Janik, J M Janik, I Natkaniec, W Nawrocik, W Olejarczyk, K Otnes, T Zaleski, Physica, 122B (1983) 217-226.
[6] G Baluka, A V Belushkin, S I Bragin, T Zaleski, M Z Ishmukhametov, I Natkaniec, W Olejarczyk, J Pawelczyk, Comm. JINR, p. 13-84-242, Dubna 1984.
[7] The Spectrometers for Scientific Researches on Pulsed Reactor IBR-2, Ed. by Yu M Ostanievich, Comm. JINR, p. 13-85-310, Dubna 1985.
[8] A V Belushkin, V D Dolganov, I Natkaniec, V G Simkin, Mol. Cryst. Liq. Cryst., Vol. 150B (1987) 187-200.
[9] A V Belushkin, I Natkaniec, M M Plakida, L A Shuvalov, J Wasicki, J. Phys. C, Solid State Phys., 20 (1987) 671-687.

[10] R Wisniewski, R Dimitrowa, I Natkaniec, J Wasicki Solid State Comm., Vol. 54 (1985) 1073-1075.
[11] I Natkaniec, J A Janik, J Mayer, J Pawelczyk, J Sciesinski, S Urban, in: Neutron Scattering in Nineteens, IAEA, Vienna 1985, p. 412.
[12] A N Gundorin, V M Nazarov, Comm. JINR, p. 3-80-721, Dubna 1980.
[13] J Penfold, J Tomkinson: Report RAL -86-019, Rutherford Appleton Laboratory, Chilton, 1986.
[14] V B Zlokazov, V V Chernyshev, J. Appl. Cryst., 25 (1992) 447-451.
[15] User Guide - Neutron Experimental Facilities at the JINR, Ed. by Yu V Taran, Frank Laboratory of Neutron Physics, JINR, Dubna 1992.

# PERFORMANCE OF ROTAX

H. Tietze-Jaensch[1,2,3], W. Schmidt[1,2], R. Geick[1]

1.) Physikalisches Institut der Universität Würzburg, Am Hubland, 8700 Würzburg, F.R.G.
2.) ISIS Facility, Rutherford Appleton Lab., Chilton OX11 0QX, U.K.
3.) Institut f. Festkörperforschung, KFA Jülich, Pf. 1913, 5170 Jülich, F.R.G.

## Abstract

The rotating crystal analyser spectrometer ROTAX started commissioning in October 1992, yet a general survey about the state of the project is given.

The general capability of ROTAX has been presented and discussed in detail at the last ICANS XI held at KEK, Japan in 1990. Therefore, we now concentrate on improvements, new developments and particular problems: A) technical feasibility and reliability; B) multiplex advantage, intensity and background; C) basic and advanced operation scheme of ROTAX, in particular synchronisation and veto action; D) operation schedule.

## 1. ROTAX instrument

Unlike other crystal analyser neutron spectrometers ROTAX uses a programmable non-uniformly spinning analyser crystal in order to scan almost freely the energies of the neutrons scattered and deflected by a single crystal sample placed in a white pulsed beam. On ROTAX this gives a superior flexibility and versality to perform particular scans throughout the $(Q,\omega)$-space when compared with competetive machines. The principles and many details about ROTAX have been discussed in length elsewhere [1-3]. In a series of test experiments using a provisional setup of the ROTAX spectrometer on the ISIS Test Beam facility it has been proved that ROTAX does fulfill standard expectations to an inelastic coherent neutron spectrometer. In fact, the intensity performance was competetive with a setup of a standard crystral analyser spectrometer [3], angular accuracy and technical reliability of the ROTAX motor drive and the overall scan versality were proved satisfactory under realistic conditions at the ISIS test beam. This has lead to the decision to finally build ROTAX at its own construction site behind PRISMA [4] on the N2 beamline of ISIS.

Fig. 1 shows what ROTAX looks like: a large area Tanzboden-like concrete floor is enclosed to a wax tank blockhouse for shielding. The spectrometer components are remotely operated and moving on air pads. Three different sample positions are provided to adjust the scattering geometry to the individual requirements of a

particular experiment. The sample tank is made to the RAL standard granting access to all sample environment equipment available at ISIS. The Germanium analyser crystal is of cylindrical shape, 5 cm in height and 1.2 cm in diameter. Other analysers are under consideration for later use. The linear position sensitive JULIOS scintillaton counter, devised by KFA Jülich [5], is used on ROTAX.

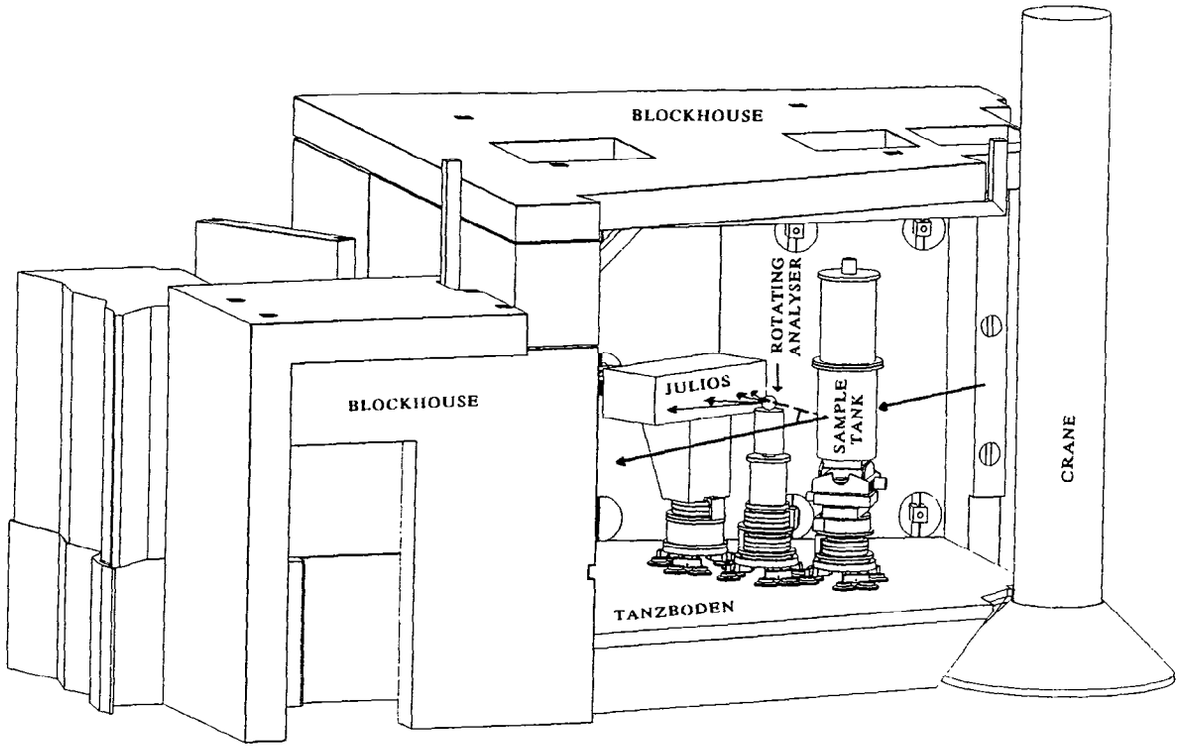


Fig. 1: The ROTAX hardware installed at the N2 beamline at ISIS

## 2.) present status

Very recently, ROTAX has become operational, but still runs at a first stage of limited operation control comfort.

After basic development and construction was finished, ROTAX started commissioning on 20 October 1992 with actually opening the neutron beam in the ROTAX shielding blockhouse. All major components, i.e. the detector, the analyser drive and the whole mechanics, i.e. the various rotational stages, sample alignment, analyser and detector support frames and double pivoting arm, are installed and at present operated by individual PC controls. In fact, the JULIOS detector actually used is a loan from KFA Jülich. Our own unit is in manufactoring process and expected for installation later this year.

A major improvement has been achieved with the accuracy and reliability of the ROTAX analyser drive: the digitally controlled gear-less direct drive is now entirely

software controlled. The advantages are: a) much improved angular accuray, now at a max. angular misfit of $\Delta\Theta_A < 0.15$ deg, b) on-line verification of desired and achieved performance at 10kHz sampling rate (100 $\mu$s), c) on-line dynamic correction scheme according to the dynamic response function of the regulator/motor drive system [6], d) permanently guaranteed and stabilised regulation parameters over the whole range of technically feasible drive parameters without any operator's interaction, e) hardware independence and portability of the drive control program. All the user of ROTAX needs to do is to think of a desirable and suitable TOF-scan throughout $(Q,\omega)$ space and then to check technical feasibility for his particular ROTAX-scan with the aid of our instrument control program and finally dump the desired anayser scan curve in a file that is read by the signal processor running the analyser motor control.

At present we are working on the integration of all the individual components to one whole system. Nevertheless, all major components (mechanics, analyser, detector) are individually operational already. The timers of the detector and the motor drive are not yet synchronised, which needs the full implementation of the transputer board and interface. Until now, they are externally triggered by a common pulse signal that indicates the start of a neutron pulse at the moderator. Time resolution now is ca. 2-3 $\mu$s.

## 3.) results

### 3.1.) multiplex advantage

Longitudinal acoustic phonons of Aluminium were measured with ROTAX using the Ge-(220) analyser. Within the accessible time window of 3.5msec and 11.5msec of an ISIS frame the Al-(200) and Al-(400) Brillouin zones were scanned simultaneously with a constant-$\Psi$ scan. In fact, 3 individual phonons of the LA(100) branch of Aluminium were traced with only one TOF-curve, namely the phonons at a) $\hbar\omega = 3$meV, $q = 0.05$, b) $\hbar\omega = 10$meV, $q = 0.1$, c) $\hbar\omega = 12$meV, $q = 0.11$. This multiplex advantage can be quantified as follows: If n time channels are used simlutaneously the spectrometer performance is improved by a factor $\sqrt{n}$ as compared to measuring each time channel separately ain a sequence of measurements with the same total measuring time in both cases.

Additional multiplex advantage is obtained from the 2-dimensional neutron data acquisition. The JULIOS detector counts neutrons in position (x) and total time-of-flight (t) channels; the position channel is correlated with the analyser Bragg angle. Hence, every single detector pixel is uniquely correlated with one particular space element $(\Delta Q, \Delta\omega)$ in $(Q,\omega)$ space, thus, we can plot the original detector data in (x,t) coordinates together with the traces of the sample's reciprocal space and the traces of energy transfer $\hbar\omega$. Fig. 2 presents such a plot; for reason of clarity, only 3 levels of intensities are shown. No further intensity correction or background suppression has been applied. The long dashed lines correspond to $Q_x$ and $Q_y$, short dashed lines to energy transfer. The solid track along $Q_y = 0$ is, in fact, the scan path used by ROTAX. It is worth to monitor the distribution of intense pixel along and aside the actual scan path, because this is an immediate image of the actually achieved resolution in $(Q,\omega)$ for that particular scan. Furthermore, from this 2-dimensional data-set cuts along constant energy or constant-Q directions can be calculated to obtain directly the peak

width in these dimensions. However, computational problems in proper normalisation may occur, because every detector pixel is linked to a ($\Delta Q, \Delta\omega$) element of different and varying size. For details, refer to W. Schmidt, session A6, this ICANS XII workshop.

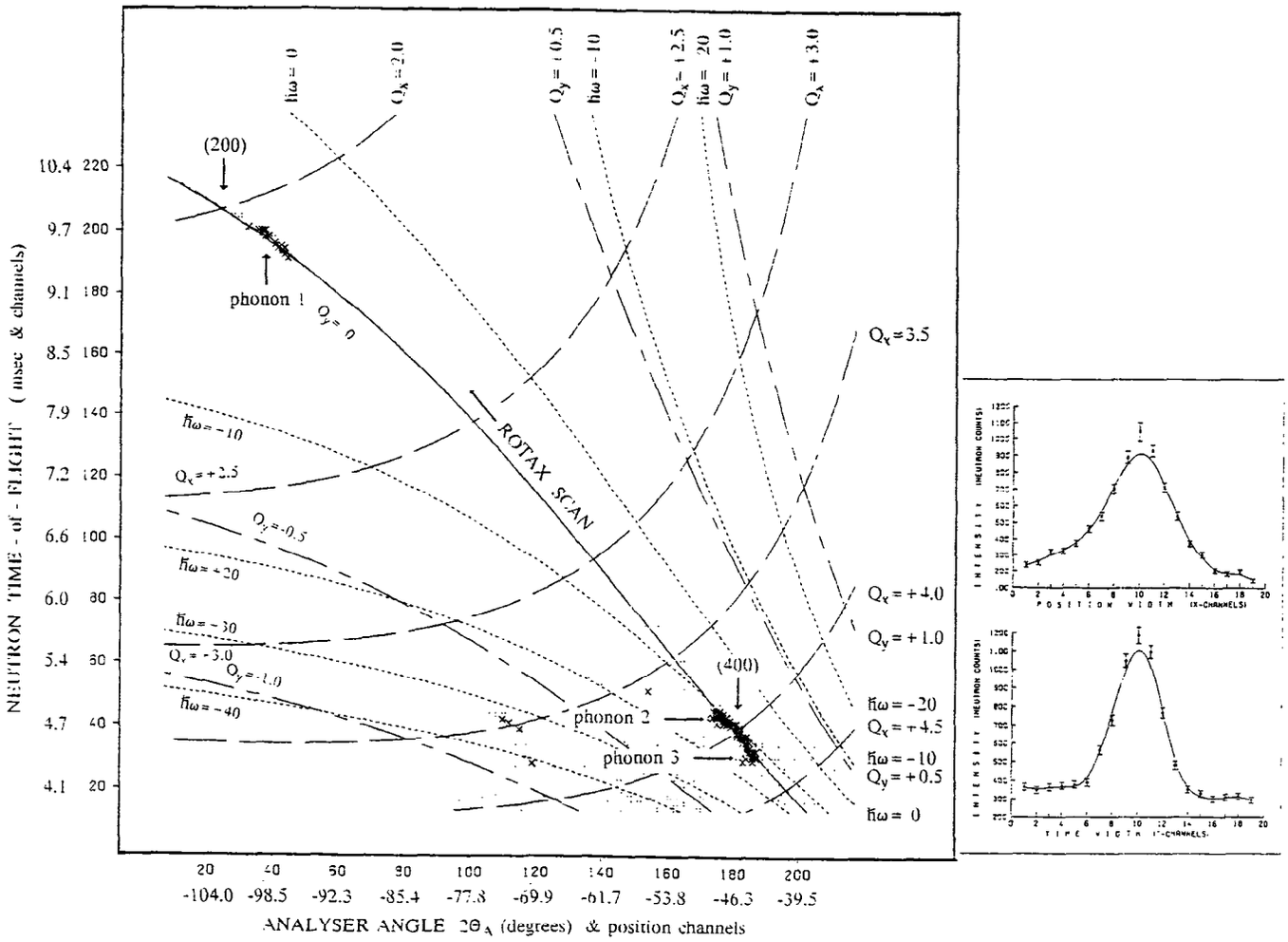


Fig 2: Inelastic neutron scattering on ROTAX showing several LA(100) phonons of Aluminium in the original position and time coordinates of the detector display. The traces of i) the ROTAX constant-$\Psi$ scan, ii) the Q-space in units of the reciprocal lattice of Al and iii) of the energy transfer $\hbar\omega$ in meV are also shown. On the right the intensity profile of phonon 1 is shown along position and time channels

## 3.2.) background suppression with ROTAX

A very interesting and more general feature of ROTAX is its dynamic background suppression, because the rotating analyser grants access to the detector only those neutrons, that fulfill the analyser's Bragg condition at the desired time channel. This pronounced effect can be seen very clearly in fig. 3a) showing 3 Al-Bragg peaks, that are rotaxed simlutaneoulsy in 10 min total measuring time. To perform the same experiment with an idle, non rotating analyser needs to perform 3 individual measurements consecutively, fig. 3b. This does not only take more then twice the total time, neglecting spectrometer setting and positioning time, even more

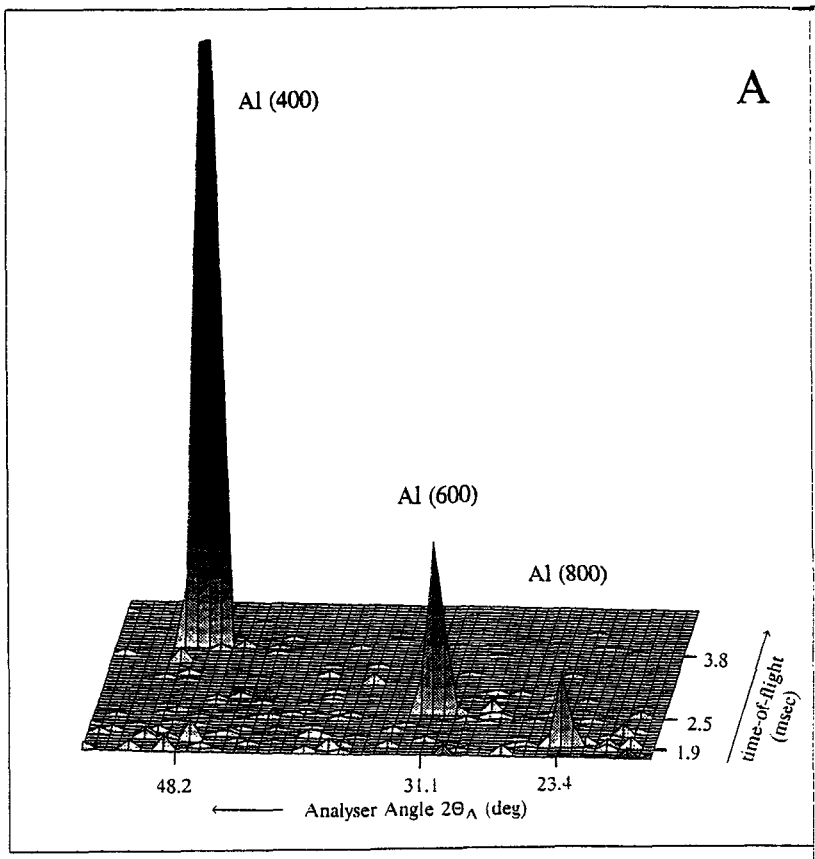


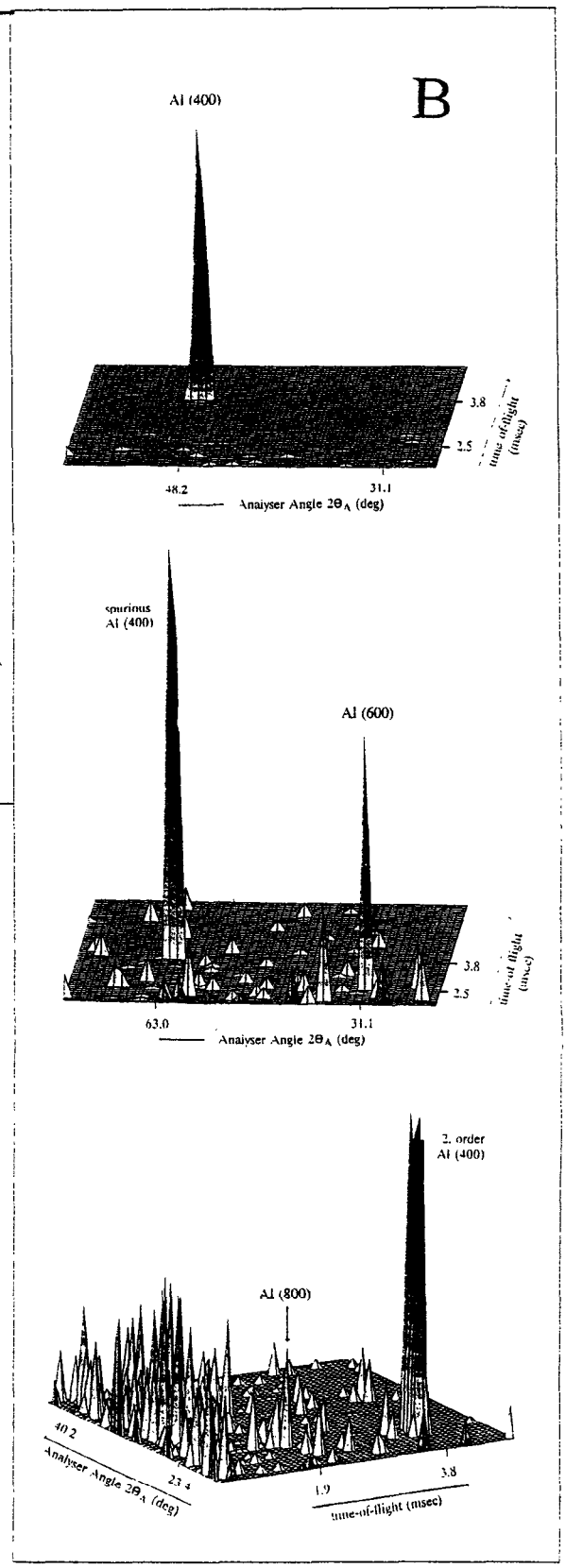


Fig. 3: a) series of simultaneously rotaxed Al-(h00) Bragg peaks with considerably reduced spurious background scattering; b) the same series of AL-(h00) Bragg peaks in 3 consecutive measurements using a non-rotating analyser: terribly increased spurious and second order scattering.

striking is the effect of additional spurious background and second order scattering, that cannot be suppressed by the static analyser condition used on all conventional crystal analyser spectrometers. In fact, it would be very hard to detect the weak Al-(800) Bragg peak from the bottom intensity pattern shown in fig. 3b, unless it was known precisely where about to search for. This particular pattern was obtained after the same total measuring time of 10 minutes as the one shown in fig. 3a.

## 4.) basic and advanced ROTAX operation

In principle ROTAX consists of 3 major parts: i) the rotating analyser and its drive control, ii) the detector and iii) the control of all auxiliary equipment such as the suite of rotational stages, goniometer, sample environment etc. that are needed to set up an experiment properly. In fact, all these units are operational on ROTAX in a stand-alone mode yet. This may be considered satisfactory as a fall back level and is very suitable for error checking and maintenance. It is, however, not very recommendable for a user run mode, where the control of the machine from one unique command level is admired. In addition, there are technical reasons as well to fully integrate namely the detector and analyser motor control into one single interaction shell.

In fact, the correct visualisation and interpretation of detector data relies crucially on the proper knowledge and, hence, monitoring of the actual motor performance. And, last not least, it must be guaranteed, that both the detector and rotating analyser are well synchronised with the neutron source ISIS and that they both run at the same and unique absolute instrument time. Naturally, neutrons travel at their own time scale, that has to be matched. However, neutron pulses start with a certain unpredictable irregularity and this fact means that every active spectrometer component has to be triggered on and rephased with every incoming neutron master pulse. The logic to synchronise active (moving) components of ROTAX with ISIS is shown in fig. 4. ISIS issues an absolute time-zero signal to start a neutron frame. Its repitition frequency is 50 Hz ± a tolerance value, which is usually very small: approx. ±400ns. The ISIS time zero refers to the time-zero channel of the digities desired motor curves, in fact, there are two, one for the analyser angle $\Theta_A$, a second one for the analyser's angular speed $\omega_A$. For both, a certain bandwidth is tolerated. The event of the ISIS time zero signal causes the signal processor to reset to its time zero channels for $\Theta_A$ and $\omega_A$. This causes the first regulation amplitude on the ROTAX motor drive, it can be as much as 2 degrees. However, the regulator would not realise this angular error until the next ISIS signal to occurr. Therefore, it is inevitable to fine tune the synchronisation with an additional 1 MHz counter for the time Z (cf. fig. 4) between the ISIS zero signal and the next subsequent signal processor clock tick. The fine tuning produces another offset to the desired scna curve in every frame and guarantees the syncjronisation between the processor clock and ISIS.

The same logic is also used to synchronise the anticipated frame length of 20ms to the real frame length of ISIS that is not always at 50 Hz. There are periodic undulations in minute time scale as well as unphased statistical beam trips. On ROTAX the analyser goes immediately stand-by if only one missing ISIS pulse was to be detected. And it will not resume operation, unless an adjustable number of consecutive frames (100 at present, i.e. 2 sec) in the appropriate repitition frequency window has been encounted for.

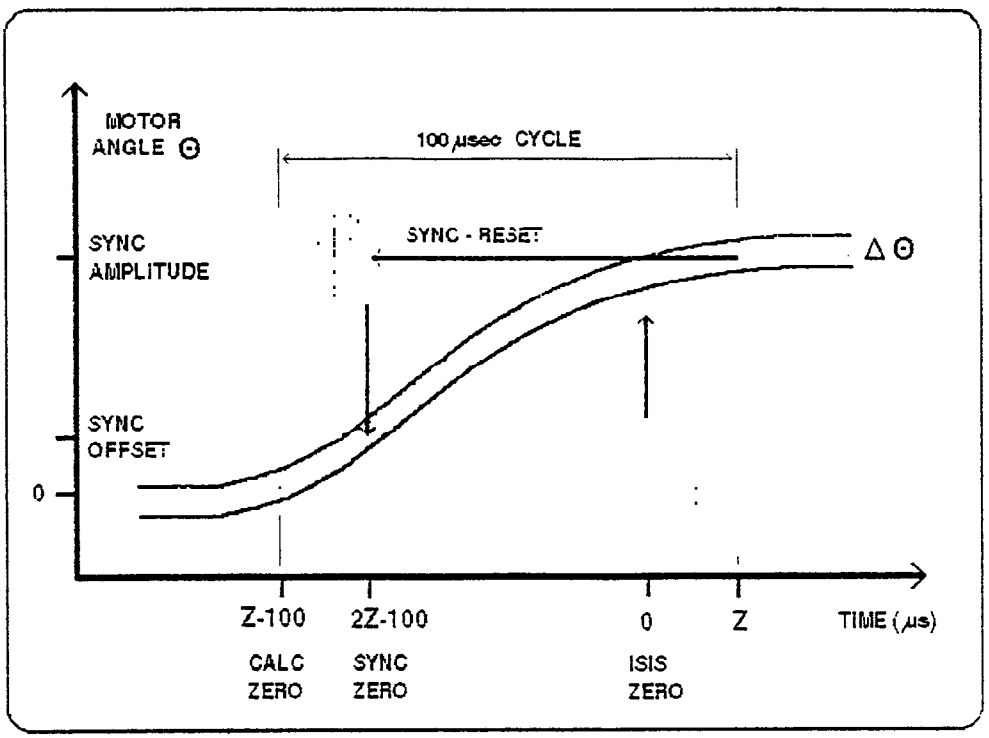


Fig 4: the scheme to synchronise the ROTAX analyser motor with ISIS

This veto scheme for the ROTAX analyser can be used also to hook up other kinds of vetos or machine disruptions. Moreover, a whole individual veto and action scheme can be put into force. On ROTAX, for instance, it will be likewise:

A) vetos:

analyser motor out of desired range
motor running hot
ISIS off 50 Hz
detector idle
shutter closed
sample environment out of range
...

B) automatic action scheme:

control program to monitor vetos
encount absolute time
determine event type
analyser motor to go stand-by or resume
detector suspend/resume counting
issue user information/warnings
...

The logical structure of ROTAX is compiled in fig. 5 and as more and more recently designed spectrometers employ dynamic or active components, we feel that our specific solution may be of general interest. The user of ROTAX does not neccessarily take much notice of the automatic veto/action scheme unless a severe malfunction has occurred that could not be rectified by the machine itself. In this case the experiment will be aborted or in minor case a warning will be issued onto the console terminal and logfile. His job, however, is to create an initial experimental set-up with an idea of the scattering geometry and particular ROTAX scan he requests. By then, typing in a number of commands, the mechanics will move to the anticipated angles, the detector starts counting and the signal processor reads the desired ROTAX scan curve of the analyser and starts rotating it. The actually achieved motor position is montiored by a fast incremental decoder and fed back to the regulation unit every 100$\mu$s, i.e. 10 kHz sampling rate. At this rate, regulation feed-back action can be taken by the motor's main amplifiers. However, the actual motor performance can be read with much higher sampling rate of 1 MHz into the transputer system. If ROTAX is operated at its power limits, then its real TOF-trace in (Q,$\omega$) space can be calculated within a few ISIS frames. The user can then decide to veto out these frames or to keep them, if they are not too far from their anticipated target. In addition, the user can create a modified, more precise ROTAX scan to run. Fig. 5 shows ROTAX of its final design. At present, there is not yet a synchronisation between detector and analyser motor, nor is there any on-line data feed-back to the computer system. Instead, a scope is used to verify the analyser motor performance and all control commands are to be issued on different computer keyboards of the $\mu$VAX and 2 PCs.

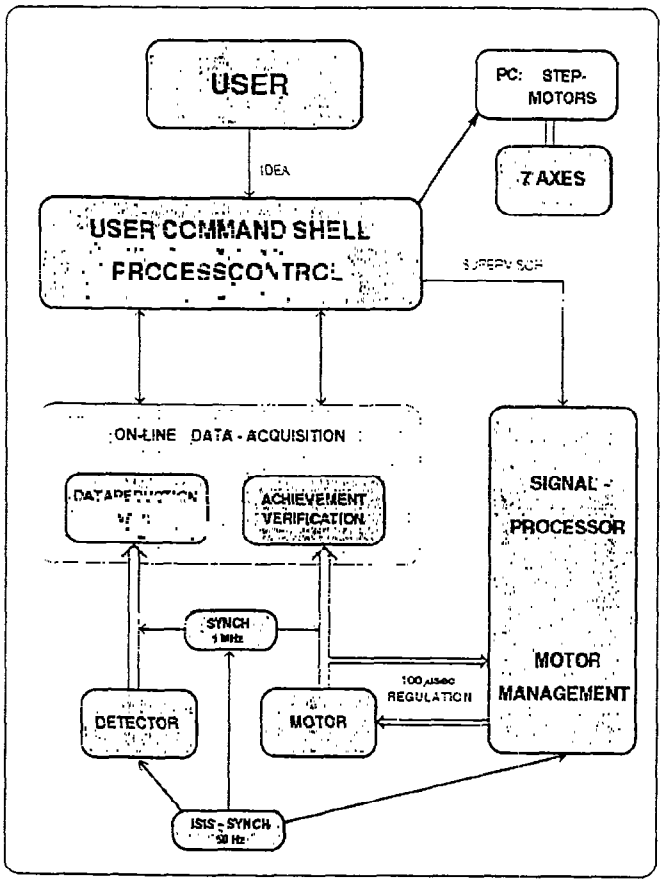


Fig 5: Logical structure of ROTAX

Technically, the full ROTAX design structure can only be accomplished by using one general computer with one common interface and a precise real-time clock. Because of the very high data rates to be acquired, on ROTAX we have an input load of 2 x 16 bit parallel data at 1 MHz rate, in total 3.2 Mbaud, this cannot be done with present PC, VAX or RISK workstation machines. A technical solution for ROTAX is currently developed, using a specifically designed transputer interface board with 4 dual SRAM input buffers and the general real time clock. A number of transputer links are set up in a few $\mu$s of time to forward the data to subsequent transputer nodes

that run the veto-interaction and data reduction software. All data are finally stored in VAX accessible files. The hardware was tested successfully, the software still needs further development and improvement.

## 5.) ROTAX operation schedule

ROTAX has become operational at its first stage already. Further improvements are to come, the final detector will be installed later this year and we look forward to opening ROTAX as a scheduled instrument to the public by the late autumn 1993. One half of the available beam time on ROTAX will be under control of the ISIS selection panel, the other half will be controlled by a German board, still to be installed.

The fully advanced feature of ROTAX will be in place as soon as resources will allow us to complete.

## Acknowledgement

We are grateful to many people who helped us in the design and installation of ROTAX. The Bundesminister für Forschung und Technologie has provided the funds for ROTAX under contract number 03-GE3-WUE.

## References

[1] R. Geick, H. Tietze; Nucl. Instr. Methods A **249** (1986) 325

[2] H. Tietze, R. Geick
Proc. Int. Collab. Advanced Neutron Sources ICANS IX 1986, CH-Villigen, Switzerland, SIN-rep. 40926, 389 (1987)

[3] H. Tietze, W. Schmidt, R. Geick, U. Steigenberger, H. Samulowitz;
Proc. Int. Collaboration on Advanced Neutron Sources ICANS XI 1990, KEK Japan, KEK report 90-25, 774 (1991)

[4] U. Steigenberger, M. Hagen, R. Caciuffo, C. Petrillo, F. Cilloco and F. Sacchetti
1990 RAL-90-004 and Nucl. Inst. and Meth. **B53** (1991) 87

[5] E. Jansen, W. Schäfer, A. Szepesvary, R. Reinartz, H. Tietze, G. Will, K.D. Müller, U. Steigenberger;
Proc. Int. Conf. on Neutron Scattering ICNS 91, Oxford (1991), Physica B **180 & 181** (1992) 917

[6] H. Tietze, W. Schmidt, R. Geick, H. Samulowitz, U. Steigenberger;
Proc. Neutron scattering data analysis conf. WONSDA II, Rutherford (1990), IOP Conf. Series 107, 253 (1990)

# Less Background, Better Contrast by Cooling Analyser Crystals

C.J. Carlile, M.A. Adams, P.S.R. Krishna, M. Prager‡,
K. Shibata‡‡ and P. Westerhuijs

ISIS Pulsed Source, Rutherford Appleton Laboratory,
Chilton, Oxon OX11 0QX, UK

*Cooling the pyrolytic graphite analyser crystals of the IRIS spectrometer to 25 K has proved to be very effective in suppressing the background from thermal diffuse scattering and in improving the contrast of the analysers. In this paper we show that a 12 times drop in background has been realised and that it would fall by an additional factor of 3-4 by further reducing the analyser temperature to 5 K.*

## 1. Introduction

Inelastic neutron spectroscopy on pulsed sources is carried out using two distinct methods: direct geometry spectrometers which use a monochromatic incident pulsed beam and detect energy changes at the sample by time of flight after scattering; and inverted geometry spectrometers which allow a white neutron beam to fall on the sample, energy sorted by time of arrival, which is then analysed after scattering at a single energy by an array of single crystals analysers.

Unlike equivalent direct-geometry instruments, inverted-geometry spectrometers can still be employed when carrying out measurements at high resolution and wide energy transfers from cold samples in their ground state. Using the inverted geometry neutron energy-loss technique the energy and momentum transfer ranges are largely independent from the energy resolution, which is a function of the selected analyser reflection energy and take-off angle.

Present addresses:

‡ KFA Jülich, Germany
‡‡ Tohoku University, Japan

One reason why inverted-geometry spectrometers are a comparatively recent development is that it has generally been considered that the white beam falling on the sample in these spectrometers would cause more background than could be obtained with a direct-geometry machine. Indeed the neutron current passing through the sample is about one hundred times higher than on a similar performance direct-geometry spectrometer. However, in recent years, spectrometers such as IRIS at ISIS and LAM80 at KEK Japan, following on from the success of the backscattering spectrometers at KFA Jülich and ILL, have demonstrated that the problem of the background resulting from the white beam in the spectrometer can be overcome quite satisfactorily.

Nevertheless white-beam techniques do mean that collimation of the incident and scattered beams must be very effective and that internal shielding must be well-defined and universal. A crucial factor in the sensitivity of such instruments is that the crystal used as the analyser must have a very high contrast for the analysing energy compared with all other energies in the incident beam. In practice this means that the coherent elastic cross section of the analyser must be very large compared to the sum of the coherent inelastic and the total incoherent cross sections.

For the IRIS spectrometer a 12 times drop in background has been achieved by cooling the pyrolytic graphite analyser crystals to 25 K and consequently reducing the coherent inelastic cross-section from thermal diffuse scattering (TDS) by this factor. Recent measurements have shown that the TDS will fall by a further factor of around 4 if the graphite were to be cooled to 5 K. The overall gain in analyser contrast between room temperature and 5 K would then be close to a factor of 50 and the analyser contrast would approach 5000.

## 2. Description of IRIS

The IRIS spectrometer is illustrated in Figure 1. It consists of a long incident flight path from the liquid hydrogen moderator of the ISIS pulsed source which delivers a white pulsed neutron beam via a curved neutron guide to the sample sitting at 36.5 metres from the moderator. This flight path serves to time-sort the neutron beam such that the incident neutron energy is defined to microelectronvolt precision by time-of-flight. The neutrons scattered from the sample are analysed by two large arrays of single crystals which reflect a single scattered neutron energy back to an array of scintillator detectors situated close to backscattering geometry ($\theta_B$=87.5°). The resolution of the primary spectrometer is then matched to that of the secondary spectrometer. Scattering angles from 15° to 165° are continuously covered with 51 scintillator detectors. Each analyser is 2.25 metres long, and 6 cm and 20 cm high respectively. The two sets of analysers on IRIS are pyrolytic graphite and muscovite mica. The resolution $\delta E$ of the instrument can be changed in steps by choosing the appropriate diffraction order of the analyser crystals: one obtains $\delta E$=50 μeV for PG 004, 15 μeV for PG 002, 4.5 μeV for mica 004 and 1.1 μeV for mica 002. The former options select 3.3 and 6.6 Å neutrons and the latter options utilise 9.9 and 19.8 Å neutrons at the analyser. An important aspect of inverted geometry spectrometers is the ability to measure diffraction patterns simultaneously, thanks to the white incident beam. IRIS has a diffraction detector array situated at $2\theta_B$=170° giving a resolution in $\Delta d/d$ of 2.5 $10^{-3}$ over the d-spacing range from 2 Å to 13 Å. The whole instrument is housed in a 2 m diameter stainless steel vacuum tank held at a pressure of 2 $10^{-5}$ mbar. A fuller description of the IRIS spectrometer is given in Ref.[1].

## 3. Cooling the analysers

The analyser geometry of IRIS is very open as can be seen in Figure 1 - there is a line of sight between virtually each detector and each point on the analyser. A given detector is thus able to see a wide area of analyser surface whilst Bragg scattered neutrons are reflected to that detector from only a very limited area. The detector is therefore very sensitive to any non-specular scattering processes in the analysers. For graphite, since its incoherent cross-section is virtually zero (carbon is 98.9% $C^{12}$), these non-specular processes refer only to inelastic coherent scattering: thermal diffuse scattering from phonons. The contrast of the mica analyser on the other hand is determined by incoherent scattering since it contains a significant proportion of $OH^-$ ions and the contribution from TDS is relatively low.

As a consequence, the resolution function from the graphite analysers on IRIS at room temperature has the asymmetric shape characteristic of instruments on pulsed sources superimposed upon a broad almost flat underlying feature due to TDS. The ratio of elastic peak height to "flat" background with the analyser at room temperature is only 120.

The origin of the TDS is illustrated in Fig. 2 where the scattered spectrum from a pyrolytic graphite analyser illuminated by a white beam is shown as a function of angular offset from the Bragg condition. These patterns were recorded in the IRIS diffraction detector with a graphite crystal at the sample position. As the crystal is turned off the Bragg condition, where the underlying TDS is centred on the intense diffraction line, two distinct 'wings' representing phonon creation and phonon annihilation emerge [2].

It is the sum of these offset patterns from a wide angular range of analysers which are recorded in each detector on the spectrometer and which results in the broad underlying feature centred on the elastic line. The Bragg line itself is reflected from only a restricted analyser area to each detector. The TDS intensity is approximately 1% of the elastic peak height, but the integrated intensity over the whole spectrum approaches that of the elastic line itself. One method of reducing the off-Bragg TDS intensity would be to introduce a coarse collimator between the analyser and the detector but this would leave unaffected the most intense contribution to the TDS signal which lies at or close to the Bragg reflection itself, and would significantly reduce the total signal.

A second method, which is the solution taken on IRIS, is to cool the analyser to reduce the phonon population in the graphite and minimise the effects of TDS. Tests were carried out on IRIS with a graphite crystal in a helium cryostat at the sample position and scattering patterns were recorded in the diffraction detector as a function of offset from the Bragg condition at a series of temperatures down to 5 K. In Fig.3 the scattering patterns as a function of temperature are shown for an offset of 4° from the (002) reflection of graphite at a wavelength of 6.6 Å. The phonon annihilation and phonon creation peaks are clearly observed as is their drop with temperature.

In Fig. 4 the integrated TDS intensity for phonon annihilation and creation is shown to be almost linear with fall in temperature even down to 5 K, because of the extremely soft phonon spectra which graphite possesses. The phonon energy of the TDS peaks observed as ~2 meV [4]. From these data, a graphite analyser operating at 25 K would be expected to produce a background from TDS sources which is more than an order of magnitude lower than it would be at room temperature. The elastic intensity itself hardly rises at all with the fall in temperature.

As a result of these tests the graphite analyser on IRIS has now been cooled to 25 K, by a combination of cold compressed helium gas and liquid nitrogen cooling circuits, described in next section. The effect has been to improve the signal to background in the scattered spectrum (as defined by the peak intensity in the elastic line to the flat background from a 1 mm plate sample of vanadium) from 120-to-1 to 1350-to-1, more than a factor ten. This improvement in background is crucial in the reliable study of quasielastic neutron scattering (QENS ) and low intensity inelastic spectroscopy such as tunnelling. From Fig.4 it can be seen that the background would fall a further factor of about 4 by reducing the analyser temperature to 5 K. This is technically possible and a design is now being considered.

## 4. Technical Description of the Cooling System

The graphite analyser comprises 1350 1 $cm^2$ graphite pieces of grade ZYB ($\eta$~0.8°) pyrolytic graphite supplied by Le Carbone of France. Each piece of 2 mm thickness is held to a single solid aluminium backing plate by miniature electronic plugs and sockets. The graphite is arranged in a 225x6 mosaic rectangular array, the overall length of the analysers on their backing plate being 2.30 metres. The front surface of the aluminium backing plate was cut by computer controlled machinery to the necessary quasi-spherical shape for focusing onto the detector bank. The analyser itself is supported by low conductivity convoluted stainless steel piping with a long heat path inside an aluminium radiation shield. A cross section of the analyser design is shown in Figure 5. The aluminium radiation shield is cooled to 80 K by flowing liquid nitrogen drawn through pipes by a gas pump. The analyser support plate itself is further cooled to 25 K by circulating helium gas at 20 bar which has been pre-cooled by a closed-cycle Displex refrigerator. The front surface of the radiation shield is made from thin aluminium foil to minimise background scattering in the detectors and exposed parts of the analyser plate and shield are covered in 0.5 mm cadmium sheet. The temperature of the analysers and its shield is recorded by standard sensors and the position in time of flight of the elastic line itself acts as a monitor of the reducing d-spacing of the analyser with temperature.

## 5. Conclusions

The effectiveness of cooling the large graphite analyser on the IRIS spectrometer has been demonstrated. The analyser contrast of 120 at room temperature is improved to 1350 at 25 K by more than an order of magnitude reduction in TDS. Measurements show that further cooling the analysers to 5 K will increase this figure to beyond 5000. The energy gain process will fall almost to zero whereas energy loss processes will only drop marginally. At temperatures lower than 5 K other background effects will begin to become apparent at this level of sensitivity.


[1] C.J. Carlile and M.A. Adams, Physica B **182** (1992) 431

[2] B.T.M. Willis, C.J. Carlile, R.C. Ward, W.I.F. David and M.W. Johnson, Europhys. Lett., (1086) **2** 767

[3] E.A. Kellett and B.P. Richards, J. Appl. Cryst. (1971) **4**, 1

[4] P.S.R. Krishna (private communication)

## Figure Captions

Figure 1: The IRIS high resolution spectrometer at the ISIS pulsed neutron source.

Figure 2: The scattering patterns from a single crystal of pyrolytic graphite measured by time of flight white beam diffraction at a series of offset angles from the Bragg condition. Peaks due to phonon creation at shorter times and phonon annihilation at longer times are clear as the offset angle increases.

Figure 3: Scattering patterns from pyrolytic graphite taken at a fixed offset angle from the Bragg condition of 4° showing the reduction in intensity of the phonon peaks with fall in temperature. Structure caused by harder phonon branches can just be observed at the base of the remaining Bragg line in the centre of the pattern.

Figure 4: The integrated intensities of phonon creation and phonon annihilation peaks in graphite as a function of temperature.

Figure 5: A cross-section of the pyrolytic graphite analyser on IRIS showing the cooling mechanism and the analyser thermal shield and support.

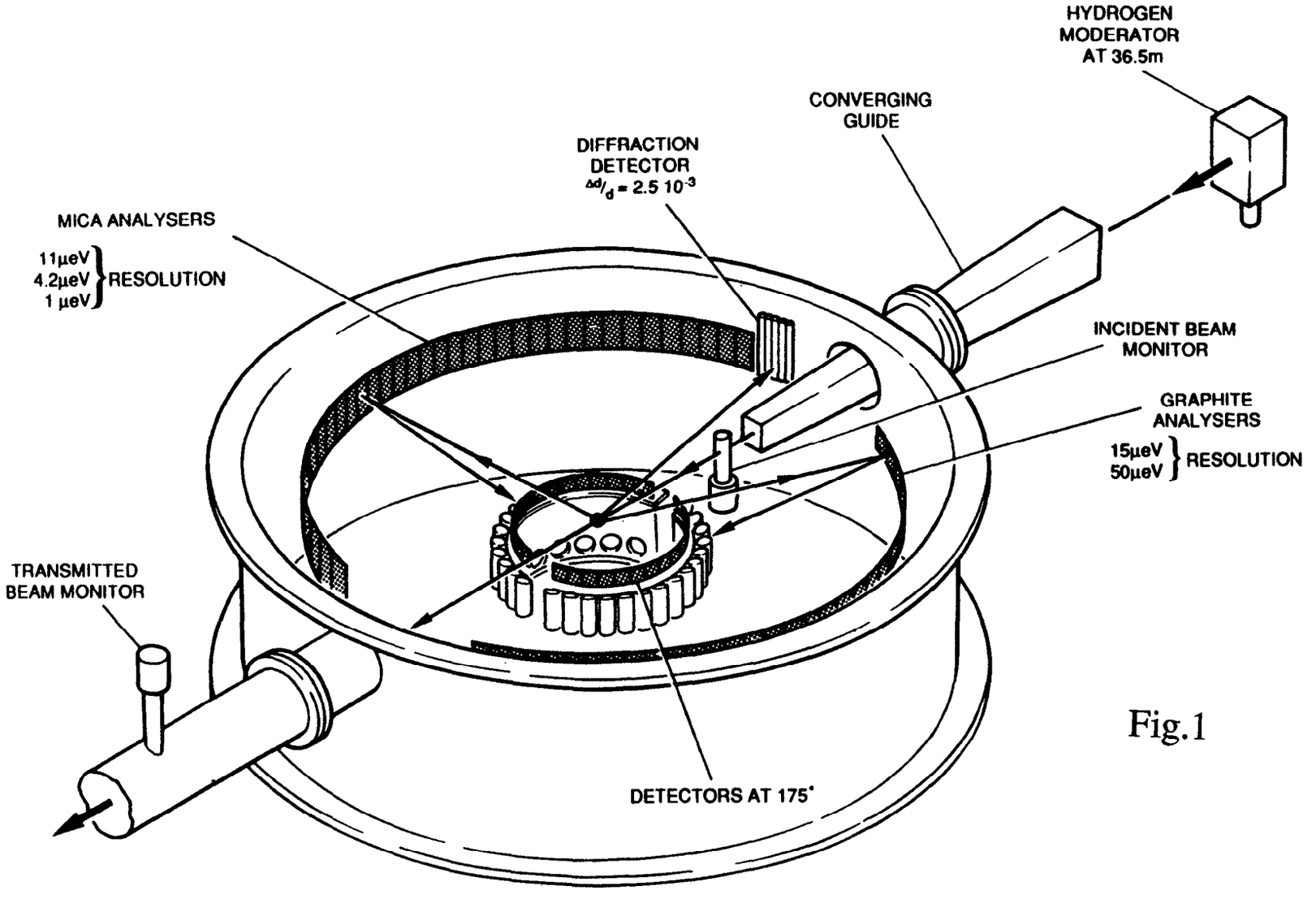


Fig.1

THE IRIS SPECTROMETER

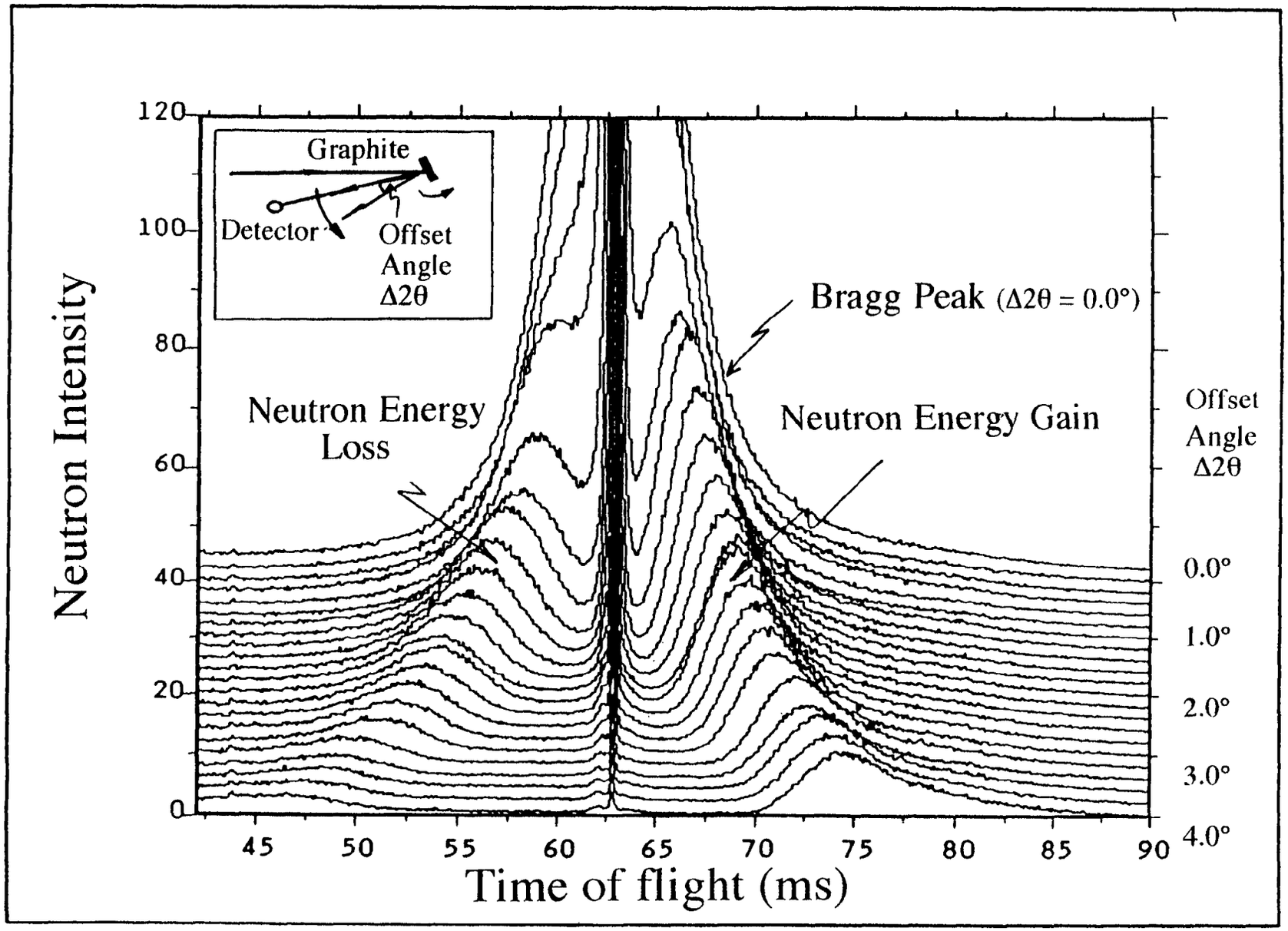
Graphite
Detector
Offset
Angle
Δ2θ
Bragg Peak (Δ2θ = 0.0°)
Neutron Energy
Loss
Neutron Energy Gain
Offset
Angle
Δ2θ
0.0°
1.0°
2.0°
3.0°
4.0°
Neutron Intensity
Time of flight (ms)
0
20
40
60
80
100
120
45
50
55
60
65
70
75
80
85
90

Fig.2

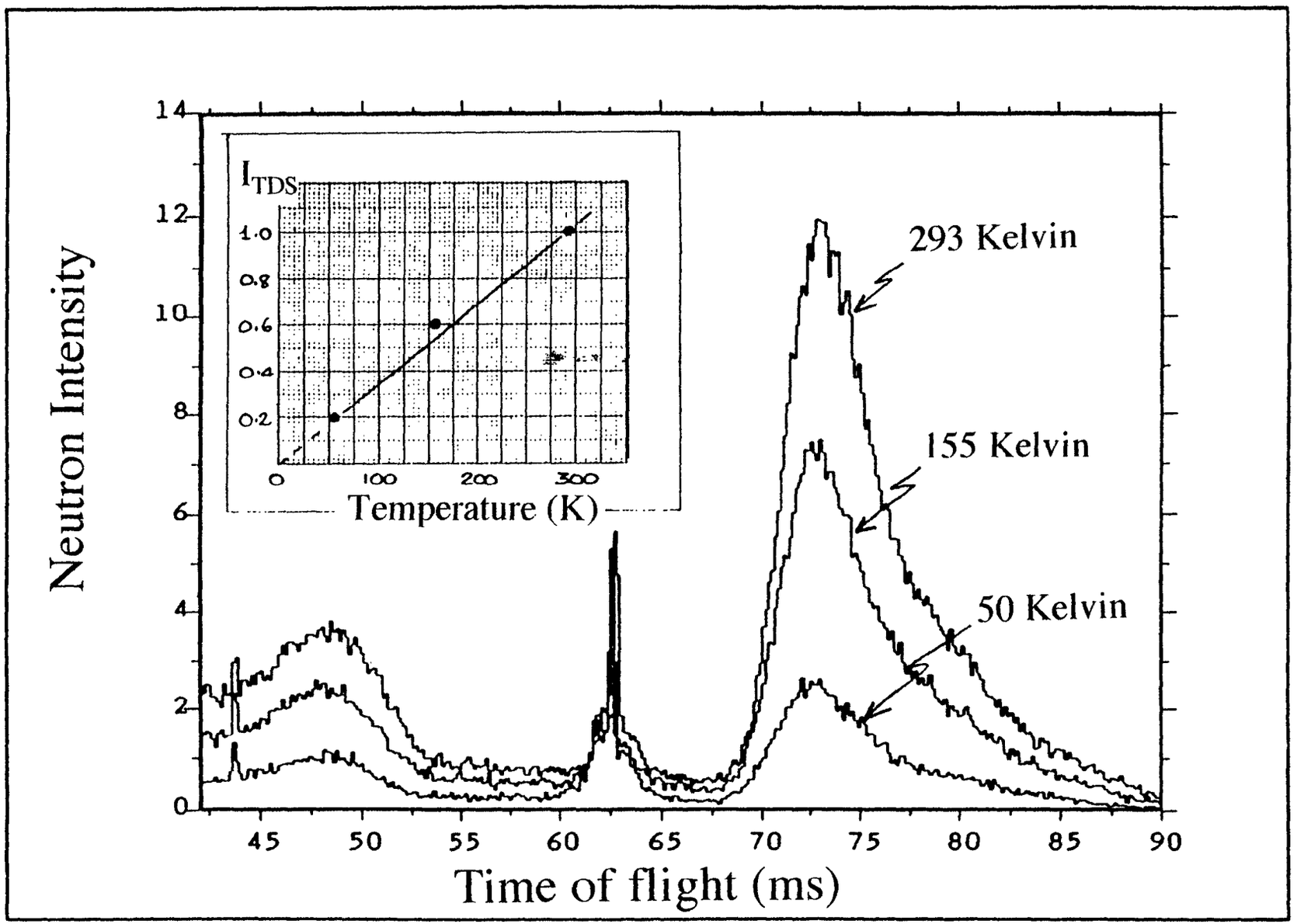
Neutron Intensity
Time of flight (ms)
293 Kelvin
155 Kelvin
50 Kelvin
$I_{TDS}$
Temperature (K)
0
100
200
300
1.0
0.8
0.6
0.4
0.2
0
2
4
6
8
10
12
14
45
50
55
60
65
70
75
80
85
90

Fig.3

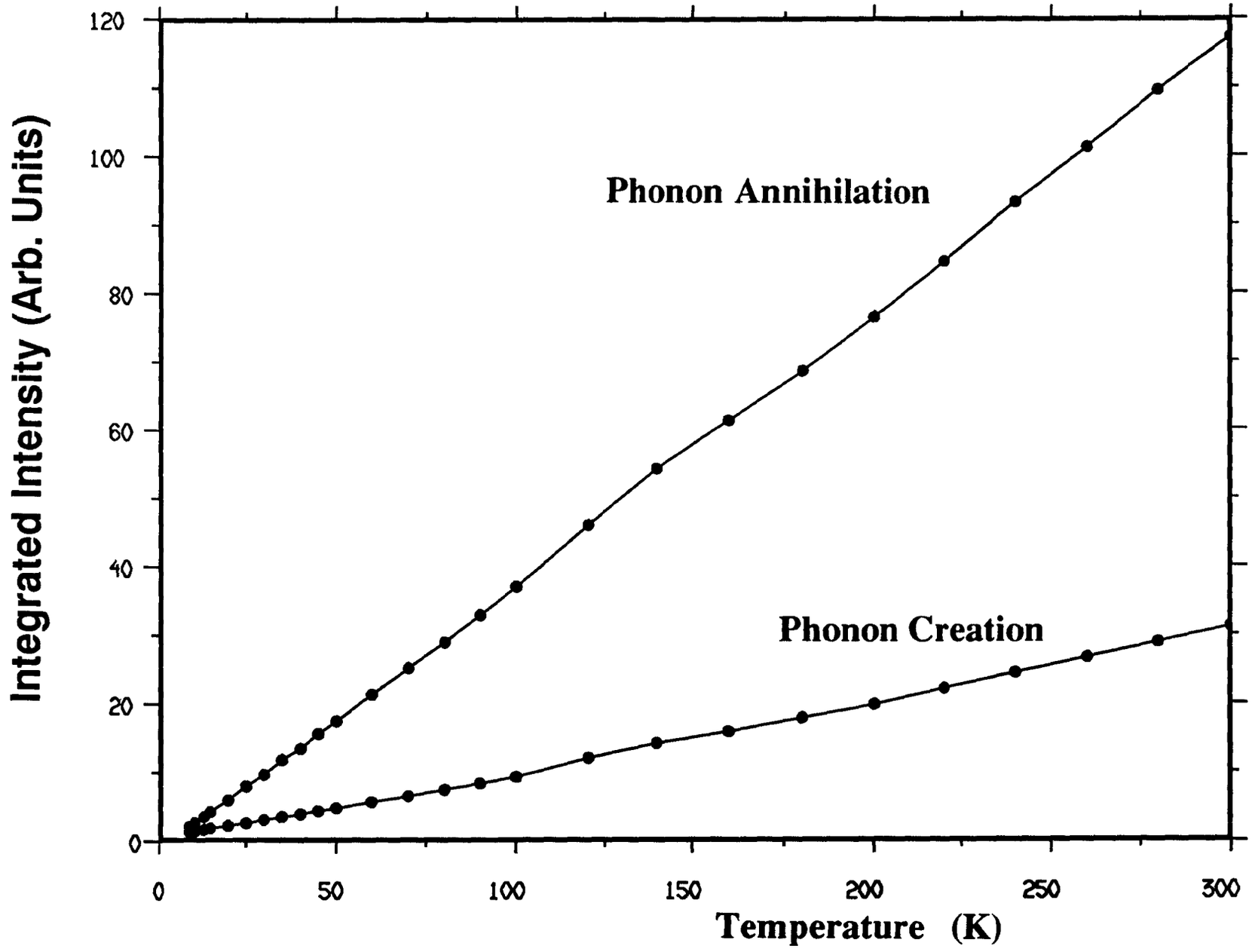
Integrated Intensity (Arb. Units)
120
100
80
60
40
20
0
Phonon Annihilation
Phonon Creation
0
50
100
150
200
250
300
Temperature (K)

Fig.4

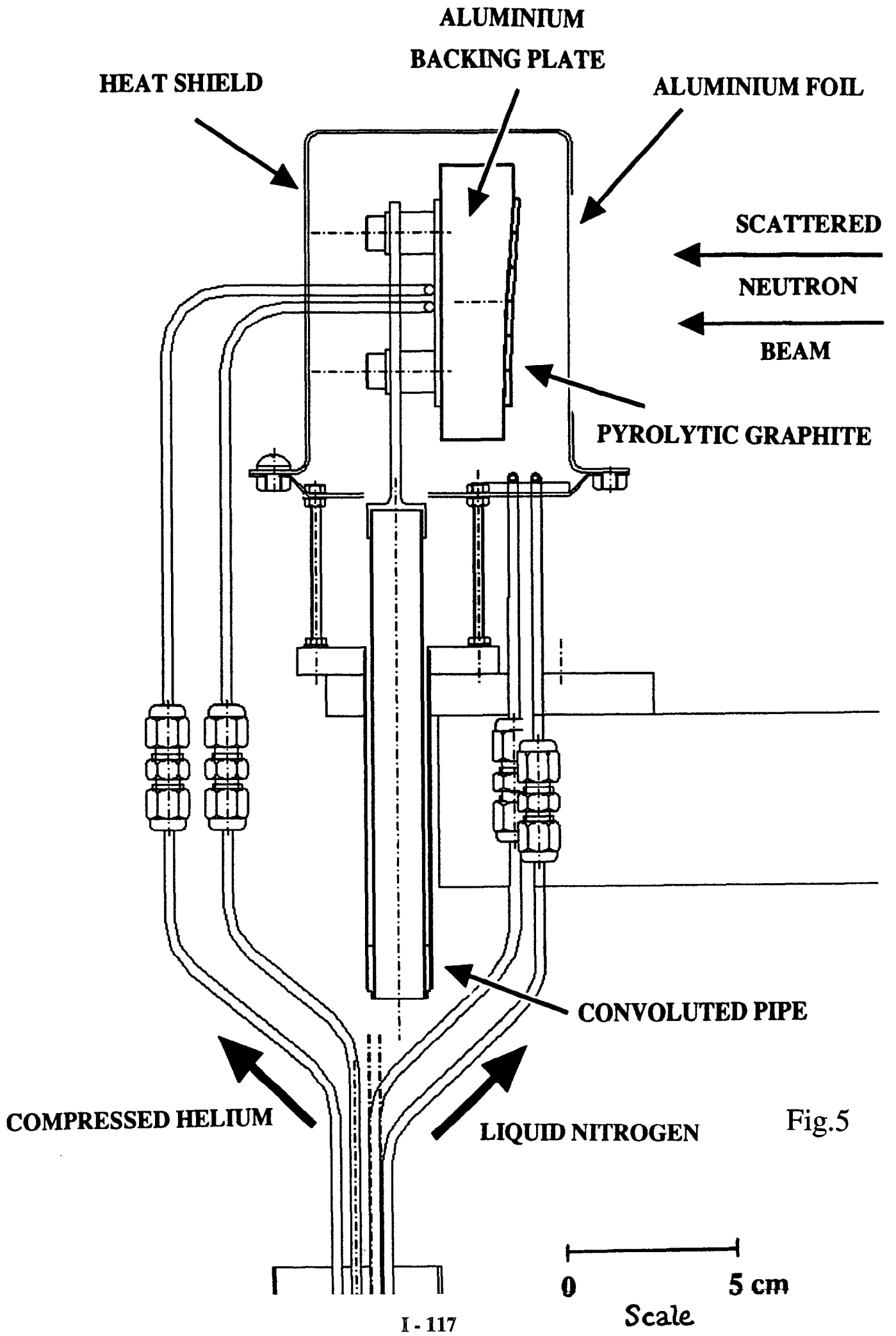
ALUMINIUM
BACKING PLATE
HEAT SHIELD
ALUMINIUM FOIL
SCATTERED
NEUTRON
BEAM
PYROLYTIC GRAPHITE
CONVOLUTED PIPE
COMPRESSED HELIUM
LIQUID NITROGEN
0
5 cm
Scale

Fig.5

# VESTA - A new Beamline for Cold Neutron Storage Experiments on ISIS

E. Jericha[1,2], H. Rauch[1], M. Schuster[1] and C.J. Carlile[3]

1. *Atominstitut der Österreichischen Universitäten, A-1020 Wien, Austria*
2. *Institut Laue-Langevin, F-38042 Grenoble, France*
3. *Rutherford Appleton Laboratory, Chilton, Oxon OX11 0QX, UK*

In the past 3 years we have shown that long wavelength neutron pulses can be trapped between 2 perfect single crystal silicon plates 1 metre apart using magnetic switches to allow the neutrons entry to and exit from the storage device. Neutrons were stored for up to a quarter of a second undergoing 156 reflections in the process. A special set-up of the IRIS beamline was used for these measurements which meant that the spectrometer could not be used at the same time. We have now installed a graphite monochromator into the IRIS guide which will reflect out neutrons of 6.27Å into the storage device so that experiments can be carried out concurrently. The storage device itself has been upgraded so that its performance should be enhanced by a factor of at least 10. Amongst planned experiments are the storage of more than one ISIS pulse, an investigation into the question whether the motion is a coherent or an incoherent process and the possibility of observing electromagnetic interactions during this motion. The monochromatic beam could well find other uses in fundamental neutron physics and neutron scattering in the future.

## 1. Introduction

The method of storing cold neutrons by Bragg reflection from perfect crystal plates has been successfully tested at the ISIS pulsed neutron source [1,2]. A *1072 mm* long perfect single crystal of silicon, consisting of 2 rectangular endplates and a connecting crystal base was cut as one piece for the purpose of neutron storage. The surfaces of the crystal plates are parallel to the *(111)* lattice planes of the crystal. Neutrons of wavelengths about *6.27 Å* are Bragg reflected at a Bragg angle of exactly *90°* between the two crystal plates. For a small region in the neutron's wave vector space ($\Delta k/k \sim 4 \cdot 10^{-5}$) the reflectivity of the crystal plates is almost unity (a lower limit for the reflectivity was determined to be *0.9978* by this method [2]). Pulsed electromagnets mounted on each of the end plates are used to shift the k-vector of these neutrons out of the total reflection region of the crystal, thus enabling a magnetic field dependent transmission probability through the crystal plates to be switched. The magnetic pulses have the shape of half a sine wave and their duration is long compared to the pulse width of the neutron beam (~ *150 μs*) but shorter than the flight time of the neutrons between the crystal plates (*3.38 ms*). The magnetic field required to shift the k-vectors of the neutrons by the Darwin width of the total reflection region is *1.26 T*. The loss of neutrons due to the angular divergence of the incoming beam is minimized by inserting a neutron guide between the reflecting crystal plates. The guide is made of float glass with an angular acceptance range of about *± 7 mrad*. The stored neutrons are therefore characterized by their position in k-space and their angle in respect to the axis of the neutron storage system.

The beamline for neutron storage at the pulsed neutron source ISIS is that used by the IRIS spectrometer. The main part of the IRIS neutron guide is hidden within a tunnel of shielding. Between this tunnel and the IRIS spectrometer there is a 3 m long

freely accessible guide section surrounded by an interlocked area perfectly suited for the installation of the neutron storage system. A schematic survey is given in Fig. 1.

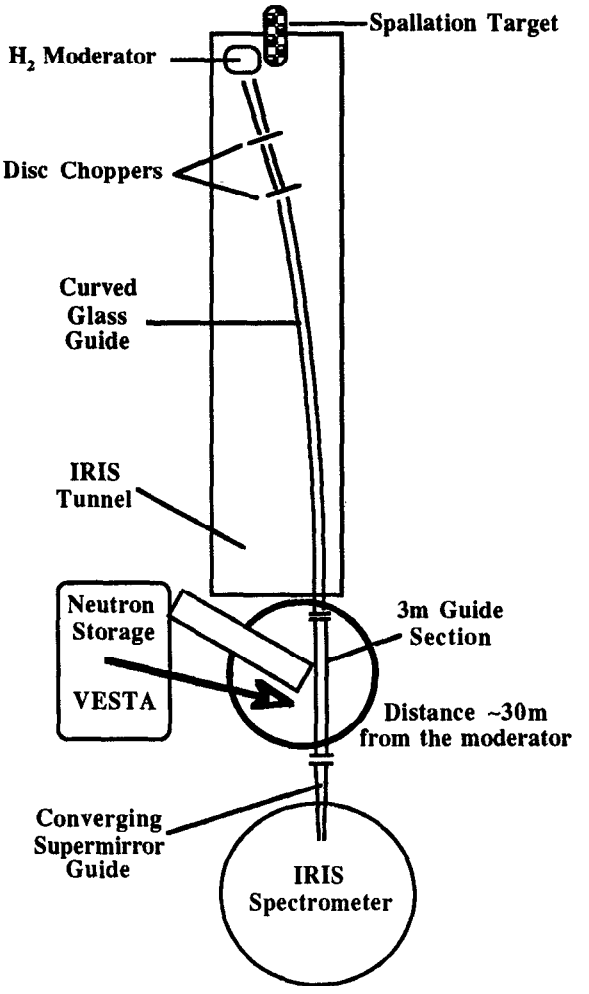


*Fig.1* Area for Neutron Storage Devices on the IRIS beam line

## 2. The Prototype Storage Device

For our earlier feasibility studies the 3 m IRIS guide section was removed and replaced by the neutron storage device (Fig. 2). Its performance was characterized by the following quantities. The neutron guide had a length of *1000 mm* and a cross section of *26x40 mm*. The magnetic pulses reached a maximum field of *1.06 T*. A graphite crystal after the storage device was used to deflect the stored neutrons into the detector, therefore acting as an *analyzer* crystal. The detector consisted of 2 He-3 tubes of 1" diameter which were arranged side by side. (cf. Fig.2).

The main problem of this location was the fact that this mode of operation allowed *either* the use of the IRIS beamline for experiments on the standard inelastic neutron spectrometer *or* for experiments with the neutron storage apparatus. Considering the number of applications for the use of the IRIS spectrometer this situation needed a proper solution for future developments. It was decided that the neutron storage device should become an independent instrument which will be described in section 3

of this article. This also gave a timely opportunity to optimise the components of the neutron storage device itself [2-4].

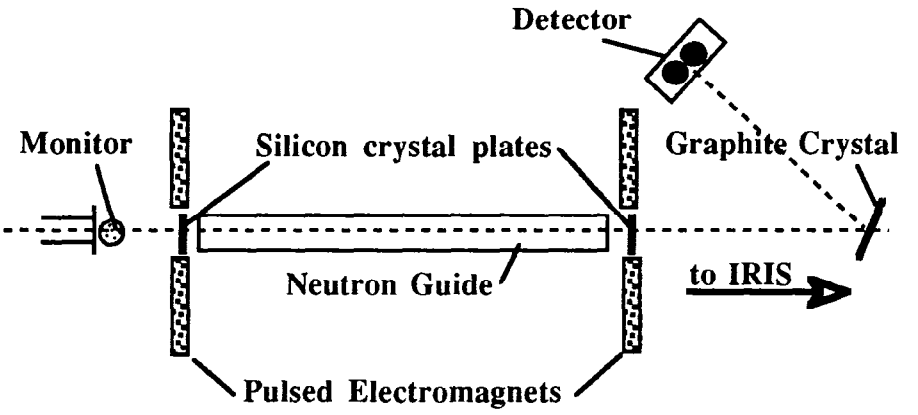


*Fig. 2* The prototype neutron storage set-up

The loss in stored neutron intensity was found to be due to two different sets of factors. The first set contains factors external to the storage process such as the magnetic field, the graphite crystal and the detector. The second set deals with the storage process itself and has to take factors like the geometry of the neutron guide, vibrations of the system due to the pulse of the electromagnets or absorption and scattering by air molecules into account. The factors relating to the external storage process are independent of storage times, since they represent single loss events of the storage process. The factors relating to the internal storage process are time dependent with a varying influence in respect to increasing storage times, since they represent loss events associated with the travel of the neutrons through the storage device.

Due to electronic limitations the maximum magnetic field could not be greater than *1.06 T,* which was not sufficient to shift the wave vector of the neutrons by the full width of the total reflection region. The transmission probability for neutrons in the total reflection range is calculated to be *0.656* after applying a magnetic field of *1.06 T.* The height of the graphite analyzer crystal was *40 mm* corresponding to the height of the neutron guide in the storage device but was reduced by the clamps of the crystal holder. The loss of stored neutron intensity due to this fact was slightly more than 10%. The arrangement of the detector created an artificial loss in efficiency in the central region. Compared to a detector volume with rectangular cross section of 1" thickness the efficiency in the central region was reduced to *78%.* Monte Carlo simulations showed the gap between the crystal plates and the neutron guide to be one of the major loss factors. In the old set-up the width of the gap was *32 mm* on each side of the neutron guide representing a loss per traverse of 6%. The influence of vibrations on the storage process had not been taken into account by any damping system for the crystal supports.

### 3. VESTA - The Optimised Storage Device

The problems with the exclusive use of the IRIS beamline either for the standard instrument or for neutron storage experiments led to the concept of the neutron storage device as an independent instrument on ISIS. The instrument will be called **VESTA**, *the Viennese nEutron STorage Apparatus* (cf. VESTA, Roman Goddess of the hearth and household) and operated as a collaborative project between ATI (Atominstitut der Österreichischen Universitäten) and RAL (Rutherford Appleton

Laboratory). VESTA will be fed by a monochromatic beam of neutrons reflected from the IRIS beamline (cf. Fig. 3). A hole was cut into one of the neutron guides of the 3 m guide section, allowing a pyrolytic graphite crystal to be inserted into the IRIS guide, acting as a *monochromator* crystal which deflects neutrons of wavelengths around *6.27 Å* out of the IRIS guide into the neutron storage apparatus. The graphite crystal is mounted on an orientation unit allowing it to be aligned with respect to the IRIS beam as well as being able to insert and retract it according to the VESTA/IRIS operational modes. Fully inserted, the graphite crystal covers slightly less than half of the IRIS neutron guide cross section (*43x65 mm* ).

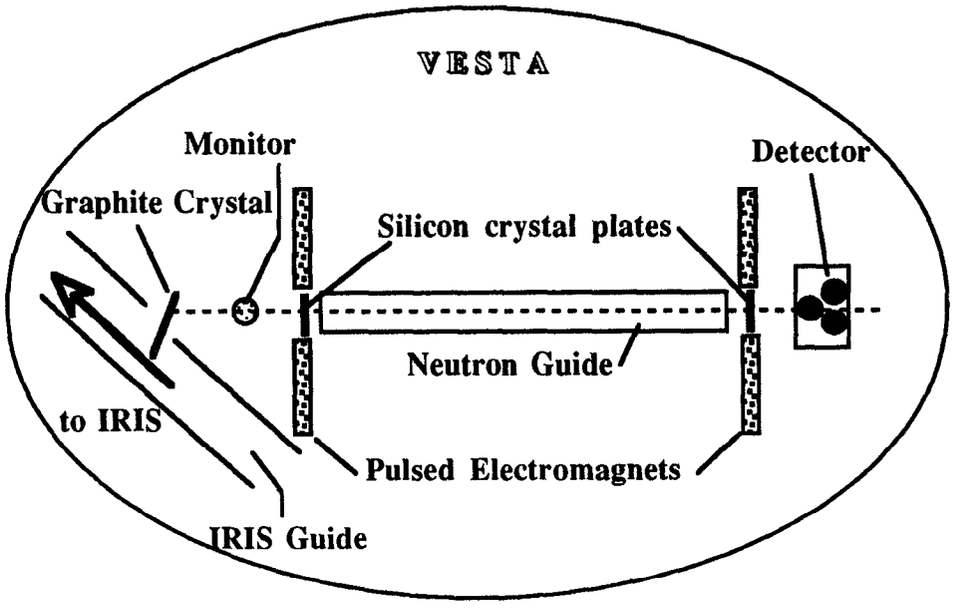


*Fig. 3* The new neutron storage set-up

As a consequence of the loss factors of the old neutron guide, VESTA will be equipped with a new guide. The new guide is *1063 mm* long, reducing the gaps on each side between the neutron guide and the silicon storage crystal to *0.5 mm.* Assuming a linear dependence of neutron losses due to the gap width, this would reduce the influence of the gap by a factor *64* on each reflection. The cross section of the new guide is *26x43 mm*, while material and critical angle remain the same. The parallelism of opposite guide surfaces has slightly improved from $8 \cdot 10^{-5}$ *rad* to $7 \cdot 10^{-5}$ *rad.* The increase of the height of the guide cross section from *40* to *43 mm* now covers the total height of the silicon crystal plates (diminished only by the thickness of the neutron guide bottom plate and a vertical gap between the neutron guide and the storage crystal base which assures movability of the neutron guide and prevents the guide and the crystal from touching each other). A new graphite crystal, about *60 mm high* and *2 mm thick,* will ensure both good illumination of the storage device and acceptable transmission to the IRIS spectrometer. Furthermore an increase in the maximum magnetic field from *1.06 T* to *1.3 T* should raise the transmission probability from *0.656* to *0.826* at each plate. A third He-3 tube was added to the detector, thus increasing its geometrical efficiency by a factor *1.28* (cf. Fig. 3). To reduce the influence of vibrations a simple damping system was added to the support of the electromagnets. Putting together the gain in stored neutron intensity as a result of improving factors relating to the external storage process, i.e. height of graphite crystal and neutron guide, magnetic entrance and exit field and arrangement of the detector, a gain factor of *1.35* at the beginning and of *1.93* at the end of the storage process should be achieved. The influence of the improved conditions for the inner

storage process have not been treated analytically but Monte Carlo simulations suggest an increase in efficiency of the inner storage process by a factor between 10 and 100 for longer storage periods. In addition the storage device will not be in the full IRIS beam. The wavelength band illuminating the storage device will be much narrower than previously, resulting in lower background effects.

## 4. Future plans

The initial commissioning runs of VESTA will show whether the improvements described in section 3 will have the expected influence with respect to loss factors and storage times. In 1989 neutrons were stored for *20.2 ms* [1] and in 1990 for up to *263.1 ms* [2]. The improved set-up should allow storage times well beyond 1 second to be achieved. The standard ISIS Data Acquisition Electronics (DAE) has been modified to create time frames up to *10 s*. Since, with increasing storage time, the neutron storage device will accept a correspondingly smaller number of ISIS pulses, e.g. 1% when ISIS operates at *50 Hz* and VESTA is storing with *0.5 Hz,* a special interaction scheme between the standard DAE and the Storage Control Electronics (SCE) was created to take the new mode of operation into account. The SCE was modified also to suit the advanced needs of the planned neutron storage experiments. The main goal will be the characterization of all the loss factors, again enabling a significant increase in storage time. It will also enable us to set an improved limit for the reflectivity of a perfect silicon crystal plate (presently *0.9978;* cf. Ref. 2). As the spatial length of a stored neutron pulse is about *10 cm*, compared with a flight path of 2 m between the crystal plates, the possibility of storing several neutron pulses at the same time has been considered [3,4]. With the present set-up a storage of 2 or 3 neutron pulses together seems feasible. Using neutrons of *2.09 Å* wavelength, which fulfils the backscattering condition for the silicon *(333)* reflection, neutrons of another wavelength band could be stored within the same neutron storage device. A demonstration of this capability is also amongst our future plans.

After a complete characterization of the instrument with its anticipated lower loss factors, two fields of application arise for a neutron storage device such as VESTA. *i)* The set-up offers the possibility of observing weak neutron interactions with other radiation in a defined area. If one considers for example the interaction of a neutron with an electro-magnetic field, one can observe this interaction for several seconds over a flight path which exceeds one kilometre while the characteristics of the electromagnetic field have to be controlled over a distance of only 1 m. As one could imagine observing the effect of such an interaction as an increase or decrease of stored neutron intensity, the knowledge of all loss factors of the neutron storage device has to be the first goal of its characterization. *ii)* The instrument could serve as a preparation stage for subsequent experiments. The advantages of this preparation are the flexible choice of measurement time, performing the subsequent experiment without disturbances and with excellent background conditions. It offers high monochromaticity *(0.15 μeV)* and low angular divergence of the beam. To obtain an effective preparation tool, the losses of the neutron storage apparatus have to be minimized. It is hoped to achieve this further step in perfect crystal storage techniques with the new VESTA set-up at the pulsed neutron spallation source ISIS.

## 5. Concluding remark

The intense monochromatic neutron beam out of the IRIS neutron guide can also be used for purposes different from neutron storage experiments. It is intended to be used as a test beam for new developments in fundamental physics experiments and advanced spectrometer set-ups for future pulsed sources such as AUSTRON and the European Spallation Source ESS.

**Acknowledgement**

The financial support from the Hochschuljubiläumsstiftung der Stadt Wien 1990 is gratefully acknowledged, as is the technical assistance of ISIS staff, in particular Mr. M.A. Adams and Mr. J. Hirst.

[1] M. Schuster, H. Rauch, E. Seidl, E. Jericha and C.J. Carlile, Phys. Lett. A **144** (1990) 297
[2] M. Schuster, C.J. Carlile and H. Rauch, Z. Phys. B **85** (1991) 49
[3] M. Schuster, E. Jericha, C.J. Carlile and H. Rauch, Physica B **180** & **181** (1992) 997
[4] M. Schuster, C.J. Carlile, E. Jericha, H. Rauch, SPIE Vol. **1738** (1992) 406

# THE NEW FOURIER DIFFRACTOMETER AT THE IBR-2 REACTOR: DESIGN AND FIRST RESULTS

**V.L.Aksenov, A.M.Balagurov, V.G.Simkin, Yu.V.Taran**
Frank Laboratory of Neutron Physics, JINR, Dubna, Russia

**V.A.Trounov, V.A.Kudrjashev, A.P.Bulkin, V.G.Muratov**
Petersburg Nuclear Physics Institute, Gatchina, Russia

**P.Hiismaki, A.Tiitta, O.Antson**
Technical Research Centre of Finland, Espoo, Finland Abstract

**Abstract**

A high-resolution neutron powder Fourier diffractometer (HRFD) has been realized at the pulsed reactor IBR-2 in Dubna. The HRFD avails of both the high luminosity of the IBR-2 reactor and the high resolution of the Fourier chopper. The resolution very close to 0.001 has been achieved over a wide range of *d*-spacings and the value of $\Delta d/d$ equal to 0.0005 is expected to be reached after the diffractometer units are aligned. Neutron flux at the sample position is about $10^7$ n/cm$^2$/s providing a good data accumulation rate. The new diffractometer is thought to be very suitable for structural refinement of low symmetry crystals and for residual stress studies.

## 1. TOF diffractometers at the IBR-2 reactor

It is well known that a powder diffractometer can be optimized in two alternative modes: high resolution or high intensity. Precise structural studies and real-time experiments are the examples of the investigations which are destined for these two kinds of instruments. The pulsed reactor IBR-2 /1/ in Dubna has a very high peak flux of thermal neutrons from moderator surface — $10^{16}$ n/cm$^2$/s. At the same time the resolution the conventional TOF spectrometers at the IBR-2 is not too good due to the large width of the neutron pulse (320 μs). As a result good prospects exist for the experiments that require high intensity but moderate resolution. For example, the DN-2 diffractometer at the IBR-2 makes it possible to measure the entire diffraction pattern within a fraction of a minute. The examples of such experiments are reported elsewhere /2/. However the precise structural studies of high level seemed impossible to be carried out with the IBR-2.

## 2. How the resolution can be improved?

The expression for the resolution of the time-of-flight powder diffractometer has two terms (in the first approximation):

$$R = \Delta d/d = \left[(\Delta t_0/t)^2 + (\gamma\, ctg\theta)^2\right]^{1/2}, \qquad (1)$$

where $\Delta t_0$ is the width of the neutron pulse, $\gamma$ includes all geometrical uncertainties, $t = 252.778L\lambda$, $L$ is the total flight path, $\lambda$ is the neutron wavelength, $\theta$ is the Bragg angle. It is clear that the time-of-flight contribution can be reduced either by shortening the source pulse or by lengthening the flight path. For example, the HRPD diffractometer /3/ at ISIS exploits both ways: the pulse width is as short as ~15 μs/Å and the flight path is as long as ~100 m. This permits one to get $\Delta t_0/t$ as small as $6\cdot10^{-4}$ in a wide *d*-range.

From the practical viewpoint these two ways are not good, if one wants to the resolution of the TOF diffractometer at the IBR-2 reactor to be of such a small value. Another and more promising possibility is the utilization of the correlation technique, pseudostatistical or Fourier-type. The Fourier method proved itself to be more preferable for elastic scattering because it allows use of narrow chopper slits together with wide neutron beam /4/.

### 3. The resolution of the neutron Fourier diffractometer

The key part of the Fourier diffractometer, the Fourier chopper, is the ultimate case of a multislit Fermi chopper when the widths of slits and the spacings between them are equal. For a 1 mm slit and 9000 rpm speed of a chopper the neutron pulse width is about 2 μs. But due to the frequency sweeping the width of resolution function is not so small. In the simplest case, this frequency sweep $g(\omega)$ is Blackman distribution from zero frequency up to the maximum one, $\omega_m$. It was shown, for example in /5/, that the time-of-flight part of the resolution function, $R_c(t)$, in this case is equal to:

$$R_c(t) \sim \int_0^{\Omega_m} g(\omega) cos(\omega t) d\omega, \tag{2}$$

where $\Omega_m = N\omega_m$ is the maximum modulation frequency of neutron beam, with $N$ denoting the total number of chopper slits. Roughly, the full width at the half maximum of $R_c(t)$ is equal to $\Omega_m^{-1}$ and can be pushed down to about 7 μs. In this case the first term in (1) is (for backscattering):

$$\Delta t_0/t = \Delta t_0/253L\lambda \approx 7\cdot 10^{-4}/d, \tag{3}$$

where $d$ is in Å . The divergence of the initial beam, sample and detector dimensions contribute to the second term in (1). For the time-focused detector system the calculated value for this term can be equal /6/ to $3.5\cdot 10^{-4}$, so the total width of the resolution function can be about $5\cdot 10^{-4}$, if $d$ equals 2 Å.

### 4. Existing neutron Fourier diffractometers

At present two neutron Fourier diffractometers are in practical use: mini-SFINKS facility /7/ in Gatchina (Russia) and FSS /8/ in Geesthacht (Germany). They both are installed at steady state reactors, use the Reverse Time Of Flight (RTOF) method /5/ of data acquisition and reveal good prospects for structural and residual stress studies. The mini-SFINKS diffractometer is the first result of Finnish - Russian cooperation aimed at the development of Fourier TOF techniques for diffractometry applications. In improved configuration it has been operating at the 16 MW reactor since 1986 for routine structural investigations. The maximum beam modulation frequency, $\Omega_m$=120 kHz, allows a FWHM of ~8.5 μs to be achieved. For the total flight path of 7.6 m the resolution changes in the useful interval of $d$-spacings 0.5-2.6 Å from $\Delta d/d \approx 0.005$ to about 0.002.

### 5. Some special features of Fourier diffractometer operation at a pulsed neutron source

For the better understanding of the situation with the Fourier chopper at a pulsed source let us compare three types of instruments: the conventional TOF machine and the Fourier diffractometer at a steady state and a pulsed source. In the first case the detected intensity is proportional to the convolution integral:

$$I(t) \sim \int R_s(t-\tau)\sigma(\tau)d\tau + B(t), \tag{4}$$

where, in the rough approximation neglecting all geometrical contributions, $R_s$ is the source pulse, $\sigma$ is the scattering cross section of the sample, $B$ is the conventional background. The situation with a Fourier diffractometer at a steady state reactor is a little more complicated as there is the modulation of the incident neutron beam by the Fourier chopper. Then the relation for the intensity looks like

$$I(t) \sim \int R_c(t-\tau)\sigma(\tau)d\tau + c\int \sigma(\tau)d\tau + B(t), \tag{5}$$

here $R_c$ is the resolution function of the Fourier chopper, the second term, which can be called "the correlation background" is proportional to the total detected intensity, $c$ is a certain constant. The situation with the Fourier chopper at a pulsed neutron source is, in some sense, the combination of the two previous cases:

$$I(t) \sim \int R_s(t-\tau)R_c(t-\tau)\sigma(\tau)d\tau + c\int R_s(t-\tau)\sigma(\tau)d\tau + B(t). \tag{6}$$

One can see, that in (6) both resolution functions $R_s$ and $R_c$ are present, thus the diffraction peaks are very narrow ($\Delta t \approx 7$ μs), the correlation background is not constant and it is proportional to the resolution function of the source. Additional modulation with $R_s$ is very important for decreasing the correlation background, which is now proportional to a small portion of the total intensity, namely, the intensity in the time interval $2\Delta t$, where $\Delta t$ is equal to the width of $R_s$, i.e. 320 μs for the IBR-2 reactor. Due to the Maxwellian distribution of the incident beam intensity the signal to noise ratio for steady state and pulsed sources is quite different. There is some gain in this ratio in the pulsed source case, being especially high for the long wavelength neutrons.

## 6. The HRFD design (Fig.1)

The High Resolution Fourier Diffractometer (HRFD) at the IBR-2 pulsed reactor is the spinoff from the cooperation of the Joint Institute for Nuclear Research, Dubna, Nuclear Physics Institute, Gatchina and Technical Research Centre of Finland, Espoo. The project started in 1988, when all calculations were performed. The electronics and mechanical devices were ready for operation late in 1991. The neutron beam was formed in the beginning of 1992 and in June 1992 the first diffraction patterns were measured /9/.

HRFD is located on beam N5 of the IBR-2 reactor. Immediately after the reactor shielding the mechanical filter and the auxiliary neutron guide tube are placed. The filter is a stainless steel disk-chopper of about 1 m diameter with a $\Delta\phi$=60° window. It is to remove the thermal neutron background off the beam. Through the biological shielding the beam is conducted over a straight neutron guide. Immediately after this shielding wall the Fourier-chopper is placed. The focusing guide tube acts both as the forming element of the neutron beam and filter of fast neutrons and γ-rays. Its incoming and outgoing window cross-sections are as large as 30x200 and 10x100 mm$^2$, respectively, and its total length is about 19 m. Before the sample the Soller collimator is installed to reduce the angular divergence of the neutron beam. The detector assembly consists of two blocks. At a lower scattering angle two position sensitive detectors are placed on the moveable arms. The main detector is located at a larger angle (≈156°), it is time-focused and has a total solid angle of 0.08 sr. The flight path between the chopper disk and the sample position is 20.0 m. The electronics of HRFD is created using the modular RTOF analyzer based on a polarity correlator ASIC circuit of special design. Each Correlator module contains 1024 channels. The analyzer consists of a master module, acting as the signal interface and the master clock unit, and eight correlator modules. Two these 8192-channel analyzers operate simultaneously with the Fourier chopper pickup signals in opposite phases. The RTOF analyzers are connected to a PC/AT-386 by a BITBUS standard serial interface. The PC is used as interface between the user and the measuring unit. Principal technical data and performance characteristics of HRFD are summarized in the Table. At the present they all correspond to the actual ones, except for the high resolution detector at 90° scattering, which will be ready

for operation at the end of 1993.

## 7. Instrument performance and first experimental results

As it follows from eq. (6) the experimental spectrum measured with each of the two analyzers consists of three components: the high resolution diffraction peak, the low resolution diffraction peak and the background. The sign of the term, representing the high resolution peak, is different for the first and second analyzer. Therefore, simple subtraction allows to separate the high resolution spectrum only. One can easily see that in Fig.2, which shows a small part of the spectrum from $Al_2O_3$. It is natural that dispersion of the resulting spectrum depends on the statistics collected by the analyzers.
The high resolution spectrum of the *Ge* powder is shown in Fig.3, while Fig.4 gives comparative raw diffraction patterns of $Al_2O_3$ obtained with HRFD (bottom) and HRPD diffractometer at ISIS. One can see that both diffractometers have practically the same resolutions. At the same time it is clear that the HRPD creates better background conditions. The resolution was measured at various chopper speed (Fig.5) and *d*-values. Then the measured and expected resolution functions were compared. The result was that the TOF contribution to the resolution function was very close to the expected value but the geometrical term was three times larger. We believe it is mainly due to the detector contribution, as no careful detector alignment has been done yet. An attempt of Rietveld refinement was also done (Fig.6) with the help of MRIA program /10/. For profile shape function we used one of the diffraction peaks, measured with good statistics, as it is possible with MRIA. Details will be presented in a separate paper.

## 8. Conclusions

The high resolution Fourier diffractometer has been realized at the IBR-2 pulsed reactor. The most important result of the preliminary measurements performed consists in the fact that the idea has received confirmation that the Fourier technique in combination with a pulsed neutron source, such as the IBR-2 reactor, gives the diffraction patterns of very good quality. The resolution of 0.0015 in $\Delta d/d$ was achieved at first attempt. It is approximately 10 times better than was before achieved at the IBR-2 (Fig.7). The expected value of $\Delta d/d$ equal to 0.0005 can be reached after the diffractometer units are aligned and their assembly completed.

The authors wish to acknowledge the help of many members of the FLNP, PNPI and VTT staff in engineering, fabrication and installation of this instrument.

Special thanks are due to Drs. B.I.Voronov, E.V.Serochkin, V.I.Aparin, V.G.Tishin, V.E.Novozchilov, A.I.Ostrovnoy, I.P.Barabash, A.A.Bogdzel, A.I.Sirotin, A.P.Trofimova, G.F.Zhironkin and V.V.Zhuravlev.

The work was financed by the Joint Institute for Nuclear Research in the frame of the JINR and BMFT (Germany) agreement on co-operation and supported by the Russian State Commission on HTSC materials within projects 90169 and 90287.

## References


[1] V.D.Anan'ev et al, Neutron Scattering in The 'Nineties, Conf. Proc., p.63, Vienna, IAEA, 1985
[2] A.M.Balagurov et al, J.Appl.Cryst., 1991, 24, p.1009
[3] W.I.F.David, W.T.A.Harrison, M.W.Jonson, Communication of RAL, RAL 86-068, Chilton, 1986
[4] P.Hiismaki, H.Poyry, A.Tiitta, J Appl.Cryst. 1988, 21, p.349
[5] H.Poyry, P.Hiismaki, A.Virjo, Nucl.Instr.Meth., 1975, 126, p.421
[6] V.A.Kudryashev et al, Communication of LNPI, 1562, Leningrad, 1989 (on Russian)
[7] P.Hiismaki et al, Neutron Scattering in The 'Nineties, Conf. Proc., p.453, Vienna, IAEA, 1985
[8] H.G.Priesmeyer, J.Schroder, Mat.Res.Soc.Symp.Proc., 166 (1990) 299
[9] V.L.Aksenov et al, Communication of JINR, E13-92-456, Dubna, 1992
[10] V.B.Zlokazov, V.V.Chernyshev, J.Appl.Cryst., 1992, 25, p.447


## Table. HRFD details

| | |
|---|---|
| Beam | $^{58}$Ni-covered guide tube |
| Guide aperture | 10 mm x 100 mm, variable |
| Moderator - sample distance | 30 m |
| Chopper - sample distance | 20.00 m |
| Fourier-chopper (disk-type) | Ti-Zr-alloy |
| outside diameter | 540 mm |
| slit width | 0.6 mm |
| number of slits | 1,024 |
| max speed | 9,000 rpm |
| max beam modulation frequency | 150 kHz |
| Thermal neutron pulse width: | |
| low-resolution mode | 320 μs |
| high-resolution mode | 7 μs |
| High-resolution detectors | $^{6}$Li, time-focusing |
| Low-resolution detector | $^{3}$He, position-sensitive |
| Aperture of the detectors: | |
| high-resolution 156° | 0.08 sr |
| high-resolution 90° | 0.04 sr |
| low-resolution 0° - 60° | 0.006 sr |
| Wavelength interval | 0.9 - 8 Å |
| *d*-spacing interval: | |
| high-resolution | 0.5 - 6 Å |
| low-resolution | 4 - 60 Å |
| Flux at sample position | $10^7$n/cm$^2$/s |
| Sample volume | ~ 2 cm$^3$ |
| Resolution for: | |
| $2\theta = 156°$, $d = 2$ Å | 0.0005 |
| $2\theta = 90°$, $d = 2$ Å | 0.002 |

**Fig.1. The HRFD design**

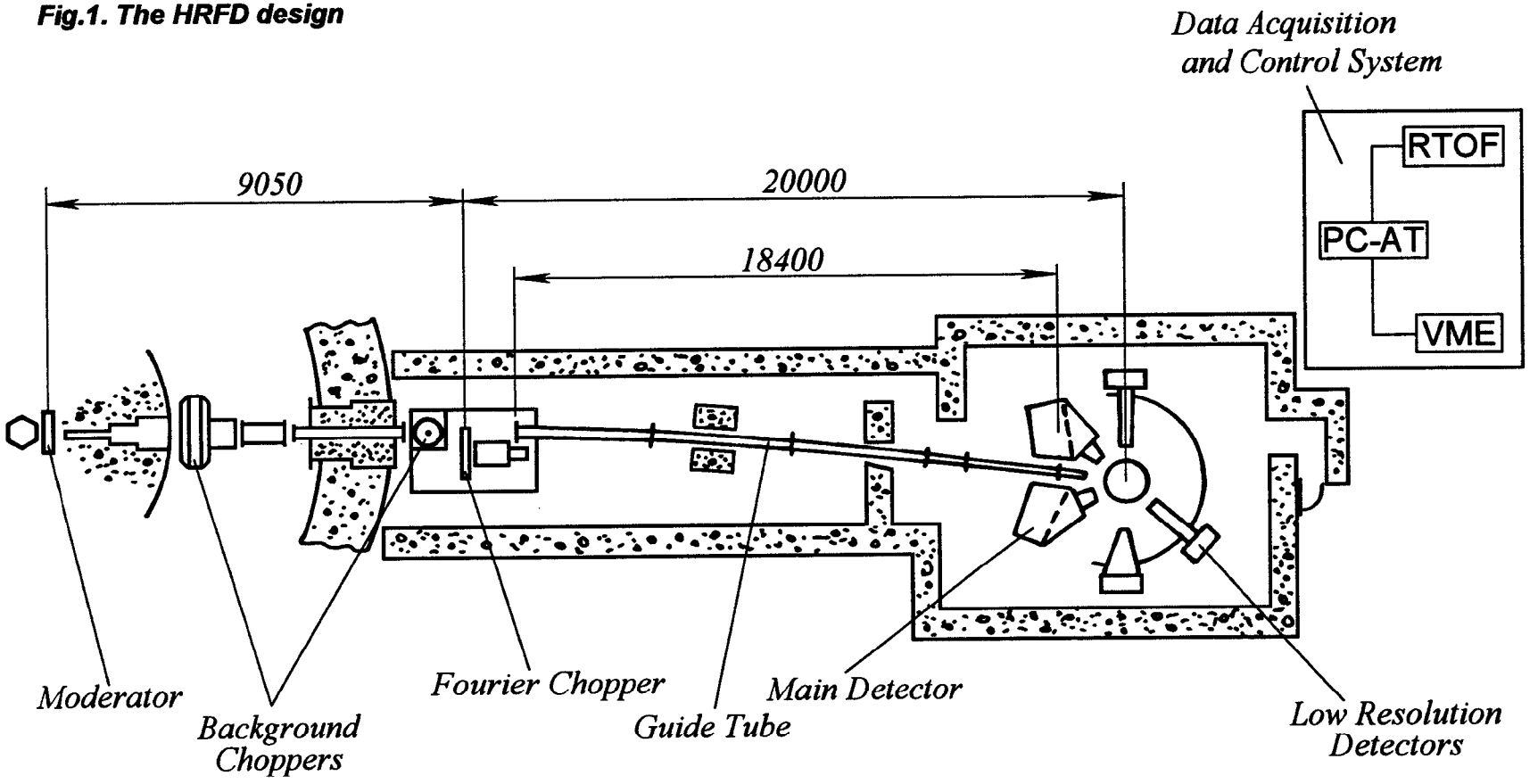

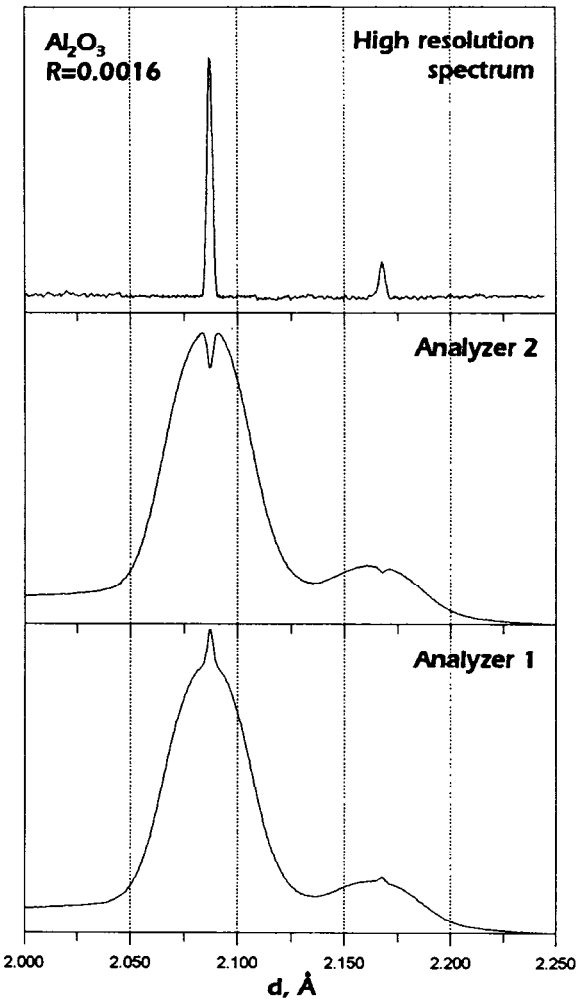


**Fig.2.** A small section of the $Al_2O_3$ diffraction pattern measured with analyzers 1 and 2 and their difference (upper).

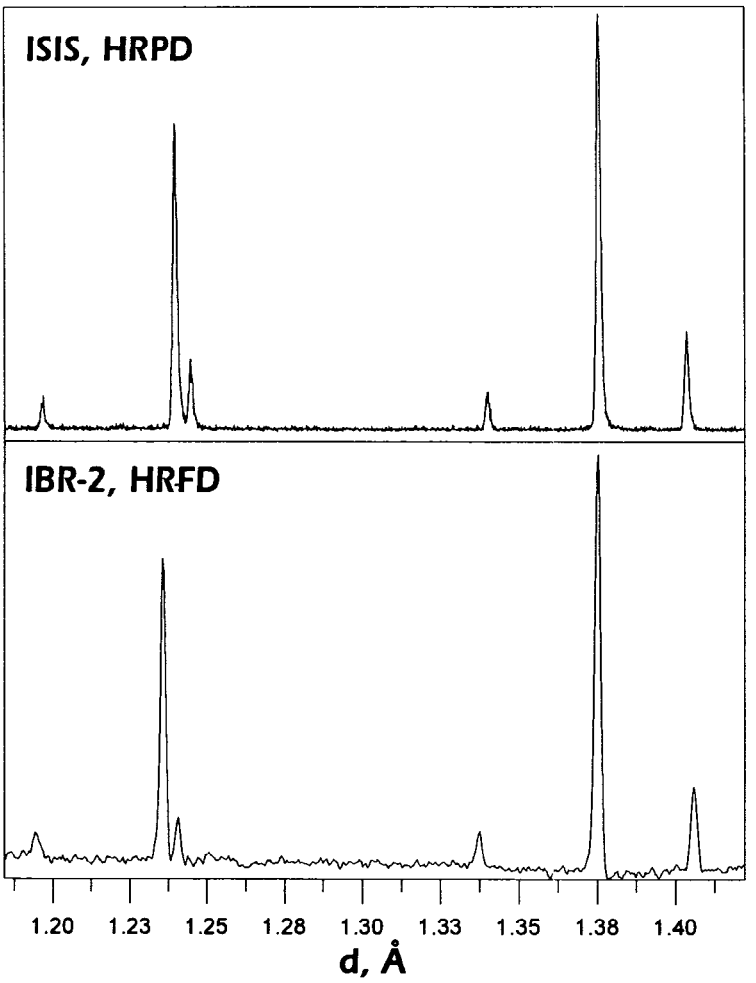


**Fig.4.** A small section of the $Al_2O_3$ diffraction pattern measured on the HRPD diffractometer at ISIS (top) and on HRFD (bottom). The horizontal scale is slightly different for the patterns.

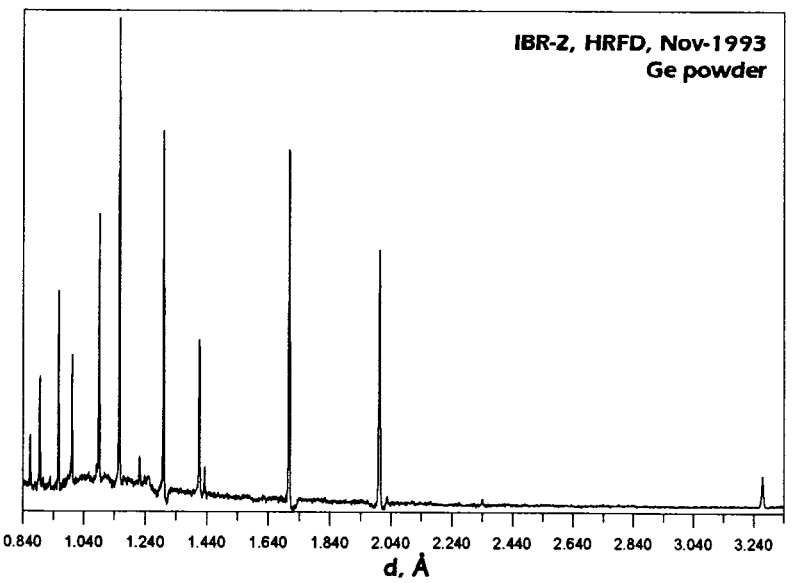


**Fig.3.** The Ge powder diffraction pattern measured at the IBR-2 reactor with the new Fourier diffractometer. The sample was packed in an Al-foil whose small diffraction peaks are also visible.

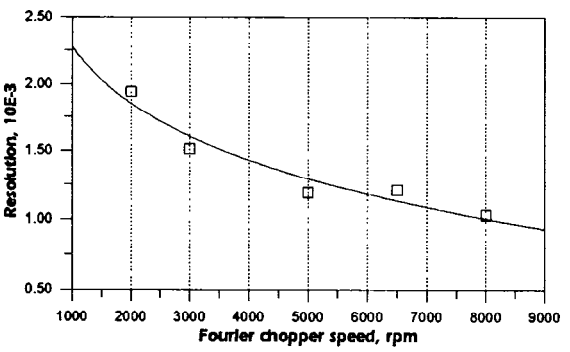


**Fig.5.** The dependence of the resolution ($\Delta d/d$) on the speed of the chopper rotation for the diffraction peak at d = 1.67 Å

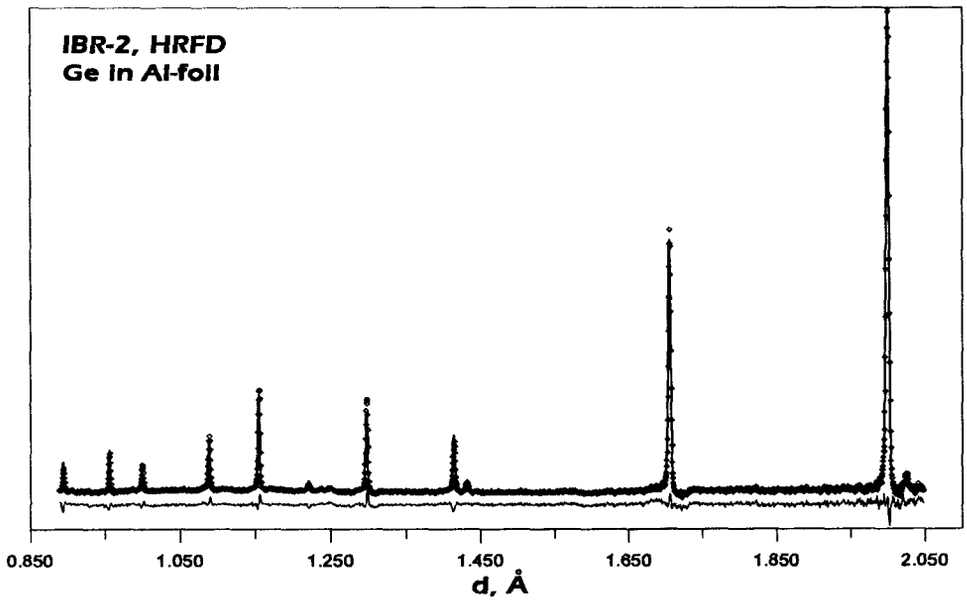


**Fig.6.** A section of Rietveld refinement pattern for Ge after normalization shown in Fig.3.

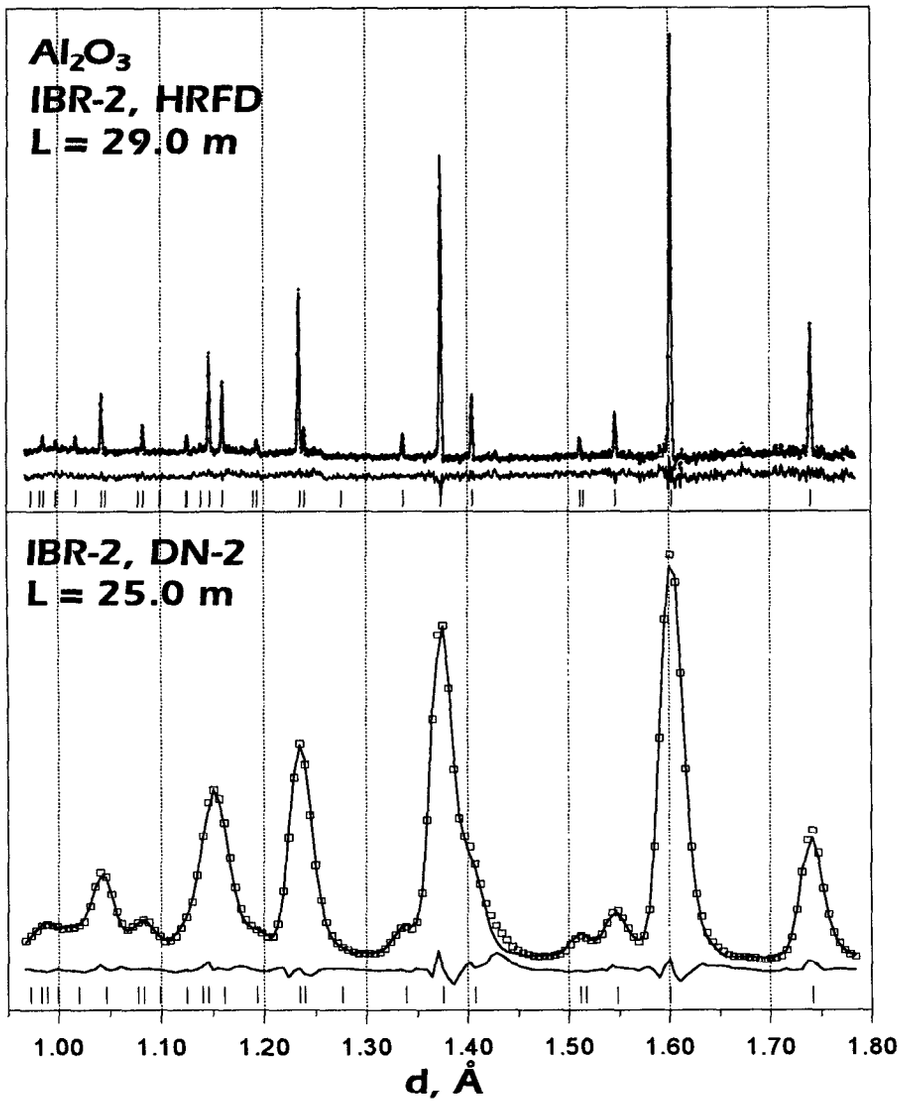


**Fig.7.** The comparison of $Al_2O_3$ diffraction patterns measured at the IBR-2 reactor with the DN-2 TOF-diffractometer and the new Fourier diffractometer. *L* is the total flight path equal to 25 m and 29 m for these two instruments, respectively. The resolution of HRFD is approximately 10 times better than that of DN-2. Experimental points, calculated profile and difference curve are shown.

# SXD: Novel Single Crystal Studies using the Time-Of-Flight Laue Technique

C C Wilson

ISIS Facility, Rutherford Appleton Laboratory, Chilton, Didcot, Oxon OX11 0QX, UK

## Abstract

Some of the novel applications of time-of-flight Laue diffraction performed on the SXD instrument at ISIS are discussed. The power of the technique both in structural refinement and in diffuse scattering studies is stressed.

## Introduction

SXD, the single crystal diffractometer at ISIS (Figure 1), uses the Laue time-of-flight diffraction technique (Wilson, 1993a) for structural studies. This method exploits the ability of an instrument equipped with a 2D position-sensitive detector (PSD) on a pulsed neutron source to access large volumes of reciprocal space in a single measurement and has significant advantages in many areas of structural work.

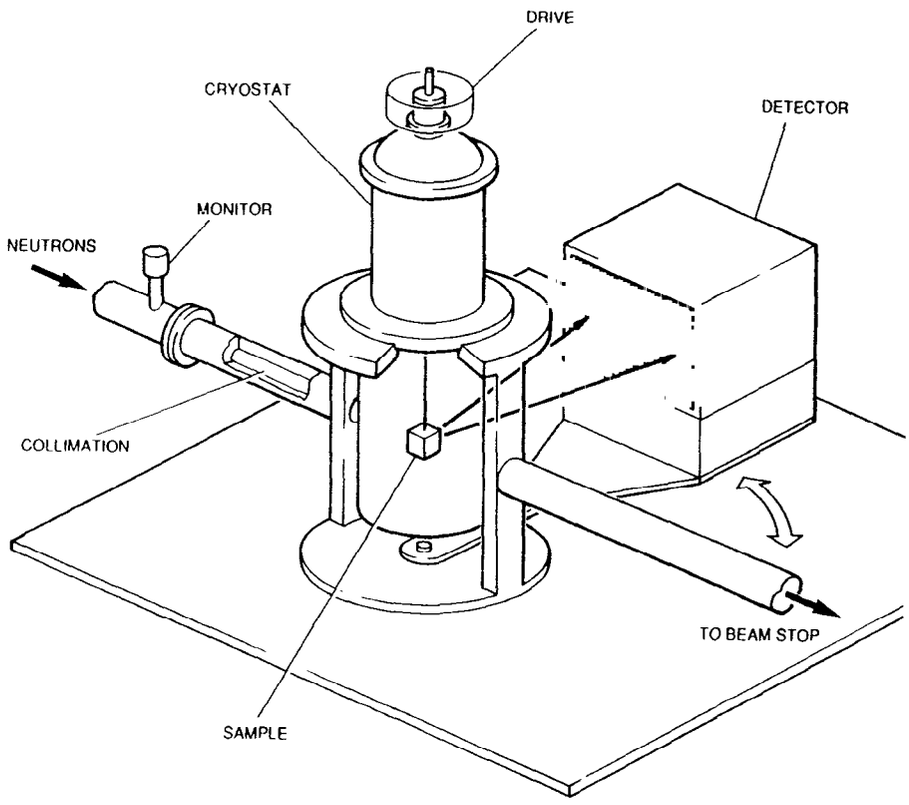


*Figure 1 - The time-of-flight Laue instrument SXD at ISIS.*

The first areas in which SXD was successful (Wilson, 1990) were those of the examination of incommensurate structures and the more qualitative aspects of diffuse scattering, these being the most obvious areas in which an ability to conveniently measure the regions between Bragg peaks is especially useful.

More recently, however, improvements in the instrumentation, especially the provision of larger, more reliable PSDs, have enabled the extension of the scientific programme. SXD is now fully capable of routinely performing a full range of single crystal studies, for example:

- Structural studies - chemical crystallography, the location of hydrogen atoms (Wilson, Stewart and Keen, 1992; Wilson, 1993b), the study of long range static disorder (Artioli et al, 1993), the exploitation of the high sin $\theta/\lambda$ measurements possible on a spallation source (Keen, Hannan and Wilson, 1993);
- Diffuse scattering studies - the study of short range order and disorder, quantitative atomic level cluster modelling (Hull and Wilson, 1992), quantitative Reverse Monte Carlo type modelling (Li et al, 1993).
- Incommensurate structures and phase transitions - the study of magnetic structures, the monitoring of structural changes from single data histograms (Wilson, 1993c).

**Structural Studies**

The application of time-of-flight Laue diffraction in routine structural studies broadly mirrors that of any neutron single crystal diffractometer, primarily involving the location of hydrogen atoms or the differentiation of atoms with similar atomic numbers. The nature of the time-of-flight Laue technique, however, is such that the data collection and reduction are significantly different from traditional techniques. By using the wide wavelength range available from a pulsed source such as ISIS, which with time-of-flight is uniquely non-prejudicial in terms of overlap, and combining this with large area PSDs, an instrument such as SXD is found to measure many reflections simultaneously (see Figure 2). Thus the coverage of reciprocal space is achieved in a series of histograms, typically a dozen or so, rather than by scanning individual reflections. The angle- and wavelength-dependent corrections are more severe (but occasionally, in favourable cases, more informative) than in the fixed wavelength case, and this tends to lead to slightly poorer agreement factors than are available from a fixed wavelength, step scanning instrument. In addition, there is some evidence that the non-uniform statistical distribution of intensities measured using time-of-flight Laue can also adversely affect the resulting crystallographic R-factor (Wilson, 1993d). Nonetheless, both accuracy and precision can be obtained in structural studies on SXD, as shown in the following examples:

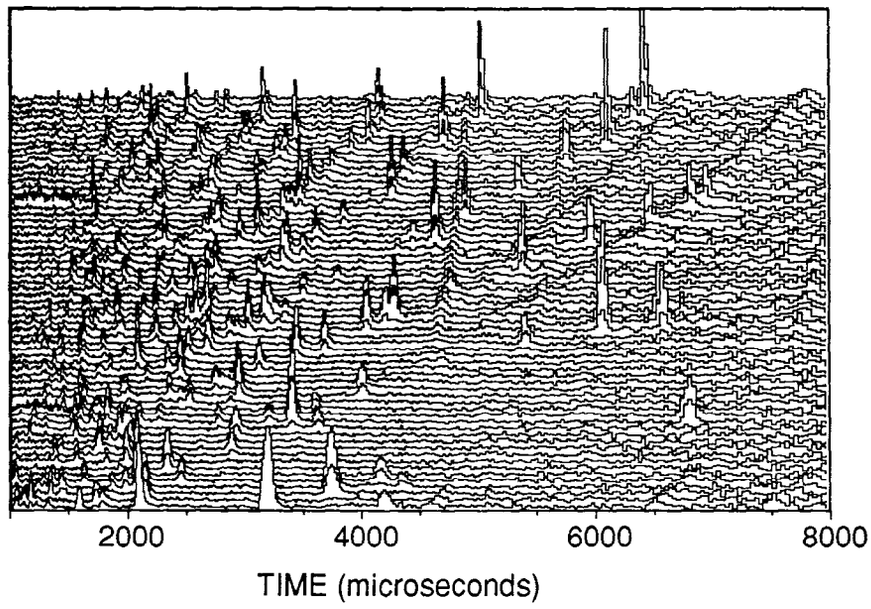


*Figure 2 - Representation of the large number of reflections (around 400) measured in a single histogram on SXD from urea phosphoric acid.*

### *(i) Hydrogen atom location in the organic structure 3-deazauracil*

X-ray studies of this material had yielded the heavy atom framework and indicated a strong (~ 2.5 Å) O-H...O hydrogen bond. However, the combination of the poor visibility of hydrogen atoms for X-rays and the obviously high non-bonding electron density in this region precluded hydrogen atom location. As this hydrogen bond is thought to play a crucial role, in the cytostatic properties of the parent drug 3-deazauridine, location of this hydrogen atom is important. Two experiments were carried out on SXD to investigate this material. In the first, using a smaller area PSD, a "quasi-equatorial" data set was collected, roughly equivalent to one or two layer lines in Weissenberg geometry, and the resulting 80 neutron structure factors were used in combination with the earlier X-ray data in a joint X-n refinement. This revealed unambiguously the location of the vital H atom on O4, rather than the alternative O2 site (Wilson, Stewart and Keen, 1992). A subsequent full data set collected on SXD using the larger detector led to neutron-only refinements which agreed well with the joint refinement (Wilson, 1993b). In addition to confirming the obvious utility of neutron data in cases such as this, the ability of even a limited data set to reveal correct and useful information in combination with other data, was extremely encouraging.

### *(ii) Fe/Mg ordering in olivine at high temperatures*

Olivine, $(Mg,Fe)_2SiO_4$, is the most constituent of the upper terrestrial mantle and a common rock forming mineral. In the structure of olivine, Mg and Fe can be distributed over two structural sites, M1 and M2, which have slightly different octahedral configurations. There are, however, conflicting crystallochemical factors which influence the Mg-Fe ordering onto the two sites, which superficially seem to

suggest that there is more likelihood of $Fe^{2+}$ occupying M1. There are also, however, other effects such as composition, oxygen fugacity, pressure and especially temperature, which can affect the relative distribution of the two cations.

The determination of the equilibrium in the exchange reaction

$$Fe_{M1} + Mg_{M2} \Leftrightarrow Fe_{M2} + Mg_{M1}$$

as a function of temperature can provide important information on the cooling history of the host rocks. Recent X-ray experiments on olivine samples quenched from various temperatures seem to indicate that iron tends to concentrate in site M1 as the temperature increases. However, olivines quenched from temperatures above 800°C show the same equilibrium constant as those of crystals quenched from 700°C, indicating that the maximum temperatures which can be determined by this technique is in the region of 700-800°C. This is because the rate of cooling, even for very rapid quenching techniques, is lower than the speed of the exchange reaction at temperatures above 800°C. The only way to truly monitor this equilibrium above 800°C is to carry out an *in situ* experiment at these temperatures. The convenience of high temperatures experiments using neutron diffraction allows a single crystal neutron scattering experiment to measure this equilibrium.

The sample used in the SXD experiment (Artioli et al, 1993) was an olivine single crystal of volume some 5 $mm^3$ taken from a pallastic meteorite from Kansas, whose iron content (> 10%) is sufficient to allow a reliable determination of the site content. Data were collected at two temperatures (880°C and 1060°C) and the results of the refinements at the two temperatures are shown in Table 1. All atoms were refined with anisotropic temperature factors, with the site occupancies refined both with Mg/Fe temperature factors fixed and with these parameters varying, with essentially identical results. The Fe temperature factors were fixed to be identical with those of the equivalent Mg atom and the overall site occupancies were constrained to add up to one on each site.

**Table 1**

Neutron refinement parameters for olivine

T=880°C, $R_w$=0.058 for 319 data, 42 refined parameters
a=4.788(3), b=10.349(3), c=6.061(2) Å; V=300.3 $Å^3$
$K_D$=1.45, Fe(M1)=0.140(26), Fe(M2)=0.100(26)

T=1060°C, $R_w$=0.062 for 238 data, 42 refined parameters
a=4.792(3), b=10.361(3), c=6.082(2) Å; V=302.0 $Å^3$
$K_D$=0.47, Fe(M1)=0.081(40), Fe(M2)=0.159(40)

The most remarkable result is that, while the Fe occupies the site M1 preferentially at 880°C as expected from the previous experiments on quenched samples, there are clear indications that at the higher temperature Fe preferentially occupies site M2. This result, unexpected from all previous X-ray results, indicates that there is a significant alteration in the Fe/Mg equilibrium above 880°C. This shift in equilibrium occupancy is obviously masked in studies of quenched samples by the speed of the exchange reaction, and is therefore only accessible in an experiment performed at

the higher temperature. This shift in preferential occupancy will also have implications for the position of the equilibrium in those samples quenched from above 800°C. Such a conclusion has significant implications for our understanding of rock-forming processes.

### *(iii) High sinθ/λ measurements - the exploitation of epithermal neutrons*

In previous measurements on the fluorite material $SrF_2$ on SXD (Forsyth, Wilson and Sabine, 1989) it was found to be possible to refine the anharmonic thermal vibrations in this structure to high precision even at room temperature, where the effect is obviously smaller than at elevated temperatures. However, even at room temperature there remains a significant contribution to the scattering at and around the Bragg peaks from thermal diffuse scattering (TDS). The simplest way to reduce TDS effects is to reduce the temperature but unfortunately this will also reduce the thermal vibrations of the atoms and hence make any anharmonic effects still more difficult to measure. However, the effect of anharmonicity on structure factors and hence on reflection intensities, increases with Q (and hence sinθ/λ) and given that higher Q data ought to be accessible at lower temperature as the Debye-Waller factors reduce, it may be possible to measure and refine anharmonic effects, uncorrupted by TDS, even at low temperatures. SXD is an ideal instrument with which to attempt this, as the combination of the favourable properties of the neutron (no form-factor fall-off with Q) and of ISIS (high flux of epithermal neutrons, especially on the ambient water moderator on which SXD is sited) should allow very

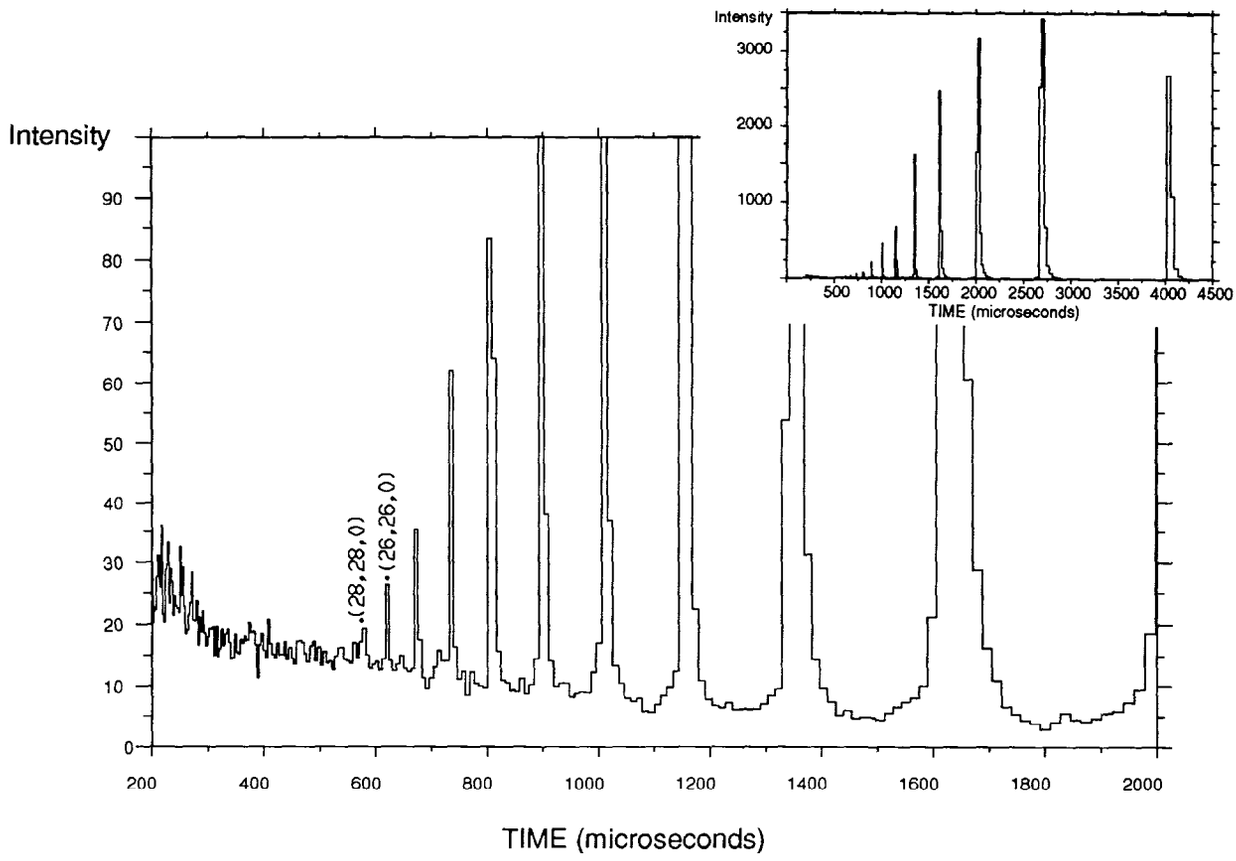


*Figure 3 - The (hh0) row of reflections in $SrF_2$ measured at 25 K on SXD, showing the (28,28,0) reflection at sinθ/λ of > 3.3 Å$^{-1}$.*

high resolution data to be accumulated. Accordingly, a data set was measured from $SrF_2$ at 25 K on SXD. The data are in the process of being analysed, but the promise of this approach is indicated by the observation of the (28, 28, 0) reflection (from a cubic crystal, with a = 5.8 Å; Figure 3), representing a $\sin\theta/\lambda$ value of > 3.3 $Å^{-1}$ (Q > 40 $Å^{-1}$). Since the earlier work extended the $\sin\theta/\lambda$ range to < 1.7 $Å^{-1}$, the prospects for analysing detailed thermal effects at this low temperature seem realistic, and work is continuing on this (Keen, Hannan and Wilson, 1993).

## Diffuse scattering studies

While SXD remains an extremely powerful surveying instrument for examining diffuse and/or incommensurate scattering patterns, the emphasis of the diffuse scattering programme has now shifted from elegant demonstrations of this capability to much more quantitative applications of the technique. Unlike routine structural refinement, interpretation of results in this field is still difficult, but is extremely rewarding and informative when successful. Detailed results have now been obtained using both cluster modelling and Reverse Monte Carlo type analysis. The rapid, accurately quantitative results obtained using SXD, and in particular the combination of these with simultaneous Bragg reflection measurements, are extremely favourable for further advances in these areas.

### *(i) Defect clusters in $(Ca,Y)F_{2+x}$ as a function of temperature*

Structural information concerning defect clusters within non-stoichiometric compounds can be obtained from both Bragg and diffuse scattering measurements. The average unit cell structure is determined from the Bragg scattering, while direct information concerning the local arrangement of the defect cluster is obtained from the coherent diffuse scattering, which often exhibits broad maxima between the Bragg peaks. Both types of data are readily accessible on SXD.

The defect structure of the anion-excess fluorite $Ca_{0.94}Y_{0.06}F_{2.06}$ was investigated using both Bragg and diffuse scattering measurements on SXD at 20° and 900°C. It is found that the best agreement with both Bragg and diffuse scattering information at low temperatures (Figure 4) is obtained by adopting a defect cluster which results from the conversion of six edge-sharing $(Ca,Y)F_8$ cubes into corner-sharing square antiprisms (Hull and Wilson, 1992). These cuboctahedral clusters are a general feature of ordered anion-excess yttrofluorites, and the SXD results, by combining the two types of diffraction information, indicate that these clusters are also present, but randomly distributed, in the disordered solid solution of $(Ca,Y)F_{2+x}$.

At higher temperatures, approaching the fast-ion transition, the diffuse scattering has a radically different appearance (Figure 5). Again both Bragg and diffuse scattering data were used in the analysis and clearly indicate that at 900°C the cuboctahedral clusters have broken up and the main type of defects in the structure are now Frenkel type anions, with further relaxation of anions into positions previously unoccupied at 20°C (Hull, Hoffmann and Wilson, 1993). The high temperature pattern thus closely resembles that from stoichiometric $CaF_2$ in which these Frenkel defects are the medium for fast-ionic conductivity. The availability of such **quantitative** information from a combination of Bragg and diffuse scattering lends great power to this area of application.

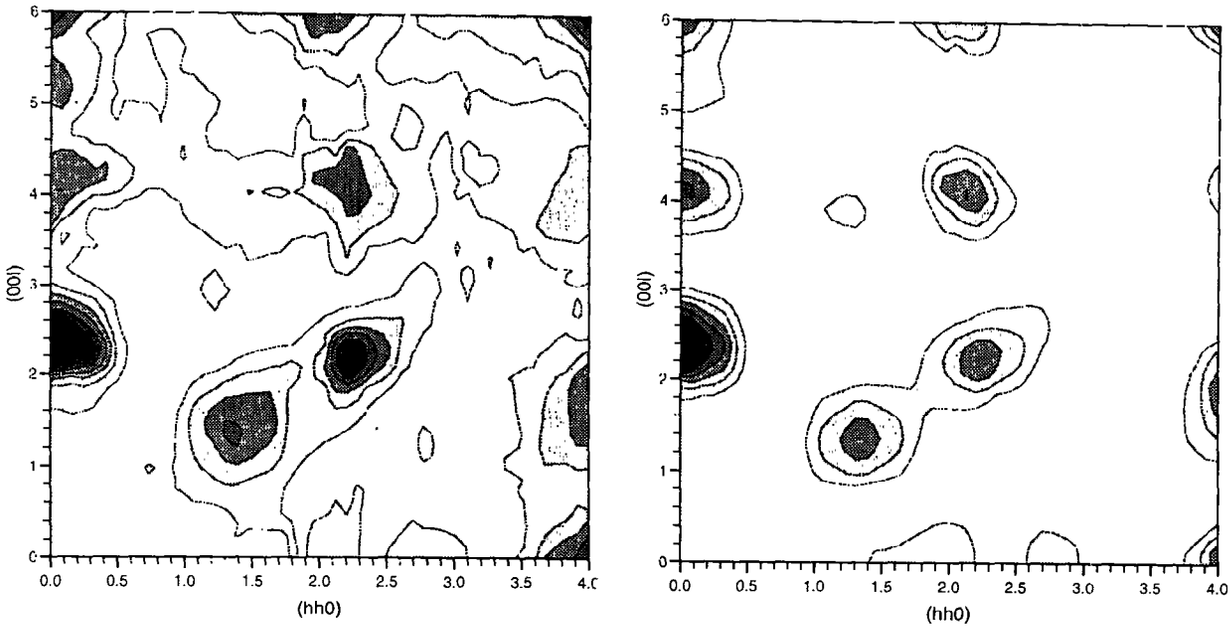


*Figure 4 - Observed (left) and calculated (right) coherent diffuse scattering from $(Ca,Y)F_{2.06}$ at 20°C. The latter is calculated using isolated cuboctahedral clusters to accommodate the excess fluorine atoms.*

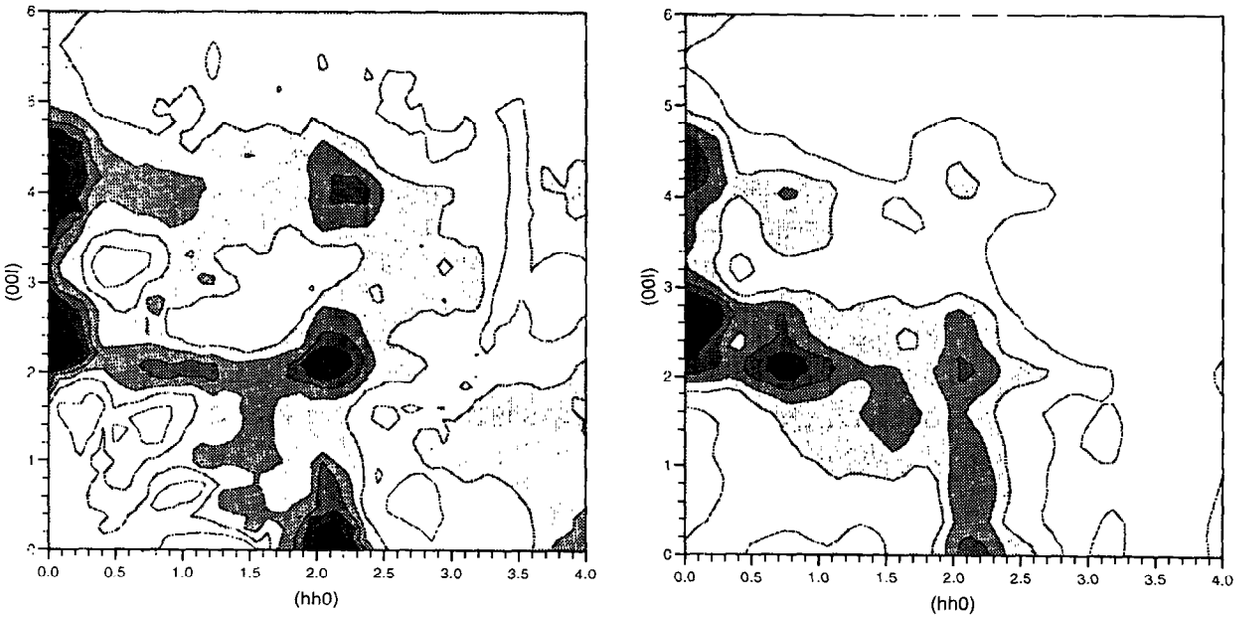


*Figure 5 - Observed (left) and calculated (right) coherent diffuse scattering from $(Ca,Y)F_{2.06}$ at 900°C. The latter is calculated using isolated Frenkel defect-like excess fluorine atoms.*

### *(ii) Short range proton ordering in Ice Ih*

The normal form of ice, ice Ih, consists of a tetrahedrally coordinated oxygen network, with the hydrogen atoms arranged so as to obey the Bernal-Fowler 'ice rules'. These state that each oxygen is bonded to two hydrogens, with one hydrogen on each O...O bond. In ice Ih the hydrogens obey these rules but are disordered with respect to one another. In order to examine this disorder and to see whether there is any local ordering of the protons a comprehensive study of the diffuse scattering from single crystal $D_2O$ ice Ih has been made on SXD, where the large region of reciprocal space measured is of particular benefit. To date the diffuse scattering has been measured in the (hhl) and (h0l) planes at 20 K and in the (hk0) plane at 10, 20, 110, 160 and 250 K.

The scattering in the (hhl) plane is shown in Figure 6 This is found to be very structured as the most significant features result from static disorder. A simulation in which the standard crystallographic positions for the atoms were used with the hydrogens completely disordered within the Bernal-Fowler rules (Figure 6) clearly reproduces the hexagonal rings. However, it fails to pick up the very strong diffuse streak stretching along (00l) from the (330) position. Further investigation suggests that this feature originates from a slight change in the H-O...H bond angle. No evidence has yet been found for any local ordering of the hydrogens beyond that expected from the 'ice rules'. Simulations are continuing using various innovative fitting techniques, such as RMC, and this work again stresses that the possibility of quantitative analysis of such diffuse scattering patterns is adding to our understanding of the underlying structural processes.

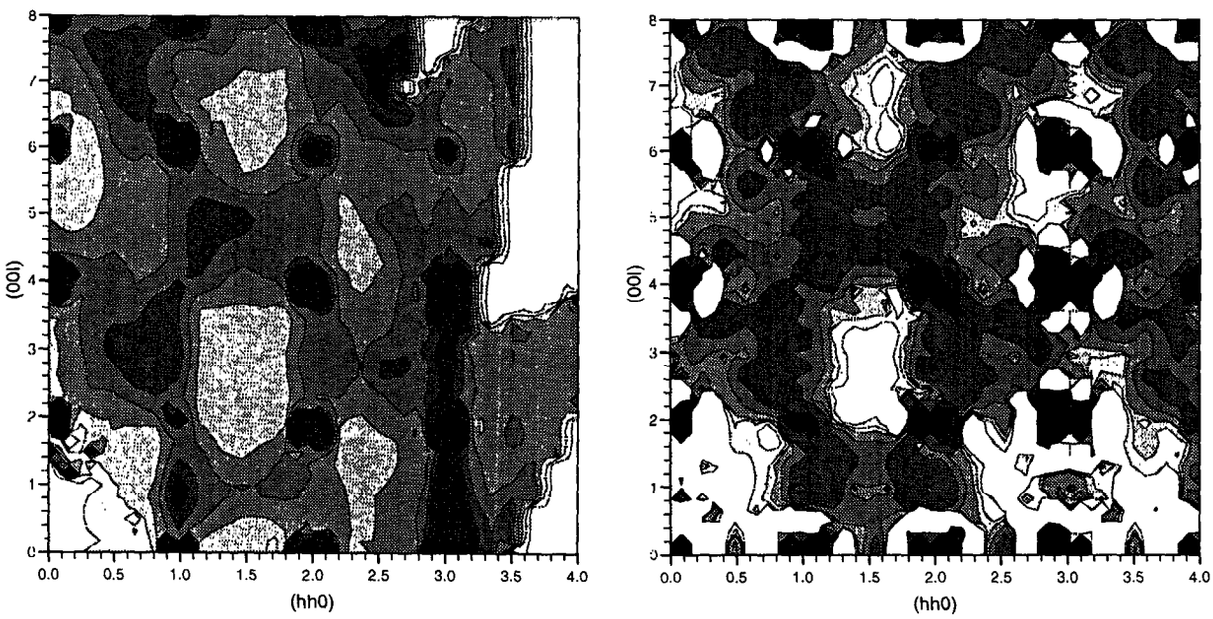


*Figure 6 - Observed (left) and simulated (right) scattering in the (hhl) plane of Ice Ih at 20 K.*

## Phase transitions

The study of phase transitions can be carried out in two ways using time-of-flight Laue diffraction. The first is the conventional manner in which full data sets are collected under each set of physical conditions, from which full refinements can yield the significant changes. This is most convenient for high symmetry systems if a single crystal sample is used, as then the amount of data comprising a more or less complete data set can be minimised. The alternative is to take advantage of the fact that frequently a phase transition can be characterised by the changes in a small subset of reflections - in this case the use of relevant $\Delta(F)/\Delta(\text{parameter})$ methods (Wilson, 1993c) on this subset can yield sufficient information. Ultimately, for the time-of-flight Laue method, the aim is to reduce the amount of data collected to a single histogram, with optimisation of the sample orientation to maximise the amount of unique information available in this single shot. In this way the experimental set-up is the most convenient for the alteration of sample environment parameters as the sample and detector can remain completely stationary throughout the entire experiment.

### *(i) Single histogram dynamic scanning of the simulated dehydration of cytosine monohydrate*

Single crystals of the nucleic acid base cytosine monohydrate ($C_4H_5N_3O_2.H_2O$) undergo an unusual dehydration reaction in which the water of crystallisation is lost while leaving the crystal structure essentially unaltered. The dehydration reaction occurs over a period of some 50 hours at 40°C, and thus "real-time" crystallographic monitoring of the reaction would require data collection periods of the order of 1-2 hours. This means there would be time for only histogram snapshot at each set of conditions (in this case elapsed time). In this respect time-of-flight Laue diffraction has a major advantage in that the group of reflections measured in a single shot are measured at genuinely the same time and under the same conditions - the usual scanning restriction that conditions change as a set of scans are performed does not affect this type of measurement.

The unit cell of this material is moderately complex, and more importantly in the context of extracting useful structural information from limited data, is of low symmetry. The cell is monoclinic, $P2_1/c$, $a = 7.78$, $b = 9.82$, $c = 7.67$ Å, $\beta = 99.6°$, and there are some 656 reflections accessible to a $d_{min}$ of 1.0 Å.

This system is thus ideal for an investigation of the possibilities for single histogram dynamic scanning in time-of-flight Laue diffraction as the end points of the refinement will be well fixed. The general strategy is to perform full structural refinements on the end members of the reaction and use these to fix appropriate parameters within the necessarily limited refinements from the single histogram data. In an ideal case the experiment can also be designed to focus on a histogram in which the structure factor changes throughout the transition are maximised, that is the optimal $\Delta F$-$\Delta(\text{parameter})$ path can be exploited. Thus it might be possible to focus on rather subtle changes in reaction path, reaction rate etc, given this optimal set of $\Delta F$ values.

To date only a simulated experiment has been performed, to test the principle. Structure factor sets were generated for various $H_2O$ occupancies in the range 1.0

(monohydrate) to 0.0 (fully dehydrated). The generated structure factors were allocated quasi-random errors based on their magnitudes (not at this stage on intensity statistics) and extinction was assumed not to be present. For each of the six occupancy levels generated, there were some 605 reflections in the full data set, with some 83 of these in the single histogram selected for the limited data set. This histogram was selected essentially at random - it was not chosen in this case to optimally reflect the expected structure factor changes during the reaction.

The structure chosen as the starting point was that reported by McLure and Craven (1973) for cytosine monohydrate. It was assumed that any cell contraction during the dehydration reaction would be isotropic and that the only significant changes in the structure would be to the scale factor and the occupancies of the water molecule. Variations in the scale factor were taken account of in the simulated data, and all other parameters were fixed at their values from the monohydrate structure. In the refinements, therefore, there were three parameters related to the dehydration reaction, the occupancies of the oxygen and two hydrogen atoms. All refinements commenced from full $H_2O$ occupancy and converged in five or fewer refinement cycles. The data from the refinements are summarised in Table 2 and Figure 7.

**Table 2**

Full and single histogram refinements of the simulated dehydration of cytosine monohydrate

| | Full data | | | Limited data | | |
|---|---|---|---|---|---|---|
| | *O1 occ* | *H1 occ* | *H2 occ* | *O1 occ* | *H1 occ* | *H2 occ* |
| *OCC=1.0* | 0.999(2) | 1.001(4) | 1.006(4) | 0.999(4) | 1.021(12) | 0.978(11) |
| *OCC=0.8* | 0.801(2) | 0.811(4) | 0.805(4) | 0.779(5) | 0.811(8) | 0.828(9) |
| *OCC=0.6* | 0.605(2) | 0.606(4) | 0.616(4) | 0.589(5) | 0.585(9) | 0.623(9) |
| *OCC=0.4* | 0.406(2) | 0.412(4) | 0.398(4) | 0.387(5) | 0.404(8) | 0.414(8) |
| *OCC=0.2* | 0.208(2) | 0.224(4) | 0.196(4) | 0.196(5) | 0.182(8) | 0.204(8) |
| *OCC=0.0* | 0.001(2) | -0.005(4) | -0.003(4) | 0.007(4) | -0.002(8) | 0.015(7) |

It can be seen from these that the results from the limited data show great promise. In spite of necessarily reduced precision, the values obtained for the occupancies are in good agreement with those from the full data refinements. This illustrates that it is in fact possible to obtain useful structural information from single histogram 'dynamic' scanning measurements from single crystals on a time-of-flight Laue instrument. While the precision of such dynamic refinements will necessarily be limited, as a consequence of the limited data accessed in a single shot, substantive information can be obtained, yielding important transitory structural information. Further investigations are in progress on this system, including optimising the $\Delta F$-$\Delta$(parameter) path and further refinements in which the temperature factors and positional parameters are perturbed (Wilson, 1993c).

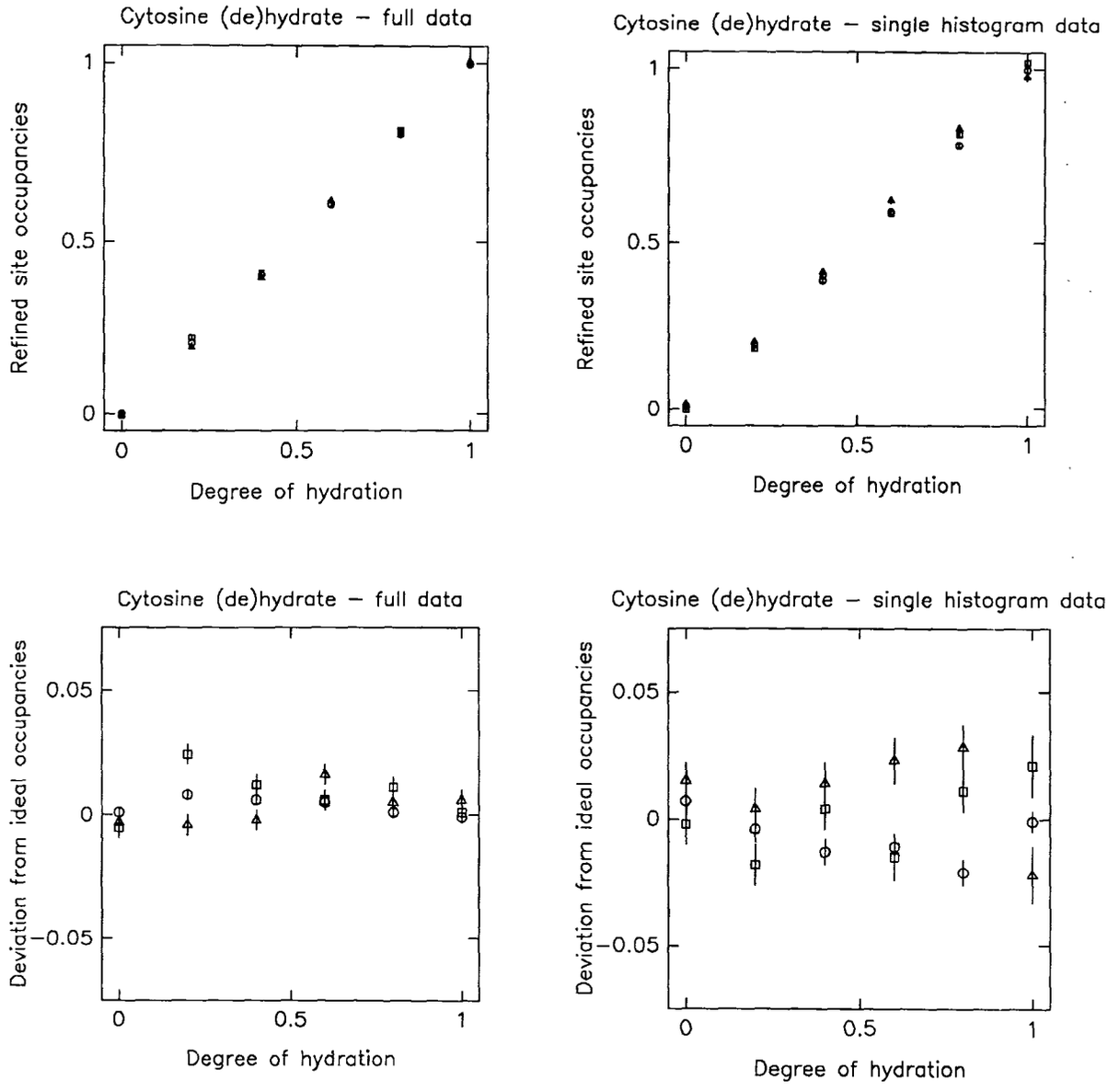


*Figure 7 - Dehydration of cytosine monohydrate. (top) Refined site occupancies from full (left) and single histogram (right) data sets. (bottom) The deviations of these occupancies from the ideal values in the full (left) and single histogram (right) data sets. Key: (O) - O7 occ; (□) - H11 occ; (Δ) - H12 occ.*

## Conclusions

It is clear that the time-of-flight Laue technique has useful and often quite original contributions to make in the field of neutron single crystal diffraction. While those applications involving more routine structural refinement remain of general interest and the high Q capability of SXD promises to yield great insight into the basic physics of simple materials, the use of the surveying capability of the technique in either diffuse scattering or the study of phase transitions remains the most exciting area of application.

## References


G Artioli, R Rinaldi, P-F Zanazzi and C C Wilson (1993) *High temperature Fe/Mg partitioning in olivine crystals: ordering reversal above 1000°C.* Nature, submitted.

S Hull and C C Wilson (1992) *The defect structure of anion-excess $(Ca_{1-x}Y_x)F_{2+x}$ with x=0.06.* J Sol State Chem **100** 101-114.

S Hull, M Hoffmann and C C Wilson (1993) *The defect structure of $(Ca,Y)F_{2.06}$ at high temperature.* In preparation

D A Keen, L R Hannan and C C Wilson (1993), work in progress.

J-C Li, V M Nield, D K Ross, R W Whitworth, C C Wilson and D A Keen (1993) *Disorder in $D_2O$ ice Ih studied using pulsed neutron single crystal diffraction.* Phil Mag B, submitted.

R J McLure and B M Craven (1973) *New investigations of cytosine and its monohydrate.* Acta Cryst B**29** 1234-1238.

C C Wilson (1990) *The data analysis of reciprocal space volumes.* in "Neutron Scattering Data Analysis 1990", ed M W Johnson, pp 145-163, IOP Conf Series **107**, Adam Hilger, Bristol.

C C Wilson (1993a) *Understanding the time-of-flight Laue diffraction technique - interpretations and comparisons.* J Appl Cryst, submitted.

C C Wilson (1993b) *A pulsed neutron single crystal diffraction study of the structure of 3-deazauracil.* J Cryst Spect Res, submitted.

C C Wilson (1993c) *Monitoring phase transitions using a single data histogram in neutron time-of-flight Laue diffraction.* J Appl Cryst, in preparation.

C C Wilson (1993d) *Reflection statistics in single crystal diffraction on a pulsed neutron source.* Acta Cryst A, in preparation.

C C Wilson, N S Stewart and D A Keen (1992) *On hydrogen atom positions in 3-deazauracil.* Chem Comm **1992** 1160-1162.

# Performance of the Amorphous Materials Diffractometer "GLAD" at IPNS

A. J. G. Ellison, K. J. Volin, D. L. Price and R. K. Crawford
Argonne National Laboratory, Argonne, IL 60439

ABSTRACT

The Glass, Liquids, and Amorphous Materials Diffractometer (GLAD) at IPNS has now been commissioned and the first scientific measurements have been carried out. Details of the performance of this instrument, including background, calibration, resolution, data rate, data quality, and data reduction and analysis will be discussed.

## I. Introduction

Until recently, neutron diffraction measurements of the structure of disordered materials at pulsed sources were carried out on diffractometers designed essentially for powder diffraction. While much work of high quality was carried out, these instruments fall far short of meeting the requirements for state-of-the-art measurements on disordered systems. Because of this, a few years ago a group of Argonne and university scientists decided to build a new instrument optimized for structural measurements in glasses and liquids at the Intense Pulsed Neutron Source (IPNS). The requirements for this instrument included a large Q range, a nearly continuous range of scattering angles extending to angles as low as possible, and a range of wavelengths extending to ones as short as possible; coupled with the need to maximize intensity while still preserving reasonable Q resolution. These demanding requirements have been met by the design of the Glass, Liquids, and Amorphous Materials Diffractometer (GLAD). This design and various novel features incorporated in the instrument have been described in detail elsewhere.[1-5] Therefore, only a brief description of the instrument is presented below, and the remainder of this article is devoted to discussion of the performance of this instrument.

## II. The GLAD Instrument

Figure 1 presents a top view of GLAD. As shown in the figure, GLAD has two sample positions, an upstream position 9.0 m from the moderator for the highest resolution measurements and a downstream position 10.5 m from the moderator, which provides higher data rates at some sacrifice in resolution. Crossed converging soller collimators focused on the forward detector bank collimate the thermal and epithermal neutrons used by GLAD. With this collimation scheme the sample size does not contribute significantly to the resolution,[6] so samples up to ~2.5 x 2.5 $cm^2$ (1.25 x 1.25 $cm^2$) can be used at the upstream (downstream) position. A series of massive apertures upstream from the soller collimators defines the beam, and provides the primary collimation for those higher-energy neutrons (hundreds of eV and higher) for which the soller collimators become transparent. The last of these massive apertures

* Work supported by U.S. Department of Energy, BES, contract No. W-31-109-ENG-38.

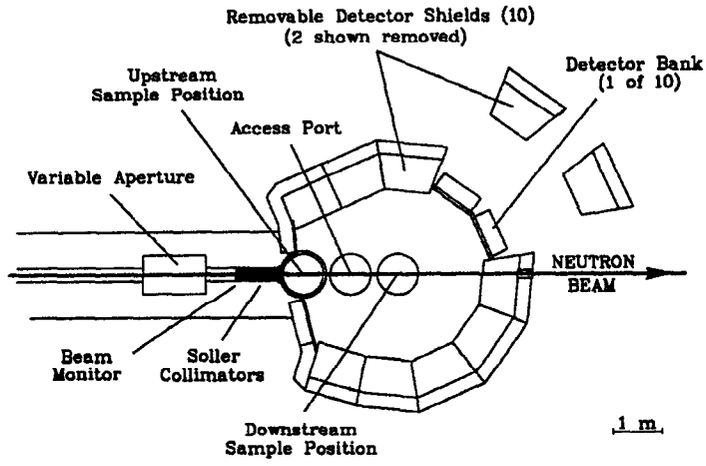


**Figure 1. Top view of the GLAD instrument. Two of the ten detector shields are shown removed to reveal the associated detector banks in their positions just outside the evacuated flight path.**

is adjustable and can be varied to control the beam size to minimize the amount of background when smaller sample sizes are used. The flight path is evacuated and the detectors are located outside this vacuum (Fig. 1), viewing the sample positions through thin aluminum windows.

GLAD uses linear position-sensitive detectors (LPSDs), which permit it to handle high data rates and to cover low scattering angles. GLAD contains 235 cylindrical aluminum-walled $^3$He-proportional-counter LPSDs at the present time; eventually to be expanded to a total of 408. These detectors are mounted in 10 banks (Fig. 1); each bank contains from 38 to 53 LPSDs, depending on the location of the bank in the instrument. Each LPSD has a diameter of 1.27 cm and an active length of 60 cm, and contains 10 atm of $^3$He plus appropriate stopping gases (mostly Ar). Each detector is encoded into 64 segments using charge-division encoding; the resulting full width at half maximum (FWHM) position resolution is currently measured to be ~14 mm. (These detectors and the mounting arrangements are similar to those used earlier on a steady-state small-angle diffractometer at the University of Missouri reactor[7] and on the SAN small-angle diffractometer at the KENS pulsed neutron source,[8] but the encoding and data acquisition electronics for GLAD are quite different from those used in either of these other two instruments.[3]) Segments of the LPSDs located in line with the direct beam have been successfully used to monitor sample transmissions[4] concurrently with the scattered neutron measurements which utilize the remainder of the segments of these same LPSDs.

The currently-installed detectors cover scattering angles from -9° to +18° and +37° to +95° for the upstream sample position and from -17° to +35° and +73° to +150° for the downstream sample position, with the negative sign implying scattering angles measured clockwise from the direct beam (at 0°) when viewed from above as in Fig. 1. Angular coverage is continuous over these ranges except for very small angles and for the small gaps between the detector banks. A beam attenuator, which protects the LPSDs near 0° from overload by the direct beam, obscures the scattering angles $2\theta < 1.7°$ when the upstream sample position is used

and $2\theta < 3.4°$ when the downstream sample position is used. The locations of the detector banks on the two sides of the flight path are not symmetric (Fig. 1), so that the scattering angles not covered on one side of the flight path can be covered on the other.

An experiment on GLAD is started by first setting up a run file which contains information about how LPSD segments are grouped together and how the time-of-flight (TOF) histograms are organized. There are virtually no restrictions on how this is achieved; for example, detector segments may be grouped into Debye-Scherrer cones (preferable for isotropic scattering) and the time binning may be chosen with a channel width which is proportional to the TOF. In addition the run file contains calibration information concerning scattering angles, distances, etc. which are used in the subsequent data analysis. The run files are large (up to ~12 Mbyte), so managing the volume of data generated by GLAD presents some problems. A typical experiment results in several run files generated in a short period of time, so efficient programs have been developed for analyzing the data and compressing it to more manageable sizes. The raw run files are archived on secondary mass storage devices (currently 8-mm tapes holding about 2 Gbytes each) after the first-step analysis.

## III. Resolution

The best experiments performed on GLAD use detector segments binned in common Debye-Scherrer cones with a user-defined width $\Delta\theta$. Most experiments performed to date have been in the downstream sample position using $\Delta\theta$ of 0.6°, corresponding to roughly 2 detector segment widths over a nominal scattered flight path of 1.5 m. In this operational mode instrument resolution is almost entirely geometric. This is illustrated using the FWHM of the strong (111) peak in the powder diffraction pattern of diamond to determine the resolution $\Delta Q/Q$, where the momentum transfer Q is defined as

$$Q = \frac{4\pi\sin\theta}{\lambda} \tag{1}$$

and

$$\frac{\Delta Q}{Q} = \frac{\Delta d}{d} = \Delta\theta\cot\theta \quad , \tag{2}$$

where d is the crystalline d-spacing. The results are plotted in Fig. 2 as a function of the scattering angle $2\theta$ from 2-95°. The line through the data is 0.006 $\cot\theta$, where 0.006 is the average of the ratio $(\Delta Q/Q)/\cot\theta$ for each angle. Essentially identical curves are obtained using FWHM of other Bragg peaks - thus the resolution function is almost entirely geometric. Resolution improves by roughly a factor of two for samples run in the upstream sample position, but is still dominated by geometry.

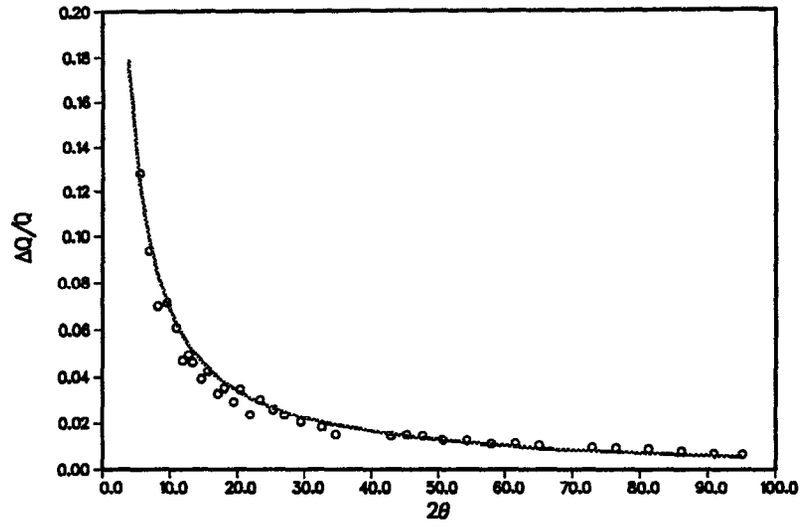


**Figure 2. Resolution of GLAD, measured as the FWHM of the (111) peak in the powder diffraction from diamond.**

The comparatively low resolution at low scattering angles places limits on the angles at which data are used in routine analyses. While some materials have relatively broad features at low Q, in general the best results for vitreous and liquid samples run in the downstream position are obtained when analysis is confined to data collected at scattering angles > 7°. At the same time, for liquids formed from light atoms and for nearly all oxide glasses, Placek corrections become quite large for values of Q corresponding to wavelengths of 1.5-2.5 Å. This places a practical limit upon the lowest reliable Q obtained from a sample in the downstream sample position of 0.2-0.3 $Å^{-1}$, depending upon the wavelength range appropriate for a particular sample. In the upstream sample position, the minimum reliable scattering angle decreases to 4°, and thus the minimum reliable Q decreases to roughly 0.1 $Å^{-1}$. Work underway is expected to improve the spatial resolution of the low-angle detectors to better than the size of a detector segment, in which case the minimum Q in the downstream sample position will improve by at least a factor of two. Even with the present set-up, however, GLAD provides relatively good overlap with the highest Q values obtained on conventional small-angle neutron diffractometers.

## IV. Calibration

At present time-of-flight data is corrected to wavelength using a simple linear relation between t and λ. This is justified empirically in that addition of quadratic or higher-order terms to the equation had a negligible impact on $\chi^2$ for wavelength-calibration data collected on the GLAD prototype.[5] Software is in place for performing wavelength calibrations, and efforts are

underway to automate it. Detector segment positions are currently assumed to be equally spaced along LPSDs, with exactly the same active lengths. Flood patterns collected using a moderated PuBe source show that differences in counting rates from one segment to another - a potential rationale for determining detector segment boundaries - are within the counting error for each segment, as might be expected given the fact that the resolution at any point is almost twice the size of a detector segment. Nevertheless, anticipated changes in the resolution of the low-angle detector banks will necessitate a calibration of detector segment positions. Hardware for measuring detector segment positions is in place and has been tested, and software has been developed to calculate detector segment boundaries using data collected with this hardware. A trial position calibration will be performed this Spring, and will hopefully be fully automated and routinely performed by the end of this year.

## V. Backgrounds

Amorphous materials display an unfortunate tendency to be weak scatterers, compounded in some instances by a tendency to be very efficient absorbers of thermal neutrons as well. In these cases a successful analysis depends strongly on the reproducibility and magnitude of background scattering in the instrument. We have devoted considerable attention to sources of background in GLAD, and over the wavelength range for which GLAD is optimized its background is currently the lowest among diffractometers at IPNS. Moreover we know the sources of the background that remains, and are taking steps this Spring to greatly reduce the contributions of the most prominent of these. We demonstrate the current state of affairs in Fig. 3, a plot of normalized intensity vs. Q for $Li_2Si_2O_5$ glass for data collected at roughly 30°. Natural Li has a 70 barn absorption cross section (1.8 Å), a negative scattering

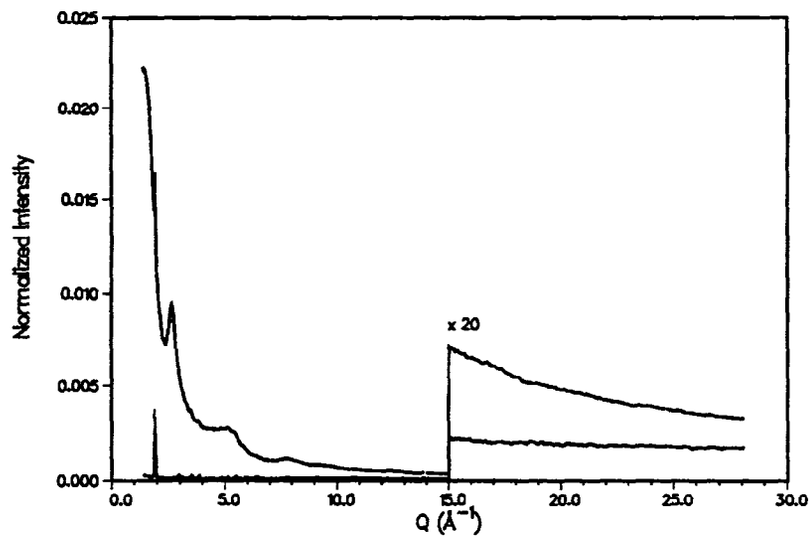


**Figure 3. Normalized scattered intensity for $Li_2Si_2O_5$ glass. The lower curve is the measured background with the sample removed.**

length, and a relatively large incoherent scattering cross-section, and its presence at the level of 22 atom% not only results in significantly attenuated scattering at long wavelengths but also greatly reduces the amplitude in the interference function. As is clear in the figure, even for this "difficult" sample the sample scattering is far greater than the background at all points.

## VI. Data Normalization

Even with low backgrounds, analysis of scattering data in real-space is extremely sensitive to the normalization of the data. Unfortunately, there are no universal criteria for a determining whether or not one has obtained a "good" normalization, except perhaps the success or failure of a real-space representation of structure to replicate the coordination numbers of the various atoms in a known sample. We have adopted an alternative criterion: when a well-characterized sample of known geometry is placed in a beam of known dimensions and flux, and if absorption and multiple scattering corrections are relatively small, then the differential cross-section $d\sigma/d\Omega$ obtained for relatively high-energy neutrons (> 1 eV) should approach the calculated self-scattering (SLF) obtained using the methods described by Placek[9] - in other words, $(d\sigma/d\Omega)/(SLF) \rightarrow 1$ as $Q \rightarrow \infty$. When true, we have correctly accounted for the most important instrument-dependent factors contributing to raw scattering intensity. This criterion is indeed satisfied on GLAD. Figure 4 shows the ratio $(d\sigma/d\Omega)/(SLF)$ for a rod of v-$SiO_2$ collected at scattering angles of roughly 30, 45, 60, and 90°. Data from the various angles all fall on the same curve, and the ratios clearly converge to 1.0 at high Q.

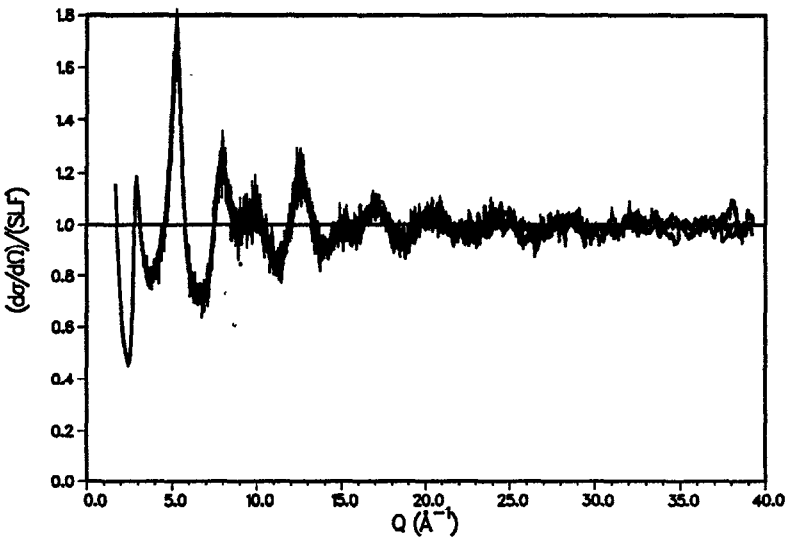


**Figure 4. Ratio of the differential scattering cross-sections measured for v-$SiO_2$ at different scattering angles to the corresponding calculated self-scattering.**

## VII. Example

These results confirm that the data from GLAD meets or exceeds its design specifications, and thus "all" that remains is to develop optimized procedures for instrument operation while leaving enough flexibility to adapt to the needs of a particular experiment. We confine our demonstration of the capabilities of GLAD to a single example, the structure factor of $D_2O$. This is germane because the study of amorphous materials containing light atoms figured prominently in the design criteria for GLAD. Briefly stated, analysis of neutron scattering from materials containing light atoms is plagued by the importance of inelasticity corrections. While the Placek correction is adequate for relatively high energy neutrons scattering from atoms with "fixed" equilibrium positions, it is a comparatively poor approximation when the mass of the atoms in question approaches the mass of the neutron, particularly at high scattering angles. Therefore a premium is placed upon collecting data over as broad a Q-range as possible using the highest energy neutrons collected over the smallest range of scattering angles. Moreover, it must be possible to perform these experiments in the extremely limited amount of time typically allotted to experimenters!

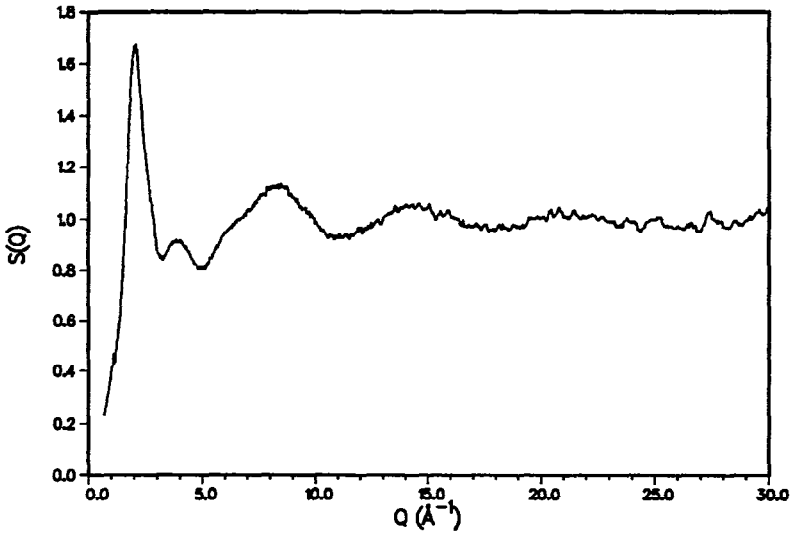


**Figure 5. Structure factor for $D_2O$, based on a measurement range of 8-30° and 0.1-1.0 Å.**

Figure 5 shows the structure factor of $D_2O$ obtained using detector segments from 8-30° over a wavelength range of 0.1 - 1.0 Å. The sample was in a 4 mm x 8 cm vanadium container and was run at ambient temperature for 12 hours in the downstream sample position. Although the wavelength and angle range employed here is very restrictive, the Q range of the resulting structure factor encompasses all major diffraction features in $D_2O$, including the prominent low-Q pre-peak and its much weaker satellite at slightly higher Q, and extends to nearly 30 $Å^{-1}$. When a broader range of scattering angles and/or a larger wavelength range can be employed, the statistics at all points are improved significantly, and the structure factor data can be extended to far higher Q (analyses are routinely performed using data through Q = 40 $Å^{-1}$, and occasionally to Q = 50 $Å^{-1}$).

**Acknowledgments**

The success of GLAD is due in large part to the innovative mechanical design by Bob Kleb and the state-of-the-art data acquisition system designed and developed by Joe Haumann. The instrument was assembled and installed by the IPNS operations team headed by Don Bohringer and Dave Leach, and Merlyn Faber managed the fabrication and installation of the position encoding electronics. Sherman Susman has played a lead role in the development of the ancillary equipment for GLAD. Funding for the construction of GLAD was provided primarily by the Department of Energy through a proposal submitted by a Participating Research Team (PRT) headed by Simon Moss at the University of Houston.

**References**

1. R. K. Crawford, D. L. Price, J. R. Haumann, R. Kleb, D. G. Montague, J. M. Carpenter, S. Susman, and R. J. Dejus. *Advanced Neutron Sources 1988*, Proceedings of the 10th Meeting of the International Collaboration on Advanced Neutron Sources (ICANS X), held at the Los Alamos National Laboratory, Oct. 3-7, 1988. Institute of Physics Conference Series Number 97, IOP Publishing Ltd, New York. pp 419-426 (1989).
2. R. K. Crawford, J. M. Carpenter, R. Dejus, J. R. Haumann, R. Kleb, D. G. Montague, D. L. Price, and S. Susman. Proceedings of the 11th Meeting of the International Collaboration on Advanced Neutron Sources (ICANS XI), held at the National Laboratory for High Energy Physics, Tsukuba, Japan, October 22-26, 1990. KEK Report 90-25. pp. 820-829 (1991).
3. R. K. Crawford and J. R. Haumann. *IEEE Trans. Nucl. Sci.* **NS-37**, 72-81 (1990).
4. D. G. Montague, J. M. Carpenter, R. K. Crawford, R. Dejus, D. L. Price, and S. Susman. Proceedings of the 11th Meeting of the International Collaboration on Advanced Neutron Sources (ICANS XI), held at the National Laboratory for High Energy Physics, Tsukuba, Japan, October 22-26, 1990. KEK Report 90-25. pp. 830-839 (1991).
5. R. K. Crawford, J. R. Haumann, and G. E. Ostrowski. Proceedings of the 11th Meeting of the International Collaboration on Advanced Neutron Sources (ICANS XI), held at the National Laboratory for High Energy Physics, Tsukuba, Japan, October 22-26, 1990. KEK Report 90-25. pp. 943-956 (1991).
6. A. C. Nunes. *Nucl. Instrum. Methods* **119**, 291-293 (1974).
7. R. Berliner, D. F. R. Mildner, O. A. Pringle, and J. S. King. *Nucl. Instrum. Methods* **185**, 481-495 (1981).
8. Y. Ishikawa, M. Furusaka, N. Niimura, M. Arai, and K. Hasegawa. *J. Appl. Cryst.* **19**, 229-242 (1986).
9. G. Placek, The Scattering of Neutrons by Systems of Heavy Nuclei, *Phys. Rev.* **86** 377-388 (1952).

# SPIDA : A Special Intense Diffractometer For Amorphous Materials

A.C.HANNON, A. K. SOPER, R. J. NEWPORT*, and W. S. HOWELLS.

*ISIS Facility, Rutherford Appleton Laboratory, Chilton, Didcot, Oxon OX11 0QX, UK*
**Physics Laboratory, The University, Canterbury, Kent CT2 7NR, UK*

A design concept is presented for a special intense neutron time-of-flight diffractometer for amorphous materials (SPIDA). This is a new-generation diffractometer for the study of the structure of amorphous and liquid systems requiring special environments and for a wide range of novel amorphous materials.

## 1. Introduction

It is now becoming clear that time-of-flight diffractometers for non-crystalline samples may be divided into two distinct and complementary types. The first type involves a very open design with a large number of detectors at low scattering angle $2\theta$. The designs of two such instruments, one at the ISIS source (SANDALS[1]) and one at the IPNS source (GLAD[2]), were reported at the ICANS-X conference in 1988, and both of these have now been constructed and are operating successfully. This type of diffractometer achieves a high count rate by the use of a large number of detectors, and the effects of inelasticity are minimised by the use of low values of $2\theta$. The study of the structure of non-crystalline samples of low atomic mass at ISIS has been significantly advanced by SANDALS since its start of operation in 1989. However, the necessary lack of secondary collimation (ie. shielding around the secondary flight path from sample to detector) in this first type of instrument has the consequence that whilst excellent results may be obtained for samples under ambient conditions, these instruments are not at all well suited to experiments which make use of extensive sample environment equipment due to the very high background signal always associated with an open design. Furthermore the lack of a large angular range is a severe disadvantage in the study of novel amorphous materials, firstly due to the lack of detectors with a high Q-resolution (where momentum transfer $Q=4\pi\sin\theta/\lambda$) and secondly due to the inability to perform anisotropy studies.

The second type of diffractometer involves a significant level of secondary collimation in the detector tank, and the detectors cover a very wide range of scattering angle. The LAD diffractometer[3], which has been essentially unchanged since it was constructed for use at the relatively low intensity Harwell Linac source[4], currently performs this role at ISIS. Experiments may be performed successfully on samples requiring a large amount of sample

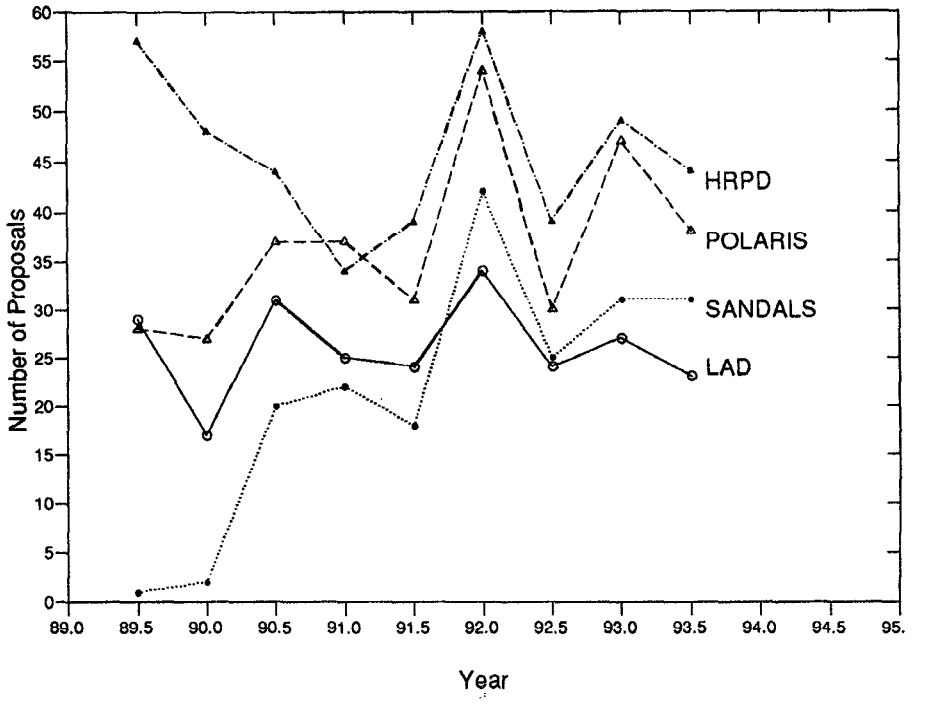


**Figure 1. The number of ISIS diffractometer proposals since 1989.**

environment equipment due to the high level of secondary collimation. The backward angle detectors in such an instrument have good Q-resolution, which can be of great importance in the characterisation of novel amorphous materials (in practice these may be crystalline to some extent), and also of use in the study of molten systems.

As an illustration of the demand for a non-crystalline diffractometer with good secondary collimation figure 1 shows the demand for diffractometer use at ISIS since the first receipt of proposals to use SANDALS. The steady demand for the present LAD diffractometer has been unaffected by the arrival of SANDALS, demonstrating that the two types of non-crystalline diffractometer are truly complementary and that there is a clear scientific need for diffractometers of the second type discussed above.

## 2. Design Criteria

For a diffractometer of the type discussed here the foremost design criterion concerns the secondary collimation; this must be designed so that each detector element views the whole of the illuminated volume of the sample, but as little of the surrounding sample environment equipment as possible so as to minimise background counts. The detector arrangement should then be designed so as to achieve the maximum intensity and the maximum range in both Q and $2\theta$ without compromising the secondary collimation requirements.

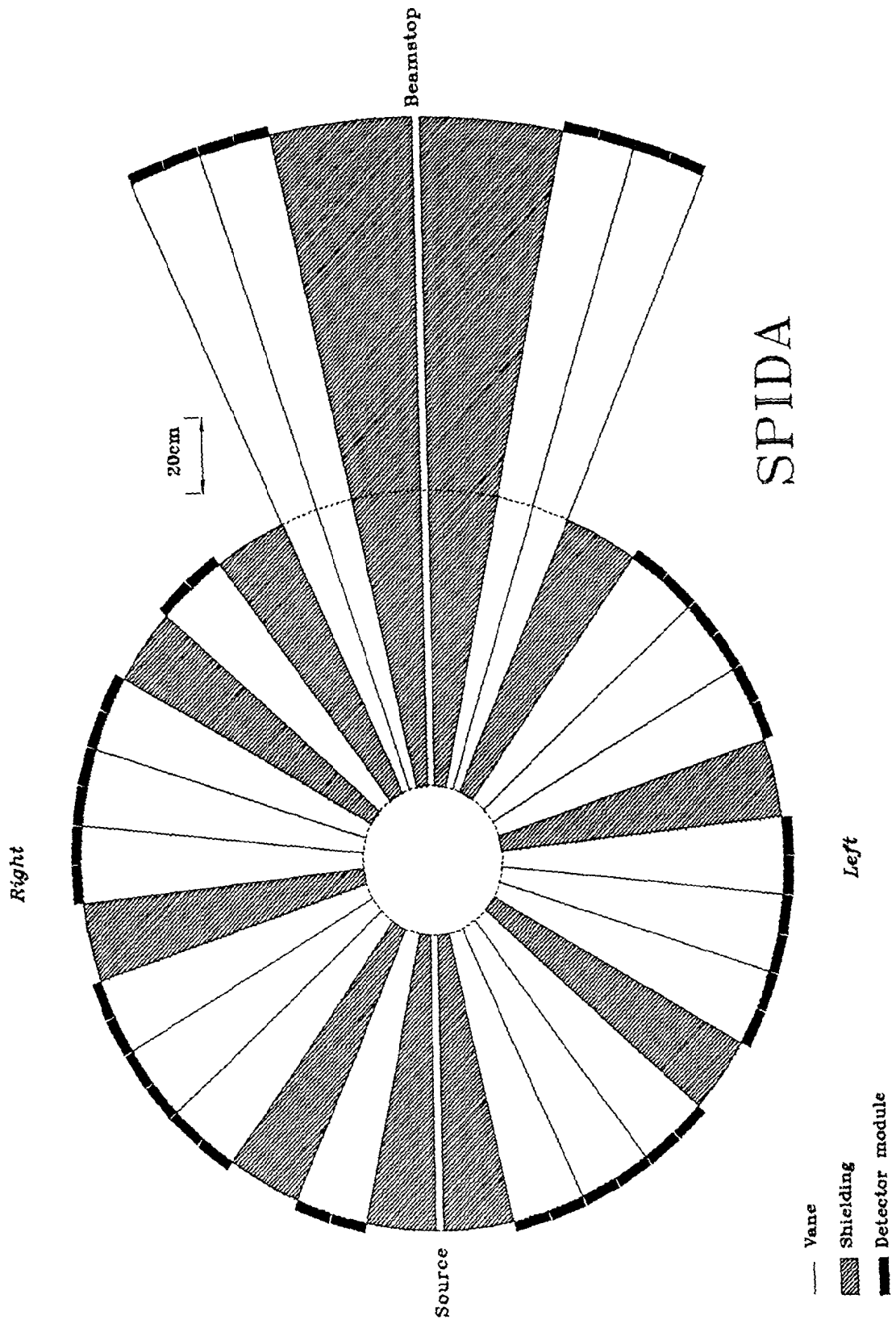


Figure 2. A plan view of the SPIDA instrument.

## 3. Specification

The SPIDA instrument, as shown in figure 2 and specified in tables 1 and 2, has been designed to meet the scientific requirements described above in section 1 and the design criteria given in section 2.

| | |
|---|---|
| Moderator: | methane 110K |
| Incident flight path: | 10m |
| Scattered flight path: | 1m |
| Scattered flight path (low angle): | 2m |
| Beam size: | rectangular 15mm wide and 40mm high |
| Beam: | S7 |
| Detectors: | ZnS scintillator modules 10cm wide and 30cm high |
| Sample tank: | standard ISIS 'Tomkinson hole' |

**Table 1. Some design specifications for SPIDA**

Howells[5] has shown that a cooled moderator is to be preferred for non-crystalline time-of-flight diffraction since this gives rise to inelasticity corrections which are better behaved than for an ambient moderator. Hence SPIDA is designed for use on the 110K liquid methane moderator at ISIS.

At all but the lowest and the highest scattering angles the SPIDA design involves having one detector module situated in the horizontal plane with two more situated above and below. In this way the detector solid angle, and hence the count rate, is maximised.

Theoretically the minimum Q which can be achieved by the low angle detector bank is 0.19Å$^{-1}$. However, in practice the lowest reliable Q is determined not by this theoretical limit but by the point at which the data become unreliable due to strongly rising background contributions at low Q. For this reason it is necessary for the low angle detector banks to have a very low intrinsic background level. The secondary flight path of the low angle detectors is longer than that of the other detectors firstly to facilitate a high level of secondary collimation to reduce backgrounds and secondly to improve resolution.

| *right* | *left* |
|---|---|
| 12°-24° (2m) | 12°-24° (2m) |
| 36°-48° | 36°-72° |
| 60°-96° | 84°-120° |
| 108°-144° | 132°-168° |
| 156°-168° | |

**Table 2. The range of scattering angle 2θ covered by the detector banks**

The detector arrangement is asymmetric in order to achieve a wide and continuous angular coverage, without compromising the secondary collimation requirements. A notable application of this arrangement is in the study of anisotropy in planar samples in which case a wide range of relative orientations between scattering vector **Q** and sample can be achieved simultaneously[6].

Soper[1,7] has described how the intensity of diffractometers may be compared by use of the C-number, defined to be the count rate per inverse Ångstrom per unit volume of standard scatterer (usually vanadium);

C-number = neutrons /second /$Å^{-1}$ /$cm^3$ of vanadium (1)

Figure 3 shows the measured C-number of the LAD diffractometer together with calculations of the C-number for a completed SANDALS and for the SPIDA design, based on data from the present SANDALS. For comparison note that the D4B diffractometer at the ILL reactor has C-number=53 n/sec/$Å^{-1}$/$cm^3$V at a wavelength of 0.7Å. Clearly the SPIDA design presented here is capable of a very good count rate, compatible with its secondary collimation requirements.

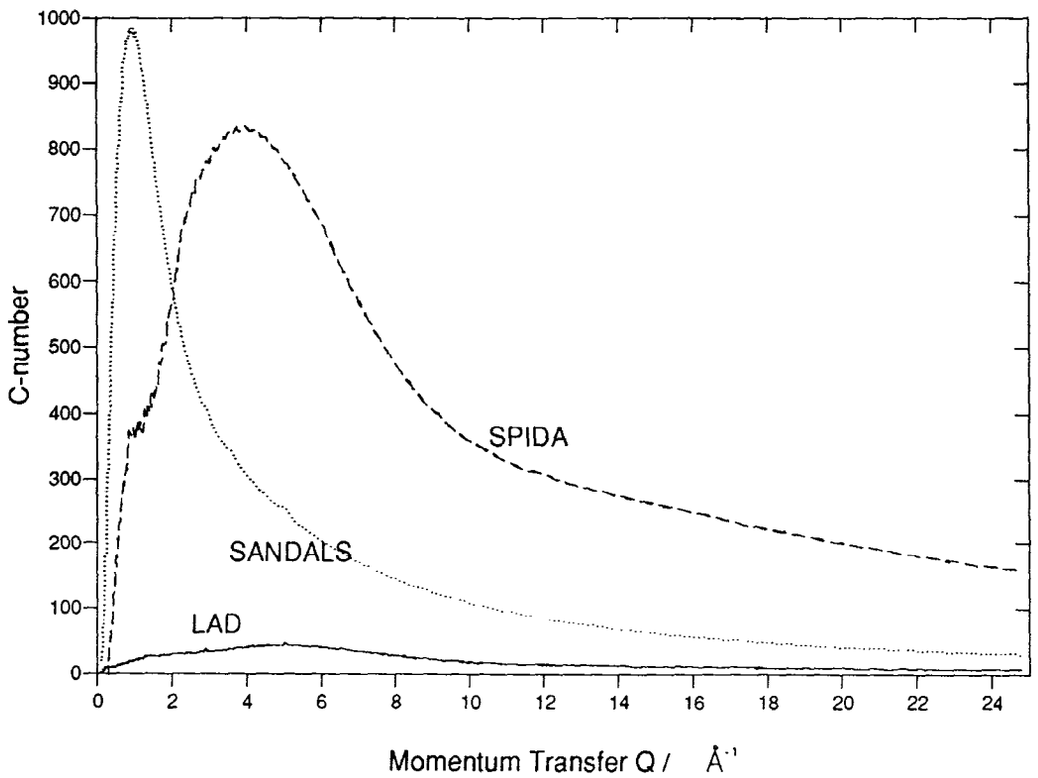


**Figure 3. The C-number for SPIDA (dashed line), for a completed SANDALS (dotted line) and for LAD (continuous line).**

## 4. Conclusions

A design concept for a new-generation non-crystalline time-of-flight diffractometer with good secondary collimation has been presented and shown to be able to produce a high count rate. Such an instrument is well-suited to the study of novel amorphous materials and liquid systems in high background sample environment conditions which continue to be of major scientific importance, and also to anisotropy studies on oriented samples.

## References


[1] A.K.Soper, in 'Advanced Neutron Sources 1988' ed. D.K.Hyer, IOP Conf. Series **97**(1989)353.

[2] R.K.Crawford, D.L.Price, J.R.Haumann, R.Kleb, D.G.Montague, J.M.Carpenter, S.Susman and R.J.Dejus, in 'Advanced Neutron Sources 1988' ed. D.K.Hyer, IOP Conf. Series **97**(1989)427.

[3] W.S.Howells, 'A Diffractometer for Liquid and Amorphous Materials at the SNS', RAL Report RAL-80-017 (1980).

[4] C.G.Windsor and R.N.Sinclair, Phys. Bull. **33**(1982)290.

[5] W.S.Howells, Nucl. Instr. and Meth. **223**(1984)141.

[6] G.R.Mitchell, F.J.Davis, R.Cywinski and A.C.Hannon, Polymer Commun. **30**(1989)98.

[7] A.K.Soper, W.S.Howells and A.C.Hannon, 'ATLAS - Analysis of Time-of-Flight Diffraction Data from Liquid and Amorphous Samples', 1989, Rutherford Appleton Laboratory Report, RAL-89-046.

# Engin: An Engineering Strain Scanner at the ISIS Facility

M W Johnson[1], L Edwards[2], H G Priesmeyer[3], F Rustichelli[4], P J Withers[5] & J S Wright[1]

1: Rutherford Appleton Laboratory, Chilton,Didcot,Oxon OX11 0QX, UK.
2: Faculty of Technology, The Open University, Milton Keynes, MK7 6AA, UK
3: Universität Kiel c/o GKSS Research Centre, POB 1160, D-2054 Geesthacht, Germany
4: Instituto di Fisica Medici, Universita degli Studi, Via Ranieri- Monte d'Ago, 60131 Ancona, Italy
5: Dept. of Mat. Sci. & Metallurgy, University of Cambridge, Pembroke St., Cambridge CB2 3QZ, UK

*Introduction*

Under an EC initiative (the Brite EuRam programme) funding has been made available to develop the measurement of internal stress using the time-of-flight neutron diffraction technique. The project, which has the title 'PREMIS' (PREcise Measurement of Internal Stress) is being jointly undertaken by researchers from Germany (Kiel), Italy (Ancona) and the UK (Cambridge, Open University and RAL). While the technique of neutron strain measurement has been developed considerably since its inception in 1980 [1], this has largely been on reactor neutron sources. The use of the time-of-flight method offers some potential advantages, but requires development to realise these advantages.

The PREMIS project includes the construction of a dedicated strain measurement instrument ENGIN, incorporating for the first time the use of radial collimators to achieve a sampling volume < 2 mm, and a 2-D array of detectors to shorten data acquisition times and improve strain sensitivity. In addition, two 90° scattering angles will be used to enable the simultaneous measurement of strain in two perpendicular directions. The primary advantages of a dedicated facility will be:

- reduced setting up time
- precision sample positioning
- an optimised detector array offering efficient data collection
- the simultaneous measurement of strain in orthogonal directions.

With pulsed sources, a white incident spectra is used with the result that the entire diffraction pattern from a single volume element within the sample is measured simultaneously. By measuring the entire diffraction pattern, a number of major advantages are obtained:

- the strain in both phases of a composite material may be measured simultaneously
- anisotropic sample behaviour can be identified, quantified and, if necessary, allowed for

- the presence of texture can be determined
- the lattice parameter (and hence the strain) may be determined to a greater precision.

The initial aim of the programme is to build a dedicated strain scanner together with its ancillary equipment (furnaces, stress rig etc.) and analysis software. The final aim of the programme is to use this equipment to develop the technique in a number of key areas:

- determination of full stress tensors
- the stroboscopic study of thermally cycling material
- the study of fatigue cracks

The economic justification for such a programme has been given elsewhere [2], and this paper will concentrate on the technical aspects of the instrument design.

*Instrument Design Criteria*

These may be simply listed:

1. To measure internal strain to better than 50 microstrain.
2. To make this measurement on a gauge volume which may have any dimension 2 mm or less.
3. The gauge volume may be up to 50 mm below the surface.
4. The gauge volume should be positioned with an accuracy of 0.01 mm for specimens of up to 100 kg in weight. Heavier specimens (up to 200 kg) should be accommodated with reduced precision.
5. Small samples should be able to be temperature controlled to $\pm$ 5K in a range up to 1000c.

*Instrument Design*

The traditional collimation design of neutron strain measuring instruments on reactor sources is shown in Figure 1a [3]. A parallel, monochromatic neutron beam is masked down to the size required (typically 1-5 mm) and similar masks on the outgoing collimation define the gauge volume. This technique is extremely effective for measuring the d-spacing of one reflection chosen such that $2\theta \sim 90°$.

Such a design may be copied for use on time-of-flight instruments, but since the flux over a given wavelength range is generally lower, individual neutron peaks take longer

to record. The white beam, time-of-flight technique is able to record diffraction patterns at any scattering angle, and thus the intensity of time-of-flight diffraction peaks can be improved if the collimation geometry shown in Figure 1b can be realised. This uses a radial collimator to define the gauge volume and allows the solid angle of the detectors to be increased by a factor of ~ 50.

The theory of such collimators is straightforward. Assuming the vanes of the collimator to be black, the ray diagram for a single element of the collimator is shown in Figure 2. Calculation of the solid angle subtended by the detector for each point on the incident neutron beam (e - g) shows that the gauge volume is defined along the beam direction by a triangular response function with

$$FWHMH = jl/(L-l)$$

In the other orthogonal directions the shape of the gauge volume is determined by the incident beam.

In the PREMIS instrument it has been decided that the gauge distance along the beam direction should be 1.41 mm (FWHMH), which corresponds to a rectangular distribution with a width of 2 mm. It was further decided that the radial collimator should start 150 mm from the gauge volume. This distance is obviously a compromise: making it larger makes the instrument easier to use, but makes the collimator vanes closer together (for a given gauge size). As the collimator vanes become closer, the radial collimator loses efficiency (from its mark/space ratio) and becomes progressively prone to manufacturing error.

The collimator design used in ENGIN is in fact an extension of the parallel 'Rutherford Collimators' that have been used for many years. They are constructed from mylar film coated with gadolinium-oxide loaded paint and are manufactured by L&H Designs Ltd. Gloucester, GL3 4AA,UK.

Detectors will be located at the rear of the radial collimator, and occupy a solid angle of 0.125 sr. They will consist of 46 vertical, 5 x 300 mm strips of Li-loaded scintillator, each directly viewed by two photomultipliers. The width of the detectors is, coincidentally similar to that of the spacing of the large end of the collimator. This is purely a coincidence: the dimension of the collimator is chosen to define the gauge volume, the width of the detector is determined by the $\Delta d/d$ resolution required. This resolution is largely dictated by the primary flight path (15m), and the detector width has been chosen to match the beam divergences in the incident and diffracted beam.

The instrument will also include a large XYZω translator, to enable the sample to be accurately positioned in the beam. A diagram of the translator is shown in Figure 3, and a plan view of the instrument in Figure 4. Also shown in the plan view of the instrument are the 2 theodolites which are rigidly mounted and aligned to intersect on the axis of the ω-rotation.

In addition, a glass walled furnace is being constructed to enable precisely positioned components to be thermally controlled, thus permitting the in-situ study of thermal relief procedures or thermal cycling effects. Design criteria for this device include a low thermal inertia to provide quick response times and temperature control allowing for well-defined heating and cooling conditions up to 1000°C as well as synchronisation of the temperature in neutron-stroboscopic thermal-cycling studies.

*Results from an ENGIN Prototype*

The instrument described above is the instrument that will be installed between June - December 1993. In advance of this construction programme some results have been obtained using a similar (but smaller) collimator, also positioned on the TEST beam at ISIS.

The aims of these tests were to establish that a radial collimator of this type could be successfully constructed and to measure the gauge volume defined by the radial collimator. The prototype radial collimator contained 20 vanes, was 600 mm long and had dimensions of 150 x 117 mm at the detector end which was 750 mm from the sample. To achieve the required gauge volume (1.4 mm FWHMH) at a working distance of 150 mm from the sample, the mylar sheets were 1.12 mm apart at the front of the collimator. To investigate the gauge volume definition achieved by the collimator, a nickel rod of 2 mm diameter was scanned along the incident neutron beam (i.e. across the collimator's field of view) and the intensity of the (111) reflection plotted as a function of position (see Figure 5). The width of this distribution is the convolution of the viewing window of the collimator and the specimen itself. It is straightforward to show that the second moment of the observed convolution ($\sigma_0$) is related to those of its constituent functions by:

$$\sigma_0^2 = \sigma_g^2 + \sigma_r^2$$

The observed $\sigma_0$ = 0.832 mm, and since $\sigma_r$ = 0.5 mm the derived value of $\sigma_g$ for the gauge volume is 0.66 mm, in close agreement with that expected (0.58) for a triangular distribution with FWHMH = 1.4 mm.

The experiments with the prototype also enabled us to evaluate the resolution and counting times that would be required in the full scale instrument. Figure 6 shows a typical spectrum recorded for a steel sample in 10 minutes. Extrapolation to the larger, ENGIN detector shows that such patterns will be recorded in 3 minutes with a similar $\Delta d/d$ resolution of $1.4 \times 10^{-4}$.

*References*


1. Allen A J, Andreani C, Hutchings M T, & Windsor C G (1981) 'Measurement of internal stress within bulk materials using neutron diffraction', NDT International, October, pp249-54.
2. BRITE-EURAM II proposal #5129, submitted to CEC in March 1992.
3. Hutchings M T, 'Neutron diffraction measurement of residual stress fields: overview and points for discussion' pp 3-18 in ' Measurement of Residual and Applied Stress Using Neutron Diffraction' Eds. M T Hutchings & A D Krawitz, Kluwer Academic Pub. , NATO ASI Series Vol.216 (1992)

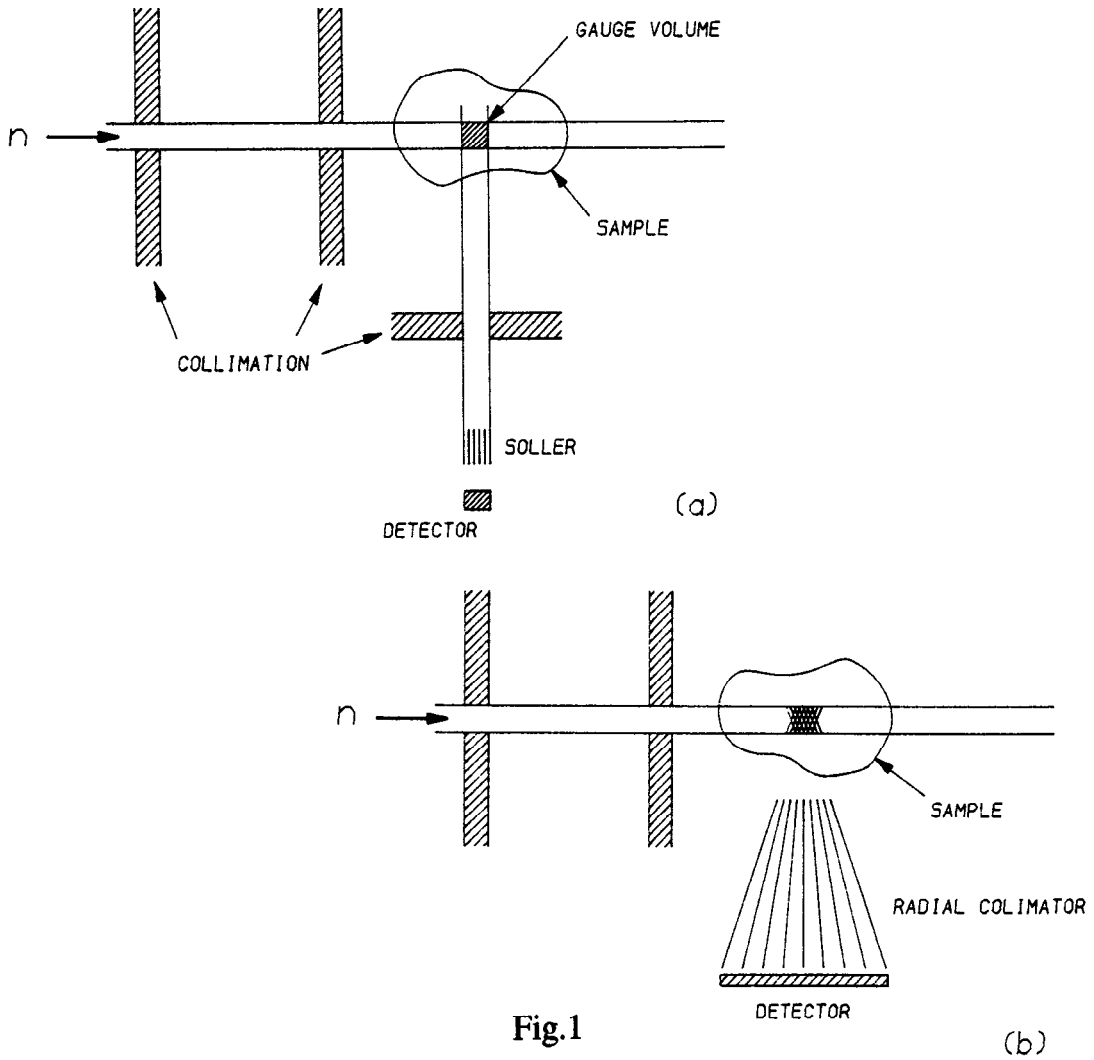
GAUGE VOLUME
n
SAMPLE
COLLIMATION
SOLLER
DETECTOR
(a)
n
SAMPLE
RADIAL COLIMATOR
DETECTOR
(b)

Fig.1

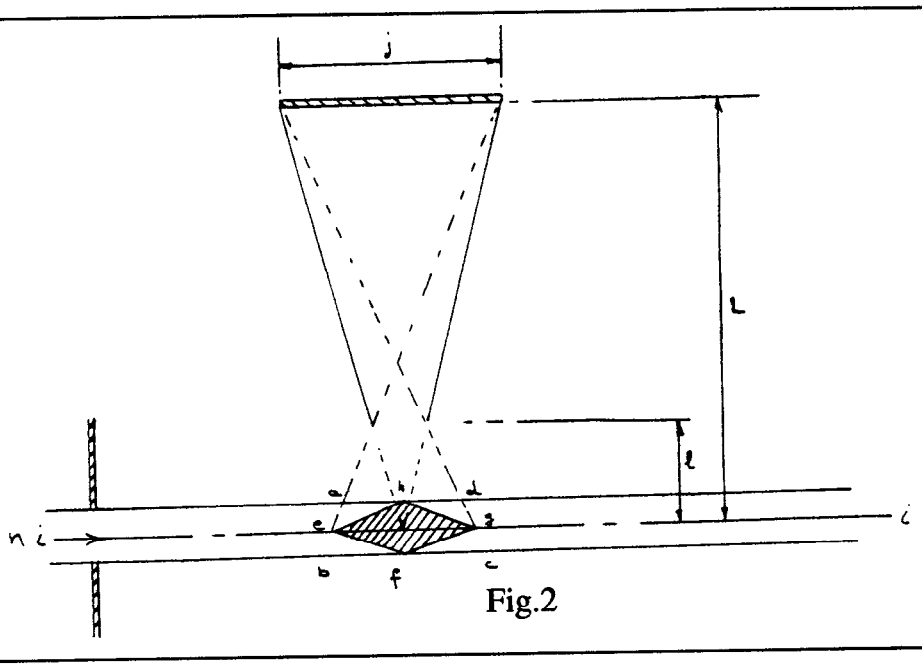
j
L
l
n i
i
a
b
c
d
e
f
g
h

Fig.2

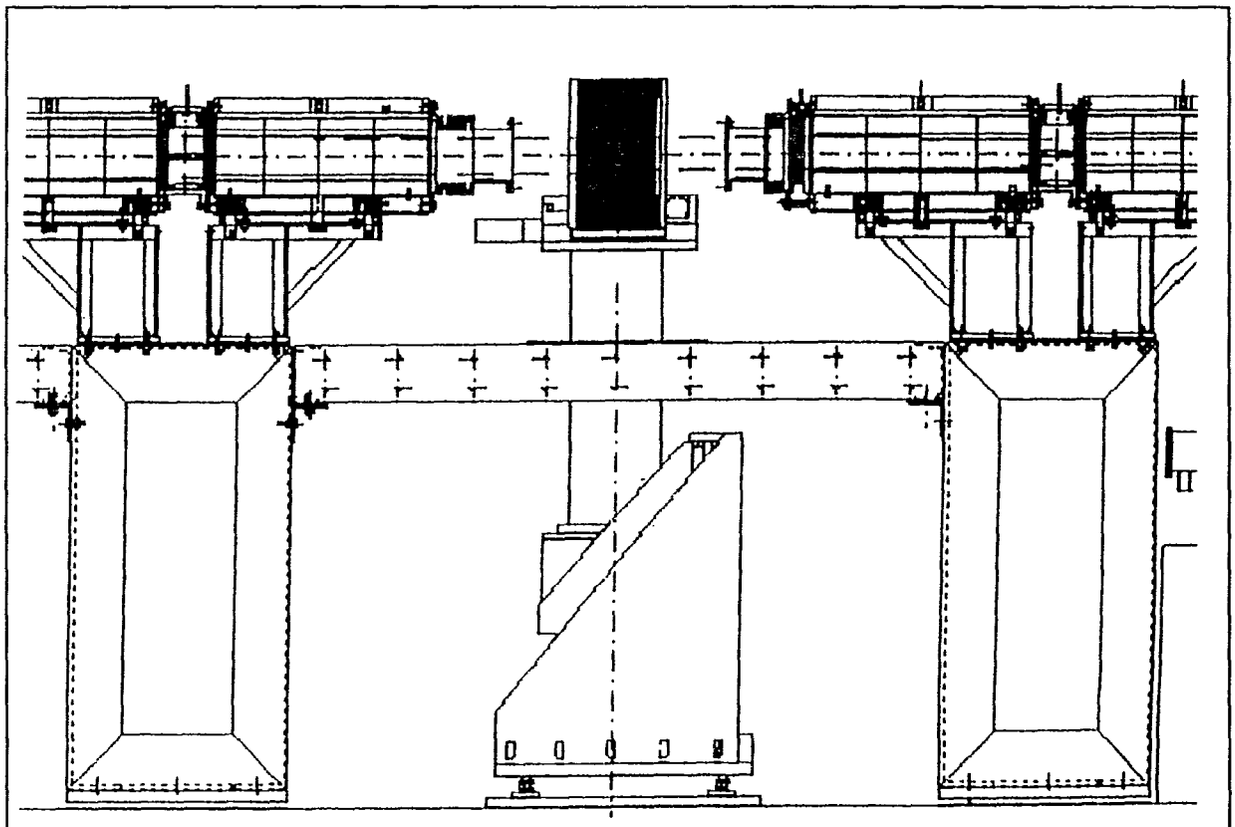

Fig.3

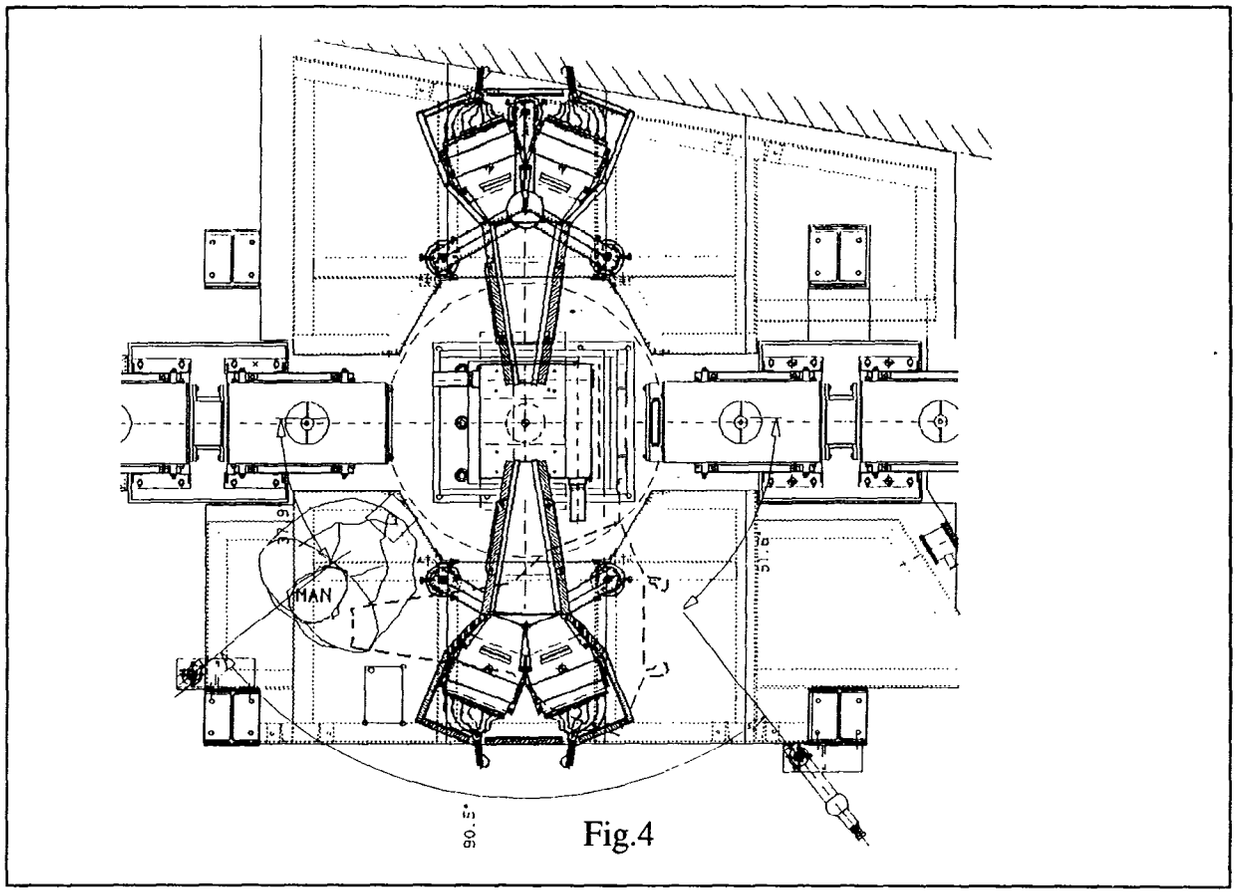


Fig.4

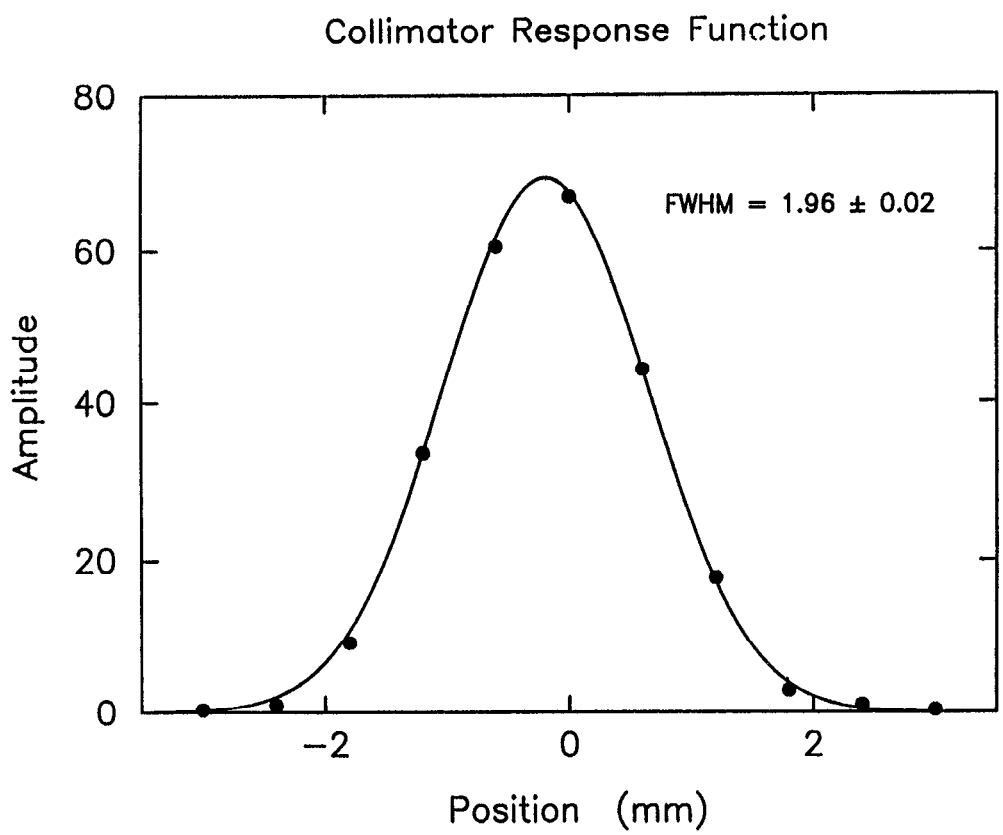
Collimator Response Function
FWHM = 1.96 ± 0.02
Amplitude
80
60
40
20
0
−2
0
2
Position (mm)

Fig. 5

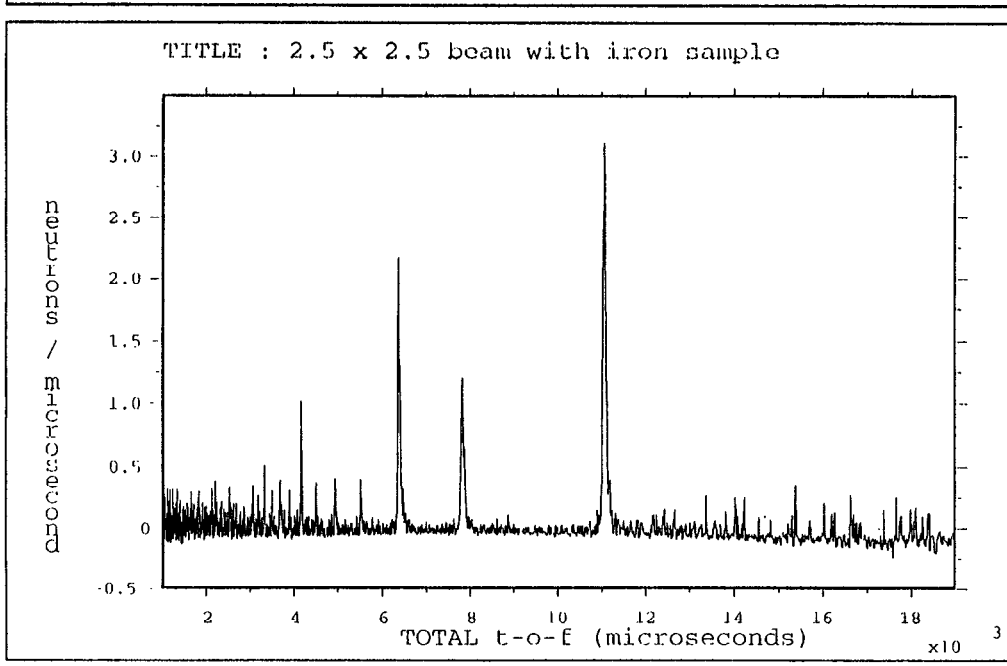
INSTRUMENT: TEB
USER: JSW
RUN NUMBER: 2910
RUN START TIME: 19-SEP-1992 09:50
SPECTRUM : 20
PLOT DATE: Tue 29-SEP-1992 08:36
NO GROUPING OF BINS
LOCATION: TEB$DUA0:[TEBMGR.DATA]TEB02909.RAW
TITLE : 2.5 x 2.5 beam with iron sample
neutrons / microsecond
3.0
2.5
2.0
1.5
1.0
0.5
0
-0.5
2
4
6
8
10
12
14
16
18
TOTAL t-o-f (microseconds)
x10 3

Fig. 6

# SMALL/MEDIUM-ANGLE DIFFRACTOMETER WINK

M. Furusaka, K. Suzuya, N. Watanabe, *M. Osawa, I. Fujikawa and S. Satoh
National Laboratory for High Energy Physics, Tsukuba 305
*Institute of Materials Science, University of Tsukuba, Tsukuba 305

## Abstract

WINK is a special instrument which covers very wide momentum transfer range ($0.01 \leq Q \leq 20$ Å$^{-1}$) by using incident neutrons of wide wavelength band ($1 < \lambda < 16$ Å), together with wide scattering-angle coverage ($2° \leq \theta \leq 145°$). To show the capabilities of WINK, we performed measurements of SiC fibers which have very complex mesoscopic structures. We also performed conventional X-ray small-angle and wide-angle diffraction to compliment the analyses. WINK was proved to be a very powerful instrument to analyze such complex materials; i) concentrations of hydrogen atoms were determined from incoherent scattering intensity at around $Q = 1$Å$^{-1}$, ii) voids as little as 4Å in diameter were observed, iii) the size of β-SiC obtained by SANS was different from that by diffraction at high angle, iv) glassy carbon and vitreous silica were detected in the power scattering.

## Introduction

WINK is a special instrument which is a combination of a small-angle instrument, a medium-resolution powder diffractometer and a total-scattering instrument. It is designed for characterization of various materials which have mesoscopic scale structures, like biology samples, micelles and emulsions, membranes, polymers, "hard" materials, magnetic materials and so on. To show the capabilities of WINK, we performed measurements on SiC-fibers, and detailed structure analysis was done. SiC-fiber is a material which has very high tensile strength even at high temperature. As common in such materials, it shows very complex mesoscopic structures[1]; it is not a homogeneous system and consists of several components and phases.

This study is also a good example of using both X-ray (SAXS) and neutron (SANS) small-angle scattering method to analyze very complex structure; the differences in the scattering amplitude density for both probe between the components are significant in this sample.

## Current status of WINK

Fig. 1 shows a side view of WINK. Design specifications of WINK are described elsewhere[2]. Last two years, we focused our effort to establish how to analyze data taken by WINK, since the use of such wide incoming neutron wavelength band together with wide scattering angle range has never been realized. For example, we found a deviation from Maxwellian distribution above 12Å in incident neutron spectrum. We also found that we could distinguish frame overlapped scattering by comparing scattering in the same Q bin obtained from different detector at different angle and wavelength. Therefore, there is no need for a frame-overlap eliminating chopper.

For the hardware side, we now have nearly 100 conventional $^3$He detectors working, mainly in a small-angle detector bank. We will have additional 40 detectors working in a 1.1m detector bank by the end of this fiscal year. We still have tentative setup for a higher-angle detector bank which surrounds the sample position.

## Sample preparation

SiC fibers were produced from Polycarbosilane ($Si_{1.93}CH_{4.71}O_{0.01}$). The first step for making commercial SiC fibers (Si-C-O fibers) are a thermal oxidation curing process to make

bridges between microscopic fibers. However, oxygen introduced into the fibers by the curing process causes a drastic thermal degradation of the fibers. Electron beam irradiation is a good alternative to the curing process, and it can produce oxygen-free SiC fibers[2)] (Si-C fibers). Following these curing processes, the samples are heat treated at various high temperatures (heat treatment temperature: HTT). We studied samples prepared by the above two curing processes, at the HTT's of 1273K, 1473K, and 1673K for each case.

## Results and Discussions

First, residual hydrogen contents were determined from the scattering at medium-Q range, as shown by the line denoted by $I^N_{inc}$ in Fig. 2, where coherent cross-section is negligible. We assumed that incoherent scattering from hydrogen atoms is the only contribution to the scattering in such a Q range. The hydrogen contents thus obtained were in good agreement with that from chemical analysis. Because of the large incoherent cross-section of the hydrogen atom, sensitivity is very high for the neutron scattering.

In the case of small-angle scattering, neutron (SANS) and X-ray (SAXS) scattering looks quite different at a first glance, as shown in Fig. 2, especially at higher Q range ($0.1 < Q < 1$ Å$^{-1}$), even after subtracting the incoherent scattering from hydrogen atoms.

SAXS shows $I(Q) \sim Q^{-4}$ power law in the Q range $0.1 < Q < 0.2$ Å$^{-1}$), whereas, SANS has a shoulder at around $Q = 0.3$ Å$^{-1}$. Therefore, we assume that the SANS data consist of three components; a broad peak, a shoulder and a constant spectrum. Those components are expressed by the scattering functions $I_1(Q)$, $I_2(Q)$ and $I_{inc}$, respectively. The SAXS data should also consist of these functions, although such a shoulder and a constant spectrum are not observed distinctly in Fig. 2. Consequently, the neutron and X-ray scattering cross-sections can be expressed by the following equation:

$$\left[\frac{d\Sigma}{d\Omega}(Q)\right]^{N,X} = C_1^{N,X} I_1^{N,X}(Q) + C_2^{N,X} I_2^{N,X}(Q) + I_{inc}^{N,X}, \qquad (1)$$

where $C_1$ and $C_2$ are the coefficients, N and X refer to neutron and X-ray.

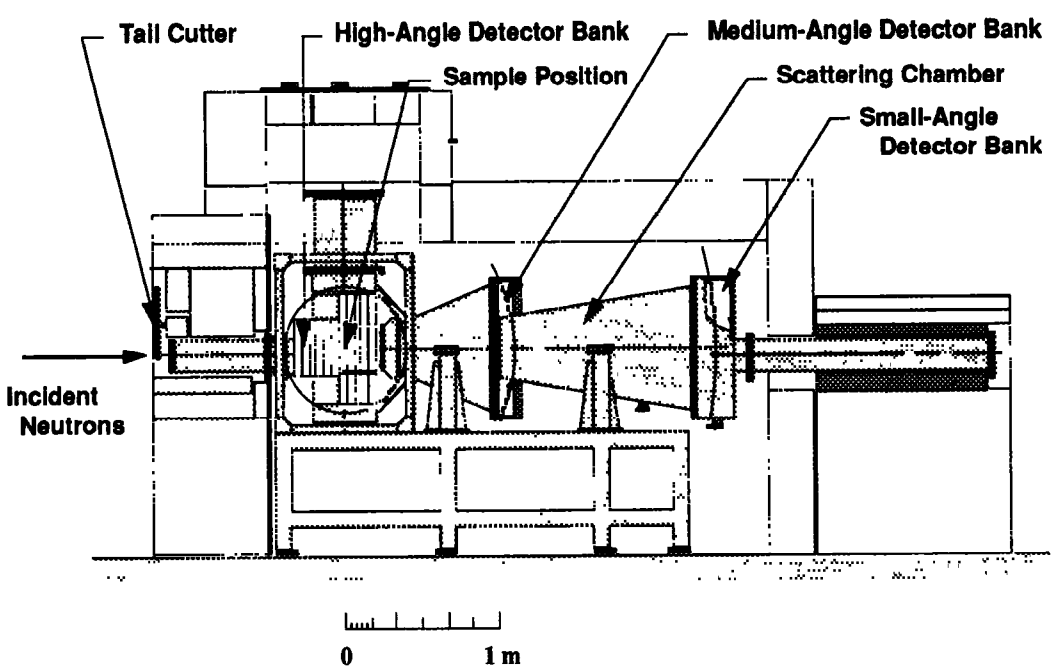


Fig. 1. Schematic diagram of WINK.

As a first step of the data analysis, we made the following assumptions; i) $I_1(Q)$ obeys Porod law at high Q (0.1 ~ 0.2 Å$^{-1}$) as obtained from the SAXS data, ii) $I_2(Q)$ is represented by the Debye-Bueche formula. Therefor the scattering cross-section at high Q is expressed as follows:

$$\left[\frac{d\Sigma}{d\Omega}(Q)\right]^{N,X} = C_1^{N,X}Q^{-4} + \frac{C_2^{N,X}}{(1+Q^2\xi^2)^2} + I_{inc}^{N,X}, \qquad (2)$$

where $\xi$ is a correlation length. First, we fitted high-Q part of the SAXS data with equation 2, and obtained $I_1^X(Q)$. We then fitted SANS data assuming that the $I_1^N(Q)$ has the same Q dependence as the $I_1^X(Q)$ for the whole Q range. Since SANS has much more pronounced shoulder around Q ~ 0.3 Å$^{-1}$, we could determine the $\xi$ in the second term of equation 2 more reliably than the SAXS data fitting. By using the same $\xi$, we fitted the SAXS data again using equation 2. Finally, we fit the SANS data using more reliable $I_1^X(Q)$. Figure 3 shows the result of the fitting to the SANS data.

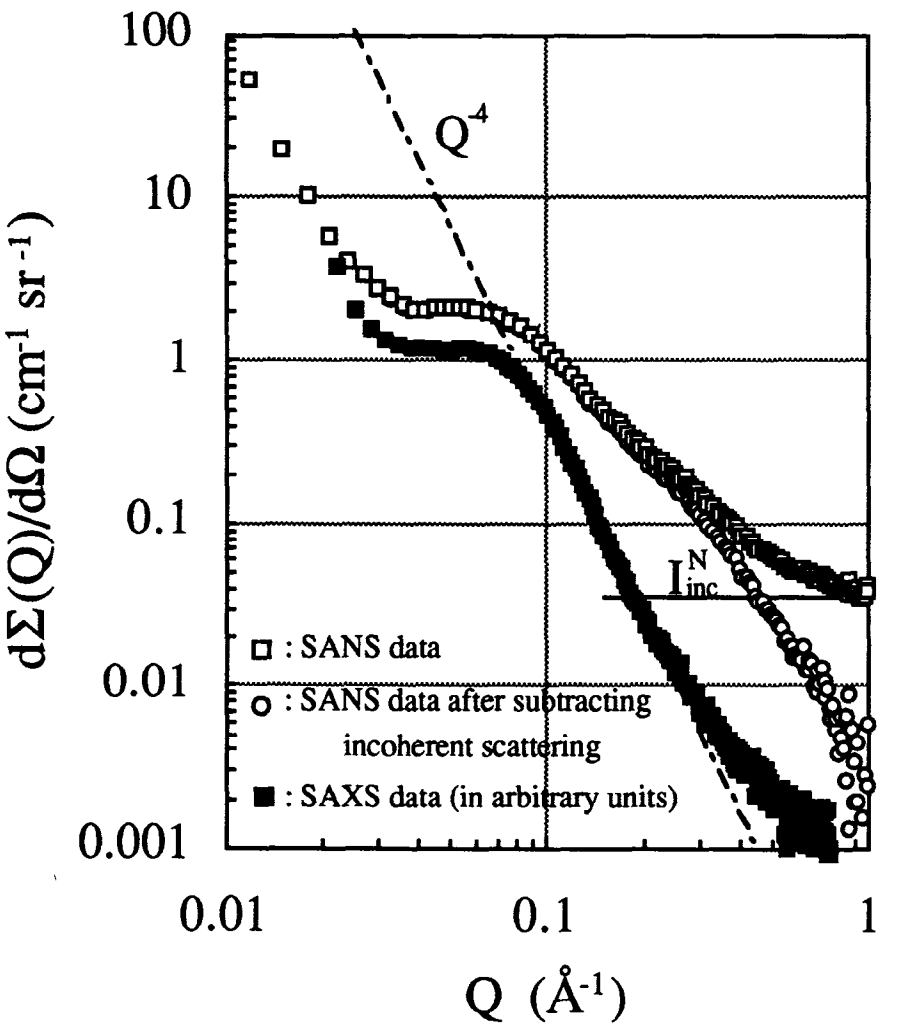


Fig. 2. SANS and SAXS data for SiC fibers (HTT=1473K).

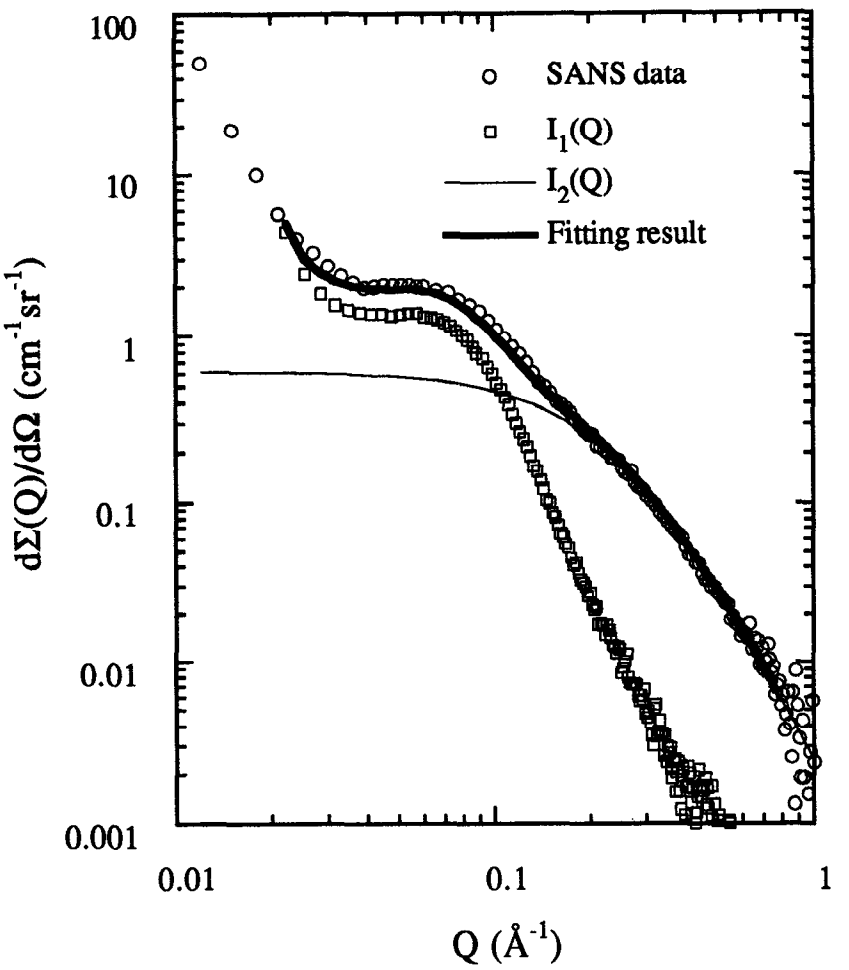


Fig. 3. Result of SANS data fitting for SiC fibers (HTT=1473K)

From macroscopic density measurements and chemical analysis, together with the results from the above fittings, we concluded that the SiC fibers consist of four basic phases; β-SiC($I_1(Q)$), vitreous $SiO_2$, glassy carbon and void($I_2(Q)$)[1]. Since the main component should be β-SiC, and void has higher contrast in SANS than in SAXS, the conclusion is quite natural.

The radius $R_v$ of the voids were obtained from the ξ, using the following equation,

$$R_v = \frac{3\xi}{4(1-\phi_{void})}, \tag{3}$$

where $\phi_{void}$ is a volume fraction of the voids. The diameter of the voids thus obtained were from 4Å to 13Å, depending on the curing processes and HTT's. It is almost impossible to measure small voids of such size with other methods; we have to use incoming neutrons of long wavelengths which are longer than Bragg-cutoff to avoid multi-Bragg reflections, and simultaneously, have to cover up to relatively high Q to about $1Å^{-1}$. WINK was designed for this purpose and it was very good at measuring such things.

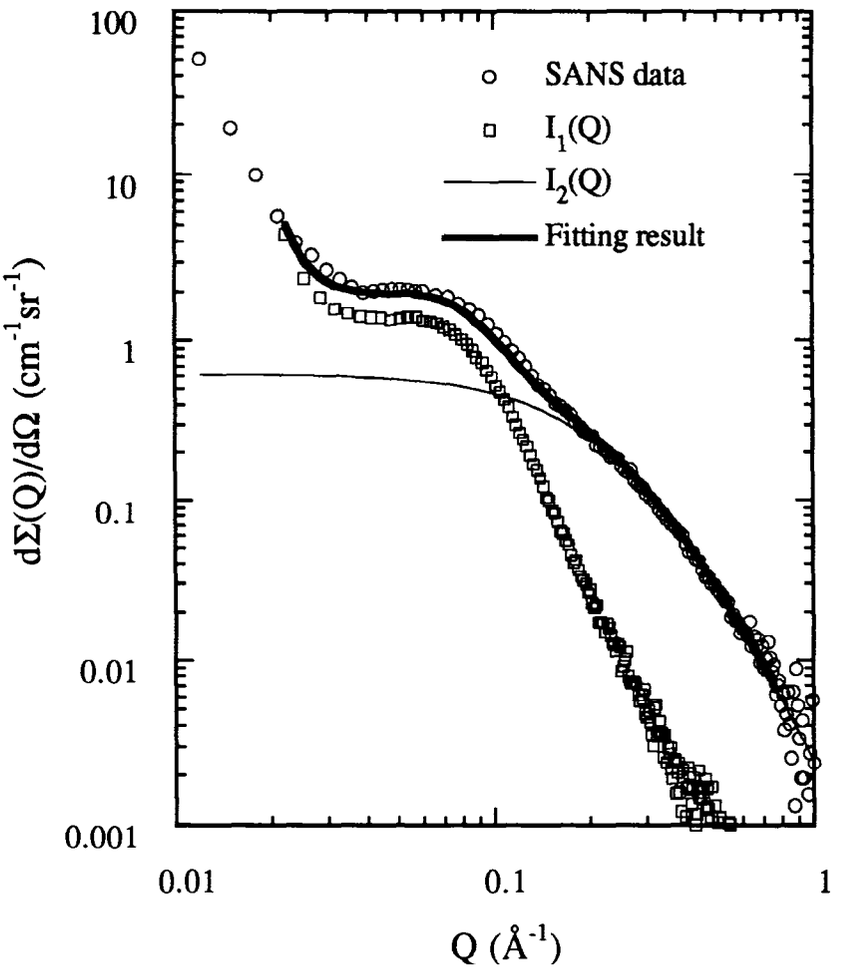


Fig. 4. Neutron diffraction patterns for Si-C and Si-C-O fibers (HTT=1473K).

We estimated the size of β-SiC crystallites L from the peak position of $I_1^N(Q)$ and volume fraction of the β-SiC. We also determined the size D from a diffraction peak width obtained from the high-angle neutron (see Fig. 4) or X-ray diffraction using Scherrer equation,

$$D = \frac{0.9\lambda}{W\cos\theta}, \tag{4}$$

where λ is the wavelength of the incident neutrons or X-ray, W the full-width at half maximum (FWHM) of a Bragg peak and θ the Bragg angle. Fig. 5 shows both L and D as a function of HTT. It is note worthy that the size of the crystallites observed by small-angle scattering L was much bigger than that obtained from the powder diffraction D. The size observed by the small-angle scattering did not reflect the size of a single crystallite, but it is a measure of a particle which consists of small crystallites which were observed by the powder diffraction.

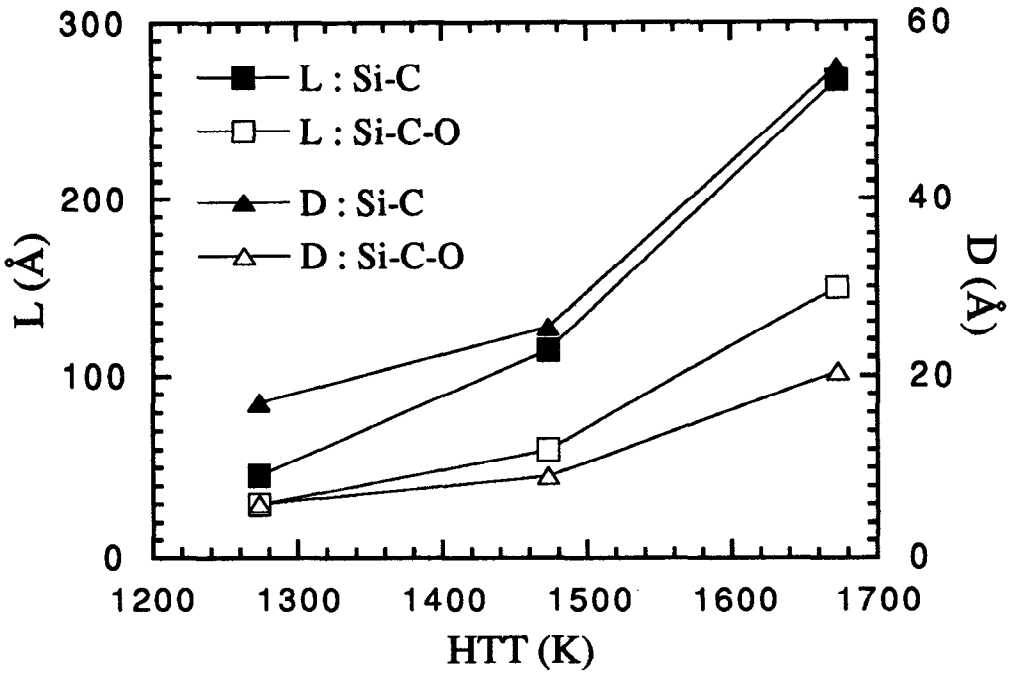


Fig. 5. Sizes of particles L and crystallites D of β-SiC.

Figure 4 shows diffraction patterns from SiC fibers. Besides the powder diffraction from β-SiC particles, small diffuse peaks were observed. We made a separate measurement for vitreous carbon, and plotted on the same figure. We scaled it by the peak around 1.7Å$^{-1}$ of the glassy carbon to the diffraction pattern. The figure shows that not only could we reproduce the first peak, peaks around 3 and 5.2 Å$^{-1}$ were also attributed to the vitreous carbon. We also performed measurement on vitreous silica, and plotted on the bottom half of the Fig. 4. This time, the peak around 1.5Å$^{-1}$ has different shape from Si-C fibers, and again it was well reproduced by the combination of vitreous silica and glassy carbon. In principle, we will be able to do a total fitting to multi-phase powder pattern and to total scattering simultaneously.

## Conclusions

We performed measurements on two kinds of SiC fibers using WINK and conventional SAXS and X-ray diffraction. WINK was proved to be a very powerful instrument to analyze such a complex material, especially when combined with X-ray diffraction.

## References

1. K. Suzuya, M. Furusaka, N. Watanabe, M. Osawa, K. Okamura, T. Kamiyama and K. Suzuki; submitted to J Am. Ceram. Soc.

2. M. Furusaka, N. Watanabe, K. Suzuya, I. Fujikawa and S. Satoh; ICANS-XI International Collaboration on Advanced Neutron Sources (KEK, Tsukuba, Oct. 22-26, 1990) P. 677.

# A Very-Low-Q Diffractometer for an Advanced Spallation Source

Philip A. Seeger and Rex P. Hjelm, LANSCE, Los Alamos National Laboratory
Los Alamos, NM 87544-1663, USA

Abstract

Proposals to build new, more powerful spallation sources and the introduction of advanced moderator concepts will result in neutron sources that are 20 times more luminous than the brightest available today. These developments provide opportunity and challenge to expand the capabilities of present low-Q instruments using new designs. A particularly interesting case is the design of an instrument capable of measurements to "very low" momentum transfer, say $Q \approx 0.0007$ Å$^{-1}$. We consider an instrument to be built on a 20 Hz, 330 kW target and viewing a coupled liquid-hydrogen moderator. The instrument would use a frame-definition chopper to select a wavelength band suitable for the required Q-domain. Monte Carlo optimization of the geometry was performed by choosing the minimum observable Q always to be 0.0007 Å$^{-1}$ and then maximizing intensity/variance at $Q = 0.0020$ Å$^{-1}$ while maintaining reasonable constraints. The resulting design is 48 m long, with a maximum wavelength band 16.8 Å $\leq \lambda \leq$ 20.5 Å.

The Monte Carlo simulations of instrument performance include wavelength-dependent effects from aluminum and fused silica windows, air, chopper opening and closing times and phase jitter, measured spectrum and detector efficiencies, sample transmission and multiple scattering, and gravity. The results were normalized by the measured flux from the present LANSCE moderator, and scaled by the expected performance of a coupled hydrogen moderator. The results compare well with the 76-m configuration of the D11 instrument at ILL in both count rate and Q-precision, due in part to the ability to correct for gravitation effects using the time of flight of the detected neutrons. The validity of these comparisons was demonstrated by comparison of measurements and Monte Carlo simulations made on the present LANSCE Low-Q instrument (LQD) and on D11.

## Introduction

Neutron scattering with "small" momentum transfer gives information about the scattering system at "large" length scales: $Q = (4\pi \sin\theta)/\lambda \sim 1/d$ to $2\pi/d$. For example, determination of a radius of gyration $R_g$ requires data for Q ? $1.3/R_g$. The technique of small-angle neutron scattering (SANS) also relies on use of long wavelengths to achieve low Q. Thus when performing measurements in the size range 300 Å or more, steady state (reactor) neutron sources with large cold moderators appear to have an advantage over spallation sources, whose spectra emphasize the epithermal regime. On the other hand, several successful SANS instruments have been built at spallation sources[1] and with careful attention to optimization of resolution[2,3] these instruments are

competitive with reactor SANS instruments over at least a portion of the "low-Q" range.

As part of the design study for a suite of instruments to be recommended for a proposed high-power pulsed neutron source, we were asked to consider the capability to measure length scales greater than 1000 Å, which are of particular interest in metallurgy, materials science, colloids, and polymers. To this end we chose to design a Very-Low-Q Diffractometer (VLQD) which would have comparable resolution to the 76-m configuration of D11 (D11-76) at the Institut Laue-Langevin[4]. Taking parameters for D11-76 from ref.[4], the collimation length is 40.5 m, sample-to-detector distance is 35.7 m, the maximum practical wavelength $\lambda$ is 12 Å, and the minimum Q recorded is 0.00074 $Å^{-1}$.

In assessing the resolution of D11-76, we discovered that the effect of gravity is very deleterious. The velocity of a 12-Å neutron is 329.7 m/s, so the flight time is 0.234 s and the neutron falls 269 mm due to gravity. Parabolic trajectories defined as being on-axis at the entrance and exit of the collimation strike the detector below axis by an amount proportional to $\lambda^2$; specifically 0.84 $\lambda^2$ mm/$Å^2$. The resulting average droop of 121 mm is not in itself significant, but the variance of vertical position on the detector resulting from the spread of wavelengths of the velocity selector is the dominant term in the Q-resolution for any value of $Q \leq 0.002$ $Å^{-1}$. Thus the possibility to extend the Q range below about 0.002 $Å^{-1}$ is very limited at a steady-state source, because without knowledge of the velocity of each individual neutron there is no direct way to correct for the effect of gravity. A narrower velocity spectrum could be used, at the expense lowering the count rate below the already meager number available. In principle, image enhancement techniques could be applied to the data, but only if very high quality data are obtained.

At a pulsed source, on the other hand, it is trivial to correct for gravitational droop because the time of flight of each neutron *is* measured, and the droop is easily calculated. Therefore gravity does not limit the instrument length nor the wavelength range which may be used. We have designed the VLQD to operate on a 20-Hz , 330-kW target viewing a coupled liquid hydrogen moderator. Monte Carlo simulations of many geometries were tested, assuming a $\delta$-function scatterer at $Q \equiv$ 0.0020 $Å^{-1}$, and requiring a minimum recorded value of Q of 0.0007 $Å^{-1}$.

Instrument Geometry

Figure 1 illustrates the general instrument geometry which has been used in the design and analysis of a family of SANS instruments for the high-power source. The most significant variables are the total instrument length DT, the sample-to-detector distance L2, and the maximum wavelength $\lambda_{max}$; the search for an optimum is carried out over these three variables. Other elements which can be adjusted are the entrance aperture of the collimator (radius R1, located distance D1 from the moderator), the massive $T_0$ chopper (distance Dt from the moderator), the disk frame-definition chopper (distance Df from the moderator), the collimator exit aperture (radius R2, distance D2 from

moderator), and the beamstop. For the VLQD, we take D1 = 4.6 m, Dt = 5.0 m, Df = min{DT/2, DT −L2} − 1 m, D2 = DT − L2 − 0.15 m, and R1 and R2 determined by the cone rule[5] and the beam penumbra radius which results from computing the minimum scattering angle which must be measured to attain the required minimum Q. Similarly the nominal opening and closing times of the choppers are computed to assure closure during the initial pulse, and to give the maximum counting time without frame overlap. The $T_0$ chopper is two-lobed, rotating at half the proton pulse rate with an assumed phase jitter of 60 μs (rms), and the frame-definition chopper makes one revolution per proton pulse with phase jitter 30 μs (rms).

The detector is a very critical element in the performance of a SANS instrument, and we cannot give this presentation without stating very strongly our belief that detector development is the most crucial problem in improving existing instruments as well as being essential for instruments on a high-power neutron source, either pulsed or steady-state. The parameters of the detector which enter the Monte Carlo simulations are its overall size, the size of one pixel, the rms position encoding, the absorbing thickness of the entrance window, and the efficiency as a function of wavelength. We have assumed pixel size and rms to be similar to our existing $^3$He detector (to facilitate comparison with actual measurements), but we hope for much larger area. (The simulations assume a detector 3 m wide by 1 m tall.) We have also retained the 1-cm Al entrance window, which greatly reduces efficiency at long wavelengths, and used the same gas fill pressure, which leads to lower efficiency at short wavelengths. Improved detectors will greatly affect our predicted instrument performance, but will probably not greatly affect the optimization procedure. In particular, elimination of the thick entrance window would vastly improve efficiency at the wavelengths we propose to use.

The effect of gravity in a long instrument with slow neutrons is that the trajectories have a high arch (proportional to $\lambda^2$) through the collimator. The intermediate baffles indicated in fig. 1 are not practical, so we are limited to a single-aperture collimation system instead of the multiple apertures shown. Also, the vertical motion required for the gravity focuser would be too large, so the VLQD is assumed not to have gravity focus. This means that all of the transmitted neutrons in the wavelength band of interest will droop *below* the beamstop, which will thus only intercept neutrons which scatter upward. We therefore plan to omit the beamstop in the VLQD; however since the wavelength bandpass is small, an adjustable beamstop could be included.

Monte Carlo Calculations

1. Neutron source

The direct spectrum of neutrons from the LANSCE liquid hydrogen moderator at 29 K was measured with a $^3$He monitor detector of known efficiency at the sample position. The data were fitted by least squares with a semi-empirical function. This function was multiplied by $\lambda^2$, and integrated to give a cummulative probability distribution. A table of values of neutron energy was

generated such that the cummulative probabilities are the same as those of a normal distribution (truncated at $\pm 3\ \sigma$). Then to find a random neutron energy from the distribution, we use a standard routine to generate a random normal deviate and interpolate in the table to get E. Note that because the distribution has been weighted by $\lambda^2$, more histories will be generated at the wavelengths which have higher scattering probability; each history is given an initial weight of $(\lambda_{max}/\lambda)^2$. This distribution accounts for absorption in the Al can of the cold moderator, but not the detector window.

After the neutron energy is determined, its emission time is selected from probability distributions including "slow" and "fast" components depending on wavelength. The parameters of the distributions are derived from early ISIS data; we have not felt the need to re-measure these distributions because the time spread is not a major contribution to SANS resolution.

2. Apertures and phase space

Only neutrons which pass through both apertures of the collimator need be tracked. We therefore begin by choosing a random point within each aperture, and projecting back (including the acceleration of gravity) to the moderator. Thus only a limited volume of phase space is sampled, namely $[\pi\ R1\exists R2/(D2\#D1)]^2\ \mu ster\exists mm^2$. Given the moderator surface brightness in neutrons/$\mu$ ster/mm$^2$/MW/s, the Monte Carlo results are normalized to MW$\exists$s (or, in the case of a steady-state source, to s). Note that we have scaled the measured LANSCE source brightness upward by a factor of 4 for the expected gain of thermal flux from a strongly coupled moderator. Composite moderators may also be considered, which could have a similar gain.

3. Choppers

When a neutron track is projected to a chopper location, the location of the nearest moving edge is computed including a random normal deviate times the phase jitter. If the neutron position is on the closed side of the edge it is absorbed; otherwise it passes unaffected. Part of the program initialization is to set the nominal opening and closing times of the choppers to guarantee closure at $T_0$, including the time it takes to close fully and $)3\sigma$ of jitter. The open duration of the frame-definition chopper is similarly set to give a maximum counting frame, and its phase is set to pass the requested $\lambda_{max}$.

4. Absorption in windows and air

A subroutine computes the aluminum scattering probability as a function of wavelength and compares it to a random number to decide whether the neutron was removed from the beam. The algorithm is taken from a note by Jack Carpenter[6], and explicitly includes Bragg edges up to the (820) reflection. Air and fused silica are treated simply by taking cross sections from the barn book[7].

5. Sample transmission and scattering

Sample thickness is expressed as transmission probability at $\lambda_{max}$, and is assumed to vary as $T(\lambda) = \exp(-\alpha\exists\lambda^2)$. When optimizing, $T(\lambda_{max})$ was arbitrarily set to 50%, but in comparisons with

D11 the sample thickness was kept constant such that transmission at 10 Å was always 75%. Every neutron history which strikes the sample is transmitted with its weight multiplied by $T(\lambda)$, and is also scattered with its initial weight multiplied by $[1 - T(\lambda)]$. The scattering law used to determine system performance is a $\delta$-function; *i.e.*, every neutron scatters with exactly the same magnitude of Q, but the azimuthal angle is random. After the first scatter the probability of escaping the sample is computed by selecting a penetration depth from an exponential distribution, dividing the remaining thickness by the longitudinal direction cosine, and comparing the transmission probability to a random number. The scattering process is repeated until the neutron escapes.

6. Detector tallies

Transmitted neutrons and scattered neutrons that are still aimed downstream are projected to the plane of the detector (always including gravitational droop). If the X-Y position is within the physical bounds of the detector, encoding uncertainty is introduced by applying random normal deviates separately in X and Y, and the weight of the neutron is added to the corresponding X-Y-t cell. Time slices are logarithmic, defined using the algorithm of the LANSCE data acquisition system. At the completion of the Monte Carlo run, the X-Y-t data file is essentially identical to an LQD experiment, and is reduced to I(Q) using our standard procedures[8]. A typical result is shown in fig. 2. This figure also illustrates the effects of multiple, which is the only mechanism in the simulation which contributes to the "background" under the peak. These effects become severe whenever the sample transmission is low, as it was in this simulation.

7. Figure of merit (FOM)

A figure of merit (FOM) is needed to compare different configurations. The fundamental criterion is to maximize count rate at a given resolution, or equivalently to minimize the variance of Q at fixed count rate. The FOM is therefore $I(Q)/V[Q]$. We estimate scattered count rate by weighting the transmitted flux by $\lambda^2$ to account for variation of scattering probability. Because of the large number of terms which contribute to the $\delta$-function response resolution in fig. 2, we can expect the shape to be Gaussian. We have estimated the variance $V[Q]$ by fitting Gaussians to each of these plots. The units of the FOM as described are $Å^4/s$, but for comparing configurations at the same value of Q we normalize by multiplying by $Q^4$ so that the units are $s^{-1}$.

8. D11

As far as possible, the same code has been used to compute resolution and intensity at D11. One obvious difference is the neutron source function: the velocity selector is emulated by a triangular probability distribution with a full-width-half-maximum of 10%. There are no choppers and no gravity focuser, and time of flight is not recorded. When comparing optimum configurations the cone rule for collimator apertures is applied, but when comparing the real experiment the non-optimum practice of ILL is followed and there is no aperture at the guide exit.

Monte Carlo Results

After the first round of iteration on the three parameters (DT, L2, and $\lambda_{max}$), the proposed instrument was 46 m long, with L2 ≈ DT/2 (*cf.* fig. 3a) and $\lambda_{max}$ > 20 Å (*cf.* fig. 3b). For the next series of simulations, $\lambda_{max}$ was always adjusted (as DT was varied) so that the detector is never counting at the instant when protons are being delivered to the target; this will eliminate background problems associated with beam delivery and room background in the first 4 ms after each pulse. Note that the counting frame begins after three or four additional proton pulses have already been delivered to the target, so that there are four or five pulses in the instrument at any one time. The resulting plots of FOM *vs.* DT are given in fig. 3c. As usual, optimization leads to as long an instrument as possible. The selected design is 48 m long, and uses the counting frame from 204 to 249 ms after the proton pulse, corresponding to wavelengths from 16.8 to 25.6 Å. The frame-definition chopper (at 23.0 m) is open from 96.56 to 120.52 ms for each pulse, but its phase may also be adjusted to use shorter wavelength neutrons to extend the dynamic range in Q. The resulting resolution (at Q = 0.002 $Å^{-1}$) is 0.00031 $Å^{-1}$. The estimated integrated neutron flux on sample (area = 3.6 $cm^2$) is 1400 per second.

Figure 4 illustrates the Q-range and precision for the VLQD, compared to identical simulations of D11-76. (Three other pulsed-source instruments and three other D11 configurations are also shown.) The four lines represent setting the frame-definition chopper to count in the fifth, fourth, third, or second frames after $T_0$, while the box for D11 corresponds to varying the velocity selector between 12 Å and 6 Å. The resolution for VLQD frame 4 is identical to D11-76 for 10 Å neutrons, so it is appropriate to compare their intensities; see fig. 5. The computed VLQD intensity is a factor of 2.5 lower, but this is partly due to absorption of the long-wavelength neutrons in the detector window. With improved detectors, the intensity (for a 330 kW target) would be very comparable to D11-76. Thus these simulations show that a VLQD is completely feasible on the proposed high-power pulsed sources.

Code Validation

A comparison experiment between the present LQD and D11 at total lengths of 10 m and 20 m (sample-to-detector distances of 5 m and 10 m respectively) has previously been reported[1]. To test the validity of the Monte Carlo procedure, we have also simulated that experiment. The line labeled "LANSCE LQD" in fig. 4 shows our computed resolution. The value at Q = 0.020 $Å^{-1}$ (corresponding to the peak in the experiment) is 0.0023 $Å^{-1}$, while that computed for D11 at 10 m is 0.0020 $Å^{-1}$. This supports our statement in ref.[1] that the data for the two experiments are of the same quality. Furthermore the computed count-rate ratio is within 20% of the observed (which must be considered fortuitous), so that we can be reasonably confident in our comparisons.

## Conclusions

The Monte Carlo calculations which are the basis of this report have proven to be extremely useful in understanding both existing and proposed future instruments. Each new feature added to the simulation seemed to produce an "ah-ha!" result – something obvious in retrospect but which we had previously overlooked. The first of these was the effect of gravity of steady-state sources which use long wavelength neutrons *and* long flight paths. Because droop is proportional to $\lambda^2$, the effect of the spread of wavelengths from a velocity selector is amplified. A second insight is that multiple-scattering effects can be extremely strong, and can lead to artifacts and high "incoherent" background even for scatterers which are purely coherent. For the simulatioin describing the comparison experiment, 30% of the detected neutrons were multiply scattered. We plan to use this simulation technique in the near future to study the possibility of correcting the experimental data.

Finally, and not surprising, the calculations again emphasize the need for detector development.

## Acknowledgement

This work was performed at the Manuel Lujan Jr. Neutron Scattering Center (LANSCE), a national user facility operated by the US Department of Energy under contract W-7405-ENG-36 with the University of California.

## References

1. P. A. Seeger and R. P. Hjelm Jr. (1991), "Small-Angle Neutron Scattering at Pulsed Spallation Sources," *J. Appl. Cryst.* **24**, 467-478.
2. P. A. Seeger and R. Pynn (1986), "Resolution of Pulsed-Source Small-Angle Neutron Scattering," *Nucl. Instrum. Methods* **A245**, 115-124.
3. R. P. Hjelm Jr. (1988), "The Resolution of TOF Low-Q Diffractometers: Instrumental, Data Acquisition and Reduction Factors," *J. Appl. Cryst.* **21**, 618-628.
4. P. Lindner, R. P. May and P. A. Timmins (1992), "Upgrading of the SANS Instrument D11 at the ILL," *Physica* **B 180&181**, 967-972.
5. P. A. Seeger (1980), "Optimization of Geometric Resolution in Small-Angle Scattering," *Nucl. Instrum. Methods* **178**, 157-161.
6. J. W. Carpenter (1986), "A Simple Formula for the Total Cross Section of a Monatomic Polycrystal," IPNS Note 32.
7. S. F. Mughabghab, M. Divadeenam and N. E. Holden, Neutron Cross Sections (Academic Press, New York, 1981).
8. R. P. Hjelm Jr. and P. A. Seeger (1988), "Time-of-Flight Small-Angle-Neutron-Scattering Data Reduction and Analysis at LANSCE with Program SMR," in Advanced Neutron Sources 1988, D. K. Hyer, ed., IOP Conference series **97** (Institute of Physics, Bristol and New York, 1989) pp 367-387.

Figure Captions

1. Generalized diagram of a Low-Q Diffraction instrument for a pulsed spallation neutron source. The nomenclature is discussed in the text. This arrangement has been used in the design of a family of diffractometers for a new high-power source.
2. Computed response function for a δ-function scatterer at $Q \equiv 0.0020$ Å$^{-1}$. The shape of the peak at $Q = 0.0020$ Å$^{-1}$ gives the Q-resolution. The underlying background and the secondary structures are all results of multiple scattering. Data below $Q \approx 0.0007$ Å$^{-1}$ have larger error bars because of subtraction of a background run including spreading of the direct beam.
3. Figure-of-Merit plotted *vs.* the three main parameters. a) variation of the secondary flight path with total length and wavelength held constant. b) variation of maximum wavelength with path lengths constant. c) variation of total instrument length with proportional changes in secondary path and wavelength.
4. Computed statistical resolution in Q as a function of Q for a number of SANS instruments. The various D11 configurations and the Biological LQD are shown as boxes representing continuous choices of wavelength. The present LQD and the proposed MQD record all wavelengths at a single setting, and the VLQD is expected to be operated at a few selected wavelengths.
5. Intensity of SANS instruments, weighted by $\lambda^2$. Only instruments with the same resolution on fig. 4 should be compared; *e.g.*, MQD and D11(11 m), Biology LQD and D11(21 m), or VLQD frame 4 and D11(76 m).

# Low-Q Diffractometer

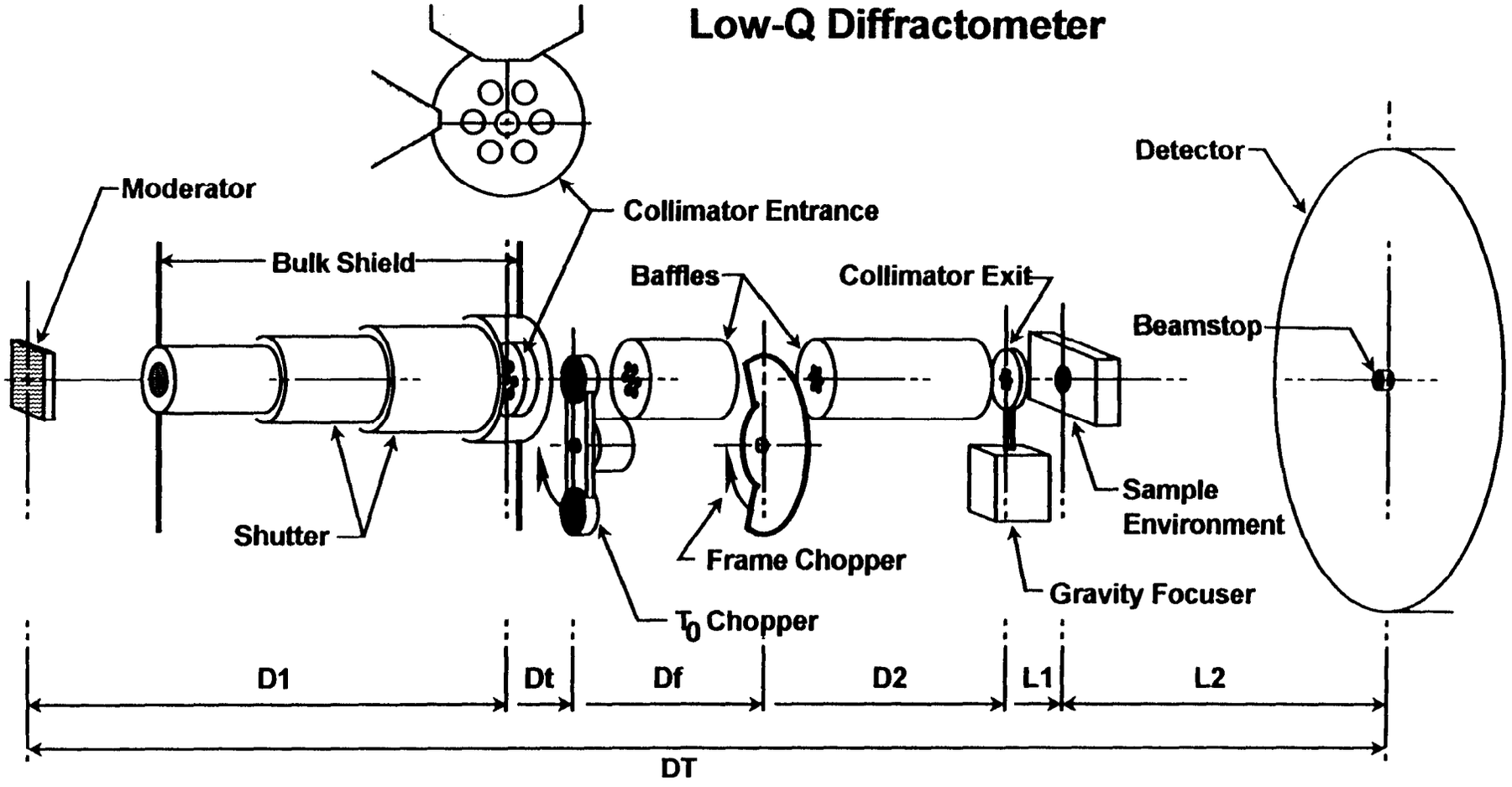

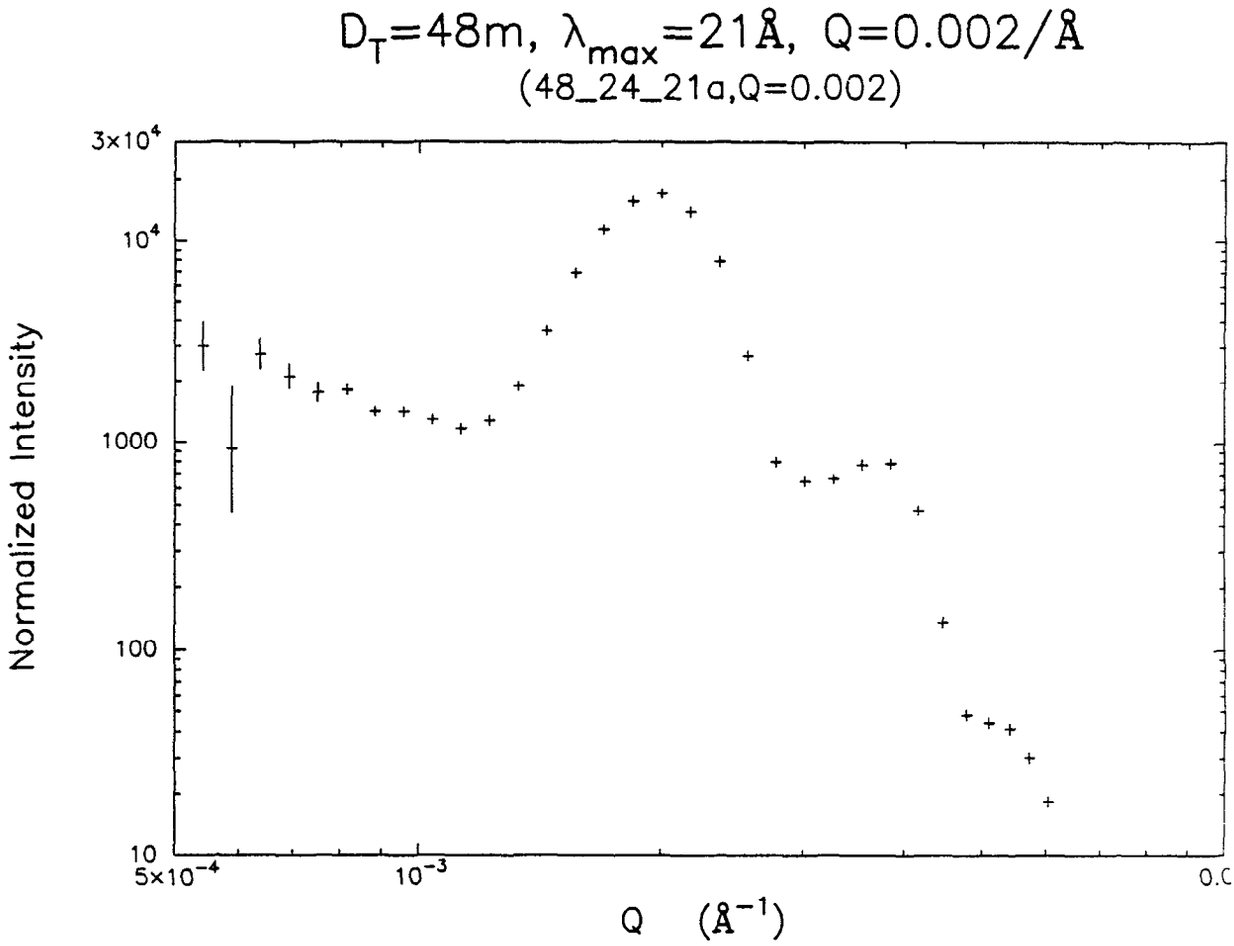
$D_T$=48m, $\lambda_{max}$=21Å, Q=0.002/Å
(48_24_21a,Q=0.002)
3×10⁴
10⁴
1000
100
10
Normalized Intensity
5×10⁻⁴
10⁻³
0.0
Q (Å⁻¹)

Fig.2

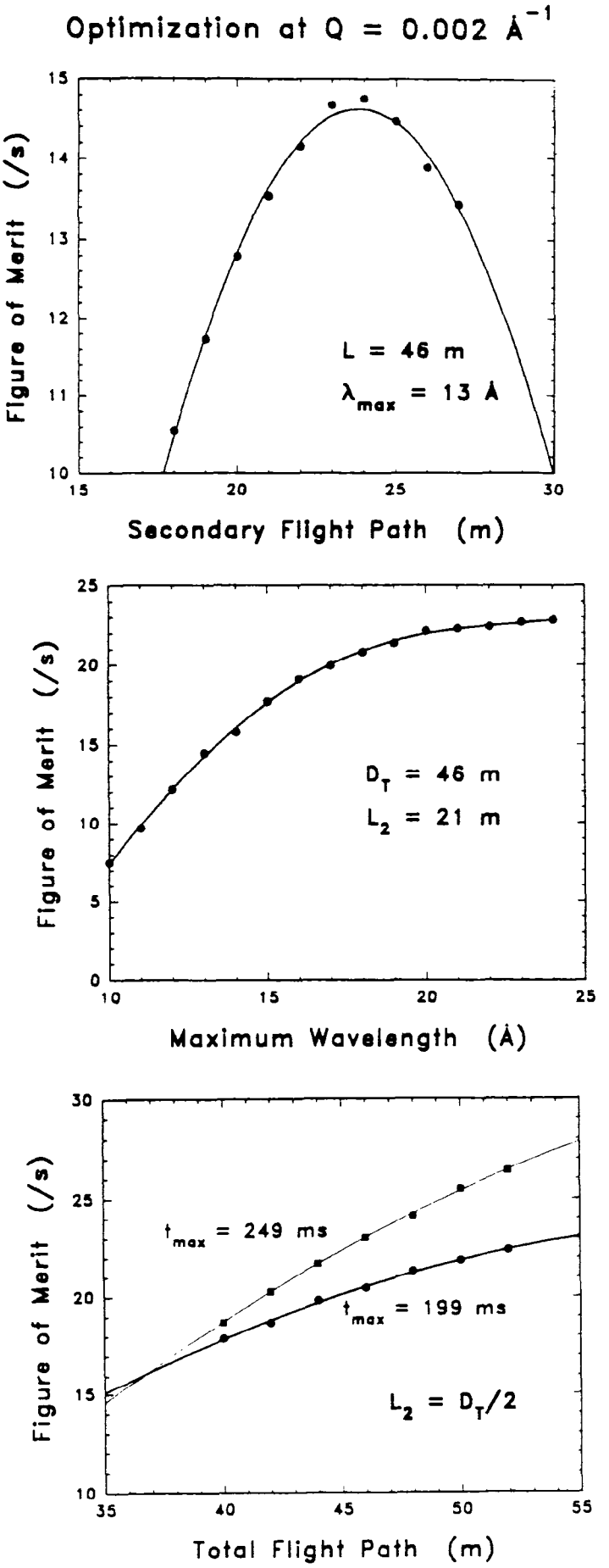
Optimization at Q = 0.002 Å$^{-1}$
Figure of Merit (/s)
L = 46 m
$\lambda_{max}$ = 13 Å
Secondary Flight Path (m)
Figure of Merit (/s)
$D_T$ = 46 m
$L_2$ = 21 m
Maximum Wavelength (Å)
Figure of Merit (/s)
$t_{max}$ = 249 ms
$t_{max}$ = 199 ms
$L_2 = D_T/2$
Total Flight Path (m)

Fig. 3

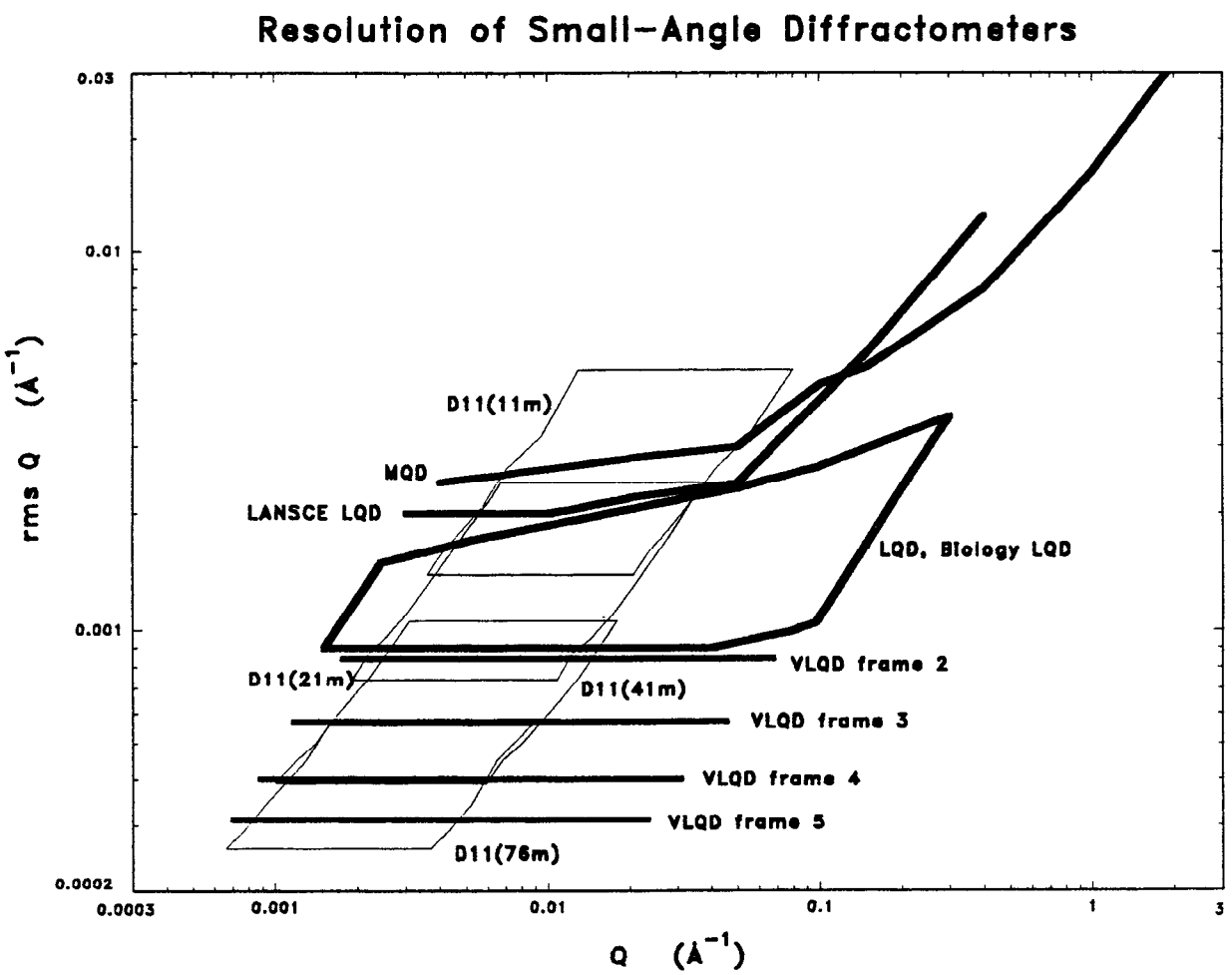
Resolution of Small-Angle Diffractometers
0.03
0.01
0.001
0.0002
rms Q (Å$^{-1}$)
0.0003
0.001
0.01
0.1
1
3
Q (Å$^{-1}$)
D11(11m)
MQD
LANSCE LQD
LQD, Biology LQD
VLQD frame 2
D11(21m)
D11(41m)
VLQD frame 3
VLQD frame 4
VLQD frame 5
D11(76m)

Fig. 4

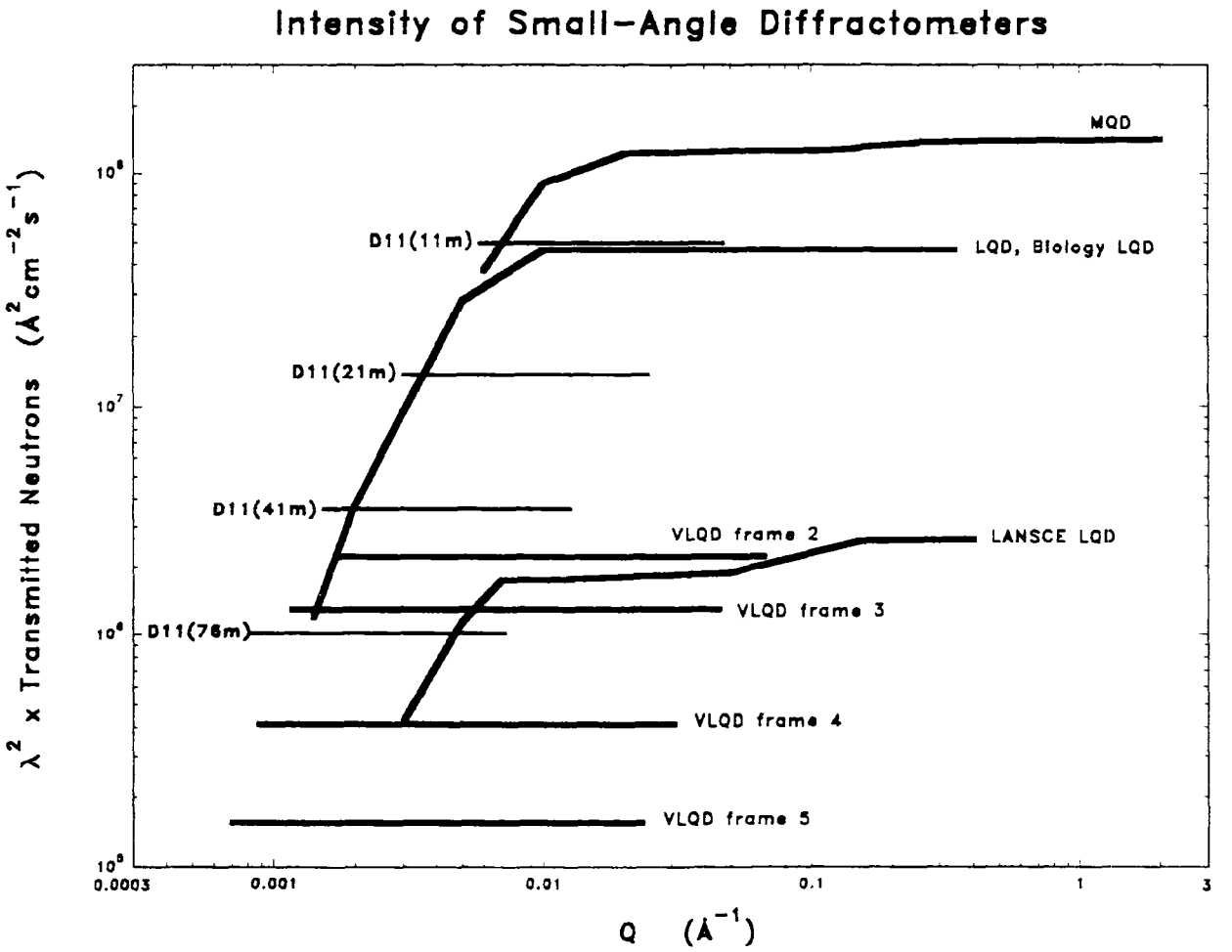
Intensity of Small-Angle Diffractometers
MQD
D11(11m)
LQD, Biology LQD
D11(21m)
D11(41m)
VLQD frame 2
LANSCE LQD
VLQD frame 3
D11(76m)
VLQD frame 4
VLQD frame 5
$\lambda^2$ x Transmitted Neutrons ($Å^2 cm^{-2} s^{-1}$)
$10^8$
$10^7$
$10^6$
$10^5$
0.0003
0.001
0.01
0.1
1
3
Q ($Å^{-1}$)

Fig.5

# ISIS NEUTRON DETECTORS

**RHODES, N.J., BORAM, A.J., JOHNSON, M.W., MOTT, E.M. and WARDLE A.G.**

**Rutherford Applton Laboratory, Chilton, Didcot, Oxon. OX11 0QX.**

## ABSTRACT

ISIS is currently operating 14 instruments for neutron scattering measurements. Of paramount importance to each of these instruments is its neutron detector system. The detector systems on ISIS include a variety of scintillator detectors which have been developed in house, together with $^3$He proportional counters which have been obtained commercially. The detectors may be characterised by their shape, neutron and gamma efficiencies, intrinsic background, dead time and the stability of these quantities with time. The characteristics of the ISIS detectors are discussed in relation to the different ISIS instrument requirements.

## INTRODUCTION

The ISIS neutron scattering instruments comprise of 6 diffractometers, HRPD, LAD, SXD, POLARIS, LOQ and SANDALS and 6 spectrometers MARI, eVS, HET, TFXA, IRIS and PRISMA, together with the neutron reflectometer CRISP. In addition there is a TEST BEAM which can quickly be configured into a number of different roles including a facility for measuring neutron scattering from samples under high pressures in the Paris/Edinburgh High Pressure Cell and an instrument for residual stress analysis. These instruments will shortly be joined by ROTAX, a rotating analyser crystal spectrometer. Each of these instruments operates one or more types of neutron detector.

An overview of the types of neutron detector operational at ISIS is shown in Figure 1. These detectors can be divided into $^3$He gas proportional counters which are available commercially and scintillator detectors which have largely been developed at the Rutherford Appleton Laboratory, RAL. The scintillator detectors can be differentiated according to the type of

scintillator used; whether the scintillator is $^{6}Li$ loaded zinc sulphide, ZnS, or $^{6}Li$ loaded glass. Each of the three groups can be sub divided according to the degree of position sensitivity; whether it be a single counter, a linear counter with one dimensional position sensitivity or an area detector with two dimensional position sensitivity. The scintillator detectors can be further characterised according to the method of coupling the scintillator to photomultiplier tubes, PMT's. The PMT's may either view the scintillator directly or via fibre optic light guides.

In assessing the performance of each of these detector types then a number of characteristics need to be considered. These include the following:

1) Neutron detection efficiency as a function of energy.
2) Sensitivity to gamma radiation.
3) Intrinsic detector background.
4) Spatial resolution and detector geometry.
5) Pulse pair resolution, ppr.
6) Stability of detector characteristics with respect to time.
7) Ease of maintenance.
8) Cost.

The efficiencies of gas proportional detectors can be calculated from a knowledge of the gas pressure of the neutron absorbing component. For the scintillator detectors the efficiency with which light is generated from a neutron event, the efficiency of light transmission to the PMT's and the quantum efficiency of the PMT's can all result in a decrease in neutron detection efficiency compared with that calculated from the concentration of neutron absorber in the scintillator. Neutron detection efficiencies of the scintillator detectors have therefore been determined experimentally from neutron count rates measured near to a PuBe source which has a broad neutron energy spectrum centred around 1 Angstrom. The neutron flux from the PuBe source is calibrated using a 10 mm x 10 mm scintillator sheet directly coupled to the end window of a PMT. For a glass scintillator this gives a detector with an excellent pulse height resolution of 12 %. In most cases scintillator detection efficiencies have been confirmed on

ISIS by comparing count rates from standard $^3$He single proportional counters under similar conditions. The sensitivity of neutron detectors to gamma radiation has been measured using a 1 curie $^{60}$Co gamma source placed 100 mm from the active detector area. Gamma sensitivity is expressed as a ratio of photons detected to photons incident on the detector, account being taken of intrinsic detector background levels where significant. Pulse pair resolution is used as a means of comparing the time response of the detector types and is a measure of the shortest time in which successive neutron detector events can be recorded.

Detector characteristics are discussed in detail for the various types of detector operational at ISIS. It is the optimisation of these parameters to meet the requirements of a particular instrument which leads to a successful detector design.

## SINGLE $^3$He PROPORTIONAL COUNTERS

Nine of the ISIS instruments make use, either in part or in total, of single $^3$He proportional counters. Over 1000 of these detectors will be operational on ISIS by the end of the year. By far the largest user is the MARI spectrometer which operates Reuter Stokes detectors at 10 atmosphere $^3$He and generally 300 mm long and 25 mm diameter. Typical detector characteristics are given in Table 1. For these detectors the neutron detection efficiency at wavelengths of 1 Angstrom and greater is good, the gamma sensitivity and intrinsic detector backgrounds are low while the pulse pair resolution is moderate. The single neutron proportional counter has been in use for many years at neutron scattering centres throughout the world and its detector characteristics have become a yardstick by which the performance of other more novel detector systems can be measured.

## ONE AND TWO DIMENSIONAL POSITION SENSITIVE $^3$He PROPORTIONAL DETECTORS

ISIS operates three position sensitive $^3$He proportional counters. The CRISP reflectometer uses a linear position sensitive detector while LOQ and SXD/TEST BEAM use two

dimensional area detectors. All theses detectors have been purchased from the Ordela company, ref 1, and use rise time encoding methods to determine position sensitivity. Detector characteristics as published by the Ordela company are summarised in Table 2.

## DIRECTLY COUPLED LINEAR ZINC SULPHIDE SCINTILLATOR DETECTORS

SANDALS, IRIS, POLARIS and TEST BEAM all operate one dimensional position sensitive ZnS scintillator detectors in which the PMT's directly view the scintillator elements. In each of these detectors scintillator elements are contained in aluminised mylar light guides and the PMT's are displaced laterally a half tube diameter from the light guide axis. Each PMT views two scintillator elements, while each scintillator is viewed by segments of two adjacent PMT's. Neutron events in any one scintillator are determined by the coincident output from adjacent pairs of PMT's. This PMT arrangement uses on average one PMT per detector element while allowing detector noise due to random PMT events to be largely eliminated.

The detectors of this type on POLARIS and TEST BEAM have become known as 'BRICK' detectors due to a design requirement to achieve a self stacking detector. The POLARIS BRICK detector modules are used for diffraction measurements while two BRICK detector modules on TEST BEAM have been incorporated in an instrument for residual stress analysis, ref. 2. Essential differences between the SANDALS, IRIS and BRICK detectors are associated with the arrangement of the scintillator in the detector element, Figure 2.

The SANDALS elements consist of 20 strips of ZnS, 200 mm x 10 mm x 0.4 mm stacked one behind the other and separated by crown glass strips of similar dimensions. This arrangement gives a neutron path length, p, through the scintillator of 8 mm. In the IRIS detector the strips are non-overlapping, but are oriented at an angle of 60 degrees to the neutron beam giving a neutron path length of 0.8 mm. This arrangement has a much lower ZnS scintillator density compared with the SANDALS detector elements and a corresponding improvement in the collection of the scintillator light. In the BRICK detector the scintillator elements are arranged

as a smaller version of the SANDALS sandwich. Each element is made up of 4 strips of ZnS scintillator sandwiched between crown glass strips of similar dimensions giving an average neutron path length of 1.6 mm. The number of detectors of each type operational on ISIS together with their characteristics are given in Table 1.

Detector characteristics are largely determined by the magnitude of the neutron path length, p, through the scintillator elements. For SANDALS where p is high, neutron detection efficiency is relatively high, even at 10 eV. Although gamma sensitivity and intrinsic detector background is also high, this is an acceptable compromise for SANDALS requirements. In the IRIS detectors, p is low and neutron efficiency at 1 Angstrom is correspondingly low. However IRIS operates at wavelengths of 3 - 10 Angstroms and in this region neutron detector efficiency is relatively high. Full advantage is therefore obtained from the excellent gamma rejection and low intrinsic detector background available with this detector geometry. These characteristics are comparable with the best $^{3}$He detectors. The BRICK detectors exhibit characteristics intermediate between these extremes with a relatively high neutron detection efficiency for a detector which is only 5 mm deep.

## FIBRE COUPLED LINEAR ZINC SULPHIDE SCINTILLATOR DETECTORS

A detector system has been designed specifically for data collection from samples in the Paris/Edinburgh high pressure cell. Four modules of this type have been installed on POLARIS and a further two modules are operational on TEST BEAM. All six modules have been operating since November 1992. Each module has 36 elements, 300 mm high and 3.5 mm wide, connected by a fibre optic array to 9 PMT`s. The fibres are arranged in a 2CN code so that any pair of PMT` outputs uniquely specifies one of 36 detector elements. This is an extension of the detector design employed on the 90 degree HRPD detector described previously, ref. 3. In this detector 6 modules are vertically stacked one on another. Each module has 66 scintillator elements 200 mm high and 3 mm wide. The scintillators are again viewed by a fibre optic 2CN coded array in which pairs of outputs from 12 PMT`s specify one of 66 elements. The characteristics of these detectors are very similar and given in Table 1.

Neutron detection efficiencies are 30% - 36% at 1 Angstrom with gamma sensitivities and intrinsic detector backgrounds only marginally worse than those of the IRIS detector or the standard 10 atmosphere $^3$He proportional counter. Since only one electronic channel is needed per 36/9 or 66/12 detector elements this gives rise to a relatively cost effective detector system.

## FIBRE COUPLED AREA ZINC SULPHIDE SCINTILLATOR DETECTORS

The 4096 SXD detector is a fibre coupled two dimensional ZnS scintillator detector. The detector consists of a single sheet of ZnS scintillator, 192 mm x 192 mm, which is located onto the front of a mylar light guide grid. The grid divides the detector into a 64 x 64 array of pixels, each of 3 mm x 3 mm resolution. Each pixel is viewed by four 1 mm diameter fibre optic light guides arranged in a quad coincident code, Figure 3. In this manner 4096 detector pixels are encoded by 32 PMT's and associated electronics. This detector has been in continuous use on SXD since April 1992 and has become the principle means of data collection on this instrument. Detector characteristics are given in Table 1 and show exceptionally low gamma sensitivities, low intrinsic detector backgrounds and moderate pulse pair resolution. There are a number of other interesting features regarding this detector. The active detector element is only 0.4 mm thick and thus a short 250 mm sample to detector distance may be used on SXD without causing a parallax error and enabling a large solid angle to be covered. The fibre coded array ensures that detector resolution is linear across the whole of the detector and there is no degradation of resolution at the detector edges. Position sensitivity is achieved by the disposition of the fibre optic array , complex encoding electronics is largely avoided and detector stability is more easily achieved.

## SINGLE GLASS SCINTILLATOR DETECTORS

A new glass scintillator detector is under construction for the Electron Volt Spectrometer, eVS. eVS measures neutron energy transfers between 4 and 30 eV and requires efficient neutron detectors within this range. Due to the high neutron flux on the detectors pulse pair

resolution is also a detector characteristic of prime importance. The eVS detector consists of four 8 element detector modules. Each element contains a block of 200 mm x 25 mm x 10 mm GS20 scintillator glass purchased from Levy Hill Laboratory, ref. 4. Each block is viewed at the end of an aluminised mylar light guide by a single PMT. Thus the eVS detector is a directly viewed single glass scintillator detector. The detector characteristics are given in Table 1 where the high gamma sensitivity and high intrinsic detector background associated with a detector of this type are readily apparent. However, eVS uses a filter difference technique where these effects can be largely eliminated. Figure 4 shows time of flight spectra recorded on eVS using an experimental detector of this type compared with a 300 mm long 25 mm diameter 10 atmosphere $^3$He detector. Despite the larger area of the helium detector the glass scintillator count rate is 12 times that of the helium tube. This is a combination of an increase in detector efficiency and a reduction by a factor of two in the sample to detector distance, a feature made possible by the improved pulse pair resolution of the glass scintillator detector.

## FIBRE COUPLED LINEAR GLASS SCINTILLATOR DETECTORS

The back scattering detector of the High Resolution Powder Diffractometer, HRPD, has been described previously, ref. 5. Briefly it consists of six detector modules, each module containing 20 elements arranged in concentric annuli. The annuli of each module span radii of 70 mm to 370 mm perpendicular to the beam axis, with 15 mm resolution and an included angle of 45 degrees. Each element consists of two strips of GS20 glass 1 mm thick arranged one behind the other and connected to set of eight PMT's by a fibre optic array arranged in a 3CN code. The concentric detector geometry approximates the Debeye Scherrer cones of diffraction and largely eliminates geometrical contributions to the profile line shape. Detector modules of this type have been operational on ISIS since December 1984 and detector characteristics are given in Table 1. Although this detector has good neutron detection efficiency at wavelengths greater than 1 Angstrom and has produced some outstanding results on HRPD, detector performance is limited by the high gamma sensitivity and high intrinsic detector background.

## FORTHCOMING DETECTORS

Currently under development is a fibre coupled zinc sulphide detector to replace the high angle glass scintillator detector on HRPD. This new detector will exhibit lower gamma sensitivity and lower intrinsic background associated with ZnS. The arrangement of the scintillator elements to match the Debye Sheere cones of diffraction has been maintained while the spatial resolution has been improved from 15 mm to 5 mm. The scintillator light guide and the precise scintillator geometry has been modified to increase the neutron detection efficiency compared with the fibre coupled ZnS HRPD 90 degree and pressure cell detectors. The fibre code is arranged to enable data to be collected separately from two orthogonal strips across the detector if so desired. This will yield improved spatial resolution in single crystal diffraction experiments on HRPD.

SANDALS is an ongoing detector project. A further 10 detector modules are expected to be operational this year, followed by 20 and 22 modules in the subsequent two years. SANDALS electronics design is undergoing a major overhaul. The amplifier discriminator/decoder and HT being made more compact, of less power consumption and relocated onto individual detector modules inside the detector block house. This removes the need for extensive cabling and racks, reduces the likelihood of electronic interference from pickup and maintains the detector electronics in a temperature controlled environment. Remote control of the detector HT and discriminator level is provided. Eventually these parameters will be under computer control which will not only facilitate detector set up but also provide a means of automatically checking detector performance.

A second ZnS fibre coupled two dimensional position sensitive detector is soon to be commissioned on the CRISP reflectometer. This detector has an active area of 50 mm x 100 mm which is divided into 440 pixels of 5 mm x 2.5 mm resolution and is decoded by 21 PMT's. Detector characteristics similar to the SXD 4096 detector are anticipated.

## SUMMARY OF DETECTOR PERFORMANCE

In general standard $^3$He proportional counters exhibit high detection efficiencies for thermal neutrons, very low gamma sensitivity and low intrinsic detector backgrounds. Choice of spatial resolution and geometry is limited, pulse pair resolution is moderate and the cost is relatively high.

Two dimensional position sensitive gas technology can provide high spatial resolution, but pulse pair resolution is low and the cost is high. To achieve an acceptable neutron detection efficiency the gas pressure inside the detector is high which necessitates a thick detector window, 10 mm in the Ordella 2250n detector. Detector depth can be significant for some instrument applications leading to position errors due to parallax while non linearity in position sensitivity at the detector edges can also degrade the data. In the rise time encoded position sensitive detectors, breakdown in the high resistive wire coating may lead to a maintenance problem which can only be solved at the site of manufacture.

Scintillator technology offers the opportunity to exploit a different set of detector characteristics from those currently available with gas technology. The most obvious difference is the ability to exploit a more flexible detector geometry as in the HRPD back scattering glass scintillator detector. Neutron detector efficiency in the epithermal region, detector resolution and cost can be emphasised as in the case of SANDALS. Neutron detection efficiency and pulse pair resolution are the major requirements in the eVS glass scintillator detector. The HRPD 90 degree and the Paris/Edinburgh pressure cell ZnS fibre coupled detectors are cost effective detectors which maintain low gamma sensitivities and low intrinsic detector backgrounds. The two dimensional position sensitive ZnS scintillator detectors offer good spatial and pulse pair resolution, insignificant distortions due to parallax, while maintaining low gamma sensitivity and low intrinsic detector background.

In considering the detector requirements of a particular instrument it is necessary to optimise a variety of characteristics. To date no single technology is superior in every respect.

## FUTURE DETECTOR DEVELOPMENTS

Improvements in gas technology must centre around a more flexible geometry and a greater pulse pair resolution. It is possible that both these needs can be met by the development of the gas micro strip detector first introduced by Oed in 1988, ref. 6. Solid state technology which has been successful in so many detector technologies has yet to make a major impact in neutron detector systems. Much development is needed to determine whether it is possible to incorporate neutron absorbing materials into solid state detectors in sufficiently high concentrations to obtain viable neutron detector systems. Scintillator technology requires faster, more efficient scintillators which nevertheless maintain the excellent low gamma sensitivity and low intrinsic detector background associated with ZnS.

To meet the needs of future spallation sources which will generate much higher neutron fluxes some or all of these technologies will have to be developed in the near future.

## REFERENCES


**1.** Ordela, inc., 139 Valley Court, Oak Ridge, Tennessee 37830, USA.

**2.** Johnson, M.W. et al., These proceedings.

**3.** Davidson, P.L. Johnson, M.W. and Rhodes, N.J. Proceedings of the 11th meeting of International Collaboration on Advanced Neutron Sources, KEK Report 90-25, (1990) 957.

**4.** Levy Hill Laboratories Ltd, 5 Sheffield House, Fieldings Road, Cheshunt, Herts. EN8 9TJ

**5.** Davidson, P.L. Rhodes, N.J. and Wroe, H. Proceedings of the 8th Meeting of International Collaboration on Advanced Neutron Sources, RAL Report RAL-85-110 (1985) 725.

**6.** Oed, A. Nucl. Instr. and Meth. A263 (1988) 351.

| INSTRUMENT | DETECTOR | MODULES x ELEMENTS | TYPE | ELEMENT SIZE/MM | NEUTRON EFFICIENCY | GAMMA SENSITIVITY | QUIET COUNT/hr | PPR/us |
|---|---|---|---|---|---|---|---|---|
| MARI | HELIUM | 500 x 1 | Gc | 300 x 25 dia. | 70 % at 1 A | 10 ( EXP - 8 ) | 5 | 2.5 |
| SANDALS | SANDALS | 23 x 20 | SZLD | 200 x 10 | 1.7 x std He at 10 eV | 10 ( EXP - 8 ) | 360 | 2.5 |
| POLARIS | BRICK | 4 x 20 | SZLD | 150 x 5.7 | 45 % at 1 A | 3 x 10 ( EXP - 8 ) | 23 | 2.5 |
| TEST BEAM | BRICK | 2 x 20 | SZLD | 150 x 5.7 | 45 % at 1 A | 3 x 10 ( EXP - 8 ) | 23 | 2.5 |
| IRIS | IRIS | 2 x 51 | SZLD | 52 x 12 | 36 % at 1 A | 10 ( EXP - 8 ) | < 2 | 2.5 |
| HRPD | HRPD 90 DEG. | 6 x 66 | SZLF | 200 x 3.0 | 36 % at 1 A | 10 ( EXP - 7 ) | 3 to 10 | 2.5 |
| POLARIS | PRESS. CELL | 4 x 36 | SZLF | 300 x 3.5 | 32 % at 1 A | 10 ( EXP - 7 ) | 12 | 2.5 |
| TEST BEAM | PRESS. CELL | 2 x 36 | SZLF | 300 x 3.5 | 32 % at 1 A | 10 ( EXP - 7 ) | 12 | 2.5 |
| SXD | SXD | 1 x 4096 | SZTF | 3.0 x 3.0 | 20 % at 1 A | < 10 ( EXP - 8 ) | 0.6 | 2.5 |
| eVS | eVS | 4 x 8 | SGsD | 200 x 25 | 3 x std He at 6 eV | 2 x 10 ( EXP - 2 ) | 150 / min. | 0.3 |
| HRPD | HIGH ANGLE | 6 x 20 | SGLF | 45 deg x 15 | 60 % at 1 A | 10 ( EXP - 3 ) | 0.2/min/cm2 | 0.05 |

TABLE 1. Detector characteristics of scintillator detectors operational on ISIS compared with characteristics of MARI 3He gas proportional counters. Gc = gas proportional counter, S = scintillator, Z = Zinc Sulphide, L = linear, D = directly coupled, F = fibre coupled, T = two dimensional, G = glass, s = single.

| INSTRUMENT | DETECTOR | MODULES x ELEMENTS | TYPE | ELEMENT SIZE / MM | ACTIVE DIMS. L x W x D / MM | NEUTRON EFFICIENCY | WINDOW THICKNESS / MM | PPR / us |
|---|---|---|---|---|---|---|---|---|
| CRISP | ORDELA 1202N | 1 x 100 | GcL | 50 x 2 | 200 x 50 x 25 | 45 % at 1 A | 3.8 | 10 |
| SXD/TEST | ORDELA 2250N | 1 x 16 364 | GcT | 2 x 2 | 254 x 254 x 25 | 32 % at 1 A | 10 | 10 |
| LOQ | ORDELA 2651N | 1 x 4 096 | GcT | 10 x 10 | 640 x 640 x 44 | 22 % at 1 A | 12 | 10 |

TABLE 2. Detector characteristics of Ordela rise time encoded position sensitive detectors operational on ISIS. Detector type specification is as given in Table 1.

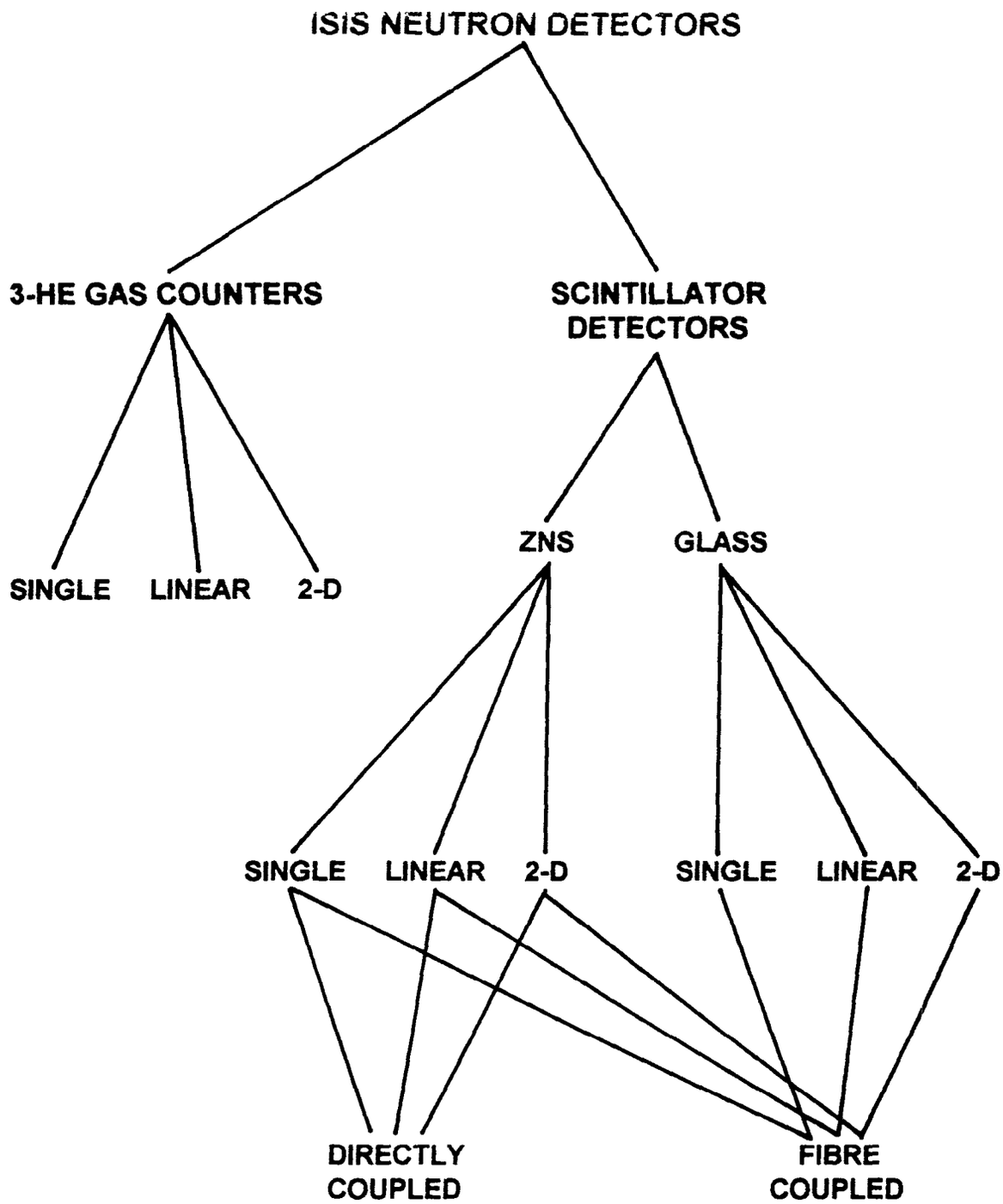


**FIGURE 1. Neutron detector types operational on ISIS**

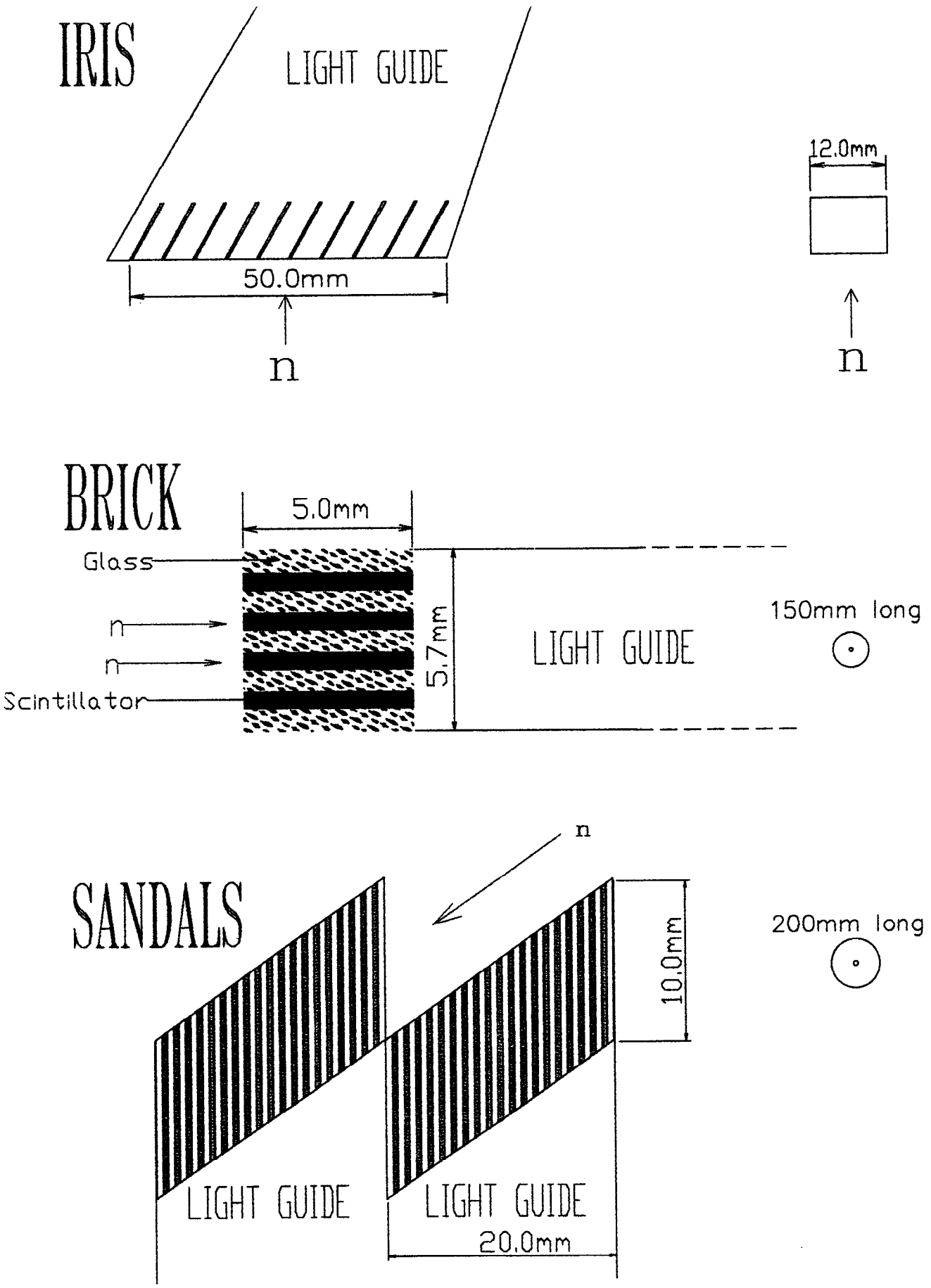


**FIGURE 2.** Scintillator arrangement in the IRIS, BRICK and SANDALS directly coupled linear Zinc Sulphide scintillator detectors.

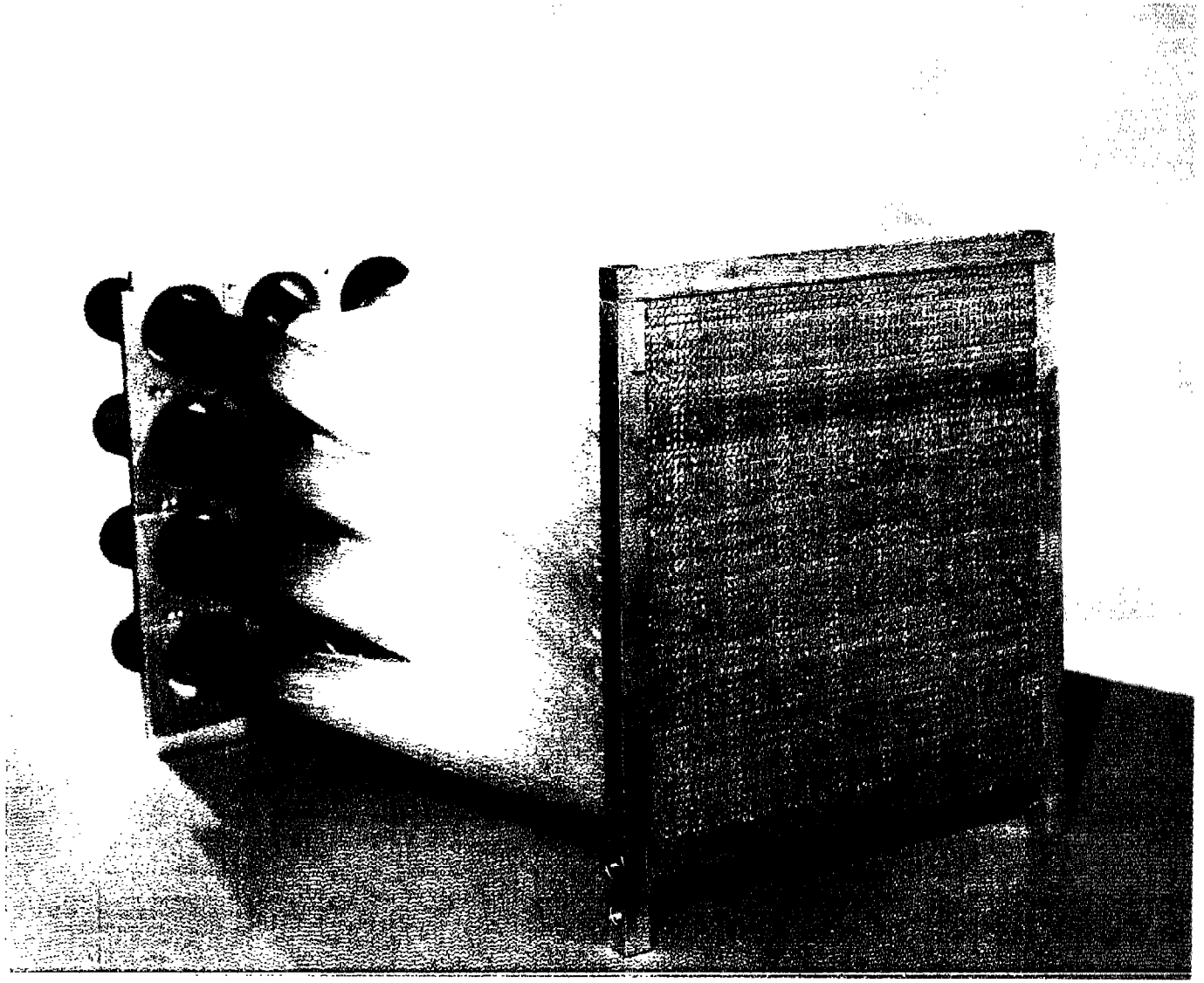

91 FC 5020

**FIGURE 3.** The front end of the SXD 4096 detector showing the mylar light guide grid and the fibre optic array.

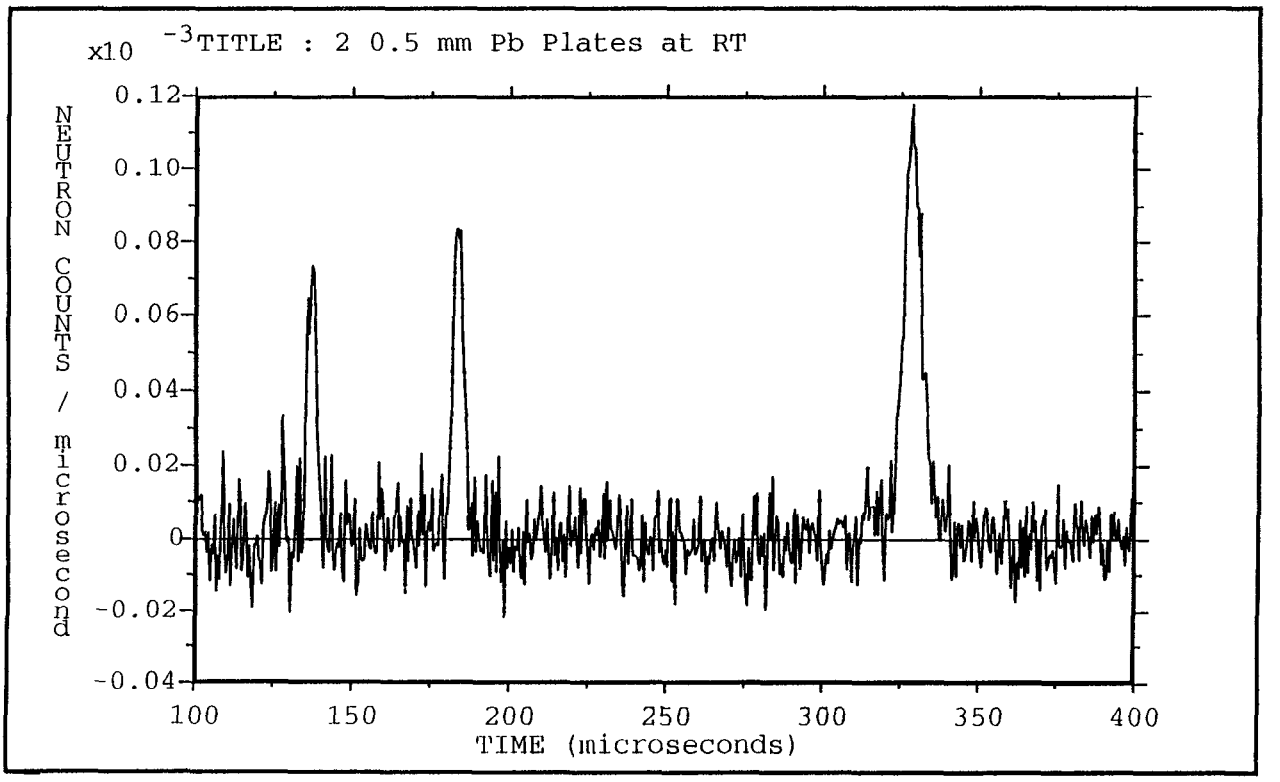


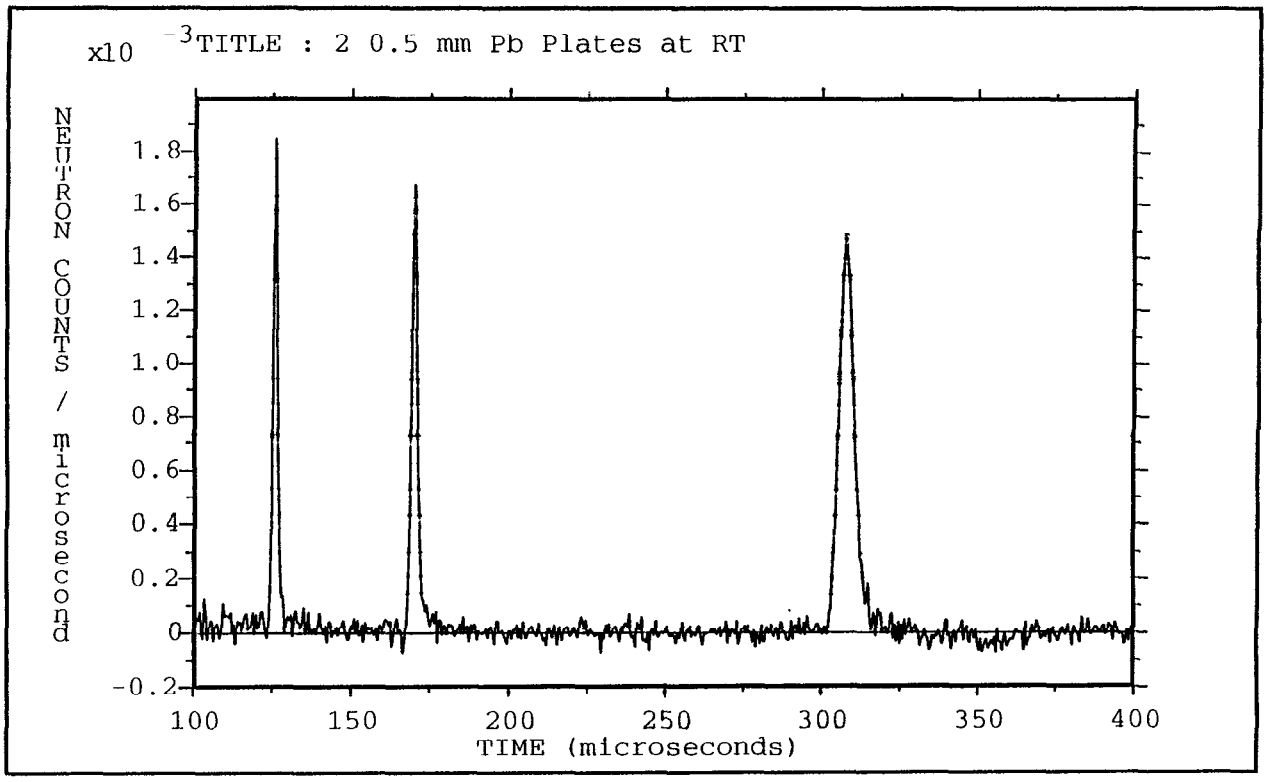


**FIGURE 4.** Uranium foil resonances recorded on eVS from a lead sample using a foil difference technique. The upper spectrum is obtained using a 300 mm long 25 mm diameter 10 atmosphere $^3$He detector, the lower spectrum is from a 200 mm long 25 mm wide GS20 glass scintillator detector.

# THE SCINTILLATION PSD JULIOS AND ITS USE IN TOF-DIFFRACTOMETRY AT ISIS

W. Schäfer, E. Jansen, A. Szepesvary, R. Skowronek, G. Will

Mineralogisches Institut, Universität Bonn, Poppelsdorfer Schloß, D-53115 Bonn, Germany

and

R. Reinartz, K.D. Müller

Zentrallabor für Elektronik, Forschungszentrum (KFA), Postfach 1913, D-52425 Jülich, Germany

## Abstract

JULIOS is a plane linear position-sensitive neutron detector based on a modified Anger technology and aimed at applications in time-of-flight experiments at pulsed spallation sources. Three versions differing by the type of photomultipliers used are developed: (1) standard version of 680 x 25 $mm^2$ sensitive area and 2.3 mm spatial resolution, (2) small version of 200 x 20 $mm^2$ size and 1.0 mm resolution, and (3) large version of 940 x 75 $mm^2$ size and 3.5 mm resolution; resolution values are based on the light output of 1 mm $^6$Li glass scintillator. The use of other neutron scintillators like $^6$LiI(Eu) and $^6$LiF/ZnS;Ag is discussed.

Concept and design of the JULIOS electronics including provisions for long-term stability of the detector, and high resolution timing modules to synchronize detector activities with the time structure of the neutron source, are described. Events are registered in 32 bit data words containing 12 bit position and 16 bit time information each. The detector can be operated as a standalone system controlled by an EISA-bus PC with the memory under the control of a 28 bit increment module; alternatively, it can be connected to the ISIS DAE.

The detector was tested under ISIS conditons in white beam angular dispersive time-of-flight diffractometry. A permanent installation of a JULIOS diffractometer at ISIS aimed at crystallographic and magnetic structure and texture research is envisaged.

## Introduction

JULIOS stands for 'JUelicher LInear Ortsauflösender Szintillationsdetektor'; it is a linear position-sensitive scintillation detector and it operates on the basis of a modified Anger technology [1]. In standard configuration, Li-6 scintillator glass is used as neutron absorber. The solid state absorber implies a rather thin detection zone of only 1 mm depth and simultaneously high sensitivity over the thermal wavelength spectrum. The scintillation detector is specially suited for applications in time-of-flight (TOF) technology at pulsed spallation sources. The JULIOS development had been started in Jülich originally in connection with the SNQ spallation source project. Design and construction were performed in collaboration between KFA Jülich and Bonn University.

In the meantime, eight JULIOS detector units have been built or are under construction for installation at conventional powder and texture diffractometers at steady state neutron sources. Besides the standard detector configuration we have developed two more types devoted for high resolution or high intensity application, respectively; the corresponding physical characteristics will be given in the next chapter. There is now a ten years experience with JULIOS in routine operation at the University Bonn service instruments at the FRJ-2 in Jülich (see [2] to [5]).

In 1990, an additional timer unit has been added to the JULIOS electronics, in order to run the position-sensitive detector also in a time resolved mode as a standalone system. We have performed test measurements in TOF technique under spallation source conditions at ISIS [6]. First results from d-spacing patterns obtained with JULIOS in a short term experimental setup at the testbeam facility at ISIS have been reported in [7]. Those results encouraged us to do further experiments at ISIS with JULIOS positioned in forward-, 90°- and backscattering diffraction geometry. These measurements were done in 1992 at TEST and ROTAX instrument positions. The ROTAX spectrometer at ISIS [8] being currently under commissioning, is equipped with one unit of the JULIOS PSD; test results of ROTAX are reported in a separate paper during this conference by H. Tietze-Jaensch et al. [9].

JULIOS installations at both a steady state reactor and a pulsed spallation source were used for a direct comparison of the efficiency of conventional diffractometry with monochromatic neutrons and of TOF diffractometry with the sample positioned in the primary white beam, respectively [10]. Angle dispersive TOF-diffraction in a pulsed beam is an efficient technology to exploit the thermal neutron spectrum. In constant wavelength diffraction at a continuous source, monochromatization reduces the utilization rate of the thermal neutron beam to about one percent. The PSD can only serve for an optimum detection of this small fraction. In pulsed white beam TOF-diffractometry, however, principally the total thermal spectrum can be used simultaneously; and the crucial element for the potential of the diffractometer is the PSD-system and its electronic ability for high resolution time encoding and count rate capability.

## JULIOS construction

Neutrons are absorbed via the $^6Li(n;\alpha)$-reaction in a transparent $^6Li$ containing solid state scintillator of about 1 mm thickness. Photons emitted by each capture event are transmitted and confined into a cone inside a plane rectangular light

disperser, which is arranged behind the scintillator and in front of the photocathodes of a linear row of 24 photomultipliers (PM) (Fig. 1).

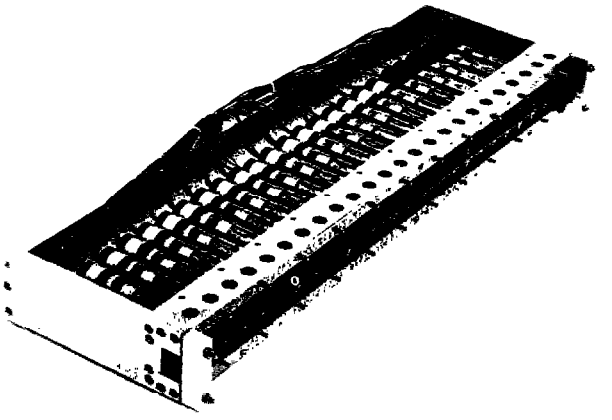

Fig. 1: JULIOS detector head (without light-proof box) in its standard version

The position analysis of an absorbed neutron is based on the determination of the light distribution on three adjacent PMs; for physical and constructive details see [1] and [2]. The digitized PM signals are processed in a dedicated hardwired computer to calculate the final position by means of special lookup tables; for electronical details see [3] and [11]. The spatial resolution of the detector is limited due to the statistics in distributing light on the PMs and in the light-to-photoelectron conversion. While the conversion rate is an intrinsic property of the PMs, the statistics of light distribution can be influenced by the total light output of the neutron scintillator and by the size of PM cathodes and suitable dimensions of the disperser. Model calculations were performed by Schelten and Kurz [12] to optmize the resolution function of the detector. The shape of the resolution function can be described by a gaussian function. The spatial resolution is given by the full width at half maximum (FWHM) according to the empirical formula

$$\mathrm{FWHM} = c \frac{a}{\sqrt{N}} \qquad (1)$$

where N is the total number of photoelectrons per capture event and a is the linear size, i.e. the separation of the adjacent PMs; c is a constant (see also [13]).

**Neutron scintillators**

The total number of photoelectrons depends strongly on the light output of the scintillator. By default, the JULIOS detector is equipped with $^6$Li scintillator glass manufactured by Levy Hill Ltd. For details of $^6$Li scintillating glasses we refer to papers of A.R. Spowart [14,15]. The glass thickness used in the JULIOS detector is 1.0 mm with absorption efficiencies of about 65% and 85% for 1 Å and 2 Å neutrons respectively. The Ce doped $^6$Li glass creates about 4000 photons of 400 nm wavelength per neutron capture event and at least 200 photoelectrons are finally generated in the photocathode of the PM. Based on these values the linear spatial resolution of the JULIOS detector can be roughly estimated to about one tenth of the diameter of the PM tubes. This is in fair agreement with experimental results of 2.3 mm spatial resolution for the standard JULIOS unit, which is equipped with cylindrical PMs of 28 mm cathode diameter.

In the pulse height spectrum of $^6$Li-glass, there is a certain overlap of neutron pulses with gamma pulses. A gamma quantum, which is absorbed by photoeffect in the interior of the scintillator, produces the same amount of light, provided it has an energy of more than 1 MeV. Although the JULIOS electronics (see next chapter) provides for pulse height discrimination, a rest gamma sensitivity of about $2 \times 10^{-4}$ has been measured for the $^6$Li glass. It should be mentioned, however, that the gamma sensitivity depends strongly on the purity of the scintillator glass as was experimentally shown on the example of the KG- and GS-type glasses [3]. Other neutron scintillator materials are desirable with respect to higher light output and improved gamma discrimination. By comparison, the light output of the neutron glass scintillator ammounts to only 2% of the light output of a NaI(Tl) crystal for gamma rays. There are two other neutron scintillators, which have been and are being tested with the JULIOS detector.

One is $^6$LiI(Eu). The light output for neutrons was found to be twelve times larger with single crystalline $^6$LiI than with $^6$Li-glass; therefore a $\sqrt{12}$ better resolution is achieved. Another advantage of $^6$LiI is that this detector is practically insensitive to gamma rays of energy below 3.5 MeV due to more favourable conditions in the pulse height spectrum [16]. However, $^6$LiI is highly hygroscopic and therefore encapsulation is required. We have built a JULIOS prototype detector with an encapsulated $^6$LiI single crystal scintillator produced by Harshaw. Technical details are described in [11]. A spatial resolution of 0.5 mm was measured. Due to its difficult technical handling the use of $^6$LiI is restricted to detector dimensions of about 100 mm.

$^6$LiF/ZnS;Ag is another neutron scintillator of rather simple technical handling and without any size restrictions for the detector. $^6$LiF-ZnS;Ag is known for a much higher light production during the scintillation process compared to $^6$Li glass. The problem here is the reduced transparency of the material in getting the light out. In the very beginning of the JULIOS development we did comparative tests with both the $^6$LiF/ZnS;Ag and $^6$Li glass scintillators with the result of a poorer photoelectron production by a factor of 10 in the case of $^6$LiF/ZnS;Ag. Encouraged by different experiences in the scintillation detector development at RAL more recently [17], we are about to do new tests with the JULIOS detector using $^6$LiF/ZnS;Ag sheets of 0.1, 0.4 and 0.6 mm thickness. It is an essential advantage of the JULIOS construction that the scintillator material can be exchanged very easily.

**Different types of photomultipliers**

Besides the neutron scintillator the characteristic properties of the JULIOS detector are determined by the photomultipliers. Three different types of JULIOS have been constructed (Table 1). They differ by the PM tubes installed in the detector head (Fig. 2). Position resolution and size of sensitive detector window depend on the size of PM photocathodes. Development started with PMs of circular photocathodes of 28 mm diameter (standard-type A in Table 1 and Fig. 2). When using PMs of circular shape there is a conflict between two aims of the detector: spatial resolution and effective detector height. In normal powder diffractometry spatial resolution should be as small as possible for optimum peak separation and the detector should be rather high in order to profit from the vertical divergence of the neutron beam for intensity reasons. According to equ. (1) spatial resolution depends linearily on the PM diamter a, thus limiting the

detector height. Type A PMs are a compromise between good resolution and reasonable detector height (see Table 1).

Table 1: Technical and physical specifications of three JULIOS types constructed with different photomultipliers.

| Specifications | type A | type B | type C |
|---|---|---|---|
| scintillator-material (Levy Hill) | 6-Li-Glas | 6Li-Glas | 6-Li-Glas |
| thickness of scintillator (mm) | 1.0 | 1.0 | 1.0 |
| detector form | plane | plane | plane |
| number of photomultipliers | 24 | 24 | 24 |
| type of photomultiplier (Hamamatsu) | R268 | R2937 | R1612 |
| form of photocathodes | circular | rectang. | rectang. |
| effective detector length (mm) | 682 | 200 | 940 |
| effective detector height (mm) | 25 | 20 | 75 |
| max. 2Θ-coverage in 1.0 m distance (°) | 38 | 11 | 50 |
| max. 2Θ-coverage in 1.5 m distance (°) | 26 | 7 | 34 |
| linear spatial resolution (mm) | 2.3 | 1.0 | 3.5 |
| gamma sensitivity | $< 10^{-4}$ | $< 10^{-4}$ | $< 10^{-4}$ |

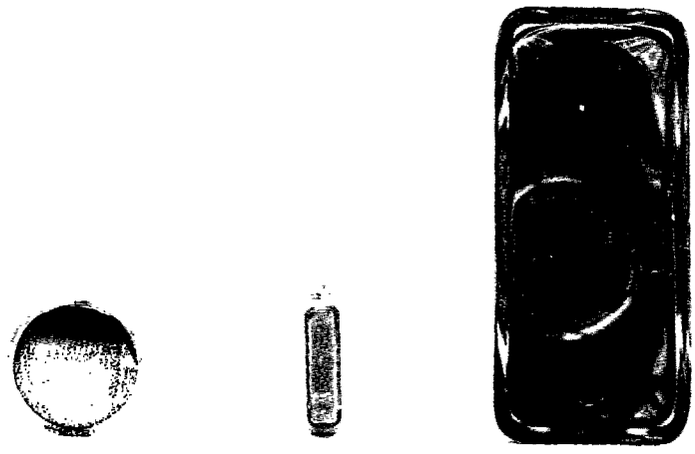

Fig. 2: View on the photocathodes of three PMs used for JULIOS type A (left), type B (middle) and type C (right); compare Table 1.

Advanced PM developments resulted in a large variety of PMs with also rectangular shaped photocathodes matching special detector requirements. Two different rectangular types are used (Table 1 and Fig. 2). PM type B enabled the construction of a higher resolution version of JULIOS; 1.0 mm is obtained with the light output of the normal $^6$Li glass scintillator. Type C being composed of PMs with photocathodes of 40 x 80 mm cross section is a wide window version with still reasonable resolution; the effective detector height is enlarged by a factor 3 in comparison with type A.

**Electronic signal processing and stabilisation**

The signal processing of the JULIOS detector with respect to position computation can be followed by the blockdiagram depicted in Fig. 3. PM output signals, fed into voltage preamplifiers followed by a shaping amplifier, are preselected according to highest signals and multiplexed into four ADCs. The ADC signals

are processed in a dedicated hardwired computer (Q-calc in Fig. 3) to perform the position analysis. Position computation of an event is performed stepwise by (1) selection of those three PMs yielding the largest output signals, (2) calculating the center of gravity Q with the digitized output signals by using a fast look-up table scheme, and (3) correcting Q according to nonlinearities and inhomogenity of either scintillator or photocathode by means of a special look-up table. Position computation is performed within 70 ns. Look-up tables are generated once by a calibration measurement. For further details we refer to [11].

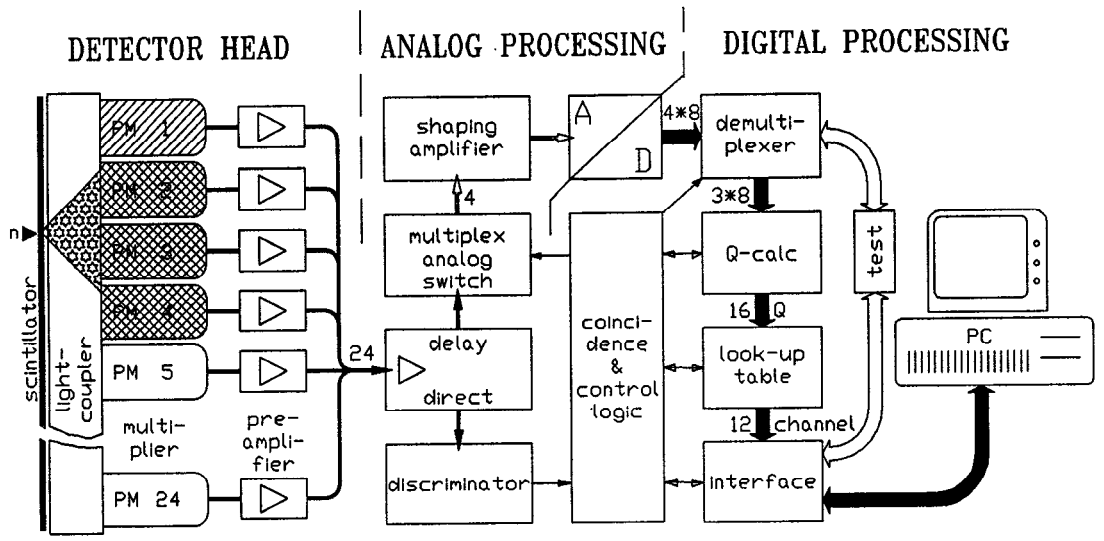


Fig. 3: Blockdiagram of the signal processing of the JULIOS electronics.

Long-term stability of the JULIOS detector is achieved by stabilising the gains of the PMs, knowing that drift rates of about 10% within several days are possible. Gain stabilisation is achieved by adjusting the PM high voltage according to reference light pulses, which are distributed via light guides from a LED to the PMs. The cathodes of the PMs are connected to high voltage DACs for changing the gain. The stabilisation runs completely automatic and takes about half a minute for the whole detector unit. For details of the gain stabilizing circuitry we refer to [18]

**Timing module and interface**

For operating the detector in a time resolved mode, the JULIOS electronics is supplemented by a new timing module to synchronize the detector activities with the time structure of the neutron source. High flexibility in timing is achieved by using XILINX devices, which are programmable to assume various desired functions. XILINX devices in combination with a programmable timing generator allow those timer specifications listed in the central box of Fig. 4 with respect to channel width, delay and window. Detector events can electronically resolved up to 12 bit position and 16 bit time information each; the configuration of position and time addresses on the MUX-module (Fig. 4) can be chosen arbitraryly.

The electronic concept provides for two alternatives. One is the operation of JULIOS as a standalone system without any mainframe computer, the other is the provision of a well defined interface to central data acquisition systems like DAE at ISIS. The realisation of this concept can be seen in Fig. 4.

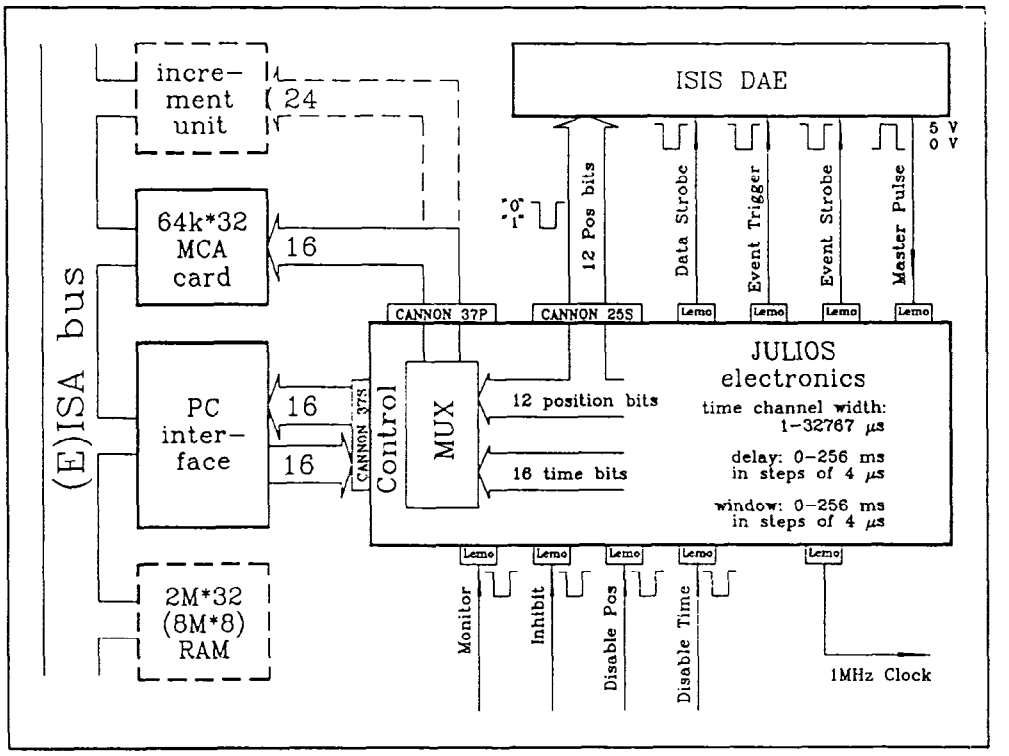


Fig. 4: Interface to JULIOS electronics

As a standalone system the JULIOS electronics is connected to a 32 bit PC with EISA-bus architecture. The PC is equipped with specially developed interface and data storage devices. Events are registered via a 24 bit increment module and stored in 2M*32 PC-RAM. Additonally, there is a 16 bit multichannel analyser card of 64K*32 capacity to be used as on-line monitor during the experiment. The 16 bit may be variably configurated for position and time information.

When connecting the JULIOS electronics to DAE at ISIS, only the 12 bit positon information has to be transferred and to be synchronized to the DAE timing. The corresponding interface provides three outputs: (1) event trigger to define the arrival time of an event at the detector, (2) event strobe to define the time of an event being in a pipeline for position analysis, and (3) data strobe to transfer the positon synchronized to the external DAE time information.

## TOF-diffractometry with JULIOS at ISIS

A detector like JULIOS performing simultaneous position and time encoding of detected events can be used favourably for angular dispersive TOF diffractometry at a pulsed neutron source. The pulsed beam diffractometer consists of only sample and detector device; the sample is positioned directly in the primary beam and no further mechanical components like monochromator or chopper are needed. Test measurements have been performed on standard materials like mica, quartz, corundum and nickel (Fig. 5); we refer to [6,7,10]. A JULIOS type diffractometer is designed to consist of three detector units, which are positioned under fixed scattering angles in forward-, 90°- and backscattering geometry, respectively. A total flight path of about 20 m is envisaged; the intensity spectrum of every ISIS neutron frame can be utilized. d-spacings to be analysed lie between about 0.3 and 30 Å and d-spacing resolution is within $1 \times 10^{-3}$

and 5 x $10^{-2}$, respectively. The instrument can be accomodated by opening up the downstream end of an existing ISIS beam line. The diffractometer is aimed at crystallographic and magnetic structure and at texture research.

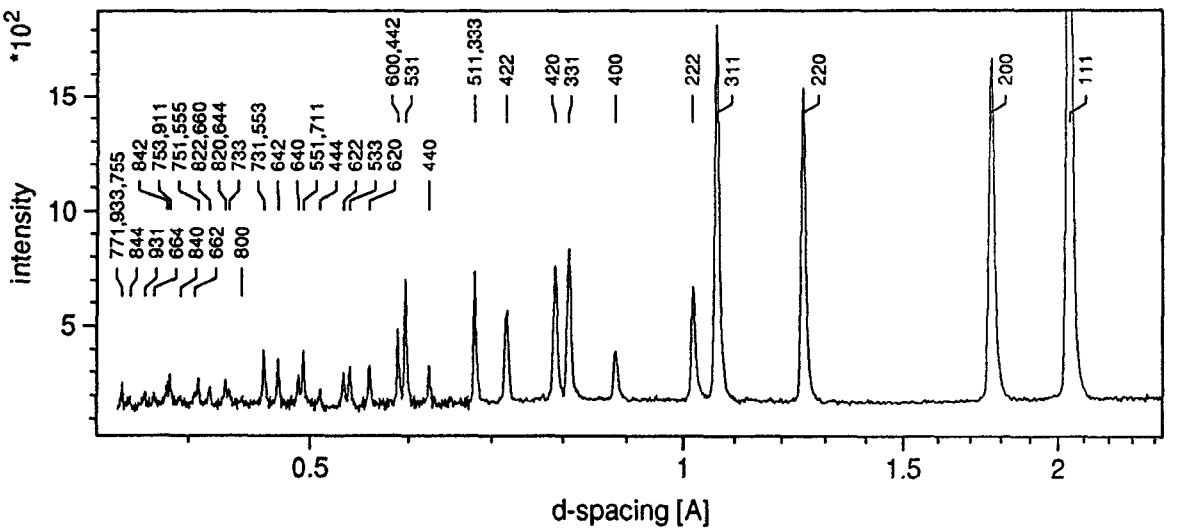


Fig. 5: d-spacing pattern of Ni, which was contained in a V-can of 11 mm diameter. The total neutron flight path up to the JULIOS detector was about 16 m. Detector window: $\Delta 2\Theta$ from 136.1° to 152.9°, $\Delta\lambda$ from 0.675 to 1.344 Å. The detector was operated in a 8 bit mode for time and position information each.

*Acknowledgement*: The detector project is funded funded by the German Federal Minister for Research and Technology (BMFT) under contract no. 03WI3BON.

**References**

[1] J. Schelten, R. Kurz, I. Naday, W. Schäfer, Nucl. Instrum. Meth. 205 (1983) 319.
[2] W. Schäfer, E. Jansen, F. Elf, G. Will, J. Appl. Cryst. 17 (1984) 159.
[3] E. Jansen, W. Schäfer, A. Szepesvary, G. Will, R. Kurz, Physica B 156 & 157 (1989) 584.
[4] W. Schäfer, P. Merz, E. Jansen, G. Will, Acta Cryst. A 46 Suppl. (1990) C-407.
[5] W. Schäfer, P. Merz, E. Jansen, G. Will, Textures and Microstructures 14-18 (1991) 65.
[6] E. Jansen, W. Schäfer, A. Szepesvary, G. Will, R. Reinartz, K.D. Müller, H. Tietze, U. Steigenberger, Physica B 180 & 181 (1992) 917.
[7] W. Schäfer, E. Jansen, R. Skowronek, G. Will, K.S. Knight, J.L. Finney, Nucl. Instrum. Meth. in Phys. Research A317 (1992) 202.
[8] H. Tietze, W. Schmidt, R. Geick, Physica B 156 & 157 (1989) 550.
[9] H. Tietze-Jaensch, W. Schmidt, R. Geick, this report
[10] W. Schäfer, E. Jansen, G. Will, J. Appl. Cryst., in print
[11] R. Kurz, K.D. Müller, J. Schelten, A. Szepesvary, W. Schäfer, G. Will, IEEE Trans. on Nucl. Science 35 (1988) 78.
[12] J. Schelten, R. Kurz, Proc. Conf. Position-Sensitive Detection of Thermal Neutrons, eds. P. Convert, J.B. Forsyth (Academic Press, London) 1983, p 203.
[13] M. Heiderich, R. Reinartz, R. Kurz, J. Schelten, Nucl. Instrum. Meth. in Phys. Research A305 (1991) 423.
[14] A.R. Spowart, Nucl. Instrum. Meth. 135 (1976) 441.
[15] A.R. Spowart, Nucl. Instrum. Meth. 140 (1977) 19.
[16] R. Kurz, J. Schelten, Proc. Conf. Position-Sensitive Detection of Thermal Neutrons, eds. P. Convert, J.B. Forsyth (Academic Press, London) 1983, p 192.
[17] P.L. Davidson, M.W. Johnson, N.J. Rhodes, Proc. ICANS-XI, eds. M. Misawa, M. Furusaka, H. Ikeda, N. Watanabe (KEK-report 90-25), 1991, p 957.
[18] I. Naday, W. Schäfer, Proc. Conf. Position-Sensitive Detection of Thermal Neutrons, eds. P. Convert, J.B. Forsyth (Academic Press, London) 1983, p 197.

**Linearity and Calibration of Charge-Division and Rise-Time Encoded Gas PSDs***

R. K. Crawford, P. Thiyagarajan
Argonne National Laboratory, Argonne, IL 60439, USA
J. Chen
Massachusetts Institute of Technology, Cambridge, MA 02139, USA

ABSTRACT

Both linear and area gas proportional counter position-sensitive detectors (PSDs) are used at IPNS, and both charge-division and rise-time encoding schemes are used for these detectors. Impedance mismatching at the detector ends can lead to nonlinearities in the analog portion of the encoding circuits, and digitization errors can lead to local channel-to-channel variations in the position encoding. Some of these nonlinearities can be eliminated by appropriate circuit design, and a calibration scheme has been devised to effectively eliminate the remaining problems. Both the circuit improvements and the calibration methods are discussed.

## I. Introduction

### Encoding Methods

Figure 1 provides a schematic representation of a one-dimensional position-sensitive detector and preamplifiers. Typical voltage pulses from the preamplifiers are also shown for a neutron detected at a particular position x. In "charge-division encoding" the remainder of the encoding circuitry is designed to determine the peak amplitudes $V_A$ and $V_B$ from the two ends of the detector, and to determine an "encoded position" x' for this event from the relationship

$$x' = \frac{V_B(x)}{V_A(x) + V_B(x)} L_D + x_o \tag{1}$$

where $L_D = x_B - x_A$ is the detector length, $x_A$ and $x_B$ are the positions of the detector ends, and $x_o$ is a constant which allows adjustment of the encoding offset. Figure 1 also shows the rise times $t_A(x)$ and $t_B(x)$ of the pulses at the two ends of the detector resulting from an event at position x. In "rise-time encoding" the rest of the encoding circuitry determines these "rise times", and the encoded position x' for this event is based on the relationship

$$x' = \frac{L_D}{2}\left[1 - \frac{t_B(x) - t_A(x)}{t_B(x_A) - t_A(x_A)}\right] + x_o \tag{2}$$

The normalizing constant $t_B(x_A) - t_A(x_A)$, which must be determined empirically, is roughly equal to the "detector time constant" RC, where R and C are the total resistance and capacitance associated with the detector electrode.

* Work supported by U.S. Department of Energy, BES, contract No. W-31-109-ENG-38.

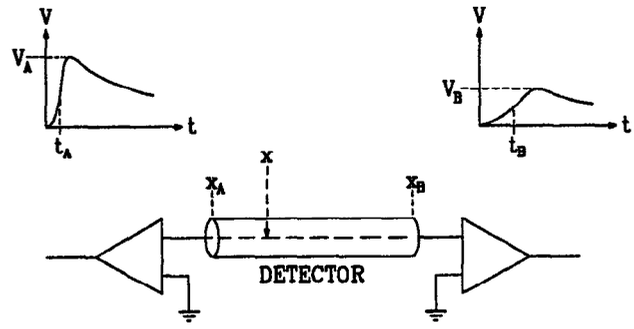


**Figure 1. Schematic representation of the charge-division and rise-time encoding schemes.**

Linearity Measurements

The linearity of the encoding for position-sensitive detectors can be readily assessed by a "flood pattern" measurement to determine the response of the detector to a uniform flux of neutrons. If $N_i$ is the number of counts measured in the encoded segment i when a detector with detection efficiency $\varepsilon$ is under uniform illumination $I_o$, then

$$N_i = I_o \varepsilon (x_{i+1} - x_i) \tag{3}$$

where $x_i$ and $x_{i+1}$ are the physical positions corresponding to the boundaries of the $i^{th}$ segment and statistical fluctuations have been ignored. Assuming $\varepsilon$ is constant, the variation of $N_i$ from segment to segment gives a direct measure of the variation in the ranges of physical detector positions which are mapped into the segments by the encoding process, and hence a direct measure of the differential nonlinearity of the detector encoding.

## II. Impedance Mismatching Problems and Solutions

Significant effort has been invested in understanding the position encoding for the PSDs on the GLAD (charge-division encoding) and SAD (rise-time encoding) instruments at IPNS. Figure 2 shows a typical flood pattern measured with one of the GLAD one-dimensional PSDs at an early stage in the development of the charge-division encoding electronics. The large nonlinearities seen near the detector ends affect roughly 20% of the total detector length. In an effort to understand these nonlinearities, the detector was modeled as a uniformly distributed resistance-capacitance (RC) line, and a computer program was used to numerically invert the Laplace transforms for the system comprised of this RC line and its associated analog encoding electronics (charge-sensitive preamplifiers and shaping amplifiers).[1] The calculated pulses at the end of the detector close to the event are large, and show the usual rapid rise to a peak value proportional to the charge collected on the capacitor at that end, followed by a slow decay through the associated discharging resistor. However, for x near either end of the detector, the

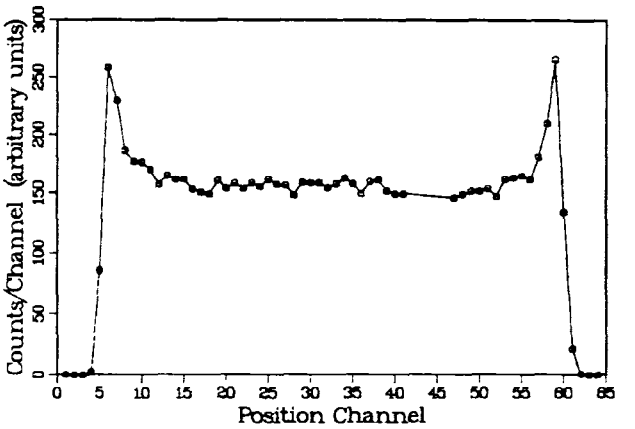


**Figure 2. Flood pattern measured with an unterminated GLAD linear PSD.**

pulses at the opposite end of the detector are very small, and are distorted from this expected behavior. These small pulses show the rapid rise proportional to the initial charge collected on the capacitor at this end, but this is followed by a substantial additional slow rise due to the discharge of the capacitor at the far end of the detector. While most of that charge is dissipated through the associated resistor, some of it is transferred back through the detector and appears on the capacitor at this end. (This can also be thought of as a "reflection" of part of the initial waveform from the impedance mismatch between the detector and the preamplifier.) The curve labeled "not terminated" in Figure 3 demonstrates this type of behavior. Since the remainder of the electronic circuitry senses the peak of the voltage pulse rather than just the initial rapidly-rising portion, this "double counting" of some of the charge causes the encoded voltage at the end away from the event to be higher than it would be based on the initial charge division alone. This effect disappears rapidly as the event position is moved away from the detector end; analytical expressions have been derived which quantitatively explain this behavior.[1]

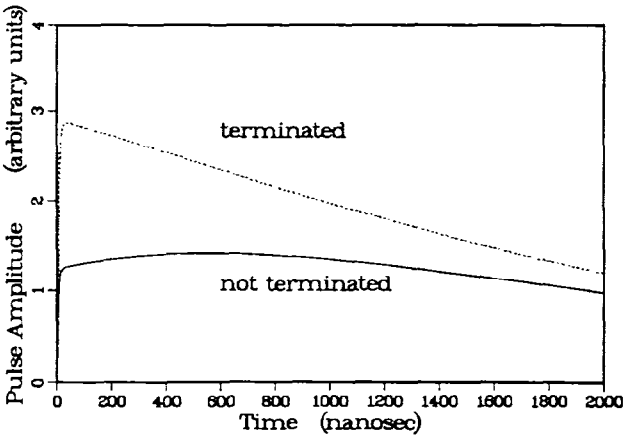


**Figure 3. Calculated pulse shape at end B of a GLAD detector for an event at $x=0.05L_D$ in the unterminated and terminated cases.**

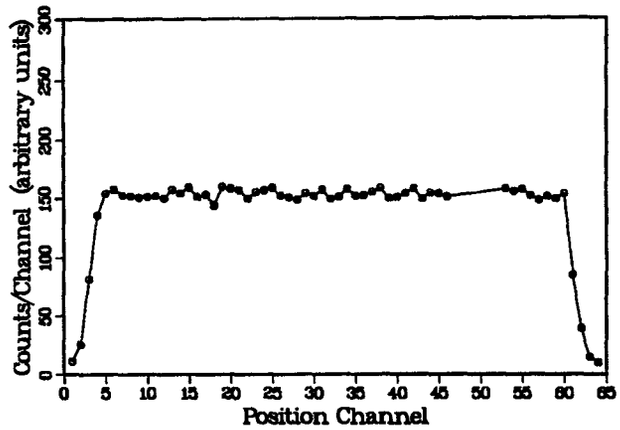


**Figure 4. Flood pattern measured for a GLAD detector after the termination was added.**

These calculations made clear a number of changes to the encoding circuitry which would partially or entirely alleviate the problem. These included using preamplifiers with much higher open-loop gain, using very fast pulse shaping electronics to filter out the slow-rising component, and simply adding small terminating resistors to the ends of the detector. In this latter procedure, which was adopted for the GLAD detectors, these resistors appear to the circuit as neutronically-inactive extensions of the detector. Then since the active regions of the "modified detector" are all farther away from the effective electronic ends of the modified detector, all the active regions fall within the portion where the encoding is linear. The curve labeled "terminated" in Figure 3 shows the calculated voltage pulse under these conditions, and indicates that while there is still some distortion of the pulse at the end away from the event, this distortion affects only the long-time portion of the pulse shape and does not affect the peak value. Figure 4 shows the almost completely linear flood pattern measured for a GLAD detector which has had such resistors added.

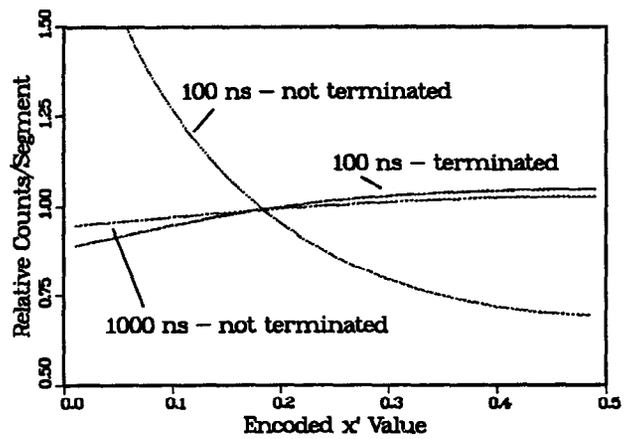


**Figure 5. Calculated flood patterns for rise-time encoding with different pulse shaping times and different types of termination. Because of symmetry, only half of the detector is shown. $L_D$=1 in this example.**

Impedance-matching also plays an important role in the linearity of rise-time encoding, but the mechanism is much more complicated than in the case of charge-division encoding. Figure 5 shows one-dimensional flood patterns calculated for a rise-time encoded PSD, using pulse-shaping time-constants of 100 ns and 1000 ns for the analog portion of the of encoding electronics. System parameters for the calculations were chosen to match those of the 20 x 20 $cm^2$ two-dimensional rise-time-encoded PSD used on SAD. The figure shows considerable nonlinearity, with better linearity when longer time constants are used. This behavior is also seen in flood patterns measured on the SAD detector, and is consistent with the empirically-determined linearity rules of Borkowski and Kopp.[2] However, the calculations also indicate that with properly chosen resistance-capacitance termination networks at the ends of the detector electrodes, the detector encoding can be made essentially linear while using much shorter pulse-shaping time constants. Calculations for such a "terminated" configuration with a shaping time constant of 100 ns are also shown in the figure, where it can be seen that in this "terminated" case the linearity is nearly as good with the shorter time constant as it was with the much longer time constant in the "not terminated" case. Since the shorter time constants permit operation at higher data rates, such termination networks may be a useful addition to the detector electronics.

## IV. Digitization Problems

Close inspection of Figs. 2 or 4 shows significant segment-to-segment variations in the encoded flood patterns for the GLAD detectors. These variations are systematic, and far exceed the expected statistical fluctuations. These are a result of the nonlinearities in the charge-division-encoding digitization circuitry, and are generally different for every different set of digitization electronics, and hence for every detector. It has not been possible to eliminate such variations without resorting to much more expensive circuitry. However, the calibration procedures discussed below can correct for these variations as well as for the segment-to-segment variations sometimes associated with the digitization process for rise-time encoding.

## V. Calibration Methods and Correction Algorithms

We have developed a procedure, valid for both charge-division and rise-time encoded data, for correcting for any remaining nonlinearities in the encoded data.[3] Consider a one-dimensional PSD which has been binned into n spatial segments. In the analog portion of the encoding process, an event occurring at position x will be encoded to have occurred at x' with a probability given by the resolution function P(x,x'). If the incident intensity per unit length is $I_o(x)$ and the detection efficiency is $\varepsilon$, then the measured intensity will be I(x') given by

$$I(x') = \varepsilon \int_{-\infty}^{\infty} I_o(x) P(x,x') dx \qquad (4)$$

The number of counts $N_i$ recorded for segment i is just

$$N_i = \int_{x_i}^{x_{i+1}} I(x')dx' \tag{5}$$

If we assume that the resolution function is gaussian with standard deviation $\sigma$ and that the illumination intensity has the uniform value $I_o$ over the length of the detector, then this becomes

$$N_i = \frac{I_o\varepsilon}{\sqrt{2\pi}} \int_{x_i}^{x_{i+1}} \int_{x_A}^{x_B} \frac{1}{\sigma(x)} e^{-(x-x')^2/2\sigma^2(x)} dx\,dx' \tag{6}$$

In the case of infinitely sharp resolution ($\sigma = 0$), Eq. (6) reduces to

$$N_i = \left\{ \begin{array}{rll} 0 & \text{for} & x_i < x_{i+1} < x_A \\ I_o\varepsilon(x_{i+1} - x_A) & \text{for} & x_i < x_A < x_{i+1} \\ I_o\varepsilon(x_{i+1} - x_i) & \text{for} & x_A < x_i < x_{i+1} < x_B \\ I_o\varepsilon(x_B - x_i) & \text{for} & x_i < x_B < x_{i+1} \\ 0 & \text{for} & x_B < x_i < x_{i+1} \end{array} \right\} \tag{7}$$

If the encoded positions are accurately known for two physical positions, say $x_\alpha$ and $x_\beta$, which are a distance L apart, then

$$I_o\varepsilon = \frac{1}{L} \sum_{x_i = x_\alpha}^{x_i = x_\beta} N_i \tag{8}$$

where some interpolation may be required to handle the end segments in the sum. If one of these known positions is then used to find one of the $x_i$ (by interpolation to the end of the corresponding segment), then Eq. (7) can be used to find all of the other $x_i$ in terms of the $N_i$ from the flood pattern. If all of the intensity from the ends of the detector is recorded in the flood pattern data, then $x_A$ and $x_B$ can be determined from the conservation of intensity, as

$$x_A = x_\alpha - \frac{1}{I_o\varepsilon} \sum_{x<x_\alpha} N_i \tag{9}$$

$$x_B = x_\alpha + \frac{1}{I_o\varepsilon} \sum_{x>x_\alpha} N_i \tag{10}$$

If the resolution $\sigma(x)$ is not infinitely small, but can be assumed to vary only slowly with x (the usual case), then it can be replaced with $\sigma(x')$ in the integral in Eq. (6). In regions of the

detector which are several $\sigma$ from the ends, the limits of integration $x_A$ to $x_B$ in Eq. (6) can be replaced with $-\infty$ to $+\infty$, and the integral over x can be evaluated to give

$$N_i = I_o\varepsilon \int_{x_i}^{x_{i+1}} dx' = I_o\varepsilon(x_{i+1} - x_i) \qquad \text{for} \quad x_A << x << x_B \tag{11}$$

which is independent of the value of $\sigma$ and is equivalent to Eq. (7). Thus resolution effects can be ignored for the central portion of the flood pattern, and the procedure outlined above with Eqs. (7) and (8) can still be used for calibration of the central portion of the detector.

Near the ends $x_A$ and $x_B$ of the detector, the resolution must be taken explicitly into account in Eq. (6). For segments near end A, $x_B$ can be replaced by $+\infty$ as the limit of integration, giving

$$N_i = \frac{I_o\varepsilon}{\sqrt{2\pi}} \int_{x_i}^{x_{i+1}} \frac{1}{\sigma(x')} \int_{x_A}^{\infty} e^{-(x-x')^2/2\sigma^2(x')}\, dx\, dx'$$

$$= \frac{I_o\varepsilon}{2}(x_{i+1} - x_i) + \frac{I_o\varepsilon}{2} \int_{x_i}^{x_{i+1}} \operatorname{erf}\left(\frac{x' - x_A}{\sqrt{2}\sigma}\right) dx' \tag{12}$$

This equation can be solved for $x_i$ if $x_{i+1}$ is known, so it is only necessary to start at a point where $x_{i+1}$ is known from Eq. (7) and then solve Eq. (12) repetitively for successively smaller values of i. A similar procedure can be used for calibration near end B. Equations (9) and (10) can still be used to determine $x_A$ and $x_B$ in this case.

For most area detectors, the encoding of the x and y positions is done independently, so the calibration procedure involves such a one-dimensional calibration in each dimension. Figure 6 shows a uniform-illumination flood pattern for the SAD area detector. Separate measurements made with a mask in front of the detector were least-squares fit to determine the local values of $\sigma(x)$ and $\sigma(y)$, and the encoded x' and y' values for the known x and y coordinates of the center of each hole in the mask. These values were used for $x_\alpha$ and $x_\beta$ (and also for $y_\alpha$ and $y_\beta$), and the above procedure was applied to the data of Fig. 6 (averaged over the central portion of the detector) to determine the set of $\{x_i\}$ and $\{y_j\}$. Once these boundaries of each encoded segment of the detector were known, the data from the original pattern could be corrected to determine the "true" resolution-broadened efficiency-weighted intensity pattern $I(x,y)\varepsilon$ according to

$$I_{i,j}(x,y)\varepsilon = \frac{N_{i,j}}{(x_{i+1} - x_i)(y_{j+1} - y_j)} \tag{13}$$

Figure 7 shows the data of Fig. 6 corrected to produce I(x,y) in this manner. This procedure has proven to be quite satisfactory, and is now used for much of the data collected on SAD.

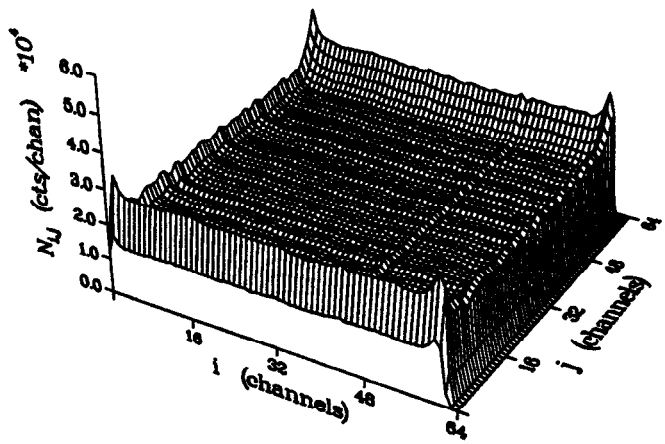


**Figure 6. Measured flood pattern for the rise-time encoded detector used on SAD.**

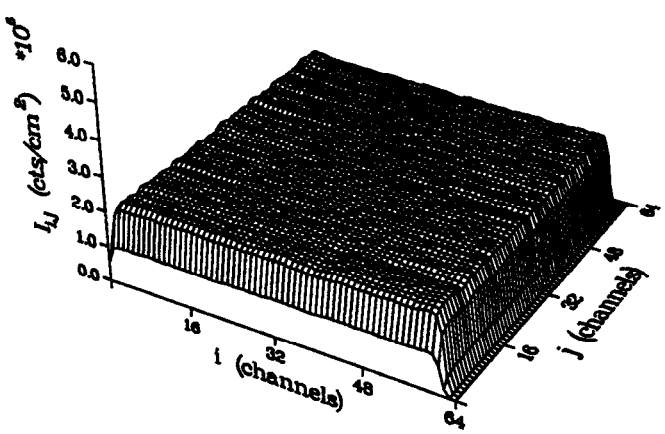


**Figure 7. Flood pattern of Fig. 6 corrected for detector nonlinearities by the method discussed in the text.**

## References


1. R. K. Crawford and J. R. Haumann. *Nucl. Instrum. Meth.* **A292**, 656-670 (1990).
2. C. J. Borkowski and M. K. Kopp. *Rev. Sci. Instrum.* **46**, 951-962 (1975).
3. P. Thiyagarajan, K. F. Bradley, R. K. Crawford, J. E. Epperson, D. G. Wozniak and J. M. Carpenter. Proceedings of SPIE's 1992 International Symposium on Optical Applied Science and Engineering, San Diego, Calif., July 19-23, 1992, Vol. 1737, pp. 243-254.

# THE ISIS SECOND GENERATION DATA ACQUISITION ELECTRONICS

J.Norris, S.Quinton, D.Allen
ISIS Facility, Rutherford Appleton Laboratory, Chilton, Didcot
Oxfordshire, OX11 0QX, United Kingdom

*Abstract*

The ISIS Data Acquisition Electronics has been in successful operation since 1984. However, improving neutron detector technology, an ever-changing computing environment and more exacting experiments are challenging its design specification. A second generation data acquisition electronics system is needed to accommodate increased detector numbers and allow more varied data acquisition control and monitoring. Real-time display and a pre-processing capability of the acquired data are also required. This paper outlines the current electronics, the issues that dictate the need for change and the new system that will replace it.

## I. INTRODUCTION

The design of the existing ISIS Data Acquisition Electronics was first proposed back in 1979. Its specification was derived from detailed discussions between the instrument scientists and the Rutherford Appleton Laboratory's Electronics Division. Three systems were commissioned for the first ISIS neutron run in December 1984. Since then, the number of systems has grown to fourteen, with two 'hot spares' used for testing and evaluation purposes. Although each ISIS neutron scattering instrument differs in characteristic, it is the same data acquisition electronics design that supports them all.

## II. THE ISIS DATA ACQUISITION ELECTRONICS

### *A. System Overview*

The Data Acquisition Electronics (DAE-I) is an integral part of the ISIS PUNCH Data Acquisition and Display System. It is made up of two component parts, the Instrument and the System Crate (See Fig. 1). The Instrument Crate is connected to the detectors via detector processing electronics. Its role is to capture the detected neutron position with a corresponding time-of-flight timestamp to form a descriptor word. The System Crate is responsible for generating the acquisition timing, processing the descriptors, and histogramming them. This crate is attached to the Front End Minicomputer (FEM) which controls the whole acquisition process.

As many as 16 Instrument Crates can be attached to a single System Crate. Generally, the Instrument Crates reside close to the detectors whilst the System Crate is located near the FEM in the instrument cabin. A maximum distance of 30Metres between the two crate types can be catered. This is achieved by a three cable interconnection of a 28Bit good descriptor data bus, an acquisition timing signal bus and an acquisition control signal bus. All these interconnections use balanced complimentary ECL signals in twisted pair format to cope with the long distance between crates and to counter externally generated noise pickup. In a multiple Instrument Crate implementation this interconnection is daisy chained between the crates.

The Instrument Crate is based mechanically on CAMAC but with an in-house designed backplane incorporating a detector readout bus. This bus can achieve a peak raw descriptor readout rate of 10MHz from the detector modules. The raw descriptor is partitioned into a 24Bit wide detector position and time-of-flight descriptor word part. The backplane also contains the 16Bit time channel bus which distributes the time-of-flight descriptors to the detector modules. The System Crate uses the standard Multibus-I bus architecture with its 24Bit address and 16Bit data bus. The read and write operations are undertaken as a command from a master card and completed by an acknowledge issued from an accepting slave card. The bus is used in three ways, to set up parameters within the System Crate cards defining the experimental run, to perform the histogramming process and finally to readout the histogram data.

### *B. The Instrument Crate*

The Instrument Crate modules and their functionality will now be described. There are two types of input module in which data is captured. These are Instrument Beam Monitor Modules (MIM's) and Detector Input Modules (DIM's) of which several variations exist. The DIM1 module takes data from 8 independent detector inputs, whilst the DIM2 module accommodates 4096 detectors through a 12Bit binary coded input. Lastly the DIM3 module encodes upto 64 detector inputs into a 6Bit coded event position word. The MIM module accepts 4 beam monitor inputs. Apart from the input stages, both MIM's and DIM's follow the same design. An input latch captures the neutron position and the time-of-flight word. This is stored in a 16Word deep Last-In-First-Out (LIFO) memory. A peak event input rate of 20MHz can be absorbed by each module. If event data is written into the LIFO quicker than it can be readout, then the module can flag a LIFO overflow veto.

The 24Bit raw descriptors output from the monitor/detector modules are stored in two Ping-Pong Frame Memory (PPFM) modules, on an acquisition frame by frame

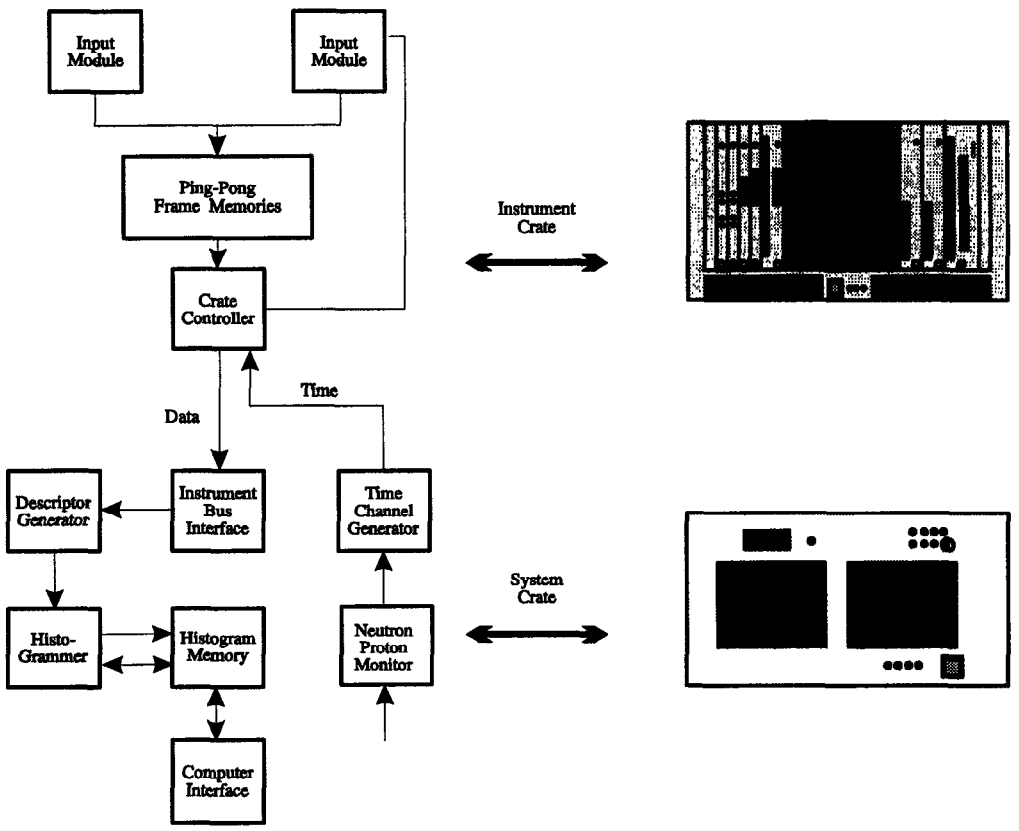


Fig. 1. The DAE-I Electronics

basis. Whilst one PPFM is acquiring descriptors the other is transferring descriptors to the System Crate. Each module contains 20KWords of SRAM, where each word is made up from the 24Bit raw descriptor and a 4Bit MIM/DIM identifying word. The number of descriptors acquired in a frame is counted and if this goes above 20000, then a PPFM overflow is flagged. This veto and a crate global MIM/DIM LIFO overflow are checked prior to data transfer to be ensure that the collected data is valid.

The 24Bit raw descriptors output from the monitor/detector modules are stored in two Ping-Pong Frame Memory (PPFM) modules, on an acquisition frame by frame basis. Whilst one PPFM is acquiring descriptors the other is transferring descriptors to the System Crate. Each module contains 20KWords of SRAM, where each word is made up from the 24Bit raw descriptor and a 4Bit MIM/DIM identifying word. The number of descriptors acquired in a frame is counted and if this goes above 20000, then a PPFM overflow is flagged. This veto and a crate global MIM/DIM LIFO overflow are checked prior to data transfer to be ensure that the collected data is valid.

The last module in the Instrument Crate is the Instrument Crate Controller (ICC). It determines the arbitration of input modules seeking permission to write raw descriptors into the PPFM. The modules are serviced on a priority basis, with the priority determined by the module position. A second function it has is to generate the 16Bit time-of-flight channel bus words which are required by the input modules. Its final role is to handle the transfer of the PPFM descriptors to the System Crate, generating the required bus timing protocols.

*C. The System Crate*

The System Crate splits into seven functional component parts. The Neutron-Proton Monitor (NPM) covers three cards. One of these is responsible for the timing and synchronisation of the data collection to the ISIS neutron pulses. It takes in the ISIS Frame Synch pulse (or a chopper system synchronising pulse), and adds a user-settable delay before distributing it as the Delayed Frame Synch time reference, for the Instrument Crate data acquisition and transfer. Run data logging is also performed within this group of boards. This data includes the good/raw accumulated beam current values received from the Protons-Per-Pulse (PPP) Receiver card.

The Time Channel Generator (TCG) card is responsible for setting up the time channel boundaries in the histogrammed spectra. On this card is a 32KWord lookup table holding the time channel boundaries relative to the Delayed Frame Synch pulse. A 32MHz clock drives a counter which generates a word for comparison with the first time channel boundary word in the lookup table. When they are equal a pulse is sent to the ICC which increments the 16Bit time-of-flight word to the input modules. This continues until either the maximum number of time channels is reached or the

next ISIS pulse occurs. These conditions reset the lookup table back to its beginning.

The Instrument Bus Interface (IBI) control and driver cards initiate the data collection process and readout the PPFM 28Bit descriptors synchronised to the Delayed Frame Synch pulse, at a rate of 1MHz. It adds the Instrument Crate address (4Bits), and Period Count (8Bits), generating a 40Bit descriptor which is then pipelined through the other cards in the System Crate. The second function of the IBI is veto handling, where something external has gone wrong in an acquisition frame, with likely data corruption resulting. The IBI would flag to the Instrument Crate not to transfer that particular frame. Included in this veto monitoring are the detector/monitor input module global LIFO and PPFM overflow veto's sourced from the Instrument Crate. Also external vetoes such as chopper out of phase and moderator temperature are monitored. The IBI also holds counts of the number of raw and good (transferred) PPFM data frames.

The 40Bit descriptor passes to the Descriptor Generator, (DG) which is responsible for mapping it to a 24Bit histogram address. Various on-board lookup tables allow efficient mapping which includes the ability to gang detectors to a particular spectra. The 24Bit output of the DG is passed to the Incrementer card (INC) which performs the actual histogramming process by generating Read-Increment-Write cycles to the Histogram Memory (HMEM). As much as 16MBytes is available to be used as Histogram Memory.

The final stage is the Computer Interface (CI) linking the System Crate to the FEM via DEC's QBus standard. The card contains QBus mapped registers controlled by a software driver resident on the FEM. These registers act as gateways to the System Crate histogram and run set-up address locations. Within the System Crate this card acts as master sharing this role will the Incrementer. Arbitration logic between the two cards allows dual access to the Histogram memory.

*D. DAE-I Software Interaction*

A brief overview of the DAE-I software interaction is necessary to highlight some of the problems now being faced by DAE-I.

The most important interaction occurs through the Instrument Control Program (ICP). This allows the user to set-up detector to spectra mappings, time channel widths and veto enables. When these parameters are ready then a BEGIN can be typed at the terminal screen. This has the effect of clearing the histogram memory, setting up the various lookup tables and initialising registers and counters. The final operation is to set a control bit within the IBI which instructs data acquisition to start on the next ISIS Frame Synch pulse. Each of these memory/register access operations is undertaken by the FEM, which means that for large histogram instruments there is a delay of ten's of seconds before the run starts. This is also apparent when an END instruction is typed, where the histogram memory contents are readout with the total number of frames and the total accumulated beam current.

Another DAE-I software interaction is with the DASHBOARD process. Approximately every five seconds the good/raw frame counts, the beam current, and monitor counts between pre-set time limits are readout. In the case of the monitor counts, a block access to the histogram is made and the integrated counts calculated in the FEM. The problem here is with the randomness to which this process access's the DAE , holding up the transfer of data from the PPFM to the histogram memory. Also the block transfer of the monitor counts data is inefficient.

The other major interaction with the DAE-I can be done through the GENIE spectra display and manipulation software. It has a command which allows runtime access to the DAE-I histogram memory so that whilst the run is executing, the detector spectra can be displayed. Again the randomness of this access and the ability to examine multi-spectra plots (large block data transfers) tends to hold up DAE-I descriptor transfer and histogramming.

## III. THE NEED FOR CHANGE

The forward looking design of the DAE-I system has enabled it to cope with many instrument design changes. After some nine years of continuous operation, it is only now that the design of ISIS Instruments are starting to stretch its operation. This section looks at those factors influencing the need for change.

*A. Expanding Data Acquisition Parameters*

With the increase of detector numbers through continual instrument upgrading, the most pressing issue on DAE-I is the histogram memory size. This is related to the number of detectors the instrument has, and the number of time channels used to 'time stamp' the detected event. The amount of memory store allocated to hold the number of counts for each event histogram channel is also important. This must be large enough to avoid data loss through count overflows. This store can be programmed to 8, 16 or 32Bits long but is generally set to the latter. The current DAE-I histogram memory is thus limited to 4MEvent histogram channels, restricted by the 24Bit (16MBytes) addressing range of the System Crate Multibus-I backplane.

The 16MByte histogram limit is now being reached by ISIS Instruments SXD and MARI. The detector upgrades for SANDALS, SXD and the SURF detector system easily surpass this limit as shown in Table 1.

Another issue concerns long flight path instruments such as HRPD and IRIS. Within DAE-I both the incident beam monitor and detector time-of-flight data share the same time regime. Where the monitor is close to the detector this is fine, but where there is some distance between the two, the resulting monitor spectra needs some manipulation before

normalisation can take place. Hence the need to run the monitors and detectors on different timing regimes relative to the ISIS Frame Synch Pulse.

| Instrument | Detector Elements | Time Channels | Histogram Memory |
|---|---|---|---|
| SANDALS (1994) | 1500 | 5000 | 30MBytes |
| SXD (1994) | 2 x 4096 | 4000 | 128MBytes |
| SURF (1995) | 20000 | 2000 | 160MBytes |

Table 1. Instrument Future Histogram Requirements

A final point concerns the introduction of glass scintillator detectors to EVS. This has increased the overall detector event rate for the instrument. Whilst the DIM peak input rate of 20MHz is not reached, the overall event rate readout to the PPFM's shared across four DIM modules is approaching the DAE-I limit of 10MHz.. There is also the implication that more than 20KEvents could be collected per frame, thus overflowing the PPFM's. The ability to scale data acquisition to accommodate higher event rate detectors in a manageable way is necessary.

*B. Instrument Diagnostics*

This area concerns the ability of the DAE to be used as an instrument fault diagnostic tool. A major concern is DAE-I's lack of effective handling of a detector going noisy. The Instrument HET used to minimise the number of detector spectra by ganging detectors together in the Descriptor Generator lookup tables. However a detector going noisy within a group corrupted the ganged spectra and the instrument reverted back to individual detector spectra. The second problem concerns identification of that noisy detector. In the DAE-I Instrument Crate each monitor/detector module LIFO output is ganged together to produce a single LIFO overflow veto. Because of the ganging it makes identification of a noisy detector, within a module, and/or within a crate of modules difficult to trace. It is therefore necessary to be able to trap and identify this faulty condition quickly.

Another problem relates to the moderators and their performance in the ISIS target station. Current moderator performance is monitored by software taking neutron and proton counts periodically and displaying the results over a 24Hr time frame. This method tends to reveal problems only after trouble has occurred with potential data corruption in the spectra. The ability to compare the proton value with the incident bean monitor counts on a frame by frame basis and veto the acquired frame if outside a tolerance, would minimise data corruption and flag to the user quickly that something is wrong.

A further related veto issue is the ability to identify which veto condition is causing problems. With DAE-I, the only way that vetoes are noticed is when there is a mismatch between good and raw frame counts. This doesn't reveal the source nor identify trends where for example a chopper phase veto may increase its occurrence over many runs signifying a degradation in chopper performance.

*C. Data Pre-Processing*

Increasing the histogram memory size to accommodate extra detectors has further consequences for the DAE. The time taken to transmit the histogram between the DAE-I histogram memory and the FEM is important. If these transfers become too long they could delay the start of the next data acquisition run. The transfer rate between the DAE-I and FEM is 100KBytes/sec and is limited by QBus and the controlling software.

Another consequence of larger histograms is the time it takes for the FEM to clear the histogram ready for the next run. This is already approaching nearly a minute to clear 8MBytes of memory. It is currently undertaken by the FEM issuing block writes of zero data into the histogram memory locations. This is an unnecessary drain on the FEM computing resource. Also the block reading of the monitor counts between time limits seems an inefficient use of the interconnecting bus.

Methods of efficiently using the DAE/FEM interconnecting bus in control and data transfer need to be considered. One way is to introduce some pre-processing of the data. Rather than sending single bytes of DASHBOARD information, a packet of runtime data could be assembled and a block move of that data transferred. Further pre-processing would come in the form of data compression techniques used to minimise the size of the large histograms before data transfer.

## IV. THE NEXT GENERATION DAE

*A. System Overview*

Like the current DAE-I, the second generation data acquisition electronics (DAE-II) is based on two crate types, the Interface Crate and the Control Crate (See Fig. 2). The Interface Crate is the link between the detector processing electronics and the Control Crate. The many different detectors offering varying types of connectors, electrical level and transmission formats, has led to many interface cards being built. Therefore, there is a need to buffer the more expensive control crate cards from these varying interfaces. The interface modules will cater for the standard DIM1 and DIM2 detector outputs, routing the signals into a high density 68-way shielded connector. Crate fan and power supply failure monitoring will be done on selected modules. Notification of a faulty condition will be sent to the Control Crate as a veto signal.

The Interface Crate can be either a CAMAC Crate or a DAE-I Instrument Crate. Interface modules running in these

crates will only be drawing power from the backplane, so no adaptation of these crates is required. The reason for choosing these crates is that they are well designed, known technology with ample power supplies and spares available. In re-cycling the DAE-I Instrument Crate this also circumvents a disposal problem as more DAE-I systems move to the DAE-II solution.

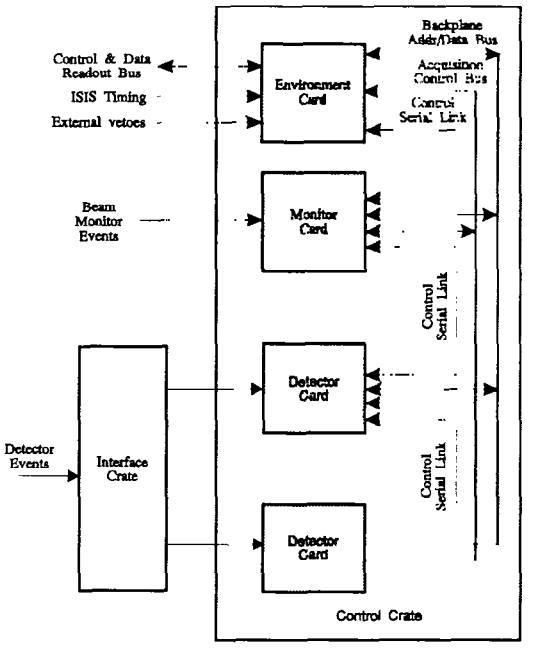


Fig. 2. DAE-II System Block Diagram

The DAE-II Control Crate is based on the VME Extended for Instrumentation (VXI) Bus [1]. The reason for choosing VXI is that it conforms to the VMEBus standard, which is well understood and proven technology. But VXI extends VME by introducing an inter-card daisy chain bus, dedicated inter-slot lines, more bus lines and extra power supplies. The enclosure provides an almost continuous surround of metal to minimise electromagnetic interference. Attention to this issue is becoming more an more important because of the increasing background electrical noise within the ISIS experimental hall.

All cards and modules will be manufactured in multi-layer PCB technology as oppose to the DAE-I which was fabricated using wirewrap. A PCB implementation will improve reliability with inner layer ground planes aiding screening as well as minimising ground bounce induced false triggering. For the Control Crate cards, a VXI D size card will be used. This 9U board size allows a high density of components to be laid out with fewer inter-connections needed. Further screening will be achieved by adding card sidecovers that will connect to the ground plane and totally enclose the card.

Surface mount components will help in making effective use of the board real estate. Also much use will be made of Programmable Logic Devices (PLD) and Xilinx Field Programmable Gate Arrays (FPGA) [2]. These allow many standard logic gates to be programmed into a single package so reducing interconnections and increasing reliability. The reduced component inventory and re-programmability make these devices very attractive.

Three cards will exist in the Control Crate. These are the Environment card, the Monitor card and the Detector card and will now be described.

*B. Environment Card*

The function of Environment Card is two-fold, to act as the interface between the FEM and DAE, and to generate system data acquisition timing/control signals. A major change to the DAE environment is the FEM moving away from the MicroVax 3200 QBus series machines to the more powerful Alpha and SCSI workstations. For this reason the FEM/DAE-II interconnect bus chosen is SCSI-2 [3]. This is a proper communications bus geared towards block data transfers with error checking built-in.

The DAE-II SCSI interface will run either in 10MBytes (8Bit) SCSI-1 mode or at the full SCSI-2 mode at 20MBytes (16Bit). Which mode is used depends on the SCSI implementation in the workstation. Currently the DEC workstations support 8Bit mode. Single-ended and differential transmission formats will also both be supported allowing flexible positioning of the crate. Both Target and Initiator modes will be allowed enabling the DAE to act as a receiving data slave and/or as a bus master sending data to the workstation.

To set-up the SCSI interface, control data acquisition and readout/pre-process the histogram data an on-board processing element is required and this will be a Transputer [4]. This is a powerful microprocessor, simple to interface and has the ability to easily undertake parallel tasks with other Transputers. The Transputer board controller will be a 20MHz T805 floating point processor. It will have access to 16MBytes of DRAM for program workspace, 4MBytes EPROM for the program itself and 0.5MBytes Flash EPROM for runtime program variables. This last type of storage memory will be used to store parameters about the DAE configuration (how many cards, how much memory, etc.) and current run parameters (such as what vetoes are enabled, and time channel boundary information). This is necessary in case the Transputer descends into an error condition and needs re-initialising. The design of the data acquisition parts of the system will ensure that data acquisition continues in the event of this happening.

The VME Interface will be undertaken by an commercial VME Interface ASIC handling all the bus single cycle/block accesses, interrupts, master/slave bus arbitration and DMA control. Like the SCSI Controller it is set up and controlled by the Transputer. Bus transfer rates can be up to a maximum of 40MBytes/sec using 256Byte block transfers. The interface will be able to function as a master device, issuing read/write commands to other devices, or as a slave

receiving read/write commands. It will support 32Bit aligned and unaligned transfers over a 4GByte addressing range.

The VXI additions to the VME standard bring extra bus and interslot lines to the backplane. The bus lines will be used to distribute the ISIS Frame Synch pulse, a System DAQ Running flag and other DAQ control signals so as to synchronise all the cards in the system. The inter-slot lines will be used to distribute the Transputer 20MBit/sec serial links. It is envisaged that these links will be used to transfer small packets of data, leaving the larger histogram, block transfers to be done over the VME.

Turning to the system data acquisition control, this will be performed by several FPGA's. The Card FPGA has the responsibility for resetting the system and synchronising the run to the ISIS Frame Synch pulses. It will also distribute these signals to other cards in the crate.

The chopper FPGA will look after all the control logic concerned with running the DAE from a Chopper system. This includes generation of the DAQ Frame Synch pulse and the monitoring of the chopper out of sync with the ISIS neutron pulse. This will generate a veto which will be logged by a veto counter. Also in this FPGA will be a user-settable window that will monitor a Fast Fermi Chopper position pulse. If the position pulse falls outside the window then a veto is generated, and again this will be logged.

The new neutron-proton ratio veto will be on this card. A small lookup table will be loaded with values corresponding to the particular target. When the delivered proton value arrives, this is latched into the lookup table which generates a high and low band value to compare against the accumulated Incident Beam Monitor neutrons count. Towards the end of the frame the test is made to see if the actual neutron value lies within the band. If it does not then a veto is raised.

Another new feature on this card is what is labelled the Diagnostic Pulse Generator. This is essentially a replication of the TCG sub-circuit where values are loaded into a lookup table and compared with a running counter value. A trigger signal can be generated when the counter and lookup table values match. This is useful when trying to relate a noise spike appearing in the spectra to a detector signal allowing an oscilloscope to trigger precisely around the noise spike's position in time. The detector's signal at that point can then be inspected for strange pickup effects.

The Transputer/VME/VXI sub-system parts will be replicated on the Monitor and Detector cards. This standardises the boards maintaining consistency in their designs, and so minimising errors.

*C. The Detector Card*

This card (See Fig. 3) is responsible for capturing the neutron position events and histogramming them. In effect, it reproduces the functionality of the DAE-I Instrument and System Crates onto a single card. As detector systems expand, it would then be a matter of duplicating extra cards of this type in the Control Crate. The functionality follows almost exactly as for the DAE-I system. Where the difference lies is in the use of FPGA's which allow DAE-I board functionality to be implemented almost as a single chip.

For the generation of the time channels a 64K*32Bit SRAM lookup table is used under the control of the TCG FPGA. This increases the number of time channels available to 64KTime Channels per Acquisition Frame. Integrating much of the TCG scalar and control logic onto a single chip allows a minimum time channel resolution of 100nS to be achieved. Widening the width of the lookup table from 20Bits (DAE-I) to 32Bits means a maximum acquisition frame length of 128 Seconds is possible.

The DIM module functionality in DAE-I can similarly be achieved in an FPGA solution. A personality PROM configures the FPGA allowing it to function either as a DIM1 or DIM2. Upto to sixteen Detector Input Gate Arrays (DIGA's) can be fitted on the card each handling 4096 detectors in the DIM2 format. Each DIGA will have a 32Bit data capture latch (16Bit for time channel, 16Bit for position) and a 32Deep*32Bit true FIFO. This FIFO will enable the 20MHz peak event rate to maintained whilst using slower CMOS technology as a oppose to the ECL technology used to achieve this on DAE-I.

Arbitration of the DIGA's to allow their events to be written into the PPFMs will be controlled by the Arbiter FPGA. The DAE-I arbitration method is priority based but this has led to some problems with the EVS glass scintillator detector event rates. For DAE-II a round-robin method of arbitration will be employed. Also included in this Arbiter will be a Detector Raw/Good Neutron Counters with registers to allow start and stop times between which event data is collected. This register will be a useful diagnostic aid to see that the card is collecting data. Access to these counters would be simpler in operation than obtaining the same information from the histogram.

The final FPGA in this area of DAE-II is a veto counter FPGA that will log the DIGA FIFO Overflow vetoes. This will allow the identification of a noisy detector to be more accurately pinpointed.

The DAE-II PPFM's will have their size increased from 20K to 64K allowing many more events to be collected in a frame. The FPGA functionality is expanded to allow a user-settable maximum number of events per frame to be collected (PPFM overflow veto). This is to trap a noisy detector from corrupting a frame and hence the spectra (especially when detectors are ganged). It may not be possible to predict the actual number of events per frame that will occur, hence the incorporation into this FPGA of a counter that simply logs the maximum number of counts occurring in a frame. This counter could log the maximum value readout

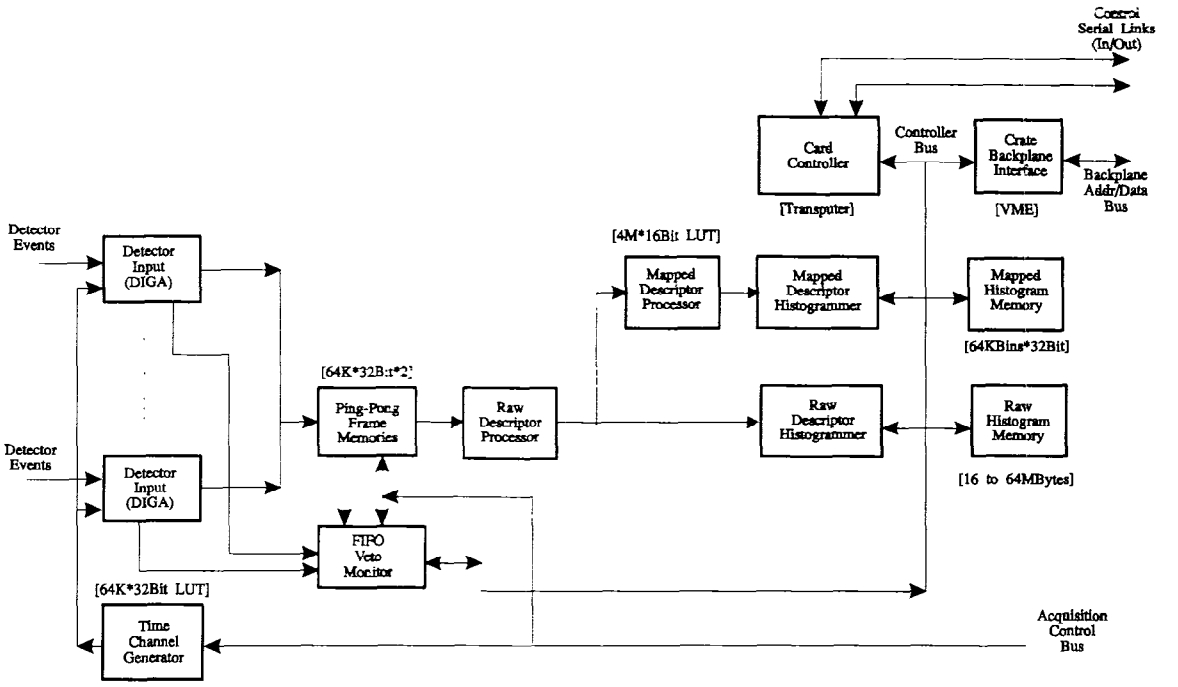


Fig. 3. Detector Card Block Diagram

over the first hour of the run, a tolerance value then added to that value and the result being used to set-up the PPFM overflow veto.

Within the Raw Descriptor Processor is a 2KDeep*32Bit FIFO used to buffer the block moving of descriptors from the PPFM through the Descriptor Processor to the Histogrammer. The pipeline architecture of the Descriptor Processor, Histogrammer and the actual histogramming process to the Histogram memory tends to slow the transfer of descriptors. Hence the need for the FIFO to maintain a balanced throughput. The Descriptor Processor also contains a coarse detector position mapping table. This is needed to map the detectors efficiently to the histogram memory. The mapping calculation is performed by a multiplier/accumulator device which can be set-up to perform either the (Tmax *P) + T or the (Pmax * T) + P algorithm.

After coming out of the Descriptor Generator the raw histogram descriptors are passed into another FIFO before going into the Raw Histogram Histogrammer. This FIFO's purpose is to ensure there is no holding up of data transfer, when the Transputer is accessing the Histogram Memory. This was a problem with DAE-I where data transfer from the PPFM was being held up when the FEM was doing large block reads of the histogram memory.

A Raw Histogrammer FPGA takes the Raw Histogram Descriptor and performs the Read-Increment-Write operation on the Histogram Memory. The size of the histogram memory will be either 4M *32Bit or 16M*32Bit depending on the instrument requirements, using the latest 16MBit DRAM's in an array. This means that 4M or 16MHistogram channels per detector card will be available to the user.

A design departure from the DAE-I architecture is the introduction of a Mapped Histogram Lookup table, Histogrammer and Histogram Memory. With higher density DRAM memory devices available, large lookup tables can be created in a small real estate area. What the Mapped Histogram Lookup table allows is the mapping of the Raw Histogram Descriptors to a particular bin. This means that focusing of time shifted detector spectra can be done to produce a single spectra achieving a significant reduction in data. The 64KBin Mapped Histogram memory can then be used to check instrument data integrity quickly rather than having to search the full Raw Descriptor Histogram which could be processor intensive.

The second departure from DAE-I is the use of an on-board processor to manipulate data in the Raw histogram. Transputers were chosen as the processor because of their ability to work in parallel. It is envisaged that many detector cards will be used with Transputers linked together via the backplane by their serial links. At a minimum level a single command could be passed to each, instructing the clearing the histogram memories. A second higher level use of the Transputer would be the data reduction of the raw histogram using Delta (shift level) encoding and/or Huffman encoding data compression techniques. On-board EPROM would contain a suite of programs that could be selected to perform the desired operation.

*D. Monitor Card*

This card almost follows exactly as for the Detector card, in that it carries the same VME/VXI interface with the option of a Transputer to be fitted to the board for future processing requirements.

The data acquisition parts are scaled down versions found on the Detector card. Four monitors will be accommodated each having the same PPFM, Descriptor Processor, Histogrammer structure as the Detector card. In splitting the monitors into four separate identical data acquisition circuits a gain in acquisition and data transfer speed is possible. It also allows redundancy should a monitor circuit fail. The Histogram memory for each monitor is 64KBins*32Bit in width and the same PPFM overflow veto setting and logging as found on the Detector card can be made.

## V. SUMMARY

The need for the DAE-II second generation data acquisition electronics system is clear. The current DAE-I is unable to meet the future instrument detector and operational requirements. Implementing DAE-II in VXI with its electromagnetic interference suppression and the PCB method of manufacture will bring reliability benefits. The use of PLD and FPGA re-programmable technologies will allow the design to accommodate future changes. The project schedule is for the Instrument SANDALS to have an operational DAE-II system for the 3rd Quarter of 1994.

## VI. REFERENCES

[1] VMEBus International Trade Association, VXIBus System Specification, Rev 1.3, July 14, 1989

[2] XILINX, The Programmable Gate Array Databook, 1992

[3] Small Computer System Interface (SCSI-II), American National Standards, X3t(.2/86-109 Rev.10h, Nov 11, 1991

[4] INMOS, The Transputer Databook, 2nd Edition 1989

# Measurement of Strain in Individual Phases of Composites Before, During, and After Mechanical Loading

Joyce A. Goldstone, M. A. M. Bourke, Dan Davis, LANSCE; Ning Shi, LANSCE/CMS; A. C. Lawson, MST-5; Los Alamos National Laboratory, Los Alamos, NM 87545 USA
and
John E. Allison, Ford Motor Company, Dearborn MI, USA

At LANSCE, we have measured residual strains in a variety of metal-matrix systems using the Neutron Powder Diffractometer. In 1992, we developed a compact stress rig for *in-situ* strain measurement during applied loading. Comparison of experimental measurements made with the stress rig on aluminum titanium carbide with numerical predictions showed the importance of the influence of initial thermal residual strains in composites In Al/TiC, normal to the loading direction, the increase in the average matrix and reinforcement lattice strains was in a "zigzag" manner. Finite element modeling indicated that this resulted from residual strains induced during cooling from fabrication temperatures. Data and modeling are presented herein.

## Introduction:

In metal matrix composites the presence of a hard minority phase can promote localized or non-homogeneous plastic flow during loading. This leads to internal elastic strains that are superimposed on initial strains due to thermal expansion mismatch. Even in single phase polycrystalline materials, strain incompatibility and directionally dependent yield stresses in individual grains can lead to strain differences in adjacent grains following plastic deformation [1]. In some cases, microstrain effects can result in some grains experiencing a tensile residual stress even when the macroscopic stress is compressive. This may affect crack initiation and is likely to affect mechanical properties such as strength and fracture toughness.

In a metal-matrix composite (MMC), the situation is even more complex because processes distinct from crystalline anisotropy may be contributing [2]. Numerical codes are frequently used to predict the development of residual strains as a result of such processes, but the complexity of the situation increases the importance of experimental validation before, during, and after thermo-mechanical conditions that simulate service. Neutrons have already been used and identified as a valuable method for validation of numerical codes [3,4]. Measurements have largely concentrated on residual stresses following heat treatments or deformation. By making measurements during the application of a load, we can improve our understanding of the performance of MMCs during loading.

## Experimental Method:

Diffraction methods of measuring strain by x-rays or neutrons have been extensively covered in the literature [5-9] and only a brief overview is given here. Changes in the lattice spacings of crystalline materials experiencing a residual or applied load are the basis of strain measurement by diffraction. When x-rays or neutrons of an appropriate wavelength fall on a polycrystalline material, diffraction peaks are produced corresponding to the spacings of atoms within the material. Bragg's Law relates the lattice spacings to the angle and wavelength of the diffracted

radiation. If these values are known, the lattice spacing for a set of crystals in specific orientations can be determined. The direction in which strain is measured lies along the scattering vector and is dictated by the scattering geometry.

In contrast with x-rays, whose penetration is limited, neutrons can penetrate several tens of millimeters into most materials of engineering interest. The low attenuation enables many grains to be examined, giving a representative value of the elastic internal strains in grains of particular orientations. Strains are determined from changes in lattice spacings from their "stress-free" values. For measurements under load, if the unloaded state is used as a "stress-free" value, it must be noted that the initial stress state will include residual stresses from fabrication. The strains of interest are usually less than $2x10^{-3}$. Particularly for the ceramic reinforcement residual strains are often less than $10^{-3}$ and high-resolution instruments are needed to discern them.

The neutron powder diffractometer (NPD) at the Manuel Lujan Jr. Neutron Scattering Center (LANSCE) is the highest resolution spectrometer of its type in the United States and is particularly appropriate for this work. On the NPD a favorable diffraction geometry offers simultaneous strain measurement in three directions. The loading axis is horizontal and at 45º to the incident beam allowing simultaneous axial and transverse strain measurements to be made in opposing 90º detector banks.

**Stress Rig:**

Stress rigs have been used at reactor [2,10,11] sources but it is only with the advent of relatively intense pulsed neutron sources like LANSCE, IPNS at Argonne National Laboratory, or ISIS in the UK that comprehensive assessment of strains in composite materials or any crystalline multiphase system has become possible. Spectrometers at pulsed sources require more shielding than reactors because the former have more high energy neutrons and gamma rays. This background necessitates more shielding around the sample position and has been the inhibiting feature in developing a stress rig at most pulsed neutron sources. For the NPD the loading apparatus and frame had to fit into a cylindrical space with an ID of 0.74 m. This precluded any commercial system and forced a design in which the actuator was in parallel with the specimen and the load was transferred to the specimen through a pivot arm [figure 1]. Care was taken to ensure that the loading on the sample remained axial.

**Table I Specifications NPD stress rig**

| | |
|---|---|
| Control: | Load or Stroke |
| Max. Load: | »50kN, Uniaxial tension or compression |
| Sample Size: | 50 to 150 mm in length |
| Sample geometry: | Cylindrical: Grips for different geometries could be made |
| Irradiated volume: | Center 14mm [10mm diameter specimen »1000mm$^3$] |
| Temperature: | I Cartridge Heaters to »300º C<br>II Planned 1000º C furnace |
| Environment: | Atmospheric, Inert gas, vacuum |
| Control System: | Instron, includes fatigue capability, Macintosh with LabView 2™ |
| Count times: | 1/2-12 hours / load level [depending on the material, sampling volume and beam reliability] |

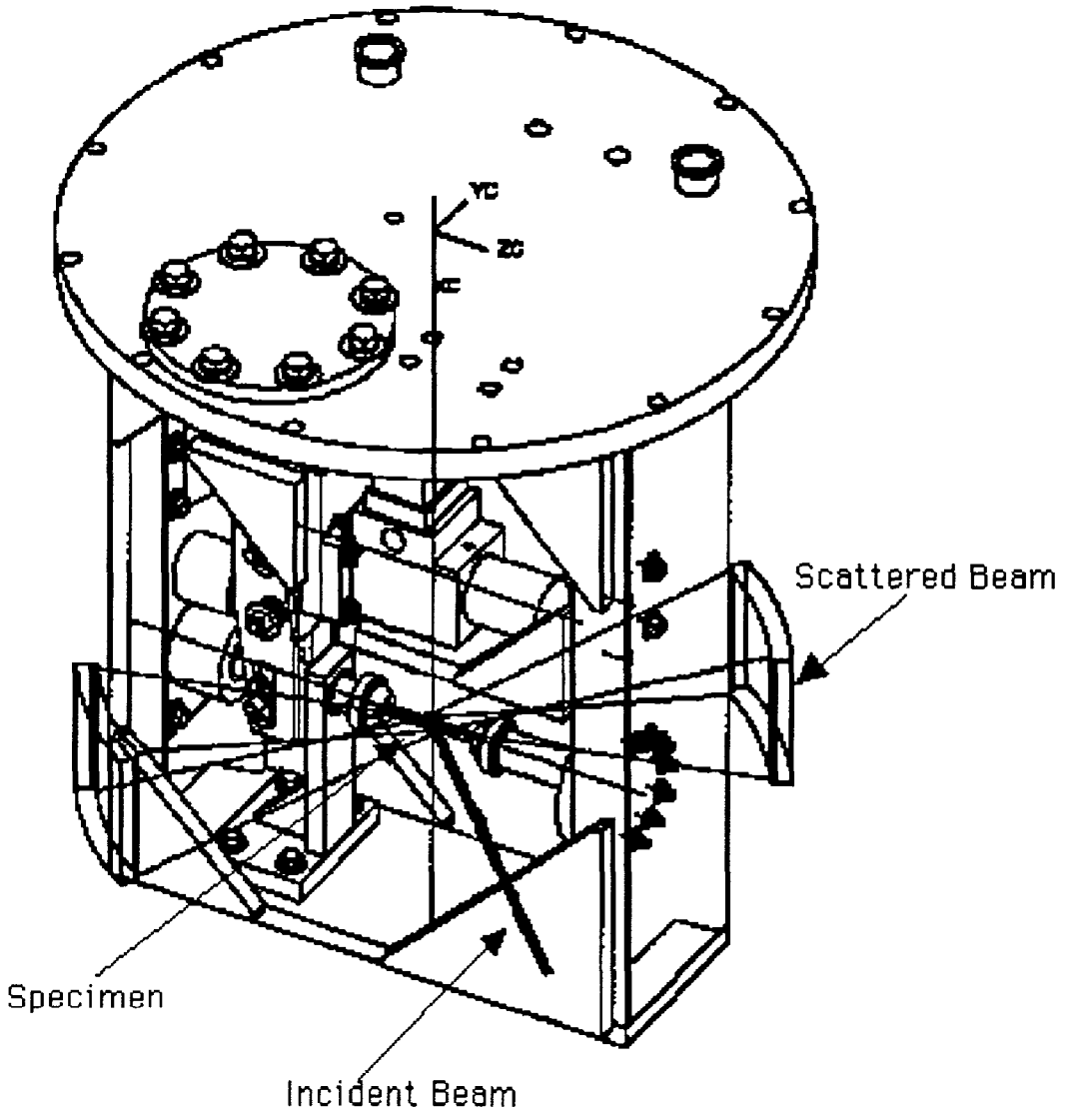


**Figure 1**: To operate a stress rig in the limited volume of the NPD sample chamber careful design was needed to ensure that the incident and diffracted beams were unimpeded.

**Experiments**:

Ford Motor Company in the US has been investigating a variety of metal matrix composite

systems for use in the automotive industry [12]. However most of these potential components are subjected to cyclic thermo-mechanical loading and an understanding of the factors influencing their mechanical behavior is needed to ensure their durability. In the summer of 1992, *in-situ* loading up to and beyond yield were made on two composite materials Al/TiC and Al/SiC. Only the results from the Al/TiC will be reported here. The Al/TiC was an artificially aged Al-2219 alloy reinforced with 15vol% TiC particles formed *in-situ* using a process developed by Martin Marietta Laboratories under the tradename XD. Although Al/TiC is unlikely to be used in production, the TiC particles produced via the XD process have a number of technological and theoretical advantages. They are spherical, possess clean matrix/reinforcement interfaces and do not appear to fracture under monotonic or cyclic loading.

A cylindrical specimen shape with a length of 160 mm and a diameter of 10 mm was used. The central portion of the specimen was in the neutron beam giving a gauge length of 14 mm and a total irradiated volume of 1100 $mm^3$. The rig was operated in cross-head displacement control and measurements were made at series of static tensile loads. The time for each measurement was approximately 4 hours at a beam current of 75 μA. Experiments were carried out under ambient temperature conditions. The initial loading sequence involved measurements at the static loads up to 200 MPa, in 50 MPa steps which maintained the samples in the elastic region. This was followed by unloading in one step, reloading to 200 MPa in one step, and finally 50 MPa step loads to 327 MPa for Al/TiC and 411 MPa for Al/SiC, which were sufficient to introduce 1% total strain as measured by a strain gauge. During final unloading, data were collected at 200, 100 and 0 MPa. Upon completion of the experiment, the Al/TiC was left with a total plastic strain of »0.67% and the Al/SiC with »0.61%.

Data were analyzed by two methods. To obtain a value of the lattice phase strain averaged over all reflections, the entire diffraction pattern was fit using the Rietveld refinement code GSAS[13]. To obtain information about the anisotropy of strain, peaks were fit individually using the same profile function as the Rietveld refinement. Figure 2 shows the (111) and (200) strains for the matrix. Figures 3 and 4 show the lattice parameter data obtained from the Rietveld refinements for the matrix and reinforcement with the numerical predictions from the finite element model. Strain is obtained from the initial unloaded value of the lattice parameters for the Al and reinforcements. See references 14 and 15 for further details.

**Discussion:**

Some interesting features can be discerned in figures 2-4. Polycrystalline anistropy in the Al was noted both parallel and perpendicular to the loading direction. In the parallel direction, it becomes apparent above 200 MPa (see figure 2) and results in the variation of final residual strains upon unloading. Perpendicular to the loading direction, there is a significant difference in the behavior of the Al [111] and Al [200] directions. Compared to the starting state, the latter is left in a state of »500μstrain tension compared to the initial matrix and the former is in »150μstrain compression. A similar effect was noted in the Al/SiC specimen. The origin of the difference has not been identified, but measurements are currently being made to assess whether any unusual texture is present and whether the effect is associated with Al or the composite.

In figures 3 and 4, the average measured phase strain (calculated from the lattice parameters) is displayed with the results of a finite element model. At this time, finite element modeling has

only be carried out for the Al/TiC composites. The composite was assumed to be infinite with cylindrical particles periodically embedded in the matrix. Two models were computed: one with no thermal residual strains (TRS) from cooling and one with residual strains developed from a ÎT of 180º C from 200º C [16]. The model without TRS does not give good agreement with the data, so only the model including TRS is shown with the data. In the direction parallel to loading, monotonic increases in the slope are observed. As the matrix strain rate decreases with increasing load, the particle strain increases. This indicates load transfer to the reinforcement as the matrix starts to yield plastically.

One interesting feature of the average matrix strain perpendicular to the loading direction is its "zigzag" behavior (see fig 5). Previous observation of this behavior in an Al/SiC composite has been explained by diffusional stress relaxation processes [2]. Our current data do not show a non-monotonic increase in the parallel direction so that diffusional relaxation cannot explain our observations. In addition, the stress decrease during a measurement was less than 1%, again indicating that relaxation does not play a signifcant role. We find that inclusion of TRS significantly changes the morphology of the strain behavior. Inclusion of TRS in the finite element model changes the region around the reinforcement which first plastically yields. Without TRS the plastic yield begins above the particle, parallel to the load direction. With the inclusion of TRS, plastic yield begins in the region perpendicular to the load direction. The Eshelby-type Mean Field Theory employed in explaining previous Al/SiC data [2,10] in not capable of predicting spatial fluctuations in the local strain fields. Further details are discussed in ref. 16.

## Summary:

Despite the constrained volume of the NPD, we have constructed a compact stress rig for *in-situ* measurements. The ability of pulsed neutron sources to examine multiple phases and all lattice reflections simultaneously has been shown to be a valuable tool. Despite the assumption of a continuum for finite element modeling, comparison with the data have shown reasonable accurate predictions and insight into deformation mechanisms. In the future, we will make measurements above room temperature »300º C and measurements at total applied strains greater than 1%.

This work performed under the auspices of DOE contract W-7405-ENG-36.

## References:

1. S. R. MacEwen, J. Faber, and P .L .Turner, "The use of time of flight neutron diffraction to study grain interaction stresses," Acta Met., **31** (1983), 657-676.

2. A. Allen, M. Bourke, S. Dawes, M. Hutchings, and P. Withers, "The Analysis of Internal Strains Measured by Neutron Diffraction in Al/SiC Metal Matrix Composites," Acta metall. mater. **40** (1992), 2361-2373.

3. G. L. Povirk, M. G. Stout, M. A. M. Bourke, J. A. Goldstone, A. C. Lawson, M. Lovato, S. R. MacEwen, S. R. Nutt and A. Needlemann, "Mechanically Induced Residual Strains in Al/SiC Composites," Scripta Metall. Mater. **25** (1991),.1883-1888.

4. G. L. Povirk, M. G. Stout, M. Bourke, J. A. Goldstone, A. C. Lawson, M. Lovato, S. R. MacEwen, S. R. Nutt and A. Needlemann, "Thermally and Mechanically Induced Residual Strains

5. A. J. Allen, M. T. Hutchings, C. G. Windsor and C. Andreanni, "Neutron diffraction methods for the study of residual stress fields," Advances in Physics **34** (1985) 445-473.

6. I. C. Noyan and J. B. Cohen, Residual Stress --- Measurement by Diffraction and Interpretation (New York, NY: Springer Verlag, 1987).

7. M. James, M. Bourke, J. A. Goldstone, and A. C. Lawson, "Residual stress measurements in continuous fiber titanium matrix composites," Advances in X Ray Analysis, (New York, NY: Plenum Press, 1992, in press)

8. M. A. M. Bourke, J. A. Goldstone, and T. M. Holden, "Residual stress measurement using the pulsed neutron source at LANSCE," in Measurement of Residual and Applied Stress Using Neutron Diffraction, (ed. M. T. Hutchings and A. Krawitz, Netherlands: Kluwer Acd. Pub., 1992), 369-382.

9. A. Majumdar, J. P. Singh, D. Kupperman, and A. D. Krawitz, "Application of Neutron Diffraction to Measure Residual Strains in Various Engineering Composite Materials," Journal of Eng. Mat. and Tech. **113** (1991) 51-59.

10. A. J. Allen, M. A. Bourke, W. I .F. David, S. Dawes, M. T. Hutchings, A. D. Krawitz, and C. G. Windsor, "Effects of elastic anisotropy on the lattice strains in polycrystalline metals and composites measured by neutron diffraction," Proceedings of ICRS2, (London, UK: Elsevier , 1988) 78.

11. T. Lorentzen and N. Sorensen, "A new device for in-situ loading of samples during neutron diffraction strain measurements," Proc. 12th Riso Int. Symp. on Mat. Sci., 489-496.

12. John. E. Allison and Gerald. S. Cole, "Metal Matrix Composites in the Automotive Industry: Opportunities and Challenges," Journal of Metals **45** (1993) 19.

13. Allen C. Larson and Robert B. Von Dreele, "GSAS - Generalized Structure Analysis System," Los Alamos National Laboratory, Unclassified Report -- LAUR-86-748.

14. M. A. M. Bourke, J. A. Goldstone, M. G. Stout, A. C. Lawson, and J. E. Allison, "Strain Measurement in Individual Phases of an Al/TiC Composite during Mechanical Loading," in Residual Stresses is Composites: Measurement, Modeling, and ThermoMechanical Modeling (ed. E. V. Barrera and I. Dutta, TMS , Proceedings 122nd TMS Annual Meeting) Denver CO, Feb 21-25, 1993.

15. M. A. M Bourke, J. E.. Allison, J. A. Goldstone, N. Shi, M. G. Stout, A. C. Lawson, "Measurement of the Strain in Individual Phases of Aluminum Titanium Carbide during Loading and Comparison with Prediction," in preparation for Scripta Met. Mater.

16. N. Shi, M. A. M. Bourke, J. A. Goldstone, M. G. Stout, A. C. Lawson, L. C. Davis, J. E. Allison, "Influence of Thermal Residual Stresses on the Development of the Average Lattice Elastic Strain during External Loading in the Al/TiC Composites, in preparation for Acta Metall Mater.

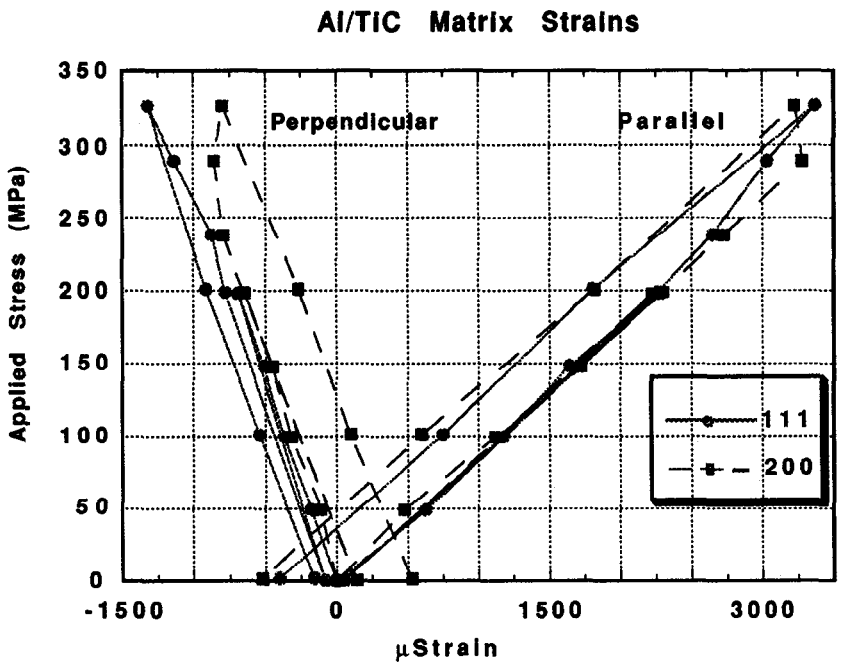


**Figure 2:** Strain data for the (111) and (200) reflections for the aluminum matrix of Al/TiC. Note the large difference in the (111) and (200) final residual strains in the direction perpendicular to the applied load. [ref. 14].

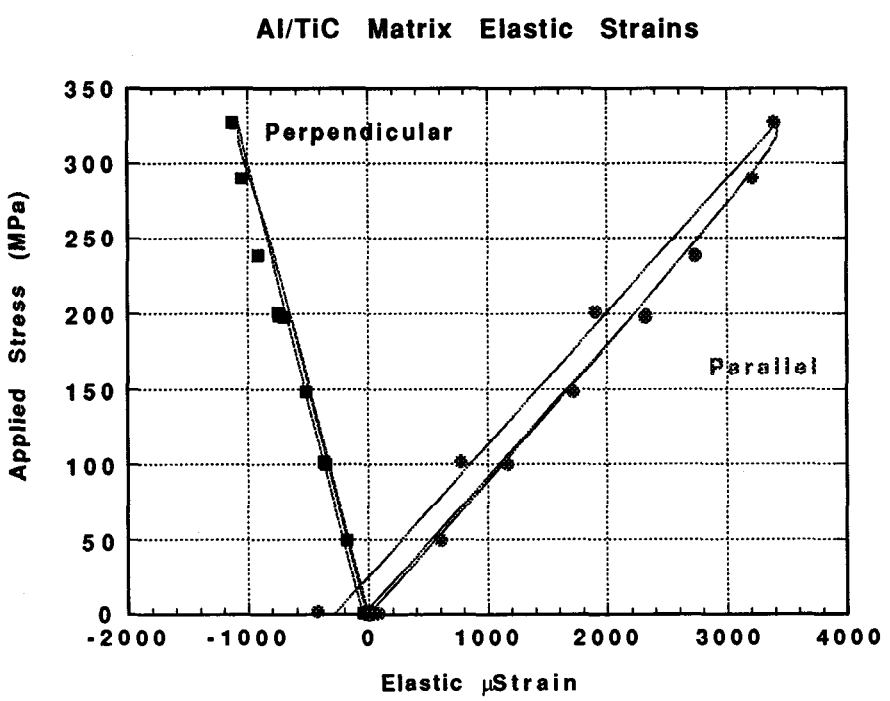


**Figure 3:** Elastic strain data (points) and FEM calculation [solid lines] for the average matrix strain in Al/TiC

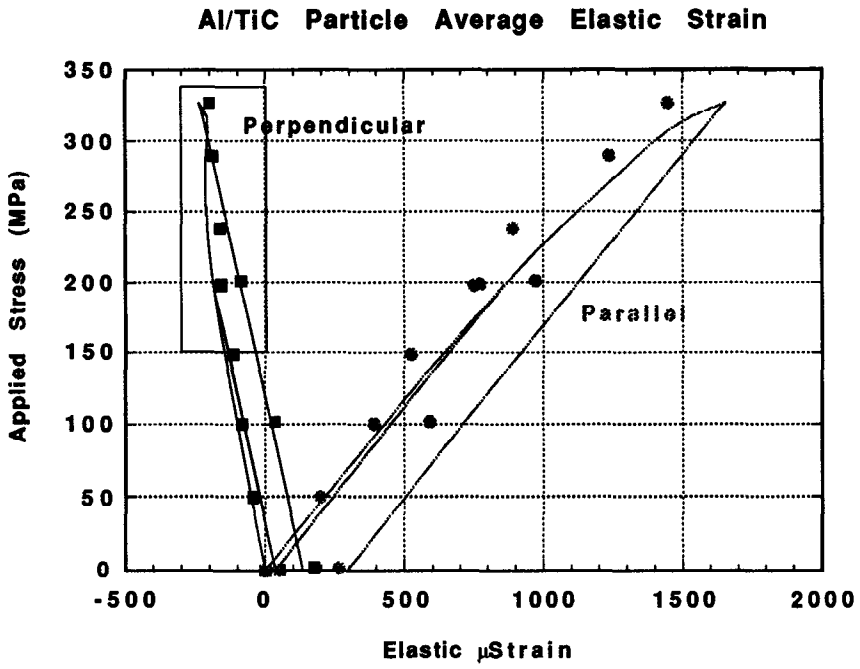


**Figure 4:** Elastic strain data (points) and FEM calculation (solid lines) for the average particle strain in Al/TiC. Boxed area is expanded in fig. 5.

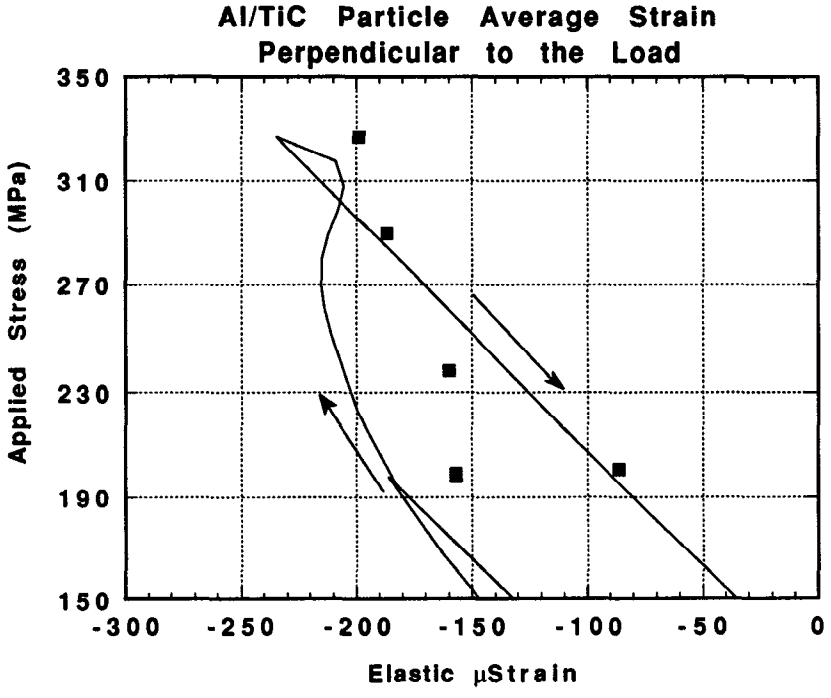


**Figure 5:** Particle elastic strain in the region of "zigzag" behavior (see zoom box in fig. 4).

# Time Resolved Studies on a Millisecond Time Scale: Transient Properties of the Ferroelectric Phase Transition in $Rb_2ZnCl_4$

U.Steigenberger[1], G.Eckold [2,3] and M.Hagen[1,4]

[1]ISIS Facility, Rutherford Appleton Laboratory, Chilton, Didcot, OXON OX11 0QX, UK

[2]Institut für Festkörperforschung, Forschungszentrum Jülich, 52425 Jülich, Germany

[3]Institut für Kristallographie, RWTH Aachen, 52056 Aachen, Germany

[4]Department of Physics, Keele University, Keele, UK

## Abstract

Using time resolved neutron scattering, the evolution of the phase transition between the paraelectric incommensurate (IC) phase and the ferroelectric commensurate (C) phase in $Rb_2ZnCl_4$ has been observed on a microscopic scale. The transformation was driven by a strong rapidly cycling electric field of 8kV/cm applied along the ferroelectric a-axis of the crystal. The response of the sample was monitored by measuring satellite reflections corresponding to the IC- and the C-phase respectively. Synchronization of the electric field to the time structure of the ISIS pulsed neutron source allowed us to observe field induced structural changes on a time scale of **milliseconds**. Characteristic relaxation times were found to depend strongly on temperature.

## 1 Introduction

Studying the evolution of a phase transition as a function of real time provides unique information on possible driving mechanisms. Different intermediate non-equilibrium phases can be passed through and knowledge of these may shed light on the questions **why** and **how** a particular final state is reached. An area of particular interest are transitions between modulated phases where one of the phases is ferroelectric and can be stimulated by an externally applied electric field.

Neutron scattering is a very powerful tool which provides unique information on the properties of condensed matter on a microscopic scale. The wavelengths of thermal neutrons are of the same order of magnitude as interatomic distances and their energies are comparable to those of the elementary lattice vibrations. The measurement of structures and excitations in crystals under equilibrium conditions has therefore been a mainstay of neutron scattering for many years now. However the inherently more difficult measurement of crystal structures under non-equilibrium (time-varying) conditions is a relatively new avenue of investigation. Recently Eck-

old [1] reported the first measurements of processes with typical relaxation times between one to several hundred seconds, using a triple-axis spectrometer at a reactor neutron source. At a pulsed neutron source it is possible to take advantage of the fact that the neutrons are time stamped, to develop special techniques for time resolved studies on shorter time scales.

In this paper we describe a technique for measuring processes with relaxation time scales of order milliseconds at pulsed neutron sources and present some of the results which we have obtained on the ferroelectric phase transition in $Rb_2ZnCl_4$ using this technique.

In section 2 we briefly outline some of the features of $Rb_2ZnCl_4$ relevant to our measurements and then describe in section 3 our technique for time resolved measurements on the millisecond scale which we have developed at the ISIS pulsed neutron facility using the PRISMA spectrometer.

## 2 The ferroelectric phase transition in $Rb_2ZnCl_4$

$Rb_2ZnCl_4$ undergoes two phase transitions [2, 3]. In the normal, high temperature, phase the crystal symmetry is orthorhombic with space group Pmcn. Below 303K the crystal enters an intermediate phase which is characterised by an incommensurate modulation wavevector $q_{IC}=(\frac{1}{3}-\delta)c^*$ where $\delta$, the misfit parameter, is a function of temperature. At $T_c(E=0)=193K$, $Rb_2ZnCl_4$ becomes ferroelectric with the spontaneous polarisation along the a-axis and at the same time the modulation wavevector locks into the commensurate value $q_C=\frac{1}{3}c^*$. The crystal structure of the ferroelectric phase remains orthorhombic, but the space group is now $P2_1cn$.

In the vicinity of the transition temperature $T_c$ (for $T>T_c$) the phase transition from the high temperature IC-phase to the low temperature C-phase can also be driven by applying a strong electric field along the a-axis [4], (cf. figure 1). The electric field induced IC-C transition has been experimentally determined to be first order. The IC and C (for $\delta = 0$) phases give rise to fundamental satellite peaks at $(h,0,l\pm(\frac{1}{3}-\delta))$ satellite positions (for l=odd) and also to higher order harmonics. We have chosen for our investigation of $Rb_2ZnCl_4$ to study the $(2,0,1+(\frac{1}{3}-\delta))$ satellite.

The size of the $Rb_2ZnCl_4$ single crystal used was $4.7\times8\times9mm^3$ and the crystal was of nearly optical quality resulting in a thermal hysteresis of the ferroelectric transition of less than 0.2 K. The sample was mounted with the $b^*$-axis perpendicular to the scattering plane on a boron nitride support inside a closed cycle refrigerator. A thin aluminium container, diameter 40mm, was positioned around the crystal in order to minimize thermal fluctuations. A platinum resistor was mounted very close to the sample to measure the temperature which was controlled to better than 0.1° and measured to 0.01° with a high sensitivity digital voltmeter. The two opposite a-faces of the crystal were coated with silver paint in order to act as electrodes and a high voltage generator was used to produce an electric field of up to 8kV/cm along

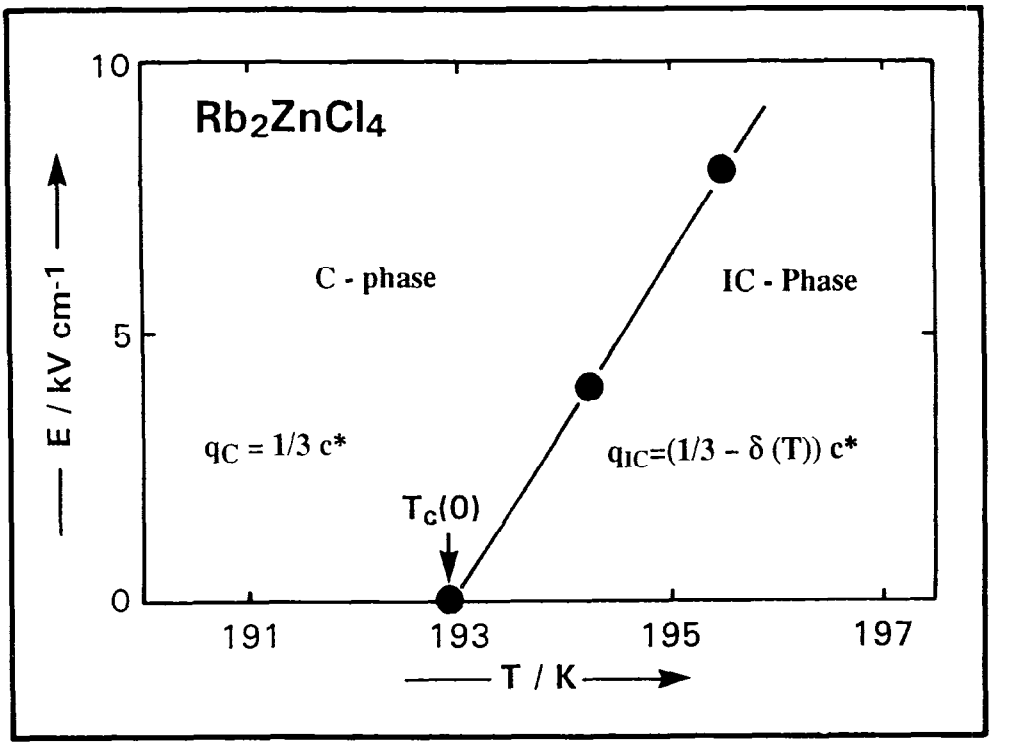


Figure 1: The phase diagram of $Rb_2ZnCl_4$ in the presence of an electric field along the ferroelectric a-axis. The regions of the commensurate C-phase and the incommensurate IC-phase are marked.

the ferroelectric a-axis. This field could be applied either statically or cycled at various frequencies up to 25Hz.

## 3 Time resolved measuring technique

The type of approach to a real time neutron scattering experiment at a pulsed neutron source depends upon whether the relaxation time ( $t_S$ ) of the sample is comparable or not to the frame length ( $\tau$ ) of the source.

Relaxation processes where $t_S$ is of the order of $\tau$ can be studied if the process is reversible and can be triggered by an external perturbation. Instruments at pulsed neutron sources can be used for such measurements by synchronising the external trigger to the production of the neutron pulse. If the relaxation process is contained within one frame, then the real time dependence can be scanned by varying a time delay between the production of the neutron pulse and triggering the external field. If the relaxation process is longer than one frame, of order a few frames, then it is possible to "daisy-chain" frames together to perform a measurement. We have developed this technique at ISIS as described below.

The time resolved neutron scattering measurements reported here were performed at the ISIS spallation neutron source at the SERC Rutherford Appleton Laboratory, U.K., using the PRISMA spectrometer. At a spallation source, sharp pulses of

neutrons are produced with a high peak intensity, separated by a time which is given by the frequency of the proton accelerator. At ISIS this frequency is 50Hz and hence the separation time between two pulses, $\tau$, is 20 milliseconds. This time structure of the neutron source means that the energies of the elastically scattered neutrons can be determined from the time-of-flight they take to travel a distance L from the moderator to the detector. For a single crystal aligned with a scattering plane (h,k,l) in a ($\Theta$,2$\Theta$) configuration with respect to the detector, the corresponding Bragg peaks will be measured at times

$$t_{B,hkl} = \frac{d_{hkl} \cdot m_N \cdot L \cdot sin\Theta}{\pi \cdot \hbar}$$

where 2$\Theta$ is the scattering angle, $m_N$ is the mass of the neutron and $d_{hkl}$ is the d-spacing between the (h,k,l) planes. By rotating the crystal in small steps the rocking curve can be measured.

In a standard pulsed neutron diffraction experiment the scattered neutrons are recorded within the entire time frame of 20 ms and stored in channels of 1 $\mu$s width in the memory of the data acquisition electronics. Subsequent frames are added together until sufficient counting statistics are achieved. For the time resolved measurements an electronic system was installed between the master pulse input and the data acquisition electronics which allowed us to create "superframes" consisting of n standard ISIS frames (the superframe being 20·n ms long), with n=2,4,6,8,10 etc. The electronic system did this by preventing the data acquisition electronics from being reset to t=0 for the subsequent n-1 frames after the first pulse.

The first ISIS master pulse is used to trigger the electric field which is switched on at $t_{on}$ for a length of time $t_{E,on} = \frac{1}{2} \cdot n \cdot 20$ ms ( ie. $\frac{1}{2}$ of the length of the superframe) and then switched off at $t_{off}$. In the first subframe the Bragg peak is measured at a time $t_B$ after the field has been switched on, in the second subframe the Bragg peak is recorded at a time $t_B + 20$ ms and so on.

The starting time $t_{on}$ can be electronically delayed with respect to the ISIS pulse in units of 1 millisecond, thus allowing a coarse tuning of the measurement of the relaxation times. The delay can also be varied by changing the scattering angle 2$\Theta$, shifting the diffraction pattern to a different time which allows for a finer tuning. For example a change in scattering angle by 2° produces a shift in $t_B$ of $\approx$ 0.12 ms at a scattering angle of 2$\Theta \approx 90°$ and a wavelength of 2.83 Å.

The rise time of the electric field was determined to be about 2ms. The time $t_B$ was corrected for the time the neutrons took to travel from the sample to the detector, using the relation $t'_B = t_B L_i/(L_i + L_f)$ where $L_i$ is the moderator to sample distance of 9.03m and $L_f$ is the sample to detector distance of 0.76m. We used different cycling frequencies of the electric field, ranging from 5Hz to 25Hz, resulting in superframes of different lengths, from 200ms to 40ms respectively.

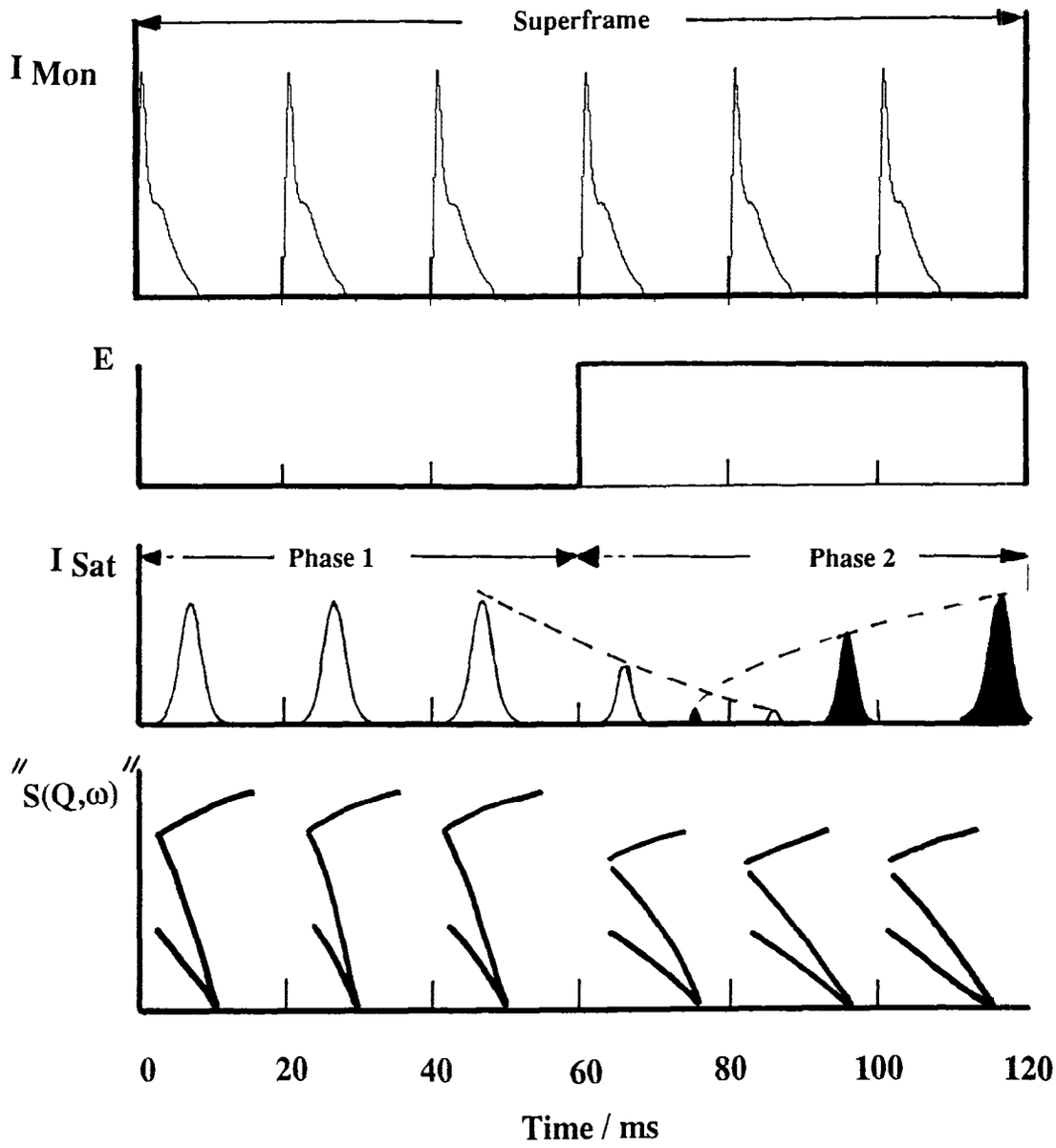


Figure 2: Schematic representation of the measuring technique illustrated for a superframe consisting of six standard frames. In the first line the six individual monitor spectra of the superframe are plotted. The next line shows the variation with time of the electric field. In line 3 the intensity of the satellite peaks is indicated schematically. When the electric field is switched on, the satellites of phase 1 gradually disappear and the satellites of phase 2 (black peaks) appear at a *different* time and their intensity increases as a function of time in the subframes 4 to 6. The last line indicates schematically how the kinetics of phonons can be measured using an inverted geometry PRISMA-type spectrometer at a pulsed neutron source.

Figure 2 shows schematically the variation with time of the various signals: 2a) the incident monitor spectra for 6 ISIS pulses which constitute a superframe in this example, 2b) the time dependence of the electric field, and 2c) the variation in time of the intensity of two sets of Bragg peaks characteristic for two different phases of the system.

Although the primary role for the PRISMA spectrometer at ISIS is to measure excitations in single crystals [5], the presence of horizontal and vertical Soller collimation makes it well suited for single crystal diffraction studies with good Q-resolution. In this diffraction mode the instrument is used without the analyser crystals in place. On PRISMA the moderator to detector distance is 9.79m and therefore at a scattering angle of 20° the commensurate $(2,0,1+\frac{1}{3})$ peak in $Rb_2ZnCl_4$ appears at 2766 $\mu$s and the $(2,0,1+(\frac{1}{3}-\delta))$ satellite peak at 2781 $\mu$s. The angular separation of the two peaks is 0.25° and their rocking curve widths are each 0.24°, which is essentially determined by the instrumental collimation.

## 4 Experimental results

A detailed description of the experimental results will be published elsewhere. Here we present some selected data to illustrate the measuring technique and the wealth of information that the results can provide.

Figure 4 shows the rocking curve of the $(2,0,1+(\frac{1}{3}$ - $\delta)$ satellite at three different times after the electric field has been switched on. The sample temperature was $T=T_c(E=0)$-0.3K, i.e. 0.3K below the phase transition temperature in zero electric field. At t=0 the incommensurate phase is fully developed, 0.2ms after the field has been switched on, a significant part of the crystal has already transformed into the commensurate phase and another 0.5ms later no trace is left of the incommensurate phase. After the electric field has been switched off, the back transformation takes place and hence at the beginning of the next cycle the sample is again in the well defined incommensurate state. For these measurements the electric field was cycled at 25 Hz. We found that on cooling through $T_c$ in an electric field cycled at 25Hz the incommensurate phase is preserved in a small temperature range even below $T_c(E=0)$ and it is therefore still possible to switch between the two phases. A detailed discussion of this unexpected behaviour will be given elsewhere.

Figure 4 summarizes our results for two different temperatures $T=T_c(0)+1.3$K and $T=T_c(0)+1.1$K. Here we have plotted the relative volume fraction of the commensurate phase (the integrated intensity of the IC satellite divided by the sum of the total intensities of the IC and the C satellites) as a function of time. The time dependence of the electric field is also plotted for the cycling frequency of 6.25Hz which we used for these measurements. The relaxation time into the incommensurate phase increases with decreasing temperature suggesting a slowing down behaviour. On the other hand, there appears to be almost no change of the time constant for the transition into the commensurate phase. Here the volume fraction of the C-phase

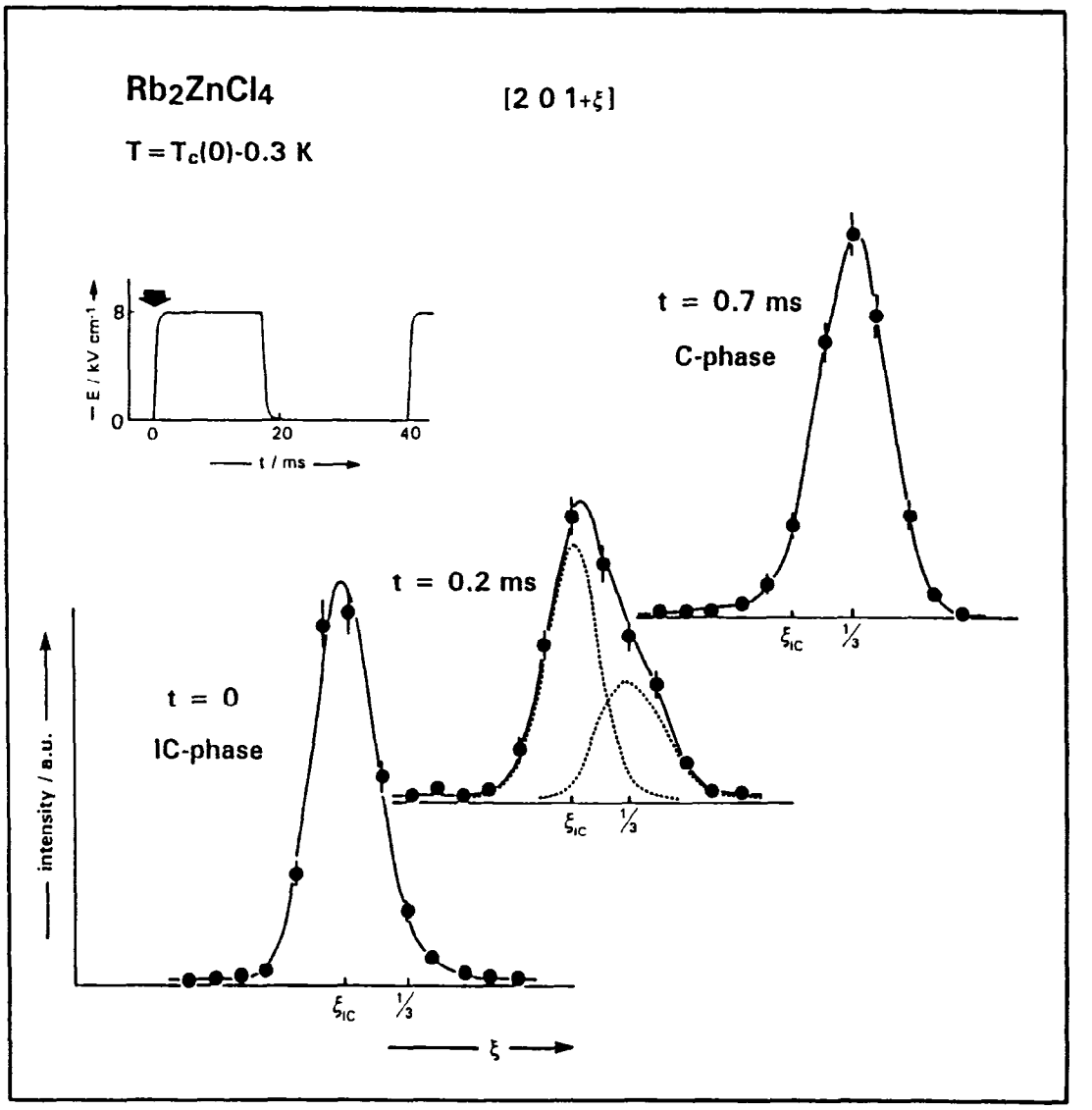


Figure 3: At T=$T_c$(E=0)-0.3K $Rb_2ZnCl_4$ is in the incommensurate phase and the satellite reflection is centred at $\xi=\xi_{IC}$. When the electric field is applied the intensity of the commensurate satellite builds up at $\xi=\frac{1}{3}$ as a function of time. For these measurements the electric field was cycled at 25Hz.

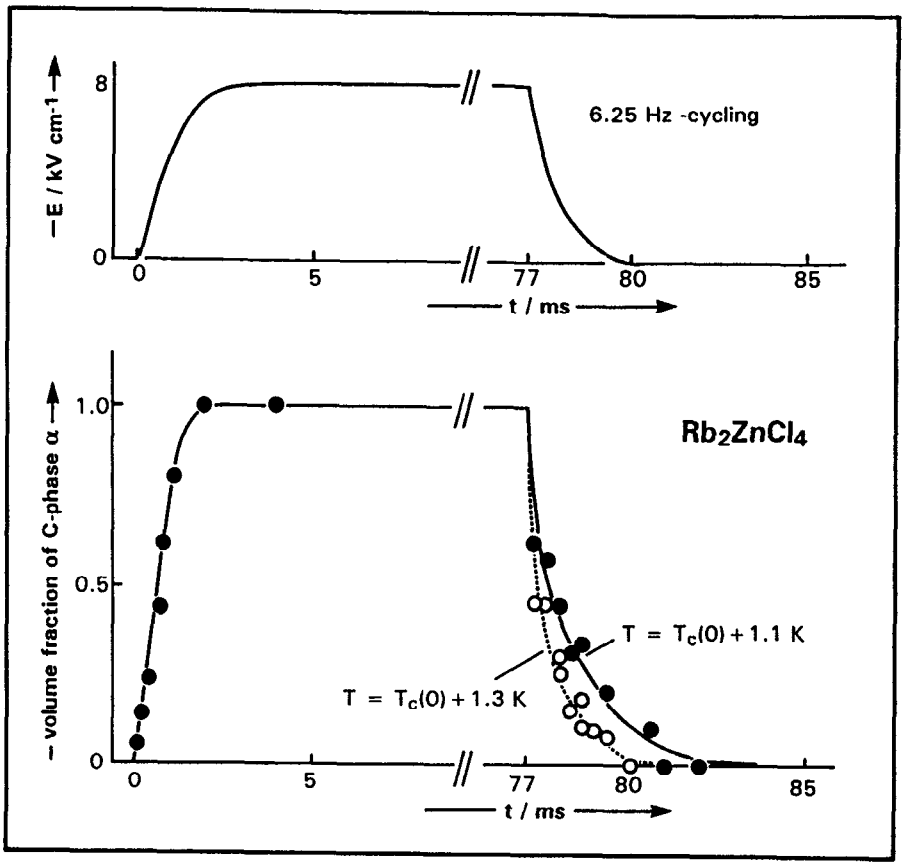


Figure 4: The volume fraction of the commensurate phase is plotted as a function of time for two different temperatures above $T_c(E = 0)$. Here the electric field was cycled at 6.25Hz.

develops with the rise time of the electric field. Within the resolution of the present experiment there are no indications for the existence of intermediate states.

## 5 Conclusion and Outlook

We have developed a technique which allows us to exploit the characteristics of a pulsed neutron source for time resolved measurements on a millisecond time scale. We have demonstrated this technique in an investigation of the ferroelectric phase transition in $Rb_2ZnCl_4$. We found that the IC-C phase transformation occurs spontaneously, whereas the reverse transformation from the C to the IC phase is clearly delayed. The relaxation times vary significantly with temperature and increase when $T_c(E=0)$ is approached.

These experiments were performed using the PRISMA spectrometer as a single crystal diffractometer. However, PRISMA is designed for *inelastic* measurements in single crystals and its capability to measure in one instrumental setting a whole phonon dispersion curve will be exploited in future experiments to investigate the *kinetic behaviour of the dynamic properties* of a system in conjunction with a phase transition (see also figure 2, last line). Each subframe will record the phonon dispersion curve at a particular time during a phase transition and these measurements will provide new insight into the real time behaviour. At present pulsed sources such experiments are time consuming, since the creation of superframes does not

only yield time dependent information but also proportionately increases the total counting time of a measurement (eg. for a superframe 160ms long the counting time is increased by a factor of 8). The advent of new, more powerful spallation sources, such as the planned ESS, will make these time resolved inelastic experiments more manageable and it is therefore timely to develop these techniques.

## 6 Acknowledgements

We would like to thank Professor H.G.Unruh for providing us with the $Rb_2ZnCl_4$ crystal and H. Mitlacher, K. Gascoyne, J. Norris and K. Knowles for technical assistance with the experiment.

## References

[1] G.Eckold, Nuc.Inst. and Meth., **A289**, p221, 1990 ; G.Eckold Jül-2675, Jülich 1992

[2] S Sawada et al., J.Phys.Soc.Jpn. **43**, p2099, 1977

[3] K.Gesi et al., J.Phys.Soc.Jpn. **46**, p697, 1979

[4] K.Deguchi et al., J.Phys.Soc.Jpn. **56**, p208, 1987

[5] U.Steigenberger et al., Nuc.Inst. and Meth., **B53**, p87, 1991

# The effects of inelastic scattering upon small angle diffraction measurements.

R.K.Heenan, ISIS, Rutherford-Appleton Laboratory, Didcot, OX11 0QX, England;
& A.R.Rennie, Cavendish Laboratory, Madingley Road, Cambridge, CB3 0HE, England.

## Abstract.

*The coherent scattering from the large objects studied by small angle scattering (SANS) is predominantly elastic. Experimental measurements show however that the incoherent "background" may have a significant amount of inelastic scattering. For a hydrogenous sample, such as 1 mm of water, roughly half the transmitted neutrons are inelastically scattered, largely to shorter wavelengths. The proportion of the inelastic scatter detected will depend upon relative detector efficiencies at these shorter wavelengths. Experimenters should be aware of this multiple incoherent inelastic scattering when subtracting "incoherent backgrounds" and when comparing such data between different instruments. The use of incoherent scattering for detector calibration also presents some problems. It is profitable for SANS instruments on both pulsed and reactor sources to be able to operate with a pulsed, monochromatic incident beam and time-of-flight analysis in order to be able to examine these effects.*

## Introduction

The success of the SANS technique in many and varied fields of science often relies on data being obtained in absolute units prior to model fitting or Fourier inversion procedures [1]. The precision with which an often relatively large background subtraction can be made, notably from hydrogenous solvents, becomes very important. This is particularly so with techniques that emphasise asymptotic limits of the data such as Porod or Kratky plots [1]. Measurements made at long wavelength at a reactor source, D17, ILL [2] and at shorter wavelengths on LOQ at ISIS [3] demonstrate that the incoherent scattering from hydrogenous materials is highly inelastic. Those familiar with inelastic scattering of neutrons will realise that the slow neutrons used by SANS instruments (wavelength ~ 1 - 20 Å ) are thermalised by these hydrogenous samples, which are typically 1 mm thick. Since the sample is normally at ambient temperature the neutrons are predominantly accelerated to shorter wavelengths, as illustrated below. An uneducated user of a SANS instrument believes that "hydrogen is a strong absorber of neutrons", as verified by sample transmission measurements, so instead expects the neutrons to be slowed down. The purpose of this paper is to illustrate the actual effects and to consider their practical consequences in terms with which the average SANS user will be familiar. For this reason we show inelastic neutron spectra against wavelength rather than energy.

## Experimental

The LOQ small angle scattering diffractometer at ISIS is equipped with a variable aperture chopper synchronised to the source neutron pulses. In normal use, at 25 Hz, the chopper transmits a range of wavelengths from 2 to 10 Å. For the measurements here a small open duty cycle was selected to provide a nearly monochromatic neutron

beam at 50 Hz. Small angle scattering was observed on the two-dimensional $^3He$ multidetector and the energy transfer was determined by the normal time-of-flight electronics. The detector has a useful area of about 64 cm diameter and is at a distance of 4.4 m from the sample, centred on the primary beam . In order to accumulate reasonable statistics, the entire data were summed together to give a single spectrum.

Typical raw data, with time of flight converted to apparent elastic neutron wavelength are shown in Figure 1. Corrections were then made for the background scattering from the empty cell and for the expected wavelength variation of detector efficiency, some results being shown in Figures 2 and 3 against inelastic wavelength. Corrected data for a 1 mm thick sample of $H_2O$ at 25 C using three different incident neutron energies are shown in Figure 3 . The spectra show clearly the peak corresponding to the incident beam at wavelengths of 2.5, 4.1 and 8.8 Å as well as a significant signal of neutrons with a lower wavelength (higher energy). At the shorter wavelengths particularly a small fraction of the neutrons are also slowed down.

A simple consideration of sample transmissions shows that not only is roughly half the scattering inelastic but that it must be dominated by multiple scattering events. Simple fitting of Maxwellian profiles of different temperatures indicates however that the SANS samples are not sufficiently thick for the neutrons to be fully moderated. This makes such scattering inherently difficult to model [4], especially as the $S(Q,\omega)$ cross section for thin samples of materials such as water are not well known.

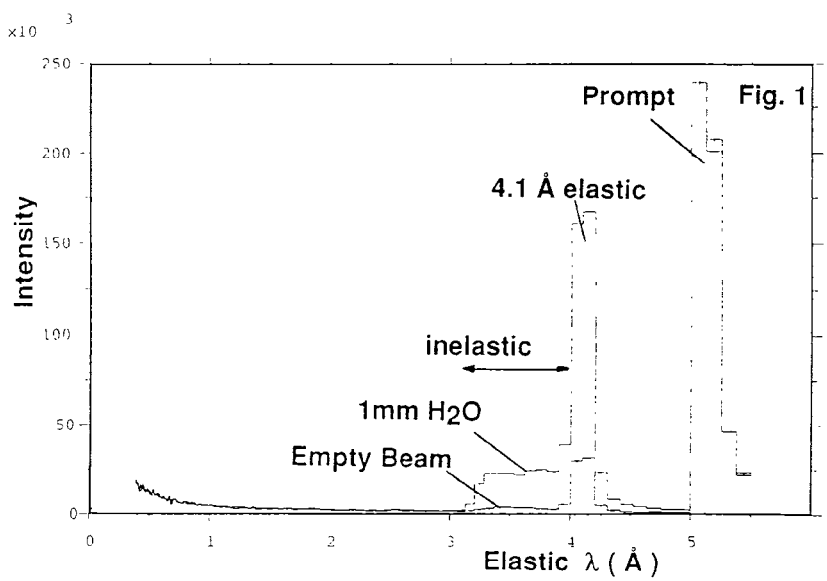


*Figure 1. Raw time of flight spectra ( as apparent wavelength from the total flight time) from LOQ at ISIS, summed over whole area detector, for 1 mm $H_2O$ at 298K and an empty beam run (of the same number of incident neutrons), with a monochromatic incident wavelength of 4.1 Å. The "prompt" peak is a background spike from the next ISIS accelerator proton pulse.*

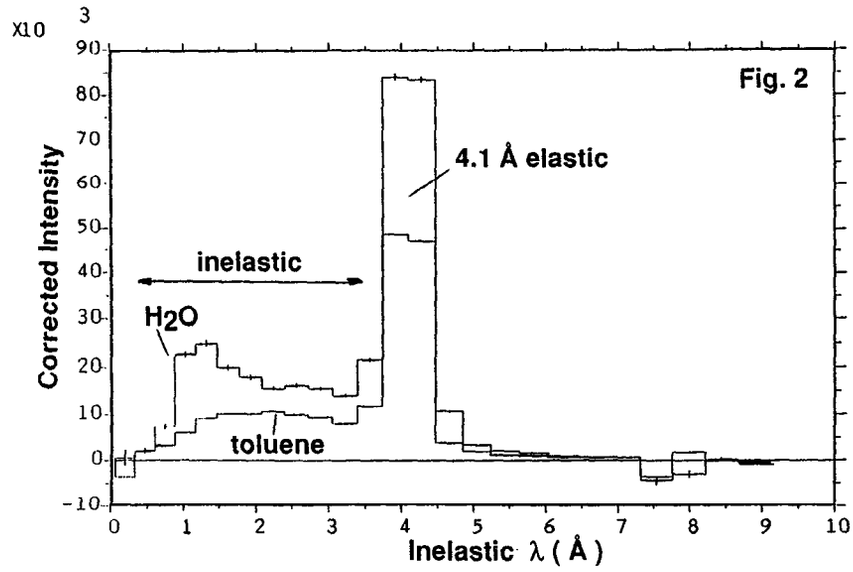


*Figure 2. $H_2O$ data of Figure 1 after conversion to the scattered beam inelastic wavelength and allowing approximately for detector efficiency. Also shown is the inelastic spectrum for 1 mm of toluene $C_6H_5CH_3$, also at 298 K, for the same number of incident neutrons.*

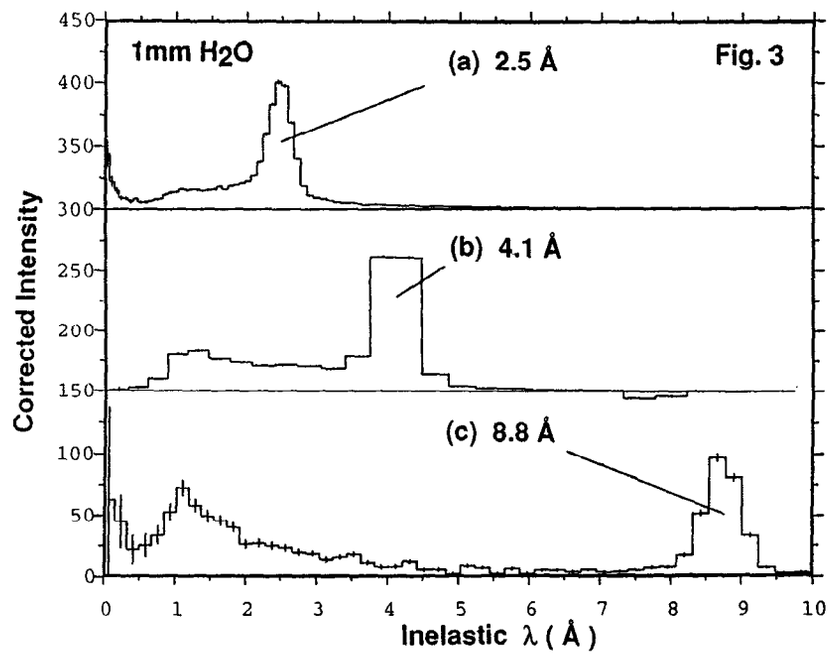


*Figure 3. Time-of-flight spectra of a 1 mm water sample at 298 K measured with incident beams of (a) 2.5, (b) 4.1 and (c) 8.8 Å wavelengths, corrected for expected detector efficiency at the inelastic scattered wavelengths shown.*

## Incoherent background subtraction

The best choice of "incoherent background" material, to subtract from a sample with a coherent elastic SANS signal should have the same multiple inelastic, incoherent spectrum. Summation of proportions of the scattering from separate measurements of fully deuterated and fully hydrogenated samples will not, in detail, be accurate as

their multiple scattering components will not be the same. A mixed $D_2O$ plus $H_2O$ sample will be a reasonable background for a water based sample where the SANS scatterer is at a low volume fraction and itself contains little or no hydrogen [12]. At higher volume fractions, with other types of solvent, or with say a bulk polymer sample, a $H_2O/D_2O$ background might not work so well. We note (for example in Figure 2) that the spectrum from $H_2O$ is quite different from other hydrogenous samples, even when normalised to the same proton density. Perhaps the most ingenious answer, at least for systems such as single polymers where all the coherent scatter is generated by D/H substitution, is to prepare a background sample in which the positions of all H and D atoms have been randomised but are on average in the same chemical sites.

In general it should be noted that an absolute subtraction of a large incoherent signal from beneath a small coherent SANS signal will be difficult to achieve and that the consequences, in terms of systematic errors, of a residual background should always be allowed for in any subsequent model fitting, inversion procedure, or graphical interpretation.

## Data normalisation and comparisons between instruments

Water has frequently been used as a secondary standard for SANS experiments [5]. It is used both as an 'isotropic' scattering material to determine cell by cell variation in detector efficiency and to calibrate the absolute intensity. For the second purpose it is normally necessary to use empirical formulae to obtain the effective scattering cross-section as a function of wavelength or temperature [6-8]. To examine these assumptions, the corrected data for the 1 mm water sample with an incident wavelength of 4.1 is shown as a function of radius (from the beam centre) on the detector in Figure 4. The two curves correspond to the elastic peak (3.9 to 4.3 Å) and the neutrons scattered to higher energies (1.5 to 3.9 Å). In this case no allowance has been made for the variation of detector efficiency with wavelength. Over this rather limited angular range, it appears that, within statistical errors, both the elastic and inelastic parts of the spectrum are "flat", in agreement with earlier results at 12 Å [2]. More detailed measurements of the scattering from different thicknesses of $H_2O$ at the ILL [9] showed that the total scattering scales non-linearly at larger radii on the detector, though the effects are small compared to other geometric effects allowed for by the usual "water normalisation".

It is important to note however that the proportion of the short wavelength inelastic scatter of Figure 4 that will be detected will depend on the nature of the detector used on a particular SANS instrument. For example a high pressure $^3He$ detector will record considerably more than a low pressure $BF_3$ based detector. The apparent cross section of $H_2O$ will thus vary from instrument to instrument, thus it should be regarded as only a secondary standard in relation to intensities from agreed coherent SANS scatterers [10].

On a pulsed neutron source the actual effect of inelastic incoherent scatter depends not only on the detector type but also on the incident spectrum shape and the distance of the detector from the sample. The inelastic incoherent signal (Figure 1) arrives in

different time channels to its elastic part, mostly to shorter wavelength. On following the normal data reduction route [11] into Q space the flat total signal of Figure 4 becomes distorted, dipping at the lowest Q values (longest apparent elastic wavelengths). In fact at the longest wavelength (lowest Q) a nearly pure elastic incoherent signal is seen. Thus in general, and particularly at the lowest Q, the combined data from a range of incident wavelengths from a hydrogenous material need not give a flat cross section. This will be true even though the normalisation procedure for coherent SANS data is correctly allowing for the wavelength dependencies of sample transmission, incident beam spectrum and detector efficiency. LOQ and other pulsed source SANS instruments avoid the use of water as a primary calibrant by making a direct measurement of the efficiency ratio of the main detector to the beam monitor as a function of wavelength. Absolute scaling of cross sections is then checked against coherent SANS scatterers [10]. Vanadium is not used as its cross section is too small to obtain good statistics at all wavelengths in a reasonable time. It is also prone to having small angle scattering from voids or adsorbed hydrogen unless carefully prepared and stored.

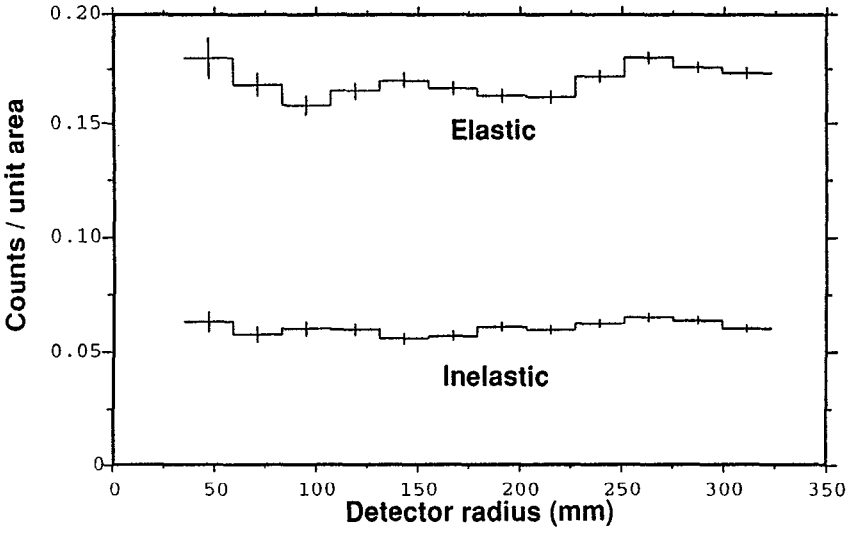


*Figure 4. Elastic and inelastic scattering from 1 mm $H_2O$ with an incident beam of 4.1 Å as a function of the radial position on the detector.*

## Transmission measurements

Absolute SANS scattering cross sections are normally obtained by dividing the recorded scattering by the sample transmission. This is particularly important on a pulsed source instrument where coherent SANS signals from different wavelengths are combined since the transmission varies with neutron wavelength [11]. This in itself may pose difficulties as the largest variations of transmission with wavelength are for incoherent scatterers. A detail discussion of all the possible effects is beyond the scope of this paper. One must consider exactly how the "cross-section" is defined, generally SANS results assume it to be proportional to the probability of coherent scattering only from the particles of interest, and assume that the total scattering cross

section for all processes is low. The optimal method for measuring the transmission will depend on the size of the coherent SANS signal compared to any incoherent background, how the data will be processed, and on all the instrumental factors mentioned above, such as detector type ! In the ideal some iteration of the derived cross section back into the transmission measurement may be required. Some compensation for the variation of the recorded inelastic incoherent scatter with detector type may occur in that the apparent transmission, if measured with the same detector, will also be higher with detectors that are more efficient at short wavelengths.

Various semi-empirical methods for either incoherent background subtraction or data normalisation between different detector positions use the assumption that, for a sample such as $H_2O$, the total incoherent scatter is proportional to $( 1-T(\lambda) )I(\lambda)$ where $I(\lambda)$ is the incident flux. Again it should be noted that due to the presence of considerable inelastic scattering the counts detected will vary from instrument to instrument, thus the scaling parameters used will not be universal constants. The same warnings made above about changes of inelastic spectra between a sample and the chosen "background" material will also apply to $(1-T(\lambda))$ methods of compensating for background subtraction of different D/H ratios of water [12-14], polymer solutions [15] or solid polymers [16].

## Conclusions

As outlined above the effects of inelastic incoherent scattering on a SANS instrument can be subtle, and vary from one instrument to another and even with different detector types on the same instrument. The results described here and in earlier work [2] both required an ability to operate SANS instruments in an unfamiliar mode, namely with time of flight data collection and a pulsed, monochromatic neutron beam. It would be useful for those designing or upgrading SANS equipment to include such a facility to empirically quantify inelastic effects on their particular instrument.

Care needs to be taken when subtracting a large incoherent background from a small coherent SANS signal, though only general guidelines rather than quantitative formulae can at present be offered to help to do this in an absolute sense.

For most SANS experiments the effects of inelastic scattering will be minimal compared to other effects such as detector inhomogeneities or resolution smearing. As far as normalisation of data is concerned the "incoherent" scattering from 1 mm of $H_2O$ at a given temperature, or any other hydrogenous material, though so far appearing to be "flat", should not be regarded as universally constant as the proportion of the considerable inelastic component detected will vary from one detector type to another.

## REFERENCES


[1] Glatter O., Kratky O. (Eds.) "Small Angle X-Ray Scattering", Academic Press, London (1982)

[2] Ghosh R. E. and Rennie A. R., Institute of Physics Conference Series **107**, 233-244 (1990).

[3] Rennie A.R. & Heenan R.K., proceedings of ISSI Meeting, Dubna 1992 ( copies available from RKH).

[4] Copley J.R.D., Journal of Applied Crystallography **21**,639-644 (1988).

[5] Jacrot B., Reports on Progress in Physics **39**, 911-953 (1976).

[6] Jacrot B., Zaccai G., Biopolymers **20**, 2413-2426 (1981).

[7] Ragnetti M., Geiser D., Höcker H., Oberthür R.C., Die Makromolekulare Chemie **186**, 1701-1709 (1985).

[8] Ragnetti M., Oberthür R.C., Colloid & Polymer Science **264**, 32-45 (1986).

[9] Rennie A.R., unpublished data from D17

[10] Wignall,G.D. & Bates, F.S., Journal of Applied Crystallography **20**, 28-40 (1987).

[11] Heenan R. K. & King S.M., proceedings of ISSI Meeting, Dubna 1992 ( copies available from RKH).

[12] May R.P., Ibel K., Haas J., Journal of Applied Crystallography **15**, 15-19 (1982).

[13] Knoll W., Schmidt G. & Ibel K., Journal of Applied Crystallography **18,** 61-64 (1985).

[14] Stothart P.H., Journal of Applied Crystallography **20,** 362-365 (1987).

[15] Geissler E., Hecht A.M., Duplessix R., J.Polymer Sci. Polymer Phys. **20**, 225 (1982).

[16] W.S.Dubner, J.M.Schultz & G.D.Wignall, Journal of Applied Crystallography **23,** 469-475 (1990).

# A MEASUREMENT OF THE PROTON WAVEFUNCTION IN MOLECULAR HYDROGEN BY NEUTRON COMPTON SCATTERING

**J Mayers (Rutherford Appleton Laboratory, Chilton, OX11 0QX)**

## Abstract

The momentum distribution of the proton in liquid and solid hydrogen has been measured by neutron Compton scattering (NCS), at energy transfers between 3 and 50 eV. The data display features due to interference between the proton and neutron wavefunctions and are accurately described by a simple quantum mechanical model, incorporating previous spectrocopic data. The excellent agreement between calculation and data in this simple system demonstrates that the NCS technique can provide accurate information about the behaviour of the proton in condensed matter. There are many applications of NCS to more complex physical systems of fundamental interest in physics, chemistry and biology.

# A MEASUREMENT OF THE PROTON WAVEFUNCTION IN MOLECULAR HYDROGEN BY NEUTRON COMPTON SCATTERING

The possibility of measuring nuclear momentum distributions in condensed matter sytems by neutron scattering was first suggested by Hohenberg and Platzmann [1] nearly 30 years ago. The method is analagous to the measurement of electron momentum distributions by Compton scattering [2] and measurement of nucleon momenta by Deep Inelastic Scattering [3] and is known as Neutron Compton Scattering (NCS) or Deep Inelastic Neutron Scattering (DINS). The theoretical basis of all three techniques is the impulse approximation (IA), which is exact when the momentum transfer $\vec{q}$ and energy transfer $\omega$ are infinite [4,5,6]. When the IA is valid, the scattering cross section is proportional to the distribution of nuclear momentum components along the direction of $\vec{q}$ and can be used to determine $n(\vec{p})$, the distribution of nuclei (and hence atoms) in momentum space.

NCS measurements on protons have a particularly simple interpretation, as the interaction of protons with other atoms can usually be accurately accounted for [7,8] in terms of a single particle potential and hence by a proton wavefunction. From elementary quantum mechanics, $n(\vec{p})$ is related to the Fourier transform of the proton wavefunction $\Psi(\vec{r})$ via,

$$n(\vec{p}) = \frac{1}{(2\pi)^3}\left|\int \Psi(\vec{r})\exp(i\vec{p}.\vec{r})d\vec{r}\right|^2 \qquad (1)$$

and an NCS measurement of $n(\vec{p})$ can be used to determine the wavefunction in an analagous way to the determination of real space structure from a diffraction pattern. In principle such measurements can provide very detailed information about the behaviour of the proton in a variety of systems of fundamental interest in physics, chemistry and biology.

NCS measurements on protons have only become possible since the construction of intense accelerator based neutron sources , which have allowed accurate inelastic neutron scattering measurements with energy transfers in the eV region [9]. For NCS measurements on the proton in molecular hydrogen, energy transfers much greater than the vibrational frequency of the molecule (516 meV [10]), are required before the IA can be used to reliably determine $n(\vec{p})$. At lower energy transfers the IA is no longer valid and $n(\vec{p})$ is not related

in a simple way to the observed scattering intensities. In sytems with weaker binding, lower energy transfers can be used and many early NCS measurements were performed on helium at relatively low energy and momentum transfers, ($\omega$ < 300 meV and $q$ < 15 Å$^{-1}$). These studies were motivated primarily by the possibility of directly observing the Bose condensate fraction in superfluid $^4$He [11,12,13,14,15]. More recently NCS measurements with 15<$q$<40 Å$^{-1}$ and incident energies up to 2 eV have been made on condensed phases of helium[16] and neon[17]. There have been a few pioneering studies on various systems at eV energy transfers [18,19,20]. Measurements on molecular hydrogen have also been made, with $\omega$ insufficient to excite vibrational transitions [21,22]. This allows a measurement of the centre of mass motion of $H_2$ molecules rather than the momentum distribution of individual protons. The measurements described here were made with 3<$\omega$<50 eV and 30<$q$<130Å$^{-1}$. At such high values of $q$ and $\omega$, accurate NCS measurements can be made even in strongly bound systems such as hydrogen.

The formal statement of the IA in neutron scattering is [23]

$$S(\vec{q},\omega) = \int n(\vec{p})\delta\left(\omega + \frac{p^2}{2M} - \frac{(\vec{p}+\vec{q})^2}{2M}\right)d\vec{p} \tag{2}$$

where $S(\vec{q},\omega)$ is the dynamic structure factor, $n(\vec{p})$ is the nuclear momentum distribution, $\vec{p}$ is the atomic momentum and $M$ is the nuclear mass. The $\delta$ function expresses the conservation of kinetic energy, which applies to the collision between the nucleus and the neutron when the IA is satisfied. When the scattering sample is isotropic it can be shown that [5],

$$S(q,\omega) = \frac{M}{q}J(y) \tag{3}$$

where

$$y = \frac{M}{q}\left(\omega - \frac{q^2}{2M}\right) \tag{4}$$

and

$$J(y) = 2\pi\int_{|y|}^{\infty} pn(p)dp \tag{5}$$

$J(y)dy$ is the probability that an atom has momentum component along $\vec{q}$ with magnitude between $y$ and $y+dy$ and is known as the Compton profile. Equations 3 to 5 express the `$y$ scaling' property of the neutron cross section at sufficiently high $q$ [24].

The measurements were performed on the electron volt spectrometer eVS at the ISIS neutron source [25]. A filter difference technique [26], with a gold foil anlayser, was used to fix the energy of the scattered neutron at 4.922 eV. Time of flight techniques [27] were used to determine the energy of the scattered neutron and hence $S(q,\omega)$. The sample of para hydrogen was measured at temperatures of 20K and 4K (the liquid and solid phases respectively) and was a 5% scatterer, contained in a planar aluminium can with a sample thickness of ~1mm and with the sample plane perpendicular to the incident beam. Measurement times were 24 hours at each temperature. Due to the $y$ scaling property mentioned above, all scans through $q,\omega$ space map on to the same function $J(y)$. Thus providing the IA is well satisfied the measurements of $J(y)$ at different angles differ only in the width of the instrument resolution function and can be averaged to improve statistical accuracy. As the differences observed between the 4.9K and 20K data were at the limits of measurement accuracy, the data sets at the two temperatures were also averaged to further reduce the statistical error.

Figure 1a shows the average of Compton profiles measured in 10 $^3$He gas detectors at angles between 35 and 45°, Figure 1b that for 10 detectors between 45 and 55° and 1c for 20 detectors at angles between 55 and 75°. The instrument resolution function [25,28] is also shown for each of these data sets, together with the energy and momentum transfers corresponding to the detector at the centre of each bank. There is a small multiple scattering component in the data which is visible at large positive $y$ values , particularly in the data sets at the two lower angles and this has been fitted by a second order polynomial. The data shows small systematic shifts of the peak of the distribution towards negative $y$, due to inaccuracies in the IA which are present at the finite $q$ of the measurement. It has been shown by Sears [5] that symmetrisation of data about $y=0$ removes most of these inaccuracies and this procedure has been followed to produce the data shown in Figure 2. The data from all detectors between

35° and 55° has been averaged and the multiple scattering background subtracted before symmetrisation.

The results are well described by a simple quantum mechanical model. It is assumed that the hydrogen molecule is bound by a harmonic potential and that its centre of mass translational motion is independent of its vibration along the bond axis. $J(y)$ is then the convolution of the momentum distributions for the vibrational and translational motions considered separately.

$$J(y) = \int J_T(y')J_V(y'-y)dy' \tag{6}$$

The translational momentum distribution $J_T(y)$ is approximated by a Gaussian function.

$$J_T(y) = \frac{1}{\sqrt{2\pi\sigma_T^{\,2}}}\exp\left(\frac{-y^2}{2\sigma_T^{\,2}}\right) \tag{7}$$

From previous measurements [21] the kinetic energy of the centre of mass motion is 63 ±6K in the liquid at 17K and 76±9 in the solid at 10K. Taking the average of these values as 70K, the translational kinetic energy of each atom is 35K $=3\sigma_T^{\,2}/(2M)$ and $\sigma_T$=0.70 Å$^{-1}$.

The momentum distribution $J_V(y)$ associated with vibration along the bond can be determined from the wave function of the proton in the molecule. Since the binding is assumed harmonic, each atom will have a Gaussian probability distribution along the bond axis, centred at its mean position at distance $R$ from the centre of mass, where $2R$ is the bond length. In parahydrogen below 20K only the J=0 state of rotation is thermally occupied and the molecular wavefunction has no directional dependence. Thus the wave function of each proton is a spherical shell.

$$\Psi(r) = \left[2\pi^{3/2}\sigma(\sigma^2+2R^2)\right]^{-1/2}\exp\left[\frac{-(r-R)^2}{2\sigma^2}\right] \tag{8}$$

where the mean square displacement of the atom from its mean position along the bond is $\sigma^2/2$ $(=\int r^2|\Psi(\vec{r})|^2 dr)$. Neglecting terms of order $erfc\left[R^2/(2\sigma^2)\right]$ equations 1 and 8 give,

$$n(p) = \frac{2\sigma}{\pi^{3/2} p^2 (\sigma^2 + 2R^2)} \left(p\sigma^2 \cos pR + R \sin pR\right)^2 \exp\left(-\sigma^2 p^2\right) \qquad (9)$$

The bond length is accurately known from spectroscopic measurements ($R$=0.3405 Å [10]) and the value of $\sigma$ can be determined from the frequency of molecular vibration as $\sigma = 0.1269$ Å . The solid line in Figures 1a-1c is fit to a convolution of the model $J(y)$ with the resolution function. The only fitting parameters are a scale factor, the position of the distribution and the polynomial coefficients, which account for the multiple scattering background. The values of $\sigma$ ,$R$ and $\sigma_T$ were fixed at the values given above. It can be seen that the model gives excellent agreement with the measurements at all angles. The solid line in Figure 2a is the calculated $J(y)$ after convolution with the resolution function- there are no free parameters. The difference between the predictions of the model and the symmetrised data is shown in figure 2b as the points oo. A fit to the data shown in figure 2a, with $R$ and $\sigma$ as free parameters gave $R$=0.356± 0.003 Å and $\sigma$=5.70±0.03 Å$^{-1}$, in good agreement with the values of 0.37 and 5.577 obtained from spectroscopy, although outside the quoted statistical error, due to small systematic errors.

The importance of including the oscillatory terms in equation 9 is demonstrated by the predictions of a classical model, which neglects the wave nature of the proton. It is assumed that the molecule is a classical linear vibrator and that each proton has a Gaussian momentum distribution along the bond. Averaging over all possible directions of the bond axis in space, to take account of the isotropy of the sample gives

$$n(p) = \frac{1}{2\pi p^2} n_V(p) \qquad (10)$$

where $n_V(p)$ is the distribution of momentum components along the bond. A calculation using equations 5,6,7 and 10 gives the results shown as the dashed line in Figure 2a. The difference between the classical and the quantum models is shown as the solid line in figure 2b and displays oscillations with a first maximum at $y \approx \pi/(2R)$. This is well reproduced by the data points xx, which are the difference between the data and the classical prediction. The oscillations in

the data are the first observation of interference between the proton and neutron wavefunctions.

The future applications of NCS measurements from protons and deuterons are very wide. An example is the hydrogen bond where NCS can determine whether the observed bi-modal distribution of the proton in hydrogen bonds is the result of statistical or quantum disorder [29]. The information obtained from NCS is qualitatively different to that given by neutron diffraction measurements. The latter determine an infinite time average of the spatial distribution of the proton wheras the former measures the proton wavefunction on a very short timescale. Thus NCS can distinguish between quantum tunneling and thermally induced hopping of the proton between different sites. One application is to the study of the mechanism of protonic diffusion in metals, semiconductors and ionic conductors. Another is to the determination of the proton wavefunction in molecules which undergo rotational tunnelling [30].

The very close agreement between data and calculation in this simplest of protonic condensed matter systems, demonstrates that NCS measurements have now reached a high level of accuracy. It shows that wavefunctions of protons can be determined even in isotropic samples, such as liquids, powders, amorphous materials and polymers. Much more detailed information about the proton wavefunction can be obtained from single crystal samples, where NCS allows a model independent reconstruction of both the proton wavefunction and the potential well of the proton in three dimensions [29]. Orders of magnitude increases in the accuracy of NCS measurements will soon be produced by improvements in countrate and resolution and it seems certain that future measurements will provide precise and unique information about the short time dynamics of protons, in many condensed matter systems of fundamental physical interest.

**Acknowledgements**

Thanks to Dr. J. Tomkinson for many stimulating discussions, to Dr. E. Pace for pointing out the inadequacy of the classical model, to Dr A. D. Taylor for support and encouragement and to the ISIS sample environment group, particularly I. Bailey, for help with the experiment.

## References


1 P. C. Hohenberg and P. M. Platzmann, Phys Rev **152**, 198 (1966)

2 P. M. Platzmann in `Momentum Distributions', ed R. N. Silver and P. E. Sokol (Plenum Press,New York, 1989, p249)

3 I Sick in ref 2, page 175.

4 R Newton, 'Scattering Theory of Waves and Particles', (Springer, Berlin, 1981)

5 V. F. Sears Phys. Rev. B **30**, 44 (1984)

6 J. Mayers Phys. Rev. B **41**,41 (1991)

7 R. Hempelmann, D. Richter and D. L. Price Phys. Rev. Lett. **58**, 1016 (1987)

8 M. Warner, S. W. Lovesey and J. Smith Z. Phys. B **39**, 2022 (1989)

9 R. S. Holt, J. Mayers and A. D. Taylor in ref 2 , p. 295

10 I. F. Silvera, Rev. Mod. Phys. **52**, 393 (1980)

11 R. A. Cowley and A.D. B. Woods, Phys. Rev. Lett. **21**, 787 (1968)

12 O. K. Harling, Phys. Rev. Lett. **24**, 1046 (1970)

13 H. A. Mook, Phys. Rev. Lett. **32**, 1167 (1974)

14 H. A. Mook, Phys. Rev. Lett. **51**, 1454 (1983)

15 P. Martel, E. C. Svensson, A. D. B. Woods, V. F. Sears and R. A. Cowley, J. Low Temp. Phys. **23**, 285 (1976)

16 T. R. Sosnick, W. M. Snow, and P. E. Sokol, Phys. Rev. B **41**, 11185 (1990)

17 D. A. Peek, M. C. Schmidt, I. Fujita and R. O. Simmons, Phys. Rev. B **45**, 9671 (1992) and **45**, 9680 (1992)

18 H. Rauh and N. Watanabe, Phys. Lett. **100A**, 244 (1984)

19 M. P. Paoli and R. S. Holt, J. Phys. C **21**, 3633 (1988)

20 S. Ikeda, K. Shibata, Y. Nakai amd P. W. Stephens, J. Phys. Soc. Japan **61**, 2619 (1992)

21 W. Langel, D. L. Price, R. O. Simmons and P. E. Sokol, Phys Rev B **38**,11275 (1988)

22 K. W. Herwig, J. L. Gavilano, M. C. Schmidt and R. O. Simmons, Phys. Rev. B **41**, 96 (1990)

23 S. W. Lovesey, ` Theory of Neutron Scattering from Condensed Matter', (Oxford University Press, New York,1987)

24 G. B. West in ref 2, p95.

25 J. Mayers and A. C. Evans, Rutherford Laboratory Report, RAL-91-048 (1991)

26 P. A. Seeger, A. D. Taylor and R. M. Brugger, Nuc. Inst. Meth, **A240**, 98 (1985)

27 C. G. Windsor, `Pulsed Neutron Scattering', (Taylor and Francis, London, 1981)

28 C. Andreani, G. Baciocco, R. S. Holt and J. Mayers Nuc. Inst. Meth. **A276** , 297 (1989)

29 G. Reiter and R. N. Silver, Phys. Rev. Lett. **54**, 1047 (1985)

30 W. Press, `Single Particle Rotations in Molecular Crystals' (Springer, Berlin, 1981)

## Figure Captions

**Figure 1.**

The data points are the average of the measured neutron Compton profiles obtained from detectors in three different angular ranges. (a) 35°-45°, (b) 45°-55°, (c) 55°-75°. The solid line is the fit described in the text. The resolution function is shown for each data set as a dashed line.

**Figure 2**

In (a) the points oo are the sum of data from 20 detectors at scattering angles between 35° and 55° after subtraction of multiple scattering and symmetrisation. The solid line is the calculation using equation 9 and the dashed line that using equation 10, both after convolution with the instrument resolution function. Figure 2b shows the difference between the data and the two models. oo equation 9, xx equation 10. The solid line is the difference between the quantum and classical models.

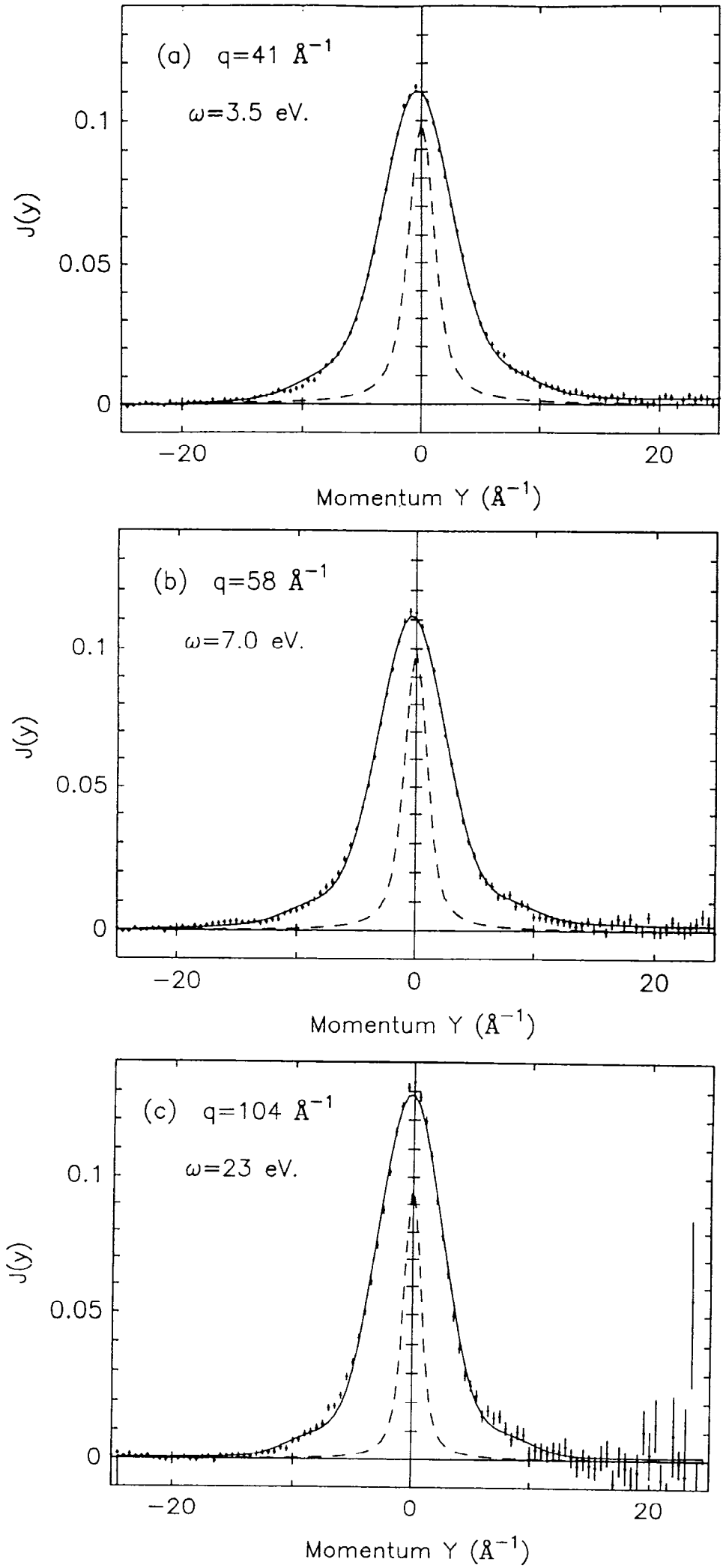
(a) q=41 Å$^{-1}$
ω=3.5 eV.
(b) q=58 Å$^{-1}$
ω=7.0 eV.
(c) q=104 Å$^{-1}$
ω=23 eV.
J(y)
0.1
0.05
0
−20
0
20
Momentum Y (Å$^{-1}$)

Fig. 1.

Figure 2a.

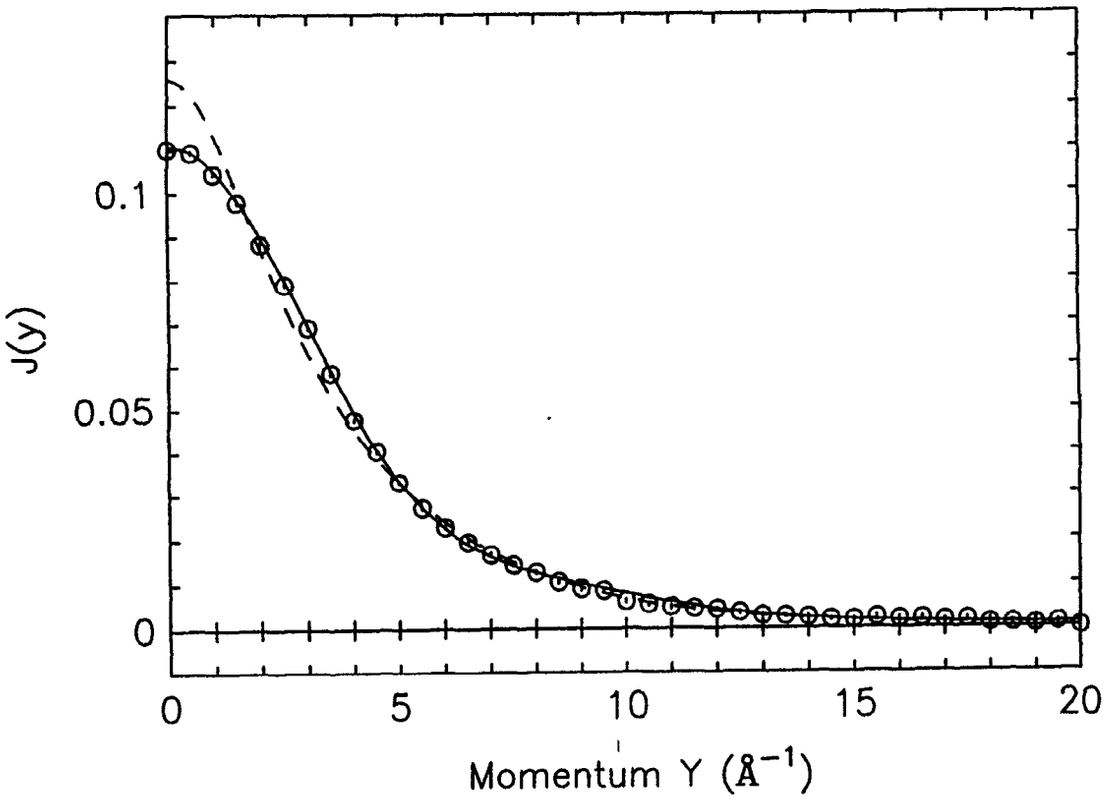


Figure 2b

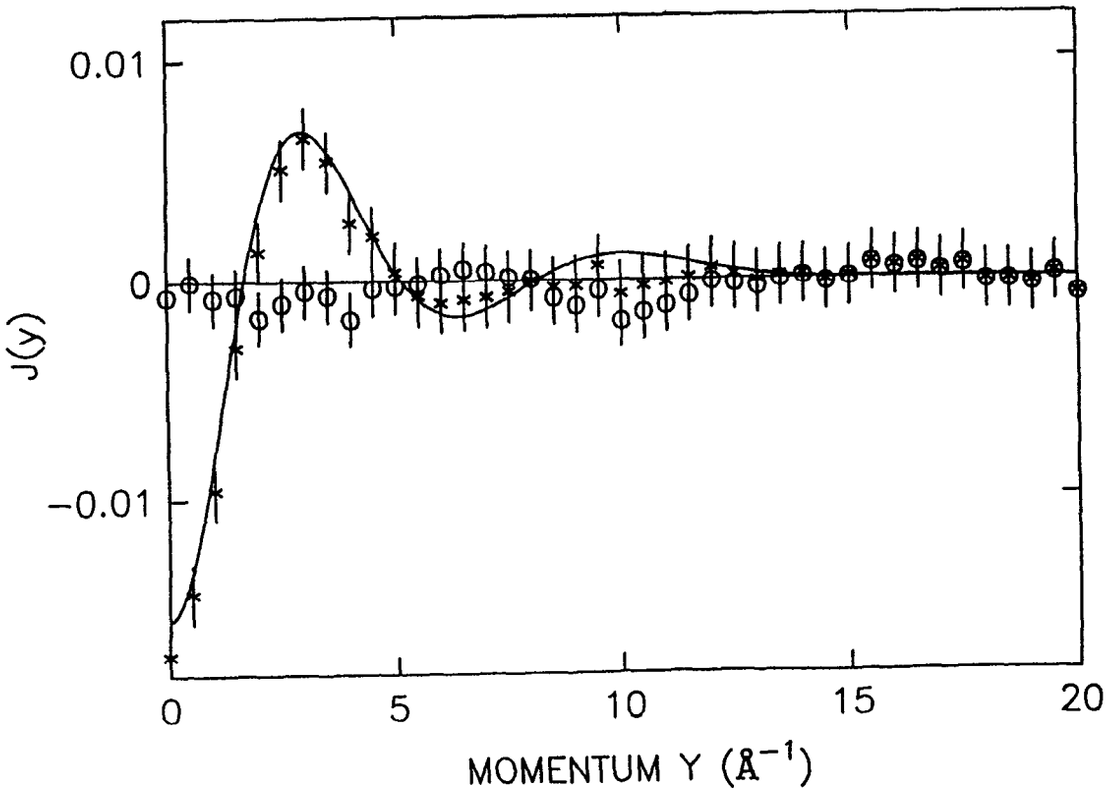

# DEVELOPMENT AND USE OF PULSED HIGH MAGNETIC FIELDS FOR NEUTRON DIFFRACTION EXPERIMENTS

M.Motokawa, M.Arai, M.Mino, K.Ubukata, T.Bokui and M.Fujita
Department of Physics, Faculty of Science,
Kobe University, Rokkodai, Nada, Kobe 657, Japan

abstract

Following the first report presented at the previous ICANS in Tsukuba on the development and use of pulsed high magnetic fields for neutron diffraction experiments, recent technical development and measurements of neutron diffraction in high fields are reported.

In addition to the 20 Tesla magnet whose field direction is horizontal and almost parallel to the neutron beam from the target, vertical field up to 16 Tesla is available. This is more convenient than the horizontal method to obtain a large scattering angle and a stable temperature by use of glass Dewar. A new magnet for 30 Tesla field is designed and now under construction by using a strong metal and by a new machining method. Another method by a copper wire coil which is immersed in a liquid nitrogen vessel is also tried.

After determination of the complicated magnetic structure of $PrCo_2Si_2$ in high field, we have performed to observe a field induced structure change due to the quantum effect in $CsCuCl_3$.

## 1. Introduction

One of the most interesting phenomena in solid state physics is considered to be the phase transition of materials induced by changing temperature, pressure or magnetic field. It is usually accompanied by a symmetry change which causes a structure transition and it is well known that the direct way to look in the symmetry of the structure is X-ray or neutron scattering. Especially the latter is useful for mapping the dispersion relations of the elementary excitations on the $\omega-\hbar$ diagram. This is one of the reasons why the combination of neutron diffraction technique with the extreme condition of low temperature, high pressure or high field is regarded as the important and urgent subject.

Regarding the general technique for high magnetic field, it has been developed intensively in this decade and now 80 Tesla field is available without destruction in a pulsed way, while the static field is now up to 30 Tesla. These high fields are under the practical use for various experiments such as the measurements of magnetization, optics, magnetoresistance, magnetic resonance and so on. As mentioned in the previous paper [1], however, such high field techniques had been considered to be difficult to use for neutron diffraction experiment. For example, a static high field up to 30 Tesla is almost impossible to use for neutron scattering experiments because of its hugeness in both size and budget. The pulsed field had been also unuseful because the data accumulation is necessary for the neutron

diffraction experiments while the pulsed field was usually single shot. So the standard method is to use a superconducting magnet with the neutron beam from a reactor. Because of the complicated configuration of equipment, i.e. installation of cryostat for the superconducting magnet, sample cryostat and goniometer, the available field has been limited lower than 10 Tesla. We considered that if the pulsed field is repeated with coincidence of the pulsed neutron beam, this method would be a breakthrough to develop the high field neutron diffraction experiments. This is the motivation of developing the repeating pulsed field. As the first step of our project, we succeeded to obtain high fields of 20 Tesla every 2 seconds [2].

## 2. Survey of the previous work

The profile of our equipment is as follows [1][2][3][4]:

(i) Capacitor bank
- Capacitance: 1.2 mF
- Maximum stored energy: 50 kJ at 10kV
- Repeating frequency: less than 0.5 Hz

(ii) Magnet
- Inductance: 80 μH
- Inner diameter: 40 mm
- Outer diameter: 144 mm
- Maximum field: 20 Tesla at 20 kA
- Duration time : 1 msecnd
- Field shape: half sine curve
- Flow rate of cooling water: 0.33 l/min
- Temperature difference: 6°C at 20 Tesla
- Life time: 20000 times at 20 Tesla
- Field direction: horizontal

(iii) Cryogenics
- Cryostat: Liquid helium flow type
- Lowest temperature: 4.2 K
- Sample size: $7 \times 7$ mm$^2$ and thickness of a few mm

(iv) Others
- Neutron beam: Spallation neutrons at KENS
- Scattering angle: $2\vartheta = 10°$
- Spectrometer: TOF method

The first successful trial of measurement was the determination of the complicated magnetic structure at high field of $PrCo_2Si_2$ [3][4] which shows a metamagnetic transition at 1.2, 3.8, 6.7 and 12.2 Tesla at 4.2 K when an external field is parallel to the c-axis.

At present time, we have to apply a pulsed field at the time when the reflection corresponding to the high field structure appears in TOF method. So if we have no idea for the high field structure, it is quite difficult to estimate the time to apply a field. This problem is technically solved by using a flat-top pulsed field and a position sensitive detector as shown in Fig.1.

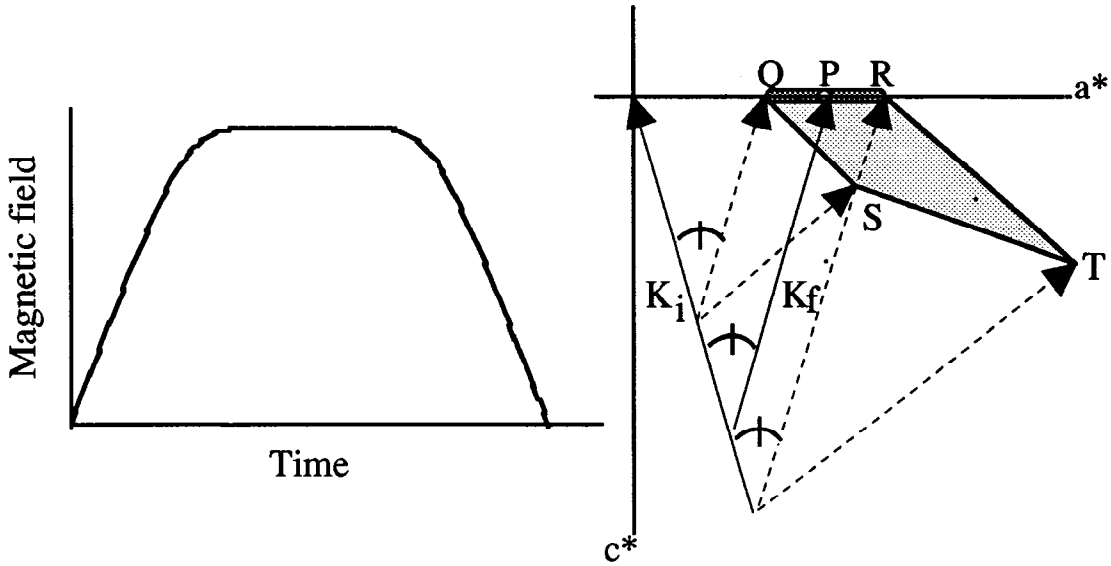


Fig.1 Shape of flat top field (left) and observable area (right). Using the present equipment, we can observe the reflection only at the point P by applying an external field. But it can be expanded to the region between Q and R by using a flat top field and more expanded to the shaded area QRST by using a position sensitive detector.

3. Vertical configuration

The magnet coil mentioned above is of the so-called Bitter type which are originally developed for static high magnetic fields. We used it for pulsed high field experiments, but when it is used for the neutron diffraction experiments, the problem is the small scattering angle [1][3]. This is one of the disadvantages of this configuration. To make a large scattering angle, we have developed a split type magnet as is shown in Fig.2 at the expense of the maximum field strength. This is set as the magnetic field is vertical. The scattering angle is arbitrary in principle but because there must be a hard spacer between the split parts of the magnet, the direction of the neutron beam is fixed as is shown in Fig.2. The available scattering angle is 30° in this case. The biggest advantage of this configuration is that a glass Dewar system is available as is shown in Fig.2. So the temperature of the specimen can be kept at 4.2 K or 1.4 K very easily and the consumption of liquid helium is small. As mentioned above, in the case of horizontal configuration, the cooling system for the specimen is a liquid Helium flow type cryostat which consumes a huge amount of liquid helium to maintain the temperature at 4.2 K. Then the sample temperature is usually kept between 5 and 10 K to save liquid helium. The disadvantage of this magnet system is the reduction of the maximum field strength. The split type magnet is also composed of Bitter disks as well. Due to the large gap at the center of the magnet, however, the available field is up to 16 Tesla. The design of this magnet is not completely finished. We still have some problems like water leak.

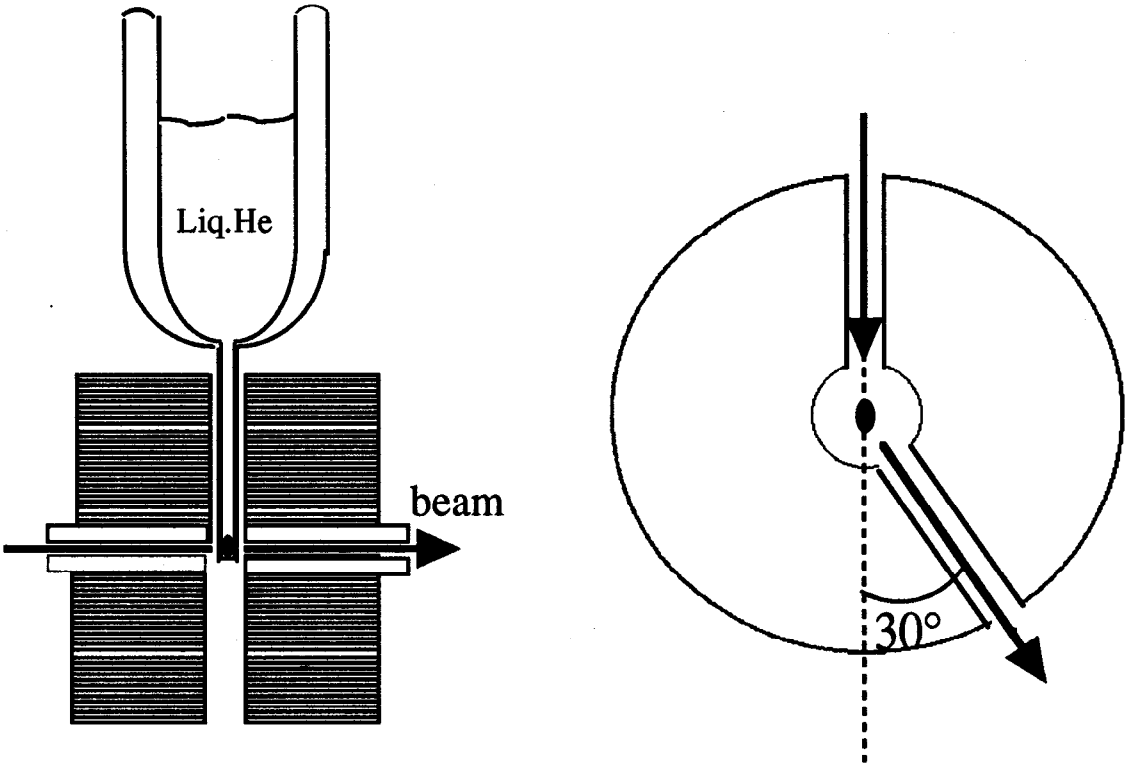


Fig.2 Cut view(left) and top view (right) of the configuration of split type magnet.

4. Design and construction of strong magnet

The magnets described in the above sections are composed of so-called Bitter disks which are copper disks with holes for water flow. The 1 mm thick disks are punched out from a large copper plate. They are stacked with insulator sheets sandwiched between the disks. 100 disks are used for the horizontal configuration magnet coil. The maximum field is limited by the strength of material and structure and by cooling rate as mentioned in the previous papers [1][2]. In our case, the material is copper which is not strong enough to produce a magnetic field higher than 20 Tesla. After 20000 times shots of the pulsed field of 20 Tesla, the inside part of the Bitter disks slightly bent[3]. The structure of the magnet is designed as the disks mechanically contact each other. This may make electrical and mechanical problems after the magnet is used for a long time. Water cooling rate is not a big problem at present. The ion exchanged water is circulated at the rate comparable to the flow rate of filling water to a bathtub. A small problem we have now is the high back pressure of the water circulation system. This problem will be solved soon by using a pump connected to the outlet of the magnet.

In order to obtain higher field than 20 Tesla, it is obvious that we have to use a strong material for the magnet. As the strong material for high field magnet, copper materials reinforced by Beryllium, almina or silver particles are known. Maraging steel is also used. These materials are strong

but low in electric conductivity. If maraging steel is used, the produced field is up to 40 Tesla but the electric conductivity is 10 times less than that of normal copper and the energy loss increases 40 times more. So it seems to be difficult to use such a steel for our purpose. The reinforced copper with Beryllium is stronger than the normal copper but brittle and electric conductivity is less than 90 %. So the reinforced coppers with almina or silver seem to be good candidates. From the yielding strength of these materials, 30 Tesla will be available by using the same capacitor bank.

We designed a new magnet using the reinforced coppers with almina and are now machining it at the machine shop in KEK. In this case, the disks mentioned above are not used. We cut a magnet coil from a big bulk material using a electric spark cutter. Suppose a bulk cylinder with a hole of inner diameter and holes for water path similar to the Bitter type magnet disk, a wire electrode is put diagonally perpendicular to the cylinder and the cylinder is rotated slowly with spark machining. After 50 rotations, 100 turns coil will be obtained as a double helix. In this case there is no mechanical connection and this magnet coil must be strong. The disadvantage is that the machining costs expensive.

5. Wire wound magnet

As another way, we are trying a different kind of magnet. When a magnet coil is wound by copper wire and a high field is produced, the force acting on the coil is outward and it is converted to the tangential force. To prevent expansion and destruction of the coil, a strong reinforcement must be used. The usual way to provide external reinforcement is to use a thick stainless steel cylinder and impregnate with epoxy resin in the space between the coil and the stainless steel shell. We suggested a novel idea to use for the reinforcement of the magnet [5]. We used almina powder and water instead of epoxy resin. Once it was frozen at liquid nitrogen temperature, this mixture was like a ceramic and very strong. By this method we have been constructing pulsed field magnets in our laboratory. The magnets usually used are multilayer, so it takes a few minutes to cool down to the initial temperature after field production. We considered if the magnet coil is single layered, the cooling time would be short. After some trials, however, it has turned out that the magnet has been broken below 20 Tesla because the electric current is so strong due to single layer. We are now improving some parts of the magnet to obtain higher than 20 Tesla.

6. Magnetic phase transition of $CsCuCl_3$

$CsCuCl_3$ is one of the hexagonal $ABX_3$ type compounds. The magnetic properties have been studied many researchers. It has linear chains of $Cu^{2+}$ inos along the c-axis and they make triangular lattices in the c-plane. The intrachain coupling is ferromagnetic, whereas the interchain coupling is antiferromagnetic. Below $T_a$=423 K, $Cl^-$ octahedron surrounding a $Cu^{2+}$ has a distortion due to the cooperative Jahn-Teller effect, and it causes the

antisymmetric Dzyaloshinsky-Moriya interaction between spins along the c-axis. This compound shows 120° magnetic structure in the c-plane and have a

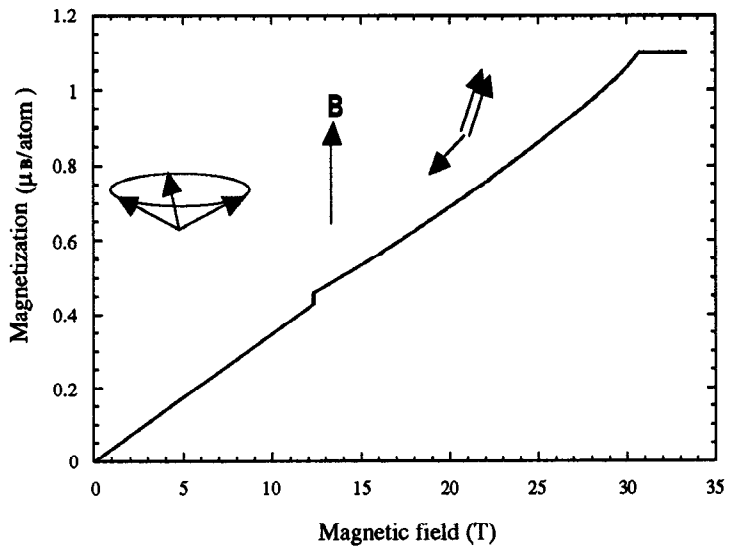

Fig.3 Magnetization curve at 1.1 K for H//c and proposed magnetic structures

long pitch helical spin structure along the c-axis below Tn=10.5K. It has been experimentally found that the magnetization has a small jump at $B_c$=12.5 Tesla at 1.1K in a field parallel to the c-axis as shown in Fig.3 [6]. It has been difficult to explain this phase transition for a long time within the classical theory. Recently, a new theoretical interpretation for this small jump has been proposed by Shiba and Nikuni [7]. They have pointed out that the quantum fluctuation is important in $CsCuCl_3$ because of S=1/2. They proposed a model that the umbrella-like structure changes to the coplanar structure at $B_c$ as shown in the inserts of Fig.4. In this model, two spins are parallel while one is almost opposite above $B_c$. This kind of magnetic phase transition have never been observed. We have studied neutron diffraction experiments in a pulsed high magnetic field in order to investigate the magnetic structure of this material.

The magnetic field was applied parallel to the c-axis at the sample temperature of 7K at which $B_c$ =10 Tesla. The intensities of the magnetic reflection (1/3,1/3,0) and (1/3,1/3,0.085) were measured as a function of the applied magnetic field, because a magnetic unit cell is three times as large as a chemical one in the c-plane. First we focused our attention on the (1/3,1/3,0.085) reflection due to the component of the magnetic moments perpendicular to the c-axis. In addition to the 120° umbrella-like structure at low field, this spin system has a helical modulation along the c-axis which makes a satellite along the c*-axis in the reciprocal lattice space. The intensity decrease as a field is increased below $B_c$ as shown in Fig.4 due to the decrease of the perpendicular component of the moments. The calculated intensity is in good agreement with the experimental results. It shows an abrupt decrease at $B_c$ and a gradual change above it. Assuming the model shown in Fig.3, we

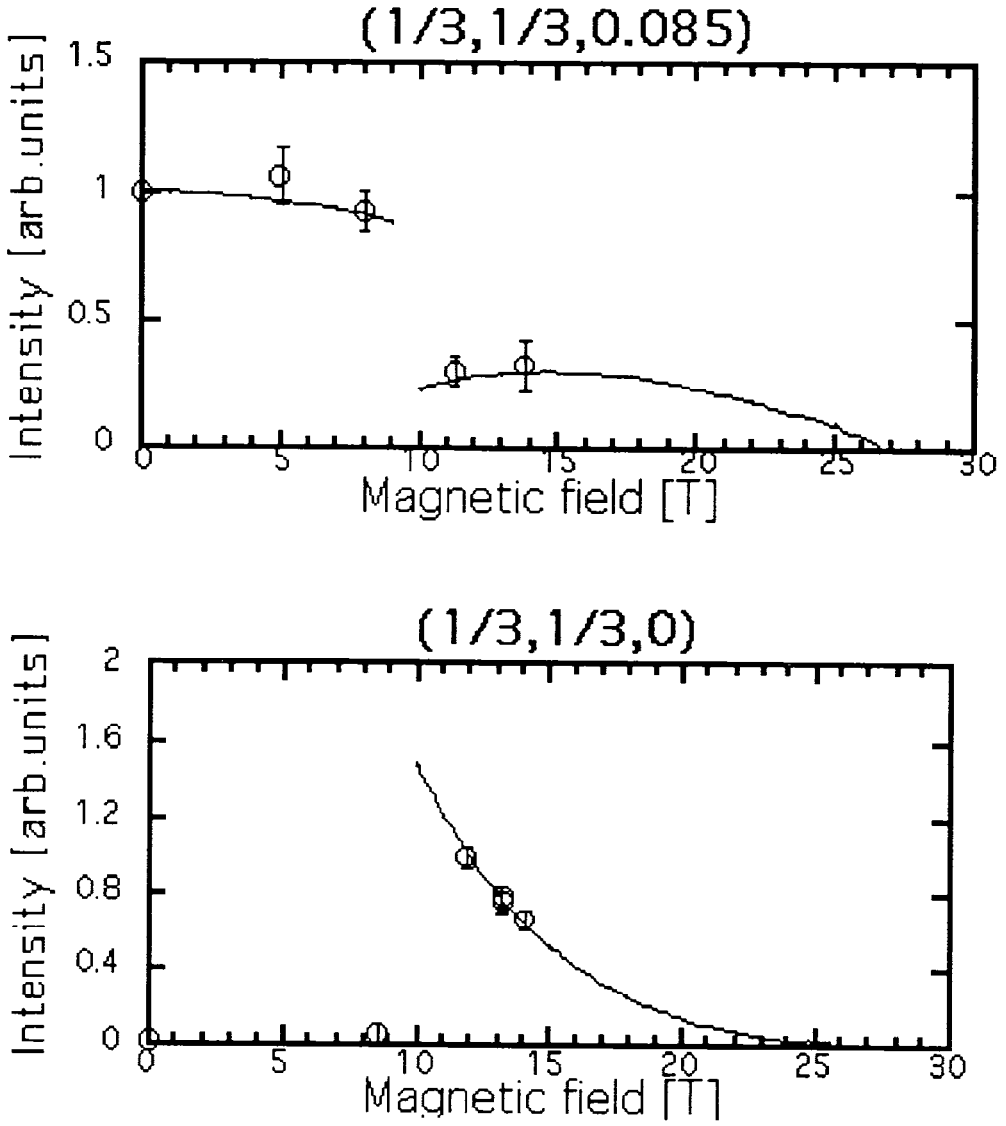


Fig.4 Field dependences of the reflection intensities. solid lines are calculated ones.

calculated the field dependence of the intensity above $B_c$ and found a good coincidence between experiment and calculation as shown by the solid line in Fig.4. The intensity is to become weak as an applied field is close to the saturation field $B_s$=27 Tesla reflecting decrease of the perpendicular component.

On the other hand, (1/3,1/3,0) reflection is due to the parallel component of the magnetic moments to the c-axis. At the umbrella-like structure below $B_c$, the c-component of the magnetic moments is identical each other and the reflection must appear at (1,1,0). This reflection overlays on the nuclear reflection and it is difficult to be discriminated from the strong nuclear one. Therefore (1/3,1/3,0) reflection can not be observed below $B_c$. Above $B_c$, however, the proposed structure shown in Fig.3 contributes to (1/3,1/3,0) reflection observed at 13.2 Tesla. This magnetic reflection disappears below $B_c$ as shown in Fig.4. We calculated the field dependence of the intensity for

the proposed structure and found a very good agreement between calculation and the experimental results as shown in Fig.4.

## 7. Summary

We have developed pulsed field system for the neutron scattering experiments at high magnetic field. It is practical and will be useful if it is used with a stronger beam intensity. We look forward to the new project in Japan and also our technique will be useful even at ISIS.

At present time, the research for high Tc superconductors are intensively progressing and the practical use of them will come in future. If superconducting magnet which is capable of producing higher fields than 20 Tesla at room temperature or even liquid nitrogen temperature may appear. The advantage of our technique will disappear.


## Acknowledgements

This work was performed under collaboration with Professor Watanabe, Professor Ikeda and other KENS staffs. We thank Professor Y. Endoh of Tohoku University for valuable discussions and Professor H. Tanaka of Nagoya University for supplying single crystals.


## References


[1] M.Motokawa, H.Nojiri, M.Uchi, S.Watamura, H.Kawai and Y.Endoh. Proceedings of The 11th Meeting of International Collaboration on Advanced Neutron Sources (KEK, Tsukuba 1990) 979-986.

[2] M.Motokawa, H.Nojiri, J.Ishihara and K.Ohnishi. Physica B**155** (1989) 39.

[3] M.Motokawa, H.Nojiri and Y.Endoh. Physica B**177** (1992) 279-285.

[4] H.Nojiri, M.Uchi, S.Watamura, M.Motokawa, H.Kawai, Y.Endoh and T.Shigeoka. J. Phys. Soc. Jpn. **60** (1991) 2380-2387.

[5] M.Motokawa, H.Nojiri and Y.Tokunaga. Physica B**155** (1989) 96-99.

[6] H.Nojiri, Y.Tokunaga, M.Motokawa. J. Phys. **49** C8 (1988) 1459

[7] H. Shiba and T. Nikuni. Private communication

# NEUTRON DIFFRACTION TO 10 GPa AND BEYOND : THE STATE OF THE ART OF THE PARIS-EDINBURGH CELL

S. Klotz[1], J.M. Besson[1], G. Hamel[2],
[1] Physique des Milieux Condensés, (CNRS URA 782),
[2] Département des Hautes Pressions
Université Pierre et Marie Curie, B 77,
4, place Jussieu, F.-75252 PARIS Cedex 05, France
R.J. Nelmes, J.S. Loveday, R.M. Wilson
Department of Physics, Univ. Edinburgh, Edinburgh EH9 3JZ, U.K.
and S. Hull
The ISIS Facility, Rutherford Appleton Lab., Chilton OXII 0QX U.K.

We review two versions of a low weight (50 kg) 250 tonne press that, for the first time, makes possible neutron-diffraction studies on powder samples of 40 to 100 $mm^3$ to 25 GPa. The assembly consists of a hydraulic ram compressing two opposed toroidal anvils, made of tungsten carbide (WC) or sintered-diamond dies, supported by steel binding rings and backed by tungsten carbide seats. An optimal signal-to-background has been achieved by an improved shielding geometry. Besides standard procedures for the studies of solid powders at ambient temperature, loading procedures for liquids and gases have been developed and represent an original characteristic of this device. The performance will be illustrated by recent results on $D_2O$ ice VIII and $B_4C$ to 10 GPa. We finally report on the first low temperature experiments to 100 K as well as recent developments towards a reduction in size (x0.8) and weight (x0.5) of the apparatus.

## INTRODUCTION

Neutron diffraction experiments on powder samples require in general samples at least 50 $mm^3$ in volume in order to collect patterns on which full profile refinement can be performed in a reasonable amount of time. Since the development of the McWhan cell[1] in the late 1960's, however, little progress has been made in the construction of standard user devices for pressures beyond 3 GPa, although presses and multianvil assemblies for compression to 10-20 GPa are commercially available. The reason for that is evident: diffraction experiments impose rather severe restrictions on the geometry of the anvils and the weight (size) of the press, rendering standard devices either useless or extremely cumbersome. The Paris-Edinburgh cell is a high pressure device which combines a toroidal anvil assembly with an optimized low weight (50 kg) 250 tonnes hydraulic ram. The anvil geometry requires measurements of the diffracted beam at a fixed angle $2\theta \approx 90°$, which is advantagous since suppression of background from illuminated parts of the cell by proper collimation is relatively easy. Therefore, it suits only measurements on pulsed sources by time-of-flight spectroscopy. The cell has been designed specifically for use at the POLARIS-station at the U.K. pulsed source ISIS.

## DESIGN AND PERFORMANCE

*Description of the cell*

Figure 1 shows two versions (V2 and V3) of the Paris-Edinburgh cell [2], which differ mainly in the shape of the hydraulic press: V2 is equipped with an axial bore at the back of the ram allowing transmission measurements, which is not present in V3. The thrust on the anvils (5) and seats (6) is generated by the piston-cylinder (7) assembly which is shown here with the piston fully recessed. With a 250 MPa (2500 bar) pressure in the hydraulic fluid which is fed in through

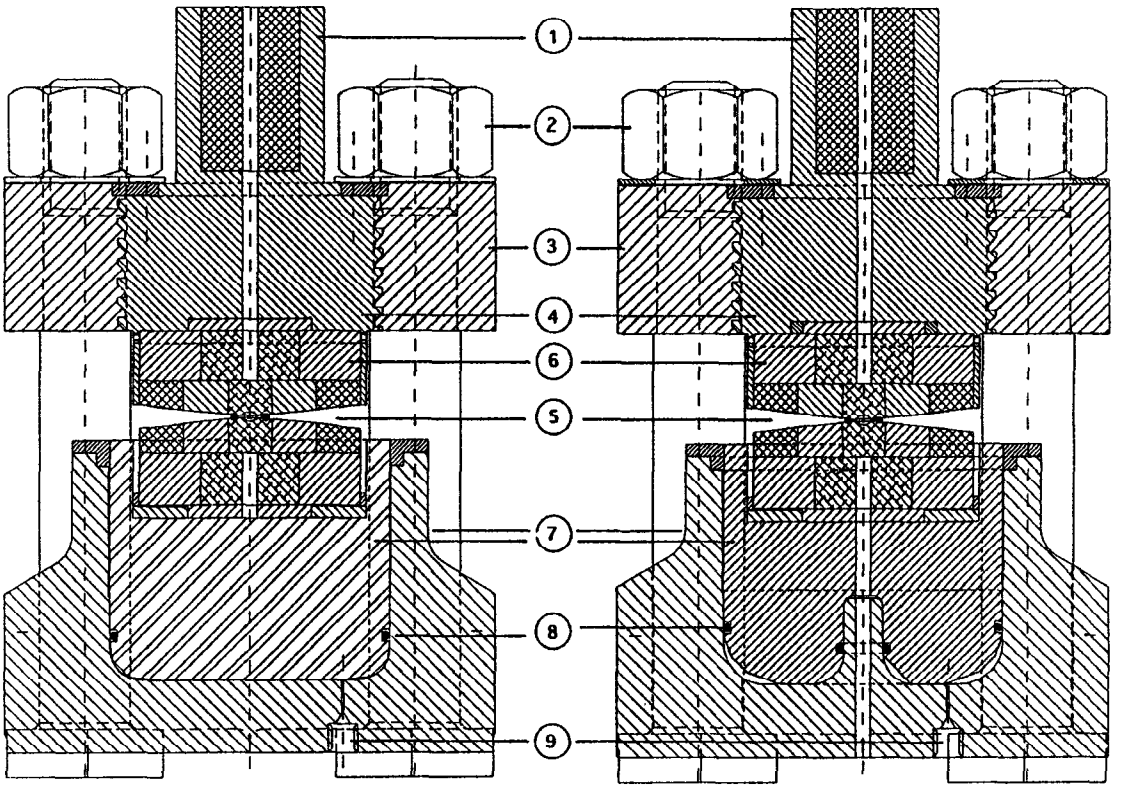


Figure 1: Cross cut of two versions of high pressure cells V3 (left) and V2 (right). (1) collimator, (2) nuts and tie rods, (3) top platen, (4) breech, (5) anvils, (6) anvil seats, (7) piston-cylinder assembly, (8) hydraulic fluid seal, (9) high pressure fluid inlet.

the inlet (9) a 250 tonnes (2.5 MN) thrust is generated by the 100 $cm^2$ piston. The tie rods with their corresponding nuts (2) connect the ram body to the top platen (3). The press is almost entirely made of high performance steel 819A by Aubert et Duval (35NCD16).

Finite element calculations were used in order to find the optimal shape and dimensions of the ram. This leads to the unusual shape shown in Fig. 1, where the deformations at the level of the O-ring seal as well as the centering ring are almost zero although some parts of the cylinder deform by 0.45 mm at 200 tonnes load. Maximum stresses of ca. 1 GPa occur at the bottom of the ram. The inlet for the hydraulic fluid was placed in a region of minimal stress.

*Toroidal anvil and gasket assembly*

Figure 2 shows an enlarged view of standard WC anvils including the gasket, consisting of a washer and a toroidal part. The high pressure chamber (sample volume V) is situated in the center of the drawing, limited laterally by the washer and vertically by the two spheroidal surfaces of the anvils.The washer is laterally supported by the toroidal gasket. High pressure is created by applying load onto the anvils which causes the sample volume to decrease both by the decrease of the gasket thickness as well as the intrusion of the washer into V. For such a profile the upper limit for the volume reduction $V_0/V$ is roughly 2. This causes no restriction for experiments on solids and liquids, where $V_0/V$ is between 1 (NaCl : 1.2) to 2 ($NH_3$, $CH_4$), between loading and ~ 10 GPa but excludes measurements on gaseous samples ($H_2$, He) if they are loaded at ambient pressure above the current low temperature limit of 100 K.

The standard anvils are made of slightly conical WC kernels (overall cone angle 3°) of 25 mm diameter and 14 mm height. They are supported by pressing them into a steel binding ring (819A by Aubert et Duval) at ambient temperature, producing a tangential stress of ca. 1 GPa. At the back they are provided with a recess of 6 mm depth and 5 mm diameter to reduce the attenuation of the incident neutron beam.

The compressive strength of WC is approximately 60 tonnes/$cm^2$, which means for

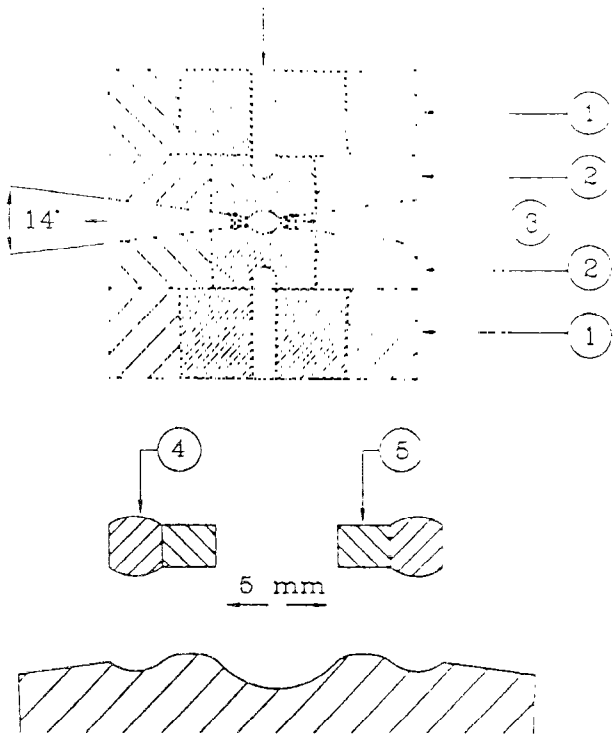


Figure 2: Toroidal anvil assembly (top) with enlarged view of the gasket and anvil profile (bottom). (1) Seats (CW), (2) anvils, (3) sealing assembly consisting of (4) toroidal gasket and (5) flat washer. Anvils are made of CW (standard) or diamond dies, supported by steel binding ring.

gaskets of 18 mm diameter a maximal load of ca. 150 tonnes. According to the empirical load/pressure characteristic of the cell (see below) this results in a maximal pressure of 12 GPa. For pressures beyond this limit, there seems at the moment to be only one feasible solution, namely compacted diamond dies. These are provided by General Electric under the commercial name COMPAX and have to be shaped to the specific anvil profile by spark erosion. Our experience at the present time is limited to a few experiments beyond 10 GPa, among them one on Ni above 20 GPa and another on $D_2O$ (ice VIII) to 13 GPa.

*Gasket materials*

Pyrophyllite and Cu:Be, were initially used as gasket materials, but are now replaced by null-scattering TiZr (52% Ti, 48% Zr by weight) to eliminate wavelength dependent absorption due to Bragg edges. Despite a much lower yield strength (900 MPa) compared to 1300 MPa for hardened CuBe the performances of the two materials in a given configuration are very [illegible] This [illegible] that the performance [illegible] by the geometry rather than the mechanical properties of the gasket material.

*Scattering geometry and shielding*

Figure 3 shows schematically the cell in its measuring position within the POLARIS tank. The incident neutrons (beam diam. 5 mm) are directed along the axial bore of the cell and have to pass through ca. 6 mm of anvil material (WC or diamond) before they reach the sample. They are scattered and collected at $2\theta=90°\pm7°$ by ZnS-detectors[3] covering 65° in the equatorial plane at each side of the cell. Proper shielding of the detectors proved to be essential for "clean" spectra i.e. without spurious peaks from the anvil material and elevated background from stray neutrons of various parts of the cell. Systematic background measurements on the

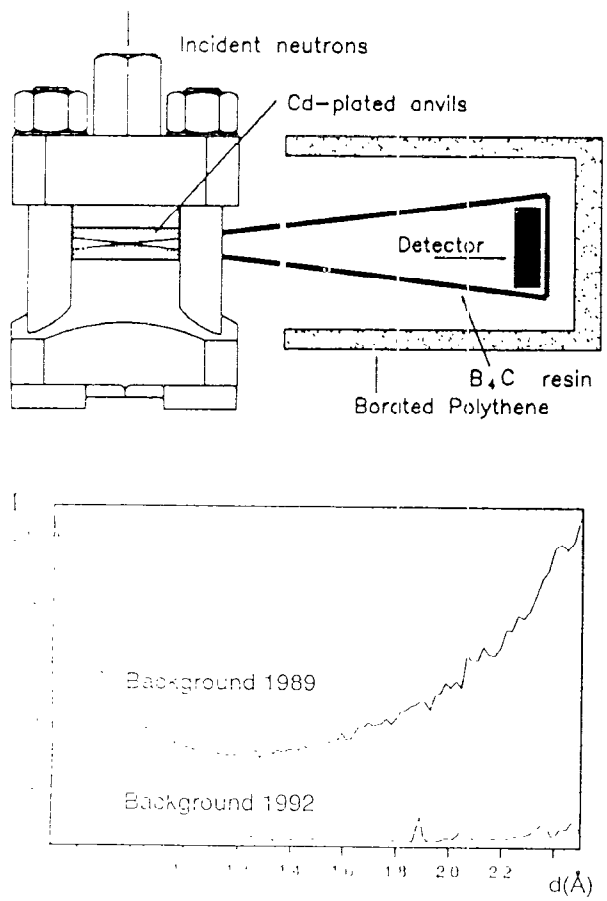


Figure 3: Top: Scattering geometry and shielding at the POLARIS station. Only half of the detectors are shown. Bottom: Background (1992) with improved shielding (see top) compared to former level (1989).

TEST-line lead finally to the set up shown in Fig. 3 (top). The detectors sit inside a conical box which comes right up to the tank. Two removable parts extend to the edge of the anvils which are plated with neutron absorbing cadmium up to 1 mm close to the gasket. The effect of such a shielding on the background is shown in Fig. 3 (bottom) in comparison with early measurements of 1989.

*Load-pressure characteristic*

After sealing the high pressure chamber under a load L of ca. 20 tonnes, P increases linearly with L to approximately 8 GPa and 90 tonnes, followed by a levelling off at 12 GPa and 130 tonnes. This holds for both solid and initially liquid samples, if the starting volume is chosen according to the specific elastic properties by using gaskets of different dimensions. The pressure/load characteristics for TiZr and CuBe gaskets are almost identical.

*Loading procedures*

To alleviate pressure broadening effects, which are commonly observed in solid powder samples at high pressures, the following procedure proved to be effective. As much as possible of the powder sample is placed into the bore of the gasket, glued to the bottom anvil. The sample is then soaked with Fluorinert and the pressure chamber is quickly sealed off by applying a load of ca. 20 tonnes.

Liquid samples are loaded directly in the cell, with no need for encapsulation: the cell is placed into its "measuring position", i.e. with its axis horizontally. Then a rubber ring is placed between the anvils, before applying a few hundred N onto them, which creates a sealed cavity around the gasket assembly. Then the sample is injected by a syringe, while a second one ensures that no air bubbles remain in the cavity. Again, 20 tonnes are applied to seal off the high pressure chamber before finally the rubber is cut off.

Gaseous samples are loaded by condensing them at sufficiently low temperatures into a loading chamber around the gaskets as in the previous case. This can be a rubber ring, or, for temperatures below 200 K a PTFE-ring, supported by a metal bracket. Such a set-up holds pressures to well beyond 50 bars, which means that some gases (Ar, $CH_4$) can be loaded close to their critical point at relatively elevated temperatures. This again is an original feature of this large volume cell. The time required for loading is mainly determined by the cooling and warming delay of the cell and thus between 1 and 6 hours.

*Low temperature experiments*

Being able to cool the cell down to moderately low temperatures (100 K) is important for structural studies (phase transitions, especially magnetic), but also for loading gaseous samples and for enabling improved structural information to be obtained because of the reduced thermal motion.

To vary the temperature, the cell and its support are placed into a thermally insulating container which fits into the existing POLARIS tank. By filling the bottom of the container with ca. 10 cm of liquid nitrogen, the cell cools down to 150 K within 2 1/2 hours and to 100 K in 5 hours. Data collection at low temperature has been successfully tested in an early experiment on .ice VIII to 110 K and recently on ammonia to 120 K.

## RECENT RESULTS

*$D_2O$ (ice VIII)*

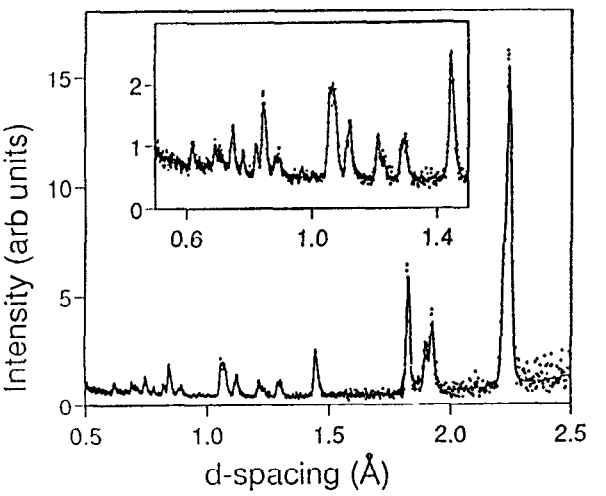


Figure 4: Spectrum of $D_2O$ (ice VIII) at 10 GPa.

The aim of this experiment was to study structural changes of the ordered high pressure phase of water, ice VIII, in particular the variation of the intramolecular O-D distances to 10 GPa[4]. Fig. 4 shows a typical spectrum at 10.4 GPa obtained after 6 hours of

data collection with only one of the two detector banks. The profile refinement of the structure gives a precision of ± 3 x $10^{-4}$ nanometers on the intramolecular O-D bondlength - the same precision as at 2.5 GPa. This is the first time that variable atomic coordinates have been successfully refined up to 10 GPa from neutron diffraction data.

*$B_4C$ ($^{11}B_4C$)*

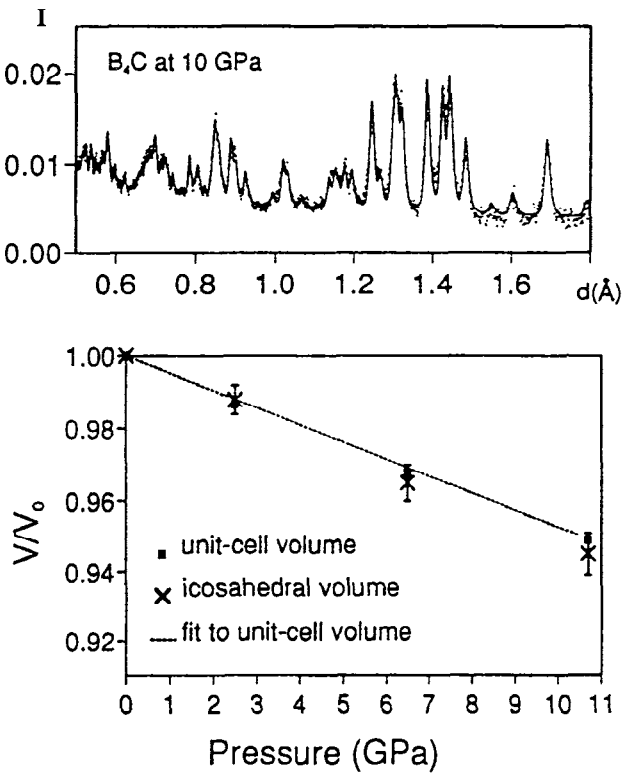


Figure 5: Spectrum of $B_4C$ at 10 GPa (top) and relative volume changes as a function of pressure (bottom).

Boron carbide is an example of a low-z material with both interesting structural features as well as applications as high temperature electronic material. Similar to many other boron compounds, the structure of $B_4C$ is made up of interconnected $B_{12}$ icosahedra, with a three-atom chain along the rhombohedral axis. Conductivity occurs by hopping of small bipolarons between icosahedra and studies at elevated pressures have revealed the that the resistivity increases with pressure. This phenomenon has been explained by the idea that the icosahedra are more compressible than the overall structure. Figure 5 shows a spectrum collected at 10 GPa, along with the behaviour of the relative volumes of the unit-cell and the icosahedra. It is clear that the icosahedra compress at a rate close to that of the unit-cell. Hence, a new explanation must be sought for the behaviour of the resistivity[5].

*Future developments*

At the moment, development is focussed on two issues: first, development of smaller presses for standard use to 10 GPa and possibly for low temperature work. All dimensions can be scaled down by a factor 0.8, leaving the anvils as they are and leading to a cell with a mass of ca. 30 kg instead of 50 kg.

A second development concerns the extension of the standard pressure range beyond 10 GPa. This requires in general not only the use of COMPAX-anvils and hence more complicated absorption corrections due to Bragg edges of the diamonds, but also an improved anvil profile.

Acknowledgments This work was supported in parts by the SERC (U.K.), the CEA (France) under contract n° W 00319/3255 and the Commission of the European Community under SCIENCE contract SC1*CT 91 0692. COMPAX diamond dies were provided by General Electric.

REFERENCES

[1] D.B. McWhan, D. Bloch and G. Parisot, *Rev. Sci. Instrum.* **45**, 634 (1974).

[2] See also: J.M. Besson, R.J. Nelmes, G. Hamel, G. Weill, J.S. Loveday and S. Hull, Physica B 180+181, 907, (1992); J.M. Besson, R.J. Nelmes, G. Hamel, G. Weill, J.S. Loveday and S. Hull, High Pressure Research 9, 179, (1992); J.S. Loveday, R.J. Nelmes, J.M. Besson, G. Hamel and S. Hull, Adv. in Powder Diffr. II, Gaithersburg USA, abstracts in the Nat. Inst. of Standards and Technology (USA), Special Publ. 864, 223 (1993).

[3] funded by the European Community.

[4] R.J. Nelmes, J.S. Loveday, R.M. Wilson, J.M. Besson, P. Pruzan, S. Klotz, G. Hamel S. Hull, *Phys. Rev. Lett.* **71**, 1192 (1993).

[5] R.J. Nelmes, J.S. Loveday, R.M. Wilson, J.M. Besson, S. Klotz, G. Hamel and S.Hull, subm.to *Phys. Rev. B*, rapid comm.

# RIETVELD REFINEMENT OF MAGNETIC STRUCTURES FROM PULSED-NEUTRON-SOURCE POWDER-DIFFRACTION DATA.

R. A. Robinson, A. C. Lawson, Allen C. Larson, R. B. Von Dreele and J. A. Goldstone
LANSCE, Los Alamos National Laboratory, Los Alamos, NM 87545, U.S.A.

Abstract

The General Structure Analysis System, GSAS, has recently been modified to include magnetic neutron-scattering cross-sections. Low-temperature diffraction data have been taken on the hexagonal noncollinear antiferromagnet UPdSn on both the HIPD and the NPD powder diffractometers at LANSCE. The low-resolution data reveal that the magnetic structure has orthorhombic symmetry (magnetic space group $P_Cm'c2_1$) between 25K and 40K, and monoclinic symmetry (magnetic space group $P_C112_1$) below 25K. The high-resolution data reveal that there are structural distortions with corresponding symmetry changes in each of these phases, to give chemical space groups $Cmc2_1$ and $P2_1$ respectively, while the paramagnetic phase above 40K has space group $P6_3mc$. Using GSAS, we have refined data sets from both diffractometers simultaneously, including both magnetic and structural cross-sections. Magnetoelastic coefficients for the distortions have been extracted and we have determined the sign of the coupling between the structural monoclinicity and the magnetic monoclinicity. The magnetic results from Rietveld refinement are in good agreement with model fitting to the integrated intensities of seven independent magnetic reflections and these, in turn, agree with measurements made on the same sample using the constant-wavelength reactor technique. Our results therefore validate, to some level, both the technique of using spallation sources for complicated magnetic structures and the specifics of the GSAS Rietveld code.

## 1. Introduction

The main impact of pulsed spallation neutron sources in the field of crystallography has been in performing high-resolution structural studies. On the other hand, there has until recently been relatively little work at spallation sources on the solution of magnetic structures, a traditional domain of reactors. There are several reasons for this dichotomy. Firstly, while high-resolution studies can be performed with good intensity in backscattering (as is very effective for structural crystallography), the backscattering geometry is of less use for magnetic problems because it forces one to use excessively long neutron wavelengths. Secondly, there has been concern that the wavelength-dependent corrections for absorption and extinction cannot be made reliably. In this article, we will demonstrate that magnetic powder diffraction can be done equally well at the present generation of spallation sources and reactors and that the former are particularly effective for the studying previously undetermined magnetic structures and the interplay between magnetism and structure. A useful tool in this field is the Rietveld refinement program GSAS[1], which now allows simultaneous refinement of data from multiple phases taken instruments with different resolutions and including magnetic cross-sections. We have validated the program for the particular case of the noncollinear hexagonal antiferromagnet UPdSn[2], on which we have data from the same sample taken on both of the LANSCE powder diffractometers as well as the BT-9 constant-wavelength machine at NIST. Not only do we get the same results at reactor and spallation source, but GSAS also gives the same quantitative results as the traditional method of fitting integrated intensities from individual reflections to the magnetic model.

## 2. Magnetic Rietveld Refinement for Spallation Source Data

Initially, magnetic diffraction data taken on the HIPD powder diffractometer[4,5] was handled by individual peak fitting using the program FIT_PEAKS[6]. This uses the same lineshape description as GSAS and corrects for the incident spectrum variation in the same manner, but does not allow explicitly for the variation of absorption or extinction with wavelength. The integrated intensities are then fitted to a model using a purpose-written program. This has been

done in various cases, including noncollinear antiferromagnetism in the case of UPdSn[2], large-cell collinear antiferromagnetism in the case of UNiGa[7] and an incommensurate structure in the case of UPtGe[8].

But calculation of magnetic diffraction intensity from commensurate magnetic structures is now explicitly included in GSAS[3]. Magnetic structures can be tackled either as an extra purely magnetic phase, or as a phase that gives both nuclear and magnetic intensity. In either case, GSAS handles the magnetic symmetry in terms of the magnetic Shubnikov space groups, which are supergroups of the regular crystallographic space groups. The magnetic space group is specified by taking the normal space group and turning on the "colours" of any combination of basis symmetry operators that define the crystallographic space group. While one uses the normal space-group section of GSAS to determine which phases are magnetic, the coloured symmetry elements are turned on or off in the atom-editing section of the least-squares option. GSAS then determines automatically the constraints on the moments imposed by the group. On the other hand, the systematic absences (as used in the reflection generator POWPREF) are calculated by a numerical sampling method. Finally, one needs a magnetic form factor and this is parameterised in the following way:

$$F(Q) = \sum_i a_i e^{-b_i Q^2} + C \qquad (1)$$

where the $a_i$, $b_i$ and C are constants, that can be fitted in GSAS to published experimental or theoretical form factors in the form of a user-provided data file, and $Q = \sin\theta/\lambda$. This is handled within the form-factor section of the least-squares option within GSAS.

3. Results

The material that we have studied most extensively is the noncollinear hexagonal antiferromagnet UPdSn. We have now studied the same powdered sample on HIPD, NPD and on the BT-9 triple-axis spectrometer (in two-axis mode) at NIST[2,9,10]. Our original powder diffraction data are shown in Figure 1, and from these we were able to solve unambiguously the magnetic structures in the two magnetic phases. In addition, we determined that the Pd and Sn atoms are chemically ordered, in contrast to other isostructural compounds. In the subsequent reactor study[9] of the temperature dependence of the order parameters, we showed that we get the same results, both for the integrated intensities of individual reflections and for the parameters in the magnetic model. While this may sound a trivial matter, at that date nobody had demonstrated that this was the case and the prevailing wisdom was that spallation sources were somehow unsuited for magnetic studies. In any case, the Lorentz factors L are completely different for the two types of experiment:

$$L \propto \lambda^4 \text{ for time-of-flight; } L \propto \frac{1}{\sin\theta \sin 2\theta} \text{ for constant wavelength} \qquad (2)$$

and in addition, the spallation source data are divided by the incident spectrum. The fact that there is good agreement indicates that these corrections are being applied properly, out to d-spacings of 8Å and beyond.

Since then, we have also done a high-resolution study on NPD, our 32-m high-resolution powder diffractometer[4], and have observed magnetically driven structural distortions. Fig. 2 shows the orthorhomic and monoclinic splittings of the 110 hexagonal reflection. These new data have been used in a Rietveld refinement together with the older low-resolution data from HIPD. While the NPD data are best for observing the structural distortion, the HIPD data are best for observing magnetism. The resultant low-temperature structure is shown in Fig. 3. In these refinements, it is even possible to determine the sign of the coupling between "magnetic monoclinicity" and "structural monoclinicity", that is whether the projected moments prefer to point across the short diagonal of the monoclinic cell or across the longer diagonal. In some

sense, these are determined independently, the magnetic monoclinicity being proportional to the amplitude of the 010 magnetic reflection, while the structural monoclinicity is primarily determined by splittings like those in Figure 2. The 120 reflection is particularly sensitive to this coupling constant, and portions of data from the +90° bank of HIPD are shown in Figure 4. The model with moments pointing across the short diagonal is clearly preferred. The Rietveld refinement included ten independent banks of data (four from NPD and six from HIPD, with parameters given in Table 1) including magnetism. At the lowest temperature, we used the crystallographic space group $C112_1$ (in the double-sized magnetic unit cell equivalent to $P2_1$) and magnetic space group $P_C112_1$.

## 4. Comparison with Reactors

We have conducted our program both at LANSCE and at the NIST reactor. With the technology presently in service, the spallation source is clearly superior for powders with unknown magnetic structures and for problems in which there are also structural concerns. Having solved the magnetic structure, one often wants to look at the intensity of a particular reflection in detail as a function of temperature, magnetic field and history. In this case the resolution can be relaxed with no loss of information, and we typically perform such measurements on a single-detector two-axis reactor diffractometer with relaxed collimation. So our philosophy is like that in other areas of neutron scattering: the broad survey work is better done at the spallation source, whereas the details are better examined at a reactor.

Of the machines currently in service, the "banana-detector" diffractometers D1B and D20 at the ILL probably have the highest total data rates of any powder diffractometers, and as comparable samples of $Bi_2CuO_4$ have been studied[11,12] on both HIPD at LANSCE and on D1B at ILL, we have made a comparison of data rates on the two machines[13]. The basis of our comparison is the intensity of the lowest order 100 magnetic reflection at d = 8.5Å. The 40° banks of HIPD have higher resolution (1.76% rather than 2.8%) and the signal-to-noise ratio is 8 times better on HIPD. But, even after correcting for the resolution difference (assuming the intensity is proportional to the square of the resolution), D1B has a count rate 60 times greater than that of HIPD! So, present-day spallation source diffractometers are not competitive on intensity, for low-resolution magnetic studies, with the best reactor diffractometers.

There are however several easy ways to make up this difference. Firstly, our measurements were made at a current of 58μA and LANSCE's design current is 100μA. Secondly, D1B has a solid angle five times that of our 40° detector banks. From an engineering point of view it would not be very difficult to increase the area of our banks by an order of magnitude, as we currently only use one sixteenth of the available Debye-Scherrer ring. Finally, we are using 5.8Å neutrons to observe the 100 reflection on HIPD which has a water moderator. A liquid-methane moderator would give three times the flux at these wavelengths[14], with no significant degradation in resolution. In Figure 5 we sketch out the design of a diffractometer that would be suitable for such studies, as well as time-resolved structural diffraction and other high-intensity applications. Such a diffractometer could be built very easily and would be competitive on intensity with the best reactor diffractometers. As a bonus, the signal-to-noise ratio is likely to be significantly better and it will automatically collect higher resolution data at the same time, for free.

## 5. Conclusions

We have shown that magnetic powder diffraction can be done very effectively at pulsed spallation sources with the present generation of sources and we have demonstrated that we know how to make all the systematic corrections. We have also demonstrated that magnetic Rietveld refinements can be performed on spallation-source data and that one gets the same result as from fitting to integrated intensities from either spallation-source or reactor data. The pulsed source is particularly effective for cases where structure and magnetism are coupled or where the magnetic structures are previously undetermined.

Acknowledgements

This work was supported in part by the Division of Basic Energy Sciences of the US Department of Energy.

References

1. A. C. Larson and R. B. Von Dreele, Los Alamos National Laboratory Report LA-UR-86-748 (1987).

2. R. A. Robinson, A. C. Lawson, K. H. J. Buschow, F. R. de Boer, V. Sechovsky and R. B. Von Dreele, J. Magn. Magn. Mater. 98, 147 (1991).

3. A. C. Larson and R. B. Von Dreele ACA Program and Abstracts Bulletin, paper J07 (1992).

4. Los Alamos National Laboratory Report LA-LP-88-04 (1988).

5. A. C. Lawson, J. A. Goldstone, J. G. Huber, A. L. Giorgi, J. W. Conant, A. Severing, B. Cort and R. A. Robinson, J. Appl. Phys. 69, 5112 (1991).

6. J. A. Goldstone (unpublished).

7. H. Maletta, R. A. Robinson, A. C. Lawson, V. Sechovsky, L. Havela, L. Jirman, M. Divis, E. Brück, F. R. de Boer, A. V. Andreev, K. H. J. Buschow and P. Burlet, J. Magn. Magn. Mater. 104-107, 21 (1992).

8. R. A. Robinson, A. C. Lawson, J. W. Lynn and K. H. J. Buschow, Phys. Rev. B47, 6138 (1993).

9. R. A. Robinson, A. C. Lawson, J. W. Lynn and K. H. J. Buschow, Phys. Rev. B45, 2939 (1992).

10. R. A. Robinson, A. C. Lawson, J. A. Goldstone and K. H. J. Buschow, J. Magn. Magn. Mater., in press (1993).

11. E. W. Ong, G. H. Kwei, R. A. Robinson, B. Ramakrishna and R. B. Von Dreele, Phys. Rev. B42, 4255 (1990).

12. J. P. Attfield, J. Phys. Condens. Matter 1, 7045 (1989).

13. Given that some of the data has been taken from figures in Ref. 12, the comparison is probably only good to a factor of 2.

14. A. D. Taylor, Rutherford Appleton Laboratory Report RAL-84-120 (1984).

Table 1 Characteristics of detector banks on HIPD and NPD

| Diffractometer (See Ref. 4) | Scattering angle (degrees) | $d_{max}$(Å) | resolution $\Delta d/d$(%) |
|---|---|---|---|
| NPD | ±148 | 3.0 | 0.15 |
| NPD | ±90 | 4.0 | 0.25 |
| HIPD | ±153 | 4.8 | 0.7 |
| HIPD | ±90 | 6.6 | 1.1 |
| HIPD | ±40 | 13.0 | 1.8 |

Figure Captions

Figure 1. Plot (from Ref. 2) of a portion of the raw data taken on a powdered sample of UPdSn in the +90° bank of HIPD at four temperatures: (a) at 13K in magnetic phase II which is monoclinic, (b) and (c) at 33.8 and 36.3K respectively in magnetic phase I which is orthorhombic and (d) at 46K in the paramagnetic hexagonal phase. The indices in the upper panel are for the magnetic reflections only, assuming the cell shown in Figure 3. The intensities have been divided by the incident spectrum.

Figure 2. Plots (from Ref. 10) of the 110 hexagonal reflection in UPdSn as a function of temperature, taken on the +148° bank of NPD. The splittings have been indexed in the orthorhombic system at 32K and in the monoclinic system below that. The intensities have been divided by the incident spectrum.

Figure 3. The crystallographic and magnetic structures at low temperature of UPdSn, with magnetic space group $P_C112_1$. The right-hand figure shows the monoclinic basal plane. The primitive crystallographic unit cell (which corresponds to the parent hexagonal cell) is shown by the dashed lines, while the magnetic unit cell is shown by the solid lines. The left-hand figure shows the projection onto a plane perpendicular to the a-axis. Neither the atom sizes nor the lattice constants are drawn to scale and the deviation from 90° of the monoclinic angle $\gamma$ has been grossly exagerated. However, the atom coordinates within the cell are drawn to scale.

Figure 4. Plots (from Ref. 10) of a portion of the time-of-flight spectra, along with Rietveld fits, reflection markers and residuals, from one 90° bank of HIPD at 13K. The data in (a) and (b) are identical, but the refinements differ in that the x-component of the uranium moment $\mu_x$ has opposite sign, as shown in the insets. Each inset shows a schematic of the projection onto the monoclinic basal plane, as in the right-hand part of Figure 3. Note that the "positively-correlated" model shown in (a) is clearly preferred by the data. The intensities have been divided by the incident spectrum.

Figure 5. Schematic diagram of the proposed next-generation high-intensity powder diffractometer suitable for magnetic diffraction studies, along with time-resolved and kinetic experiments.

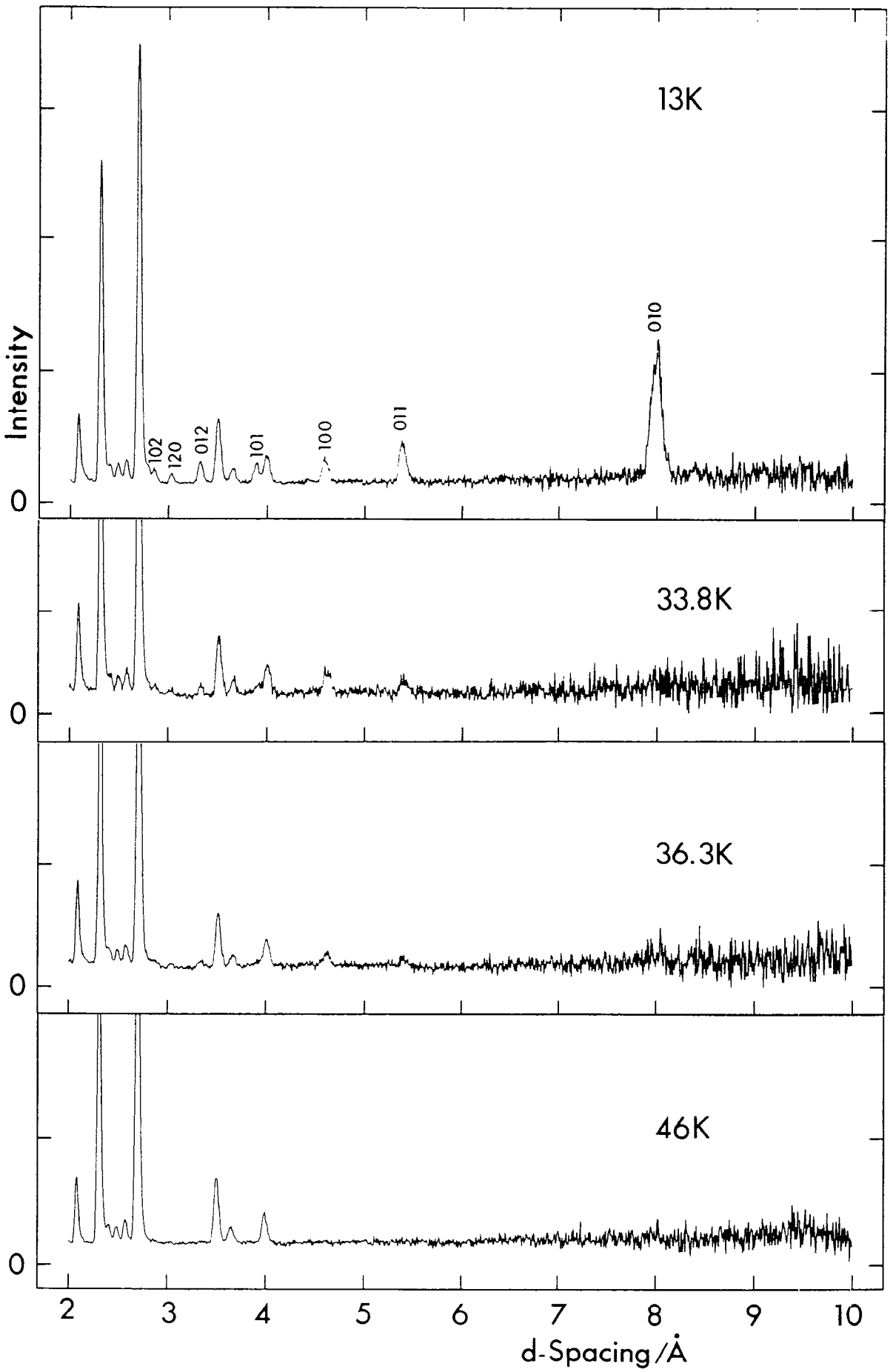
13K
33.8K
36.3K
46K
Intensity
0
102
120
012
101
100
011
010
2
3
4
5
6
7
8
9
10
d-Spacing /Å

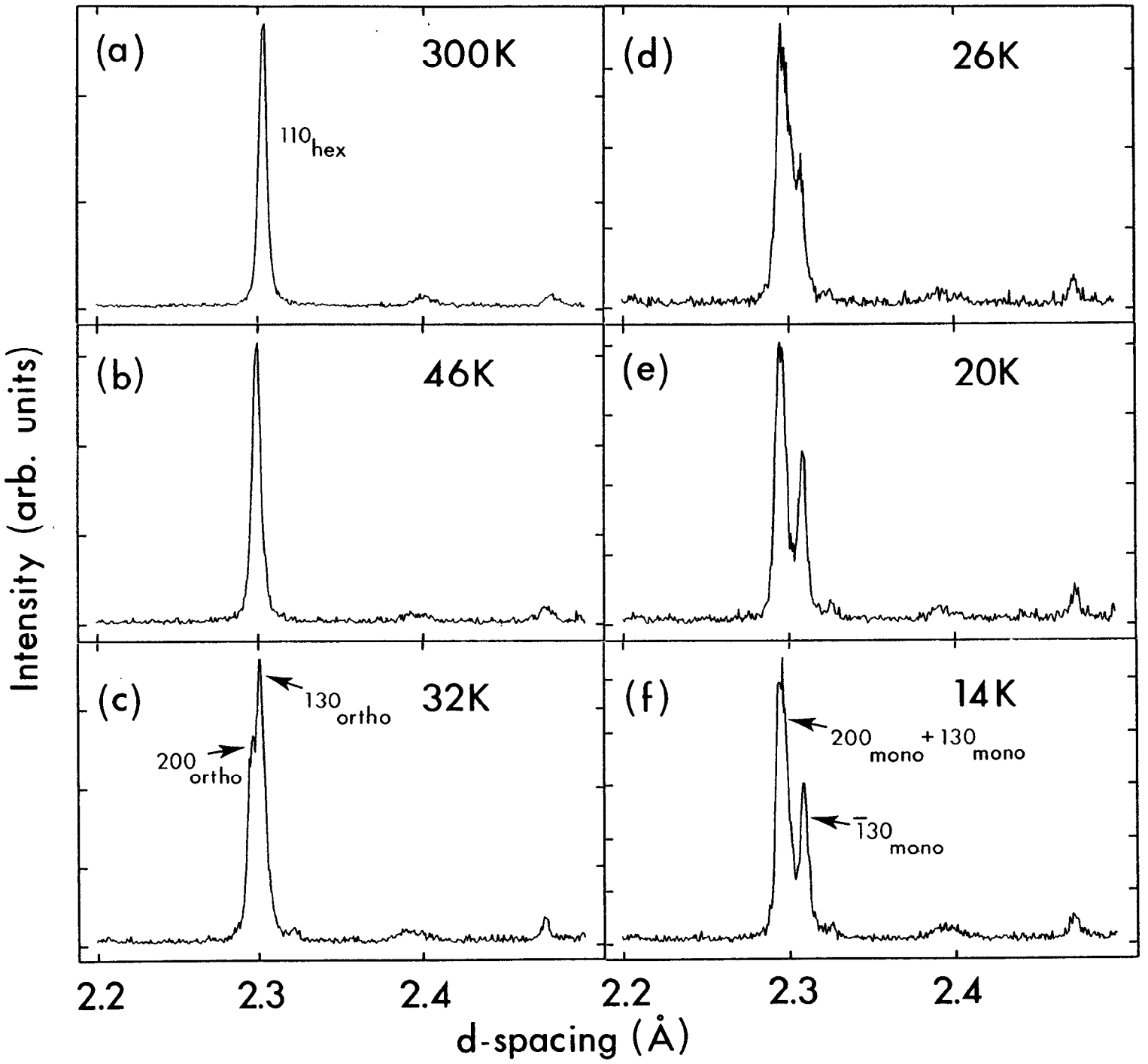
(a)
300K
110 hex
(b)
46K
(c)
32K
130 ortho
200 ortho
(d)
26K
(e)
20K
(f)
14K
200 mono + 130 mono
$\bar{1}30$ mono
Intensity (arb. units)
2.2
2.3
2.4
2.2
2.3
2.4
d-spacing (Å)

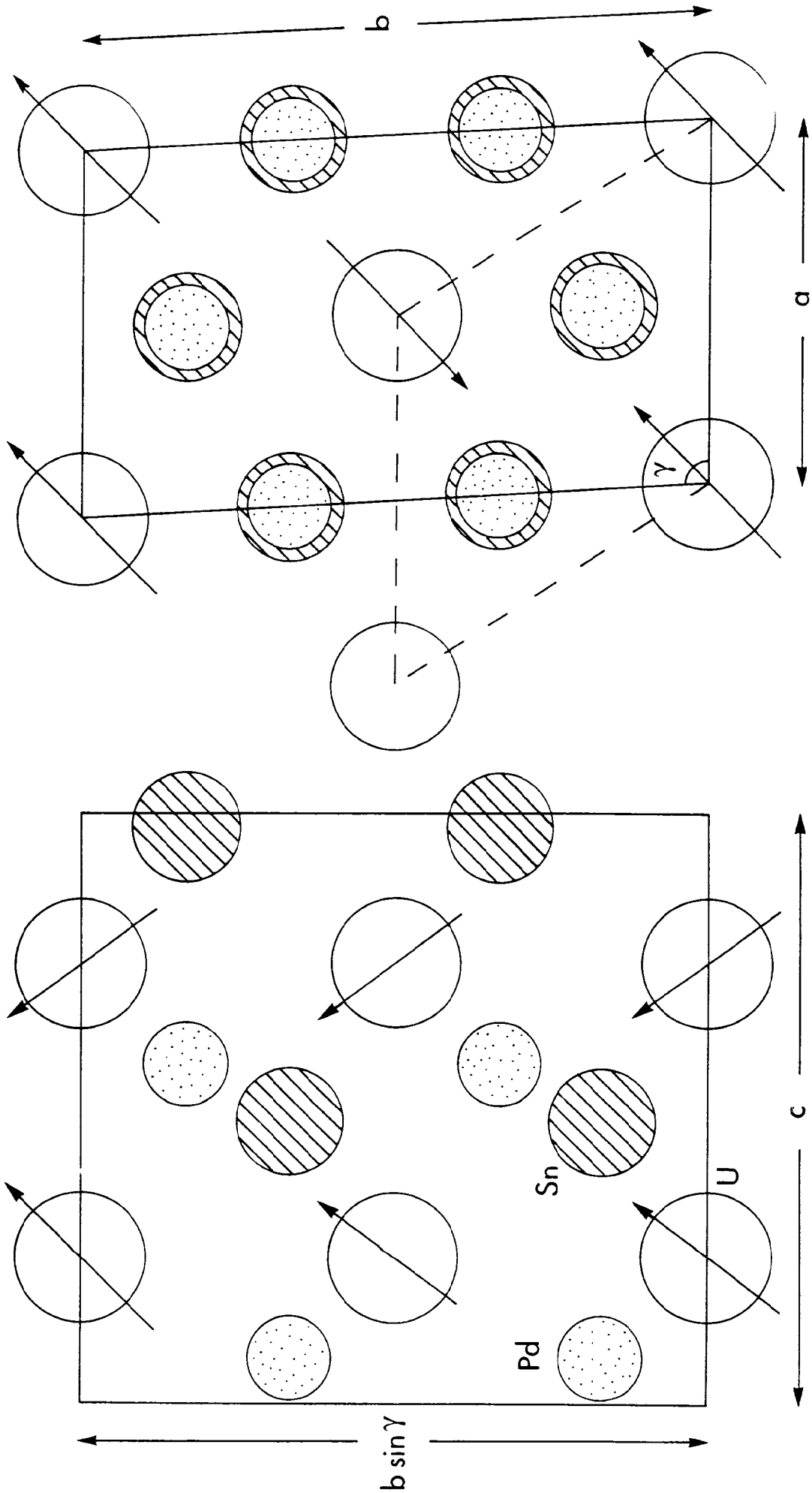
b
a
γ
c
Sn
U
Pd
b sin γ

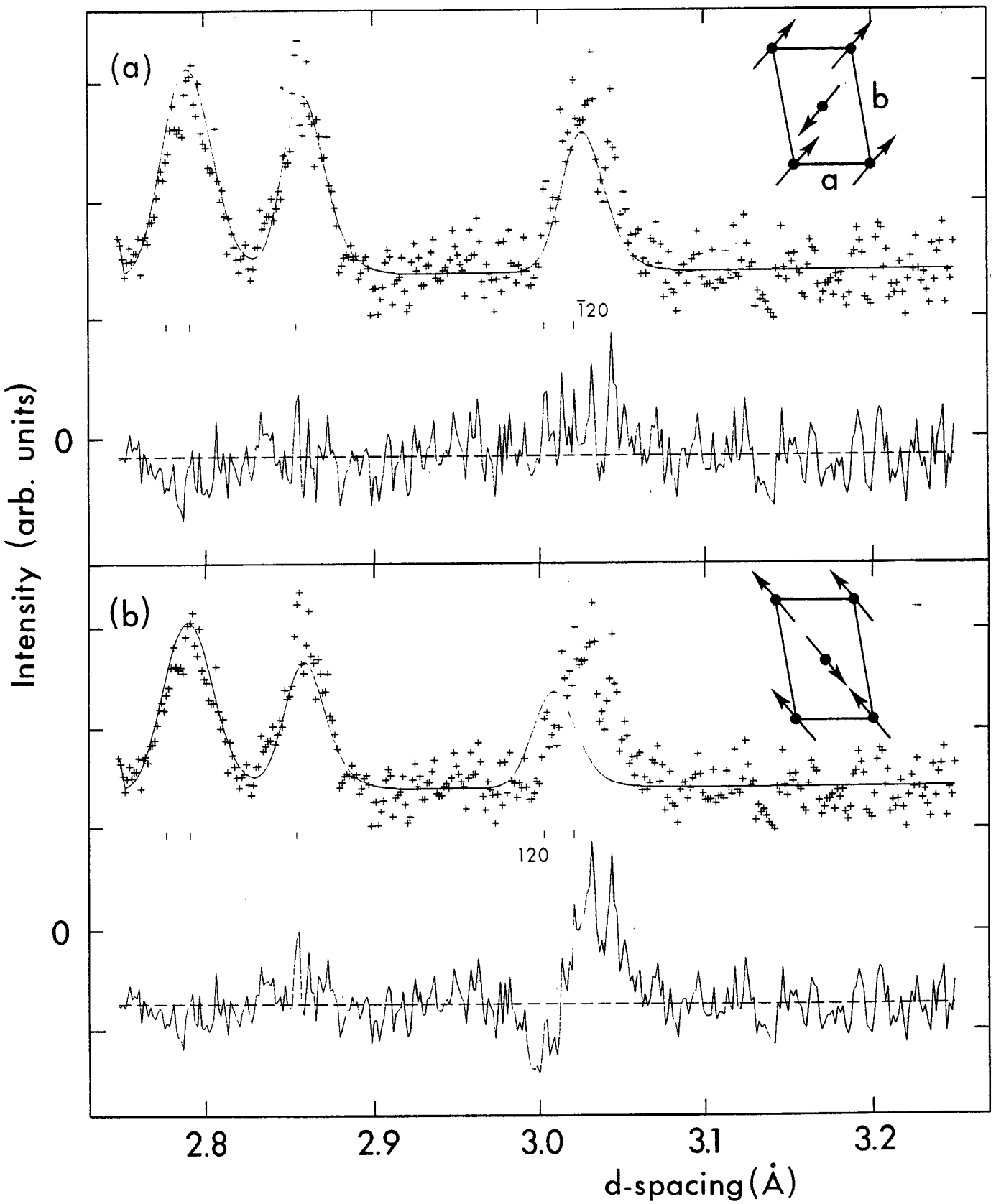
(a)
b
a
$\bar{1}20$
0
(b)
120
0
Intensity (arb. units)
2.8
2.9
3.0
3.1
3.2
d-spacing (Å)

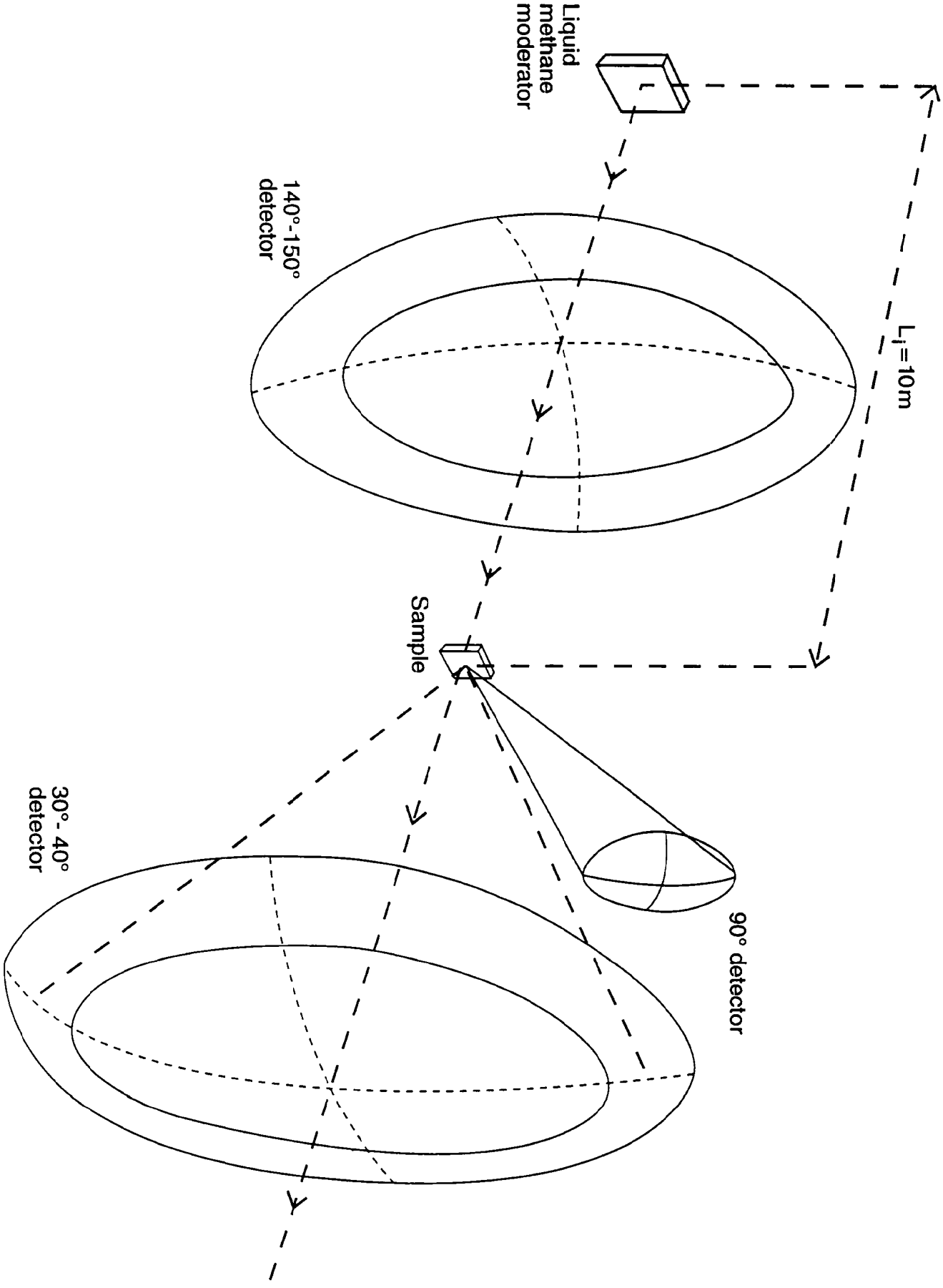
Liquid
methane
moderator
$L_i$=10m
140°-150°
detector
Sample
90° detector
30°- 40°
detector

# *A Dynamical Labelling Method for Extracting Partial Structure Factors*

*M.ARAI[1], A.C.HANNON[2] and T.OTOMO[3]*

*1) Dept. of Physics, Kobe University, 1-1 Rokkodai, Nada, Kobe 657, Japan*

*2) ISIS facility, Rutherford Appleton Laboratory, Chilton, Didcot Oxon OX11 0QX, UK*

*3) Institute for Materials Research, Tohoku University, Katahira, Sendai 980, Japan*

This paper discusses a new data analysis scheme for the scattering function S(Q,E) covering a wide range of Q-E space. The dynamic pair correlation function (DPCF) method has been developed to obtain the real space correlation at excitation energy E by analogy with diffraction data analysis. Two typical examples, $SiO_2$ glass and high-$T_c$ superconductors, have been employed to depict the potential of the DPCF method. For a material which contains significantly different masses the DPCF may provide the partial structure factor for the light atoms.

## INTRODUCTION

In recent decades neutron scattering has provided a unique probe for studying the structure and dynamics of materials; both diffraction and spectroscopic techniques may be employed. However, it is only comparatively recently that it was clearly shown experimentally that more detailed and unique information about the structure and the vibrational states can also be obtained from the momentum dependence (*Q*-dependence) of the scattering function *S(Q,E)*. A specific model calculation may be used to obtain insight into the structure apparent in reciprocal-space, i.e. in the *Q*-dependence of *S(Q,E)*. However, an alternative approach was proposed theoretically in 1975 by Carpenter and Pelizzari [1] whereby a real space correlation function is used to interpret the *Q*-dependence of *S(Q,E)*. The recently developed pulsed spallation neutron source spectrometer, MARI [2], offers an ideal opportunity to explore this idea experimentally for the first time with a very wide *Q-E* range, cf. Fig.1 [3]. In this report we will discuss how we obtain the dynamic pair correlation function (DPCF) from *S(Q,E)* by use of an approach developed by analogy with the procedure used for diffraction data. We will show two typical cases, vitreous $SiO_2$ and the high-$T_c$ superconductor $YBa_2Cu_3O_7$, studied by MARI.

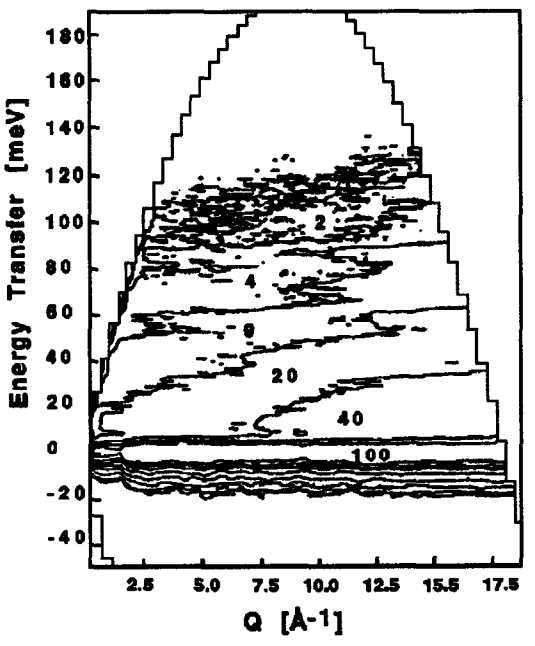


Fig.1 S(Q,E) of $La_{1.85}Sr_{0.15}CuO_4$, $E_i$=200meV

From these examples we will see:

1) The DPCF may provide partial structure factor information without isotope substitution when the material contains elements with significantly different masses.

2) The DPCF is very sensitive to some local structural instability, which may have been neglected or overlooked in previous neutron scattering studies when using conventional data analysis methods.

## DYNAMIC PAIR CORRELATION FUNCTION

The neutron cross section is written as

$$\frac{d^2\sigma}{d\Omega dE} = N\frac{k_1}{k_0} <b^2> S(Q,E). \qquad (1)$$

The dynamical structure factor $S(Q,E)$ for one-phonon scattering [4] is

$$S(Q,E)=\frac{1}{N<b^2>}[\sum_{ii'} e^{-[W_i+W_{i'}]}(b_i b_{i'})\exp(iQ.[i'-i]) \times \sum_j \frac{\hbar^2(Q.e_i^{j*})(Q.e_{i'}^j)}{2\sqrt{M_i M_{i'}}E} <n_j(\omega)+1>\delta(E-\hbar\omega_j)]_{<Q>} \qquad (2)$$

where $W_i=u_{i^2}Q^2/6$ is the Debye-Waller factor and the atomic displacement vector $\boldsymbol{u_i}$ is expressed using normalised vectors $e_i^j$ and the quantum harmonic operator $a_j$

$$\boldsymbol{u}_i(t) = \sum_j \left(\frac{\hbar}{2M_i\omega_j}\right)^{1/2} [e_i^j \exp(-i\omega_j t)\, a_j + e_i^{j*} \exp(i\omega_j t)\, a_j^+ ]. \qquad (3)$$

If the material under consideration has the long-range order of a crystal, we can apply translational invariance by using $\boldsymbol{i} = \boldsymbol{l} + \boldsymbol{d}$, where $\boldsymbol{l}$ is a translational vector of the crystal and $\boldsymbol{d}$ is a vector in the unit cell, cf. Fig.2. Thus,

$$e_i^j = \frac{1}{N^{1/2}}\sum_q e_d^j(q)\exp(iq.(l+d)) . \qquad (4)$$

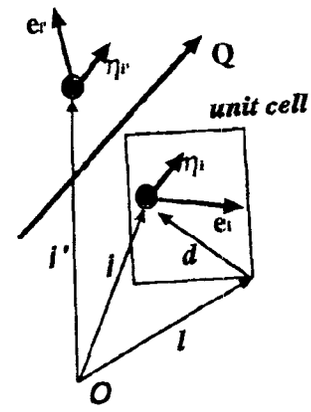


Fig.2 Relation of Vectors.

The cross-section for a crystal then takes the well-known form

$$S(Q,E)=\frac{1}{N<b^2>}\frac{(2\pi)^3}{v_0}[\sum_{dd'} e^{-[W_d+W_{d'}]}(b_d b_{d'})\exp(iQ.[d'-d]) \times \sum_{jq}\frac{\hbar^2(Q.e(q)_d^{j*})(Q.e_{d'}^j(q))}{2\sqrt{M_d M_{d'}}E} <n_j(\omega)+1>\delta(E-\hbar\omega_j(q)) \sum_\tau \delta(Q-q-\tau)]_{<Q>} . \qquad (5)$$

If the system contains local distortion or local disordering, we should start with the general expression (2). For a **mono-atomic** system (2) can be written in a simple form as follows;

$$S(Q,E) = A\left[1 + \frac{1}{N}\sum_{j}\sum_{i\neq i'} < \eta_{i^j}\eta_{i'^j} > exp(iQ.[i'-i])\ \delta(E-\hbar\omega_j)\right]_{<Q>} \qquad (6)$$

where $A=\frac{1}{3N}\frac{\hbar^2Q^2}{2M}e^{-2W}\frac{\langle n(E)+1\rangle}{E}$ and $\eta_i^j=\sqrt{3}(Q.e_i^j)$ is the directional cosine of the displacement vector of the $i^{th}$ atom to the scattering vector $Q$. $<Q>$ indicates an average over all directions of **Q**.

Therefore, in summary, the double differential cross-section is

$$\frac{d^2\sigma}{d\Omega dE} = N\frac{k_1}{k_0}<b^2>\ S(Q,E) = N\frac{k_1}{k_0}<b^2>\ [S_s(Q,E) + S_d(Q,E)] \qquad (7)$$

$$S(Q,E) = A[\ 1 + S_d(Q,E)/A] \qquad (8)$$

where $S(Q,E)$, $S_d(Q,E)$ and $S_s(Q,E)$ are the total, distinct and self scattering functions respectively. On the other hand in a total diffraction experiment the measured quantity is the static structure factor $S(Q)=\int S(Q,E)\ dE$ in the static approximation regime, i.e. $k_0=k_1$,

$$\frac{d\sigma}{d\Omega} = N<b^2>\ S(Q) = N<b^2>\ [S_s(Q) + S_d(Q)] \qquad (9)$$

$$S(Q) = 1 + S_d(Q) = \left[1+\frac{1}{N}\sum_{i\neq i} exp(iQ.[i'-i])\right]_{<Q>} \qquad (10)$$

This is related to a static pair correlation function $D_s(r)$ by

$$D_s(r) = (2/\pi)\int_0^\infty Q\ (S(Q)-1)\ sin(rQ)dQ \qquad (11)$$

where the subtraction of unity from $S(Q)$ serves to remove the self scattering contribution. From the obvious similarity between (8) and (10) and analogy with (11) a dynamic pair correlation function (DPCF) is then defined as

$$D_d(r,E) = (2/\pi)\int_0^\infty Q\ \{S(Q,E)/A-1\}\ sin(rQ)\ dQ \qquad (12)$$

$D_s(r)$ is essentially a density-density correlation function $<\rho(0)\rho(r)>$ (where $\rho(r)$ is the density at $r$ away from an origin atom), weighted according to the neutron scattering lengths at the origin and at $r$. $D_d(r,E)$ is also a density-density correlation function but with an additional weighting factor, which is $<\eta(0)\eta(r)>$ , i.e. the correlation between the directional cosine of $e(r)$ at the energy E to the scattering vector $Q$.

Since both correlation functions involve a density-density term, it is to be expected that $D_d(r,E)$ will exhibit features at the same distances as $D_s(r)$, but that the features will be weighted differently according to the atomic displacements of the relevant atoms for modes at energy $E$. Here, we should also stress that in the DPCF the contribution from light atoms is enhanced due to the mass-dependence of the cross-section.

## APPLICATIONS

### 1) Vitreous $SiO_2$

The generalized phonon density of states (PDOS) measured on MARI for vitreous $SiO_2$ by application of the incoherent approximation shows a shoulder at 10meV and clear peaks at 50,100,133 and 150meV, shown in Fig.3. The dynamic pair correlation function $D_d(r,E)$ at a particular energy E, shown to be of interest by the PDOS, was calculated from the data in the following way. The $S(Q,E)$ at constant E was fitted by the expression

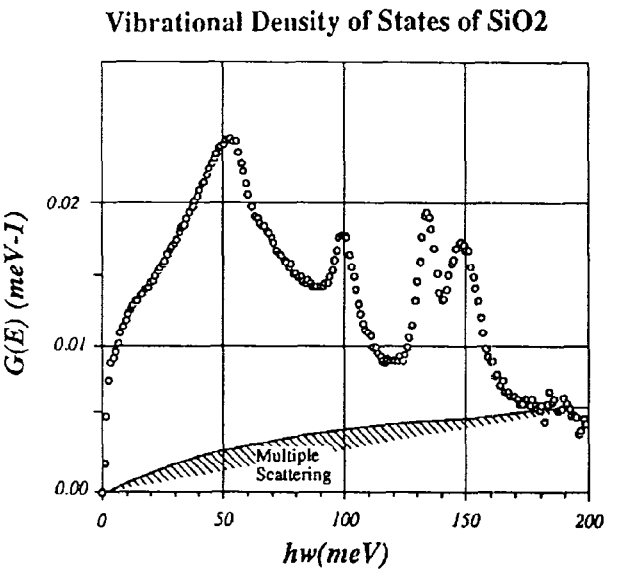


Fig.3 PDOS of g-$SiO_2$, $E_i$=220meV.

$$S_{fit}(Q,E) = C + A = C + B\,Q^2 \exp(-Q^2\langle u^2\rangle/3) \qquad (13)$$

The constant C represents the multiple scattering contribution to $S(Q,E)$ which is assumed to be independent of $Q$. The second term in (13) represents the self scattering $A$ in (8) and the oscillation about the self scattering should be the distinct scattering. The fitted function was subtracted from the data and the result divided by the fitted self scattering to yield the integrand for the Fourier transform of (12).

Figure 4 shows the energy integrated $S(Q)$ of $SiO_2$ calculated from $S(Q,E)$ together with the $Q$-dependence of $S(Q,E)$ for energy transfers $E$ of 12.5meV and 47.5meV. The 12.5meV data show a very similar form to $S(Q)$ with the exception that the first sharp diffraction peak which occurs at approximately 1.5Å$^{-1}$ in $S(Q)$ is absent from the inelastic data. Contrastingly, the 47.5meV data show an oscillatory behaviour which is essentially out of phase with $S(Q)$.

Figure 5 shows the static correlation function $D_s(r)$ according to (11) together with the dynamic correlation function $D_d(r,E)$ at 12.5meV and 47.5meV. The peaks in $D_s(r)$ may be identified as follows: 1.6Å - Si-O bond; 2.6Å - O-O distance in a tetrahedron; 3.1Å - Si-Si distance between two Si in two corner-sharing tetrahedra; 4.0Å - Si-O distance between atoms in different but connected tetrahedra, and 4.9Å - both O-O distance between atoms in different but connected tetrahedra and Si to second Si distance.

A comparison of the $D_d(r,E=12.5meV)$ with $D_s(r)$ shows a similarity in peak positions with different relative amplitudes, as expected. The first and second Si-O peaks are depressed relative to the first and second O-O peaks, indicating that the modes at this energy involve a relatively small amount of silicon motion compared to that of oxygen.

$D_d(r,E= 47.5meV)$ also exhibits peaks at the distances of the first two Si-O peaks in

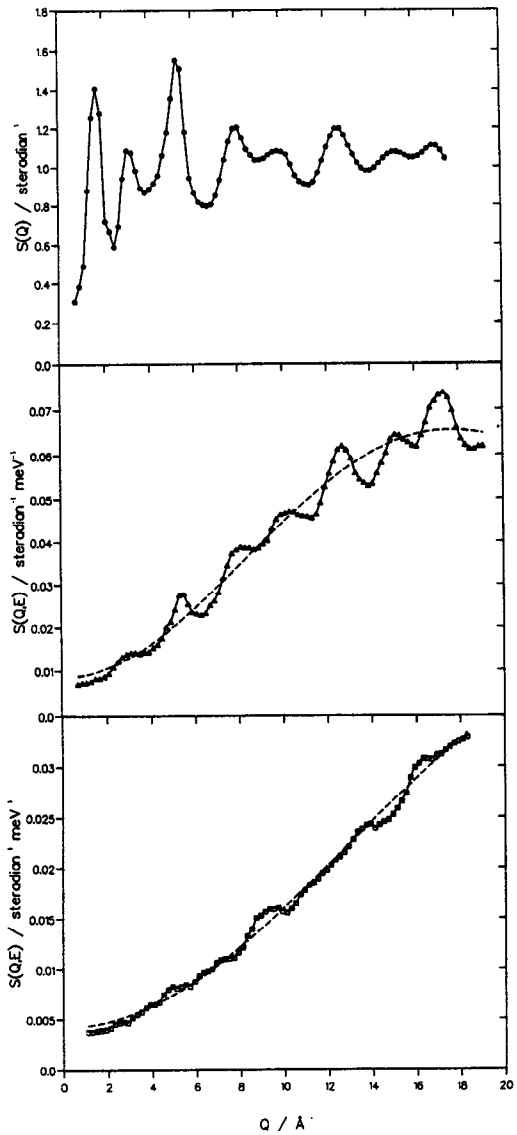


Fig.4 (a) S(Q), (b) S(Q,E=12.5meV) and (c) S(Q,E=47.5meV). The dashed lines indicate the fit described in the text.

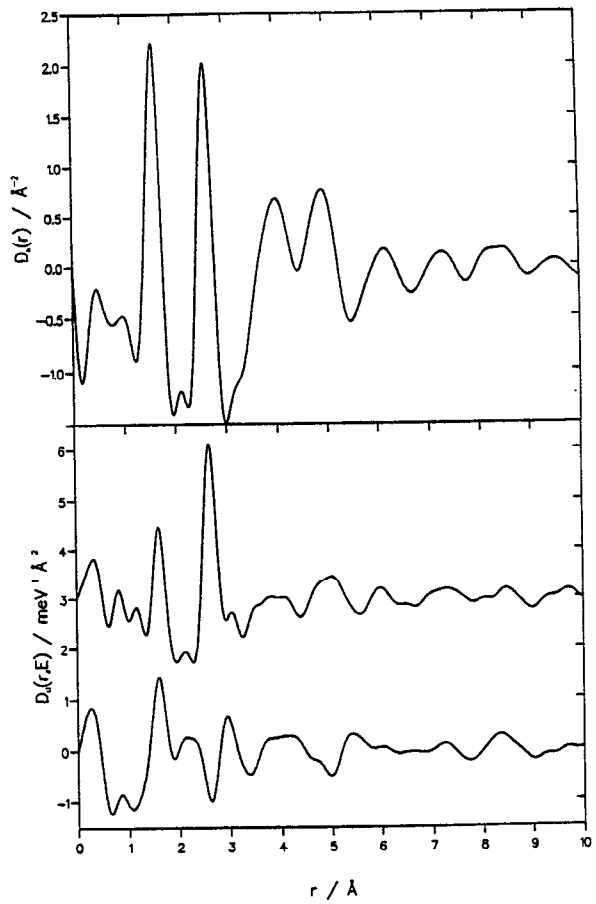


Fig.5 (a) $D_S(r)$, (b) $D_d(r,E=12.5meV)$ and (c)$D_d(r,E=47.5meV)$

$D_S(r)$. However, at the distances corresponding to both the first and second O-O peaks in $D_S(r)$ it is found that $D_d(r,E)$ has a negative-going peak. This may be explained by a negative value from the weighting factor $<\eta(0)\eta(r)>$ and other work has indicated that modes at this energy involve oxygens in a tetrahedron moving in directions which tend to oppose each other. From the results presented here it is clear that it is feasible to use a Fourier transform approach to extract information about atomic displacements in various modes from a measurement of the scattering function of a glass.

## 2) High-$T_c$ oxide superconductors

Here we apply the DPCF method to the high-$T_c$ superconductor $YBa_2Cu_3O_7$, which has very different masses for the constituent elements. In Table I we summarize the masses and the scattering cross-sections for $YBa_2Cu_3O_7$. The structure of this material has been studied by the diffraction technique and the *time averaged static structure* is well established

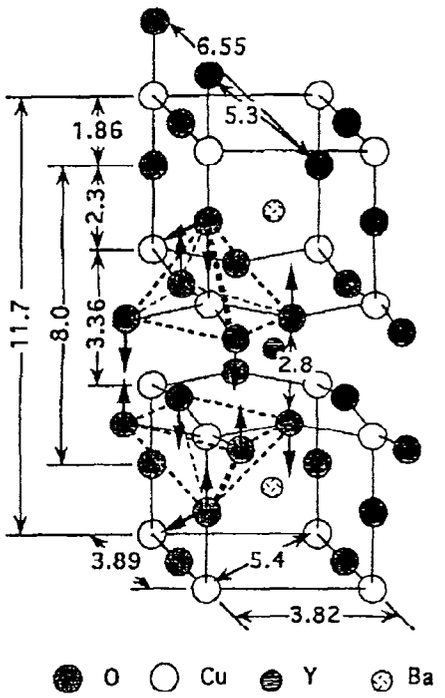


Fig.6 Crystal Structure of $YBa_2Cu_3O_7$.

by Rietveld refinement by assuming a crystal

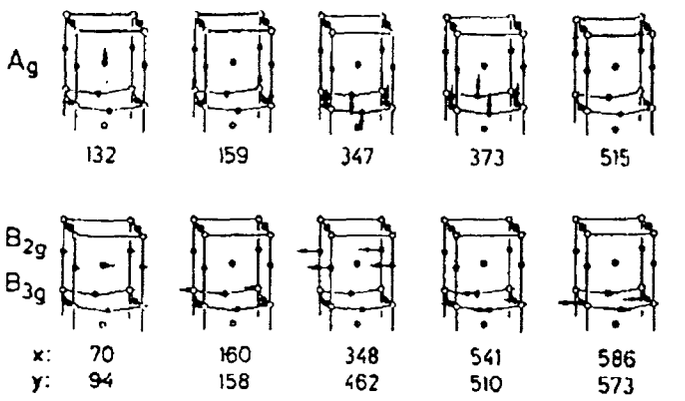


Fig.7 The 10 Raman-active vibrational modes out of 36 optical modes of $YBa_2Cu_3O_7$, taken from [6].

symmetry [5] as shown in Fig.6. From the structure symmetry group theory predicts 36 optical vibrational modes as depicted in Fig.7 [6]. Here we should note that oxygen modes dominate in the high frequency region, say above 40meV ($320cm^{-1}$). These modes have correlations dynamically only among the in-plane oxygens or among the apical oxygens, and there is no cross-correlations between these two types of modes.

The diffraction pattern will be dominated by contributions from atoms other than oxygen because of their relatively high scattering lengths. On the other hand for $S(Q,E)$ in the high energy region the dominating contribution is from the O-O correlations. The latter enhancement is due to two reasons: firstly the lighter mass of oxygen, cf. (5), secondly dominant oxygen modes in the high energy region, say above 40meV, as discussed in the previous paragraph. Therefore we can expect the $D_d(r,E)$ obtained from $S(Q,E)$ in the high energy region should have very different features from the $D_s(r)$ obtained from the diffraction pattern.

In Fig.8 the phonon density of states (PDOS) of $YBa_2Cu_3O_7$ is depicted and the dispersion relation is shown in Fig.9 [7]. The PDOS is composed of two types of features, i.e. sharp peaks and a broad feature under the peaks. The former are attributed to the flat

| elements | A(amu) | $4\pi b^2$ (barns) |
|---|---|---|
| Y | 89 | 7.8 |
| Ba | 137 | 3.5 |
| Cu | 64 | 7.4 |
| O | 16 | 4.2 |

Table I Atomic mass and scattering cross section for the elements of $YBa_2Cu_3O_7$ .

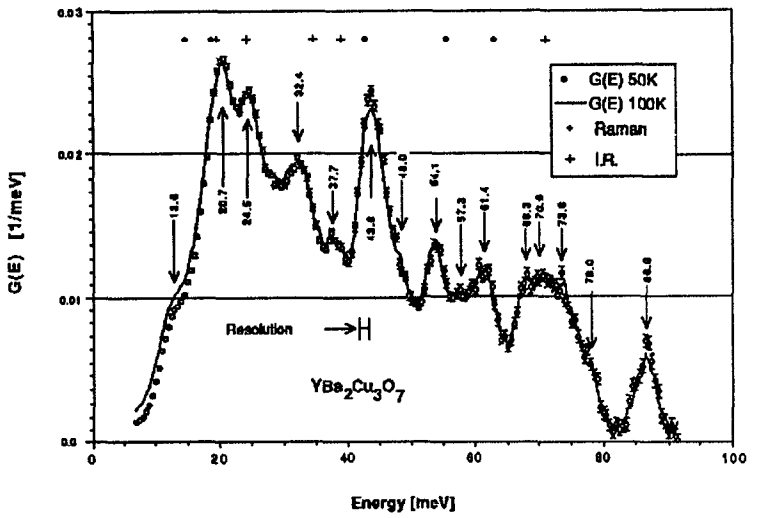


Fig.8 PDOS of $YBa_2Cu_3O_7$, $E_i$=130meV.

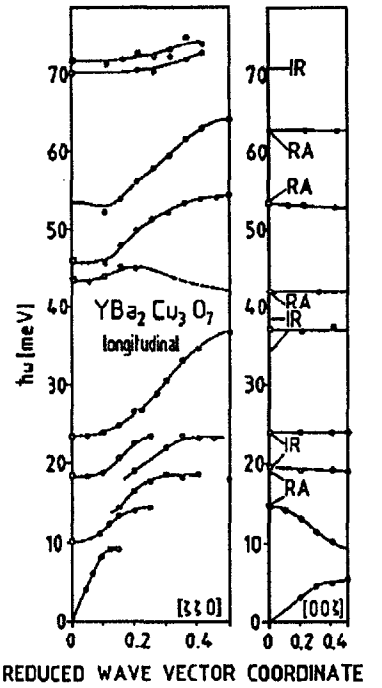


Fig.9 Phonon dispersion curve taken from [7].

dispersion in the *c*-direction and the latter is attributed to the dispersive features in the *a-b* plane. In order to obtain meaningful results by use of the DPCF, we should take some energy band, $Eo \pm \Delta E$, which completely contains the phonon dispersion curves of interest. For the first trial, the low energy limit was chosen at 40meV, where there is a gap in the PDOS and the dispersion relations. Therefore, by using the same method as described for g-$SiO_2$ in the previous section, $D_d(r,E)$ was obtained from $S(Q,Eo \pm \Delta E)$, where $Eo \pm \Delta E$ is from 40 to 90meV, whilst $D_s(r)$ was obtained from $S(Q)$, evaluated by integrating $S(Q,E)$ between -150 and 150meV. In Fig.10 $D_s(r)$ and $D_d(r,E)$ are superimposed. Obviously there are very large differences between them, and these differences are expected.

Because of the finite $Q$-range of the instrument the resolution in $r$-space does not

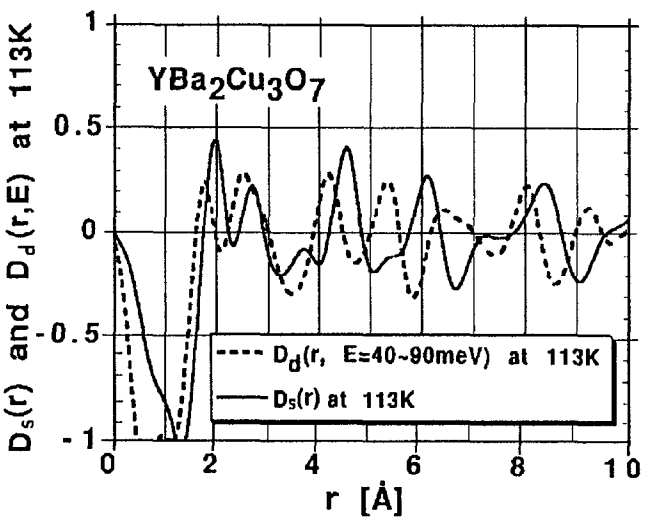


Fig.10 $D_s(r)$ and $D_d(r,E=40 \sim 90meV)$ of $YBa_2Cu_3O_7$.

resolve all details. However, $D_S(r)$ has a similar behaviour to that observed by the use of the LAD diffractometer [8]. On the other hand it is found that the peaks in $D_d(r,E)$ at 1.8, 2.4, 4.2 ,5.4, 6.5 and 8.0Å correspond to the atomic distances between oxygens as shown in Fig. 6. We should note that those correlations are among the oxygens in a group which participate to a certain mode, there is no cross-correlations between the different groups of oxygens because of the orthogonalization, for instance between the in-plane oxygens and the apical oxygens. Thus we may conclude that the DPCF method provides the specific correlations between specific atoms in the material without isotope substitution!! (ie. a Dynamical Labelling Method ) Although a quantitative understanding of the intensity of $D_d(r,E)$ has not yet been performed, we have, however, demonstrated that the DPCF provides a promising new approach to the structural study of materials. In particular the DPCF method may be applied to study local structural distortion, which may be one of the most important properties relating to high-$T_C$ superconductivity [9,10].

## FURTHER SUGGESTIONS

We may also suggest that the dynamic pair correlation function $D_d(r,E)$ contains information on the dynamically moving structure, as the name says. If the movement of the atoms is much slower than the neutron speed, $D_d(r,E)$ may show the instantaneous position of atoms. For instance, if an atom has an anharmonic oscillation in a double well potential, $D_d(r,E)$ may resolve the local stable positions, whereas the diffraction refinement may show just the time-averaged single position associated with a broad thermal diffuse factor. This argument is the direct result of the standard neutron scattering cross-section, but it has not been clearly proved so far.

## REFERENCES


[1] J.M.Carpenter and C.A.Pelizzari, Phys. Rev. B **12**, 2397 (1975)

[2] M.Arai, A.D.Taylor, S.M.Bennington and Z.A.Bowden, Recent Developments in the Physics of Fluids, Adam Hilger, F321 (1991)

[3] M.Arai, A.C.Hannon, A.D.Taylor, A.C.Wright, R.N.Sinclair and D.L.Price, Trans. ACA **27**(1991)113.
A.C.Hannon, M.Arai, R.N.Sinclair and A.C.Wright, J. Non-Cryst. Solids **150**, 239 (1992).

[4] Methods of Experimental Physics Vol.**23**, p.26, eds. K.Sköld and D.L.Price, Academic Press 1986

[5] J.D.Jorgensen, B.W.Veal, A.P.Paulikas, L.J.Nowicki, G.W.Crabtree, H.Claus and W.K.Kwok, Phys. Rev. B **41**, 1863 (1990)

[6] R.Liu, C.Thomsen, W.Kress, M.Cardona, B.Gegenheimer, F.W. de Wette, J.Prade, A.D.Kulkarni and U.Schröder, Phys. Rev. B **37**, 7971 (1988)

[7] W.Reichardt, Physica C **162-164**, 464 (1989)

[8] R.L.McGreevy, L.Borjesson, L.M.Torell and W.S.Howells, Physica B**180-181**, 443 (1992)

[9] T.Egami and S.J.L.Billinge, in: Proc. of The Fifth International Symposium on Superconductivity, Nov. 16-19, 1992 Kobe, Japan, Springer-Verlag.

# Applications of Bayesian Model Selection in Neutron Scattering

*Devinderjit Singh Sivia*

ISIS Facility
Rutherford Appleton Laboratory
Chilton, Didcot, Oxfordshire
United Kingdom OX11 0QX

Many data analysis problems in science reduce to one of model selection. For example, a materials scientist investigating the structure and properties of a new compound may wish to know: are there two peaks under these diffraction data or three? For how many layers of materials is there most evidence in these reflectivity measurements? Do these data indicate a phase transition? In 1939, Jeffreys showed how probability theory could be used to address such questions in a simple and straight forward manner. Until a few years ago, however, his method was little-known. In this short talk, we will show several examples of the use of Bayesian model selection in Neutron Scattering data analysis.

## References

Sivia, D. S., David, W.I.F., Knight, K.S., Gull, S.F. (1993). "An introduction to Bayesian model selection", *Physica D* (in press).

Sivia, D.S. and Carlile, C. J. (1992). "Molecular spectroscopy and Bayesian spectral analysis — how many lines are there?" *J. Chem. Phys.*, 96, 170-178.

Sivia, D.S., Carlile, C.J., Howells, W.S., König, S. (1992). "Bayesian analysis of quasielastic neutron scattering data", *Physica B*, 182, 341-348.

Sivia, D.S., Hamilton, W.A. and Smith, G.S. (1991). "Analysis of neutron reflectivity data: maximum entropy, Bayesian spectral analysis and speckle holography", *Physica B*, 173, 121-138.

# New Scans and Data Visualisation on ROTAX

W. Schmidt[1,2], H. Tietze-Jaensch[1,2,3], R. Geick[1]

1.) Physikalisches Institut der Universität Würzburg, Am Hubland, 8700 Würzburg, F.R.G.
2.) ISIS Science Division, Rutherford Appleton Lab., Chilton OX11 0QX, U.K.
3.) Institut f. Festkörperforschung, KFA Jülich, Pf. 1913, 5170 Jülich, F.R.G.

For the rotating analyser crystal spectrometer ROTAX we have developed a new class of scans through $(\vec{Q},\omega)$-space which will considerably enhance the flexibility of the instrument. We will show the principles of these scans and discuss their advantages and limitations.
Further we will present new developments in visualisation and interpretation of detector data based on the 2-dimensional (time versus position) display of the JULIOS scintillation detector.

## 1.) Introduction

The spectrometer ROTAX uses a non-uniformly spinning crystal analyser for the neutrons scattered by a single crystal sample. The programmable motion of this analyser enables the user to scan different paths through $(\vec{Q},\omega)$-space of the sample. In this paper we will concentrate on new developments in scan construction for the analyser and the visualisation of the corresponding data on the detector. A general description of the instrument, its performance and current status can be found in [1].
The various possibilities to construct different time-of-flight scans are the key to the flexibility of ROTAX. So far several types of scans have been introduced where a particular value, e.g. the energy transfer, is kept constant. Concerning paths along a given Q-direction we have presented the 'const.-$\psi$' scan ($\psi = \measuredangle \vec{k}_i, \vec{Q}$) to measure e.g. longitudinal phonons [2-4].
However, there is no restriction to use only those scan types. Instead, Q-scans can be performed in a much more generalized form that are feasible within the limits of the analyser drive:
In principle, the spectrometer can perform a scan along any Q-direction with respect to a chosen Q-vector. This makes it possible to scan linearly through a particular point in $(\vec{Q},\omega)$-space along a selected direction, like a symmetry axis of the crystal. As a special case we should mention the 'transverse-q' scan where the scan direction is perpendicular to a chosen Q-vector, e.g. to measure transversal phonons.
For these "linear Q-scans" we will discuss the accessible $\vec{Q}$- and $\hbar\omega$-range in accordance with geometrical factors and the limitations in the dynamics of the analyser drive.
In addition to new scan constructions we will present new developments to visualize detector data in combination with real motor performance data.

The JULIOS scintillation detector on ROTAX gives a 2-dimensional data display, time-of-flight versus position. Due to the unambiguous scattering conditions on ROTAX, these detector coordinates can be expressed in terms of $\vec{Q}$ and $\hbar\omega$, and thus, projections of the reciprocal lattice of the sample or contour lines of the energy transfer can be plotted in the same display. Furthermore, the time-of-flight scan trajectory is also transferred to these coordinates.
This simultaneous observation of detector data within the projection of $(\vec{Q},\omega)$-space and the analyser scan onto the same display provides a valuable and effective help in preparing meaningful scans on ROTAX and judging the gathered data afterwards.

## 2.) Principles of the linear Q-scans

### a) Definitions and basic relations

Before the possibilities of these Q-scans are discussed within motor dynamics and physical relevance we introduce the variables and definitions that are needed for further considerations.
The reciprocal lattice ($\vec{Q}$-space) of the sample is usually described in terms of Miller indices (h,k,l). Concerning the scattering plane these vectors can be transformed to a cartesian coordinate system with axes $Q_x$ and $Q_y$. The $Q_x$-direction (a symmetry direction of the sample) is used as a reference with respect of the incoming neutrons ($\vec{k}_i$) defining the angle $\Omega = \measuredangle(\vec{Q}_x,\vec{k}_i)$ as the orientation angle of the reciprocal lattice in the spectrometer set-up. Further we refer to the angles $\psi = \measuredangle(\vec{Q},\vec{k}_i)$ and $\varphi = \measuredangle(\vec{k}_f,\vec{k}_i)$, the scattering angle at the sample. Fig. 1 shows the details. It should be noted that all angles are counted positive when pointing anti-clockwise.

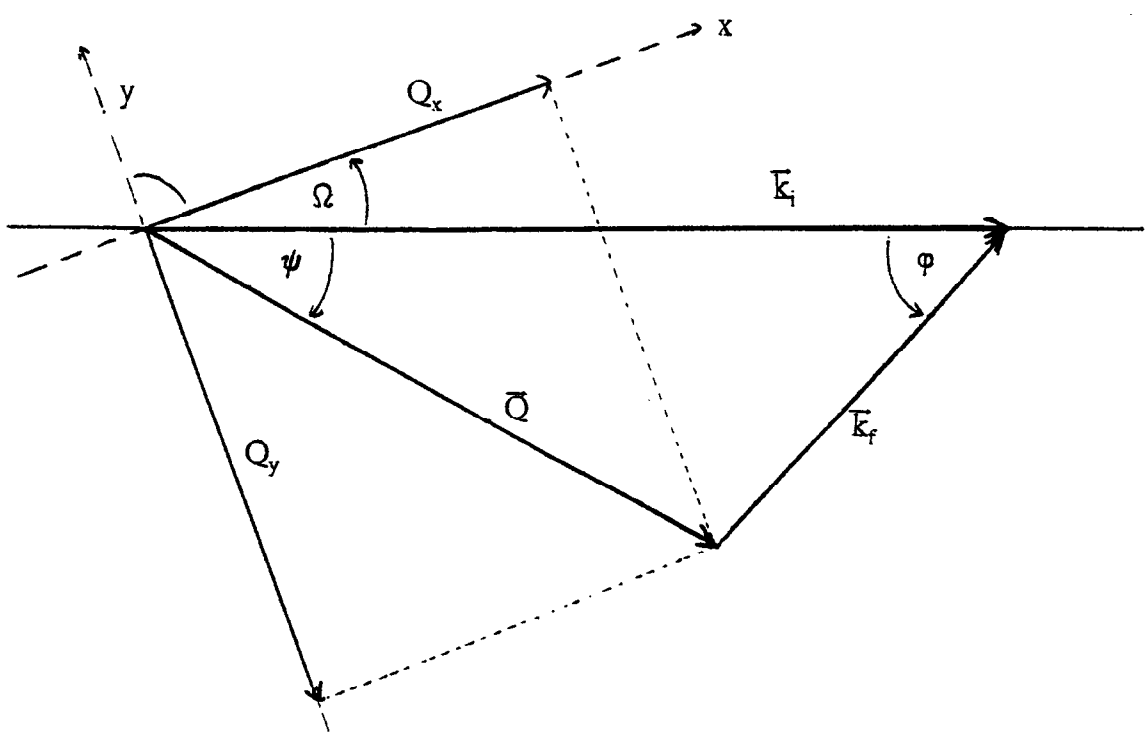


Fig. 1: Definition of the coordinate system in reciprocal space with the relevant angles.

From fig. 1 we deduce the basic relationship between Q, $k_i$ and $k_f$ :

$$Q_x = Q \cdot \cos(\psi - \Omega) = k_i \cdot \cos\Omega - k_f \cdot \cos(\varphi - \Omega)$$
$$Q_y = Q \cdot \sin(\psi - \Omega) = -k_i \cdot \sin\Omega - k_f \cdot \sin(\varphi - \Omega) \quad (1)$$

For further use we will also need the following definitions for time-of-flight and Bragg angle of the analyser:

$$t_i = m_n L_i / \hbar k_i \qquad (L_i = \text{distance moderator to sample}) \quad (2)$$

$$t_a = m_n L_a / \hbar k_f \qquad (L_a = \text{distance sample to analyser}) \quad (3)$$

$$\sin\Theta_A = \pi / d_A k_f \qquad (d_A = \text{d-spacing of the analyser}) \quad (4)$$

Now, a linear Q-scan is defined by two vectors: A starting point ($\vec{Q}_0$) and the direction to be scanned ($\vec{Q}_{sc}$). Both may be given in (h,k,l)-values or directly in the x-y-coordinate system given above. In these coordinates the two vectors define the angles $\alpha$ and $\beta$ as shown in fig. 2 .

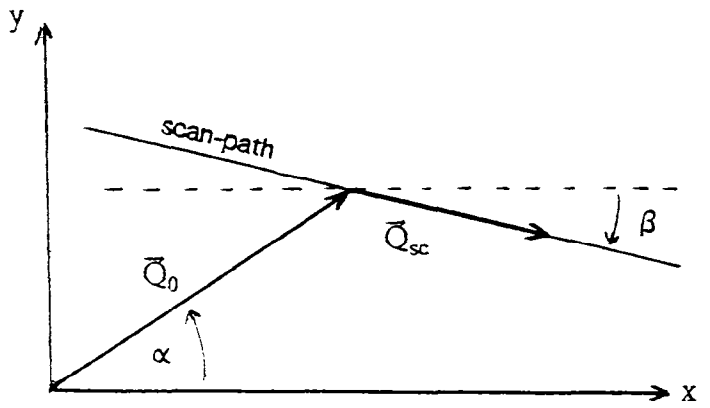


Fig. 2: Definition of the angles $\alpha$ and $\beta$ for start point $\vec{Q}_0$ and scan direction $\vec{Q}_{sc}$.

In order to perform the scan we have to vary just one value, the size of $\vec{Q}_{sc}$ . This fact is expressed by a scan parameter p in the following way:

$$Q_{sc}(p) = p \cdot Q_0 \quad (5)$$

With the angles from fig. 2 we then get a general expression for $\vec{Q}$ along the scan in dependence of p:

$$Q_x(p) = Q_0 \cdot (\cos\alpha + p \cdot \cos\beta)$$
$$Q_y(p) = Q_0 \cdot (\sin\alpha + p \cdot \sin\beta) \quad (6)$$

The starting point $\vec{Q}_0$ is included in these equation for p = 0. A scan can be performed from a value $p_{min} < 0$ to $p_{max} > 0$ which will be given by the geometrical spectrometer set-up and limitations in the dynamics of the analyser drive.

Combining eq. 6 with eq. 1 yields the variation of $k_i$ and $k_f$ during the scan :

$$k_i(p) = -Q_0 \cdot [\sin(\alpha + \Omega - \varphi) + p \cdot \sin(\beta + \Omega - \varphi)] / \sin\varphi$$
$$k_f(p) = -Q_0 \cdot [\sin(\alpha + \Omega) + p \cdot \sin(\beta + \Omega)] / \sin\varphi \quad (7)$$

For a given set of angles ($\alpha$, $\beta$, $\Omega$, $\varphi$) these equations can be used to determine the principle range for p and thus the scan length. A chosen time window for $t_i$ yields the possible $k_i$-range (eq. 2) while the $k_f$-range is given by the possible analyser angles $\Theta_A$ (eq. 4). Using these limitations for $k_i$ and $k_f$ in eq. 7 we easily get the limits for p as well.
Further, from eq. 7 we can derive an expression for the energy transfer $\hbar\omega$ during a scan:

$$\hbar\omega(p) = -\hbar^2/2m_n \cdot Q_0^2 \cdot [\sin(2\alpha + 2\Omega - \varphi) + 2p \cdot \sin(\alpha + \beta + 2\Omega - \varphi) + p^2 \cdot \sin(2\beta + 2\Omega - \varphi)] / \sin\varphi \qquad (8)$$

This equation may also be used to determine a range for p by setting lower and upper limits for $\hbar\omega$ to establish reasonable energy transfer values during a chosen scan.
Besides the range of p these equations for $k_i$, $k_f$ and $\hbar\omega$ provide a guideline for the choice of the geometrical set-up: The user may wish specific values for the wave-vectors or the energy transfer at the starting point $\vec{Q}_0$. Thus, setting p=0, eq. 7 and 8 yield conditions between the angles $\alpha$, $\Omega$ and $\varphi$. If, for example, we want $\hbar\omega = 0$ at $\vec{Q}_0$ we get the condition $2\alpha + 2\Omega - \varphi = n \cdot \pi$ from eq. 8.
In addition, even the variation of the energy transfer with respect to the scan direction can be used as a selection rule for the angles:

$$d(\hbar\omega)/dQ_{sc} = (d(\hbar\omega)/dp) / (dQ_{sc}/dp) = (d(\hbar\omega)/dp) / Q_0 \qquad (9)$$

## b) Motor dynamics

So far we have derived the basic equations and principle limitations for linear Q-scans. Another important consideration is the dynamics of the analyser drive, or in other words, can the motor drive perform the necessary rotation within its technical limits ?
In order to answer this question we have to look at motor speed and angular acceleration, i.e., the derivatives of $\Theta_A$ with respect to time. At this place we will not go through all the mathematics but instead give a short outline of the procedure and present the result for the motor speed as an example. This result is a good startpoint for discussion as well.

The arrival time $t_A$ of the neutrons at the analyser is given by the sum $t_i + t_a$ (eq. 2,3) and, like the analyser angle, it is expressed in dependence of the scan parameter p :

$$\Theta_A = \Theta_A(k_f(p)) \quad \text{and} \quad t_A = t_i(k_i(p)) + t_a(k_f(p)) \qquad (10)$$

So we can evaluate the derivatives

$$d\Theta_A/dp = d\Theta_A/dk_f \cdot dk_f/dp \quad \text{and}$$
$$dt_A/dp = dt_i/dk_i \cdot dk_i/dp + dt_a/dk_f \cdot dk_f/dp \qquad (11)$$

as well as

$$d\Theta_A/dp = d\Theta_A/dt_A \cdot dt_A/dp \quad \text{with} \quad d\Theta_A/dt_A = \omega_A \quad . \qquad (12)$$

A combination of these equations yields an expression for the motor speed $\omega_A$.

Similarly further derivatives can be calculated, too. For $\omega_A$ we get

$$\omega_A = (\pi \hbar / m_n L_i d_A) \cdot [\cos \Theta_A \cdot (\zeta + \gamma^2 \cdot x)]^{-1} \tag{13}$$

with

$$x = \sin(\beta + \Omega - \varphi) / \sin(\beta + \Omega) \ , \ \zeta = L_a/L_i \ , \ \gamma = k_f/k_i \tag{14}$$

Apart of the dependencies of $\Theta_A$, $k_f$ and $k_i$ this equation shows a dramatic influence of the parameter x which absolute value can range from zero to infinity. We will discuss the two resulting extrema for $\omega_A$ :
First, eq. 13 shows that the term in square brackets vanishes for $x = -\zeta/\gamma^2$ , i.e., we get very high speeds around that x-value which is approximately around zero since $\zeta$ is very small ($\zeta \approx 0.03$). Thus no scans are possible in a range around $\beta \approx \varphi - \Omega$ .
In terms of physics: All scattered neutrons during the scan would arrive at the analyser at one specific time.
On the other hand, we may choose $\beta = -\Omega$ which yields infinity for x and correspondingly $\omega_A = 0$ . Thus the analyser stands still and all scattered neutrons during the scan must have the same energy. This is confirmed by eq. 7 where $\beta = \varphi - \Omega$ yields $k_f$ independent of p. In fact, this mode is used on PRISMA [5].
These considerations also hold for the higher order derivatives of $\Theta_A$ since they contain the square bracket term from eq. 13 as well. But nevertheless, the motor limits for these values must be checked for each scan, especially the angular acceleration is the limiting factor rather than the speed since this parameter is directly related to the necessary motor current. In total, all the limiting factors are checked automaticly in the scan construction program so that the user always gets the maximum length of a chosen scan within the technical limits.

## c) Examples

The following figures will show some examples of possible scans using an aluminium sample (lattice constant = 6.22 Å) and a germanium analyser (4,0,0-reflection, $d_A$ = 1.414 Å). The lengths ($L_i$ = 14.1 m, $L_a$ = 0.66 m) are realised on ROTAX.
The fig. 3a and 3b both show the reciprocal lattice of the sample in relative units (h,0,0 and 0,k,0) where we take the first vector as reference direction ($\alpha = 0$). Also shown are constant energy lines to get an estimate which energy range the scans cover. The scan paths themselves are drawn for different angles $\beta$ as solid lines which spread out from $Q_0$. The step width for $\beta$ is 1° in fig. 3.
In addition to the technical limitations we have restricted the scan length to an energy transfer interval of $-20$ meV $< \hbar\omega <$ 200 meV. Therefore the scan paths either end at the corresponding energy lines or - if shorter - the motor dynamics determines their lengths. The accessible $k_i$- and $k_f$-range is also included which can partly be seen as dashed lines.
According to the discussion of the influence of $\beta$ on the motor speed we have indicated the directions $\beta = -\Omega$ (PRISMA mode) and $\beta = \varphi - \Omega$ (infinite speed). Both figures show clearly the gap around $\beta = \varphi - \Omega$ while for $\beta = -\Omega$ only the chosen energy interval determines the scan length.

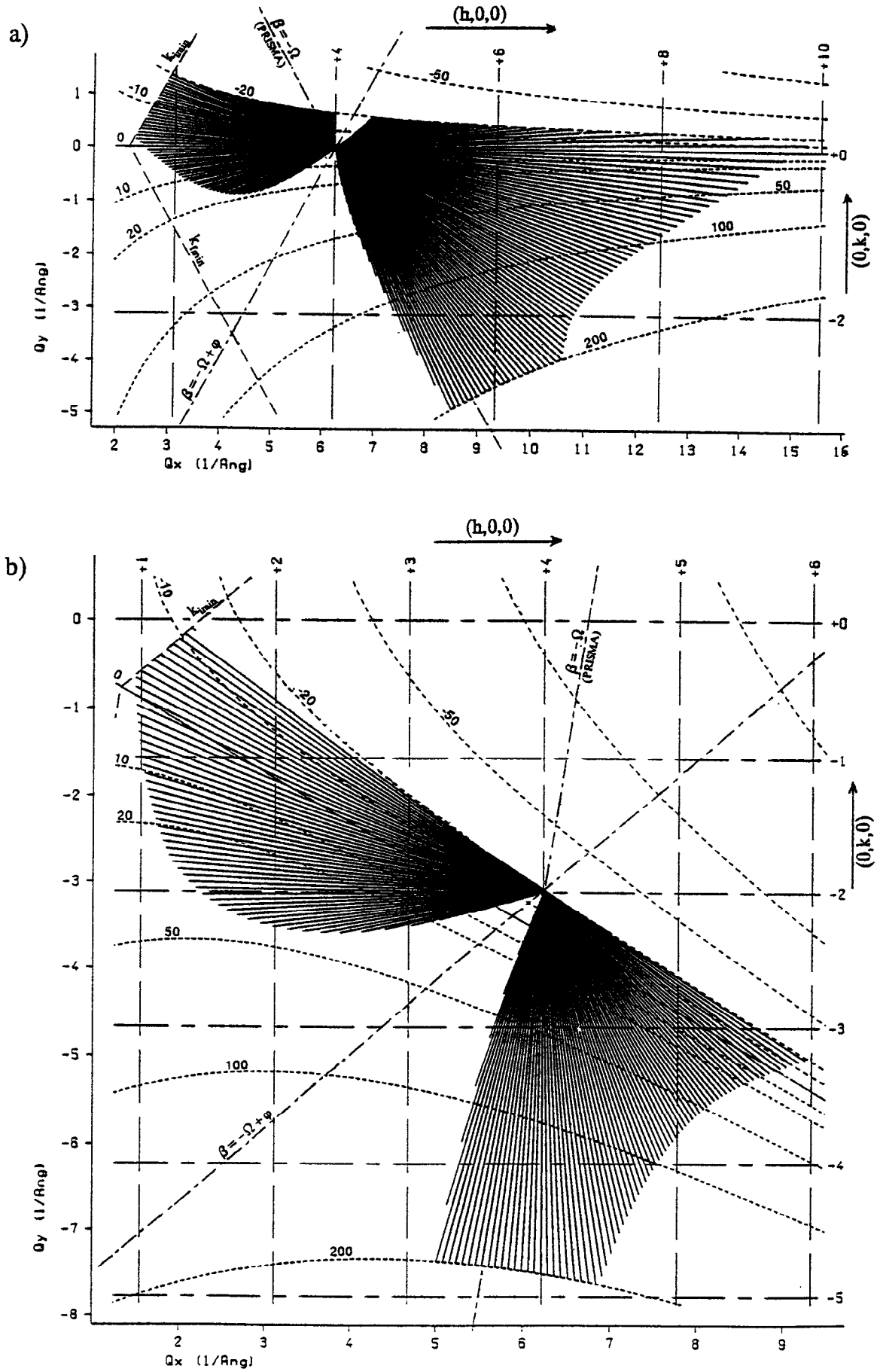


Fig. 3a,b: Feasible scan paths (solid lines) in reciprocal space for two different configurations. The dotted lines show the energy transfer in meV.

3a) $\alpha = 0°$, $\varphi = -60°$, $\Omega = 60°$, 3b) $\alpha = -25.6°$, $\varphi = -40°$, $\Omega = 100°$

Fig. 3a shows a configuration with $\vec{Q}_0$ = (4,0,0), thus $\alpha$ = 0°, and $\varphi$ = - 60°, $\Omega$ = 60° which is favourable for scans with a low energy transfer pointing approximately along the (1,0,0)-direction. In fact we have chosen $\hbar\omega(p=0) = 0$ which results from $2(\alpha+\Omega)-\varphi$ = 180° here (cf. eq. 8) and thus we are able to include an elastic scan path as well. Concerning higher energy transfers one may choose a scan along (1,-1,0).
Instead fig. 3b shows a quite different behavior. Here we have set $\vec{Q}_0$ = (4,-2,0), thus $\alpha$ = - 25.6°, and $\varphi$ = - 40°, $\Omega$ = 100°. Scans may be chosen around (1,-1,0)-direction with low energy transfer while scans with higher $\hbar\omega$-values are both possible along (1,0,0) and (0,1,0).
These two examples shall demonstrate that we get a wide range of different scan directions and different energy ranges. Certainly the technical limits of the analyser drive cut out some regions but with a proper set-up there will always be a possibility for a desired $\vec{Q}$ and energy range.

## 2.) Data visualisation

### a) The JULIOS display

The ROTAX instrument uses the JULIOS scintillation detector from KfA Jülich [6]. This detector provides a 2-dimensional display: Position channels in the horizontal direction, time-of-flight channels in the vertical.
In relation to the analyser, each position channel corresponds to a specific Bragg angle there and can therefore be related to a well-defined $k_f$. Thus, when $k_f$ is known, each time channel can be used to calculate also $k_i$. Fig. 4 shows the basic geometry with all parameters. The orientation of the detector is defined by a reference channel $n_{x0}$ with a corresponding angle $2\Theta_{A0}$.

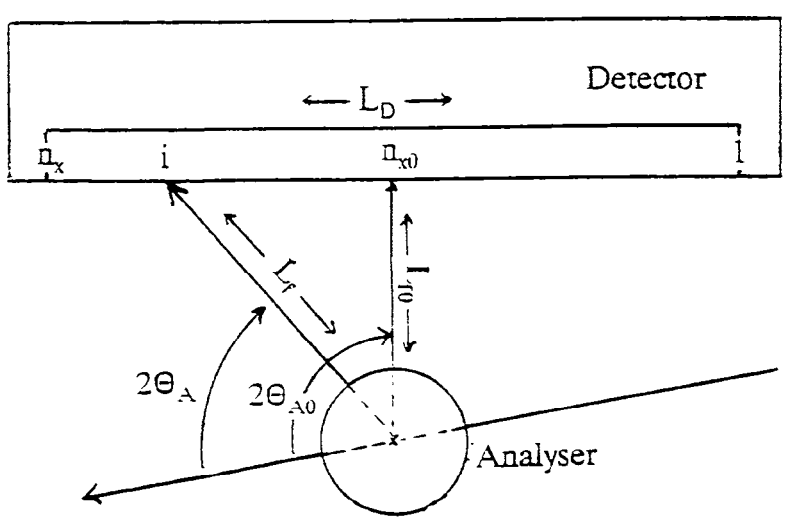


Fig. 4: Definitions of lengths and angles between analyser and detector position channels.

For a specific position channel i we get from the geometry

$$L_{f0} \cdot \tan ( 2\Theta_A(i) - 2\Theta_{A0} ) = L_D \cdot ( i - n_{x0} )/n_x \tag{15}$$

$$L_f(i) = L_{f0} / \cos ( 2\Theta_A(i) - 2\Theta_{A0} ) \tag{16}$$

$$k_f(i) = \pi / | d_A \cdot \sin \Theta_A(i) | \tag{17}$$

The time channels (from 1 to $n_y$) correspond to a user-chosen time window reaching from $t_1$ to $t_2$. For a specific time channel j we then get the total time-of-flight

$$t(j) = t_1 + (t_2 - t_1) \cdot j / n_y \tag{18}$$

and with eq. 17 the incident time-of-flight and $k_i$ :

$$t_i(i,j) = t(j) - m_n \cdot ( L_f(i) + L_a ) / \hbar k_f(i) \tag{19}$$

$$k_i(i,j) = m_n L_i / \hbar t_i(i,j) \tag{20}$$

## b) Projections of $(\vec{Q},\omega)$-space

As we have seen in the previous section we can relate every pixel (i,j) of the detector display to a pair $k_i(i,j)$ and $k_f(i)$. Therefore we are able to calculate the Q-components (eq. 1) and the energy transfer for each pixel as well. This is used to create a grid of two chosen $\vec{Q}$-vectors and energy lines similar to fig. 3. However, due to the non-linearities in eq. 15 to 20 a rectangular reciprocal lattice (as the aluminum grid in fig 3) appears highly deformed. Thus, different Brillouin-zones of actually the same size cover more or less pixels on the detector screen depending on their related values in position and time. In addition, as done in fig. 3, any scan can be plotted in the same display.

This provides a helpful tool for the user:

- The user knows in advance how the reciprocal lattice, energy transfer and the scan are related with the grid of detector channels. The size of a specific Brillouin-zone or the density of constant-energy lines gives an estimate for the expected resolution.
- During an experiment the user can easily interprete intensities, not only along the scan path but also near or perpendicular to it. This shows immediately how far a measured excitation is extended into the Brillouin-zone or how broad it is in energy.

## c) Application

All these theoretical considerations have been applied to inelastic data obtained with ROTAX [1,4] using an aluminum sample. In a scan along (1,0,0)-direction we have measured longitudinal phonons simultaneously in two different Brillouin-zones. Fig. 5 shows the results with the projection of the reciprocal lattice, energy transfer and the scan path into the display. Instead of the real colour display three different count-rate levels are selected. The graphics shows the defacing of the quadratic lattice. The zone around (2,0,0) is much larger on the display than the next zone around (4,0,0). But the display shows also interesting details confering the information perpendicular to the scan. The inelastic scattering intensity distributions are slightly asymmetric off the scan path and, with greater distance from the zone centers, tilted towards higher values of $\hbar\omega$. This is, in fact, a resolution effect, arising form the dispersion of the phonon branches, and made visible as a whole directly on the detector screen.

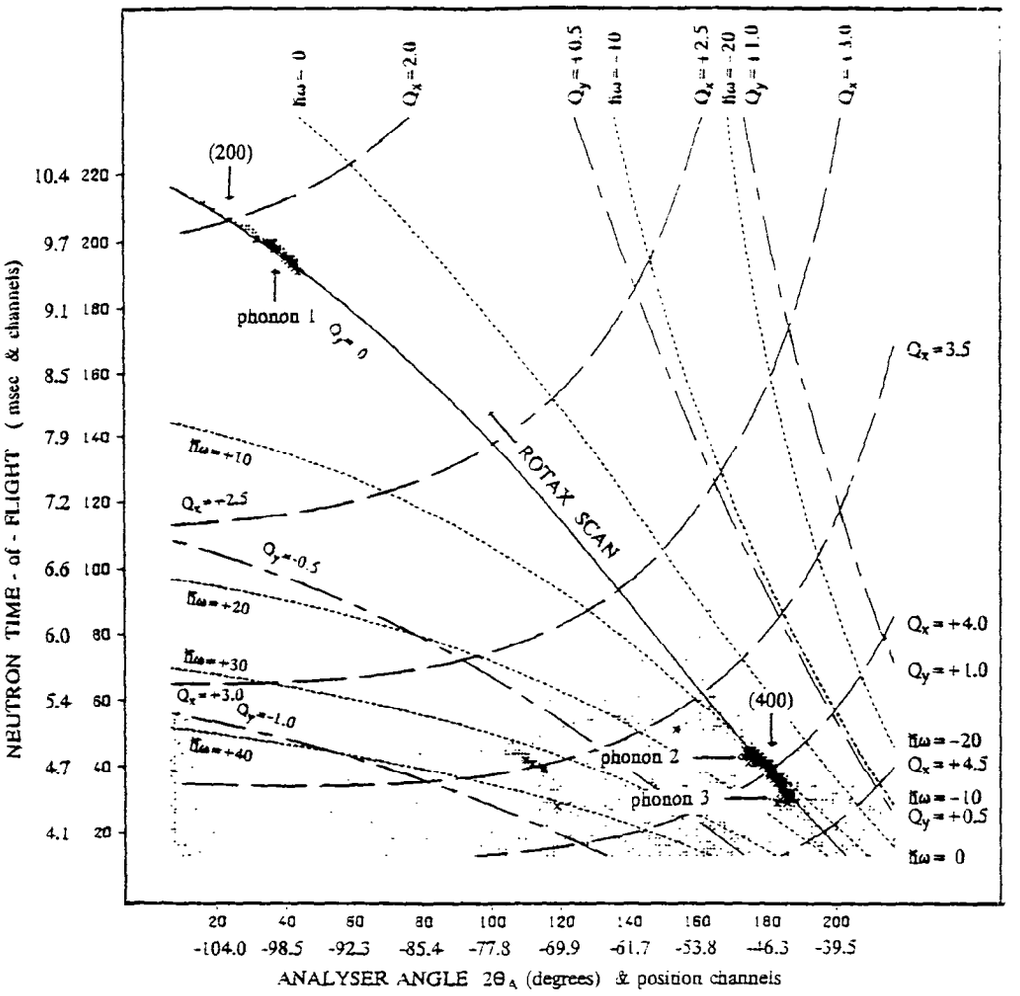


Fig. 5: The detector display with inelastic data and the projection of $(\vec{Q},\omega)$-space. The energy transfer is given in meV, the reciprocal lattice in relative units (as in fig. 3).


## Acknowledgement

ROTAX is funded by the BMFT under contract number 03-GE3-WUE.


## References


[1] H.Tietze-Jaensch, W. Schmidt, R. Geick
Proc. ICANS XII, Session A2 (1993)

[2] R. Geick, H. Tietze; Nucl. Instr. Methods A **249** (1986) 325

[3] H. Tietze, R. Geick
Proc. Int. Collab. Advanced Neutron Sources ICANS IX 1986, CH-Villigen, Switzerland, SIN-rep. 40926, 389 (1987)

[4] H. Tietze, W. Schmidt, R. Geick, U. Steigenberger, H. Samulowitz;
Proc. Int. Collaboration on Advanced Neutron Sources ICANS XI 1990, KEK Japan, KEK report 90-25, 774 (1991)

[5] U. Steigenberger, M. Hagen, R. Caciuffo, C. Petrillo, F. Cilloco and F. Sacchetti
1990 RAL-90-004 and Nucl. Inst. and Meth. **B53** (1991) 87

[6] E. Jansen, W. Schäfer, A. Szepesvary, R. Reinartz, H. Tietze, G. Will, K.D. Müller, U. Steigenberger;
Proc. Int. Conf. on Neutron Scattering ICNS 91, Oxford (1991), Physica B **180 & 181** (1992) 917

# Better visualisation of neutron scattering data using UNIRAS at ISIS

**K.M.Crennell**
***Rutherford Appleton Laboratory, ISIS Facility, Chilton, Didcot, Oxon, OX11 0QX UK***

***Abstract:*** *The pulsed neutron source, ISIS, at the Rutherford Appleton laboratory in the UK is used for many experiments to determine the structure of materials. Data is often collected over a range of operating conditions to study phase changes in the material. Older instruments collected one dimensional data, some of the newer ones have area detectors which collect two dimensional data. The old data display programs dealt only with one dimensional data so new interactive graphics programs have been written using the UNIGRAPH package to display a series of one dimensional datasets as a two dimensional image which shows the phase changes much more clearly. Experiments are described on the use of an image processing library for the display of two dimensional neutron scattering data from the small angle scattering instrument, LOQ.*

## Introduction: UNIRAS

UNIRAS(1) is a graphics system which consists of two main parts, a series of subroutine libraries and several associated interactive programs to access them. It runs on a wide range of computers including VAX, IBM mainframes, and many types of workstation including Silicon Graphics and Sun. We use it on our VAX/VMS cluster, with colour displays on the neutron scattering instrument data collection workstations and on PC clones on scientists desks. The version we are running can display graphics in a single window of an X-windows terminal, more recent versions can display graphics in many windows, so we will be upgrading soon since we plan to standardise our workstations to use OSF-Motif X-windows, and often want to see several views of our data simultaneously.

The UK Science and Engineering Research Council and the University Funding Council collaborated on a joint purchase of UNIRAS for the UK academic community, which makes it cheaply available to any UK University. It is distributed by CHEST, the Combined Higher Education Software Team, based at the University of Bath.

UNIRAS routines can be called from user programs written in the programming languages Fortran77 or C. Four associated interactive programs access most of the routines in the libraries; we use one of them, UNIGRAPH, to prototype our visualisation ideas, before writing our own interactive graphics programs if necessary. UNIGRAPH has many menus to change the type of plot, has several colouring schemes, and a simple data manipulation language. It contains many different device drivers and has a way of saving the current plot to hardcopy, including the making of monochrome or colour PostScript files.

## Visualisation of IRIS data:

### (1)Spectroscopy of hexamethyl stannate.

IRIS is a time resolution quasielastic and inelastic scattering spectrometer(2,3) at the ISIS pulsed neutron source in Oxfordshire in the UK. In June 1992 it was being used by M.Prager and C.J.Carlile to study rotational tunnelling spectroscopy with neutrons(4) on a sample of hexamethyl distannate $(CH3)_6Sn_2$ as a function of temperature between 5 and 15 degrees Kelvin. The data was normalised using the GENIE analysis and display program(5) and then written out at each temperature as a series of neutron intensities at a range of energy transfers.

Figure 1

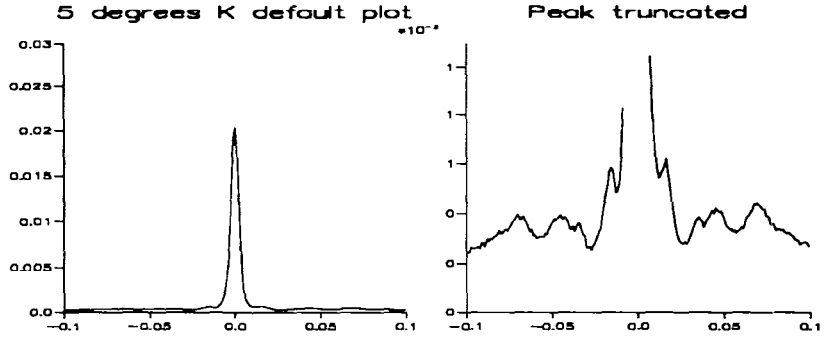


Figure 1 (left) shows the default plot for the lowest temperature made interactively using UNIGRAPH. Little detail can be seen due to the domination of the plot by the elastic peak, so data at the higher values was truncated and the data replotted as shown on the right hand side of Figure 1 where four peaks can be seen which were almost invisible before. When data is taken at a series of temperatures, it is often displayed as a series of plots displaced from one another vertically as shown in Figure 2, where different line types have been used for the different temperatures. To show all the plots on one graph, or 'multiplot', means they have to be plotted with a small scale, and although there is clearly some difference between the spectra represented by the lines at the extremes of the plot, it is hard to see exactly how they vary.

Figure 2

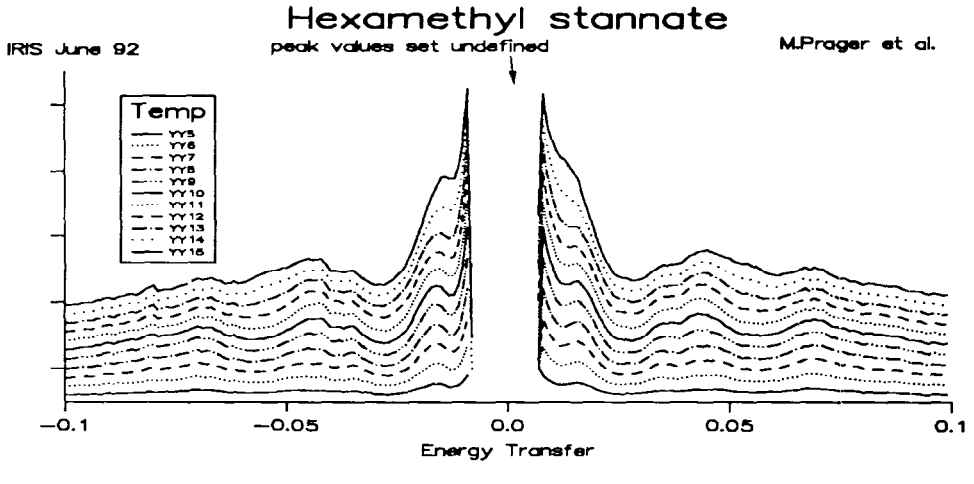

A new algorithm has been developed which considers each spectra as a slice through a three dimensional surface, with dimensions energy transfer, temperature, and intensity. The surface is made using the UNIGRAPH manipulation language to combine all the spectra into a two dimensional array, which is then displayed as an image, with spectral intensities represented as different colours or grey levels, as in Figure 3 which shows the same data as that of figure 2, but the transition at about 11 degrees Kelvin is much more obvious. This transition is thought to be due to changes in the tunnelling of the methyl groups.(4)

Figure 3

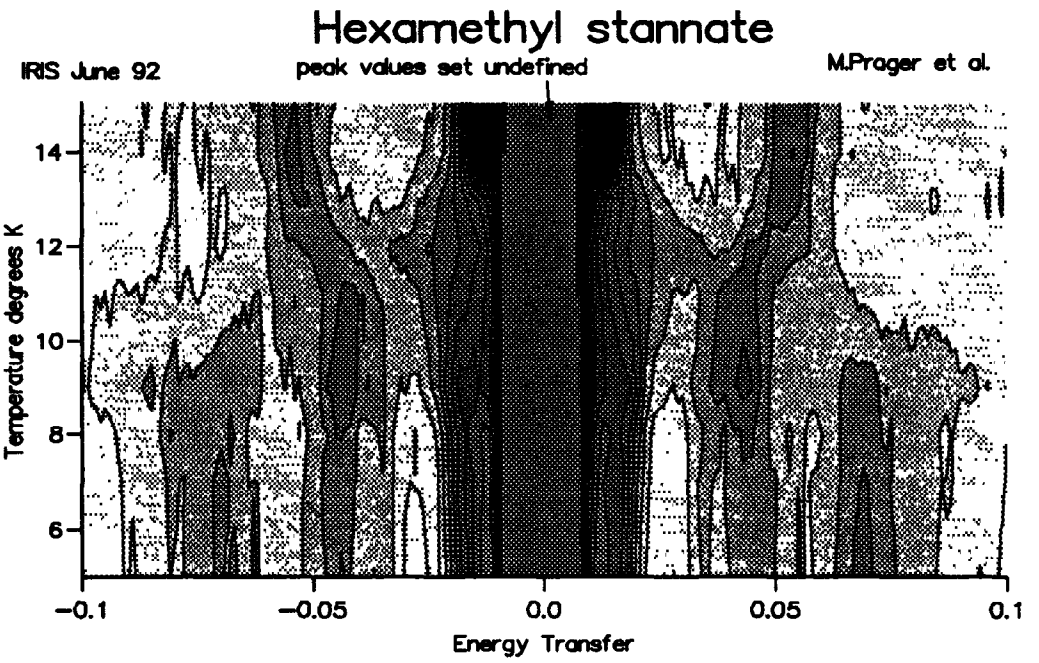


The individual datasets are read into UNIGRAPH using the command language, for example to read in a single dataset the commands are DATA IMPORT REPORT. They are given names, for example Y5, for the data taken at 5 degrees, Y6 for that at 6 degrees, and so on. These are combined together with a statement like: `Let "Y" "Y5//Y6"` where the operator // means append dataset Y6 to Y5. When all the datasets have been accumulated together they can be converted to a two dimensional array by a statement like: `Let "Y" "RESHAPE(Y,301,11,1)` where 301 is the number of entries in the X direction for each dataset, 11 the number of datasets in the Y direction, and there is only one set of values for the Z. There are many other commands in the UNIGRAPH data manipulation language; the main features it lacks are the ability to operate on a dataset and an associated error dataset in a single command, and to allow control to pass to a 'user' written routine during the data analysis.

The dataset Y can by shown as exact 'pixels', which may be necessary if measurements are to be made on the plot, but it is more difficult to see trends with that type of display. Figure 3 is a 2D contour plot, with some smoothing applied to the graphics before displaying it, and outlines added to emphasise the structure. The original data is not changed, only the graphical display is smoothed Further interactive selections of subsets of the data can be made, for example the limits of X and Y can be changed to zoom into smaller regions of the data.

Figure 4

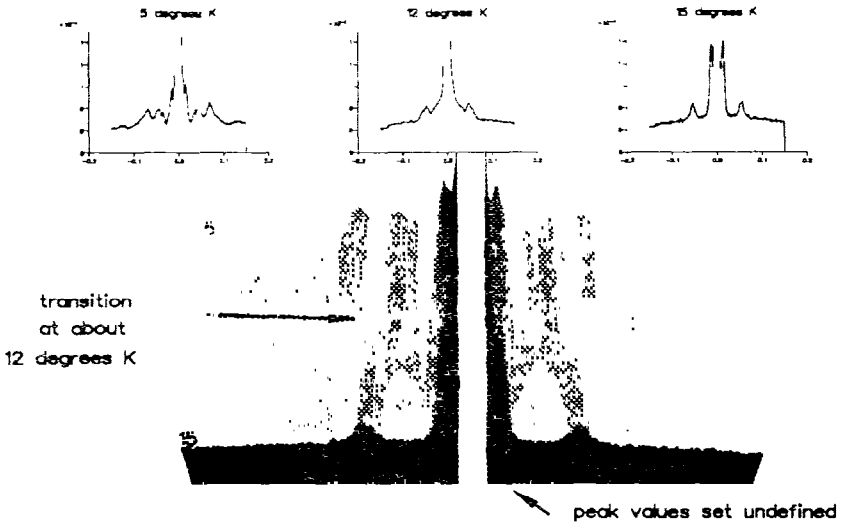


UNIGRAPH allows the superposition of several plots on the same page as shown in Figure 4, where a 3D view is shown in the centre, with 3 slices through the surface plotted at the top. The surface has been rotated relative to that of Figure 3 because it is easier to see the shape of the tunnelling peaks when viewed from the higher temperature end. These plots are normally seen in colour, where the surfaces of the peaks can be shown in a different colour. An interactive program is essential to make the optimum view by changing both the colourtable and the number of colours. We have only been using colour displays for a short time, and have found that although everyone agrees they can see the data well when displayed as grey scales, there is considerable disagreement about which colours should be used for an optimum display. We try to avoid combinations of red and green for the benefit of the colour blind.

### (2)Magnetic crystal structure of ferric vanadate

This display algorithm can be used with any sets of data taken at regular intervals. Figure 5 shows a 'multiplot' of neutron scattering data taken on IRIS for the magnetic material ferric vanadate by J.B.Forsyth and C.J.Carlile in 1992. (6)

Figure 5

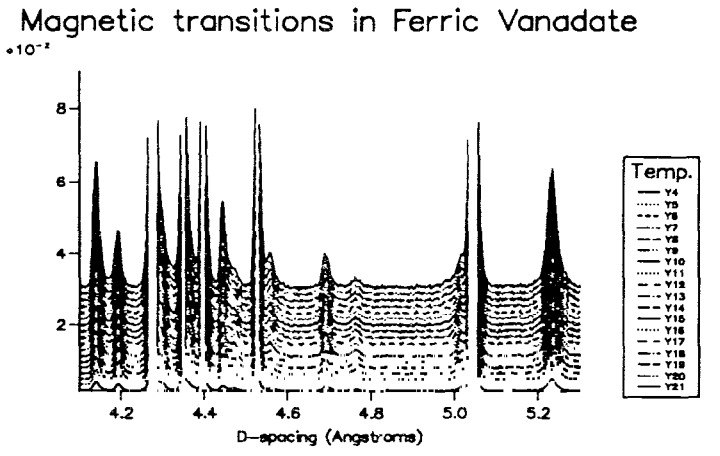

Neutrons scatter in two ways from this material; there is the usual Bragg diffraction from the structure, and additional scattering due to the interaction of the magnetic moment of the neutron with the magnetic structure of the material which is only seen at low temperatures, appearing as noise above 20 degrees K. The material undergoes two exothermic phase transitions at about 15 degrees K which involve an ordering of the electronic spins of the iron atoms.

Figure 6

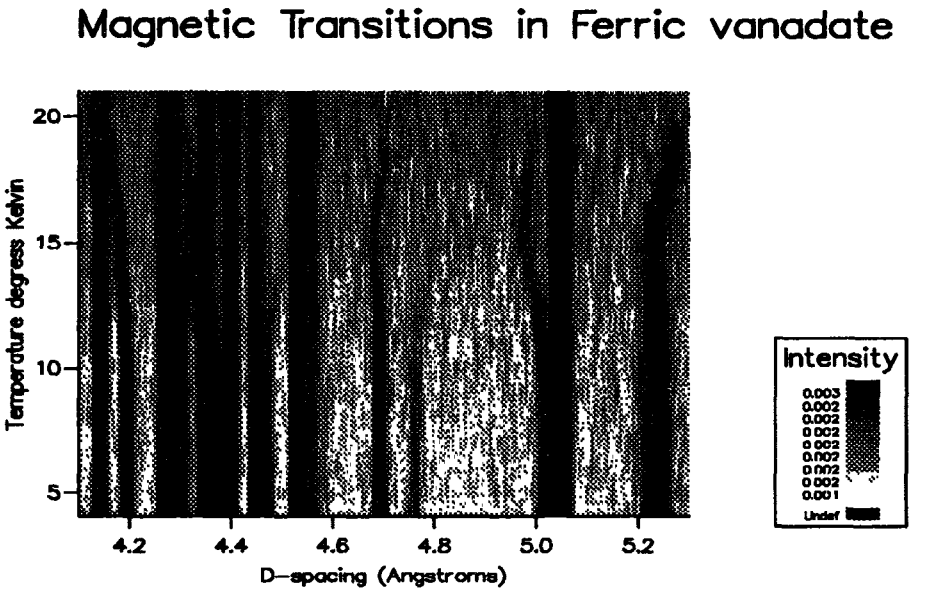


The Bragg peaks dominate this plot, so they have been truncated in order to see the detail in the magnetic diffraction lines which appear to change their position with temperature, as shown in Figure 6, a grey level 'image' plot with each line of data containing about 800 points. Between 5 and 10 degrees Kelvin the magnetic peaks show clearly as vertical lines, above that they curve dramatically. The two peaks at D spacings between 4.6 and 4.8 Angstroms curve in opposite directions as they decrease in intensity, indicating a complex ordering of the atomic moments in a helical geometry incommensurate with the atomic lattice. This can not be so clearly seen in Figure 5.

## Display of LOQ Data.

In addition to using the interactive program UNIGRAPH, we have also used the UNIRAS subroutine libraries in a program, VULOQ(7), to display data from the LOQ instrument (2) which uses small angle diffraction to investigate the shape and size of large molecules. It has an area detector coded as 128 x 128 pixels, and so unlike IRIS, naturally collects data as a two dimensional array.

VULOQ can display 2 and 3D plots similar to those of Figures 3 and 4, another example is shown in upper left of Figure 7 which shows the data displayed as the exact pixels of an image. This was part of an experiment exploring the use of a conventional image processing library for improved data display. UNIRAS has many interpolation routines, but they need to be used with caution, an injudicious choice of parameters in interpolation routines can produce spurious artefacts not present in

the data. It may be that a simpler process from an image processing library has fewer problems. The plot at upper right of Figure 7 is the result of using a 3 x 3 median filter to smooth the data of upper left. This filter will reduce the image size by a row all the way round but should not introduce other spurious effects.

Figure 7

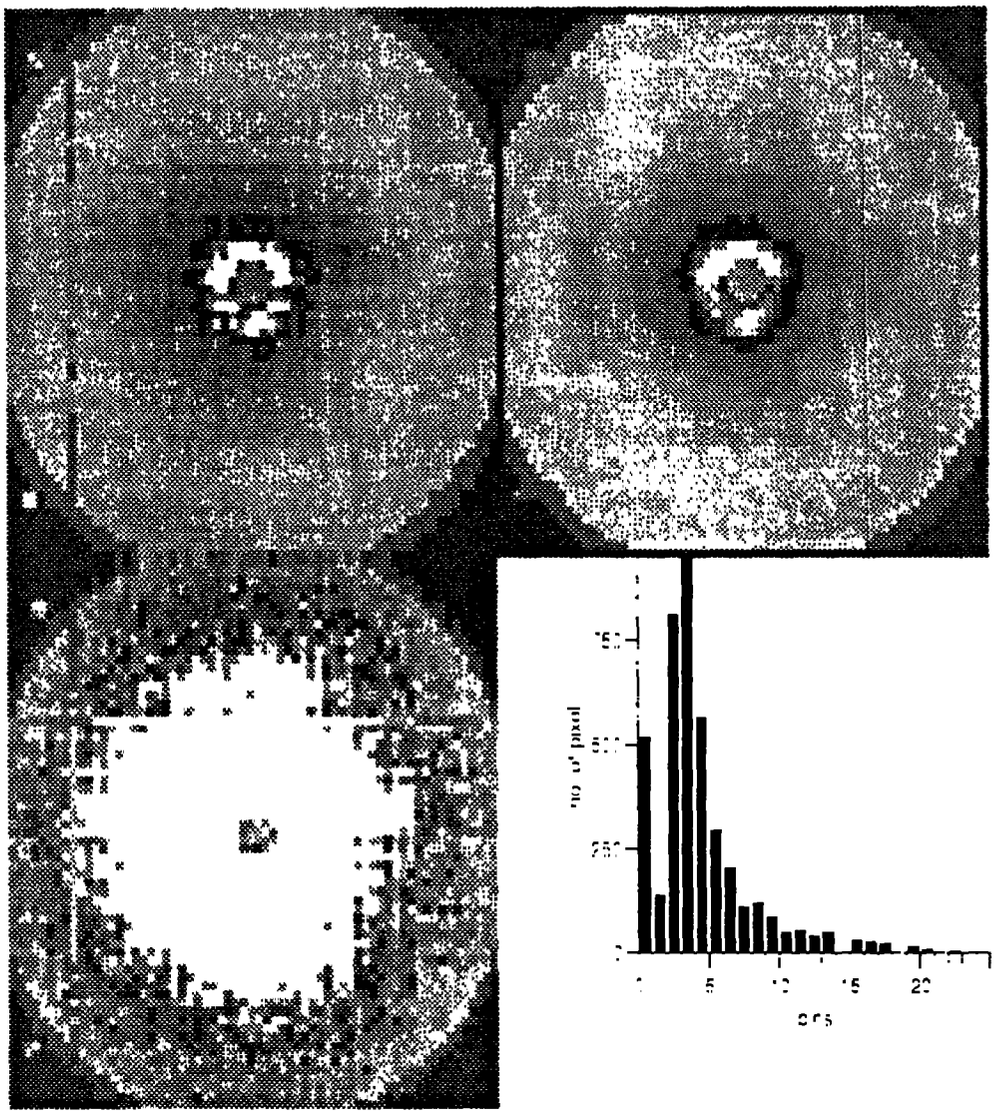

The histogram at lower right of Figure 7 shows the distribution of intensities in the image at upper left. A standard enhancement technique in image processing is to manipulate the intensities in the histogram, reducing the higher ones and increasing the lower ones, a process known as 'histogram equalisation'. As can be seen in Figure 7, lower left, it enhances image features. It might also improve the contrast in the 2D plots of Figures 3 and 6 to make the small signals more visible, but this has not yet been tried.

One problem with using conventional image processing routines on neutron scattering data is that many routines expect the intensities displayed in the image to have values less than 256, because that is the maximum intensity many optical cameras can record. Our intensities vary from many thousands to a few tens, and normalisation operations can result in negative values, so any image processing library used should not expect small positive numbers for intensities.

## Conclusions:

Visualisation is a rapidly growing field (see Brodlie (7) for an overview). There may be techniques developed in other disciplines such as astronomy or medical image processing which could be applied to the display of neutron scattering data in future. There are also a growing number of image compression algorithms which might be investigated as a possible way to reduce the amount of data in our optical disk store.

Colour graphics is not just a gimmick for publicity purposes, it has a role to play in better understanding of the data because the human eye can readily distinguish fine changes in colour and so detect features in the data which might otherwise be missed. There are many high level graphics packages which could produce similar results, we use UNIRAS because it was made available to us cheaply, has many high level visualisation routines, many device drivers and can easily be built into our data analysis programs.

### References

(1) 'Visualisation of Scientific Data' Jern M. Computer Graphics 89
ISBN 0-86363-190-3 Blenheim On-line 1989 p79-103
UNIRAS A/S, 376 Gladsaxevej, DK-2860 Søborg, Denmark
(2) ISIS User Guide Experimental Facilities, editors B.C.Boland, S.Whapham
available from ISIS Facility, Rutherford Appleton Laboratory
(3) IRIS C.J.Carlile and M.A.Adams, Physica B 182 (1992) 431
(4) Rotational tunnelling spectroscopy with neutrons C.J.Carlile and M.Prager Rutherford Appleton Laboratory Report RAL-93-028
(5) 'GENIE manual Version 2.3' W.I.F.David et al., Rutherford Appleton Laboratory report RAL-86-102 (1986)
(6) Presented by C.J.Carlile, J.B.Forsyth, C.Wilkinson at the European Condensed Matter Conference, May 93
(6) 'The visualisation of neutron scattering data' K.M.Crennell Physica B 180 & 181 (1992) 951-954
(7) 'Scientific Visualization. Techniques and Applications' K.W.Brodlie editor Springer-Verlag 1992 ISBN 3-540-54565-4

# Using databases for improved instrument operations and administration at ISIS

**K.M.Crennell**
***Rutherford Appleton Laboratory, ISIS Facility, Chilton, Didcot, Oxon, OX11 0QX UK***

***Abstract:*** *As neutron scattering instruments become more complex, often with hundreds of detectors, it becomes increasingly important to monitor their performance effectively. A program, VUSLS, is described which uses interactive colour graphics to monitor operation of the SANDALS instrument at ISIS, and future plans outlined to use a database management system. The database system is currently used to manage the administration of the proposals for the use of ISIS Beam Time, including the names and addresses of our 4000 users, and automatic letter writing.*

**Introduction.** The instrument SANDALS, is used for Small Angle Diffraction for Amorphous and Liquid Samples. It has an extensive low angle bank of zinc sulphide scintillator detectors typically 10mm wide and 200 mm tall. 360 are installed in the bank at 11 to 21 degrees scattering angle, and 120 in the 3 to 11 degree bank. Another 200 are to be installed towards the end of this year. Detectors are mounted two to a photomultiplier and arranged twenty to a module. An automated way of assessing detector performance is needed especially during commissioning. ISIS is a pulsed neutron source, counts are recorded at times up to 20000 microseconds after the passage of the main beam. In practise, few counts are seen at times of less than 200 microseconds, and there is more noise after 10000 microseconds, so counts for each detector are usually summed between these times.

**The algorithm.** We look at the data collected from a sample giving a uniform signal in all detectors. All detectors in a given module are adjusted to give a similar response, so their signals are averaged, and the ratio actual signal to average signal calculated for each detector. Any excessively noisy or low detectors are left out of the average, and out of any later data analysis. If more than half the detectors in a module are left out, the program asks the user for advice.

**Program used** An interactive colour graphics program, VUSLS, has been written in FORTRAN using the graphics package UNIRAS running on a VAX/VMS system with X-windows. The calculated ratio for each detector is displayed as a thick coloured line. The lines are drawn adjacent to one another to make the modules, with the detector numbers above. (See Figure 1) Average detectors are drawn in green, others are white, yellow, red or black. The scale in the upper part of Figure 1 shows the values of the ratios assigned to each colour. The number of detectors in each category is listed on the left of the scale. The user can change the values assigned to each colour interactively. This plot gives the user an instant appreciation of detector function, on a colour screen all the modules should be green, a few in other colours are easily seen. Notice that the very low signals occur in adjacent detectors, these probably have a defective photomultiplier.

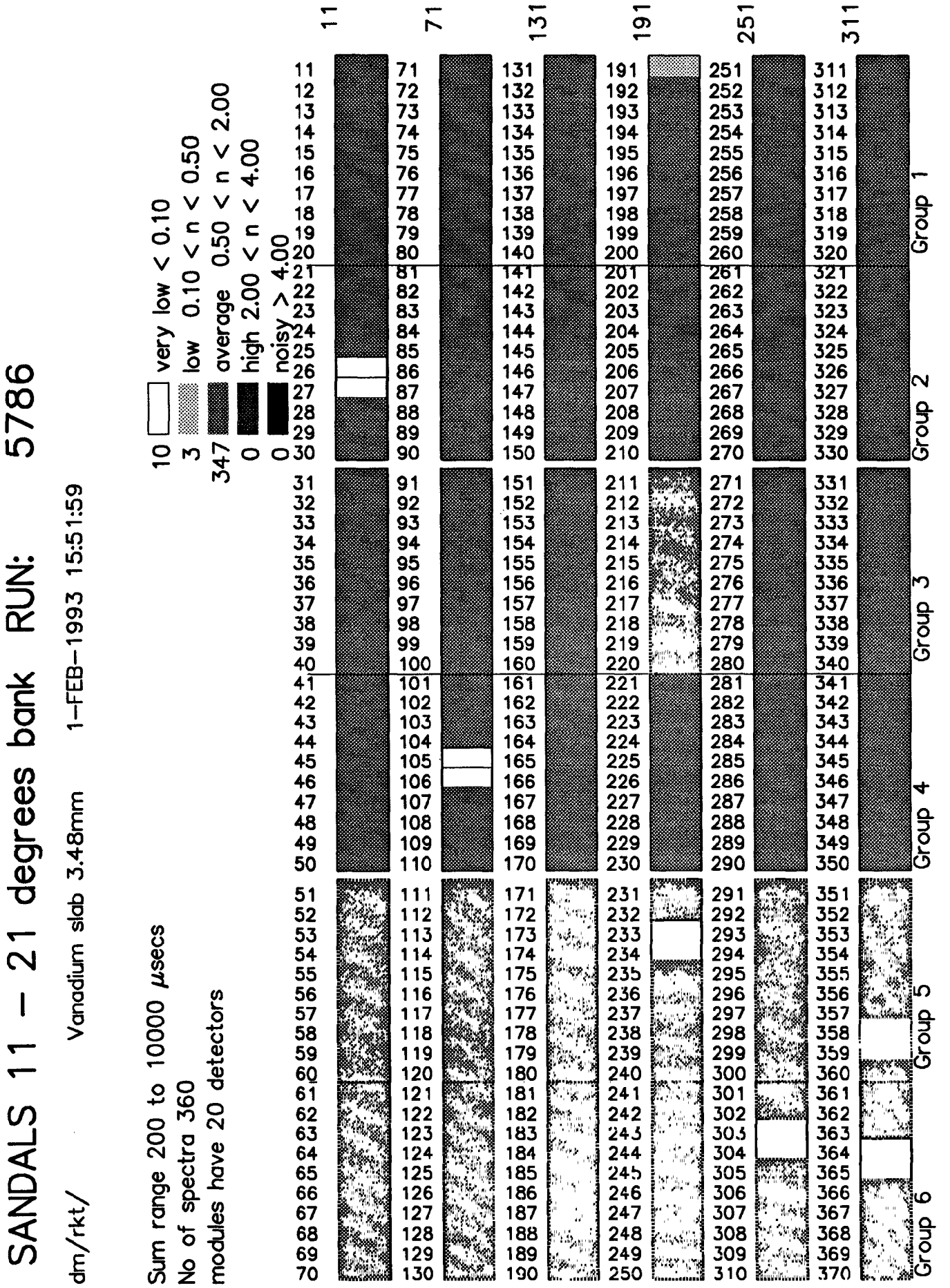


**Figure 1 Default plot for one of the SANDALS detector banks**

The detectors are arranged on a surface of constant resolution. They are used in groups whose signals are averaged together. The groups are shown by the lines crossing the modules in Figure 1 with their numbers at the bottom of the diagram.

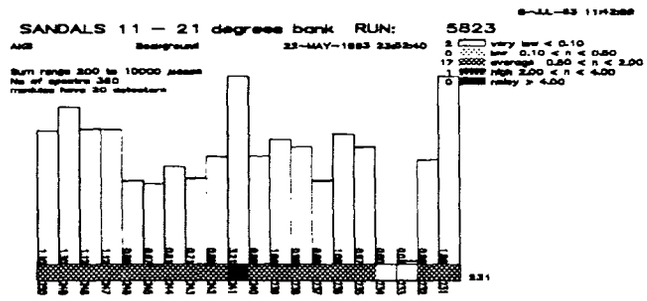


**Figure 2 Greater detail in histogram for a single module**

Another type of plot shows the counts as a histogram as well as the coloured lines, with a choice of either all the detectors in the chosen bank or a single module in greater detail. (see figure 2)

Further options allow sending the plot to hardcopy on laser or colour postscript printers, and the creation of a revised file which includes only the numbers of average detectors for use in subsequent data analysis. The revised file leaves blanks where detectors have been omitted so that it is easy for the user to see at a glance which detectors are missing.

```
9  451  452       454  455  456  457  458  459  460
8  461  462  463  464            467  468  469  470
written  18-MAY-93  11:42:50
  0 detectors not read from GROUPS90_det.DAT
 51 more detectors not average now file SLS5823.GRP
490 spectra in 1160 time channels
summed between 200 and 10000 microseconds
```

**Figure 3 Part of a revised file showing gaps for omitted detectors and the start of the history**

The operating parameters of VUSLS are written at the end of the file for future reference. The user either starts with a default file with all good detectors, or can specify one made previously with VUSLS, so that they can accumulate a single file including only detectors known to be average for all the runs of their experiment.

**Future Plans:** There may be a variation in detector noise with time. Instead of summing counts for a detector, the count at each time recorded could be plotted as a coloured point on a line for each detector, with colour used to show the magnitude of the counts, as the lines are used in Figure 1. Detector lines would be plotted adjacent to one another to create a 2D 'image'.

Each time the program runs it could append a 'history' to a log file for the instrument manager, listing the non average detectors and the time of day. A further program could scan this daily and warn the manager of any new occurrences of non-average detectors. At this stage it might be worth storing the records in a database management system, at the moment, the overheads of this are too large.

**The Administration System:** As more instruments are built for use at ISIS, we receive more proposals, and find that we can give our world-wide users a faster, more accurate service using a database management system to store information relevant to their proposals for the use of ISIS beam time.

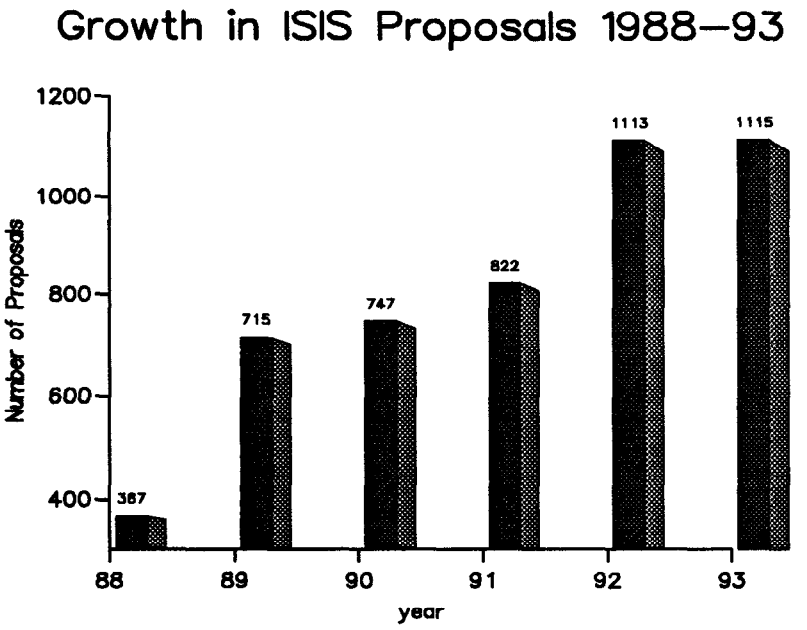


**Figure 4 Histogram using information automatically extracted from the database**

Figure 4 shows the growth in proposals submitted to ISIS over the last five years. Proposal submission rounds take place in April and October, at each one we now receive over 500 applications. On receipt, proposals are given a unique reference number which is stored with details of the experiment title, sample to be measured, instrument and sample environment needed and names and addresses of the proposer and collaborators. A relational database management system, S1032, is used, it runs on VAX/VMS on three of the workstations of our VAX cluster. Its query language can be used interactively for 'one off' queries or commands stored in a procedure file ready to make the reports we need regularly.

Figure 5 is a view of the system. The shaded area encloses the main datasets, which can be related to each other in a database as needed for production of reports. A selection panel meets in June and December to decide by peer review which proposals are awarded time. Their decisions and comments are recorded in the database, and information generated to print 'personalised' letters to each proposer giving them the results for all the proposals they submitted. Simple letters just adding name and address can use almost any 'mail merge' word processing system, we have found that only TeX can cope with more complex letters to a user who who submitted 10 proposals, some of which have been given time, some not, and any of which may have extra panel comments. We print about 300 letters for each proposals round.

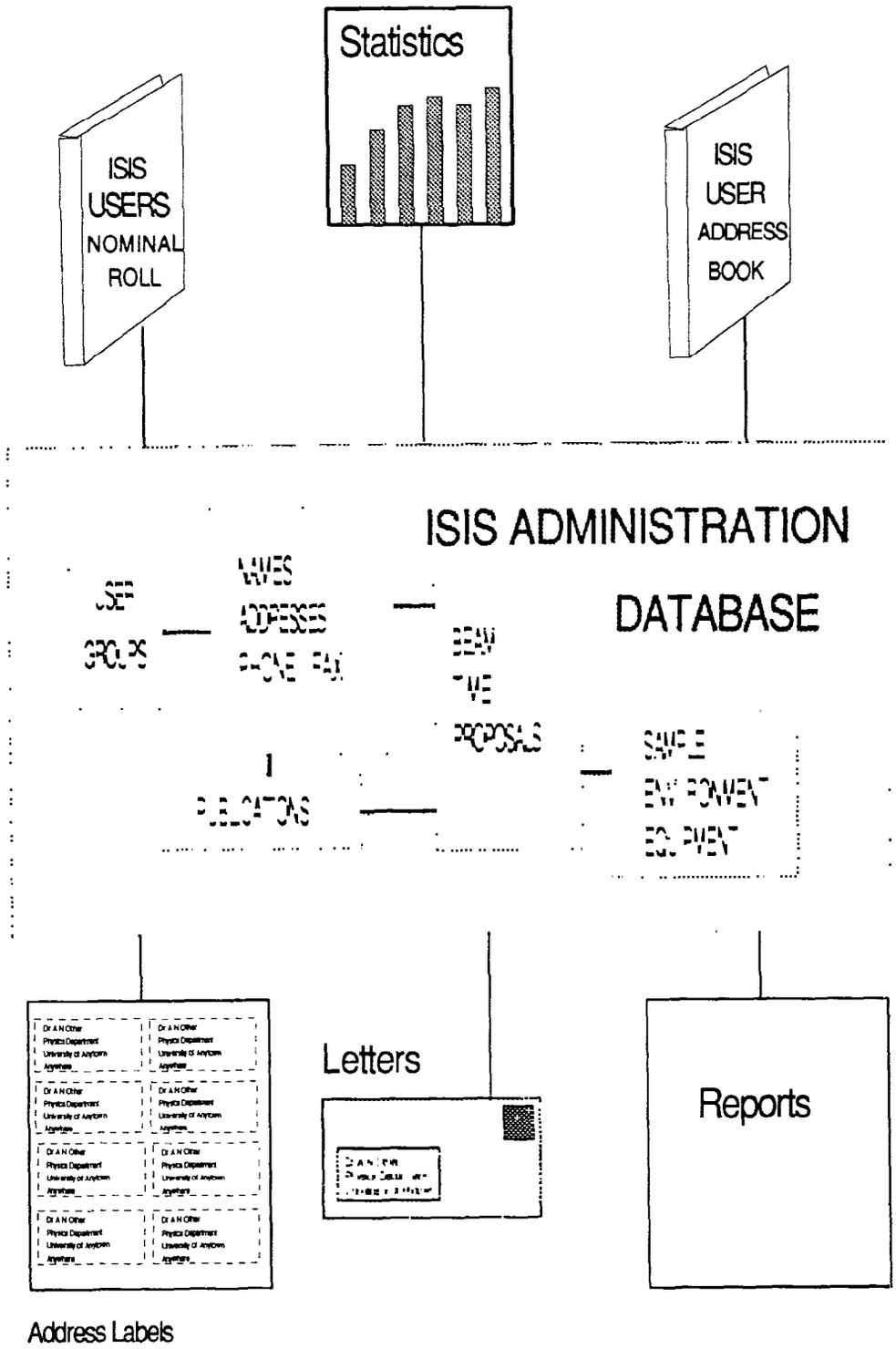


**Figure 5 An overview of the ISIS Administration database**

Most of the ISIS instruments are used for neutron scattering, a few for muons. Each instrument scientist schedules their own instrument manually and tells the operations manager what sample environment equipment is needed. He records the starting date for the experiment, resolves clashes of equipment and organises production of the 'scheduling letter' sent to the user, and the lists of equipment needed on each instrument by date. In future we hope to program the database to assist in the scheduling process. We also record the samples to be used, and whether they are hazardous, as each sample must be accompanied by a sheet of paper listing the hazards, handling precautions and first aid procedures.

Following completion of an experiment, the user sends us a report for publication in the ISIS Annual Report, and bibliographic references to published papers describing work done at ISIS. These are also stored in the database.

Statistics of ISIS usage are extracted from the database and read into spread sheet or graphics packages. Figure 4 was made using UNIGRAPH, it shows growth of number of proposals by year. Many other statistical plots are possible, we regularly make plots of usage by instrument, so have made a special procedure to do it quickly, more usually, the information is obtained interactively.

A list of UK users is printed annually in the 'ISIS Users Nominal Roll', which gives user addresses, phone and fax numbers. We have about 4000 names in our files, half of whom are UK residents; about 10% change their address during a year, so we are continually updating our files.

Over 50 procedures are in regular use producing our varied reports and we plan more to improve our instrument operations.

**Future plans:** Information from the printed proposals is currently typed into the database. We plan to accept 'electronic' proposals over the international computer networks in the near future, to improve the accuracy and reduce our typing and proof reading effort.

We are planning to integrate the system with that for issuing film badges for monitoring radiation exposure, and with a visitor registration scheme for greater laboratory security. The current forms management system will be replaced with a utility which uses 'OSF motif' window management system. We will then be able to store images in the database, possibly photographs of our equipment and users.

Raw data taken during an experiment is stored in an optical disk archive, using a 'home grown' cataloguing system. In future the location of these datasets may be stored in a database and linked to our possible instrument history records and our existing administration of the ISIS beam time proposals.

# A Resolution Function Model For A Multi-Analyser Spectrometer

M.Hagen[1,2] and U.Steigenberger[1]

[1]ISIS Facility, Rutherford Appleton Laboratory, Didcot, Oxon. OX11 0QX, U.K.
[2]Department of Physics, Keele University, Keele, Staffs. ST5 5BG, U.K.

**Abstract**
We have formulated a mathematical description of the resolution function for a multi-analyser spectrometer at a pulsed source. This formulation has been tested by a comparison with measurements carried out on the PRISMA multi-analyser spectrometer at ISIS. Previous theoretical formulations of the resolution function for multi-analyser spectrometers have assumed that that the asymmetry of the incident neutron pulse from the source could be ignored. Our measurements have shown that this is not the case for PRISMA and our formulation is such that this asymmetry has been taken into account.

## 1 Introduction

The technique of inelastic neutron scattering is unrivalled in its ability to measure phonon and spin wave dispersion relations and these measurements provide invaluable information on the inter-atomic forces in a solid. The anisotropic nature of a crystal structure means that dispersion relations can be very different in different reciprocal lattice directions and that such measurements must be carried out using single crystal samples. At reactor neutron sources this type of measurement has been carried out using the triple axis spectrometer which was devised by Brockhouse in the 1950's [1], while at spallation sources they have been carried out by multi-analyser spectrometers such as MAX [2] and PRISMA [3]. The lineshape of phonons measured on all of these instruments is given by the convolution integral of the spectrometer resolution function with the dynamic structure factor for the phonon dispersion surface. The resolution function is the relative probability of observing a neutron scattered with a wavevector and energy transfer $(\mathbf{Q}_0 + \Delta\mathbf{Q}, E_0 + \Delta E)$ when the spectrometer was positioned to measure $(\mathbf{Q}_0, E_0)$. It reflects the probability of transmission/reflection of a neutron through the various beam defining elements of the spectrometer with a wavevector or divergence other than the

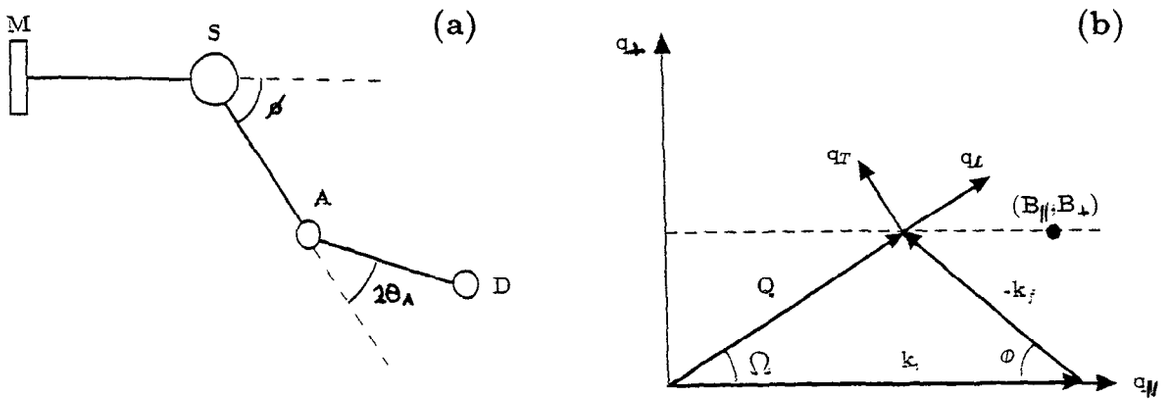


Figure 1: (a) A schematic diagram of a single analyser-detector system on a multi-analyser spectrometer is shown. (b) The path followed in reciprocal space in an indirect geometry inelastic scattering measurement is shown by the dashed line.

nominal values.

A model for the resolution function of the triple axis spectrometer was produced some time ago by Cooper and Nathans [4] in which all of the spectrometer elements are treated as having Gaussian probability distributions for their transmission/reflection elements. The combination of these elements, subject to the scattering conditions at the monochromator, sample and analyser, leads to a four dimensional Gaussian resolution function in $(\Delta\mathbf{Q}, \Delta E)$. However at a spallation source there is an intrinsically non-Gaussian component in the formulation of the resolution function, the initial neutron pulse shape in time of flight. In this paper we briefly review a recent formulation of the resolution function for a multi-analyser spectrometer which takes account of this non-Gaussian component. A detailed derivation has been given elesewhere [5].

## 2 Resolution Function Formalism

A multi-analyser spectrometer, such as MAX or PRISMA, has a bank of analyser-detector systems [2, 3]. However for the purposes of formulating the resolution function we need only consider a single analyser-detector set-up. In figure 1a a schematic representation of this single analyser-detector system is shown where M is the moderator, S is the sample, A is the analyser and D the detector. Inelastic measurements are carried out using the indirect geometry technique in which the analyser crystal defines the final wavevector and

the time of flight measurement is used to scan the incident wavevector. The wavevector transfer in the inelastic measurement, $\mathbf{Q} = \mathbf{k}_i - \mathbf{k}_f$, is therefore scanned along a path parallel to $\mathbf{k}_i$. In figure 1b we show schematically by the dashed line the path followed in such a measurement. The wavevector can be written in terms of components parallel to, and perpendicular to $\mathbf{k}_i$ as $\mathbf{Q} = Q_{\|}\hat{\boldsymbol{q}}_{\|} + Q_{\perp}\hat{\boldsymbol{q}}_{\perp}$ . Along this path the energy transfer of the neutron varies as $E = (\hbar^2/2m_N)(k_i^2 - k_f^2) = (\hbar^2/2m_N)(Q_{\|}^2 + 2(Q_{\perp}\cot\phi)Q_{\|} - Q_{\perp}^2)$.

The resolution function for the system shown in figure 1a can be therefore be written as an integral over the various paths through the different spectrometer elements weighted by their probability distributions for transmission/reflection in the form ;

$$\begin{aligned} R(\mathbf{Q},E) \;=\; & \int d\gamma_1\, d\gamma_2\, d\gamma_3\, d\varepsilon_1\, d\varepsilon_2\, d\varepsilon_3\, d\eta_{HS}\, d\eta_{VS}\, d\eta_{HA}\, d\eta_{VA}\, dk_i\, dk_f\, dk_f'\, dT_0 \times \\ & P_{H1}(\gamma_1)\, P_{H2}(\gamma_2)\, P_{H3}(\gamma_3)\, P_{V1}(\varepsilon_1)\, P_{V2}(\varepsilon_2)\, P_{V3}(\varepsilon_3)\, P_{HS}(\eta_{HS}) \times \\ & P_{HA}(\eta_{HA})\, P_{VS}(\eta_{VS})\, P_{VA}(\eta_{VA})\, P(T_0)\, \delta(T - T_0 - T_i - T_f) \times \\ & \delta((\mathbf{Q} - \eta_{HS}Q_0\hat{\mathbf{Q}}_T - \eta_{VS}Q_0\hat{\mathbf{Q}}_V) - \mathbf{k}_i + \mathbf{k}_f)\, \delta(E - \frac{\hbar^2}{2m}(k_i^2 - k_f^2)) \times \\ & \delta((\boldsymbol{\tau}_A - \eta_{HA}\tau_A\hat{\boldsymbol{\tau}}_T - \eta_{VA}\tau_A\hat{\boldsymbol{\tau}}_V) - \mathbf{k}_f + \mathbf{k}_f')\, \delta(k_f - k_f') \end{aligned} \tag{1}$$

The angles $\gamma_i$ and $\varepsilon_i$ $(i = 1,2,3)$ are the horizontal and vertical divergences of the beam from the nominal moderator to sample, sample to analyser and analyser to detector directions respectively and $P_{Hi}(\gamma_i)$ and $P_{Vi}(\varepsilon_i)$ the corresponding collimator transmission functions. The angles $\eta_{AB}$ ( $A = H,V$ , $B = S,A$ ) are the horizontal and vertical mosaic spreads and $P_{AB}(\eta_{AB})$ the mosaic spread distribution functions for the sample and analyser crystals respectively. The function $P(T_0)$ is the initial pulse shape in time of flight. The first delta-function in equation( 1) accounts for the time of flight of the neutrons, $T$ is the arrival time at the detector, $T_0$ is the time at which the neutrons leave the moderator and $T_i$ and $T_f$ are the flight times from moderator to sample and sample to detector respectively. The second and third delta functions account for the conservation of wavevector and energy transfer at the sample. The wavevector has been modified to account for the sample mosaic using the Werner and Pynn approximation [6] where $\hat{\mathbf{Q}}_T$ and $\hat{\mathbf{Q}}_V$ are unit vectors perpendicular to $\mathbf{Q}_0$ in the horizontal and vertical planes. The fourth and fifth delta functions enforce the Bragg scattering condition at the analyser, where $\boldsymbol{\tau}_A$ is the scattering vector of the analyser planes. The wavevectors $\mathbf{k}_f$ and $\mathbf{k}_f'$ are the neutron wavevectors as scattered from sample to analyser and from analyser to detector. The mosaic spread of the analyser has been included in a similar fashion to that for the sample.

If all of the $P$-functions in equation( 1) are modelled by Gaussians except for $P(T_0)$ and all of the integrals then performed, with the exception of the integral over $T_0$, then the result is ;

$$R(\mathbf{Q},E) = R_0 \exp\left[-\frac{1}{2}\left(\left(\frac{\Delta Q_V}{\sigma_V}\right)^2 + \tilde{x}^T\tilde{M}\tilde{x}\right)\right] \int dT_0\, P(T_0) \exp\left[-\frac{1}{2}\left(\frac{T_0 - \tilde{t}^T\tilde{x}}{\sigma_T}\right)^2\right] \tag{2}$$

where $\tilde{x} = \left[\Delta Q_{\|}, \Delta Q_{\perp}, \Delta E\right]$ and $\Delta Q_V$ is the vertical component. The matrix elements of $\tilde{M}$ and $\tilde{t}$ and the expressions for $\sigma_V$ and $\sigma_T$ are given in ref. [5]. As in the case of the triple axis resolution function [4] the terms in $\Delta Q_V$ separate out from those in $\Delta Q_{\|}, \Delta Q_{\perp}$ and $\Delta E$.

Equation( 2) is a general result for any pulse shape $P(T_0)$ and in order to assess the practical importance of the effect of asymmetry in the resolution function we have also considered the specific case of using the simplest asymmetric form $P(T_0) = \Theta(T_0)$ $\exp(-T_0/\tau)$. The result is ;

$$R_H(\mathbf{Q}, E) = R_K \exp\left(-\frac{1}{2}\tilde{x}^T\tilde{M}\tilde{x} - \frac{1}{\tau}\tilde{t}^T\tilde{x}\right) \operatorname{erfc}\left(\frac{1}{\sqrt{2}}\left[\frac{\sigma_T}{\tau} - \frac{1}{\sigma_T}\tilde{t}^T\tilde{x}\right]\right) \tag{3}$$

where the vertical terms, which remain unchanged from equation(2), have been omitted. In this result the slowing down time $\tau$ is energy dependent. An empirical form for this energy dependence, relevant to the PRISMA beamline, has been found from Bragg peak and powder diffraction measurements to be [5] ;

$$\tau(E) = \begin{cases} \tau_0 & E < E_c \\ \tau_0/\left(1 + (E - E_c)^2/\Gamma^2\right) & E > E_c \end{cases} \tag{4}$$

with the best fit values of $\tau_0 =$ 37.15 $\mu$secs, $E_c = 9.0$ meV and $\Gamma = 39.16$ meV. Equation( 3) therefore provides a suitable empirical representation of the resolution function of the PRISMA multi-analyser spectrometer from which the effects of asymmetry can be assessed.

## 3 Discussion

In ref. [5] Bragg peak lineshapes for various crystals and neutron energies were measured and calculated to test equation( 3). There was good agreement in all cases and all showed a significant asymmetry. A Bragg peak is probably the case where asymmetry in the resolution function will be most obvious in the measured spectra. In figure (9) of ref. [5] the spectrum measured from a Cu(220) Bragg peak with $E_f =$ 30 meV was shown and which had a clearly asymmetric lineshape. In figure 2a we show a contour map of the resolution function in the $Q_{\|}, E$ plane relevant to this measurement. Also shown in this figure by the dashed line is the measuring trajectory. Since a Bragg peak is a $\delta$-function in $\mathbf{Q}$ and E the calculated lineshape is essentially given by the intersection of this trajectory (dashed line) with the resolution function. In figures 2b and 2c contour maps of the resolution function in the $Q_{\perp}, E$ and $Q_{\|}, Q_{\perp}$ planes are also shown for this particular spectrometer configuration. The effects of asymmetry in the first of these two planes is considerably less marked than in the $Q_{\|}, E$ plane. Finally figure 2d shows a contour map of the projection of the resolution function onto the $Q_{\|}, E$ plane (ie. the result after integrating over $Q_{\perp}$). This latter form might be appropriate to the situation of phonons in the middle of the Brillouin zone where to a reasonable approximation it might be possible in certain cases to consider the dispersion surface as flat perpendicular

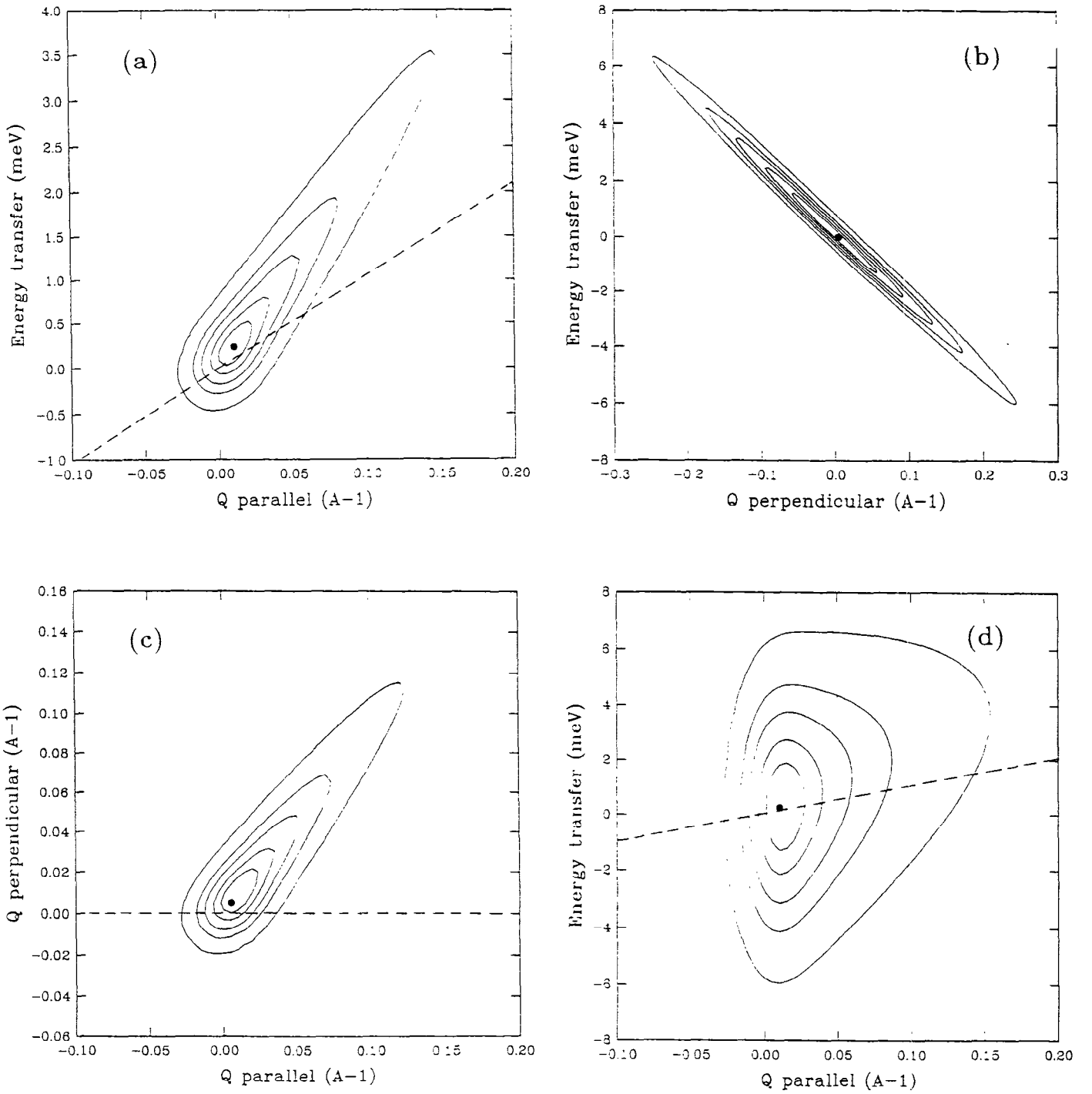


Figure 2: Contour maps of the resolution function for the measurement of a Cu(220) Bragg peak with $E_f = 30$ meV (as discussed in the text) are shown (a) in the $Q_{||}, E$ plane, (b) in the $Q_{\perp}, E$ plane, (c) in the $Q_{||}, Q_{\perp}$ plane and (d) as a projection onto the $Q_{||}, E$ plane. The levels plotted are the 75, 50, 25, 10 and 1 percent levels of the resolution function. The position of the maximum of the resolution function is shown by the dots in (a) to (d) and in (a), (c) and (d) the dashed lines show the path of the measuring trajectory.

to the measuring direction. It is clear that figure 2d is markedly different to that of figure 2a but that although the aymmetry is less marked it is still present. A conclusion that can immediately be drawn from figures 2a to d is that the measured lineshape in an experiment will depend on a detailed consideration of how the dynamic structure factor interacts with the resolution function. It is certainly not possible to replace the resolution function with a simple one dimensional function in energy and then to expect to get the correct results when convoluting with experimental data.

## 4 Conclusion

A resolution function model for the PRISMA multi-analyser spectrometer has been developed. It has been argued that the measurement of Bragg peaks given in ref. [5] has provided a critical test of the accuracy of including the asymmetry of the pulse shape into the resolution function. The complexity of the resolution function has also been demonstrated and it has been argued that it cannot simply be treated as a one dimensional function in energy only.

## References


[1] B.N.Brockhouse, in: Inelastic Scattering of Neutrons in Solids and Liquids (IAEA, Vienna,1961) p. 113

[2] K.Tajima, Y.Ishikawa, K.Kanai, C.G.Windsor and S.Tomiyoshi, Nucl. Instr. and Meth. **201** (1982) 491

[3] U.Steigenberger, M.Hagen, R.Caciuffo, C.Petrillo, F.Cilloco and F.Sachetti, Nucl. Instr. and Meth. **B 53** (1991) 87

[4] M.J.Cooper and R.Nathans, Acta Cryst. **23** (1967) 357

[5] M.Hagen and U.Steigenberger, Nucl. Inst. and Meth. **B 72**, 239 (1992)

[6] S.A.Werner and R.Pynn, J.Appl.Phys. **42** (1971) 4736

# A Parametric Formulation of the Resolution Function of a Pulsed-source Chopper Spectrometer

C.-K. Loong and J. M. Carpenter
Intense Pulsed Neutron Source
Argonne National Laboratory, Argonne, Illinois 60439-4814, U. S. A.
and
S. Ikeda
BSF, National Laboratory for High Energy Physics
Oho-machi, 305 Ibaraki-ken, Japan

## Abstract

Based on a previously developed formulation for the resolution function of a pulsed-source chopper spectrometer, we describe an algorithm which facilitates the application of resolution calculations in data analysis. The method consists of an estimate of the source pulse shape parameters from a least-squares analysis of the monitor spectra and an efficient evaluation of the spectrometer resolution functions over a wide range of energy transfers using a parametric expression.

## I. Introduction

The source pulse emission time distribution (pulse shape) bears important consequences in the energy-scale calibration and the characterization of the resolution function of a pulsed-source chopper spectrometer, of which the major components are shown schematically in Fig. 1 (see also Table I). The choppers transmit a narrow energy-band of neutrons of which the velocity distribution is not symmetric with respect to the mean velocity. As the neutrons travel along the flight path, they spread out in time, resulting in progressively skew intensity profiles, as shown in the beam monitor spectra (panels 1b and 1c). The intensity of the scattered neutron beam at a detector exhibits a similar skew time-of-flight profile that varies with the neutron energy-transfer E, as shown in panel 1d. In 1987 we demonstrated[1] how the resolution function of a pulsed-source chopper spectrometer could be calculated through an analysis of the neutron intensity distribution, $I_s(v,t)$, as a function of the neutron speed ($v$) and flight time ($t$). It involves an evaluation of a convolution integral of the source spectrum and pulse shape with the response functions of all the relevant components (moderator, choppers, collimators, detectors, etc.) of the spectrometer. The agreement between calculated and observed spectra at various configurations was borne out by experiments.

Two problems arise in the application of the resolution calculations in routine data analyses: 1) the parameters of the Ikeda-Carpenter pulse-shape function[2] under the target-moderator conditions during the experiments are usually not available; and 2) the rather long computer time required for the evaluation of the resolution functions over the measured energy

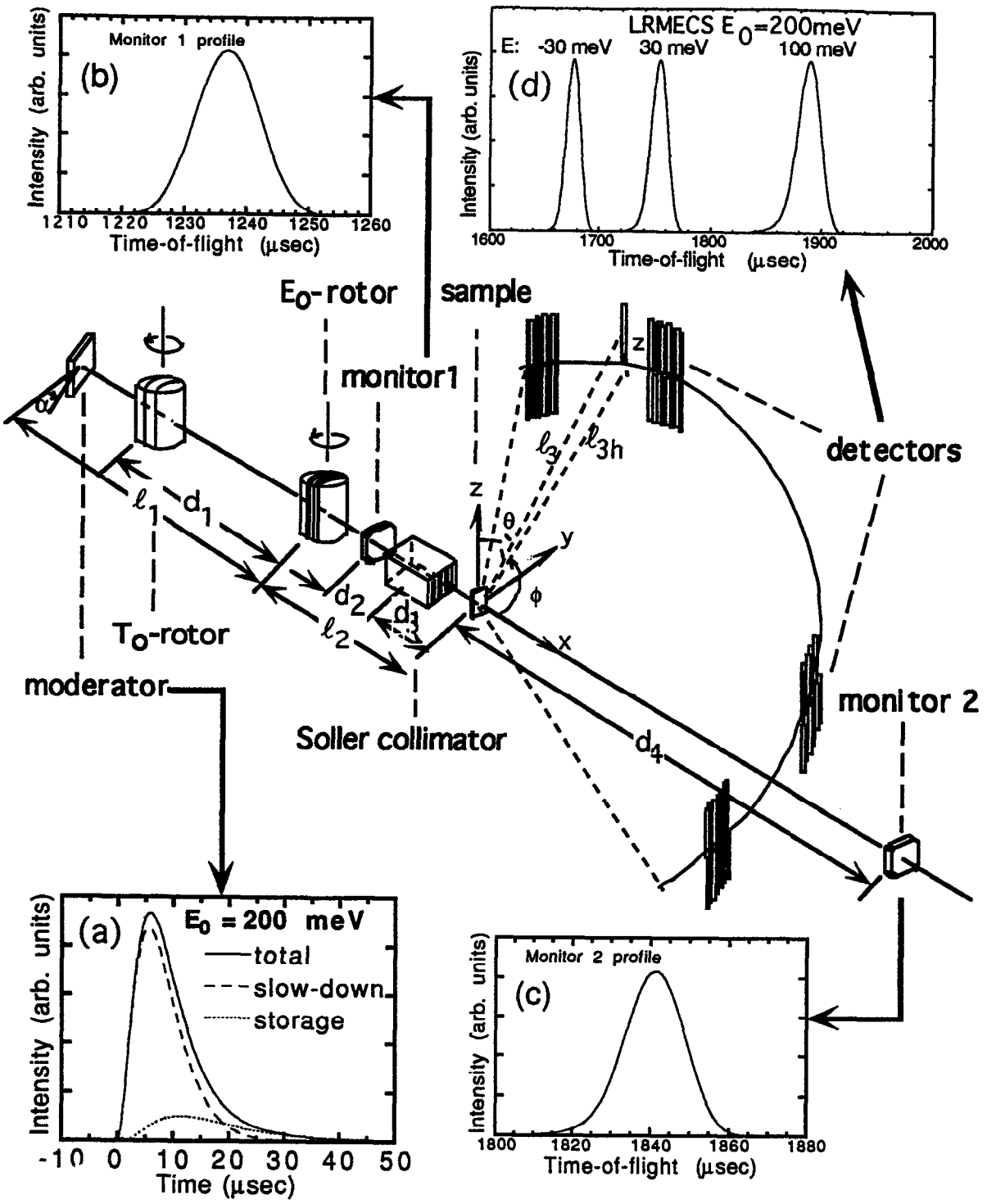


Figure 1. A schematic layout of the IPNS chopper spectrometers. The parameters for the HRMECS and LRMECS instruments are listed in Table I. Panels: (a) the source emisiion time distribution for neutron energy of 200 meV; (b-c) the calculated intensity profiles of the LRMECS monitors; and (d) the calculated resolution functions for a LRMECS detector at energy transfers -30, 30 and 100 meV.

range makes the data treatment impractical. In this paper, we present a method which overcomes these difficulties. It relies on a satisfactory parameterization of the resolution function by a simple analytic expression. In the process of data analysis the pulse-shape parameters are first obtained from a fit of the monitor spectra which are recorded as a part of the experimental data. Second, the resolution functions, calculated numerically by the convolution integral over a coarse grid of energy transfers, are fitted by an analytic expression. The process yields a set of five parameters for the resolution function at each energy. Since these parameters vary smoothly over the entire energy range of interest, their values for any specific energy transfer can be obtained from interpolation over the energy grid. Finally, the resolution functions are evaluated and applied to data analysis using the analytic formula.

Table I. Instrumental parameters for the HRMECS and LRMECS chopper spectrometers.

| Parameters | | HRMECS | LRMECS |
|---|---|---|---|
| $\alpha$ | (deg.) | -18 | 18 |
| $\ell_1$ | (m) | 12.71 | 7.02 |
| $\ell_2$ | (m) | 1.15 | 1.10 |
| $\ell_{3h}$ | (m)[a] | 4 | 2.5 |
| z | (m) | 0.23 | 0.0 |
| $d_1$ | (m) | 5.37 | 1.27 |
| $d_2$ | (m) | 0.18 | 0.13 |
| $d_3$ | (m) | 0.65 | 0.35 |
| $d_4$ | (m) | 5.12 | 3.26 |
| $\phi$ | (deg.) | -20 to 20, 80 to 140 | -10 to 120 |

[a]HRMECS detector length: 45.7 cm

LRMECS detector length: 45.7 cm for $\phi>25°$, 22.9 cm for $3°<\phi<25°$, 10.2 cm for $\phi<3°$

## II. Method of calculation

1. Parametric formulation of the resolution function

Our study shows that the pulse-shape parameters mainly control the asymmetry of the resolution profile whereas other components of the spectrometers affect the overall width. Therefore, we expect that for a given mean incident energy the counting rate as a function of time $t$ at the detector can be described quantitatively by a convolution of the pulse-shape function with a response function of the spectrometer:

$$C(t)=\frac{1}{\ell}\int_0^{\infty}dt'\int_{-\infty}^{\infty}dt''f(t')g(t'')\delta(t-\frac{\ell}{\ell_1}t_0+\frac{\ell_2+\ell_3}{\ell_1}t'-\frac{\ell}{\ell_1}t'') \qquad (1)$$

for elastic scattering, where $\ell=\ell_1+\ell_2+\ell_3$ (see Fig. 1), $t_0$ is the chopper opening time, $f(t)$ is the Ikeda-Carpenter function for a given energy (or neutron speed $v$)

$$f(t) \equiv P(v,t) = (1-R)(at)^2 \exp(-at)$$
$$+\frac{Ra^2b}{(a-b)^3}\left\{2\exp(-bt) - \left[2+2(a-b)t+(a+b)^2t^2\right]\exp(-at)\right\}, \tag{2}$$

$g(x)$ is the spectrometer response function given by a Gaussian function

$$g(x) = \frac{1}{\sqrt{2\pi}\sigma}\exp\left[-\frac{1}{2}\left(\frac{x}{\sigma}\right)^2\right]. \tag{3}$$

The advantage of this expression is its simple analytic form which requires much less computer time for evaluation than the previous formalism. It can be shown that $C(t)$ can be written as

$$C(t) = \frac{A}{\ell}\frac{1}{\sqrt{2\pi}\sigma}\left\{\begin{array}{l}(1-R)a^2C_2(a,t) \\ +\dfrac{Ra^2b}{(a-b)^3}\left[2C_0(b,t) - \left((a-b)^2C_2(a,t) + 2(a-b)C_1(a,t) + 2C_0(a,t)\right)\right]\end{array}\right\}, \tag{4}$$

where

$$C_0(x,t) = \sqrt{\frac{\pi}{2}}\left(\frac{\sigma\ell}{\ell_2+\ell_3}\right)\exp\left(v_{\min}^2 - u_{\min}^2\right)erfc(v_{\min}), \tag{5}$$

$$C_1(x,t) = \left(\frac{\sigma\ell}{\ell_2+\ell_3}\right)^2\exp\left(v_{\min}^2 - u_{\min}^2\right)\left[\exp(-v_{\min}^2) - \sqrt{\pi}v_{\min}erfc(v_{\min})\right], \tag{6}$$

$$C_2(x,t) = \sqrt{2}\left(\frac{\sigma\ell}{\ell_2+\ell_3}\right)^3\exp\left(v_{\min}^2 - u_{\min}^2\right)\left[\sqrt{\pi}\left(\tfrac{1}{2}+v_{\min}^2\right)erfc(v_{\min}) - v_{\min}\exp(-v_{\min}^2)\right], \tag{7}$$

and

$$v_{\min} = u_{\min} + \frac{x}{\sqrt{2}}\left(\frac{\sigma\ell}{\ell_2+\ell_3}\right), \tag{8}$$

$$u_{\min} = \frac{1}{\sqrt{2}\sigma}\left(\frac{\ell_1}{\ell}t - t_0\right), \tag{9}$$

$$erfc(z) = \frac{2}{\sqrt{\pi}}\int_{v_{\min}}^{\infty} dz\exp(-z^2). \tag{10}$$

For elastic scattering only three parameters, the normalization constant $A$, the Gaussian width $\sigma$ and $t_0$ need to be determined.

2. Pulse-shape parameters

An observed beam-monitor intensity profile bears an image of the transmitted neutron pulse shape that is reversed in time due to the pin-hole-camera effect of the energy selecting rotor and broadened by the instrumental response functions. Using numerical integration methods and the measured pulse-shape functions[2], we demonstrated previously[1] the ability to accurately calculate the monitor spectra over a wide range of incident energies for the IPNS chopper spectrometers. Here we show that fitting the observed monitor spectra by $C(t)$ given in Eq. (4) can provide an estimate of the energy-dependent pulse-shape parameters, $a$, $b$, $R$, for the Ikeda-Carpenter function. As an example Fig. 2 shows the results of a fit of the LRMECS

monitor 2 counting rate as a function of time for a neutron energy of 200 meV. We find that the fits can be applied successfully to estimate the pulse-shape parameters for neutron energies ranging from 4 to 2000 meV for both the HRMECS and LRMECS spectrometers. Once the pulse-shape parameters are determined for an incident neutron energy, the resolution time-of-flight profiles at a few selected energy transfers are calculated by the technique of numerical integration [Eqs. (14-15) of Ref. 1]. These calculated resolution profiles are then fitted by a parametric representation of the resolution function according the following procedure.

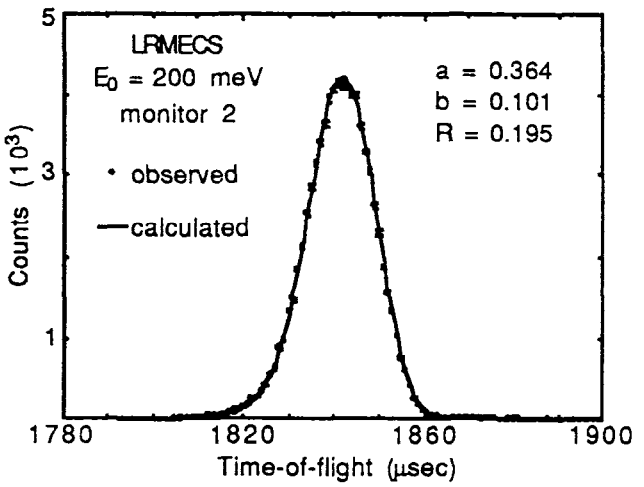


Figure 2. The monitor 2 spectrum of LRMECS with an incident neutron energy of 200 meV. The pulse-shape parameters, $a$, $b$, and $R$ were determined by a least-squares fit.

3. Calculation of the resolution function $R(E'-E)$

For inelastic scattering, we find that Eq. (1) can still describe accurately the resolution function provided that the arrival time at the detector, $t_d$, for a neutron of final speed $v_f$ is re-scaled to the elastic position, i. e.,

$$t \equiv t_d - \frac{\ell_3}{v_f} + \frac{\ell_3}{v_i}, \tag{11}$$

where $v_i$ is the neutron initial speed. In this case, in addition to $A$, $t_0$ and $\sigma$, $a$, $b$ and $R$ are also treated as adjustable parameters, which we denote as $a^*$, $b^*$ and $R^*$. They no longer carry any physical meaning as pulse-shape parameters.

Fig. 3. shows several examples of fitting the LRMECS resolution time-of-flight profiles calculated by numerical integration of the analytic expression Eq. (4). As it can be seen, the resolution profiles are adequately described by the parametric expression. The changes in the asymmetry of the profiles with energy transfer are accommodated by the varying proportions of the slowing-down and storage terms in the pulse-shape function as $a^*$, $b^*$ and $R^*$ change whereas the widths are effected by varying $\sigma$. Several sets of $a^*$, $b^*$, $R^*$, $\sigma$ and $t_0$ are first obtained this way over a coarse grid of energy transfer. Since these parameters are slowly varying variables with respect to the energy transfer, their values at any energy transfer can be

found by interpolation. The resolution functions, $R(E'-E)$, at an energy transfer $E$ can then be calculated using Eq. (4) and the relation:

$$t=\frac{\ell}{v_i}-\frac{\ell_3}{v_f}+\frac{\ell_3}{\sqrt{v_f^2-\frac{2E'}{m}}}, \tag{12}$$

where $m$ is the neutron mass. It is this computer-time saving calculation that makes the application practical for the analysis of large volume data sets. The parameters $t_0$, $\sigma$, $a^*$, $b^*$, $R^*$ and the energy transfer $E$, and the results of interpolation in the -30 < $E$ < 130 meV region are shown in Fig. 4 for LRMECS with an incident energy of 200 meV. Examples of the calculated resolution functions $R(E'-E)$ at five $E$ values are shown in Fig. 5.

## III. Results and Discussion

We have tested the application of the resolution calculations by the aforementioned method for the analyses of a variety of chopper spectrometer data[3]. The results are satisfactory. Several computer codes were written for this purpose. A typical procedure for the use of this resolution calculation is outlined in Fig. 6. We anticipate that this method can be used for data interpretation so as to simulate a predicted spectrum when a theoretical model is available, or to extract intrinsic parameters from an observed spectrum in conjunction with a least-squares or maximum-entropy analysis. This method has been applied for analysis of chopper spectrometer data, such as crystal-field studies[4] of rare-earth materials. We find that the resolution calculation is useful in providing a quantitative comparison of the theory with experiment and a measure of the intrinsic crystal-field linewidths.

In summary, we describe a parametric formulation and an algorithm which afford an efficient calculations of the resolution function for a pulsed-source chopper spectrometer.

## Acknowledgment

We thank G. E. Ostrowski for his assistance in refining some of the computer codes for the resolution calculation. Work performed at Argonne National Laboratory is supported by the U. S. DOE, Office of Basic Energy Sciences, under the contract No. W-31-109-ENG-38.

## References:

1. C.-K. Loong, S. Ikeda and J. M. Carpenter, Nucl. Instr. and Meth. **A260**, 381 (1987).
2. S. Ikeda and J. M. Carpenter, Nucl. Instr. and Meth. **A239**, 536 (1985).
3. C.-K. Loong, L. I. Donley, G. E. Ostrowski, R. Kleb, J. P. Hammonds, L. Soderholm, and S. Takahashi, this Proceedings.
4. See for example, C.-K. Loong, L. Soderholm, J. P. Hammonds, M. M. Abraham, L. A. Boatner, and N. M. Edelstein, J. Phys.: Condens. Matter. (in press)

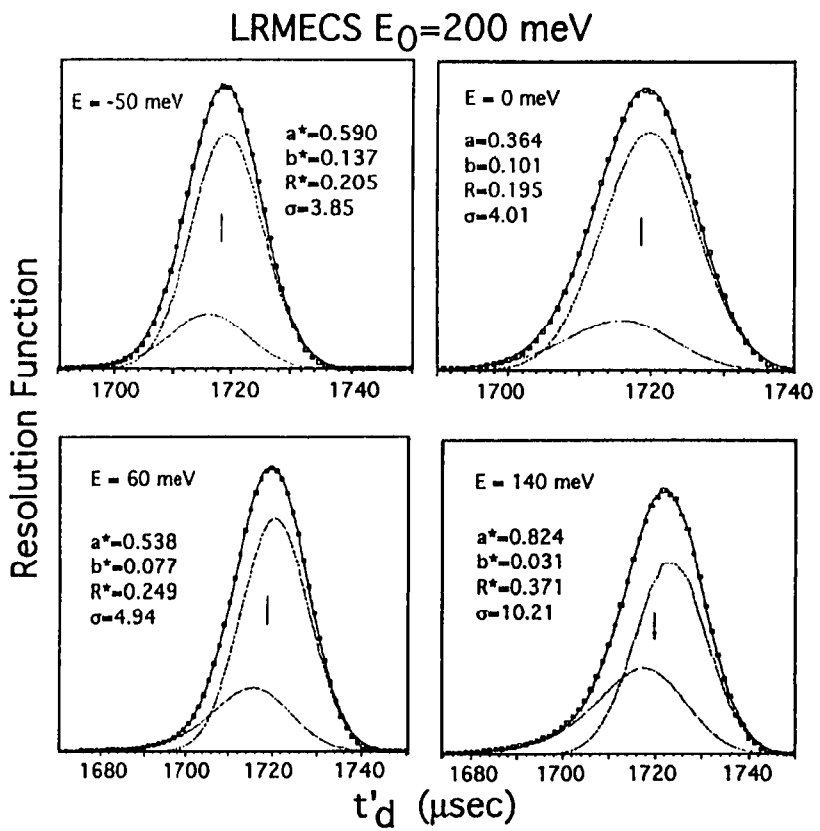


Figure 3. The least-squares fits of the calculated resolution functions for LRMECS with an incident energy of 200 meV by the analytic expression of Eq. (4). The dashed and dotted curves correspond to the two components of the pulse-shape function of Eq. (2).

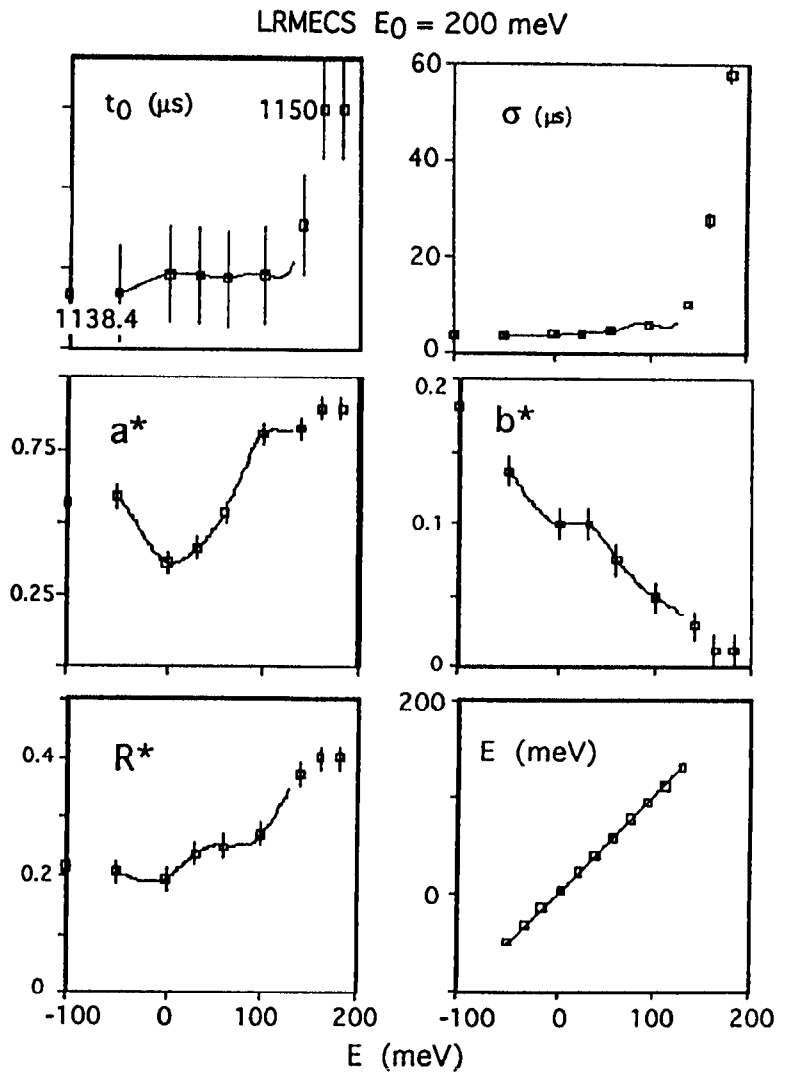


Figure 4. Variations of the parameters $t_0$, σ, a*, b*, R* and the calculated energy transfer E over the -100 to 160 meV energy region for LRMECS with $E_0$ = 200 meV. The curves represent the results of interpolation over the energy range of -30 to 130 meV.

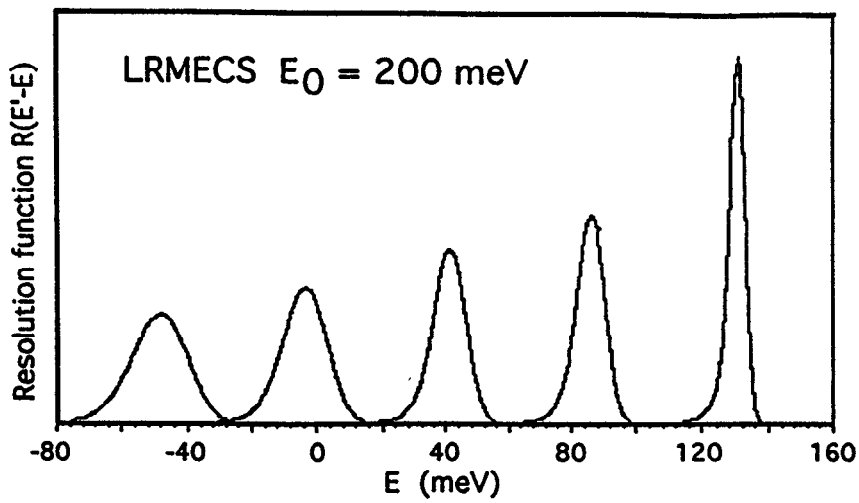


Figure 5. Calculated resolution functions R(E'-E) at five energy transfers for LRMECS with an incident energy of 200 meV.

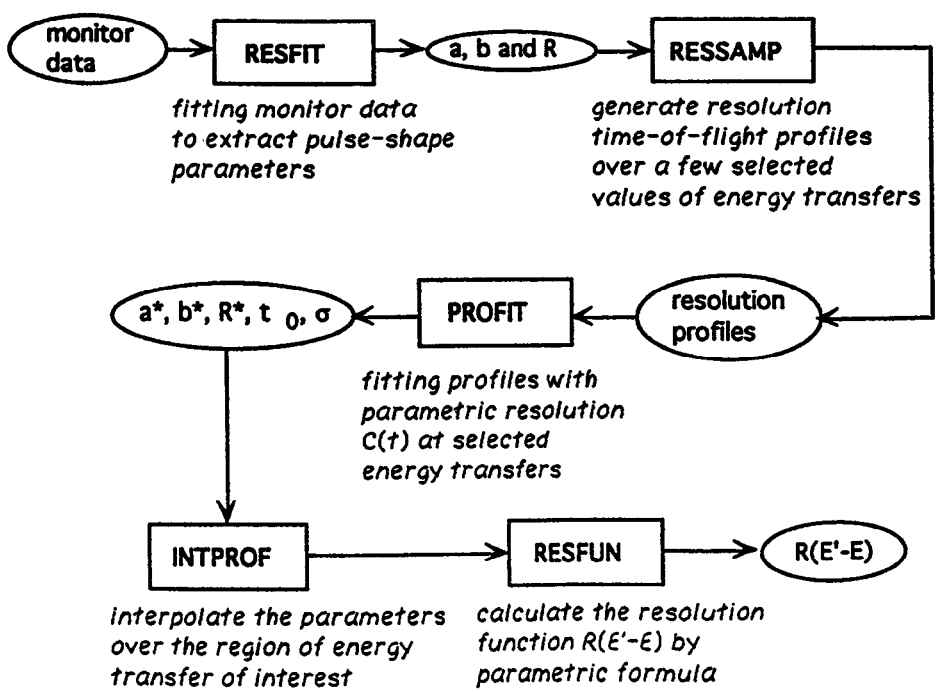


Figure 6. A flow chart for a typical resolution calculation in a data analysis.

# The Resolution Function of the Chopper Spectrometer HET at ISIS

T.G. Perring

ISIS Facility, Rutherford Appleton Laboratory,
Chilton, nr. Didcot, Oxon OX11 OQX, U.K.

## 0. ABSTRACT

The calculation of the resolution function of the chopper spectrometer HET at high incident neutron energies is described. The method is to calculate the *inverse* of the Cooper-Nathans resolution matrix, which can be achieved with much less algebra than a conventional calculation of the resolution function. A simplified version of the calculation is used to predict monitor widths, from which the moderator pulse width is parameterised and found to be much broader than expected. The data is used with the full calculation to predict linewidths of scattered neutron peaks from vanadium which are compared with experimental data. Comparison between inelastic data from single crystal MnCu and the 4-D convolution of the resolution function with a model dispersion relation is presented, which show good agreement.

## 1. INTRODUCTION

When any inelastic spectrometer is set up to observe a point $(\underline{Q}_0, \omega_0)$ in reciprocal space the spectrometer in fact accesses a region of $(\underline{Q}, \omega)$-space due to the spread of incident and final wavevectors about their nominal values. On a triple-axis spectrometer the spread arises from the range of angles that the collimators pass and the mosaic spreads of the monochromating and analysing crystals. In the case of a time-of-flight chopper spectrometer (TOFCS) the spread arises not only from the geometric collimation from the sizes of the moderator, sample and detector, but also from the distribution of flight-paths and the time-widths of the pulses from the moderator and chopper.

The resolution function for a triple-axis spectrometer is known to be a highly correlated function in $(\underline{Q}, \omega)$-space, broad in some directions but close to singular in others. This is also the case for a TOFCS. A knowledge of the form of the resolution function is important in scattering experiments from single crystals to match the resolution widths

with the problem being investigated, to focus peaks (minimise the width and maximise the height), and to determine if observed peaks widths are intrinsic to the scattering function. In section 2 the formalism of the resolution function calculation for HET is outlined and general features of the function discussed. In section 3 comparison is made between calculation and observed widths in direct-beam monitors and vanadium scattering to the detectors, and in section 4 an example of the simulation of HET data from a single crystal is presented.

## 2. FORMALISM

In figure 1 a schematic picture of the HET spectrometer [1] is shown. In the equations below, the arguments of the functions are deviations in time or distance from the values for the 'nominal' neutron. This neutron leaves the moderator face with wavevector $\underline{k}_I$, as determined from the first moments in two monitors placed in the beam behind the Fermi chopper, passes throught the chopper when the slits are parallel with the spectrometer axis, are scattered with final wavevector $\underline{k}_F$ and absorbed at the centre of the detector. The infinitesimal intensity can be written as

$$dI = [\phi(k_i)M(t_m)dy_m dz_m d^3\underline{k}_i dt_m][A(y_a)A_z(z_a)P(t_{ch}+\frac{u}{\omega})] \\ \times[\frac{\hbar}{mk_i}S(\underline{Q},\omega)s(x,y,z)dxd^3\underline{k}_f][D(x_d,y_d)D_z(z_d)dx_d.T(t_d)dt_d] \qquad [1]$$

Here $\phi(k_i)$ is the flux distribution on the moderator, $M(t_m)$ the pulse shape and $dy_m dz_m$ an element of area on the moderator face. $A(y_a)A_z(z_a)$ is the product of two hat functions that give the transmission through a beam defining aperature about 3m after the moderator, and $P(t'_{ch})$ the pulse shape through the chopper, $u$ the angle of the neutron to the spectrometer axis and $\omega$ the angular velocity of the chopper. The third pair of brackets gives the fraction of neutrons scattered by the sample into the phase space element $d^3\underline{k}_f$ by a thickness $dx$ of the sample. The function $s(x,y,z)$ is zero outside the sample volume and which gives the attenuation of the neutron beam when scattered at the point $(x,y,z)$ within the sample. The final term in brackets is the fraction of neutrons absorbed in thickness $dx_d$ in the detector and in time $dt_d$. $T(t_d)$ is a hat function with width equal to the time channel width. The variables can be changed to those that appear as function arguments to give

$$dI = \left[\frac{\hbar^2}{m^3}\frac{k_f^4 k_i\phi(k_i)}{l_0(l_a+l_1)l_2^3}\right]MAA_z sDD_z T_d dy_a dz_a dt_m dt'_{ch} dt_d\, d^3\underline{r}\, d^3\underline{r}_d.S(\underline{Q},\omega) \qquad [2]$$

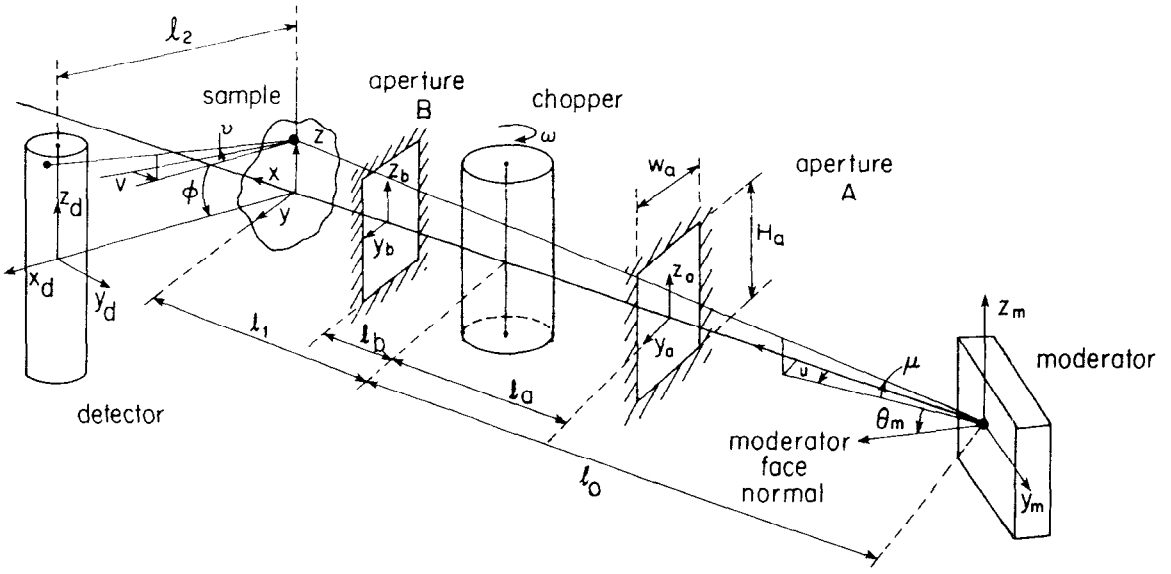


**Figure 1**: A schematic diagram of the HET spectrometer

where $l_0$ is the distance between the moderator and the chopper, $l_a$ the distance from the beam defining aperture to the chopper, $l_1$ the distance from the chopper to the sample and $l_2$ the sample -detector distance. The integral can be written in the conventional form

$$I(\underline{Q}_0,\omega_0) = \int R(\underline{Q}-\underline{Q}_0,\omega-\omega_0)\, S(\underline{Q},\omega)\, d\underline{Q}d\omega \qquad [3]$$

where

$$R(\underline{Q}-\underline{Q}_0,\omega-\omega_o) = [\ldots]\int MAA_z sDD_z T_d\, \delta(\underline{Q}-\underline{Q}_0)\delta(\omega-\omega_0)dy_a dz_a \ldots d^3\underline{r}_{\text{det}} \qquad [4]$$

In the corresponding treatment of a triple-axis spectrometer the resolution function is approximated by a Gaussian form. This simplification is not generally appropriate for a TOFCS at a pulsed source because of the asymmetry of the moderator pulse. However, at high incident neutron energies the asymmetry in the resolution is small and the approximation is valid. The conventional treatment would be to write each function as a Gaussian, change variables to $\delta\underline{Q} \equiv \underline{Q}-\underline{Q}_0$ and $\delta\omega \equiv \omega-\omega_0$ plus seven others, completing the square and integrating for each of the seven remaining variables in turn. A far simpler and more elegant method is to calculate directly from the integrand the covariance matrix $C_{\alpha\beta} = \langle \delta Q_\alpha \delta Q_\beta \rangle$, where $\alpha,\beta = 1 \rightarrow 4$ and $\delta Q_4 \equiv \delta\omega$. This is achieved by approximating the deviations $\delta Q_\alpha$ as a linear combination of the integration variables $\{X_i\} \equiv (y_a, z_a \ldots d^3\underline{r}_d)$ so that $\delta Q_\alpha = T_{\alpha j} X_j$, when

$$C_{\alpha\beta} = \langle \delta Q_\alpha \delta Q_\beta \rangle = T_{\alpha j} T_{\beta k} \langle X_j X_k \rangle \qquad [5]$$

As the integrand is largely the product of functions of one variable, most of the $\langle X_j X_k \rangle$ with $j \neq k$ are zero. The only non-zero off-diagonal elements arise potentially from the sample function $s(x,y,z)$. The diagonal terms are mostly easy to calculate apart from the variance of the depth of absorption in the gas tube detectors, which must be performed numerically. For instance, the pulse from the moderator as high energies can be approximated as [2]

$$M(t_m) = \frac{1}{2\tau^3}(t_m + 3\tau)^2 \exp\left(-\frac{t_m + 3\tau}{\tau}\right) \quad ; \quad \tau = \frac{1}{\Sigma v} \qquad [6]$$

where $\Sigma$ is the macroscopic cross-section for the moderator material and $v$ is the speed of the neutron. For this expression, $\langle t_m \rangle = 0$ and $\langle t_m^2 \rangle = 3\tau^2$. The variance of the pulse in a Fermi chopper is given in [3]. The resolution function in the Gaussian approximation is then

$$R(\delta \underline{Q}) = \frac{V_{res}}{4\pi^2 |\underline{\underline{C}}|^{\frac{1}{2}}} \exp\left(-\frac{1}{2}(\delta \underline{Q}, \delta\omega) \cdot \underline{\underline{C}}^{-1} \cdot (\delta \underline{Q}, \delta\omega)^T\right) \qquad [7]$$

where $V_{res}$ is the resolution volume, given by the integral of equation 2 with unit $S(\underline{Q},\omega)$. The method is entirely equivalent to that of [4] with $C^{-1}_{\alpha\beta}$ corresponding to the matrix elements $m_{\alpha\beta}$. It should be emphasised that the formalism takes account of all correlations introduced into the resolution function, for instance the sweep of the chopper across the moderator face and the sample, and the energy spread as well as the time spread of neutrons from the moderator that pass through the chopper. The only approximations are the ones usually made in resolution function calculations i.e. the spreads $\delta \underline{Q}$ and $\delta\omega$ are small in comparison to $\underline{k}_i, \underline{k}_f$ and $E_i, E_f$, and that Gaussian approximations are valid. It is possible to retain asymmetric functions in the formalism at the penalty of considerably more algebra, but this is not required for the high energy case being considered here.

An algorithm to calculate the resolution function according to the above formalism has been incorporated into two computer programs. RESCHOP calculates the resolution function and the peak width from a planar dispersion relation, and is similar in operation to the triple-axis spectrometer program RESCAL available at the ILL and elsewhere; and HETSIM which performs the 4D convolution of the resolution function with a model dispersion relation to simulate the results of a scattering experiment from a single crystal.

For any neutron spectrometer in the small scattering angle limit with small fractional energy transfer (the conditions in high energy magnetic scattering experiments), the resolution function can be shown to be close to singular, with [5]

$$\delta\omega \approx \frac{\hbar}{2m}\left(\underline{k}_i + \underline{k}_f\right)\cdot\delta\underline{Q} \qquad [8]$$

This result is found to be the case for HET, as shown in figure 2. Generally for HET, the fractional energy resolution $\delta\hbar\omega/E_I$ is ≈2.2% FWHH at the elastic line, reducing to 1.5% for full energy transfer. The fractional momentum resolution $\delta Q/k_I$ is about 1% both transverse and longditudinal. The vertical resolution is dominated by the height of the $^3$He gas detectors, which are mostly 30cm tall and at 4m or 2.5m from the sample.

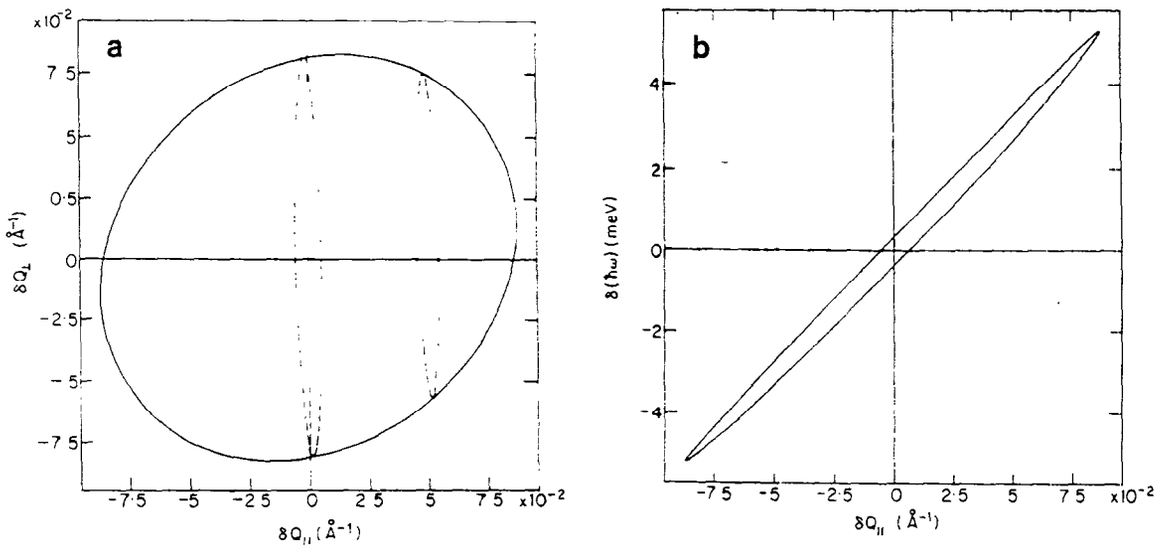


**Figure 2:** Typical resolution function for HET ($E_I$ =500meV, $\hbar\omega$ = 150meV, scattering angle =5º). (a) The solid line is the projection of the 50% surface perpendicular to the energy axis, and the dashed lines are the intersection of the function with the planes $\delta\omega = 0$ and $\delta\omega = 3$ meV. The $\delta Q_{//}$ axis is parallel to $\underline{k}_I$. (b) The projection of the 50% surface perpendicular to $\underline{k}_I$.

## 3. TESTING THE RESOLUTION FUNCTION

### 3.1 Monitor widths

HET has two monitors in the direct beam downstream of the chopper. The first is almost immediately behind the chopper so the moderator pulse width will contribute negligably to the pulse width because there is very little distance over which the transmitted spread of energies can cause the pulse to disperse. The second is 7.51m behind the chopper and so will include a moderator pulse width component. Each will also have components arising from the sweep of the chopper across the moderator face and the monitor. The expression for the pulse at the monitor position is the convolution

$$\phi(t) = \int M(t_m)A(y_a)P(t'_{ch})H(y)\,\delta(t-(a_1t_m + a_2y_a + a_3t'_{ch} + a_4y))\,dt_m dy_a dt'_{ch}\,dy \qquad [9]$$

where $H(y)$ is a hat function with width equal to that of the monitor. The coefficients $a_i$ linearly relate the deviation in time of arrival at the monitor, $t$, to the deviations $t_m, y_a, t'_{ch}, y$ and the variance of $\phi(t)$ is (expressing the $a_i$ explicitly)

$$\langle t^2 \rangle = \left(\frac{l_m}{l_0}\right)^2 \langle t_m^2 \rangle + \left(1+\frac{l_m}{l_0}\right)^2 \langle t_{ch}^2 \rangle + \left(1+\frac{l_m}{l_0}\left(1-\frac{\omega}{v}(l_0+l_m)\tan\vartheta_m\right)\right)^2 \frac{\langle y_a^2 \rangle}{\omega^2(l_a+l_m)^2}$$
$$+\left(1+\frac{l_m}{l_0}\left(1-\frac{\omega}{v}(l_0-l_a)\tan\vartheta_m\right)\right)^2 \frac{\langle y^2 \rangle}{\omega^2(l_a+l_m)^2}$$

[10]

Here $l_m$ is the distance from the chopoper to the monitor, $v$ the neutron speed and $\vartheta_m$ the angle the moderator face makes with the axis of the spectrometer. The last two terms in the equation are determined by the spectrometer geometry, as are the coefficients of the first two terms; the only uncertainties are the moderator and chopper pulse widths. Monitor_2 therefore allows the chopper pulse width to be checked against calculation, and monitor_3 will give the moderator pulse width once the chopper width is known.

The monitor widths in about 30 runs with incident energies between 130meV and 1000meV were measured with the HET Fermi chopper designed for use at high energies. Monitor_2 peaks were fitted by a Gaussian as each component (other than the moderator term) of equation 10 is comparable and arise from symmetric functions, whereas monitor_3 peaks were fitted by a Gaussian convoluted with the chi-squared function of equation 6. All the widths in monitor_2 agreed to 2% with values calculated using equation 10 with $\langle t'^2_{ch} \rangle$ calculated from the design values for the chopper slit width, radius of curvature and diameter (see figure 3). However, the widths in monitor_3 were systematically larger than calculated using equation 10. To reproduce the observed widths it was necessary to parametrise the decay constant $\tau$ as

$$\tau = \tau_0 + \frac{1}{\Sigma_{eff} v} \qquad [11]$$

with $\tau_0$=0.35μs and $\Sigma_{eff}$ =88m$^{-1}$. From the density of hydrogen in the moderator one would expect in the epithermal region $\Sigma \approx 150\text{m}^{-1}$. Typically, the observed moderator pulse width is about twice the calculated value.

3.2 Elastic scattering from vanadium

Now that the calculated chopper width has been confirmed and an empirical model for the moderator width determined, there no uncertain quantities appear in the calculation of the covariance matrix $C_{\alpha\beta}$. The element $C_{44} \equiv \langle \delta\omega^2 \rangle$ gives the variance of the elastic

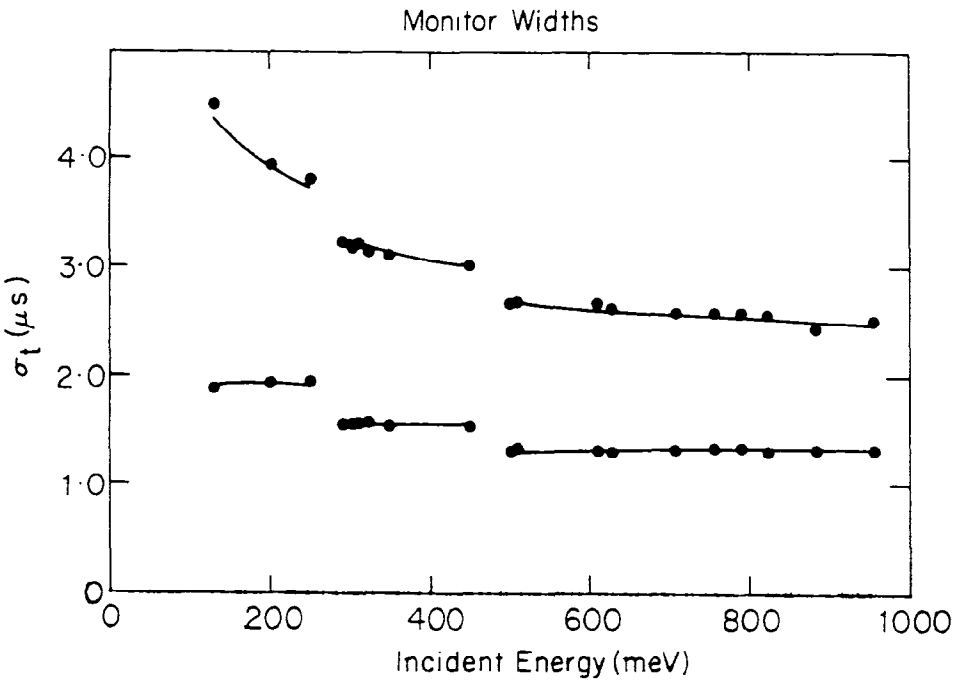


**Figure 3**: Experimental and calculated widths for monitor_2 (lower lines) and monitor_3 (upper lines). The discontinuities correspond to different chopper frequencies. Error bars on the fitted peak widths are smaller than the marks.

incoherent scattering peak ("vanadium width"). The widths of 22 such peaks with incident energies between 250meV and 880meV were measured, in detectors 4m and 2.5m from the sample position, from vanadium or cobalt (which has a comparable incoherent cross-section). The calculated widths are generally 10-20% less than the experimental widths (table 1). The origin of this discrepancy must be due to an extra component introduced to the width in the detectors that is so far unaccounted for, yet the calculation already includes the effect of sample size, detector thickness and focussing effects. One possibility is a "jitter" in the discrimination electronics of the detectors, which are $^3$He gas tubes, but which is not present in that of the monitors, which are made from beads of $^6$Li-doped scintillator glass on a wire grid. Further convolving the detector peaks widths with a function with standard deviation 1.3μs would give an excellent fit. The same effect and magnitude would also explain the observed discrepancy [6] between peaks widths in a gas tube and scintillator detector in the same position on the eVS spectrometer at ISIS.

## 4. SIMULATION OF MAGNETIC SCATTERING DATA FROM A SINGLE CRYSTAL [7]

This section describes an example of the application of the resolution function to understand some real data. MnCu(10%) is an itinerant antiferromagnet which orders three dimensionally. Near the zone centre the spin wave dispersion relation is expected to be approximately linear in reduced wavevector, $\omega(q) = \sqrt{\Delta^2 + (Dq)^2}$, with linear damping

| Incident Energy (meV) | Chopper frequency (Hz) | Sample to detector (m) | Detector width (Standard deviation) (μs) Experimental | Calculated | Error (%) | missing width (μs) |
|---|---|---|---|---|---|---|
| Vandium data | | | | | | |
| 252 | 400 | 4 m | 3.47 | 3.32 | 4 | 1.0 |
| | | 2.5 m | 3.20 | 2.92 | 9 | 1.3 |
| 303 | 500 | 4 m | 3.08 | 2.86 | 7 | 1.1 |
| | | 2.5 m | 2.64 | 2.49 | 6 | 0.9 |
| 501 | 600 | 4 m | 2.93 | 2.38 | 19 | 1.7 |
| | | 2.5 m | 2.53 | 2.07 | 18 | 1.4 |
| 629 | 600 | 4 m | 2.60 | 2.31 | 11 | 1.2 |
| | | 2.5 m | 2.37 | 2.02 | 15 | 1.2 |
| 755 | 600 | 4 m | 2.49 | 2.27 | 9 | 1.0 |
| | | 2.5 m | 2.64 | 2.00 | 24 | 1.7 |
| 884 | 600 | 4 m | 2.60 | 2.23 | 14 | 1.3 |
| | | 2.5 m | 2.43 | 1.97 | 19 | 1.4 |
| Cobalt data | | | | | | |
| 304 | 500 | 4 m | 3.09 | 2.86 | 7 | 1.2 |
| | | 2.5 m | 2.86 | 2.49 | 13 | 1.4 |
| 501 | 600 | 4 m | 2.76 | 2.38 | 14 | 1.4 |
| | | 2.5 m | 2.53 | 2.07 | 18 | 1.5 |
| 629 | 600 | 4 m | 2.59 | 2.31 | 11 | 1.2 |
| | | 2.5 m | 2.48 | 2.02 | 18 | 1.4 |
| 755 | 600 | 4 m | 2.78 | 2.27 | 18 | 1.6 |
| | | 2.5 m | 2.43 | 2.00 | 18 | 1.4 |
| 884 | 600 | 4 m | 2.60 | 2.23 | 14 | 1.3 |
| | | 2.5 m | 2.53 | 1.97 | 22 | 1.6 |

**Table 1**

$\Gamma = \Gamma_0 + \Gamma_1 q$. Here $\Delta$ is the gap at zero wavevector and $D$ the spin wave stiffness. Near the zone boundary calculations of the generalised magnetic susceptibility indicate that the dispersion relation becomes approximately flat. A highly simplified model is to assume the small $q$ dispersion relation up to a cut-off value $q^*$, beyond which the frequency and damping have the values at $q^*$. To ensure sufficient statistics it is necessary to add several adjacent detectors together, which degrades $\underline{Q}$ resolution perpendicular to $\underline{k}_F$ to a value comparable to the vertical resolution. It is important to include this resolution to understand the data, and HETSIM was used to convolve the resolution function with the proposed dispersion relation.

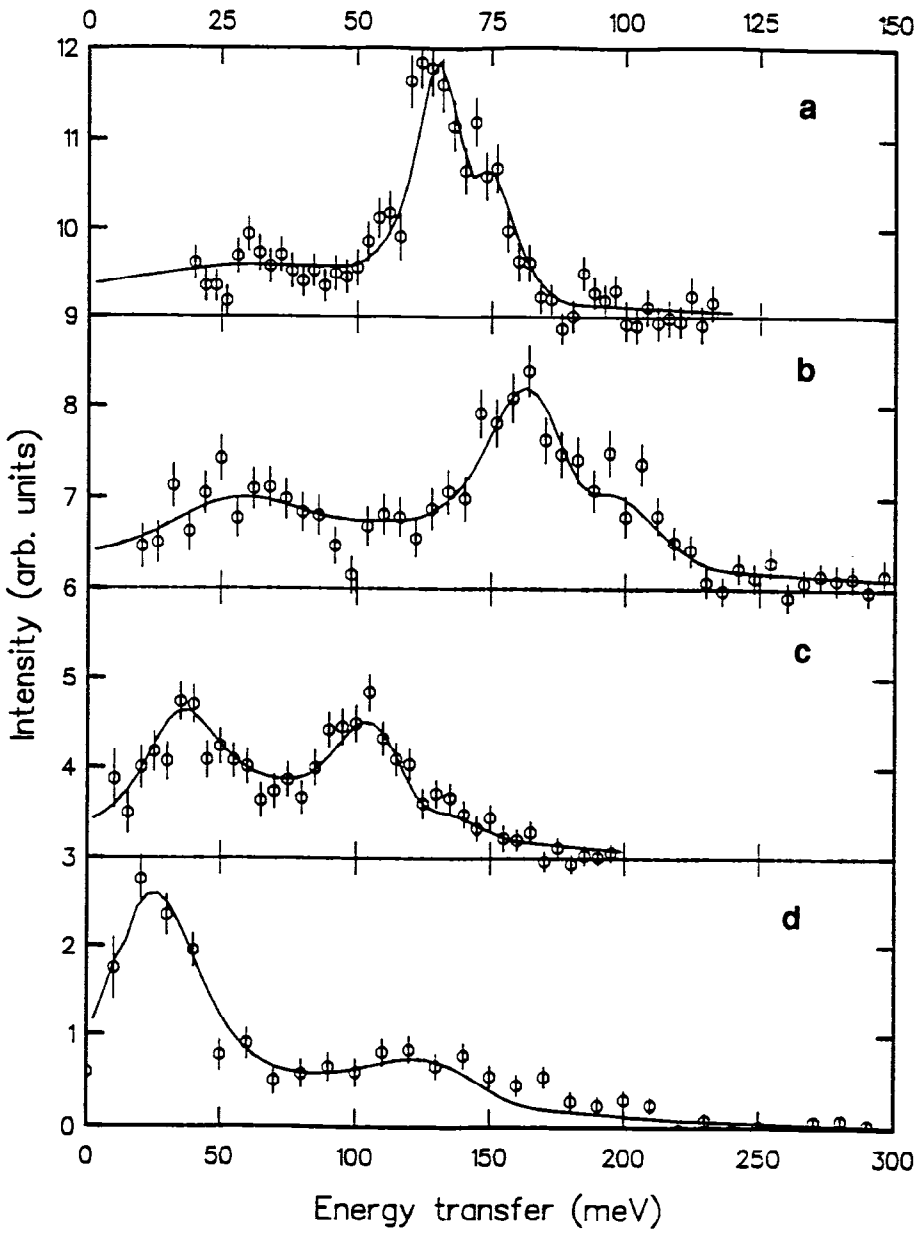


**Figure 4**: Measured spectra in the HET low angle detectors for MnCu(10%) in the [100]/[010] scattering plane. The values of $E_I$ and $\psi$ (the angle of [100] to $\underline{k}_I$) are (a) 157meV, 29.7º, (b) 262meV, 23.1º, (c) 443meV, 22.6º, (d) 813meV, 11.9º. The solid lines are the model calculations described in section 4.

Simulation of data obtained at several incident neutron energies, for which the trajectory in $(\underline{Q},\omega)$-space intersects the dispersion relation at different points, is shown in figure 4. The lower energy data is well explained using values of $\omega,\Delta,D,\Gamma_0$ and $\Gamma_1$ obtained from scattering data up to 60meV on a triple-axis spectrometer, but for the model to be consistent with tha data at high energies a cut-off wavevector $q^*$=0.8Å$^{-1}$ corresponding to $\omega^*$=190meV is required. The resulting simulation agrees closely with the data.

## 5. SUMMARY

The resolution function for HET and its sister instrument MARI has been calculated in a form suitable for high energy neutron experiments. Examination of monitor lineshapes and linewidths show that the calculated chopper pulse width agrees well with experiment, but that the HET moderator pulse width is considerably longer than expected from the water moderator. With the parametrisation of the moderator obtained from monitor data, the predicted widths in the detectors from elastic vanadium scattering are still 15% less than the experimental widths, but this discrepancy can be accounted for by 'jitter' in the detector electronics. The convolution of the resolution function with a model dispersion relation gives good agreement with magnetic scattering from a single crystal.

## REFERENCES


[1] A.D. Taylor, B.C. Boland, Z.A. Bowden, T.J.L. Jones, Rutherford Appleton Laboratory Report RAL-87-012 (1987)

[2] K.H. Beckurts and K. Wirtz, 'Neutron Physics' (Springer Verlag, Berlin, 1964)

[3] M. Marseguerra and G. Pauli, Nucl.Instr. and Meth. **4** (1959) 140

[4] M.J. Cooper and R. Nathans, Acta Cryst. **23** (1967) 357

[5] P.W. Mitchell, R.A. Cowley and S.A. Higgins, Acta Cryst. **A40** (1984) 152

[6] J. Mayers, private communication

[7] J.A. Fernandez-Baca, M.E.Hagen, R.M. Nicklow, T.G.Perring, Y.Tsunoda, J.Appl. Phys. **73** (1993) 6548

# $^3$He nuclear polarization for neutron spin analysis

Yasuhiro Masuda[1], Koichiro Asahi[2], Masashi Doi[2], Kenji Sakai[1,*], Hiromi Sato[2]
and
Z. Zhi Jian[1]

1 National Laboratory for High Energy Physics, 1-1 Oho Tsukuba-shi, 305 Japan
2 Tokyo Institute of Technology, Megro-ku Tokyo, 152 Japan
* On leave from Tohoku University

## I Introduction

The spin is a very useful probe for the space-time symmetry violation in fundamental interactions. A recent topics in this field is about large enhancement ($10^6$) of the parity ($P$) violation in the neutron-nucleus interaction in the incident neutron-energy region of eV, where the large neutron-helicity dependence is found in the cross section.[1,2,3,4] The large enhancement is also expected in the symmetry-violation effect under time reversal ($T$). A $T$-odd triple-correlation term between the neutron spin, nuclear spin and neutron momentum, which changes in sign under $T$, is measured in the $T$-violation test. The neutron spin is also used as a probe in condensed matter science. For example, the magnetic moment of the neutron and the neutron magnetic Bragg-scattering have been widely used for the study of the magnetism in condensed matter. In these studies, the neutron-spin polarization plays a decisive role. $^3$He nuclear polarization has potentially most preferable properties as a neutron-spin polarizer and analyzer. The reason is the followings.

The $^3$He nucleus has a large capture cross-section for the neutron, for example, the value of the cross section is more than ~1000 b below the neutron energy, $E_n = 1$ eV. The capture process is induced by a resonance reaction of $^3$He($n$, $p$)$t$. The resonance energy and the width are $E_0 = -518$ keV and $\Gamma = 1153$ keV, respectively.[5] The spin of the resonance state is zero. The neutron spin and the $^3$He nuclear spin are both 1/2, therefore, neutrons whose spins couple with $^3$He nuclear spins antiparallel are absorbed by $^3$He nuclei. The scattering cross-section of the $^3$He nucleus is negligible compared with the absorption cross-section. These properties are quite suitable as a neutron-spin filter. If the $^3$He polarization is 100% and the filter thickness is much larger than the neutron mean-free-path, neutrons whose spins are parallel to the $^3$He polarization transmit through the filter without attenuation, on the other hand neurons whose spins are antiparallel are absorbed completely. As a result, the transmittance of the polarized $^3$He filter becomes 50% and the polarization of the transmitted neutrons achieves 100%. This is a prominent feature of the polarized $^3$He filter as a neutron-spin polarizer. The polarized proton filter was unique method to obtain polarized neutrons in the epithermal region so far.[6,7] However, the proton has large scattering cross-section for the neutron. Therefore, the transmittance of the polarized proton filter is rather small than the polarized $^3$He filter. In addition to that, scattered neutrons may induce background in the neutron experiment. The $^3$He filter can be also applied to the neutron-spin analyzer. Namely, the neutron spin is analyzed by the neutron transmittance of the polarized $^3$He filter. A polarized $^3$He neutron counter is more ambitious application. Since the neutron of antiparallel spin induces the emission of charged particles through the nuclear reaction $^3$He($n$, $p$)$t$ , which produces an electric

signal, the polarized $^3$He counter senses only neutrons of antiparallel spin. It means a great gain of the analyzing power for the neutron spin.[8]

Although the $^3$He nucleus has the prominent properties in the application to the neutron-spin polarizer and analyzer as mentioned above, the polarized $^3$He filter has not been realized for neutron experiments. Here, we discuss development of $^3$He nuclear polarization at KEK and application to the *P*- and *T*-violation experiments.

## II Principle of $^3$He nuclear polarization

For the $^3$He nuclear polarization, a spin-exchanging hyperfine-interaction during atomic collision between polarized alkali atom and $^3$He atom is used.[9,10] The rubidium atomic-spin is polarized by an optical pumping. Namely, the rubidium atom is polarized upon the absorption of circularly polarized D1-resonant-light as it is shown in Fig. 1. The 5S1/2 state excites to the 5P1/2 state upon the absorption of the D1 light, where the magnetic quantum-state of m = -1/2 transits to the 1/2 state. The 5P1/2 state deexcites to the 5S1/2 state emitting unpolarized D1-light. If another polarized rubidium-atom absorbs the unpolarized resonant light, the atom depolarizes. A small amount of nitrogen gas is added to quench the unpolarized light. The 5P1/2 state deexcites during collision with a nitrogen molecule without emitting the resonant light. During the collision, the magnetic substates of the 5P1/2 state mixed with each other, therefore, the populations of the magnetic substates are equalized. Each magnetic substate of 5P1/2 decays into the magnetic substate of the 5S1/2 without changing the magnetic quantum number. As a result, a half of the photon spin is transferred to the 5S1/2 state. The spin-transfer rate from the photon to the rubidium atom is determined by the photon-absorption cross-section and incident laser intensity. However, the polarization of rubidium atom, $P_{Rb}$ is limited by spin destruction during Rb-Rb and Rb-$^3$He-$^3$He atomic collisions. The spin-destruction rate, $\Gamma_{sd}$ is $\Gamma_{sd}$~1 ms$^{-1}$. The incident laser power is applied to overcome the spin-destruction rate.

The rubidium atomic polarization is transferred to the $^3$He nuclear spin by a

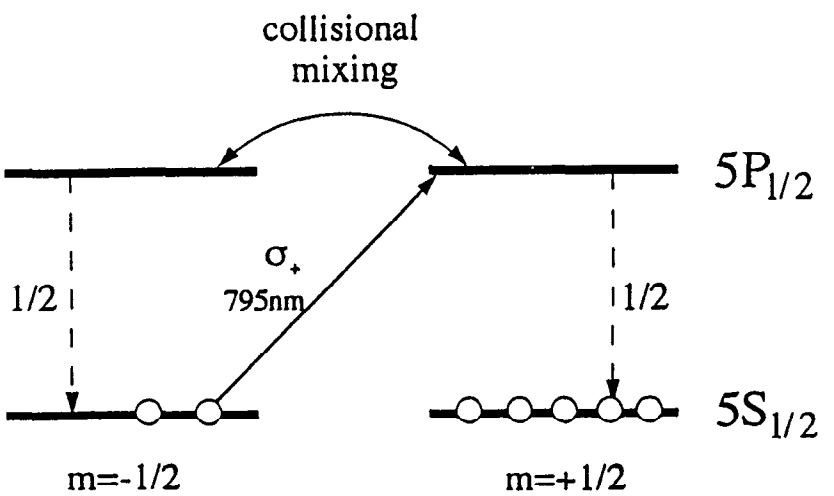


Fig. 1 Optical pumping of rubidium atom

hyperfine interaction during a Rb-$^3$He atomic collision. The spin-exchange rate from the rubidium atom to the $^3$He nuclear spin is $\Gamma_{se} = 9.4 \times 10^{-2}\ h^{-1}$ for a rubidium atomic-number-density of $4 \times 10^{14}$/cc.[10] The evolution of the $^3$He polarization, $P_{He}$ is predicted by a rate equation. The solution is

$$P_{He} = [\ P_{Rb}\Gamma_{se}/(\Gamma_{se} + \Gamma)\ ]\ [\ 1 - exp(-(\Gamma_{se} + \Gamma)t)\ ]. \qquad (1)$$

The value of $P_{He}$ is directly proportional to the value of $P_{Rb}$, since the $^3$He polarization is also depolarized upon collision with an unpolarized rubidium-atom and the optical pumping rate for the rubidium atom is very fast compared with the spin-exchange rate, $\Gamma_{se}$. $\Gamma$ is the relaxation rate of the $^3$He nuclear polarization.

The relaxation of the $^3$He polarization is induced by Brownian motion in a inhomogenous magnetic field as well as collision with an unpolarized paramagnetic center on the wall of a $^3$He container.[11,12] The $^3$He container is placed in a magnetic field in order to hold the polarization. The direction of the field is defined as $z$ axis. The $^3$He nucleus sees a magnetic field rotation in its moving frame due to a change in the $x$ or $y$ component of the magnetic field because of its inhomogeneity. The $^3$He spin rotates with the magnetic field rotation. In the frame where the magnetic field is in the $z$ axis, the effect of the magnetic field rotation on the $^3$He spin is described in terms of an effective field of $-\omega/\gamma$. $\omega$ is the angular frequency of the magnetic field rotation and $\gamma$ is the gyromagnetic ratio of the $^3$He spin. The direction of the effective field is in the $xy$ plane. The effective field fluctuates under the Brownian motion. The fluctuating field has the Fourier component of $\omega_0$ which is the Larmor frequency of the $^3$He spin. The presence of the transverse RF field of a angular frequency, $\omega_0$ induces a $^3$He-spin flip process. Thus, the $^3$He spin is depolarized by the Brownian motion in the inhomogeneous field.

## III $^3$He nuclear polarization at KEK

The apparatus for the $^3$He polarization is shown in Fig. 2.[13] An alminosilicate-glass cell was filled with 3-atm $^3$He gas, 100-torr nitrogen gas and a small amount of rubidium droplet. The size of the glass cell was 4 cm in length and 2.5 cm in diameter. The grass cell was placed in the center of a 40-G Helmholtz coil. The homogeneity of the magnetic field around the cell was designed to be lower than $10^{-3}$, in order to suppress the inhomogeneous field relaxation. The temperature of the cell was controlled at 180°C, where the number density of the rubidium atom is $4 \times 10^{14}$/cc at thermal equilibrium. The $^3$He cell was irradiated with circularly polarized light of 795 nm in wavelength, which corresponds to the wavelength of the D1 light. The circularly polarized light was supplied by a 4-W Ti-Sapphire laser system through a 1/4 $\lambda$ plate. Linear polarization of the photon is transformed into circular polarization upon transmission through the $1/4\lambda$ plate. The evolution of the $^3$He polarization was observed by a polarized neutron transmission. The method is also shown in Fig. 2.

Neutrons from the spallation source at KEK was polarized upon transmission through a polarized proton filter.[6] The neutron polarization is determined by the transmission enhancement, $\varepsilon = T/T_0$ as the following equation.

$$P_n = (1 - (T_0/T)^2)^{1/2}\ . \qquad (2)$$

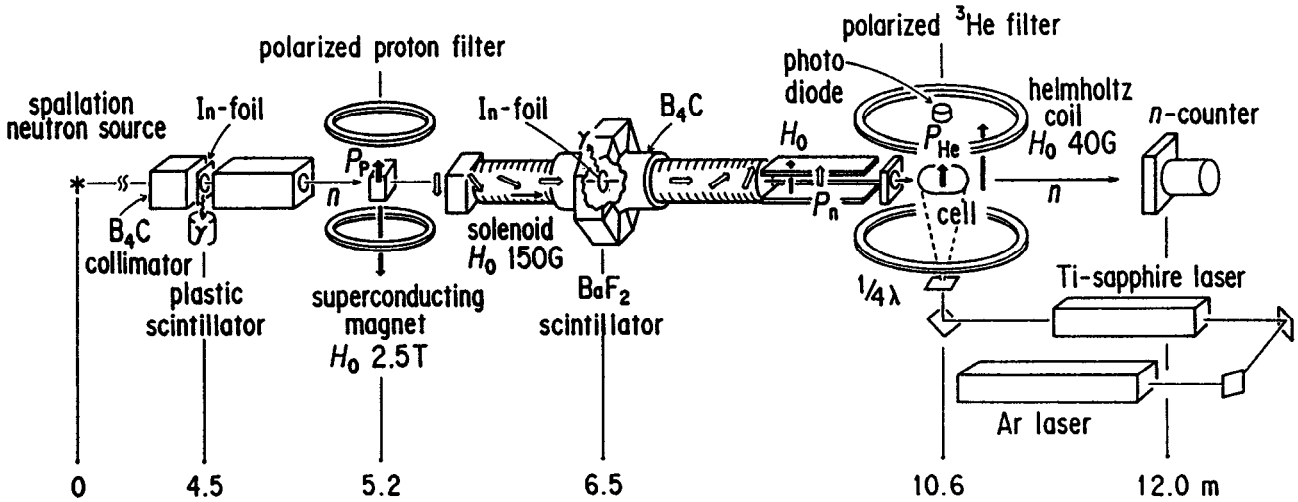


Fig. 2 Experimental set-up of $^3$He nuclear polarization

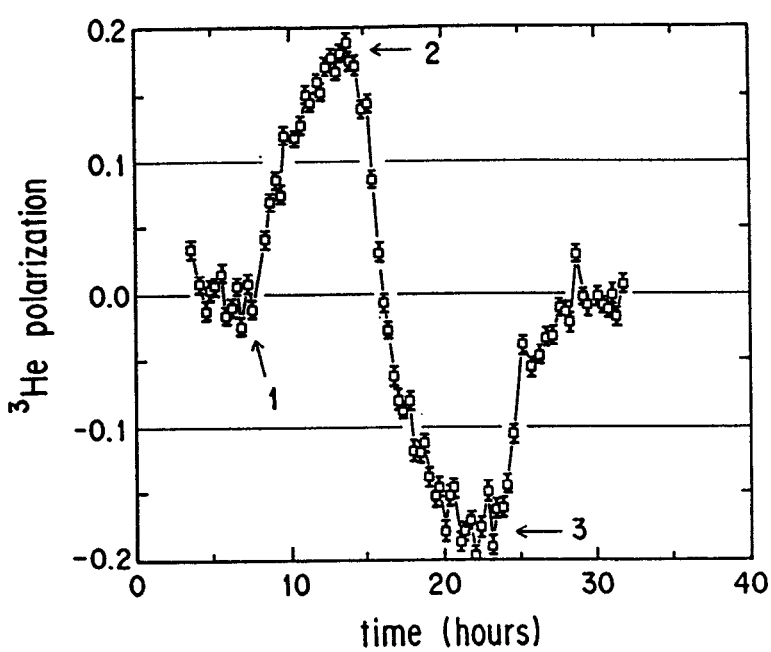


Fig. 3 $^3$He nuclear polarization

$T_0$ and $T$ are neutron transmissions in unpolarized and polarized states, respectively. The neutron transmissions were obtained by counting capture $\gamma$-rays from the two indium foil which were placed in up-stream and down-stream of the polarized proton filter. The neutron polarization was guided to the $^3$He filter from the polarized proton filter by using an adiabatic passage. Transmitted neutrons through the $^3$He filter were measured by a $^{10}$B-loaded liquid scintillator placed downstream. A typical result is shown in Fig. 3. In the figure, the laser beam was switched on at point 1 and the polarization of $^3$He started. Since the $^3$He nuclear spin was polarized parallel to the incident neutron polarization, the neutron transmittance of the $^3$He filter increased. At point 2, the circular polarization of the laser beam was reversed and $^3$He nuclei were polarized antiparallel. Therefore, the neutron transmittance decreased. The value of the $^3$He polarization is determined by the transmission enhancement,

$$\varepsilon = (1 + P_n)/2 \cdot exp(N\sigma t P_{He}) + (1 - P_n)/2 \cdot exp(-N\sigma t P_{He}). \qquad (3)$$

Here, $P_n$ is the neutron polarization, $N$ the $^3$He nuclear-number-density, $\sigma$ the $^3$He cross-section and $t$ the thickness of the filter. The sign of $P_{He}$ is assumed to be positive ,which is in the direction of the neutron polarization. The result of the calculation of the $^3$He polarization is written on the vertical scale of Fig. 3. At present, the maximum $^3$He polarization is about 50%. At point 3, the laser beam was switched off and $^3$He-polarization relaxation was observed. The value of $\Gamma$ is obtained by the time constant of the relaxation curve. The relaxation rate is also estimated by the polarization evolution. By using the value of 9.4 x $10^{-2}$ $h^{-1}$ for $\Gamma_{se}$ at a rubidium atomic-number-density of 4 x $10^{14}$/cc, the value of the relaxation rate was obtained as $\Gamma = 7.4 \times 10^{-2}\ h^{-1}$ and the value of the rubidium polarization was obtained as $P_{Rb} = 0.66$. We can improve the $^3$He polarization by decreasing the value of $\Gamma$ and increasing the value of $P_{Rb}$. We are developing surface treatment of the glass wall by HF to remove the paramagnetic

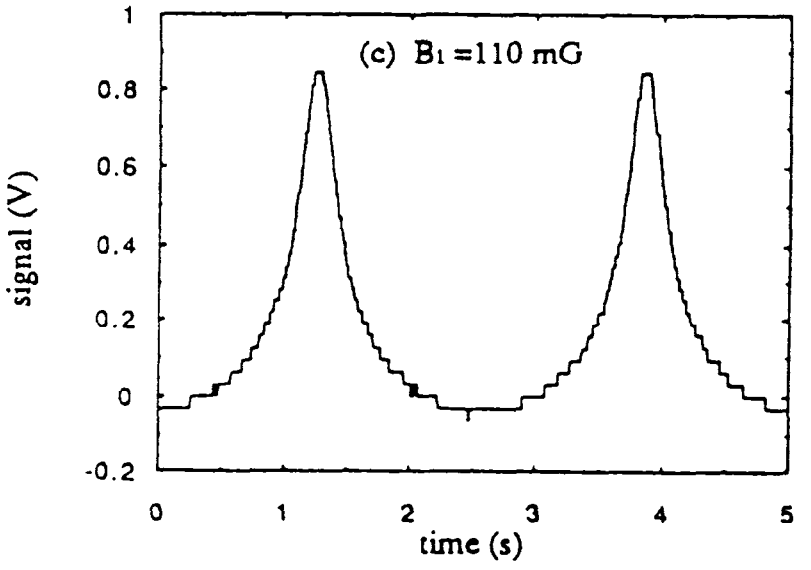


Fig. 4 $^3$He NMR signal

impurity from the glass wall. To improve the rubidium polarization, we need more laser intensity in the glass cell.

We also used a NMR method to obtained the value of the $^3$He polarization. In the 40-G Helmholtz coil, we mounted a drive coil, which applied the RF field ($H_1 \sin \omega t$) to the $^3$He cell. The effective field in the rotating frame whose frequency is same as the RF field is $-\omega/\gamma$. The total magnetic field in the rotating frame is represented as[14]

$$\boldsymbol{H}_{tot} = (\boldsymbol{H}_0 - \omega/\gamma) + \boldsymbol{H}_1. \qquad (4)$$

Here, $\boldsymbol{H}_0$ is the magnetic field of the Helmholtz coil. When the $H_0$ is swept across the resonant point, the effective field rotates from up to down or from down to up following the sweep of the magnetic field. If the sweep velocity satisfies the adiabatic condition, the $^3$He spin follows the magnetic field rotation. The change of the $^3$He spin direction was sensed by a pick-up coil. The magnetic induction signal at the pick-up coil was analyzed by a lock-in amplifier system. A typical result of the NMR measurement is shown in Fig. 4. The NMR signal amplitude was calibrated by the neutron-transmission measurement.

## IV Neutron-spin rotation experiment

We have applied the polarized $^3$He filter to the measurement of the neutron-spin rotation (NSR) during propagation through medium.[15] The NSR apparatus is shown in Fig. 5. The neutron-spin rotation-angle is converted to a projection angle on the magnetic field. In this conversion, we used a non-adiabatic passage of the neutron spin through a superconducting sheet, where the magnetic field is zero because of the Meissner effect.[16,17]

The performance of the NSR apparatus was examined by the following method. The apparatus was placed at 8.6 m from the neutron source between the $^3$He filter and the down-stream indium foil. Before the superconducting box, a dipole magnet was placed so that the neutron spin rotated from the longitudinal to transverse direction following an adiabatic passage. Since the magnetic field is zero in the superconducting sheet because of the Meissner effect, the neutron experiences a sudden change in the magnetic field at entering and going out of the superconducting sheet. Therefore, the neutron spin enters the box non-adiabatically, namely the neutron spin direction does not change. If there is no magnetic field inside the box, the neutron spin travels through the free space keeping it original direction. After propagation through the box, the neutron spin entered another transverse dipole field again non-adiabatically. If the direction of the down-stream magnetic field is rotated from the up-stream magnetic field by $\theta$, the $\cos\theta$ component of the neutron polarization is held by the down-stream magnetic field. The $\cos\theta$ component of the neutron spin is guided to the $^3$He filter by an adiabatic passage and analyzed by the transmission measurement. The transmittance of the $^3$He filter was measured as a function of $\theta$. During the experiment, the incident neutron spin was flipped by reversing the up-stream magnetic field every 4 sec. The change of the neutron transmission upon polarization reversal was observed. The flipping ratio, which is defined as

$$R = (T_+ - T_-)/(T_+ + T_-), \qquad (5)$$

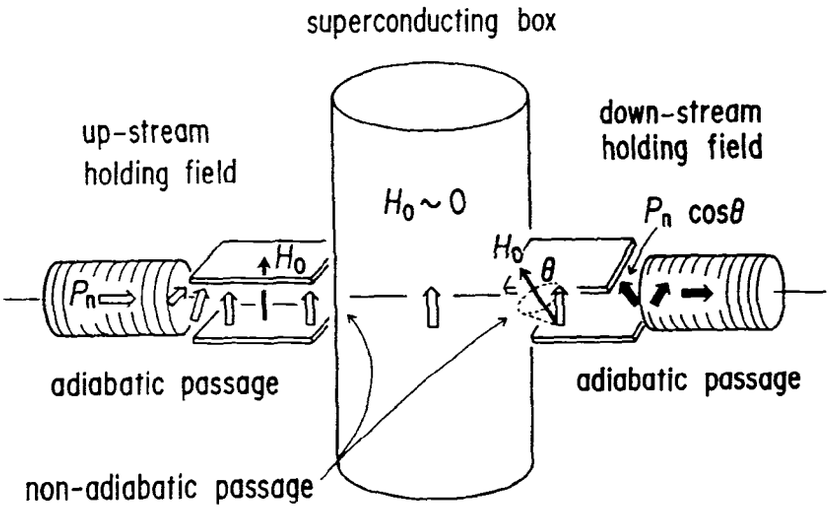


Fig. 5 Apparatus for neutron spin rotation measurement

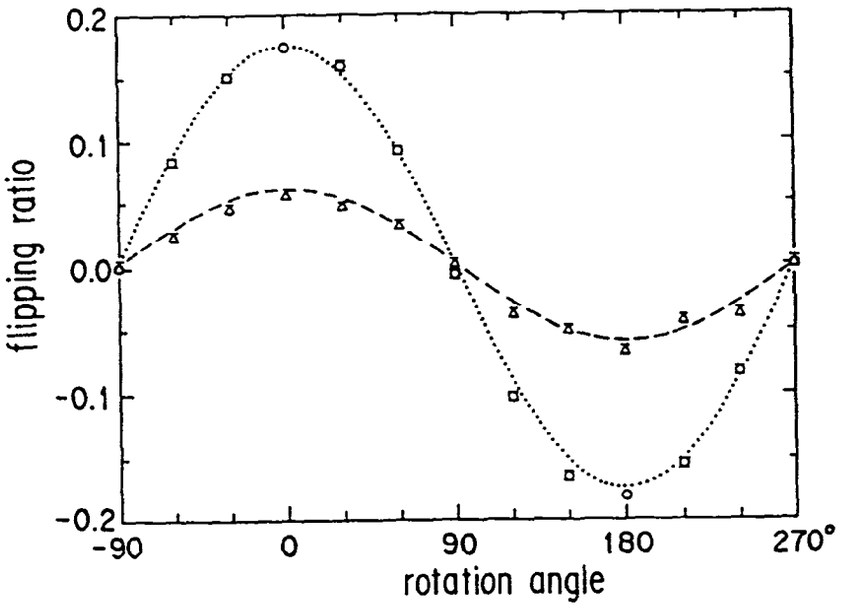


Fig. 6 Result of neutron spin rotation

was obtained. Here, $T_+$ and $T_-$ are transmittances for flipper off and on states, respectively. If we use the equation (3), the flipping ratio is represented as

$$R = P_n \cos\theta \tanh(N\sigma t P_{He}). \tag{6}$$

The result of the flipping ratio is shown in Fig. 6. A clear $\cos\theta$ distribution is found in the flipping ratio. The solid and broken lines are results of calculation for the incident neutron energy of 0.1 and 0.75 eV, respectively by using the values of $P_n$, $P_{He}$ and $N\sigma t$. The experimental results are well explained by the calculation. The result proves that the conversion of the rotation angle into the projection angle by using the Meissner effect works very well and then the direction of neutron spin in the superconducting box can be detected precisely.

The NSR apparatus can be applied to measure the neutron-spin rotation by the $P$-violating neutron-nucleus interaction.[15] For this measurement, a target is placed in the superconducting box and the down-stream magnet is set at $\theta = 90^o$ in order to get higher detection sensitivity for the rotation. More important application of the NSR apparatus is for the $T$-violation experiment.[18] A new method to detect the T-violation effect is proposed quite recently, which has a possibility to overcome the present most stringent upper limit of the T-violation obtained by the neutron electric dipole moment measurement.[19] The experimental principle is shown in Fig. 7. In the experiment, the target nuclear spin is transversely (in $x$ direction) polarized. Incident neutron spin is in $z$ direction. The neutron spin rotates upon transmission through the polarized target by $+180^o$ or $-180^o$. The $T$-violation effect is found in a transmission difference between the two opposite rotation states. The neutron-spin rotation is controlled by the following way. The neutron spin rotates around $x$ axis by the magnetic field which is used for the polarization of the target spin (Larmor precession) and the spin dependent neutron-nucleus strong interaction (pseudomagnetic precession[20,21]). In the experiment, we will adjust the magnetic field strength so that $+180^o$ and $-180^o$ rotations are realized. For the rotation adjustment we will use the NSR apparatus. The apparatus for the polarization of the target nuclear spin is now under development.[22]

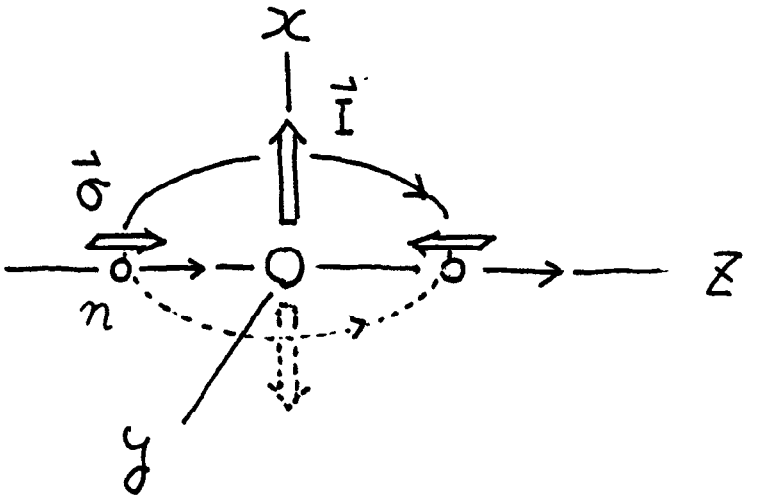


Fig. 7 Principle of spin rotation asymmetry

The authors would like to thank Prof. H. Sugawara, Prof. N. Watanabe and Prof. K. Morimoto for their warm encouragement. They also thank colleagues of PEN group at KEK for their valuable support during the experiment.

[1] V.P. Alfimenkov et al., Nucl. Phys. A398(1983)93.
[2] Y. Masuda et al., Hyp. Int. 34(1987)143; Nucl. Phys. A478(1988)737c; Nucl Phys. A504(1989)269.
[3] S.A. Biryukov et al., Sov. J. Nucl. Phys. 45(1987)937.
[4] C.D. Bowman et al., Phys. Rev. C39(1989)1721.
[5] S.F. Mughabghab et al., "Neutron Cross Section" Academic Press (1984).
[6] Y. Masuda et al., Nucl. Inst. Meth. A264(1988)169.
[7] V.I. Lushchikov et al., Sov. J. Nucl. Phys. 10(1970)669.
[8] W.G. Williams, Nucleonika 25(1980)769.
[9] K.P. Coulter et al., Nucl. Inst. Meth. A270(1988)90.
[10] B. Larson et al., Phys. Rev. A44(1991)3108.
[11] R.G. Gamblin and T.R. Carver, Phys. Rev. A138(1965)946.
[12] L.D. Schearer and G.K. Walters, Phys. Rev. A139(1965)1398.
[13] H. Sato et al., to be published in Hyp. Int.
[14] A. Abragam,"The principle of nuclear magnetism" Clarendon Press, Oxford(1961).
[15] K. Sakai et al., to be published in Hyp. Int.
[16] M. Ishida et al., KEK Progress Report 84-2(1984)207.
[17] Similar apparatus is independently developed at Grenoble. F. Tasset, Phisica B156&157(1989)627.
[18] Y. Masuda et al., Hyp. Int. 74(1992)149.
[19] Y. Masuda, to be published.
[20] V.G. Baryshevsky and M.I. Podgoretskii, Zh. exsp.teor.Fiz., 47(1964)1050.
[21] H. Glattli et al., Journal de physique 40(1979)629.
[22] Y. Masuda et al., Proc. 18th INS Int. Symp., World Scientific, 293(1991).

# RECENT PROGRESS IN SUPERMIRRORS AT PSI

P. Böni[1], I. S. Anderson[2], P. Buffat[3], O. Elsenhans[1], H. P. Friedli[1], H. Grimmer[1], R. Hauert[4], K. Leifer[3], J. Penfold[5], and J. Söchtig[6]

[1] Labor für Neutronenstreuung ETH & PSI, CH-5232 Villigen PSI, Switzerland.

[2] Institut Laue Langevin, F-38042 Grenoble, Cedex, France.

[3] EPFL, CH-1015 Lausanne, Switzerland.

[4] EMPA, CH-8600 Dübendorf, Switzerland.

[5] Rutherford Appleton Laboratory, Chilton, Didcot, Oxon OX11 0QX, United Kingdom.

[6] Paul Scherrer Institut Zürich, Badenerstrasse 569, CH-8048 Zürich, Switzerland.

## ABSTRACT

Recently, significant progress has been made in increasing the performance of supermirror coatings for neutron guide tubes. Using reactive DC-magnetron sputtering techniques we have developed at PSI a process for the series production of neutron guides with twice the critical angle of reflection of bulk Ni and with an integral reflectivity of more than 90% over a substrate area of $500 \times 300$ mm$^2$. For the optimization of the reflectivity, we have used various thin film measurement techniques, like atomic force microscopy, transmission electron microscopy and Auger depth profiling for the characterisation of the interfaces and surfaces, as well as standard X-ray and neutron scattering techniques. We shall also report on our first successful experience with the series production of supermirrors for the spallation source SINQ, which will be the first neutron source that relies almost entirely on the performance of supermirror coated guides.

## I. INTRODUCTION

Neutron guide tubes are a means to efficiently transport neutrons from the source to spacious areas of low background [1]. Until now most guide systems rely either on a coating consisting of natural Ni which has an angle of total reflection for neutrons given by $\theta_c/\lambda = 0.00173$ rad/Å. Using $^{58}$Ni this angle can be increased by a factor $m = 1.2$ [2], resulting in flux gains at the end of a guide of roughly 40%. Many years ago Turchin [3] and Mezei [4] proposed to use a sequence of thin artificial layers that increase the critical angle even further via Bragg reflection. Recently reflectivities $R$ for such superstructures have been reported that exceed 0.95 at $m = 2$ [5] and $m = 3$ [6]. In fact a group is claiming to be ready for series production of supermirrors $m = 2$ with $R > 0.95$ [7]. Therefore, in addition to flux gains of a factor of four or more that can be achieved with supermirrors, it is now possible to transport even thermal neutrons with a reasonably large divergence (i.e. $\theta \simeq 0.4^0$ at $\lambda = 2$ Å) in an efficient way.

As anounced at the last ICANS meeting in 1990 [8] a commercial DC-magnetron sputtering facility has been installed during summer 1991 at Paul Scherrer Institute. After various acceptance tests and adjustments we started the development of supermirror coatings in January 1992. During this time it became clear that the anticipated configuration of the machine proved to be right, in particular, excellent multilayers can be produced when the layers are deposited with high power and at low process pressure [8].

In Fig. 1 we show the transmission of one of our better supermirror coatings ($m = 2$) sputtered on regular float glass. In a single reflection measurement performed at a TOF

reflectometer in Saclay we obtain after deconvolution of the data a reflectivity close to $R = 0.94$ at twice the angle of total reflection of bulk Ni ($q = 4\pi m\theta_c/\lambda = 0.0435$ Å$^{-1}$). In contrast, when a measurement over the whole surface area is made using a micro-guide set-up (to be explained below), we obtain $R = 0.92$. Note that the neutrons have undergone roughly nine reflections near $m = 2$. The difference between the two results can be explained by small variations of $R$ and $m$ along the mirror surface (in particular at the beginning and at the end of the glass plate) for which the latter method is more sensitive to. In the following sections we describe the research that enables us to produce now such supermirror structures.

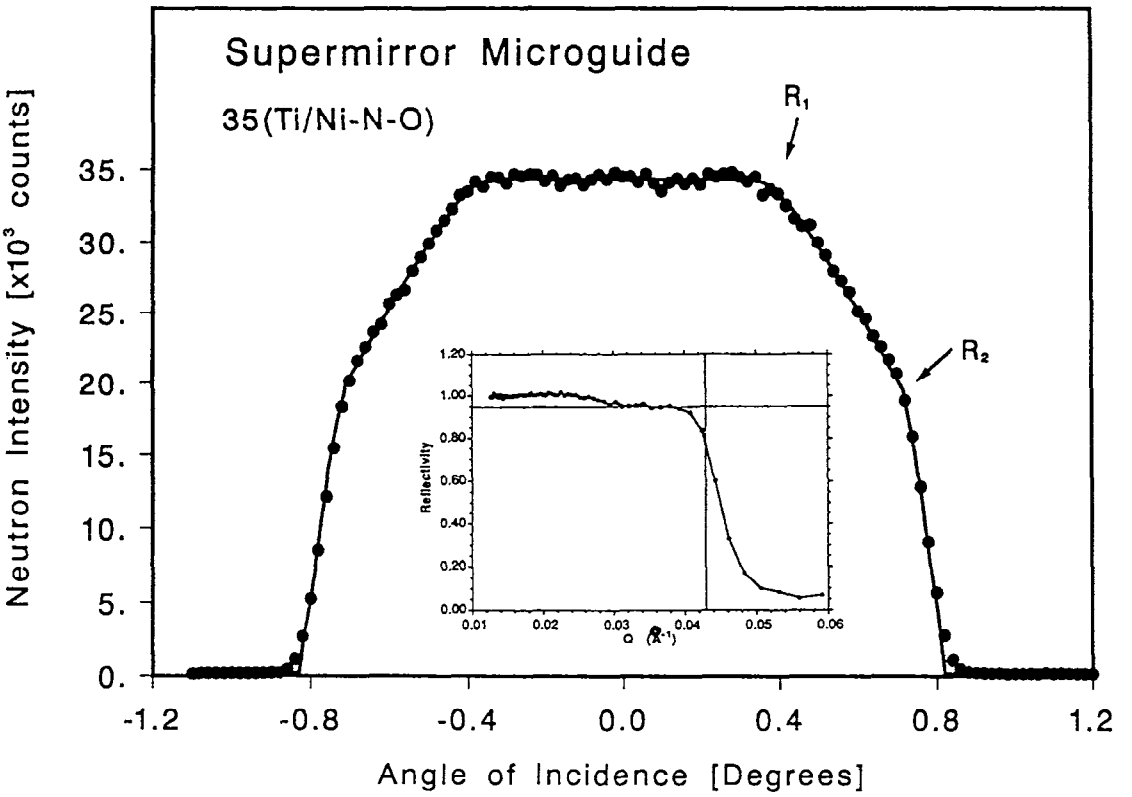


Fig. 1: Transmission profile of a micro-guide with a supermirror coating consisting of 35 Ni(air)/Ti bilayers yielding a reflectivity of 0.92. Inset: single reflection profile for same mirror, $R \simeq 0.94$ ($\lambda = 4.08$ Å).

## II. EXPERIMENTAL

For the investigation of the morphology and the interface structure of the Ni/Ti based multilayers we have produced various samples with constant bilayer spacings (usually between 50 Å and 200 Å) as well as single layers with a thickness $1000 < d < 2000$ Å on silicon wafers or regular float glass by means of DC-magnetron sputtering. The stress $S$ and $d$ have been measured directly by means of a Tencor long scan profiler P2. Combining these results with mass density measurements using quartz the density of the layers can be determined.

Conductivity measurements prove to be particularly useful because they provide an integral characterisation of the properties of the layers. In particular, the conductivity does not only depend on the thickness of the layers, it also depends on the grain size and on the amount of impurities within the layers. Fig. 2 shows a comparison between conductivity and optical transmission of a sputtered 100 Å layer of $Ti_{72}V_{28}$ on glass. The two measurements are obviously correlated along the substrate length of 500 mm, indicating that the layers have

not only a well defined thickness $d = 100$ Å±0.8%, they have also a very similar morphology. For comparison a pure Ti layer yields 165 Ω/sq.

Reflection profiles of the samples were measured on neutron reflectometers installed at the pulsed spallation source ISIS and at the Orphée reactor in Saclay using a fixed sample geometry, providing constant illumination during a wavelength scan. Most measurements at fixed wavelength have been performed on the double axis spectrometer P2ax and on the recently installed test spectrometer TOPSI (since Dec. 1992) at reactor Saphir at PSI. Usually two coated glass plates were assembled like a narrow guide with a gap of 0.4 mm (0.8 mm) for $L = 250$ mm (500 mm), where L is the length of the glass plates. This so-called micro-guide was inclined with respect to the incoming neutron beam ($\lambda = 4.08$ Å) and the transmitted intensity was recorded (Fig. 1). Near the critical edge of the supermirror the neutrons undergo up to 9 reflections.

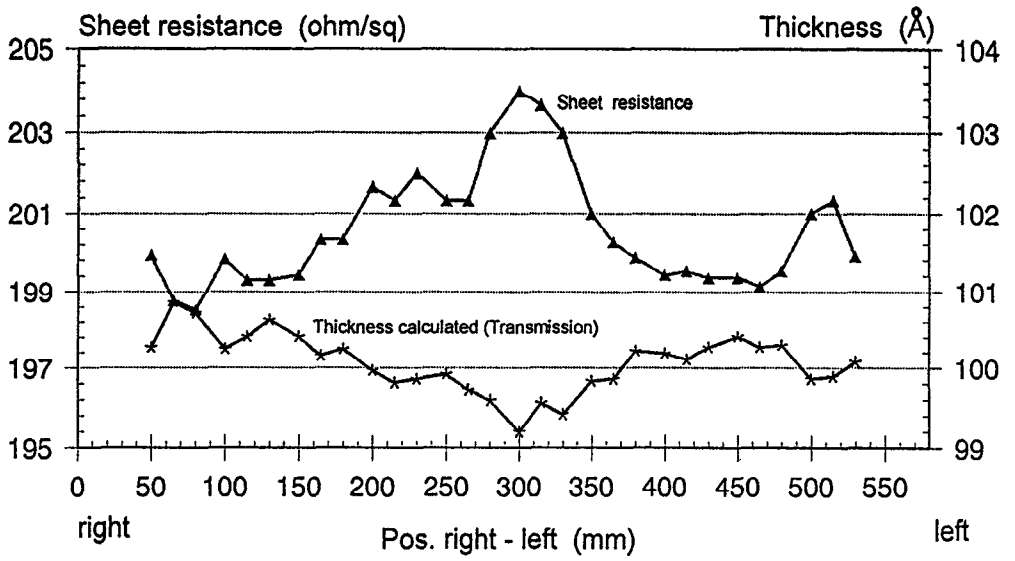


**Fig. 2:** Sheet resistance and thickness versus position of a sputtered film $Ti_{72}V_{28}$. Note the strong correlation between the two data sets.

## III. RESULTS

It is known that multilayers consisting of pure Ti and Ni tend to develop rough interfaces possibly due to the large grains in the individual layers. In additon significant interdiffusion of Ni into Ti takes place in particular at elevated temperatures. In order to reduce these effects it has become common practice to add C to the Ni layers. This procedure does not only lead to an amorphization of the layers, it also increases the scattering density of the Ni layers. Values for $bN$ of $9.6 \cdot 10^{-6}$ Å$^{-2}$ [6] and $11.2 \cdot 10^{-6}$ Å$^{-2}$ [5] have been reported. In order to further increase the contrast between the layers Vidal et al. [5] have hydrogenated the Ti layers using reactive RF magnetron sputtering. They claim that the scattering density for the TiH layers can be increased to $-7.8 \cdot 10^{-6}$ Å$^{-2}$ which is much higher than the value for the stochiometric compound $TiH_{2-x}$ ($Nb = -5.11 \cdot 10^{-6}$ Å$^{-2}$).

In a first step [9-11] we also produced multilayers consisting of these materials and observed that addition of C up to 12% reduces the size of the Ni grains (Table 1) and leads to amorphization of layers that are only a few nm thick and to reorientation of grains ([111] → [200]) in thicker layers. Further increase of C leads to the formation of $Ni_3C$ grains and to amorphous layers for C contents > 45%.

Hydrogenation of Ti in sufficient quantities leads to the formation of cubic $TiH_{2-x}$ with [111] perpendicular to the surface. Coherent interfaces are formed if the thickness of the $TiH_{2-x}$ layers does not exceed a few nm. The best interfaces are obtained with multilayers that contain either $NiC_x$/Ti or Ni/$TiH_y$ exemplified by the appearance of superlattice peaks of order 11 at scattering angles $2\theta \simeq 11^0$ for CuK$\alpha$ radiation. The quality of the interfaces of NiC/TiH multilayers was inferior.

Based on our experience with NiC and TiH we have prepared some supermirror coatings NiC/TiH on regular float glass using a sequence of layers calculated with a program from J. B. Hayter and H. A. Mook [12]. After annealing the samples during 16 h at $120^0$C the performance was $R = 0.900(2)$ at $m = 2.06(5)$ [10].

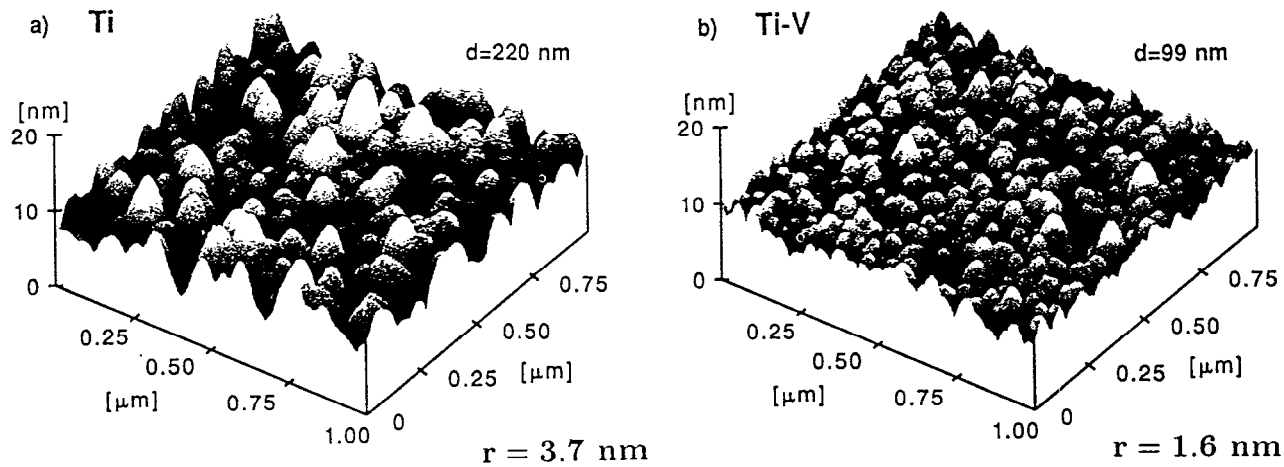


**Fig. 3:** Atomic force microscopy pattern of monolayers of a) pure Ti and b) $Ti_{72}V_{28}$

Several reasons have led us to give up the further exploration of supermirrors consisting of NiC and TiH:

- the quality of NiC layers depends on the way, how C is incorporated into the Ni target material, raising the question of maintaining the target quality
- NiC targets are very expensive
- hydrogen has a large absorption and incoherent scattering cross section for neutrons
- $H_2$ is not pumped well with turbo pumps due to the low molecular weight
- supermirrors must be annealed after production

There is not much choice for improving the structure of the Ti layers by incorporating other elements with a negativ scattering length because their number is limited (H, Li, V, Mn). Mn is known to diffuse [6], in addition it becomes activated under neutron irradiation. Li and Mn have a higher absorption than Ti. Therefore we incorporated V into Ti. Atomic force microscopy measurements [13] presented in Fig. 3a and 3b demonstrate clearly that the grain size and the amplitude of the roughness are significantly reduced in $Ti_{72}V_{28}$ when compared with pure Ti. It is interesting to note that Ni layers (RMS = 0.22 nm) are more than a factor of 10 smoother than Ti layers (RMS = 3.72 nm). The results compiled in Table 1 indicate the excellent resolution of the atomic force microscope. The roughness measurements over an area of $100 \times 100$ nm$^2$ yield in general too small values whereas samplings over larger areas are consistent with each other.

In a search for a good replacement of C in the Ni containing layers we decided to use $N_2$ which has even a higher scattering length than C. X-ray measurements show similar effects on the morphology of the layers on increasing the concentration of $N_2$ as for C. Again a reorientation Ni [111] $\longrightarrow$ Ni [200] takes place and the formation of $NiN_3$ is observed. However, an amorphisation and grain size reduction of Ni does not occur [11].

**Table 1:** Roughness and lateral extension of surface inhomogeneites measured with atomic force microscopy for different sampling areas. $d$ is the thickness of the sputtered layers.

| material | $d$ | RMS (nm) | | | lat. ext. |
|---|---|---|---|---|---|
| | (nm) | $100 \times 100$ nm$^2$ | $500 \times 500$ nm$^2$ | $6 \times 6$ $\mu$m$^2$ | (nm) |
| Si | 0 | 0.14 | 0.11 | | flat |
| Ni | 95 | 0.16 | 0.22 | 0.25 | 50 |
| $Ni_{90}C_{10}$ | 210 | 0.17 | 0.36 | 0.34 | 30 |
| $Ni_{45}C_{55}$ | 210 | 0.45 | 1.07 | 1.17 | 40 |
| Ti | 224 | 2.53 | 3.72 | 3.84 | 70 |
| $TiH_{1.1}$ | 188 | 3.40 | 5.13 | 4.18 | 60 |
| $Ti_{72}V_{28}$ | 99 | | 1.6 | | 30 |

Table 2 shows that $NiN_x$ is an excellent and cheap material for increasing the critical angle of single layer coatings. Unfortunately, multilayers consisting of $NiN_x$/Ti are not stable at elevated temperatures possibly because $N_2$ diffuses into the Ti and builds the famous hard coating (or artificial gold) TiN, thereby reducing the contrast between the Ni and Ti containing layers.

**Table 2:** Critical angle of reflection in units of the critical angle $\theta_c$ of reflection for bulk Ni for different materials sputtered on borkron glass $500 \times 150$ mm$^2$.

| material | Ni | $NiN_x$ | $Ni_{87.1}N_{7.7}O_{2.4}$ |
|---|---|---|---|
| $m$ | 0.99 | 1.03 | 1.03 |

Based on the observation of Schärpf [14], that venting an evaporation process after completion of individuel layers improves the performance of supermirrors, we replaced $N_2$ by dry air [15]. We expected that $O_2$ builds up a diffusion barrier $TiO_2$ at the interface. Indeed, the performance of the mirrors remained excellent and most importantly, the structures were stable up to $T \simeq 260^0$C (see Table 3). The highest reflectivity we obtained with this recipe on regular float glass was 92.5% at $m = 2$ when measured using the micro-guide set-up. Atomic force microscopy shows that the Ni-N-O surface is actually very smooth [13].

**Table 3:** Temperature dependence of the performance of a supermirror sputtered on regular float glass $250 \times 50$ mm$^2$. $R$ is the reflectivity at the critical angle of the supermirror $\theta = m\theta_c$. $\theta_0$ is the angle of total reflection of the top layer.

| $T(^0)$C | 20 | 180 | 220 | 240 | 260 | 270 |
|---|---|---|---|---|---|---|
| $\theta_0$ (mrad) | 1.38 | 1.36 | 1.40 | 1.29 | 1.28 | 1.00 |
| $m$ | 2.00 | 2.00 | 2.04 | 1.94 | 2.01 | 2.07 |
| $R$ | 0.90 | 0.89 | 0.87 | 0.86 | 0.85 | 0.80 |

## IV. DISCUSSION

The main advantages of supermirrors made of Ni(air)/$Ti_{1-x}V_x$ [15] are their thermal (and therefore expected long term) stability and their cheap and simple production. In April 1993 the series production of supermirror coatings for the SINQ guides began and presently we produce in one machine run two borkron glass plates $500 \times 150$ mm$^2$ in less than six hours. The coatings are characterized immediately after production using the micro-guide set-up at TOPSI. The parameters $R$ and $m$ are measured at three different heights (-40 mm, 0 mm, 40 mm) of the guide.

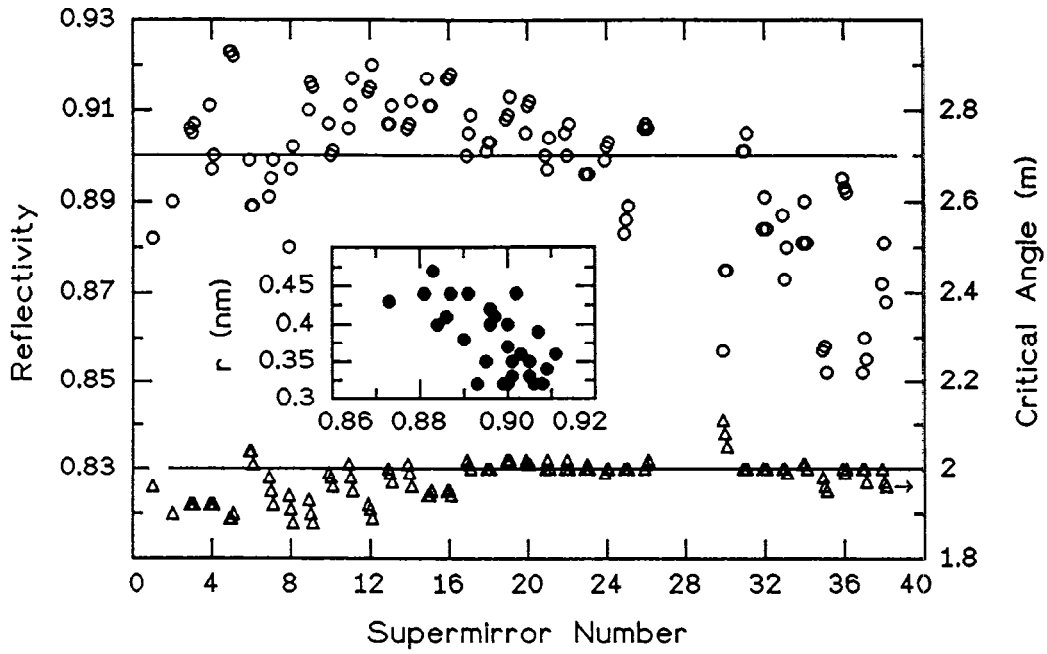


**Fig. 4:** Reflectivity (circles) and critical angle (triangles) of all supermirror coatings produced so far at PSI. Mirrors 17 to 26 have been produced within 2.5 days using an identical recipe. Note the drop in $R$ of sample 25. The inset shows roughness versus reflectivity for the samples produced with an identical recipe.

Fig. 4 shows $R$ and $m$ for *all* runs we have done in the period April 26 until May 20, 1993. After some adjustments of the sequence at the beginning of production we have now settled at $m = 2$ and $R \geq 0.90$ for substrates with a surface roughness (RMS) $r \simeq 3.5$ Å (runs 17-26). There is a trend that $R$ decreases rather dramatically if $r > 4$ Å(runs 25, 32 - 38). Such dramatic fluctuations in $R$ have never been observed when using commercial float glass. We hope that we can routinely obtain a reflectivity $R > 0.9$ when we are provided with borkron glass with $r < 3.5$ Å, or (intrinsically smooth) float glass, resulting in flux gains at SINQ [16] of a factor of three when compared with a Ni coated guide. An improvement from $R = 0.90$ to $R = 0.95$ would increase the flux only by another 20%.

One of the major problems we still have to resolve is the build-up of waveness in the mirror sequence. We have observed that the reflectivity at the critical edge $m \simeq 2$ increases by $\simeq 0.02$ if the thick bilayers are left out, whereas $R$ decreases only by $\simeq 0.01$ if 230 thinner layers are added yielding $R = 0.83$ at $m = 2.7$. We believe that the wavy parts of the supermirror reflect neutrons out of the incident beam (in wrong directions) that are supposed to be reflected by the thin layers.

Based on the scattering densities of the layers and the known roughness of the borkron glass $r \simeq 0.4 \pm 0.1$ nm [17] we have calculated $R$ for our supermirror sequence [18] and obtain $R \simeq 0.96$ at $m = 2$. Absorption and incoherent scattering has been taken into account. This

result indicates, that we loose roughly 0.02 to 0.04 because of imperfections of our mirrors.

Finally we would like to compare the performance of the supermirrors made at PSI with those, made by other groups. Vidal et al. [5] produced supermirrors composed of 49 layers NiC/TiH and obtained $R = 0.95$ near twice the critical angle of Ni. We honestly do not understand how they manage to obtain this result. In Fig. 5 we show the theoretical reflectivity for their sequence with and without taking absorption, incoherent scattering and an overall roughness $r = 4$ Å into account. The theoretical reflectivity at $m = 2$ is only $\simeq 0.92$. Indeed the recently installed supermirror neutron guide at the ORPHEE reactor in Saclay has only a reflectivity $r = 0.77$ at $m = 1.9$ [19]. Ovonic Synthetic Materials Company of Troy, Michigan have made supermirrors with $m = 2.77$ [20] and $R > 0.95$ [6]. Assuming a layer roughness $r = 4$ Å, one obtains for *the* ideal supermirror (no losses) $R \simeq \exp(-(Qr)^2/2) = 0.97$. Taking into account absorption, incoherent scattering and waveness, that amounts to at least 0.02, it is indeed surprising for us that such high quality mirrors can be produced.

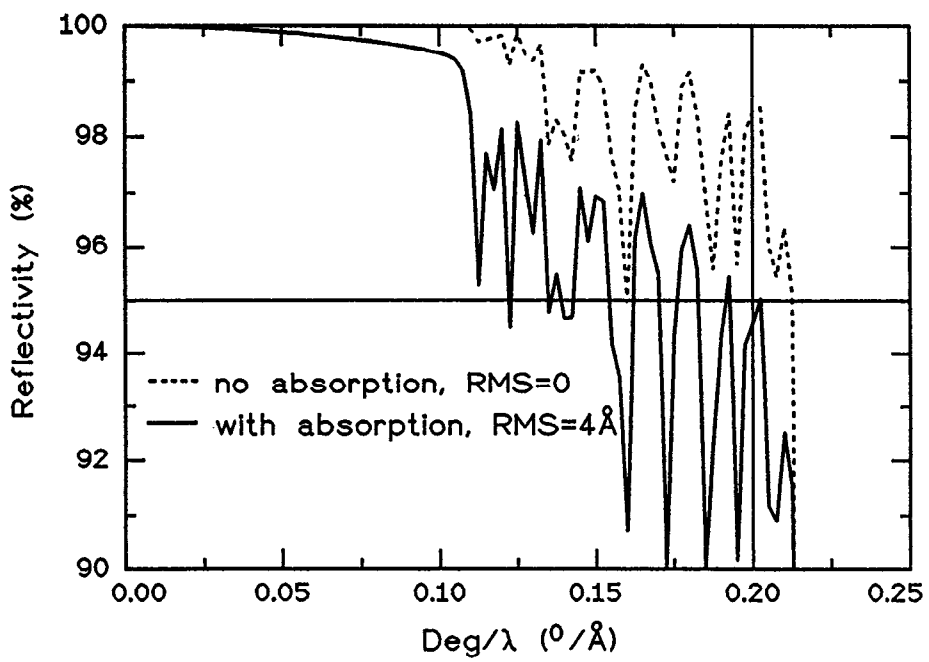


Fig. 5: Calculated reflectivity profiles for supermirrors of Ref. [5,7]. The following scattering densities have been used: $g_{NiC} = (11.2 \cdot 10^{-6} - 2.46 \cdot 10^{-9} i)$ Å$^{-2}$ and $g_{TiH} = (-6.00 \cdot 10^{-6} - 12.4 \cdot 10^{-9} i)$ Å$^{-2}$.

Concluding we remark that we are able to produce supermirror coatings reproducably on surface areas of at least 500×300 mm$^2$ on super-polished borkron glass ($r < 3.5$ Å) with $m = 2$ and $R > 0.90$ (see Fig. 4). The process can be upgraded in a straight forward way to much longer guide pieces. From our experience we learn, that absorption and incoherent scattering in the layer materials and the roughness of the substrate are very important parameters which are decisive for the performance of the supermirrors. During series production it is advisable to immediately measure $R$ and $m$ using a micro-guide set-up in order to garantee an optimum performance of the neutron guide to be produced. The production is most easily done on commercially available float glass with a deposition system located close to a neutron scattering center using DC-magnetron sputtering with materials Ni(air)/TiV [15]. We hope that it will be possible to finish the major part of the deposition process for $m = 2$ supermirror guides for SINQ until the end of 1993. Afterwards we are going to concentrate on the development of other neutron optical components like polarizers and focussing units.

## Acknowledgment

We acknowledge the efficient technical support provided by P. Keller, R. Thut, and M. Koch from the Labor für Neutronenstreuung, and for the ongoing support by W. Fischer and A. Furrer. We thank T. Krist for performing ERDA measurements at Bessy in Berlin. Financial support by the Swiss National Science foundation is gratefully acknowledged.

1. H. Maier-Leibnitz and T. Springer, Reactor Sci. & Techn. **17**, 217 (1963).
2. K. Werner, T. Springer, and J. Duppich, IAEA-CN-46/54P, 393 (1985).
3. V. F. Turchin, Deposited Paper, At. Energy 22 (1967).
4. F. Mezei, Communications on Physics 1, 81 (1976).
5. B. Vidal, Z. Jiang, and F. Samuel, SPIE Vol. 1738, 30 (1992).
6. C. F. Majkrzak and J. F. Ankner, SPIE Vol. 1738, 150 (1992); United States Patent 5,082, 621, Jan. 21, 1992, J. Wood, Ovonic Synthetic Materials Company.
7. F. Samuel, B. Farnoux, B. Ballot, and B. Vidal, SPIE Vol. 1738, 54 (1992).
8. P. Böni, I. S. Anderson, R. Hauert, P. Ruterana, K. Solt, B. Farnoux, G. J. Herdman, J. Penfold, and O. Schärpf, ICANS-XI International Collaboration on Advanced Neutron Sources KEK, Tsukuba, October 22-26, 1990, p. 910.
9. H. Grimmer, P. Böni, O. Elsenhans, H. P. Friedli, I. S. Anderson, K. Leifer, and P. Buffat, Materials Science Forum **126-128**, 615 (1993).
10. O. Elsenhans, P. Böni, H. P. Friedli, H. Grimmer, P. Buffat, K. Leifer, and I. S. Anderson, SPIE Vol. 1738, 130 (1992).
11. H. Grimmer, P. Böni, O. Elsenhans, H. P. Friedli, K. Leifer, P. Buffat, and I. S. Anderson, Proc. EPDIC-3, Vienna (1993) (to be published).
12. J. B. Hayter and H. A. Mook, J. Appl. Cryst. **22**, 35 (1989).
13. O. Elsenhans, I. Anderson, P. Böni, P. Buffat, H. P. Friedli, H. Grimmer, R. Hauert, K. Leifer, and J. Söchtig, Proc. "$9^{th}$ International Colloquium on Plasma Processes" to be held in Antibes-Juan-les-Pins, France, June 6-11, 1993.
14. O. Schärpf, Physica B **156 & 157**, 631 (1989).
15. Patent Application pending.
16. G. Bauer, this volume; W. Wagner and J. Duppich, this volume.
17. Borkron glass for part of the SINQ guides is provided by CILAS, Compagnie Indistruelle Des Lasers, F-91460 Marcoussis.
    Float glass for part of the SINQ guides is provided by NTK, Oststrasse 5, D-8939 Bad Wörishofen.
18. S. Yamada, T. Ebisawa, N. Achiwa, T. Akiyoshi, and S. Okamoto, Annu. Rep. Res. Reactor Inst. Kyoto Univ. Vol. **11**, 8 (1978).
19. B. Ballot, F. Samuel, and B. Farnoux, SPIE Vol. 1738, 159 1992).
20. Different definitions for $m$ are being used. In Ref. [6] $m$ refers to the angle of total reflection of a sputtered Ni layer. Our definition refers to the value for bulk Ni with a density of 8.9 g/cm$^3$.

# Polarized Neutron Reflection at LANSCE

*M.R. Fitzsimmons,[1] G.S. Smith,[1] R. Pynn[1] and M.A. Nastasi[2]*
[1]Los Alamos Neutron Scattering Center
[2]Materials Science and Technology Division
Los Alamos National Laboratory
Los Alamos, New Mexico 87545 U.S.A.

ABSTRACT: The integration of polarized neutron reflection (PNR) with the surface profile reflectometer (SPEAR) at LANSCE is described. To achieve a PNR capability comparable to that of CRISP at ISIS, a Co-Ti super-mirror, a flat-coil spin-flipper, and magnetic guide fields can be introduced into the SPEAR neutron beam line by simple computer command. Instrumentation, particularly with regard to the use of a flat-coil spin-flipper at a pulsed spallation source, and computer software for the optimization of such a spin-flipper and the analysis of polarized neutron reflection data are described. Recently, the ability to measure the reflection of polarized neutrons from thin-film and multilayers samples as they are manufactured *in situ,* was demonstrated. Results from such an experiment are presented.

## 1. Introduction

During 1992, polarized beam handling equipment was added to SPEAR. The purpose of this equipment is to facilitate studies of magnetic thin-films and multilayers using the polarized-neutron-reflection technique [1]. The motivation for these studies is the need to quantify the magnetization profiles of thin-films and multilayers, and correlate their magnetizations with detailed understandings of their atomic structures. Particularly in multilayer systems like those exhibiting giant-magneto-resistance (GMR), the magnetic coupling of neighboring magnetic layers is sensitive to roughness and inter-diffusion at their interfaces [2]. The attraction of PNR is that the technique can characterize the magnetizations of surfaces and interfaces in thin-films and multilayers *and* determine details about their nuclear structures with a depth resolution typically on the order of 5Å. When this technique is combined with an intense neutron source, such as LANSCE, efficient polarization devices, and an ultra-high vacuum thin-film and multilayer *in situ* fabrication capability, the surfaces and interfaces of thin-film systems can be observed in their pristine state. The magnetic structures of these spatially-limited systems can also be studied at intermediate steps during their manufacture. Not only does this capability facilitate model fitting of complicated structures, but the origin(s) of unusual magnetic properties, such as those which produce spin-flip scattering, can be identified during the fabrication of the multilayer. In §2 of this paper, details about the polarization equipment at SPEAR are described. In §3 an application of this equipment to the study of the magnetization of a thin Fe film on an MgO substrate is discussed, and in the last section, the recently installed fabrication facility in the SPEAR neutron beam line is discussed.

## 2. Polarization Equipment and its Computer Control

Neutrons with wavelengths ranging from 2 to 8Å are provided by preferentially reflecting one neutron polarization state from Co-Ti polarizing super-mirrors [3]. The super-mirrors are magnetized in a direction perpendicular to the reflection plane by a 1kG field produced by permanent magnets. The polarization of the neutron beam is maintained from the super-mirror (Fig. 1) to the sample position by magnetic guides which provide a magnetic field of 50G in the same direction as that applied to the super-mirror.

In order to measure the spin-up ($\omega_+$, neutron spin aligned parallel to the magnetic field on the polarizer) and spin-down ($\omega_-$) reflectivities of a sample, the neutron spin must be either maintained or flipped relative to the magnetization of the super-mirror. Spin-flipping at LANSCE is obtained by adiabatically precessing the neutron spin through a flat-coil spin-flipper [4]. The neutron spin can be made to precess an odd multiple of $\pi$, if the magnetic

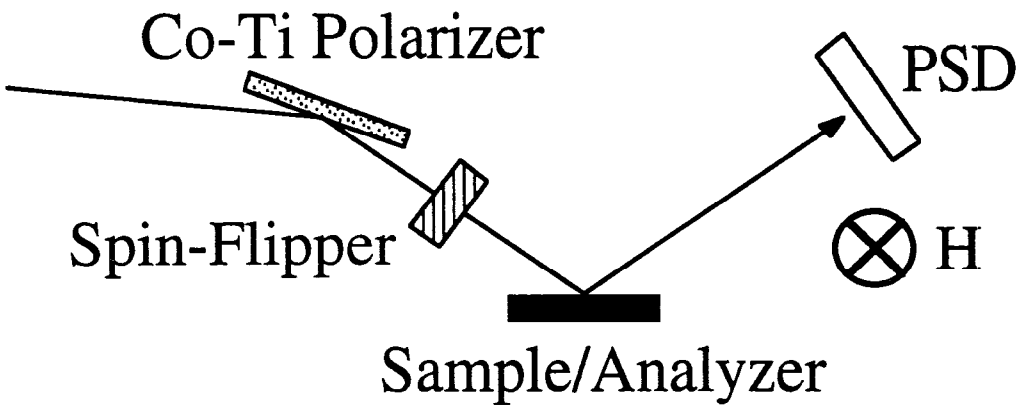


Fig. 1 Side view of the polarization components that can be introduced into the SPEAR beam line. The unpolarized neutron beam becomes polarized after reflection from the Co-Ti polarizer. The polarization state can be changed from spin-up, i.e. aligned with the magnetic field (into the figure), to spin-down by the spin-flipper. A magnetic guide field (not shown) maintains the polarization state of the neutrons from the polarizer to the sample. The spin-up and spin-down reflectivities, $\omega_+$ and $\omega_-$, are measured by a position sensitive detector (PSD).

field within the spin-flipper is:

- normal to the direction of the magnetization of the super-mirror, and
- of the correct strength for the velocity (or wavelength) of the neutron.

In the case of SPEAR, the direction of the magnetic field in the spin-flipper was chosen to lie in the vertical plane and normal to the neutron beam. The field is produced by passing current through a coil (called the flipping coil), which has a rectangular cross-section. Since the spin-flipper lies within the confines of the magnetic guide field, current passing through a second outer coil (called the compensating coil) is needed in order to cancel the magnetic field from the guide; thus, the neutron beam passes through a region with a purely vertical magnetic field, when reversal of the neutron beam polarization is desired.

In order to assure that every neutron precesses equally regardless of its wavelength, the strength of the magnetic field inside the flipping coil must be changed as a function of time so that the integral of magnetic field strength over time is constant for every neutron. This requirement is accomplished by ramping the current through the flipping coil, $I_f$, as a function of time, $t$, according to the relation:

$$I_f(t) = \frac{a}{t} + b, \tag{1}$$

The parameter $a$ is related to the precession angle of a neutron (a constant), and $b$ is related to the distance between the spin-flipper and the spallation target. Since the magnetic field due to the magnetic guide is constant with time, only a DC current is required in the compensating coil. Past experience (R.P.) with other flat-coil spin-flippers suggests that optimum performance is achieved when the compensating coil current, $I_c$, is somewhat time dependent. The relation used to change $I_c$ with time is,

$$I_c(t) = r + st, \tag{2}$$

where $r$ represents the current required to cancel the magnetic field from the magnetic guide, and $st$ is a small perturbation on the order of 10% of $r$.

The degree to which a spin-flipper is properly "tuned", i.e. the spin-flipper flips the spin of a neutron from spin-up to spin-down, can be determined by measuring the $\omega_+$ and $\omega_-$ reflectivities of a second polarizing super-mirror (the analyzer), when it is placed at the sample position. If the polarizing super-mirror and spin-flipper are functioning perfectly,

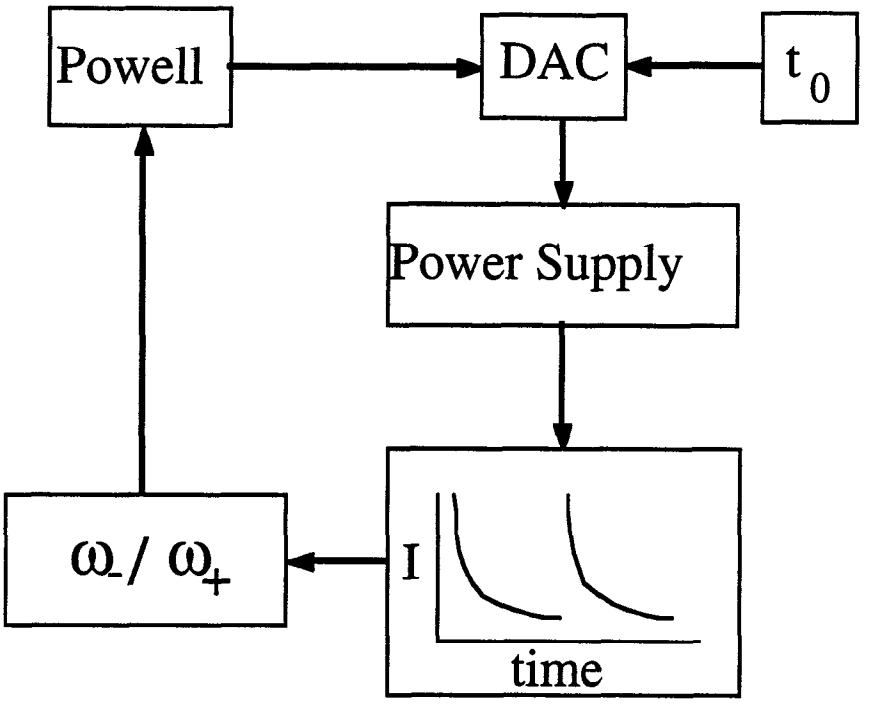


Fig. 2 The procedure for optimizing the flipping efficiency of the spin-flipper consists of loading the coefficients of a polynomial into a digital-to-analog converter (DAC), which drives a power supply to produce a time dependent variation of current through a spin-flipper. The DAC is reset when a new spallation event is detected (every 50ms). The reflectivities $\omega_+$ and $\omega_-$ are measured and used to compute the integral of the flipping ratio over time, $\varphi$, whose maximum is desired. An algorithm, called "Powell" in the diagram, perturbs the polynomial coefficients until $\varphi^{-1}$ is minimized (or the integrated flipping ratio is maximized).

then the spin-down reflectivity, $\omega_-$, of the analyzer should be zero. In other words, the ratio $\omega_+/\omega_-$, called the flipping ratio, should diverge for all neutrons with wavelengths in the range of 2 to 8Å. The optimum values of *a, b, r* and *s* are those which maximize the flipping ratio. The values of these parameters were determined from the procedure shown in Fig. 2.

This procedure first calculates $I_f(t)$ and $I_c(t)$ for an initial set of guess parameters over a 50ms (the duration between successive spallation events or proton pulses at LANSCE) time range. These values are loaded into a BiRa 12 bit digital-to-analog (DAC) CAMAC module [5], which produces two analog signals (one for each coil). The signals are triggered during every proton pulse and used to drive two Kepco programmable bipolar power supplies [6], which operate in current control mode. The currents pass from the power supplies through the flipping and compensating coils producing a magnetic field inside the spin-flipper that changes with time as prescribed by equations (1) and (2). When properly tuned, every neutron precesses in the changing magnetic field through the same angle so that the polarization of the neutron beam is anti-parallel to the direction of the magnetic field in the guide and that which is applied to the sample (spin-down). When no precession is desired, the DAC produces a constant zero voltage signal which results in no current to the spin-flipper. In this situation the magnetic field inside the spin-flipper is produced by the magnetic guide; thus, the polarization of the neutron beam is the same as that which is reflected from the polarizing super-mirror (spin-up). Since the spin-down neutron reflectivity of the analyzer (or sample) is much smaller than for the spin-up reflectivity, spin-down measurements are accumulated for longer periods of time (typically five times longer) than the spin-up measurements in order to obtain roughly equal statistical quality for both measurements.

After normalizing the $\omega_+$ and $\omega_-$ reflectivities to their respective exposures, which are measured by an incident beam monitor, the variation of the flipping ratio with time-of-flight

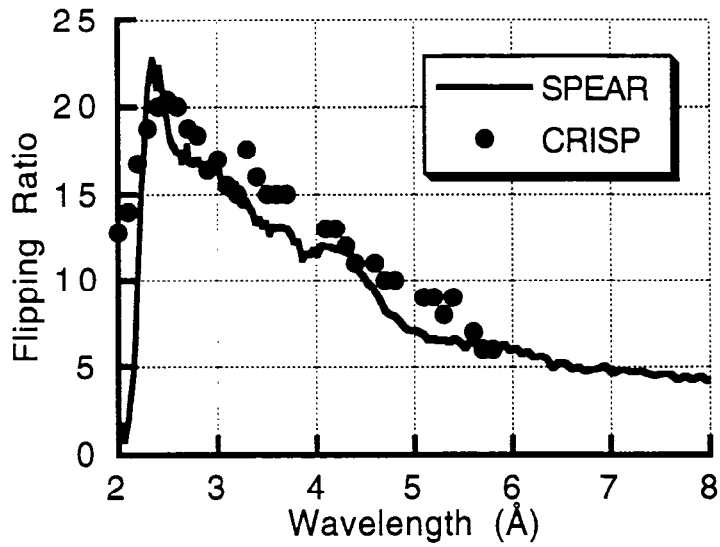


Fig. 3 Flipping ratio plotted versus wavelength as observed with SPEAR (solid curve) and CRISP (•).

(TOF) for a particular set of parameters *a, b, r* and *s*, is calculated. The problem of determining optimal values for *a, b, r* and *s*, is now one of maximizing the integral of the flipping ratio over the time-of-flight of all polarized neutrons (in practice, $\varphi^{-1}$ is minimized),

$$\varphi(a,b,r,s) = \int \frac{\omega_+}{\omega_-} dt \ . \tag{3}$$

The location of the minimum of $\varphi^{-1}$ can be efficiently determined by utilizing any number of computational algorithms which are designed to minimize a function of several arguments. The algorithm chosen for use at LANSCE is Powell's Quadratically Convergent Method [7]. While this algorithm does not converge as quickly as those that use information about the gradient of a function to locate its minimum, the Powell search algorithm can be relatively easily constrained. This is a practical consideration, since the current limits of each power supply are chosen to protect the spin-flipper coils from damage. Gradient information used in conjugate gradient and variable metric minimization methods often test parameter sets which result in currents that exceed the limits of the power supplies, consequently, causing the more sophisticated methods to fail.

The Powell procedure involves perturbing *a, b, r* and *s*, along orthogonal directions that eventually lead to the location of an extremum. After each perturbation, $\omega_+$ and $\omega_-$ are measured, and a new $\varphi^{-1}$ , $\varphi'^{-1}$, is calculated. The change of $\varphi'^{-1}$ from $\varphi^{-1}$ is used to calculate new parameters, *a', b', r'* and *s'*, representing a new set of directions, and the process is repeated until $\varphi'^{-1}$ differs from $\varphi^{-1}$ by about 1%. The optimization procedure requires approximately six hours to complete when the neutron source runs reliably at 60μA. Interestingly, the optimal value of *a* that was obtained for SPEAR, corresponded to a precession angle of $3\pi$. This angle was found to yield better flipping ratios than a precession angle of $\pi$. A plot of the flipping ratio versus wavelength measured after the optimization routine was completed is shown in Fig. 3 as the solid curve. This flipping ratio is very comparable to that obtained at CRISP (•'s in Fig. 3), which utilizes a Drabkin spin-flipper rather than a flat-coil spin-flipper [8].

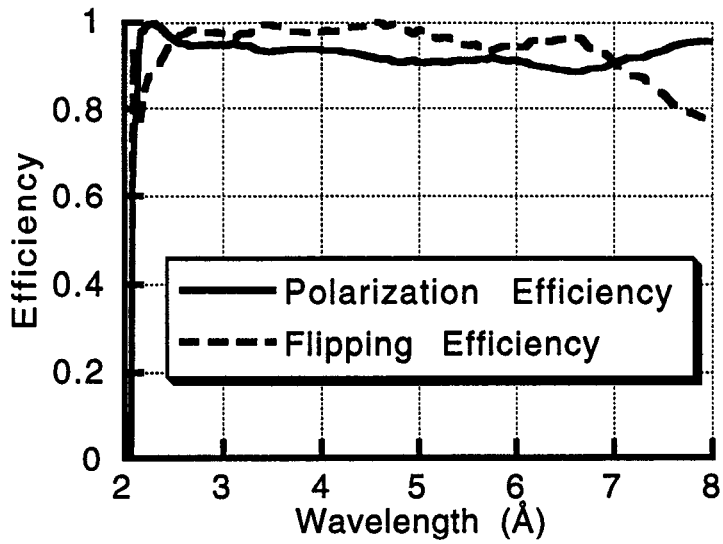


Fig. 4 The variation of polarization (solid curve) and flipping (dashed curve) efficiencies versus wavelength measured for SPEAR.

The flat-coil spin-flipper used at LANSCE is considerably larger than those in use at the ILL. Both are about 12cm by 12cm in cross-sectional area, but the LANSCE version is 2.5cm long while the ILL version is about half as long. A second much shorter (only 0.6cm long) flat-coil spin-flipper was also tested at LANSCE; however, the shorter design obtained flipping ratios only half as large as those shown in Fig. 3. The poorer performance of the shorter flipper might be attributed to an inability to obtain precession angles of $3\pi$, since the power supplies could not supply currents large enough to generate a flipping field that could precess fast neutrons through the larger angle. Based on this test the optimal flat-coil flipper design would seem to be one utilizing a relatively long flight path and high currents to precess neutron spins by at least $3\pi$.

After the spin-flipper was optimally tuned, the polarization and flipping efficiencies of the polarization components were measured in a procedure requiring four different reflection measurements of the analyzer [9]. The measurements included spin-up and spin-down measurements with and without a depolarizing Fe foil (shim) inserted between the polarizing mirror and spin-flipper. By comparing the ratios of these measurements, the polarization and flipping efficiencies, $P(\lambda)$ and $F(\lambda)$, respectively, were obtained (Fig. 4). Since the polarizer and spin-flipper are imperfect, mixtures of polarization states are actually reflected from a sample; therefore, $P$ and $F$ are used to correct the observed reflectivities $\omega_+$ and $\omega_-$ to obtain the "true" spin-up and spin-down reflectivities, $R_+$ and $R_-$. $R_+$ and $R_-$ can be compared directly to model calculations. The relationships between $R_+$ and $R_-$ with the observed reflectivities are given in equation (4).

$$R_{\pm} = \omega_+ \pm \frac{1 \mp P}{2PF} (\omega_+ - \omega_-) \tag{4}$$

## 3. Application of PNR to Measure the Magnetization Profile of a Thin Fe Film on a MgO Substrate

As an example of using PNR with SPEAR, results from measurements of a thin Fe film on MgO are presented. The thin-film (ca. 267Å thick) was epitaxially grown on a polished $4cm^2$ single-crystal wafer of MgO heated to a temperature of 500°C. The $\omega_+$ and $\omega_-$ reflectivities were accumulated after alternating between many spin-up and spin-down

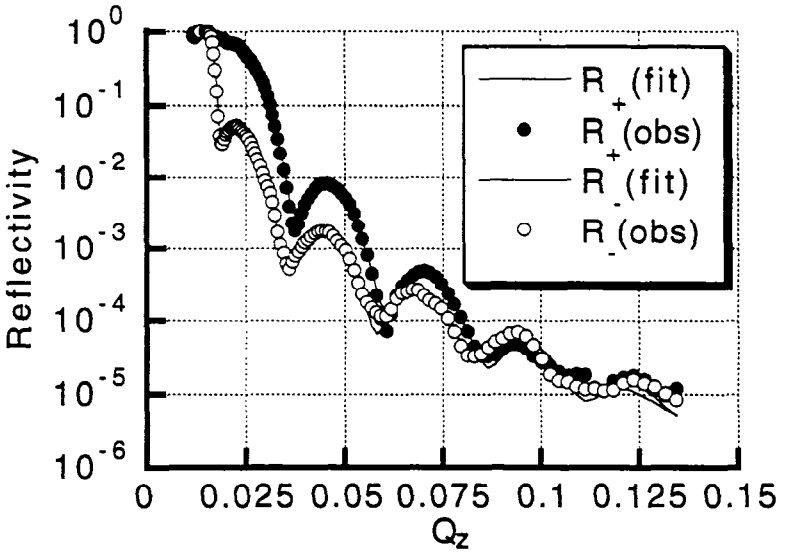


Fig. 5 Polarized neutron reflectivities, $R_+$ (•) and $R_-$ (o), from an Fe thin-film epitaxially deposited on a single-crystal MgO substrate. The solid curves are calculated reflectivities from a model structure discussed in the text.

measurements— each lasting ca. 5 and 15 minutes, respectively. In order to obtain reflectivities for momentum transfers as large as 0.15Å$^{-1}$ within the polarized wavelength range of 2 to 8Å, the data collection required three measurements at different angles of incidence. Each measurement was corrected for the variations of the incident beam spectrum and polarization and flipping efficiencies to yield $R_+$ and $R_-$ by software adapted from that which is already used to analyze unpolarized reflection data collected with SPEAR. Additional software was written which concatenates an arbitrary number of smaller reflection measurements to produce reflectivity curves, $R_+$(•) and $R_-$(o), like those shown in Fig. 5 for the Fe/MgO sample. The data in this figure required a total of eight hours to collect.

The software package used to reduce data from polarization experiments also affords the user the opportunity to optimize parameters of model structures so as to find a model that best fits both reflectivity curves (spin-up and spin-down) simultaneously. Parameters that can be optimized include: layer thickness, nuclear and magnetic scattering length densities, and interfacial roughness. This software was used in the following analysis to determine the magnetization profile as a function of depth into the Fe on MgO sample.

In the model, the Fe film was represented by three layers, consisting of a thin (25Å thick) native oxide ($\gamma$-$Fe_2O_3$, a ferrimagnet), an Fe interior, and a phase boundary region with a reduced density compared to that of the film interior. The oxide layer is motivated by Mössbauer studies of similarly grown Fe single-crystals which determined the stochiometry, phase and thickness of the native oxide [10]. The thickness of the oxide layer determined in the present study is in good agreement with that determined by the Mössbauer work. The magnetic moments of Fe atoms in the oxide (1.6$\mu_B$) and Fe interior (1.8$\mu_B$) are both somewhat smaller than those measured for bulk materials (cf. 2.3$\mu_B$ and 2.2$\mu_B$, respectively [11]). These reductions may be due to a property of the thin-film geometry or an inability to fully magnetize the sample in the 1.17kG field. If the sample had not been fully magnetized, then some spin-flip scattering from the sample may have occurred. Since the current instrument can not analyze the polarization state of the scattered radiation, spin-flip scattering is not detected and assumed not to have occurred. During 1993, polarization analysis equipment will be installed so that spin-flip scattering can be detected when it occurs.

A separate layer representing the interface between the Fe film and MgO substrate— a phase boundary, with a much reduced density (66% of the Fe interior) and enhanced magnetic moment ($2.5\mu_B$) was required in order to obtain a good fit to the data. The notion of a phase boundary region is motivated by X-ray diffraction observations taken at grazing incidence of a reconstructed interface between the Fe film and MgO substrate [12]. Like grain boundaries, which often have densities 20% less than the bulk [13,14], phase boundaries are also expected to be less dense than the bulk. The enhancement of the magnetic moments of Fe atoms in the phase boundary may be a consequence of its reduced density, since the magnetic moments of transition metal atoms, like Fe, are known to increase as their densities are reduced [15]. The present study of the Fe/MgO system is one example of the importance of interfacial structure on the magnetic character of interfaces.

## 4. Future Plans

The magnetic native oxide on the Fe film illustrates a difficulty encountered in studies of surface and interface magnetism— how can the magnetism of surfaces and interfaces be observed in their pristine state? While passivating materials can be used to prevent oxidation, these materials can also profoundly change the magnetism system they are trying to protect. For example, the diffusion of Al or V into Fe can depress the Curie temperature of the Fe film [16] so that a magnetic Fe surface may become non-magnetic. The best approach to the study surface and interfacial magnetism is to avoid oxidation in the first place by fabricating samples *in situ*. Not only is oxidation avoided, but changes in the magnetic structure of a sample can be observed during its fabrication, e.g. magnetism can be monitored as layers of different materials are deposited to form multilayer structures. This approach has been implemented at LANSCE with the construction of a fabrication system with the following characteristics:

- samples can be fabricated under ultra high vacuum conditions,
- heating filaments can raise the temperature of the sample to greater than 700°C,
- sapphire windows allow polarized neutrons to enter and exit the chamber for reflection studies, and
- magnetic fields in excess of 1T can be applied to the sample during its fabrication (if desired), and while PNR measurements are collected.

During 1992, this equipment was used to manufacture and study thin films of Fe and Ni on Si substrates *in situ*. The polarized neutron reflectivity from a thin Fe film prepared *in situ* is shown in Fig. 6. The data required one change of incident angle, and seven hours of collection time. This collection time is sufficiently long that for the vacuum in the chamber ($1 \cdot 10^{-6}$Pa), a monolayer of oxygen probably formed on the sample surface. For the 1993 experiment, an ion pump will be used to improve the vacuum by one to two orders of magnitude. Combined with improvements in the polarization optics, which decrease data collection time, studies of surface magnetism of thin-films and multilayer samples in their pristine state should be possible. In particular, the onset of spin-flip scattering like that observed in Fe/Cr multilayers [17], can be monitored after each deposition step in the fabrication of a multilayer. This experiment is planned for completion in the summer of 1993. At a next generation advanced spallation source where the incident intensity might be 25-50 times greater, these PNR measurements could be made during the actual deposition of a thin-film sample, rather than after the completion of each step in the deposition process. This capability would permit studies of dynamic processes during the fabrication of magnetic and non-magnetic thin-films and multilayers.

The construction of the polarization equipment for neutron reflection studies was supported by the U.S. Department of Energy, Office of Basic Energy Sciences, under contract W-7405-Eng-36. Funding for PNR measurements of the thin-film samples and construction of the "*in situ* fabricator" was obtained from Laboratory Discretionary Research and Development resources (project XA62).

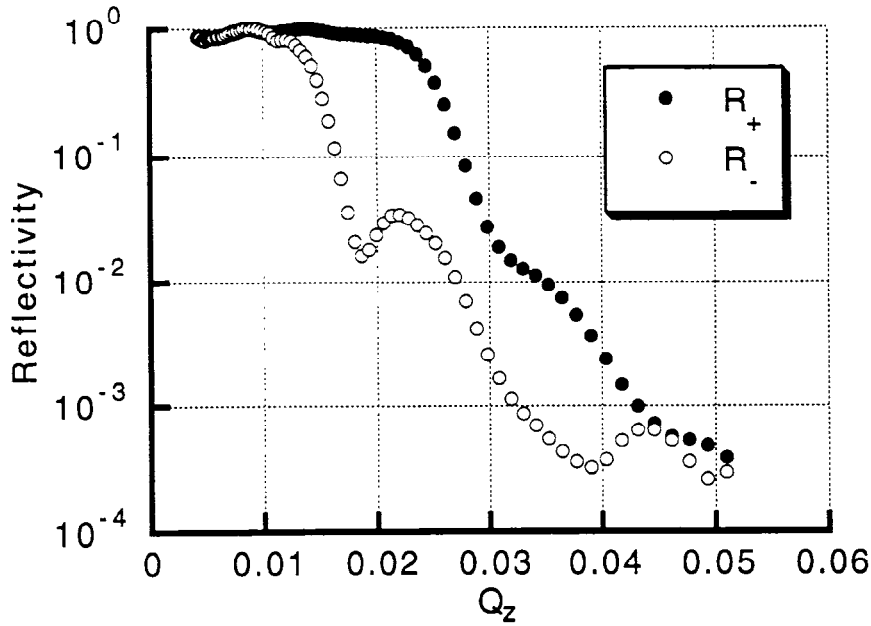


Fig. 6 Polarized neutron reflectivities, $R_+$ (•) and $R_-$ (o), measured from an Fe thin-film epitaxially deposited *in situ* on a single-crystal Si substrate.

## References


[1] G.P. Felcher, R.O. Hilleke, R.K. Crawford, J. Haumann, R. Kleb and G. Ostrowski, Rev. Sci. Instrum., **58**(4), 609 (1987).
[2] L.M. Falicov, D.T. Pierce, S.D. Bader, R. Gronsky, K.B. Hathaway, H.J. Hopster, D.N. Lambeth, S.S.P. Parkin, G. Prinz, M. Salamon, I.K. Schuller and R.H. Victora, J. Mater. Res., **5**(6), 1299 (1990).
[3] Co-Ti polarizing were kindly provided to us by Dr. O. Schärpf (ILL).
[4] O. Schärpf in *Neutron Spin Echo,* edt. by F. Mezei, Springer-Verlag, Berlin 27 (1980).
[5] BiRa Systems Inc., Albuquerque, New Mexico USA.
[6] Kepco Inc., Flushing, New York USA.
[7] W.H. Press, B.P. Flannery, S.A. Teukolsky and W.T. Vetterling, *Numerical Recipes*, Cambridge University Press, New York, pp. 294-301.
[8] R. Felici, J. Penfold, R.C. Ward and W.G. Williams, Rutherford Appleton Laboratory report #RAL-87-047 (1987).
[9] *ibid.,* RAL-87-025 (1987).
[10] T. Shinjo, T. Shigematsu, N. Hosito, T. Iwasaki and T. Takada, Jap. J. of Appl. Phys., **21**(4), L220 (1982).
[11] R.S. Tebble and D.J. Clark, Magnetic Materials, Wiley-Interscience, New York (1969).
[12] M.R. Fitzsimmons, M. Mueller-Stach and E. Burkel, to be published.
[13] M.R. Fitzsimmons and S.L. Sass, Acta. Metall., **36**(12), 3103 (1988).
[14] *ibid.,* **37**(4), 1009 (1989).
[15] V.L. Moruzzi, Phys. Rev. Lett., **57**, 2211 (1986).
[16] M. Hansen and K. Anderko, Constitution of Binary Alloys, 2nd ed., McGraw-Hill Book Co., New York, pp. 91,729 (1958).
[17] J.F. Ankner and C.F. Majkrzak, to be published in the proc. of the 37th Annual Conf. on Mag. and Mag. Mater., Houston (1992).

# New aspect in employing magnetic anisotropic FeCo thin films as neutron polarizers

D.A.Korneev

Laboratory of Neutron Physics, Joint Institute for Nuclear Research,
141980 Dubna, Moscow region, Russia

## ABSTRACT

Reversal of the beam polarization vector is a necessary procedure in carrying out experiments with polarized neutrons. At present a number of methods and set-ups (spin-flippers) are widely used in experiments utilizing thermal polarized neutrons. A new way to achieve neutron beam polarization of a necessary sign during the process of neutron specular reflection from ferromagnetic anisotropic mirrors is proposed. The results of its check-up testing with a polarized neutron beam are given. The measured spin reversal probability by this method is near to unity, and, practically, it does not depend on the neutron wavelength. The application of the given way lets one exclude the spin-flipper as an element of polarized neutrons set-ups.

## INTRODUCTION

Neutron reflection from the surface of ferromagnetic films is a widespread method of getting thermal polarized neutron beams. D.Hughes and M.Burgy were the first to use a ferromagnetic mirror as a neutron polarizer[1]. Hereafter this technique was being extensively developed (see[2], for instance). Polarizing mirrors on the base of the FeCo alloy sputtered on the absorbing sublayer TiGd, multilayer thin film structures with alternate layers of ferromagnetic and non-ferromagnetic materials are much used nowadays. Mirror polarizers make it possible to choose the right ferromagnetic alloy reflecting only the neutrons which spins are parallel to a magnetic induction vector of a mirror. As a result the spins of the reflected neutrons are directed towards an external magnetic field. A high value of polarizability ($95 - 97\%$), weak spectral dependence of polarization and ease of operation make wide use of neutron mirror polarizers at stationary as well as at pulsed neutron sources.

A change of sign of a polarization beam, i.e. mutual reverse of a polarization vector and an external magnetic field is very important during polarized neutron experiments. To realize this one needs spin-flippers - the devices for mutual reverse of the external magnetic field and beam polarization. Spin-flippers impair polarization spectral characteristics and limit the luminosity of set-ups. For example, a well-known Drabkin spin-flipper has a bounded region of neutron spin reverse.

A new way of obtaining beams of different polarization signs with the help of thin magnetic anisotropic films is discussed in this paper. The experimental results of the check-up are presented.

## THE GROUND OF THE NEW METHOD OF POLARIZATION

As it is known, the ferromagnetic with a flat boundary can be described by the following jump of the neutron optical potential

$$U\pm = U_n \pm \mu(4\pi M_p), \tag{1}$$

where $U_n = 4\pi\frac{\hbar^2}{2m} \cdot N \cdot b$ is a neutron nuclear optical potential, N is a number of nuclei per unit volume, $b$ is an average neutron scattering length, $M_p$ is the projection of a magnetic moment on a reflecting surface. The fact that a neutron spin is equal to one half results in the existence of two potentials. Thus, if one chooses the right ferromagnetic alloy, then

$$U_- = U_n - 4\pi\mu M_p = 0.$$

As a result only the neutrons with a magnetic moment facing away from the vector $\vec{M}_p$ will be reflected from the matter boundary, because $U_+ = U_n + 4\pi\mu M_p > 0$. A very important fact should be noted here: during the neutron magnetic moment interaction with the boundary of ferromagnetic matter, the derection of polarization in the reflected beam is determined only by the direction of the vector $\vec{M}_p$. The magnetic field vector does not enter into the equation (1). Thus, it is easy to show that in the system of coordinates connected with the external magnetic field $\vec{H}$ polarization in the reflected beam will depend on the angle $\theta$ between the vectors $\vec{M}_p$ and $\vec{H}$, i.e.

$$P(\theta) = P_o(\lambda) \cdot Cos(\theta), \tag{2}$$

where $P_o(\lambda)$ is mirror polarizability along the $\vec{M}_p$ direction.

From (2) it follows that

$$P(\theta = 0) = -P(\theta = \pi) \tag{3}$$

Therefore, for a polarizer where $M_p$ does not depend on $H$, the change of mutual orientations of vectors $\vec{P}$ and $\vec{H}$ in a reflected beam can be achieved by the magnetic field reverse.

Single-axis anizotropic magnetic films with a rectangular hysteresis loop, see Fig.1, are the ones which are practically free from the dependence of $M_p$ on $H$ in the interval of $|H| < H_c$. From this it follows that for the films with such a hysteresis loop the change of the field sign at $|H| < H_c$ will result in the change of sign of the reflected beam polarization.

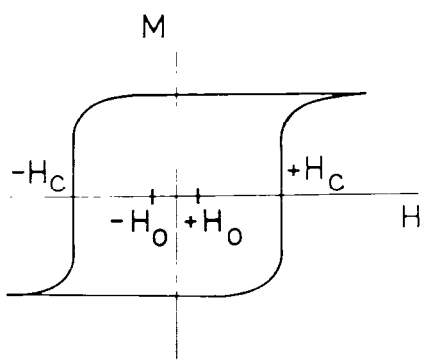


Fig.1. The typical magnetization reversal curve of a single-axis anisotropic film, when the magnetic field is directed to the "easy axis" of anisotropy of a film. In the region $-H_o < H < H_o$ the dependence of the magnetic moment $\vec{M}_p$ of a film on the volume and direction of an external magnetic field $H$ is absent.

## EXPERIMENTAL CHECK-UP OF THE METHOD

To examine the suggested technique we have used a polarizing mirror with the $Fe(40)Co(60)$ film (1500$\AA$ thick) with the $Ti(85)Gd(15)$ sublayer sputtered on a float glass plate. The film was being sputtered in the magnetic field of 250 Oe at the temperature of a glass plate equal to 150 $^oC$. Single-axis anisotropy of the film occurred due to the magnetic field. The value of the film coercive force was $H_c = 95$ Oe. The mirror was placed into a polarized beam behind a polarizing neutron guide. A change of polarization of an incident beam was performed by a spin-flipper. The mirror was put into a gap of the electromagnet allowing one to change both the value and sign of a magnetic field. The $\vec{H}$ vector coincided with the anizotropy axis of the film. Magnetic field behaviour at the electromagnet inlet provided the adiabatic guide of the spin at any field direction in the gap. Reflected intensities $N_+$ (spin-flipper "off") and $N_-$ (spin-flipper "on") for different values of fields in the electromagnet were measured with the $^3He$ detector. A combination of the measured intensities was analysed:

$$\frac{N_+ - N_-}{N_+ + N_-} = P_o \cdot P_m(H), \tag{4}$$

where $P_o$ is incident beam polarization, $P_m$ is mirror polarizability. Equation (4) is true for the case that spin reverse probability by a spin-flipper is $f = 1$. In our case the latter condition was realized with an accuracy of $5 \cdot 10^{-3}$ in the region of a neutron wave length $\lambda < 6\AA$.

## THE MEASUREMENT OF FIELD DEPENDENCE OF $P_m$

At first the mirror was magnetized by a negative magnetic field of 500 Oe. After that the field decreased to zero and then increased in a positive direction. Fig.2 shows the experimental dependence of $P_o \cdot P_m(H)$ on the magnetic field. Here $P_o$ and $P_m(H)$ are an average over the spectrum beam polarization and mirror polarizability, respectively. It is seen from the shape of a curve that in $H < 80$ Oe $P_o \cdot P_m(H)$ does not depend on the value of an applied field; in this case it is negative. It means that the magnetization vector $\vec{M}_p$ is opposite to the external field. In the fields $H > 80$ Oe the reversal of magnetization begins; the process ends in the fields of $\geq 200$ Oe. Then at a decrease of the field $P_m(H)$ does not depend on the field and it is positive. It means that the magnetization vector $\vec{M}_p$ is parallel to $\vec{H}$. Therefore the bottom and top parts of the experimental curve correspond to opposite and unidirectional orientations of the vectors $\vec{M}_p$ and $\vec{H}$, respectively.

The measurements have shown that $P_m = -P_m^{'}$ with a high degree of accuracy (about $5 \cdot 10^{-3}$) in the region $H \leq 70$ Oe, where $P_m$ and $P_m^{'}$ mirror polarizabilities correspond to the bottom and top parts of a hysteresis loop.

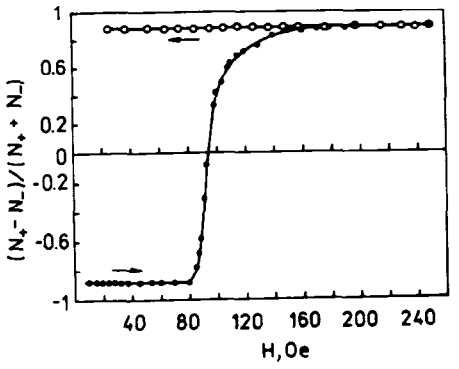


Fig.2. The experimental dependence of $P_o \cdot P_m(H) = \frac{N_+ - N_-}{N_+ + N_-}$ on the external magnetic field parallel to the "easy axis" of the anisotropic $FeCo$ film. At first the film was magnetized in the opposite direction to the external magnetic field. The reversal of magnetization of the film leads to the changing of sign of film polarizability.

## THE MEASUREMENT OF WAVELENGTH DEPENDENCE OF $P_m$

For spectral properties check-up of mirror polarizability we have measured $P_o \cdot P_m$ according to a neutron wave length in the fields $H_1 = -8$ Oe and $H_2 = +8$ Oe.

Fig.3 shows experimental functions $P_o \cdot P_m$ for these values of the fields. The ratio $\frac{P_m(\lambda,H_1)}{P_m(\lambda,H_2)}$ got from the experimental curves 1 and 2 differs from -1 no more than $5 \cdot 10^{-3}$ in the measured interval of neutron wave lengths $\lambda = 1.5 \div 6\mathring{A}$.

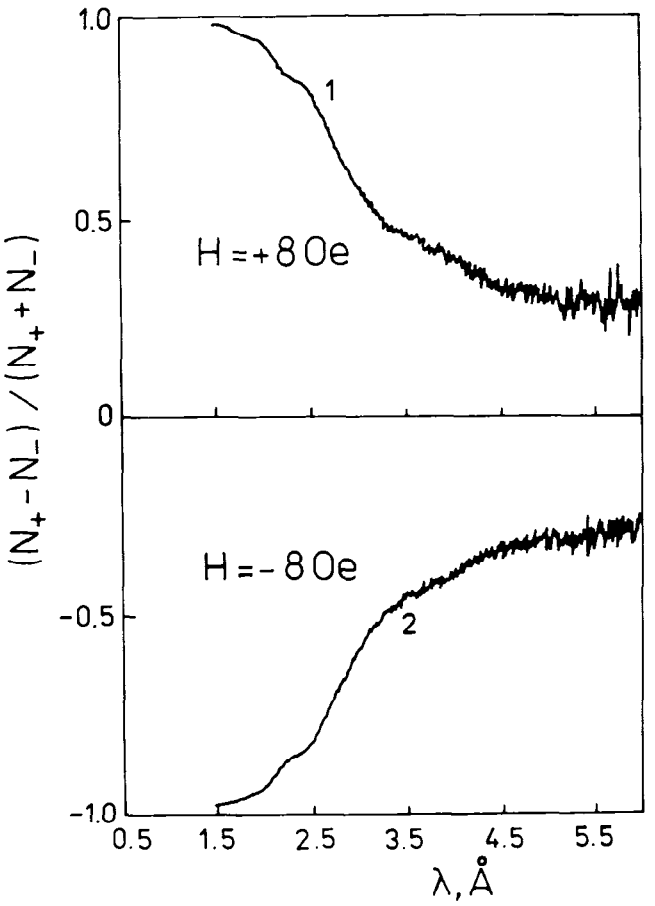


Fig.3. The experimental wavelength dependence of $P_o \cdot P_m(H) = \frac{N_+ - N_-}{N_+ + N_-}$ for the $FeCo$ single-axis anisotropic film: curves 1,2 correspond to the magnetic field equal to +8 Oe and −8 Oe, respectively. The changing of sign of the external magnetic field leads to the changing of sign polarizability of the film in a wide range of the wavelengths.

## CONCLUSION

A new method of getting polarized neutrons with a necessary sign of polarization by specular reflection from a magnetic anisotropic film is suggested. Its checkup on the single-axis anisotropic $FeCo$ film have shown that the reflected beam polarization and the external magnetic field change their sign simultaneously. The efficiency of the change of sign of neutron beam polarization due to the change of sign of an external magnetic field is near to unity and is independent of a neutron wave length.

The application of the given method allows one to perform the mutual reverse of a neutron spin and external magnetic field not using a spin-flipper.

## ACKNOWLEDGMENTS

The author is indebted to Drs. A.V.Petrenko, E.B.Dokukin, V.V.Pasyuk for the help in carrying out the measurements and to Dr. A.F.Schebetov for the FeCo films preparation.

Thanks are due to Mrs. T.A.Filimonycheva who made a translation of the paper into English.

## REFERENCES

1. D.J.Hughes, M.T.Burgy, "Reflection of Neutron from Magnetized Mirrors", *Phys.Rev.*, 81, 498, (1951)
2. W.G.Williams, *"Polarized Neutrons"*, Oxford, Clarendon Press, (1988)

# User Dedicated Neutron Guide System at SINQ

W. Wagner and J. Duppich

Paul Scherrer Insitut
5232 Villigen PSI
Switzerland

## Abstract:

The neutron guide system for the Swiss continuous spallation source SINQ is now specified in detail and entered the period of manufacturing. The design of the guide system was dominated by the intention to provide an optimum supply for dedicated types of instruments by simultaneously considering the best possible conditions for future users. It consists of seven individual guides, starting at a distance of 150 cm from the 20 l liquid $D_2$-moderator. All guides are curved to prevent the direct view to the source within a 25 m shielding bunker, thus filtering the high energy neutrons and other disturbing radiation. Supermirror coating of five guides, combined with a shallow curvature, will allow access to even thermal neutrons up to 36 meV in energy or down to 1.5 Å in wavelength, respectively.

# Introduction

The concept of the new Swiss spallation Source SINQ is that of a steady state neutron source, driven by a 590 MeV proton beam from the PSI-ring cyclotron. The time structure (51 MHz) of the proton beam is lost after hitting the spallation target and releasing the neutrons into the moderating $D_2O$ surrounding the target. The thermal flux expected in the $D_2O$-tank near the target is in the $10^{14}$ $cm^{-2}s^{-1}$ range [1]. At a distance of about 10 cm from the target surface, a 20 litre liquid $D_2$-cold moderator will be placed inside a T-shaped beam tube, as illustrated in Fig. 1. The one of the T-wings directing south will feed the neutron guide system of SINQ. The guide entrance is located at a distance of 1,50 m from the cold moderator surface, viewing a moderator cross section ("entrance window") of 135 x 80 $mm^2$. In their angular arrangement, all guides are directed towards this window to ensure optimum illumination.

## The in-shielding section

The first section of the guide system with a length of roughly 4.5 m is located inside the target shielding block . It consists of two separate bundles of guides, containing three guides each, with angular inclinations between 4° to 6° towards both sides of the central axis (cf. Fig. 1). This 4,5 m-section is enclosed in a gas-tight casing, filled with Helium (HeII) at a pressure of about 1.1 bar, which circulates by forced ventilation and is backcooled outside the plug to ensure the necessary heat removal from the guide entrance section.

Each of the two guide bundles is adjusted inside of a steel casing. Both casings together are mounted on a plug wagon (Fig. 2) which carries supporting and adjustment devices for the casings. All open space is filled with steel shielding. The wagon is set up on a high precision railway system which allows removal and reproducible re-installation of the entire plug insert with a remotely controlled handling device, attaining the correct alignment even after years of operation and severe activation of the components.

## Out-of-shielding section

Outside the plug insert the guides are continued individually, self sealed and evacuated. Following the PSI-numbering system (PKS), the guides are numbered (cf. Fig. 2) =1RNR11 to 16 inside the plug. Outside, guide =1RNR16 ist splitted horizontally into two separate guides, than numbered =1RNR16 and 17. The seven guides cross two shielding bunkers at a length of about 24 m before they penetrate a three meter thick shielding wall and exit into the guide hall. Inside these bunkers, all guides are curved to prevent the direct view to the in-shielding section and to the source.

Fig. 3 shows schematically the guide cross sections, the geometric arrangement and envisaged coating of the curved section inside the guide bunker. Fig. 4 gives an overview of the entire guide system showing the floorplan of the source, the bunkers and the guide hall.

## Characteristic data and performance

The characteristic guide data are given in Table 1 together with a list of proposed instruments for the initial operation period. These data result from the combination of various

considerations with the aim to obtain a user dedicated but still universal guide system of excellent total performance:

- The **inclinations** against the central axis were chosen as the result of the consideration of an optimum illumination from the source, flux depression, available space and geometric arrangement.

- The **dimensions in height** were determined by the height of the entrance window at the source (135 mm), combinded with the aim of an optimum illumination. These considerations led to a uniform height of 120 mm for all guides. After splitting guide =1RNR16, a square cross section of 50 x 50 $mm^2$ resulted for both subunits.

- The choice of the **width** of each guide was based on the combination and optimization of various considerations: first of all the instrument requirements on Q-resolution, useful beam divergence, characteristic wavelength and instrument position. Further, the requirement on a sufficient guide curvature to prevent the direct view to the source, and finally the given building geometry. A considerable role in this optimization process played

- the choice of **coating**: After the successful in-house development of large-scale supermirror production [2], PSI had the possibility of an ab-initio design of the guide system using supermirror (SM) coating. Thus, the maximum reflection angle for neutrons could be increased considerably compared to the critical angle of conventional single-layer coating with Ni. For the SINQ-guide system, either twice the critical angle of Ni (SM2), or a 20% increase (SM 1.2), simulating (isotopically enriched) Ni-58 coating, was taken into consideration.

The choice of coating affects two important performance parameters of the system: the transmitted **beam divergence** and the **characteristic wavelength**.

Regarding the former, a higher beam divergence of a supermirror coated guide yields on intensity gain, for SM2 by a (theoretical) factor 4 for ideal reflectivity; for realistic reflectivities one obtains a factor of 2.5 to 3. The usefulness is obvious except for instruments of high Q-resolution (e.g. SANS, high resolution powder diffractometer) where the neutrons of high divergence disturbe the resolution. For those instruments dedicated guides are foreseen coated with natural Ni, at least in the straight section, in order to suppress the unwanted high divergencies at the instrument entrance.

Regarding the latter, SM coating shifts the characteristic wavelength of a curved guide towards smaller values, proportional to the inverse of the maximum angle of reflection. This shift in wavelength yields a real spectral gain of neutrons compared to conventional coatings, allowing the approach to the range of thermal neutrons with rather comfortable or conventional geometric characteristics of the guides (cf. Table 1). For example, all guides except =1RNR11 and 16 transport neutrons of wavelengths down to 2 Å and below, the guides =1RNR13 and 15 even to 1.5 Å.

The spectral gain is achieved even if the SM-coating is made only in the curved section, and there even if only the outer (concave) guide wall carries SM-coating. Such a choice is made for =1RNR12 and 17 (cf. Fig. 3 and Table 1) where the spectral gain is wanted but not the higher divergence. Guide =1RNR17 has, in addition to the SM-coating, a vertical division of the guide along the curved section to transmit 2 Å neutrons without reducing the useful width from 50 mm.

## Filtering high energy neutrons

Compared to a fission reactor a spallation source has (besides many advantages) the disadvantage that part of the initially produced neutrons are of high energy ($E \geq 10$ MeV) which requires massive shielding. Special precautions have to be taken to prevent that those neutrons come down the beam line and penetrate into the experimenal area. For the SINQ-guide system, the precautions foreseen combine the guide curvature with high energy collimators. The collimators consist of steped steel casings tightly enclosing the guides (gap $\leq$ 3 mm) on lengths of about 3 m each. They will consequently be installe i) inside the guide insert, ii) in the 3 meter exit wall from the bunker to the guidehall, and iii) approximately half way in between inside the bunkers. Calculations prove a more-than-sufficient attenuation of the high-energy neutrons by this collimator arrangement. It must not be mentioned that other unwanted radiation, from Gammas to epithermal or fast neutrons is also very efficiently eliminated by this precaution.

## References


[1] G.S. Bauer, Status Report SINQ, ICANS XII (1993)

[2] P. Böni, I.S. Anderson, P. Buffat, O. Elsenhans, H.P. Friedli, H. Grimmer, R. Hauert, K. Leifer, A. Menelle, J. Penfold and J. Söchtig , this volume (1993)

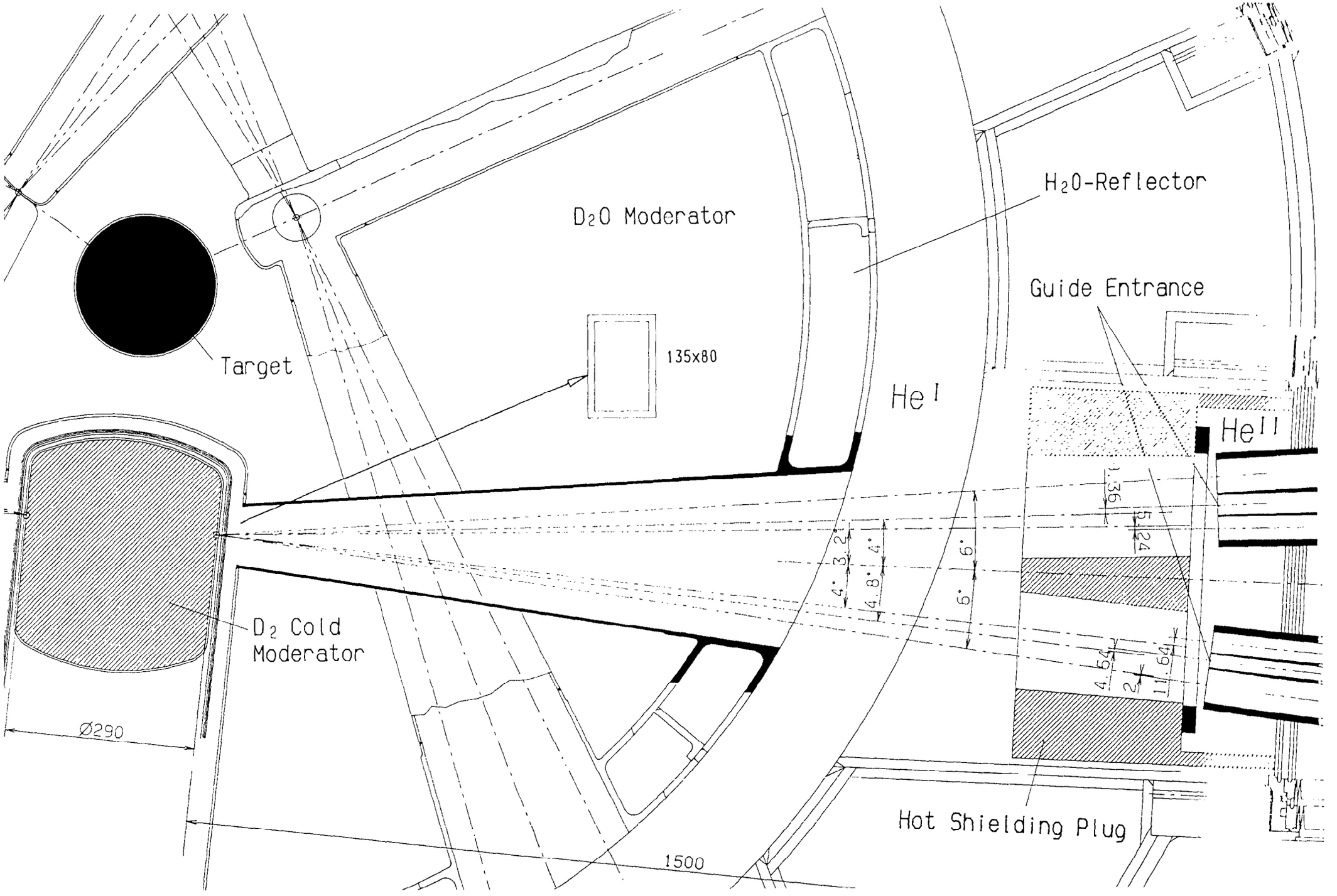


Figure 1: Schematic horizontal cross section through the SINQ target and $D_2O$ moderator tank at the height of the $D_2$-cold moderator vessel and the beam tube feeding the guide system.

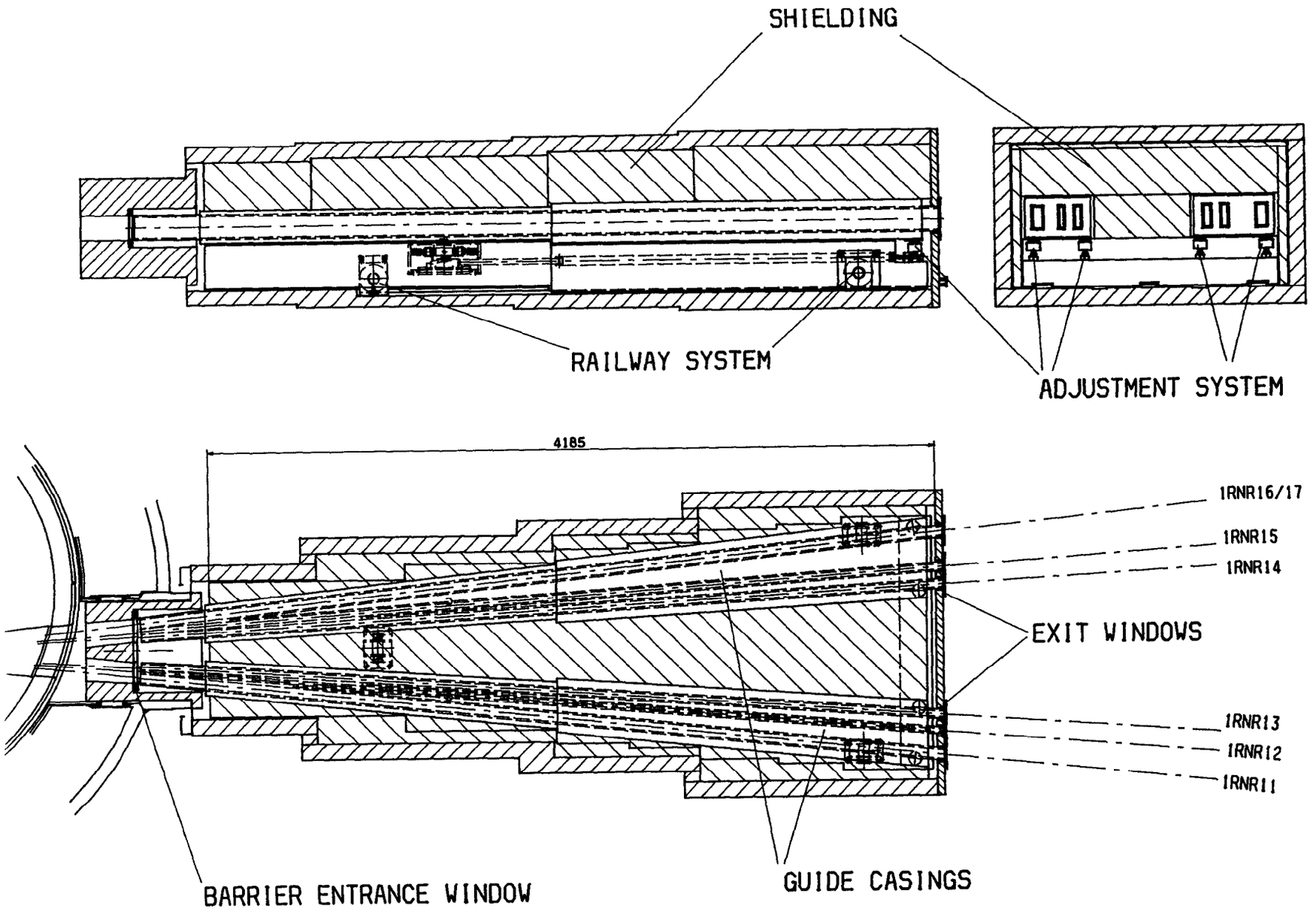


Figure 2: Triple-view of the neutron guide insert in the main shielding, showing the position of the two guide bundles and their casings, the plug wagon with railway and adjustment systems.

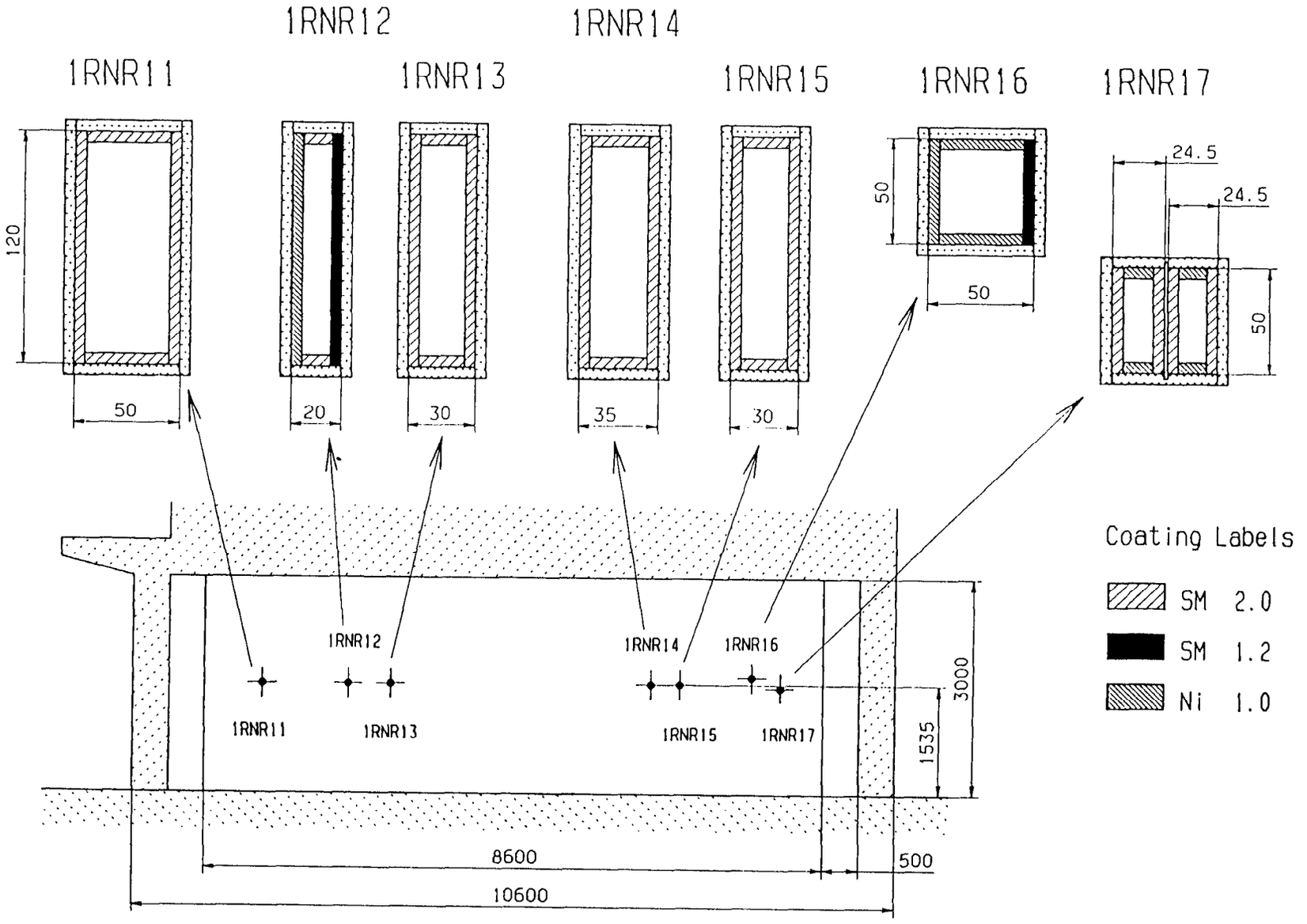


Figure 3: Guide cross sections, geometric arrangment and coating foreseen for the curved section inside the guide bunker (viewing to the source).

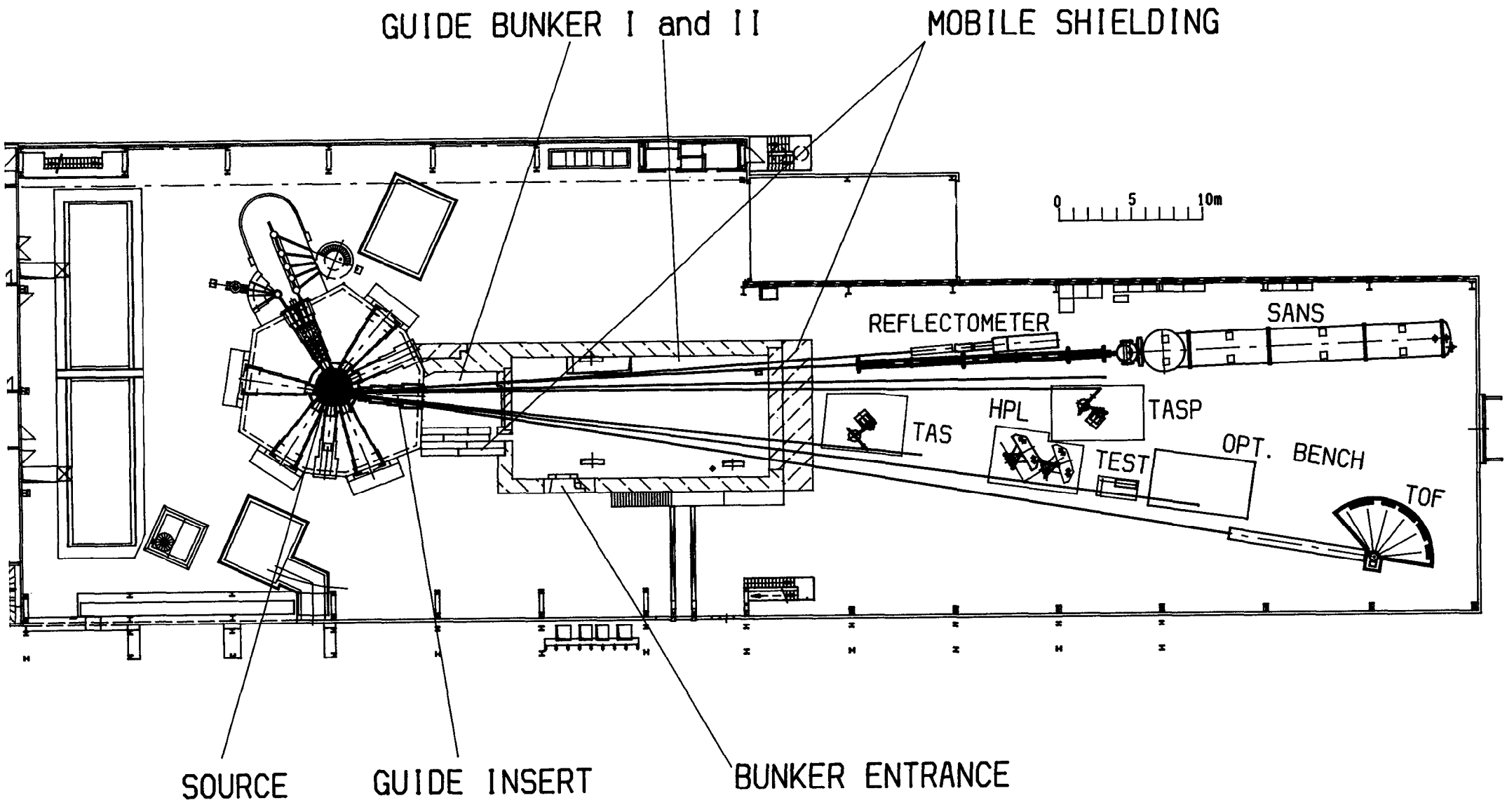


Figure 4: Floorplan of the SINQ-hall , showing the location of the source with the main shielding, the guide bunkers, the lines of the seven neutron guides and the instruments proposed for the first operation period.

| Guide (PKS) | Inclination against central axis | Dimensions width x height ($mm^2$) | $L_{CURV}$ (m) | $R_{CURV}$ (m) | Charact. wavelength $\lambda^*$ (Å) | | | Proposed instruments | | |
|---|---|---|---|---|---|---|---|---|---|---|
| | | | | | Ni | SM1.2 | SM2.0 | | | |
| 1RNR11 | -6° | 50 x 120 | 20 | 1445 ↘ | 4.9 | 4.2 | 2.4 | BSS | NN | TOF |
| 1RNR12 | -4.8° | 20 x 120 | 20 | 3612 ↘ | 2.0 | 1.7 | 1.0 | Powder Diffr. | Test | Opt. bench |
| 1RNR13 | -4.0° | 30 x 120 | 20 | 2408 ↗ | 2.9 | 2.5 | 1.5 | TAS | NN | NN |
| 1RNR14 | +3.2° | 35 x 120 | 20 | 2063 ↘ | 3.4 | 2.9 | 1.7 | | NN | TASP |
| 1RNR15 | +4° | 30 x 120 | 20 | 2408 ↘ | 2.9 | 2.5 | 1.5 | NN | NN | NN |
| 1RNR16 | +6° | 50 x 50 | 20 | 1445 ↘ | 4.9 | 4.2 | 2.4 | | | SANS |
| 1RNR17 | +6° | 2x24.5 x 50 | 24 | 1234 ↗ | 3.7 | 3.2 | 1.9 | Reflectometer | | |

↘ Curvature westward

↗ Curvature eastward

Day-One-Instrumentation

Options ready to realize

Table 1: Characteristic data of the SINQ neutron guide system, giving geometry and curvature parameters, the calculated characteristic wavelengths for three types of coatings with the decided choices labeled, and the proposed instruments for the initial operation period.

# COMPARISON OF NEUTRON EFFICIENCY OF REACTOR AND PULSED SOURCE INSTRUMENTS

F. Mezei, Hahn-Meitner-Institut/BENSC, Pf. 390128, D-14091 Berlin

## ABSTRACT

A global comparison of the luminosity of various types of neutron scattering instruments on reactors, traditional type short pulse spallation sources and a new type of long pulse spallation source show that with adapted instrumentation spallation sources outperform reactor sources of equal costs. Instrumentation ideas adequate for long pulses are described and an optimal combination of the two spallation source approaches is proposed.

## INTRODUCTION

Current common wisdom regards reactor and pulsed spallation neutron sources as "complementary" facilities. This statement is justified in the following sense: Over the spectrum of various applications a pulsed spallation (PS) source can provide some two orders of magnitude poorer luminosity (data collection rate) in some applications, and at the same time prove an order of magnitude brighter than a given reactor in other applications. (This actually roughly applies to ISIS and ILL.)

On the surface, this suggests that in order to cover all scientific opportunities offered by neutron scattering, both types of sources are needed. However, the argument of "complementarity" is incomplete: It does not include the costs aspect. What should really be compared is the "value for the money", i.e. how facilities of roughly equal costs compare in the various applications.

It is the purpose of this paper to show that an extremely simplified PS source design, (a kind of a pulsed version of the c.w. source under construction at PSI near Zurich) using a single proton linac and applying a few new instrumentation ideas can offer a very cost efficient source with a performance superior to reactors of similar price tag across the board in virtually all kinds of applications. It has to be emphasized that the new design proposed here is not an optimal PS source and that its performance can be dramatically boosted in two thirds of the applications by adding (rather expensive) storage or accelerator rings, but that it clearly outperforms reactor sources. The implication of these ideas for the design of an advanced optimized PS source facility such as ESS is that a possible way is suggested to enhance the power of the *10 Hz* target from *1 MW* to *5 MW*. This enhancement of power is necessary to make ESS a superior source compared to ILL in applications such as small angle scattering (SANS).

In what follows, the concept of a high power PS source will be described, which uses a modern linac as the only accelerator and its neutron luminosity will be compared to reactor and conventional type spallation sources. In doing this, a few new instrumentation ideas will be introduced in order to make best use of the long pulses available from a linac. These considerations will lead to the unavoidable conclusion that there is no room left for reactors in the next generation of neutron sources.

## FUNDAMENTALS

In Fig. 1 the relative luminosities of various sources [1] are compared, based on the following assumptions

a) The time averaged thermal flux from an optimized coupled, unpoisoned "slow" moderator on a 5 $MW$ beam power target is equivalent to that of ILL (conclusion of the SNQ project confirmed within a factor of two by other studies). Furthermore the cold neutron flux on a spallation source compares to reactors a factor of two more favourably than the thermal one because the cold moderator can be placed closer to the core than on a reactor.

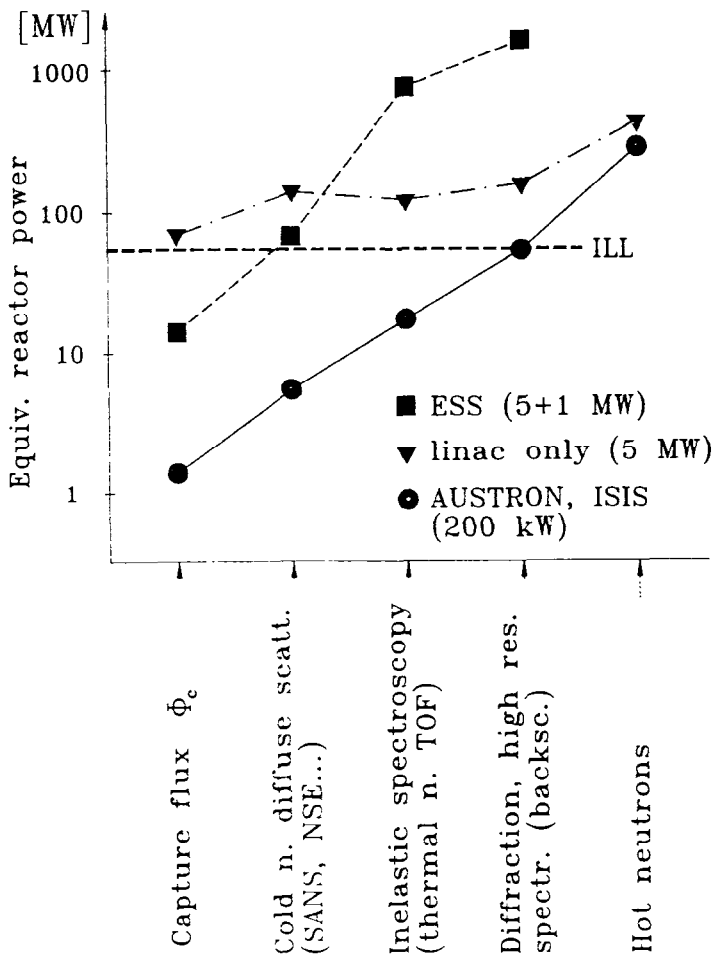


**Fig. 1.** Comparison of neutron efficiencies (typical data collection rates) in various types of instrument applications on various neutron sources.

b) The time averaged flux of a decoupled, poisonded "fast" moderator (actually most frequently used on current spallation sources) is about 10 times smaller than that of the "slow" moderator of point a).

The basic point in a comparison of the data collection rates $I$ on reactors and various types of moderators on spallation sources is to evaluate the effectively utilized fraction of the total time averaged flux $\bar{\Phi}$. Thus in scattering experiments

$$I \propto \bar{\Phi}\delta\lambda \quad (1)$$

where $\delta\lambda$ is the wavelength band usefully contributing in a given experiment. On a reactor source $\delta\lambda$ is determined by the resolution required while on a pulsed source it is most often defined by the frame overlap conditions, i.e. by the requirement to stop the fastest neutrons from catching up with the slowest ones from a previous pulse. For example at a pulse rate of *50 Hz* and a *20 m* moderator–detector distance the maximum wavelength band is *4 Å* . Thus in a powder diffraction experiment effectively using the *1 - 3 Å* wavelength band with 0.5% required resolution the wavelength band gain on PS source compared to a reactor amounts to a factor of 200 at the average flux of the "fast" moderator b). In a similar diffuse scattering experiment with a wavelength resolution of 20% the same gain factor only amounts to 5, however with respect to the 10 times more intense "slow" moderator. For neutron capture work (parity violation studies, activation analysis, in beam NMR, etc.) the whole spectrum can be used, thus simply the average (cold) flux matters.

Triple axis type spectroscopy is a rather complex case. If information has only to be collected from a single wavenumber $\vec{q}$ in a single crystal, the PS source has no wavelength band benefit, and the average fluxes have to be compared. On the other hand, if the energy scans have to be performed in the whole two-dimensional $\vec{q}$ domain (say *20* × *20 q* pixels), the simultaneous data collection on a time-of-fligth (TOF) instrument can provide a gain factor of up to 400 compared to the time-averaged flux of the "fast" source. Thus, in comparing pulsed and c.w. sources concerning typical applications of triple axis spectroscopy the average slow moderator flux ("capture flux" in Fig. 1) can be taken as the worst, and 10–100 times this value as the best estimate for the pulsed source.

Fig. 1 shows the comparison of the luminosity of a number of existing and planned sources for a selection of typical applications evaluated along the lines of the examples just discussed. Clearly, the gain of PS sources becomes stronger with increasing wavelength resolutions requirements. The comparison for hot neutrons is just indicative and not considered in any detail, since in this field most applications are just not available at reactor sources. The point dashed line corresponds to the proposed "linac only" concept which is described below.

## THE BASIC CONCEPT

As shown in Fig. 1 the two first types of applications – neutron capture and diffuse scattering (such as small angle scattering and Neutron Spin Echo) studies with cold neutrons – are those in which PS sources compare less favourably to reactors. This is largely due to the fact that here the wavelength band gain factor is 1 – 5 only. Thus, the only way to go is to increase the average power. In order to maintain a reasonable sample size, optimized small angle scattering devices have to be rather long and a low repetition rate (*10 Hz* in the ESS preliminary specifications) is required in order to maintain an adequate wavelength band. The power is than limited by the energy the ring accelerators (which typically compress the about *1 msec* long injector linac pulse into *1 μsec*) can handle in a single pulse. This leads to an expected limitation of the *10 Hz* target to about *1 MW*.

On the other hand, it turns out that for small angle scattering etc. pulse lengths of even *5-10 msec* are acceptable, since they still provide a wavelength resolution of 10-20% at $\lambda > 4$ Å and a source–detector distance of *40 m* or greater. Within such a long period a linac can provide the energy required for *5 MW* average beam power on the target even at *10 Hz*. This is the starting point of the present concept: to feed a target directly by the

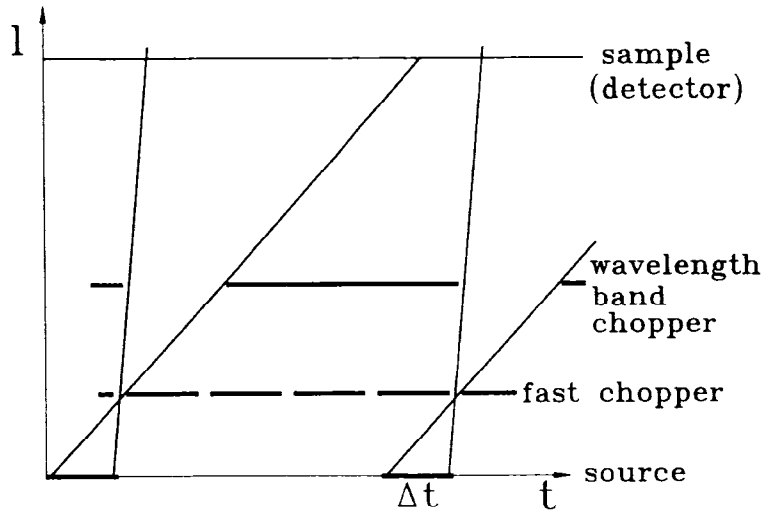


**Fig. 2.** Principle of using fast choppers for diffraction and inverted geometry inelastic scattering instruments on long pulse sources.

linac beam in order to overcome the energy bottleneck presented by the ring accelerators in the two less favourable type of applications in Fig. 1.

The second part of the proposal concerns the question of how such a long pulse source can be used for other types of experiments, i.e. where good ($\sim$ 1% or better) wavelength resolution is required. It will be shown that by the application of pulse shaping choppers the favourable comparison to reactors can be maintained over the whole spectrum of applications, while the optimized (also more expensive) PS source would provide a much superior performance in this end of the application spectrum. The new concept provides very much reactor-like characteristics, because, as it will be seen, it basically treats the source as a stationary one, which just does not have to be switched on all the time for the time-of-flight techniques proposed. Thus it can be regarded as an improved, more efficient version of the PSI c.w. spallation approach. It has, on the other hand, little in common with the SNQ concept of instrumentation, which was based on relatively short, directly utilizable pulses. This is why the present accelerator requirements are much less stringent than those of the SNQ project were.

## INSTRUMENTATION WITH LONG PULSES

In order to be more specific and to get a feeling of the orders of magnitude, in the present discussion we shall assume a state of the art $H^+$ linac with a peak beam power of *50 MW*, which can be operated at 10-15% duty cycle (very much like a possible injector in the ESS project). For SANS type experiments a pulse duration of *4 msec* will be considered with *12.5 Hz* period, i.e. *8 Å* maximal wavelength band *40 m* from the source. This provides *2.5 MW* average beam power, and with a wavelength band gain factor of at least 4 we arrive at the *200 MW* reactor equivalent flux in Fig. 1.

For the purpose of higher wavelength resolution applications let us assume 3 other pulses of a duration of *1.4 ms* each, which completes the burst rate to *50 Hz* and the total power on the target to *5 MW*. (These extra pulses will be masked by a frame overlap chopper for SANS type applications.) The instantaneous neutron flux emitted by the slow moderators during the pulses – with moderation times in the *100 μsec* range – is equivalent to the thermal flux of a *500 MW* reactor! In order to achieve the desired resolution, we shall essentially apply continuous source TOF techniques with fast choppers. This requires

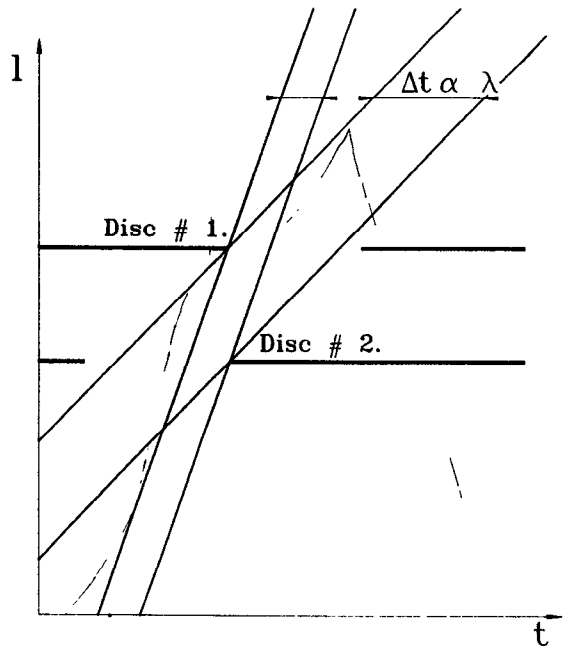


**Fig. 3.** Producing wavelength dependent neutron pulse length by a pair of chopper discs.

a source switched on long enough to provide a sufficient wavelength band in view of the finite distance between source and fast chopper, as illustrated in the TOF timetable in Fig. 2. With $l = 1.5$ $m$ source–chopper distance $\Delta t = 1.4$ $msec$ pulse length provides a wavelength band of *3.6 Å* , which will be preserved if the source–detector distance does not exceed a fair limit of *21 m*. Experts' advice differs on the technical feasibility of running choppers at *1.5 m* from the moderators, a somewhat longer distance would reduce the available wavelength band a bit, if the pulse is not made longer.

For applications such as powder diffractometry, single crystal diffractometry, inverted geometry (crystal analyser) time- of-flight inelastic spectrometry we would thus fundamentally end up with a *500 MW* equivalent reactor flux, as long as the full wavelength band allowed can be used. Compared to the TOF method crystal spectrometers occasionally offer advantages when concentrating on short scans, which will be compensated in other cases by the wider dynamic range offered by the TOF method. Nevertheless, in order to remain on the safe side, in Fig. 1 on the average only 40% of the available wavelength band is considered as useful. Note, that in the detailed analysis one often finds that the TOF method is just superior even on a c.w. source. Thus backscattering spectroscopy with a *1 meV* scan width and a resolution of *1 μeV* at a wavelength of about *6 Å* is achieved in a very efficient way by an IRIS [2] type machine at the end of an *80 m* neutron guide following a *30 μsec* pulse length fast chopper.

In direct conventional geometry, inelastic TOF spectroscopy the incoming beam is narrowly monochromatized by a sequence of fast choppers. Thus the first fast chopper does not need to be very close to the source and shorter pulses would also be sufficient. (One could even include further about *0.3 msec* long linac pulses between the *50 Hz* ones considered in order to increase the repetition rate to the *100 Hz* maximum possible for a linac.) The ideal repetition rate for TOF instruments on c.w. sources ranges from *50* to *200 Hz*, and an average of *150 Hz* has been assumed in Fig. 1 in comparison to the *50 Hz* taken for the PS sources.

## CHOPPER PERFORMANCE

The use of the TOF method for diffraction and inelastic scattering studies by applying pulse definition choppers on a long pulse spallation source is analogous to the way this could be done on a reactor source. It remains to be shown that these chopper methods are competitive to the presently more usual crystal spectroscopy, although the average flux of the here discussed source is comparable to that of ILL, so that e.g. triple axis spectrometers could be operated right away with some additional bonus from the TOF filtering of higher orders and "spurions".

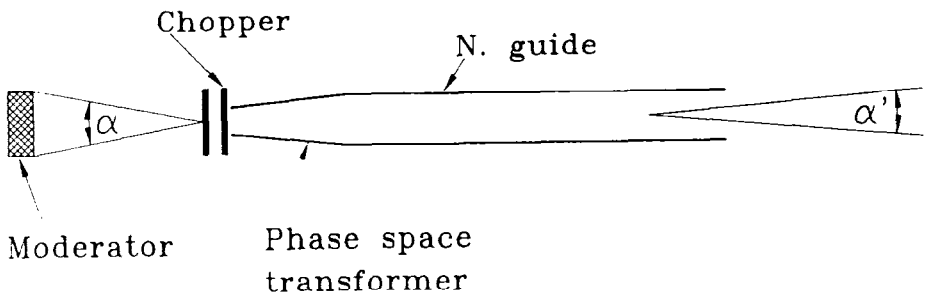


**Fig. 4.** The principle of the "eye-of-the needle" neutron beam line design, utilizing the large divergence of the beam across the narrow chopper slit.

Indeed, to start with, the resolution comparison turns out to be quite favourable for the TOF method. In diffractometry and inverted geometry inelastic spectroscopy. For example, 1% wavelength resolution at *2 Å* wavelength and *20 m* chopper–detector distance only requires a chopper pulse length of *100 μsec*, which is easily achieved by up-to-date disc choppers. Disc choppers are to be preferred here because their transmission is wavelength independent. A further advantage is that with two choppers rotating synchronously in the same direction, at the same speed and at a distance of a few *cm* from each other, one can imitate the wavelength proportional pulse width of fast PS source moderators, offering the attractive feature of constant relative resolution. Indeed, in view of Fig. 3 the FWHM pulse length becomes

$$\Delta t = max(l/v_n, d/v_c) \tag{2}$$

where $l$ is the distance between chopper discs, $d$ the beam width, and $v_n$ and $v_c$ are the neutron and the peripheral chopper velocities, respectively.

In order to achieve high resolutions – actually better ones than available with crystal instruments – some additional tricks can be used. Fermi choppers with broader slits can offer some compromise between pulse length and transmitted wavelength band. Counterrotating disc choppers at a distance of *1–2 cm* from each other give a broad band transmission and short, wavelength independent pulse lengths in the *10–20 μsec* range at *500 m/sec* peripheral velocity. This however requires a narrow slit width of *1–2 cm*, which can prove to be a serious restriction. This can be alleviated by the "eye-of-the-needle" beam line design illustrated in Fig. 4. At a narrow slit at the chopper the beam divergence $\alpha$ is considerably higher than the one useful on the sample. Than by a mirror optical "phase space transformer", e.g. widening guide section as a simple example case, the beam is transformed into a spatially wider, but less divergent beam which can feed a neutron guide. This is the inverse of the beam "compressors" such as the one used on

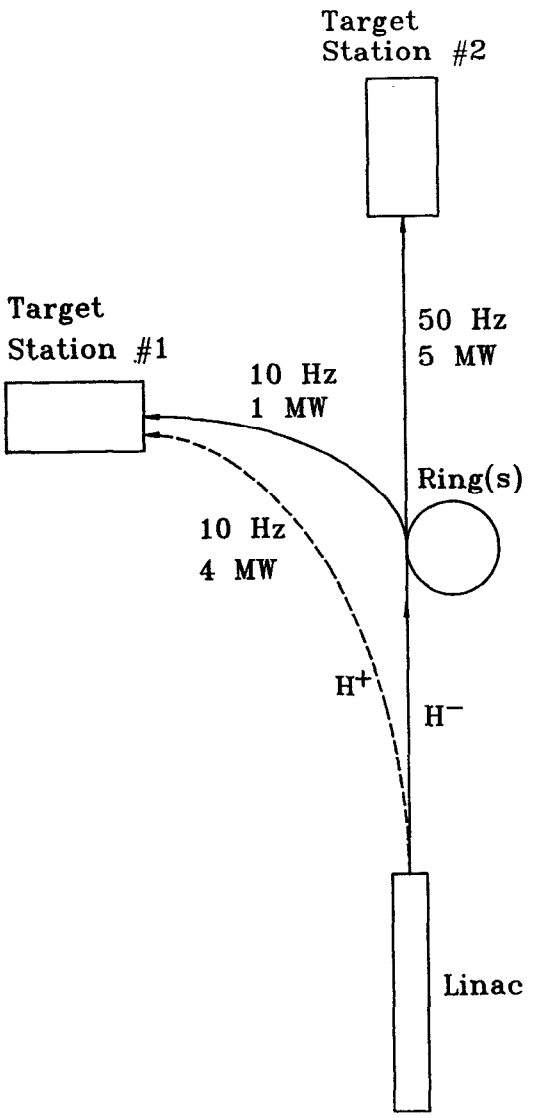


**Fig. 5.** A combination of the short and long pulse spallation approach proposed to optimize efficiency over the whole spectrum of applications.

IRIS in front of the sample. With currently routinely available supermirrors a 1:2 width compression – or decompression – can be achieved in conjunction with a neutron guide without substantial loss of neutrons [3]. The effective beam width can be further doubled by using the double slit trick for a counterrotating pair of discs, as under construction at NIST. More sophisticated optical focussing methods and improved supermirrors will also increase the flux one can concentrate on the sample downstream to the narrow slit required for the shortest pulse disc choppers.

## CONCLUSION

We have shown that a new type of spallation source set-up using a state of the art high power $H^+$ linac as the only accelerator, directly feeding the target with long pulses of *1 – 10 msec*, offers neutron source characteristics similar to reactors. An ILL equivalent performance in neutron scattering would require a *1.5 MW* total beam power on the target, half of which power concentrated into every 4th pulse in the *50 Hz* basic repetition rate. The reliability of the source should also be excellent, since the delicate problem of stripping at injection into the ring is absent. On the basis of the PSI *1 MW* source budget and various project cost estimates presented at this meeting [1], the price tag of such a source (buildings, beam guides included, instruments excluded) should not exceed $ 150–200 Mio, i.e. it is well below the construction costs of any conceivable research reactor. In the majority of the applications adding compressor or accelerator ring(s) would tremendously enhance the effective luminosity of this source, however at substantial additional costs and technical difficulties.

The most delicate point in the *5 MW* beam power, some *200 MW* reactor equivalent version considered in Fig.1 is the target design. Although the feasibility of a *5 MW* rotating target has been demonstrated in the SNQ study, and it is part of the specification of the ESS study project, concentrating half of this power in a quarter of the pulses adds to the difficulty: It would imply a *100°C* temperature jump during the longest pulses compared to *50° C* for equally distributed pulse power, unless the target used rotates at speeds comparable to that of railway wheels. (During the pulses the cooling helps little, it is only the specific heat of the target material that matters.) This leads to additional stresses, with not yet studied consequences. Nevertheless it is well possible that even at *5 MW* as in Fig. 1 this "linac only" spallation source will not cost more than an ILL type reactor, with the costs primarily determined by the target. (In contrast, e.g. a *100 mA* peak current *500 MeV* $H^+$ linac can just be considered as state of the art.) Assuming that even higher, power single pulses can be handled in the target, the present approach would allow to improve the performance of an ESS type design in small angle scattering type applications by adding long linac pulses at *10 Hz* and some *4 MW* average power to the *1 MW* delivered in form of short pulses from the ring(s) to the *10 Hz* target (Fig. 5).

In sum, the most cost efficient spallation source variant proposed here together with an adapted novel instrumentation approach offers better neutron flux conditions in virtually all applications in neutron scattering (and possibly also in the shear time averaged flux) than reactor sources of comparable costs. On the basis of current technology, optimal spallation source performance can be obtained by combining the present long pulse and the traditional short pulse approaches.

## REFERENCES


[1] The reader is referred to appropriate sections of this proceedings for specific information on the ISIS, Austron, ESS facilities/projects and on accelerator and target performance/problems.

[2] See ISIS user guide.

[3] R.E. Lechner and F. Mezei, ICANS XI Proceedings (KEK, Tsukuba, 1991) p. 919.

## List of Contributors

## Volume 1
## Instrument Workshop


Adams M A I - 73, I - 106
Aeppli G I - 60
Aksenov V L I - 124
Allen D I - 216
Allison J E I - 224
Anderson I S I - 347
Antson O I - 124
Arai M I - 260, I - 283
Asahi K I - 338
Balagurov A M I - 124
Besson J M I - 268
Böni P I - 347
Bokui T I - 260
Boothroyd A T I - 60
Boram A J I - 185
Bourke M A I - 224
Bragin S I I - 89
Brankowski J I - 89
Buffat P I - 347
Bulkin A P I - 124
Carlile C J I - 73, I - 106, I - 118
Carpenter J M I - 320
Chen J I - 208
Crawford R K I - 24, I - 144, I - 208
Crennell K I - 301, I - 308
Davis D I - 224
Doi M I - 338
Donley L I I - 36
Duppich J I - 368
Eckold G I - 232
Edwards L I - 158
Ellison A J G I - 144
Elsenhans O I - 347
Finney J L I - 1
Fitzsimmons M R I - 355
Forsyth J B I - 73
Friedli H P I - 347
Fujikawa I I - 166
Fujita M I - 260
Furusaka M I - 166
Geick R I - 97, I - 292
Goldstone J A I - 224, I - 273
Grimmer H I - 347
Hagen M I - 232, I - 314
Hamel G I - 268
Hammonds J P I - 36
Hannon A C I - 152, I - 283
Hauert R I - 347
Heenan R K I - 241
Hiismaki P I - 124
Hjelm R P I - 172
Howells W S I - 152
Hull S I - 268
Ikeda S I - 320
Jansen E I - 200
Jericha E I - 118
Jian Z Z I - 338
Johnson M W I - 32, I - 158, I - 185
Kleb R I - 36
Klotz S I - 268
Korneev D A I - 363
Krishna P S R I - 73, I - 106
Kudrjashev V A I - 124
Larson A C I - 273
Larson E I - 44
Lawson A C I - 224, I - 273
Leifer K I - 347
Loong C-K I - 36, I - 320
Loveday J S I - 268
Lysaght P I - 44, I - 52
Duppich J I - 368
Masuda Y I - 338
Mayer J I - 89
Mayers J I - 248
Mezei F I - 377
Mino M I - 260
Motokawa M I - 260
Mott E M I - 185
Müller K D I - 200
Muratov V G I - 124
Nastasi M A I - 355
Natkaniec I I - 89
Nelmes R J I - 268
Newport R J I - 152
Norris J I - 216
Nutter M I - 44, I - 52
Olivier B J I - 44, I - 52
Osawa M I - 166
Osborn R I - 60
Ostrowski G E I - 36
Otomo T I - 283
Paul D McK I - 60
Penfold J I - 347
Perring T G I - 60, I - 328
Prager M I - 106
Price D L I - 144

| | |
|---|---|
| Priesmeyer H G | I - 158 |
| Pynn R | I - 355 |
| Quinton S | I - 216 |
| Rauch H | I - 118 |
| Reinartz R | I - 200 |
| Rennie A R | I - 241 |
| Rhodes N J | I - 185 |
| Ricketts R L | I - 44 |
| Robinson R A | I - 44, I - 52, I - 273 |
| Rustichelli F | I - 158 |
| Sakai K | I - 338 |
| Sandoval J P | I - 44, I - 52 |
| Sato H | I - 338 |
| Satoh S | I - 166 |
| Schäfer W | I - 200 |
| Schmidt W | I - 97, I - 292 |
| Schuster M | I - 118 |
| Seeger P A | I - 172 |
| Shi N | I - 224 |
| Shibata K | I - 106 |
| Simkin V G | I - 124 |
| Sivia D S | I - 291 |
| Skowronek R | I - 200 |
| Smith G S | I - 355 |
| Soderholm L | I - 36 |
| Söchtig J | I - 347 |
| Soper A K | I - 152 |
| Steigenberger U | I - 232, I - 314 |
| Suzuya K | I - 166 |
| Szepesvary A | I - 200 |
| Takahashi S | I - 36 |
| Taran Yu V | I - 124 |
| Taylor A D | I - 60 |
| Thiyagarajan P | I - 208 |
| Tietze-Jaensch H | I - 97, I - 292 |
| Tiitta A | I - 124 |
| Trounov V A | I - 124 |
| Ubukata K | I - 260 |
| Volin K J | I - 144 |
| Von Dreele R B | I - 273 |
| Wagner W | I - 368 |
| Wardle A G | I - 185 |
| Watanabe N | I - 166 |
| Westerhuijs P | I - 106 |
| Will G | I - 200 |
| Wilson C C | I - 132 |
| Withers P J | I - 158 |
| Wright J S | I - 158 |
| Wilson R M | I - 268 |


## Volume 2

### Proposals for new Spallation Neutron Sources


| | |
|---|---|
| Aiginger H | P - 26 |
| Breunlich H | P - 26 |
| Brown B S | P - 13 |
| Bryant P J | P - 26 |
| Carpenter J | P - 13 |
| Cho Y | P - 13 |
| Crawford R K | P - 13 |
| Hübner K | P - 26 |
| Knox A E | P - 13 |
| Lengeler H | P - 1 |
| Pirkl W | P - 26 |
| Pynn R | P - 7 |
| Regler M | P - 26 |
| Rees G | P - 26 |
| Senichev Yu V | P - 36 |
| Schindl K | P - 26 |
| Schönauer H | P - 26 |
| Stavissky Yu Ya | P - 36 |
| Watanabe N | P - 21 |
| Wrulich A | P - 26 |


### Accelerator Workshop


| | |
|---|---|
| Bailey J | A - 57 |
| Barratt P J S | A - 109 |
| Blumberg L N | A -20 |
| Bongardt K | A - 115 |
| Brown B | A - 57 |
| Brumwell F | A - 57 |
| Carpenter J | A - 57 |
| Cho Y | A - 57 |
| Craddock M K | A - 1 |
| Crawford K | A - 57 |
| Fathizadeh M | A - 80 |
| Gardner I S K | A - 176 |
| Heinrichs H | A- 144 |
| Horan D | A - 57, A - 64 |
| Irie Y | A - 131 |
| Jason A J | A - 38, A - 49 |
| Jerng D | A - 57 |
| Johnson K F | A - 49 |
| Kleb R | A - 57 |
| Knox A | A - 57 |
| Kustom R | A - 57, A - 64, A - 159 |
| Lessner E | A - 57 |
| Macek R J | A - 25 |
| McGhee D | A - 57, A - 73, A - 80 |
| Mannix R P | A - 93 |
| Martin S A | A -153 |

Meads P F A - 153
Mills F A - 57
Moe H A - 57
Nath S A - 49
Nielsen R A - 57
Ninomiya S A - 137
Planner C W A - 4
Prior C R A - 11
Potts C A - 57
Rauchas A A - 57
Rees G H A - 168
Thompson K A - 57
Warsop C M A - 101
West N D A - 85
Wustefeld G A - 153
Yamane I A - 124
Zaplatin E A - 153
Ziegler K A - 153


## Target Station Workshop


Allen G M T - 12
Arai M T - 80, T - 90
Baker G D T - 115
Bauer G S T - 132
Beard C A T - 26
Beljakov A A T - 144
Brewton R J T - 115
Bridge A T - 115
Broome T A T - 12, T - 20, T - 128, T - 156, T - 202
Brun T O T - 26, T - 115
Cappiello M T - 115
Carpenter J M T - 1, T - 95, T - 105, T - 164, T - 206
Chiba S T - 80
Clarke-Gayther M A T - 12
Conrad H T - 61
Crawford R K T - 95
Cummings C E T - 115
Daemen L L T - 26, T - 115, T - 181, T - 202
Davis D T - 115
Dementyev A D T - 71
Elson J S T - 115
Ermilov V G T - 144
Geissmann K T - 132
Grachev M I T - 53
Grisham D T - 115
Hins A G T - 1
Hjelm R P T - 115
Hogston J R T - 156
Holding M T - 156, T - 202
Howells W S T - 156
Ishibashi K T - 44, T - 80
Iwasa H T - 164, T - 196, T - 206
Jerng D W T - 105
Kernodle A T - 115
Kiyanagi Y T - 90, T - 164, T - 172, T - 196, T - 206
Kleb R T - 95
Knox A E T - 95
Konovalov I I T - 71
Kravchuk L V T - 53
Kuzin A V T - 53
Lebedev S G T - 53
Lobashev V M T - 53
Lomidze V L T - 144
Maehata K T - 80
Maslov A A T - 71
Mateev V A T - 53
Matsufuji N T - 44, T - 80
Meigo S T - 80
Melichov V V T - 144
Merrigan M A T - 115
Miroshnichenko V G T - 53, T - 71
Mosievskaya I Y T - 71
Nakahara Y T - 44
Nakajima M T - 164, T - 172, T - 206
Nakamoto T T - 44, T - 80
Nakamura T T - 80
Nakayama Y T - 196
Numajiri N T - 80
Pitcher E J T26, T - 115, T - 181, T - 202
Planner CW T - 12
Ponomarev O V T - 53
Robinson H T - 115
Russell G J T - 26, T - 115, T - 181, T - 202
Sazanov V N T - 53
Senichev Yu V T - 53
Shabalin E P T - 144
Sidorkin S F T - 53, T - 71
Sobolevsky N M T - 53, T - 71
Spitzer H T - 132
Stavissky Yu Ya T - 53, T - 71
Takeda H T - 44, T - 80
Tretyakov I T T - 71
Trushkin V I T - 71
Wagner W T - 132
Wakuta Y T - 44, T - 80
Walker L T - 115
Watanabe N T - 90, T - 164, T - 172, T - 196, T - 206
Watanabe Y T - 80
Wilson W B T - 26
Woods R T - 115
Yoshizawa Y T - 44

## Subject Index

## Volume 1

### Instrument Workshop


| | |
|---|---|
| Calibration | I - 144, I - 208 |
| Chopper spectrometers | I - 24, I - 36, I - 44, I - 52, I - 60, I - 320, I - 328 |
| Choppers | I - 36, I - 44, I - 124, I - 377 |
| Cold neutrons | I - 1, I - 24, I - 73, I - 118 |
| Crystal analyser spectrometers | I - 24, I - 73, I - 89, I - 97, I - 106, I - 232, I - 292, I - 314 |
| Data acquisition electronics | I - 216 |
| Data analysis | I - 241, I - 283, I - 291, I - 301, I - 308 |
| Database | I - 308 |
| Data visualisation | I - 32, I - 60, I - 292, I - 301 |
| Detectors | I - 32, I - 44, I - 52, I - 144, I - 185, I - 200, I - 208 |
| Diffractometers | I - 24, I - 73, I - 124, I - 132, I - 144, I - 152, I - 166, I - 172, I - 200, I - 377 |
| Diffuse scattering | I - 132 |
| ENGIN | I - 158 |
| eVS | I - 248 |
| Fixed scattering geometry | I - 1 |
| GLAD | I - 144 |
| $^3$He filter | I - 338 |
| HET | I - 328 |
| High energy excitations | I - 1, I - 60 |
| High pressure | I - 268 |
| High resolution diffraction | I - 1, I - 24, I - 73, I - 124 |
| HIPD | I - 273 |
| HRFD | I - 124 |
| HRMECS | I - 36, I - 320 |
| Intermultiplet transitions | I - 1 |
| IRIS | I - 73, I - 106, I - 301 |
| JULIOS | I - 200 |
| Laue technique | I - 132 |
| LOQ | I - 241 |
| LRMECS | I - 36, I - 320 |
| Magnetic diffraction | I - 1, I - 73, I - 260, I - 273 |
| MARI | I - 283 |
| MAPS | I - 60 |
| Monte Carlo calculations | I - 172 |
| NERA-PR | I - 89 |
| Neutrino physics | I - 1 |
| Neutron Compton scattering | I - 248 |
| Neutron guides | I - 368 |
| Neutron storage | I - 118 |
| NPD | I - 273 |
| PHAROS | I - 44, I - 52 |
| Phase transition | I - 132, I - 232 |
| Polarisation | I - 32, I - 338, I - 347, I - 355, I - 363 |
| Powder diffraction | I - 268, I - 273 |
| PRISMA | I - 232, I - 314 |
| Pulsed magnetic fields | I - 260 |
| Reflectometers | I - 24, I - 355 |
| Resolution | I - 36, I - 89, I - 124, I - 144, I - 314, I - 320, I - 328 |

ROTAX I - 97, I - 292
SANDALS I - 308
SANS I - 166, I - 172, I - 241, I - 301, I - 377
Signal processing I - 200
Simultaneous diffraction and spectroscopy I - 73, I - 89
Single crystal measurements I - 24, I - 60, I - 132
SPEAR I - 355
SPIDA I - 152
Stress measurements I - 158, I - 224
Supermirrors I - 347, I - 368
SXD I - 132
Time resolved studies I - 1, I - 232
VESTA I - 118
WINK I - 166

## Volume 2

### Accelerator Workshop

Acceleration A - 11
Accumulator A - 25, A - 35
Amplifier A - 65
Availability A - 80
Beam-Losses A - 89, A - 125, A - 174
Buncher A - 52
Cathode-Follower A - 131
Chopper A - 104
Compressor A - 2, A - 115, A - 168
Control-System A - 93
Costs A - 148, A - 179
Database A - 93
Deflector A - 52
Diagnostics A - 105
Dual Harmonic A - 11, A - 60, A - 74
Emittance A - 43
e-p-Instability A - 30
Feed-Forward A - 112
Ferrite A - 64
FFAG A - 1, A - 153, A - 159
Funnelling A - 49
H-minus A - 35, A - 41, A - 169
H-zero A - 25
Ion-Source A - 131, A - 137
Linac A - 4, A - 20, A - 35, A - 49, A - 85, A - 115, A - 144
Magnet A - 160
Matching A - 115
NCNR A - 33
Neutron-Source A - 3, A - 20, A - 57, A - 73, A - 80, A - 115, A - 153, A - 168, A - 176
Plasma-Source A - 41
Power Supply A - 60, A - 73, A -80
PSR A - 25
Q-Values A - 105
Radio-frequency A - 64, A - 109, A - 131, A - 137, A - 154, A -160

| | |
|---|---|
| Reliability | A - 80, A - 90, A - 141, A - 180 |
| Resonant | A - 60, A - 73 |
| Room Temperature | A - 144 |
| Space Charge | A - 125 |
| Shielding | A - 179 |
| Simulation | A - 14 |
| Stability | A - 131 |
| Superconducting | A - 144, A - 154 |
| Synchrotron | A - 2, A - 5, A - 20, A - 124, A - 137 |
| Target | A - 7, A - 22 |
| Tuning | A - 111 |
| Two-Stage | A - 95 |


## Target Station Workshop


| | |
|---|---|
| Calculational Methods | T - 26, T - 44 |
| Codes | T - 26, T - 44 |
| Cooling Systems | T - 20 |
| HETC | T - 26, T - 44 |
| High Power | T - 61, T - 95, T - 105, T - 115, T - 128 |
| Hydrogen Moderators | T - 132, T - 196, T - 206 |
| Induced Activity | T - 20 |
| IPNS | T - 1, T - 95, T - 105 |
| ISIS | T - 12, T - 156, T - 202 |
| LANSCE | T - 26, T - 115 |
| Metal Hydrides | T - 206 |
| Methane Moderators | T - 144, T - 156 |
| MMF | T - 53, T - 71 |
| Moderator | T - 61, T - 132, T - 144, T - 156, T - 164, T - 172, T - 181, T - 196, T - 206 |
| Neutron Yields | T - 80,T - 90 |
| New Sources | T - 95, T - 105, T - 115,T - 128 |
| Proton Energy | T - 61, T - 164, T - 202 |
| Remote Handling | T - 20 |
| Tantalum | T - 12 |
| Targets | T - 1, T - 12, T61 |
| Tritium | T - 20 |
| Uranium | T - 1, T - 71 |

# ICANS - XII

## List of Participants


**M. ADAMS**
ISIS Facility
Rutherford Appleton Laboratory
Chilton
Oxon
OX11 0QX
UK

Tel: + 44 235 446157
Fax: + 44 235 445720

**V. AKSENOV**
Frank Laboratory of
Neutron Physics
JINR
141980 Dubna
Moscow Region
RUSSIA

Tel:
Fax: + 7 096 2165085

**M. ARAI**
Physics Department
Kobe University
1-1 Rokkodai
Nada
Kobe 657
JAPAN

Tel: + 81 78 881 1212
Fax: + 81 78 881 7593

**F. ATCHISON**
Paul Scherrer Institute
CH-5232 Villigen
PSI
SWITZERLAND

Tel: + 41 56 993256
Fax: + 41 56 992327

**I. F. BAILEY**
ISIS Facility
Rutherford Appleton Laboratory
Chilton
Oxon
OX11 0QX
UK

Tel: + 44 235 44 5881
Fax: + 44 235 44 5720

**A. BALAGUROV**
Frank Laboratory of
Neutron Physics
JINR
141980 Dubna
Moscow Region
RUSSIA

Tel:
Fax: + 7 096 21 65085

**P. J. S. B. BARRATT**
ISIS Facility
Rutherford Appleton Laboratory
Chilton
Oxon
OX11 0QX
UK

Tel: + 44 235 44 6715
Fax: + 44 235 445632

**G. BAUER**
Paul Scherrer Institute
CH-5232 Villigen,
PSI
SWITZERLAND

Tel: + 41 5699 2524
Fax: + 41 5699 3294

**S. BENNINGTON**
ISIS Facility
Rutherford Appleton Laboratory
Chilton
Oxon
OX11 0QX
UK

Tel: + 44 235 44 5193
Fax: + 44 235 44 5720

**J. R. J. BENNETT**
ISIS Facility
Rutherford Appleton Laboratory
Chilton
Oxon
OX11 0QX
UK

Tel: + 44 235 44 6379
Fax: + 44 235 44 5383

**T. D. BEYNON**
School of Physics and
Space Research
Birmingham University
Birmingham
B15 2TT
UK

Tel: + 44 21 414 4694
Fax: + 44 21 414 4725

**L. N. BLUMBERG**
National Synchrotron Light
Source
Building 725
Brookhaven National Laboratory
Upton
NY 11973
USA

Tel: + 1 516 282 4600
Fax: + 1 516 282 4745

**D. BÖHNE**
Gesellschaft für
Schwerionenforschung mbH
Planckstrasse 1
D-6100 Darmstadt
GERMANY

Tel: + 49 6151 359 411
Fax: + 49 6151 359 985

**B. BOLAND**
ISIS Facility
Rutherford Appleton Laboratory
Chilton
Oxon
OX11 0QX
UK

Tel: + 44 235 44 5679
Fax: + 44 235 44 5383

**K. BONGARDT**
KFA
D-52425 Jülich
GERMANY

Tel: + 49 2461 61 5468
Fax: + 49 2461 61 2670

**P. BÖNI**
Labor für Neutronenstreuung
ETH & PSI
CH-5232 Villigen PSI
SWITZERLAND

Tel: + 41 56 99 2518
Fax: + 41 56 98 2635

**Z. BOWDEN**
ISIS Facility
Rutherford Appleton Laboratory
Chilton
Oxon
OX11 0QX
UK

Tel: + 44 235 44 5683
Fax: + 44 235 44 5383

**B. S. BROWN**
IPNS Division Building 360
Argonne National Laboratory
9700 South Cass Avenue
Argonne
IL 60439
USA

Tel: + 1 708 252 4999
Fax: + 1 708 252 4163

**T. A. BROOME**
ISIS Facility
Rutherford Appleton Laboratory
Chilton
Oxon
OX11 0QX
UK

Tel: + 44 235 44 6255
Fax: + 44 235 44 5632

**T. O. BRUN**
Manuel Lujan Jr
Neutron Scattering Centre
LANSCE ms h805
Los Alamos
New Mexico 87545
USA

Tel: + 1 505 667 8841
Fax: + 1 505 665 2676

**D. G. BUCKNALL**
ISIS Facility
Rutherford Appleton Laboratory
Chilton
Oxon
OX11 0QX
UK

Tel: + 44 235 44 5871
Fax: + 44 235 44 5383

**C. J. CARLILE**
ISIS Facility
Rutherford Appleton Laboratory
Chilton
Oxon
OX11 0QX
UK

Tel: + 44 235 44 5684
Fax: + 44 235 44 5383

**J. M. CARPENTER**
IPNS
Argonne National Laboratory
9700 South Cass Avenue
Argonne
Illinois 60439
USA

Tel: + 1 708 972 5519
Fax: + 1 708 972 4163

**Y. CHO**
Advanced Photon Source
Argonne National Laboratory
9700 South Cass Avenue
Argonne
Illinois 60439
USA

Tel: + 1 708 252 6616
Fax: + 1708 252 4599

**M. A. CLARKE-GAYTHER**
ISIS Facility
Rutherford Appleton Laboratory
Chilton
Oxon
OX11 0QX
UK

Tel: + 44 235 44 6133
Fax: + 44 235 44 5642

**K. N. CLAUSEN**
Solid State Physics Department
Risø National Laboratory
DK 4000 Roskilde
DENMARK

Tel: + 45 4677 4704
Fax: + 45 42 370115

**R. L. S. COLEMAN**
ISIS Facility
Rutherford Appleton Laboratory
Chilton
Oxon
OX11 0QX
UK

Tel: + 44 235 44 6339
Fax: + 44 235 44 5642

**H. CONRAD**
Institut für Festkörperforschung
Forschungszentrum Jülich
Postfach 1913
D-52425 Jülich
GERMANY

Tel: + 49 2461 612610
Fax: + 49 2461 615327

**M. K. CRADDOCK**
Triumf
4004 Westbrook Mall
Vancouver BC
V6T 2A3
CANADA

Tel: + 1 604 222 1047
Fax: + 1 604 222 1074

**R. K. CRAWFORD**
IPNS
Argonne National Laboratory
9700 South Cass Avenue
Argonne
Illinois 60439
USA

Tel: + 1 708 972 5519
Fax: + 1 708 972 4163

**K. CRENNELL**
ISIS Facility
Rutherford Appleton Laboratory
Chilton
Oxon
OX11 0QX
UK

**L. De GRAAF**
IRI
Mekelweg 15
2629 JM Delft
The NETHERLANDS

Tel: + 31 15 78 55 45
Fax: + 31 15 78 64 22

**C. J. DENSHAM**
ISIS Facility
Rutherford Appleton Laboratory
Chilton
Oxon
OX11 0QX
UK

Tel: + 44 235 44 6273
Fax: + 44 235 44 5642

**J. DUPPICH**
Paul Scherrer Institute
CH-5232 Villigen,
PSI
SWITZERLAND

Tel: + 41 5699 3320
Fax: + 41 5699 3294

**R. S. ECCLESTON**
ISIS Facility
Rutherford Appleton Laboratory
Chilton
Oxon
OX11 0QX
UK

Tel: + 44 235 44 6437
Fax: + 44 235 44 5383

**Y. ENDOH**
Faculty of Science
Tohoko University
Aoba, Aramaki
Aoba-ku
Sendai-shi 980
JAPAN

Tel: + 81 22 222 1800 ext 3306
Fax: + 81 22 225 1891

**D. FILGES**
Forschungszentrum Jülich GmbH
Institut für Kernphysik
Postfach 19 13
D-52425 Jülich
GERMANY

Tel: + 49 2451 61 5232
Fax: + 49 2461 61 3930

**J. L. FINNEY**
Department of Physics and
Astronomy
University College London
Gower Street
London
WC1E 6BT
UK

Tel: + 44 71 380 7850
Fax: + 44 71 380 7145

**T. FLEMMING**
Reuter Stokes Inc.
Edison Park
8499 Darrow Road
Twinsburg
OH 44087
USA

Tel: + 1 216 425 3755
Fax: + 1 216 425 4045

**M. FUJITA**
Physics Faculty of Science
Kobe University
Rokkodai
Nada
Kobe 657
JAPAN

Tel: + 81 78 881 1212 ext 4376
Fax: + 81 78 881 7593

**T. FUKUNAGA**
School of Engineering
Nagoya University
Furo-cho, Chikusa-ku
Nagoya-shi 464
JAPAN

Tel: + 81 52 781 5111
Fax: + 81 52 782 2129

**M. FURUSAKA**
BSF
National Laboratory for High
Energy Physics
1-1, Oho
Tsukuba-shi 305
JAPAN

Tel: + 81 298 64 1171
Fax: + 81 298 64 3202

**I. S. K. GARDNER**
ISIS Facility
Rutherford Appleton Laboratory
Chilton
Oxon
OX11 0QX
UK

Tel: + 44 235 44 6109
Fax: + 44 235 44 5383

**R. GEICK**
Physikalisches Institut
Am Hubland
D-8700 Würzburg
GERMANY

Tel: + 49 931 8885898
Fax: + 49 931 8885142

**J. A. GOLDSTONE**
Lansce MS H805
Los Alamos National Laboratory
Los Alamos
NM 87545
USA

Tel: + 1 505 667 3629
Fax: + 1 505 655 2676

**M. E. HAGEN**
ISIS Facility
Rutherford Appleton Laboratory
Chilton
Oxon
OX11 0QX
UK

Tel: + 44 235 44 5805
Fax: + 44 235 44 5383

**A. C. HANNON**
ISIS Facility
Rutherford Appleton Laboratory
Chilton
Oxon
OX11 0QX
UK

Tel: + 44 235 44 5358
Fax: + 44 235 44 5383

**M. R. HAROLD**
ISIS Facility
Rutherford Appleton Laboratory
Chilton
Oxon
OX11 0QX
UK

Tel: + 44 235 44 5371
Fax: + 44 235 44 5632

**R. K. HEENAN**
ISIS Facility
Rutherford Appleton Laboratory
Chilton
Oxon
OX11 0QX
UK

Tel: + 44 235 44 6744
Fax: + 44 235 44 5720

**H. HEINRICHS**
University of Wuppertal
Gausstr 20
D-5600 Wuppertal 1
GERMANY

Tel: + 49 202 4392753
Fax: + 49 202 4392811

**M. HOLDING**
ISIS Facility
Rutherford Appleton Laboratory
Chilton
Oxon
OX11 0QX
UK

Tel: + 44 235 44 6692
Fax: + 44 235 44 5720

**W. S. HOWELLS**
ISIS Facility
Rutherford Appleton Laboratory
Chilton
Oxon
OX11 0QX
UK

Tel: + 44 235 44 5680
Fax: + 44 235 44 5383

**H. IKEDA**
BSF National Laboratory for
High Energy Physics
(KEK)
Oho 1-1
Tsukuba 305
JAPAN

Tel: + 81 298 64 5613
Fax: + 81 298 64 3202

**Y. IRIE**
BSF National Laboratory for
High Energy Physics
(KEK)
Oho 1-1
Tsukuba 305
JAPAN

Tel: + 81 298 64 5607
Fax: + 81 298 64 3202

**K. ISHIBASHI**
Dept. for Nuclear Engineering
Kyushu University
6-10-1 Hakozaki
Higashi-ku
Fukuoka 812
JAPAN

Tel: + 81 92 641 1101 ext 5822
Fax: + 81 92 641 7098

**A. JASON**
Los Alamos National Laboratory
Los Alamos
NM 87544
USA

Tel: + 1 505 667 2842
Fax: + 1 505 665 2904

**E. JERICHA**
Atom Institut
Schuttelstrasse 115
A-10020 Wien
AUSTRIA

Tel: + 43 1 21701 271
Fax: + 43 1 2189220

**M. W. JOHNSON**
ISIS Facility
Rutherford Appleton Laboratory
Chilton
Oxon
OX11 0QX
UK

Tel: + 44 235 44 5418
Fax: + 44 235 44 5383

**H. J. JONES**
ISIS Facility
Rutherford Appleton Laboratory
Chilton
Oxon
OX11 0QX
UK

Tel: + 44 235 44 5182
Fax: + 44 235 44 5720

**Y. KIYANAGI**
Hokkaido University
Kita 13
Nishi 8
Sapporo 060
JAPAN

Tel: + 81 11 716 2111 ext 6651
Fax: + 81 11 717 4745

**S. KLOTZ**
Physique des Milieux Condensés
CNRS, URA 782
Paris

**K. J. KNOWLES**
ISIS Facility
Rutherford Appleton Laboratory
Chilton
Oxon
OX11 0QX
UK

Tel: + 44 235 44 5305
Fax: + 44 235 44 5383

**R. L. KUSTOM**
Argonne National Laboratory
9700 South Cass Avenue
Building 371T
Argonne
IL 60439
USA

Tel: + 1 708 252 6533
Fax: + 1 708 252 5291

**H. LENGELER**
CERN
CH-1211
Geneva 23
SWITZERLAND

Tel: + 41 22 767 5862
Fax: + 41 22 767 8666

**C. LOONG**
IPNS/360
Argonne National Laboratory
9700 South Cass Avenue
Argonne
IL 60439
USA

Tel: + 1 708 252 5596
Fax: + 1 708 252 4163

**R. J. MACEK**
MP Division
Los Alamos Laboratory
Mail Stop H848
Los Alamos
NM 87545
USA

Tel: + 1 505 667 5670
Fax: + 1 505 665 1712

**D. MARTIN**
ISIS Facility
Rutherford Appleton Laboratory
Chilton
Oxon
OX11 0QX
UK

Tel: + 44 235 44 5718
Fax: + 44 235 44 5720

**Y. MASUDA**
c/o Dr J D Bowman
MP-9 LANL
Los Alamos
NM 87545
USA

Tel: + 1 505 667 5670
Fax: + 1 505 665 1712

**J. MAYERS**
ISIS Facility
Rutherford Appleton Laboratory
Chilton
Oxon
OX11 0QX
UK

Tel: + 44 235 44 5882
Fax: + 44 235 44 5383

**D. McGEE**
Accelerator Systems Division
Argonne National Laboratory
9700 South Cass Avenue
Argonne
IL 60439-4814
USA

Tel: + 1 708 262 2000
Fax: + 1 708 252 9480

**F. MEZEI**
HMI/BENSC
D-14109
Berlin 39
Glienicker Str. 100
GERMANY

Tel: + 49 30 80622322
Fax: + 49 30 80622523

**S. P. MØLLER**
Institute for Synchrotron
Radiation (ISA)
Aarhus University
DK-8000
Aarthus C
DENMARK

Tel: + 45 86 12 8899
Fax: + 45 86 12 0440

**M. MOTOKAWA**
Faculty of Science
Kobe University
Rokkodai
Nada
Koba 657
JAPAN

Tel: + 81 78 881 1212 ext 4379
Fax: + 81 78 881 7593

**E. M. MOTT**
ISIS Facility
Rutherford Appleton Laboratory
Chilton
Oxon
OX11 0QX
UK

Tel: + 44 235 44 5708
Fax: + 44 235 44 5720

**I. NATKANIEC**
Frank Laboratory of
Neutron Physics
JINR
141980 Dubna
Moscow Region
RUSSIA

Fax: + 7 096 21 65085

**R.D. NEEF**
Forschungszentrum Jülich GmbH
Institut für Kernphysik
Postfach 19 13
D-52425 Jülich
GERMANY

Tel: + 49 2461 61 5232
Fax: + 49 2461 61 3930

**S. NINOMIYA**
PS Div. Accelerator Department
KEK National Laboratory for
High Energy Physics
1-1 Oho Tsukuba-city
Ibaraki 3205
JAPAN

Tel: + 81 298 64 1171
Fax: + 81 298 64 3182

**J. NORRIS**
ISIS Facility
Rutherford Appleton Laboratory
Chilton
Oxon
OX11 0QX
UK

Tel: + 44 235 44 5807
Fax: + 44 235 44 5720

**J. PENFOLD**
ISIS Facility
Rutherford Appleton Laboratory
Chilton
Oxon
OX11 0QX
UK

Tel: + 44 235 44 5681
Fax: + 44 235 44 5383

**T. G.PERRING**
ISIS Facility
Rutherford Appleton Laboratory
Chilton
Oxon
OX11 0QX
UK

Tel: + 44 235 44 5428
Fax: + 44 235 44 5383

**C. W. PLANNER**
ISIS Facility
Rutherford Appleton Laboratory
Chilton
Oxon
OX11 0QX
UK

Tel: + 44 235 44 5434
Fax: + 44 235 44 5632

**C. R. PRIOR**
ISIS Facility
Rutherford Appleton Laboratory
Chilton
Oxon
OX11 0QX
UK

Tel: + 44 235 44 5262
Fax: + 44 235 44 5632

**R. PYNN**
Los Alamos National Laboratory
P O Box 1663
MS H805
Los Alamos
NM 87545
USA

Tel: + 1 505 665 1583
Fax: + 1 505 665 2676

**S. P. H. QUINTON**
ISIS Facility
Rutherford Appleton Laboratory
Chilton
Oxon
OX11 0QX
UK

Tel: + 44 235 44 5534
Fax: + 44 235 44 5383

**G. H. REES**
ISIS Facility
Rutherford Appleton Laboratory
Chilton
Oxon
OX11 0QX
UK

Tel: + 44 235 44 5595
Fax: + 44 235 44 5632

**M. REGLER**
c/o Institut für
Hochenergiephysik der
Österreichischen Akademie
der Wissenschaften
Nikolsdorfer Gasse 18
A 1050 Wien
AUSTRIA

Tel: + 43 222 55 73 28
Fax: + 43 222 55 75 89

**N. J. RHODES**
ISIS Facility
Rutherford Appleton Laboratory
Chilton
Oxon
OX11 0QX
UK

Tel: + 44 235 44 5491
Fax: + 44 235 44 5720

**R. ROBINSON**
LANSCE MS-H805
Los Alamos National Laboratory
Los Alamos
NM 87545
USA

Tel: + 1 505 667 3626
Fax: + 1 505 665 2676

**G. J. RUSSELL**
LANSCE MS-H505
Los Alamos National Laboratory
Los Alamos
NM 87545
USA

Fax: + 1 505 665 2676

**H. L. RUTKOWSKI**
Lawrence Berkely Laboratory
50-149
1 Cyclotron Road
Berkeley
CA 94720
USA

Tel: + 1 510 486 7209
Fax: + 1 510 486 6003

**W. SCHÄFER**
Forschungszentrum Jülich
Postfach 1913
D-52425 Jülich
GERMANY

Tel: + 49 2461 616024
Fax: + 49 2461 613841

**H. SCHÖNAUER**
PS Division
CERN
CH 1211
Geneve 23
SWITZERLAND

Tel: + 41 22 767 40 78
Fax: + 41 22 767 8200

**S. SCHRIBER**
Los Alamos National Laboratory
P O Box 1663
M S H811
Los Alamos
NM 87545
USA

**W. SCHMIDT**
ISIS Facility
Rutherford Appleton Laboratory
Chilton
Oxon
OX11 0QX
UK

Tel: + 44 235 44 5352
Fax: + 44 235 44 5383

**M. SCHUSTER**
Atominstitut der
Österreichischen Universitäten
Schottelstr 115
A-1020 Wien
AUSTRIA

Tel: + 43 1 557328 36
Fax: + 43 1 2189220

**P. A. SEEGER**
MS/HB05
Los Alamos National Laboratory
P O Box 1663
M S H811
Los Alamos
NM 87545
USA

Tel: + 1 505 662 7163
Fax: + 1 505 665 2676

**E. SHABALIN**
Frank Laboratory of
Neutron Physics
JINR
141980 Dubna
Moscow Region
RUSSIA

Fax: + 7 096 21 65085

**R. SIDLOW**
ISIS Facility
Rutherford Appleton Laboratory
Chilton
Oxon
OX11 0QX
UK

Tel: + 44 235 44 5219
Fax: + 44 235 44 5632

**D. S. SIVIA**
ISIS Facility
Rutherford Appleton Laboratory
Chilton
Oxon
OX11 0QX
UK

Tel: + 44 235 44 5685
Fax: + 44 235 44 5383

**A. K. SOPER**
ISIS Facility
Rutherford Appleton Laboratory
Chilton
Oxon
OX11 0QX
UK

Tel: + 44 235 44 5543
Fax: + 44 235 44 5383

**T. SPRINGER**
Institut für Festkörperforschung
Forschungszentrum Jülich GmbH
Postfach 1913
D-52425 Jülich
GERMANY

Tel: + 49 2461 61 4693
Fax: + 49 2461 61 2610

**Y. STAVISSKY**
Institute for Nuclear Research
60th October Anniversary
Prospect 7a
117312 Moscow
RUSSIA

Tel: + 7 95 334 0191
Fax: + 7 95 135 2268

**H. STECHEMESSER**
Zentralabteilung Technologie
Forschungszentrum Jülich
Postfach 1913
D - 52425 Jülich
GERMANY

Tel: + 49 2461 616740
Fax: + 49 2461 616816

**U. STEIGENBERGER**
ISIS Facility
Rutherford Appleton Laboratory
Chilton
Oxon
OX11 0QX
UK

Tel: + 44 235 44 5145
Fax: + 44 235 44 5383

**A. D. TAYLOR**
ISIS Facility
Rutherford Appleton Laboratory
Chilton
Oxon
OX11 0QX
UK

Tel: + 44 235 44 6681
Fax: + 44 235 44 5383

**H. TIETZE-JAENSCH**
ISIS Facility
Rutherford Appleton Laboratory
Chilton
Oxon
OX11 0QX
UK

Tel: + 44 235 44 5685
Fax: + 44 235 44 5383

**J. TOMKINSON**
ISIS Facility
Rutherford Appleton Laboratory
Chilton
Oxon
OX11 0QX
UK

Tel: + 44 235 44 6686
Fax: + 44 235 44 5383

**W. WAGNER**
Paul Scherrer Institute
CH-5232 Villigen
PSI
SWITZERLAND

Tel: + 41 56 992517
Fax: + 41 56 98 2635

**C. M. WORSOP**
ISIS Facility
Rutherford Appleton Laboratory
Chilton
Oxon
OX11 0QX
UK

Tel: + 44 235 44 6374
Fax: + 44 235 44 5632

**N. WATANABE**
National Laboratory for
High Energy Physics
1-1 Oho
Tsukuba
Ibaraki 305
JAPAN

Tel: + 81 298 64 5601
Fax + 81 298 64 3202

**J. R. P. WEBSTER**
ISIS Facility
Rutherford Appleton Laboratory
Chilton
Oxon
OX11 0QX
UK

Tel: + 44 235 44 5193
Fax: + 44 235 44 5383

**N. D. WEST**
ISIS Facility
Rutherford Appleton Laboratory
Chilton
Oxon
OX11 0QX
UK

Tel: + 44 235 44 6122
Fax: + 44 235 44 5632

**P. R. WILLIAMS**
Director
Rutherford Appleton Laboratory
Chilton
Oxon
OX11 0QX
UK

Tel: + 44 235 44 5533
Fax: + 44 235 44 5632

**C. C. WILSON**
ISIS Facility
Rutherford Appleton Laboratory
Chilton
Oxon
OX11 0QX
UK

Tel: + 44 235 44 5137
Fax: + 44 235 44 5383

**I. YAMANE**
PS Division
National Laboratory for
High Energy Physics
1-1 Oho
Tsukuba
Ibaraki 305
JAPAN

Tel: + 81 298 64 5268
Fax: + 81 298 64 3182

**V. YOUNG**
Reuter Stokes Inc.
Edison Park
8499 Darrow Road
Twinsburg
OH 44087
USA

Tel: + 1 216 425 3755
Fax: + 1 216 425 4045

**E. ZAPLATINE**
Hahn-Meitner Institut
Glienicker Str. 100
D-14109 Berlin 33
GERMANY

Tel: + 49 30 8062 2293
Fax: + 49 30 8062 2293

**K. ZIEGLER**
Hahn-Meitner Institut
Berlin GmBH
Glienicker Str. 100
D-14109 Berlin 39
Germany

Tel: + 49 30 8062 2498
Fax: + 49 30 8062 2293